

---

# **Solution behaviour of dissociative direct dyes in the presence of surfactants**

---

## **Dissertation**

zur Erlangung des Grades eines

Doktors der Naturwissenschaften

- Dr. rer. nat. –

von

**Wenke Müller**

geboren am 13.09.1996

in Annaberg-Buchholz

Paderborn

September 2023



Die vorliegende Arbeit wurde im Zeitraum von November 2020 bis September 2023 im Fachbereich für Physikalische Chemie der Fakultät für Naturwissenschaften an der Universität Paderborn unter der Betreuung von Prof. Dr. Klaus Huber angefertigt.

Prüfungsausschuss:

Prof. Dr. Klaus Huber	Erstgutachter
Prof. Dr. Claudia Schmidt	Zweitgutachter
Dr. Hans Egold	
Prof. Dr. Sabine Fechner	Vorsitz

Tag der Einreichung: 06.09.2023

Tag der mündlichen Prüfung: 08.11.2023



Hiermit erkläre ich, die vorliegende Dissertationsschrift selbstständig verfasst zu haben. Die dazu genutzte Literatur, zur Hilfeleistung herangezogene Institutionen sowie Beiträge anderer Personen zu dieser Arbeit werden im Rahmen der Dissertationsschrift vollständig angegeben bzw. kenntlich gemacht.

Grenoble, September 2023

Wenke Müller



## Danksagung

An erster Stelle möchte mich herzlich bei meinem Doktorvater Herrn Prof. Dr. Klaus Huber für das in mich gesetzte Vertrauen und seine Unterstützung während der Doktorarbeit bedanken. Die zahlreichen interessanten fachlichen Diskussionen haben wesentlich zum Erfolg der Arbeit beigetragen.

Weiterhin gilt mein großer Dank Dr. Ralf Schweins, der häufig mein erster Ansprechpartner war. Auch ihm möchte ich für die tatkräftige Unterstützung, die Teilnahme an vielen Messzeiten und seine guten Ratschläge danken.

Meinen großen Dank möchte ich auch an Dr. Bernd Nöcker richten, der nicht nur sehr konstruktiv an der Betreuung der Doktorarbeit mitgewirkt, sondern mir auch einen Einblick in die Forschungsarbeit in der Industrie ermöglicht hat.

Allen drei Betreuern danke ich sehr für die Freiheiten, die ich während der Doktorarbeit genießen konnte sowie für die enorme Unterstützung, konstruktiven Diskussionen, schnelle Reaktion auf meine Fragen und regelmäßigen Treffen, die mir viele Projekte sehr erleichtert haben.

Bei Frau Prof. Dr. Claudia Schmidt möchte ich mich herzlich für die Übernahme des Zweitgutachtens bedanken.

In the following I would like to sincerely thank everyone who helped me with my PhD project and otherwise throughout the last three years.

Mein Dank gilt Dr. Leonardo Chiappisi, der mir nicht nur viele gute Ratschläge zur Datenauswertung gegeben hat, sondern auch häufig bei Fragen zu bestehendem oder neuem Equipment mit Rat und Tat zur Seite stand. In the same course I would like to thank Dr. Martina Sandroni who does a great job keeping the laboratories organized and was often the first person to ask when new setups were needed. Un grand merci aussi à Sandrine Verdon qui a presque toujours pu m'aider lorsqu'il manquait quelque chose dans les laboratoires.

Furthermore, I would like to thank Dr. Sylvain Prévost, who helped me a lot with data reduction, supported me during neutron experiments and gave valuable advice for data evaluation and the design of experiments. A big thanks also to Dr. Lionel Porcar for his valuable advice on data reduction and data evaluation.

Ich möchte mich weiterhin herzlich bei Dr. Joachim Kohlbrecher für die Bereitstellung interner Messzeit am SANS-I Instrument (PSI) sowie für das in mich gesetzte Vertrauen für die Bedienung

des Instruments und für die Ratschläge zur Datenreduktion bedanken. I would furthermore like to thank Dr. Sarah Rogers for supervising our experiment at the Zoom instrument (ISIS) and helping us with data collection and reduction. In the same course, I would like to thank Dr. Lauren Matthews for guiding our experiment at the ID02 beamline (ESRF) and for always being ready to answer questions. In addition to that, I would like to thank Dr. Theyencheri Narayanan for his valuable advice concerning the design of the experiment and the beamtime proposal.

I would like to sincerely thank my colleagues and dear friends Larissa Araujo and Mohit Agarwal, who did not only make the PhD-experience more enjoyable, but also actively helped me in the laboratory and with my experiments. Larissa, I thank you for travelling all the way to Harwell Campus to participate in the beamtime at ISIS and Mohit, you for travelling to Villigen to participate in the beamtime at PSI.

Mein großer Dank gilt weiterhin der Arbeitsgruppe von Professor Huber in Paderborn. Fabian Kollmann und Leon Koch, euch danke ich für die Hilfe und guten Ratschläge während meiner Arbeit in Paderborn sowie für eure Teilnahme und tatkräftige Unterstützung während der Messzeit an der ID02 beamline am ESRF. A big thanks also to Kate Doostdar, who introduced me to the project and was always available to answer questions. Furthermore I would like to thank Dr. Sanjib Saha for the helpful discussions and valuable advice on data analysis. Ich danke der ganzen Gruppe einschließlich Benjamin Hämisch und Anne Büngeler für das positive Ambiente und die interessanten Diskussionen während der Gruppentreffen.

Weiterhin möchte ich Gisela Jünnemann-Held für ihre Hilfe im Labor sowie für das Übernehmen der Viskositätsmessungen danken. Susanne Keuker-Baumann, Rita Egert-Tiesbohenkamp und Katrin Bandzius, euch danke ich für eure Hilfe in allen organisatorischen Angelegenheiten.

Mein besonderer Dank gilt Dr. Hans Egold, welcher nicht nur einen Großteil der NMR-spektroskopischen Messungen übernommen hat, sondern auch aktiv sehr wichtige Ratschläge in der Datendiskussion gegeben hat.

I would like to sincerely thank the R&D team at KAO Germany GmbH for their support during my time at KAO. Dr. Steven Breakspear, Anna Neu, Fariba Ghiasi, Dr. Ines Rabelo de Moraes, Dr. Clarissa Lipinski, Stephani Ilham, Maria Nguyen, Qi Uellner and Niu Jian, thank you for all of your help, for answering my questions and for making the experience at KAO very enjoyable! Anna, ich möchte besonders dir für alle Vorbereitungen und zusätzlichen Experimente sowie für deine Teilnahme an unserer Messzeit an der ID02 beamline am ESRF danken. Weiterhin vielen Dank



an Dr. Tobias Miller für die patentrechtliche Prüfung der Arbeiten sowie interessanten fachlichen Diskussionen.

I would like to thank my interns, Weronika Sroka and Carlo Giorgetti, for their help in advancing the project as well as their many interesting questions.

Furthermore, I would like to thank all my collaborators who I have not mentioned yet. Dr. Jia-Fei Poon, thank you for putting a lot of time and effort into the synthesis of the deuterated nonionic surfactants, which we used during our neutron beamtime. Dr. Yvonne Hannappel, vielen Dank für die cryo-TEM Aufnahmen, die die Existenz von Wurmmizellen in unseren Proben bestätigt haben. Dr. Adrien Favier et Dr. Alicia Vallet, merci de mesurer les spectres RMN de mes échantillons.

Weiterhin möchte ich mich bei Dr. Nico Carl bedanken, der mich im Rahmen mehrerer Praktika für Neutronenstreuung begeistern konnte und mir viele hilfreiche Ratschläge gegeben hat.

I am thanking the ILL and the European Union for funding my PhD-project in the framework of the European Union's Horizon 2020 research and innovation programme under the SINE2020 project, grant agreement No 654000. I am thanking the organizers of the InnovaXN programme for the possibility to participate in many interesting workshops and events. I am furthermore thanking the Partnership for Soft Condensed Matter for providing an excellent laboratory infrastructure and many measurement instruments.

Finally, I would like to thank my friends and colleagues, who supported me during the last three years and rendered the PhD-experience more enjoyable. Thank you for the pleasant atmosphere at ILL and all the nice activities after work!

Natürlich möchte ich auch meiner Familie für all die Unterstützung der letzten Jahre herzlich danken.



## Kurzfassung

Die vorliegende Arbeit beschäftigt sich mit der Selbstorganisation der drei kommerziellen Haarfarbstoffe Yellow, Blue und Red und deren Interaktion mit Tensiden.

UV/vis- und NMR-Spektroskopie sowie Kleinwinkelneutronenstreuung (SANS) zeigen, dass Yellow nicht aggregiert, Blue gut definierte Dimere formt und Red zu größeren Strukturen aggregiert. Die Ergebnisse beziehen sich auf die Untersuchung der Selbstorganisation in einem  $\text{NaHCO}_3/\text{Na}_2\text{CO}_3$  Puffer mit  $\text{pH} = 10.5$  bei einer Temperatur von  $25\text{ }^\circ\text{C}$ .

Lösungen der Farbstoffe und des kationischen Tensids Dodecyltrimethylammoniumbromid (DTAB) phasenseparieren unter den gleichen Bedingungen oberhalb eines gegebenen Farbstoff:DTAB Verhältnisses. Dieses Verhältnis nimmt von Yellow:DTAB über Blue:DTAB zu Red:DTAB ab. SANS zeigt, dass Farbstoff-DTAB Mizellen in der Einphasenregion bei Annäherung an die Zweiphasenregion wachsen. Eine Kombination aus Kontrastangleichung in SANS und NMR-Spektroskopie an Blue-DTAB Lösungen zeigt, dass Blue sich in der Nähe der DTAB Kopfgruppe befindet. Die erfolgreiche Lokalisierung von Blue in DTAB Mizellen demonstriert die Realisierbarkeit der Kontrastangleichung in SANS für die Lokalisierung kleiner organischer Moleküle in Tensidmizellen.

Abhängig vom pD-Wert der Lösung liegt der Säurefarbstoff Blue entweder in seiner neutralen, seiner ein-fach oder seiner zwei-fach deprotonierten Form vor. Das ermöglicht die Erforschung seiner Solubilisierung in nicht pD-responsiven Mizellen des nichtionischen Tensids  $\text{C}_{12}\text{E}_5$  als Funktion der Polarität von Blue. Sterische Effekte müssen dabei nicht berücksichtigt werden. Bei  $\text{pD} = 2$  befindet sich Blue bevorzugt im Inneren der  $\text{C}_{12}\text{E}_5$  Mizellen, bei  $\text{pD} = 9$  in der Palisadenregion und bei  $\text{pD} = 13$  in der Nähe der Grenzfläche zwischen Mizelle und Lösungsmittel.

## Abstract

The self-assembly of the three commercial hair dyes Yellow, Blue and Red and their co-assembly with surfactant is studied.

UV/vis- and NMR-spectroscopy and small-angle neutron scattering (SANS) reveal, that in a  $\text{NaHCO}_3/\text{Na}_2\text{CO}_3$  buffer with  $\text{pH} = 10.5$  ( $25\text{ }^\circ\text{C}$ ) Yellow does not self-assemble, Blue forms well-defined dimers and Red self-assembles into larger aggregates.

Under the same conditions, solutions of dye and the cationic surfactant dodecyltrimethylammoniumbromide (DTAB) phase separate above a certain dye:DTAB ratio, which decreases from Yellow:DTAB over Blue:DTAB to Red:DTAB. SANS reveals that dye-DTAB micelles in the 1-phase region grow when the 2-phase region is approached. Using a combination of SANS contrast matching and NMR-spectroscopy on Blue-DTAB solutions, Blue molecules are located in the outer region of DTAB micelles. The successful localisation of Blue in DTAB micelles demonstrates the feasibility of SANS contrast matching for localizing small organic molecules in surfactant micelles.

Dependent on solution  $\text{pD}$ , the acid dye Blue is present in its neutral, one- or two-fold deprotonated form. This permits to study its solubilisation in non  $\text{pD}$ -responsive micelles of the non-ionic surfactant  $\text{C}_{12}\text{E}_5$  as a function of Blue polarity without having to consider steric effects. The preferential solubilisation locus of Blue is determined to be in the core of  $\text{C}_{12}\text{E}_5$  micelles at  $\text{pD} = 2$ , in the palisade region at  $\text{pD} = 9$  or at the surfactant-water interface for  $\text{pD} = 13$ .

## List of abbreviations

Blue	HC Blue 18 (CAS: 1166834-57-6)
C <sub>12</sub> E <sub>12</sub>	Dodecylethyleneglycolmonododecylether
C <sub>12</sub> E <sub>5</sub>	Pentaethyleneglycolmonododecylether
C <sub>12</sub> E <sub>6</sub>	Hexaethyleneglycolmonododecylether
cmc	Critical micelle concentration
cryo-TEM	Cryogenic transmission electron microscopy
CTAB	Cetyltrimethylammoniumbromide
DLS	Dynamic light scattering
DTAB	Dodecyltrimethylammoniumbromide
FID	Free induction decay
ILL	Institut Laue-Langevin
LS	Light scattering
MD	Molecular dynamics
MOLT	Molecular theory
NMR	Nuclear magnetic resonance
NOE	Nuclear Overhauser Effect
NOESY	Nuclear Overhauser Effect spectroscopy
PEO	Polyethyleneoxid
PPO	Polypropyleneoxid
PSI	Paul Scherrer Institut
RDG	Rayleigh-Debye-Gans
Red	HC Red 18 (CAS: 1444596-49-9)
ROE	Rotating frame Nuclear Overhauser Effect
ROESY	Rotating frame Nuclear Overhauser Effect spectroscopy
SANS	Small-angle neutron scattering
SAS	Small-angle scattering
SAXS	Small-angle X-ray scattering
SDS	Sodiumdodecylsulphate
SLS	Static light scattering
TEM	Transmission electron microscopy
USAS	Ultra-small-angle scattering

UV/vis

Ultraviolet/visible

WAXS

Wide-angle X-ray scattering

Yellow

HC Yellow 16 (CAS: 1184721-10-5)

# Table of Contents

Kurzfassung	ix
Abstract	x
List of abbreviations	xi
<b>1. Introduction</b>	<b>1</b>
1.1 Dye self-assembly	1
1.2 Surfactant self- and co-assembly	2
1.3 Application of dye-surfactant systems	3
1.4 Localization of additives in surfactant micelles	8
1.5 Objective of the thesis	18
1.6 References	19
<b>2. Synopsis</b>	<b>37</b>
2.1 Dye self-assembly	37
2.2 Co-assembly between dye and surfactant	40
2.3 Outlook	50
2.4 References	52
<b>3. Co-authors' contribution</b>	<b>55</b>
<b>4. Comparative study of the self-assembly behaviour of 3-chloro-4-hydroxy-phenylazo dyes</b>	<b>56</b>
4.1 Introduction	58
4.2 Experimental	59
4.3 Discussion	61
4.4 Conclusions	75
4.5 Supporting information	77
4.6 References	96
4.7 Appendix	102
<b>5. Comparative study of the co-assembly behaviour of 3-chloro-4-hydroxy-phenylazo dyes with DTAB</b>	<b>103</b>
5.1 Introduction	105
5.2 Experimental	107
5.3 Discussion	109

5.4 Conclusions	123
5.5 Supporting information	125
5.6 References	132
<b>6. SANS contrast matching for the unambiguous localization of anionic dye in cationic surfactant micelles</b>	139
6.1 Introduction	141
6.2 Experimental	142
6.3 Data analysis	146
6.4 Results and discussion	147
6.5 Conclusion	167
6.6 Supporting information	169
6.7 References	187
<b>7. Impact of dye polarity on mixed dye-non-ionic surfactant micelles: Micelle morphology and spatial dye distribution</b>	194
7.1 Introduction	197
7.2 Experimental	199
7.3 Clouding temperatures of Blue-C <sub>12</sub> E <sub>5</sub> solutions	202
7.4 Morphology of C <sub>12</sub> E <sub>5</sub> surfactant micelles with and without Blue at variable pD	204
7.5 Localization of Blue in C <sub>12</sub> E <sub>5</sub> micelles	211
7.6 Discussion	221
7.7 Conclusion	225
7.8 Supporting information	227
7.9 References	265
<b>8. List of publications</b>	271
<b>9. List of conference contributions</b>	272



# Chapter 1

## Introduction

### 1.1. Dye self-assembly

Dye self-assembly in solution has been the focus of scientific investigations for decades due to its frequency of occurrence and relevance in application.<sup>1-8</sup> Dye self-assembly is also termed dye self-aggregation and arises due to attractive interactions between dye molecules. Resulting aggregates often show new functionalities compared to individual molecules, which are caused by the electronic coupling of  $\pi$ -systems.<sup>1,9-11</sup>

With advances in optoelectronics and nanotechnology applications, dye self-assembly attracted increasing interest for “bottom-up” synthesis approaches.<sup>1,3,12,13</sup> Furthermore, dye self-assemblies in solution were suggested to constitute an intermediate state between molecularly dissolved dyes and the corresponding solid state material.<sup>2,14</sup> The investigation of such assemblies in solution is worthwhile, as it provides valuable insights into intermolecular interactions affecting the solid state system whilst reducing its complexity. In addition to that, dye molecules were suggested to be promising as protein substitutes for the investigation of biological systems. For example, the cationic dye pseudo isocyanine chloride was identified as a suitable protein-like substitute concerning the resemblance of protein aggregation.<sup>15</sup> Similar to the aggregates originating from amyloidogenic proteins, the aggregates formed by this dye exhibit a fibrillar structure.<sup>15</sup>

In aqueous solutions, dye molecules are either present in their molecularly dissolved form, as dimers or as large assemblies with aggregation numbers larger than two.<sup>1,2</sup> Owing to the amount and complexity of possible intermolecular interactions, the prediction of dye self-assembly is difficult if no distinct dominant contribution exists.<sup>1</sup> Therefore, the experimental investigation of dye self-assembly under given solution conditions often remains necessary. UV/vis spectroscopy is a valuable technique for this purpose. The formation of soluble and insoluble dye aggregates is easily detected due to deviations from the Beer-Lambert law:<sup>16</sup>

$$A_{\lambda} = \log \left( \frac{I_0}{I_{\lambda}} \right) = \epsilon_{\lambda} \cdot d \cdot c \quad (1)$$

In eq (1),  $A_{\lambda}$  is the absorbance of a sample at a given wavelength  $\lambda$ . The incident and the transmitted intensity are designated as  $I_0$  and  $I_{\lambda}$  respectively. The absorbance  $A_{\lambda}$  depends on the molar absorption coefficient  $\epsilon_{\lambda}$  at  $\lambda$ , the optical path length  $d$  and the molar concentration of the absorbing species  $c$ . UV/vis spectroscopy may even provide information on the orientation of dye

molecules within dimeric or larger assemblies. For this purpose, concentration induced changes of the dye absorption spectrum need to be analysed in the framework of molecular exciton theory.<sup>3,5,17</sup> Within this approach, the quantitative analysis of wavelength shifts and oscillator strengths may permit deductions on dye aggregate geometry.<sup>4,18</sup>

## 1.2. Surfactant self- and co-assembly

Surfactants (surface-active agents) belong to the most important products of the chemical industry. They are used in oil recovery, water treatment, mineral processing, pharmaceuticals and in many food- and consumer products.<sup>19-21</sup> Due to their amphiphilic molecular structure, surfactants alter the interfacial tension between two liquids, most often causing a decrease.<sup>19</sup> In aqueous solution, surfactant molecules assemble into a single layer at the air-water interface. At concentrations above the critical micelle concentration (cmc) they furthermore self-assemble into micelles (Figure 1).<sup>19,22</sup> Surfactant micelles can adopt different shapes ranging from small, spherical micelles over cylindrical micelles or wormlike micelles to lamellar structures.<sup>23</sup>

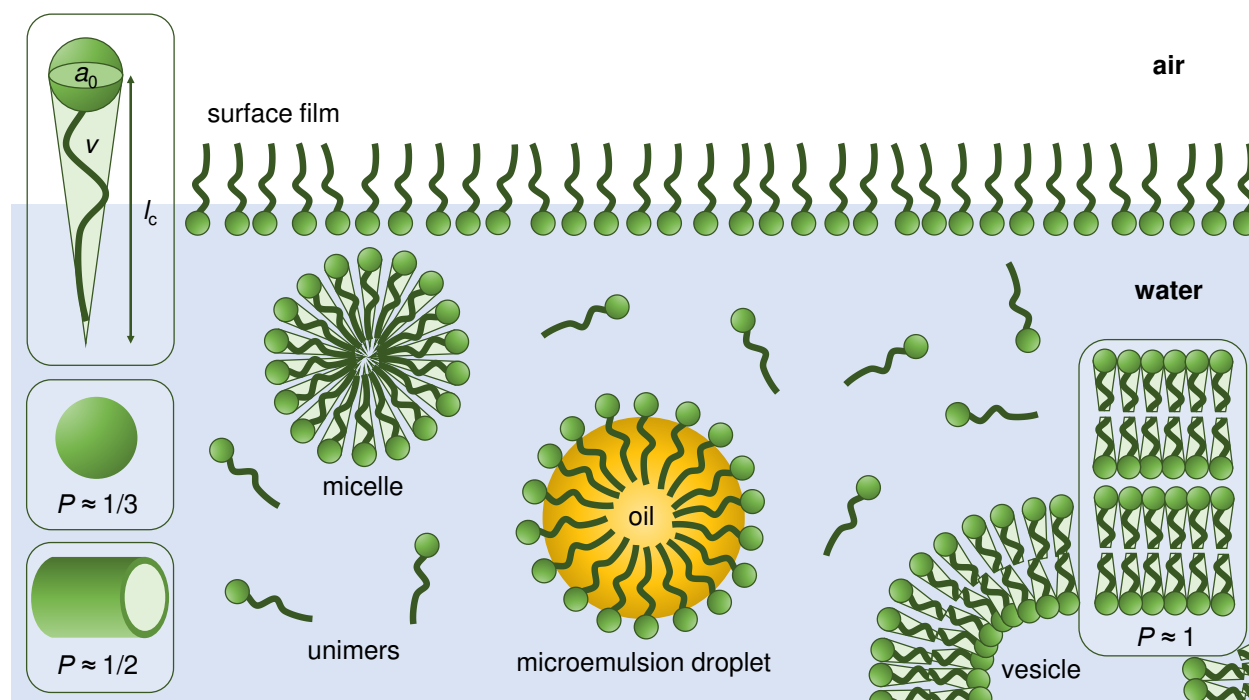


Figure 1: Schematic representation of possible surfactant self-assembled structures in solution and of a microemulsion droplet. Green spheres represent the hydrophilic surfactant head group and dark green lines the hydrophobic surfactant tail. Size parameters of surfactant molecules that contribute to the packing parameter  $P$  are illustrated in the top left corner inset. Values of the packing parameter are illustrated for important micelle morphologies in the insets.  $P \approx 1/3$  is characteristic for spherical micelles,  $P \approx 1/2$  for cylindrical micelles and  $P \approx 1$  for lamellar and vesicular structures.<sup>21,23,24</sup> If strongly hydrophobic molecules are added to a surfactant solution, microemulsion droplets can be formed.<sup>25</sup>

The concept of the critical packing parameter provides a theoretical basis to understand shape changes of micellar assemblies based on geometrical parameters of constituting surfactant

molecules. The value of the packing parameter ( $P$ ) is calculated from the effective head group area of a surfactant  $a_0$ , the length of the completely extended hydrophobic tail  $l_c$  and the volume of the hydrophobic tail  $v$ , which are illustrated in Figure 1.

$$P = \frac{v}{a_0 \cdot l_c} \quad (2)$$

An overview of possible packing parameters and corresponding geometrical shapes of micelles is given in Figure 1.<sup>23,26</sup>

The packing parameter is frequently discussed together with the concept of the “spontaneous curvature” of a micelle. Spherical micelles possess a high spontaneous curvature, whereas cylinders have an intermediate and lamellar structures a low spontaneous curvature.<sup>27</sup> As the packing parameter increases from spherical over cylindrical to lamellar assemblies, both concepts can be used interchangeably.

As visible from eq (2), the morphology of surfactant micelles depends on the molecular structure of the surfactant. However, solution conditions like concentration<sup>28–32</sup>, temperature<sup>33–36</sup>, pH<sup>37,38</sup>, ionic strength<sup>32,39–46</sup>, addition of another surfactant<sup>41,47–55</sup> and addition of hydrotropic<sup>56–62</sup> or of non-polar solutes<sup>56,63</sup> may strongly influence the shape and size of such micelles. Micelles of ionic surfactants are more sensitive to the ionic strength of the solution, whereas micelles of non-ionic surfactants often show a pronounced temperature-dependency. Strongly hydrophobic additives often reduce the size of surfactant micelles, whereas more hydrophilic compounds commonly lead to the formation of larger rod- or wormlike micelles. Due to the delicate balance of interactions influencing the micellar equilibrium, some additives might induce growth at lower additive concentrations, but shrinking at higher concentrations.<sup>25,56,64</sup> In some cases, microemulsions are formed. In the light of the variety of parameters influencing micelle morphology, synergistic effects and conflicting values reported in literature, the development of comprehensive models for the prediction of micellar morphology as a function of solution conditions remains a challenge to this day.<sup>65–67</sup>

### 1.3. Application of dye-surfactant systems

**Textile dyeing and wastewater treatment:** The interaction between dye and surfactant molecules in solution was subject to scientific investigations for decades to satisfy the needs of textile- and paper dyeing industries as well as other sectors like cosmetics and food colouring.<sup>68</sup> The use of surfactants in dyeing baths and dyeing formulations significantly improves the dyeing process and quality, as surfactants promote penetration of dye into the substrate and often cause

a more uniform distribution of colour.<sup>69–73</sup> Surfactants may furthermore improve fibre wetting or solubilize poorly soluble dyes.<sup>69</sup> Unfortunately, concomitant with the extensive use of dyeing solutions for substrate dyeing, huge amounts of wastewater arise.<sup>74</sup> To give an example, between 70 and 150 L of water are required for dyeing 1 kg of cotton fabric.<sup>75,76</sup> Due to the toxicity of textile effluents and environmental implications, the development of effective treatment techniques is crucial.<sup>77</sup> For this reason, current research considering dye-surfactant interactions tends to be mostly motivated by the need of wastewater treatment.<sup>74,76,78–85</sup>

**Optical applications:** Dye and surfactant molecules with opposite charge may form insoluble salts. This behaviour was first observed as an undesired phenomenon in the context of cmc determination with the spectral change method.<sup>86–89</sup> In the early 2000s, solid dye-surfactant complexes were investigated more systematically as a desired product due to their interesting optical properties, which could have been exploited in optical data storage applications.<sup>90,91</sup> The Faul group investigated the formation of solid crystalline complexes and liquid crystalline phases between multiply charged dye molecules and oppositely charged surfactant.<sup>91,92</sup> Some of these systems showed pronounced optical anisotropy.<sup>91–93</sup> Current research in this field mostly focuses on liquid crystalline phases. Liquid crystalline systems with good film forming properties might find application in optical layers such as retardation films and polarizers.<sup>90</sup> The successful synthesis of thermotropic and lyotropic liquid crystalline systems by co-assembly of oppositely charged dye and surfactant molecules was reported.<sup>94–99</sup>

**Diagnostics:** Dye molecules can be employed as an analytical probe for the characterization of micelle containing systems. The dye absorption spectrum is sensitive to its micro-environment, permitting the observation of general system properties, such as the presence of an analyte, solution pH or solubilizing capability of surfactant containing solutions using simple UV/vis spectroscopy.<sup>68,100–107</sup> Furthermore, fluorescence spectroscopy and fluorescence microscopy, analytical methods which are frequently applied to biological systems, rely on the emission properties of fluorescent dyes. The presence of surfactant molecules in such systems needs to be considered, as the interaction with surfactant might change the emission spectrum of a dye.<sup>108,109</sup>

**Hair dyeing:** Dyeing of hair has been performed for more than 2000 years and is nowadays an important sector of the cosmetic industry.<sup>110,111</sup> Unlike other physical attributes, hair colour can easily be changed, which makes it popular among many age groups for self-expression and to cover grey hair.<sup>112,113</sup> Hair dyes can be distinguished into oxidative and non-oxidative.<sup>110</sup>

Non-oxidative dyes are also termed “semi-permanent” or “temporary”, as the coloration of the hair is based on diffusion of dye molecules into the hair fibre. This means that they do not bind firmly and can be washed out of the hair over time.<sup>110</sup> Figure 2 shows the molecular structures of three direct dyes that could be used for this purpose. The colours yellow, blue and red are combined in dyeing formulations to cover the whole colour range by adjusting the concentration of each dye in the dyeing liquor. For a predictability of the final hair colour from the colour of the dyeing liquor, all three dyes should show similar affinity to the hair fibre and similar diffusion characteristics to and within the fibre.<sup>114</sup> However, such properties may be influenced by the interaction of dye molecules with other components of the dyeing liquor, e.g. surfactants.

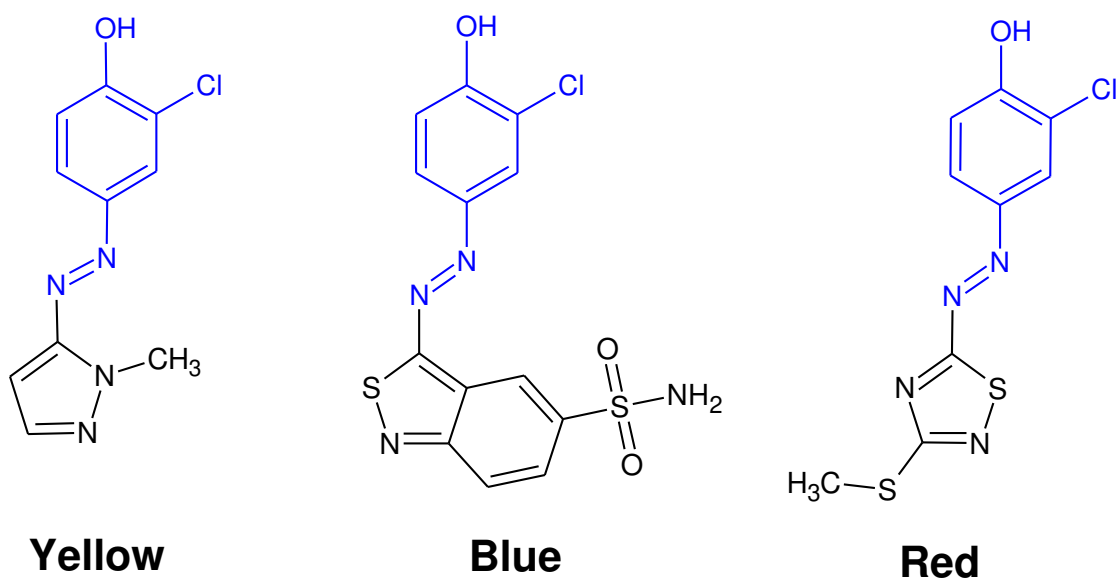


Figure 2: Molecular structures of three azo direct dyes, which are combined in dyeing formulations to enable the whole colour range for dyeing of human hair. All three dyes possess a congruent structural sub-unit, which is marked in blue. Dyeing is usually performed at an alkaline pH. Under such conditions, the phenolic hydroxyl group is deprotonated for all three dyes. Full descriptors and CAS numbers: Yellow: HC Yellow 16 (CAS: 1184721-10-5), Blue: HC Blue 18 (CAS: 1166834-57-6), Red: HC Red 18 (CAS: 1444596-49-9).

Dye-surfactant interactions are crucial for the dyeing of human hair. Surfactants are used in hair dyeing formulations to improve hair fibre wetting, to increase solubility of the dye, to achieve a uniform distribution of dye on the hair fibre due to levelling and to obtain desirable rheological properties of the dyeing liquor.<sup>69,71,73</sup> Furthermore, they may improve the exhaustion of the dyeing liquor applied to the hair fibre or reduce hair damage during oxidative pre-treatment.<sup>115</sup> However, such properties strongly depend on the system in use. An apparently suitable dye-surfactant combination in a given solvent may improve the dyeing process, but can also decrease the uptake of dye by the hair fibre or may cause inhomogeneous dyeing due to aggregation effects.<sup>113</sup> The latter is mostly observed in systems where dye and surfactant are oppositely charged.<sup>71</sup> Figure 3 shows examples of the detrimental effect surfactant addition may exert on the efficiency of hair

dyeing. Hair tresses shown in Figure 3 were dyed in alkaline solutions of the dye Yellow, Blue and Red (Figure 2) respectively. For each dye, the left image shows the result of dyeing with a solution only containing the dye in the buffer and the right image shows the result of dyeing with a solution containing dye and the cationic surfactant DTAB in the same buffer. In all cases, tresses dyed in the presence of DTAB show a less saturated colour, pointing towards reduced dye uptake compared to tresses dyed in absence of DTAB. Furthermore, the hair tresses dyed in presence of DTAB appear less homogeneously dyed, which is mostly visible when comparing the hair tresses directly rather than their pictures. These undesired effects render the cationic surfactant DTAB unsuitable for the use in dyeing formulations, but interesting for fundamental studies of dye-surfactant interactions.



Figure 3: Images of washed goat hair tresses dyed in solutions containing the specified direct dye at a concentration of [Dye] = 5 mM without or with the cationic surfactant DTAB. For each dye, the left image shows the hair tress dyed in absence of DTAB and the right image the hair tress dyed in presence of DTAB. The composition of the dyeing solution is indicated below each image. Dyeing was performed with an excess of dyeing solution and at a temperature of 25 °C for 30 min under constant mixing. A NaHCO<sub>3</sub>/Na<sub>2</sub>CO<sub>3</sub> buffer with pH = 10.5 and an ionic strength  $I \approx 0.25$  M was used as solvent. After dyeing, all hair tresses were washed under running, lukewarm water and subsequently dried using a fan.

As mentioned previously, the effect of surfactant addition on hair dyeing strongly depends on the system in use. In another example, hair tresses were dyed with a mixture of Blue at a concentration of [Blue] = 6.25 mM and the non-ionic surfactant C<sub>12</sub>E<sub>5</sub> at varying concentrations. Hair tresses dyed in absence of C<sub>12</sub>E<sub>5</sub> and hair tresses dyed with a solution containing C<sub>12</sub>E<sub>5</sub> at a concentration of [C<sub>12</sub>E<sub>5</sub>] = 6.25 mM or [C<sub>12</sub>E<sub>5</sub>] = 12.5 mM do not differ in their appearance (Figure 4). However, use of a surfactant concentration of [C<sub>12</sub>E<sub>5</sub>] = 25 mM during dyeing results in a significant colour change. This could be caused by two effects: (1) Surfactant micelles and hair fibres compete for interactions with the dye Blue. At sufficiently high surfactant excess, a

significant amount of dye interacts with surfactant micelles and is therefore not freely available to penetrate into the hair fibre. This results in a lower dye uptake of the hair fibre. (2) Surfactant molecules might penetrate into the hair fibre too, causing a change in the polarity of the environment of the dye in the hair fibre. Most dyes are solvatochromatic and their absorption spectrum changes in function of the polarity of their environment.<sup>116</sup> This behaviour would result in a colour change of the dyed hair fibre. Both effects may contribute to the result of hair coloration.

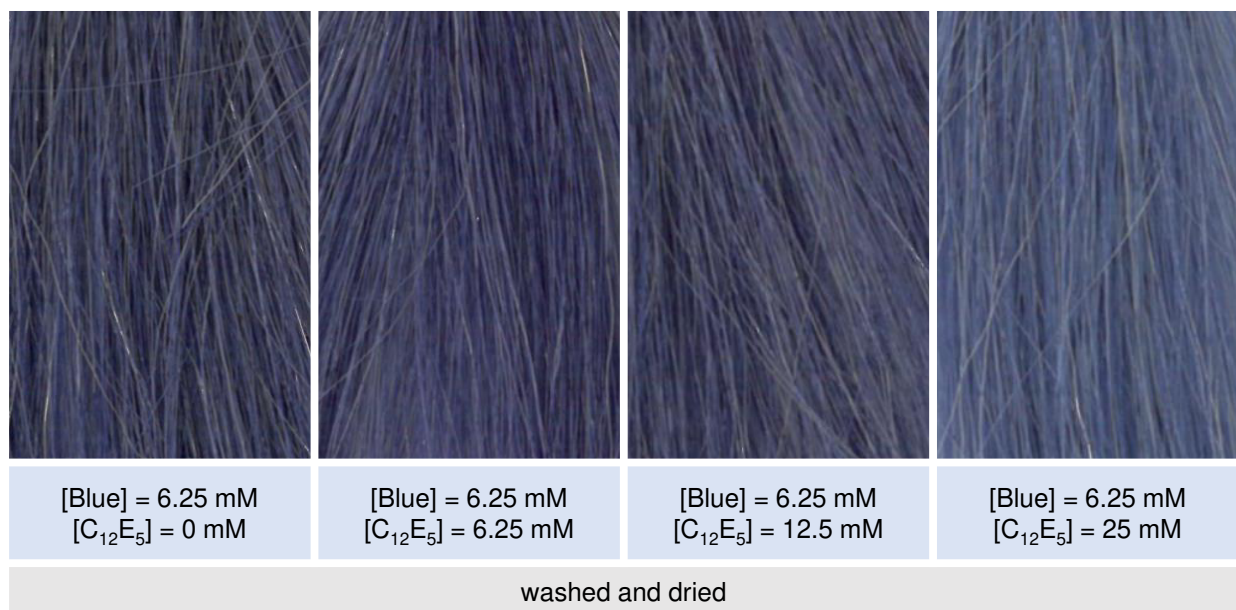


Figure 4: Images of washed goat hair tresses dyed in solutions containing the dye Blue at a concentration of [Blue] = 6.25 mM without or with the non-ionic surfactant C<sub>12</sub>E<sub>5</sub> at various concentrations [C<sub>12</sub>E<sub>5</sub>]. The composition of the dyeing solution is highlighted in blue. Dyeing was performed with an excess of dyeing solution and at a temperature of 25 °C for 30 min under constant mixing. An isotonic NaCl solution with pH = 9 (adjusted with HCl/NaOH) was used as solvent in all cases. After dyeing, all hair tresses were washed under running, lukewarm water and dried using a fan.

Dye-surfactant interactions do not only influence the design of dyeing formulations, but also require considerations on the haircare after dyeing. Shampoos usually contain anionic surfactants at a pH close to neutral and conditioners contain cationic surfactants.<sup>117</sup> As fast washing-out of hair dyes with such products or colour changes upon interaction with them are to be avoided, the interaction between dye and ingredients of haircare products needs to be considered as well.

To conclude this section, the development of hair dyeing formulations and suitable haircare products highly benefits from a fundamental understanding of dye-surfactant interactions as it facilitates a systematic approach towards the design of efficient formulations. Not all types of surfactants are suitable to be used in hair dyeing formulations and concentration conditions play an important role.

## 1.4. Localization of additives in surfactant micelles

The effect of an organic additive on the shrinking or growth of surfactant micelles strongly depends on its solubilisation locus in the micelle.<sup>25,63</sup> As the morphology of additive-surfactant micelles dictates rheological properties of the solution and influences its solubilisation capacity, it is crucial to understand intermolecular interactions and mechanisms leading to morphological transitions.<sup>25,47,67,118,119</sup>

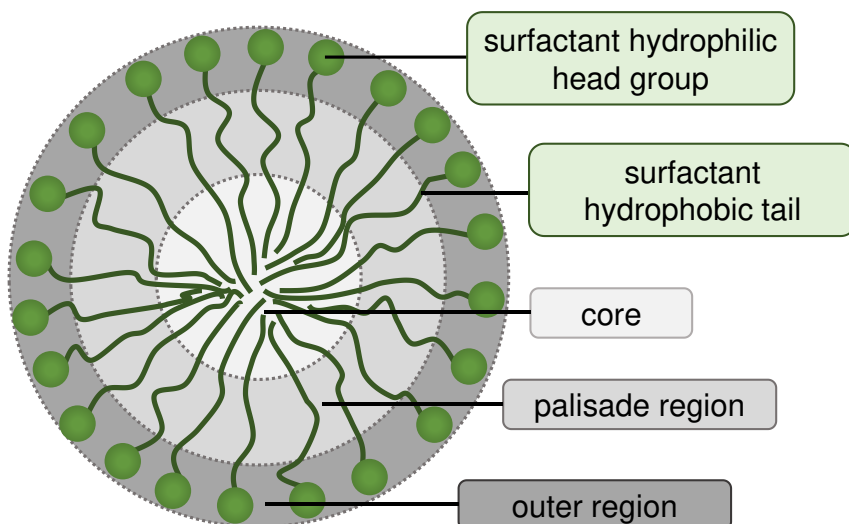


Figure 5: Classification of regions in a surfactant micelle according to their polarity.<sup>120</sup>

Figure 5 schematically shows a commonly employed division of the surfactant micelle into three regions according to their polarity or hydrophilicity:<sup>120</sup> (I) The core of the micelle constitutes the most hydrophobic part of the micelle and contains mostly alkyl hydrocarbons.<sup>121,122</sup> (II) The palisade region is described as the transition zone between the hydrophobic micellar core and the more hydrophilic outer layer of the micelle in aqueous solution.<sup>38</sup> The assignment of the palisade region in a surfactant micelle depends on the type of surfactant and is often kept rather vague. For ionic surfactants it usually corresponds to a part of the hydrophobic alkyl chains close to the head group.<sup>121</sup> (III) The outer region corresponds to the interface between the micelle and the surrounding bulk water.<sup>120</sup> It contains charged head groups, counter ions, water molecules and potentially some strongly hydrated methylene groups of the alkyl tail.<sup>121</sup> For ionic surfactants the outer region is also termed “Stern layer” and is typically addressed when evaluating the stability of solutions and dispersions containing ionic surfactants.<sup>38,120,121,123</sup> For non-ionic surfactants the outer region refers to the more hydrated part of the polar head group.<sup>38</sup>

Previous research successfully related morphological transitions of surfactant micelles upon additive addition to the solubilisation locus of such additives.<sup>51,55,63,64,124–127</sup> Apart from



experimental investigations, Zaldivar et al. modelled the distribution of highly and mildly hydrophobic additives in surfactant micelles using molecular theory (MOLT) simulations.<sup>25,128</sup> Furthermore, Molecular dynamics (MD) simulations helped to understand the solubilisation of amphiphilic indicator dyes in surfactant micelles or of drug molecules in micelles formed by high molecular weight surfactants.<sup>122,129–131</sup> Nevertheless, even though theoretical simulations might be useful for screening of pharmaceutical formulations to minimize experimental effort, important results should be verified experimentally.<sup>122,132,133</sup> In the following, UV/vis-spectroscopy, NMR-spectroscopy and small-angle neutron scattering with contrast variation will be presented as suitable analytical techniques for the localization of dye molecules in surfactant micelles.

**UV/vis-spectroscopy:** UV/vis spectroscopy can be used to investigate additive-surfactant interaction if the additive absorbs electromagnetic radiation in the UV/vis-range and if its UV/vis absorption spectrum is sensitive to polarity changes of its microenvironment. This is the case for solvatochromic dye molecules. Solvatochromism entails that, dependent on the molecule, an increase in the polarity of its environment causes a bathochromic shift of the dye absorption spectrum (positive solvatochromism) or a hypsochromic shift (negative solvatochromism).<sup>116</sup> This phenomenon is caused by a variation in the extent a given environment stabilizes bonding and non-bonding molecular orbitals of the dye and often linearly correlates with the polarity of this environment.<sup>101</sup> A polarity change in the microenvironment of dye molecules in surfactant solutions compared to in water can be induced by the incorporation of dye molecules into surfactant micelles. The extent to which the dye absorption spectrum is altered upon inclusion into surfactant micelles may provide information on the polarity of the dyes' microenvironment, which indicates its solubilisation locus. A frequently employed strategy for the quantification of such an effect is to compare the UV/vis absorption spectrum of the dye in micellar solution to UV/vis absorption spectra of the dye in solvents with variable polarity.<sup>134,135</sup> A drawback of this approach is the difficulty to quantitatively identify the polarity of various regions in the micelles, which complicates the choice of reference solvents. This approach may furthermore be hampered by dye self-aggregation and by choosing unsuitable spectral features for evaluation.<sup>136</sup> For this reason, most UV/vis spectroscopic investigations on the solubilisation locus are kept qualitative and solely distinguish between solubilisation in the core region or in the palisade- and outer region.<sup>101,137–139</sup> For these reasons, even though UV/vis spectroscopy may give a first impression about the dye solubilisation locus, it does not permit its precise determination. Other experimental techniques are required for this purpose.

**Nuclear magnetic resonance spectroscopy:** Nuclear magnetic resonance (NMR) spectroscopy is not only one of the most important analytical methods in organic chemistry but also frequently applied for the localisation of solutes or additives in surfactant micelles. In the following, theory and application of  $^1\text{H}$ -NMR spectroscopy and Nuclear Overhauser Effect spectroscopy will be presented.

Atomic nuclei with a nuclear spin quantum number  $> 0$  possess an angular momentum  $\mathbf{P}$ , which gives rise to an associated magnetic moment  $\boldsymbol{\mu}$ , due to the motion of the charged nuclei.<sup>140</sup>

$$\boldsymbol{\mu} = \gamma \cdot \mathbf{P} \quad (3)$$

The value of the magnetic moment  $\mu = |\boldsymbol{\mu}|$  is determined by the gyromagnetic ratio  $\gamma$ . When nuclei are placed in an external magnetic field  $\mathbf{B}_0$ , they align themselves relative to this field. The number of possible orientations depends on the magnetic quantum number. For  $^1\text{H}$ -nuclei, the magnetic quantum number amounts to  $1/2$ , resulting in two possible spin states with different energy (Figure 6a). These spin states can be understood as orientations relative to the external magnetic field.<sup>140,141</sup>

The magnetic moments  $\boldsymbol{\mu}$  of the atomic nuclei show a precession movement around  $\mathbf{B}_0$  with a frequency  $\nu_L$  (Larmor frequency):<sup>140</sup>

$$\nu_L = \frac{\gamma \cdot |\mathbf{B}_0|}{2 \pi} \quad (4)$$

If electromagnetic radiation with Larmor frequency  $\nu_L$  is irradiated onto the precessing nuclei, the resonance condition is fulfilled, as the energy of this radiation matches the energy difference  $\Delta E = h\nu_L$  between possible spin states. Energy differences involved in NMR spectroscopy are very small compared to IR- or UV/vis spectroscopy, which renders NMR-spectroscopy more insensitive and experimentally demanding.<sup>140</sup> The magnetic field of electromagnetic radiation causing energetic transitions of nuclear magnetic moments is designated  $\mathbf{B}_1$ . It changes the population of available spin states and causes a phase coherent precession of magnetic moments around  $\mathbf{B}_0$  (Figure 6b). The population of spin states is often expressed as the z-component of the net (bulk) magnetization vector  $\mathbf{M}_0$ , whereas its x- and y- component indicate phase coherent precession (Figure 6b). The free induction decay (FID), from which the NMR-spectrum is obtained by Fourier Transformation, can be collected due to the precession of the bulk magnetization in the x,y-plane. Over time, a recovery of z-magnetization caused by the re-establishment of equilibrium population (longitudinal relaxation,  $T_1$ ) and the loss of phase coherence and therefore the loss of magnetization in the x,y-plane (transversal relaxation,  $T_2$ ) is observed. Short  $T_2$

relaxation times often result in broad peaks and are observed for slowly tumbling analytes, e.g. for macromolecules or for aggregates.<sup>6,140,142</sup>

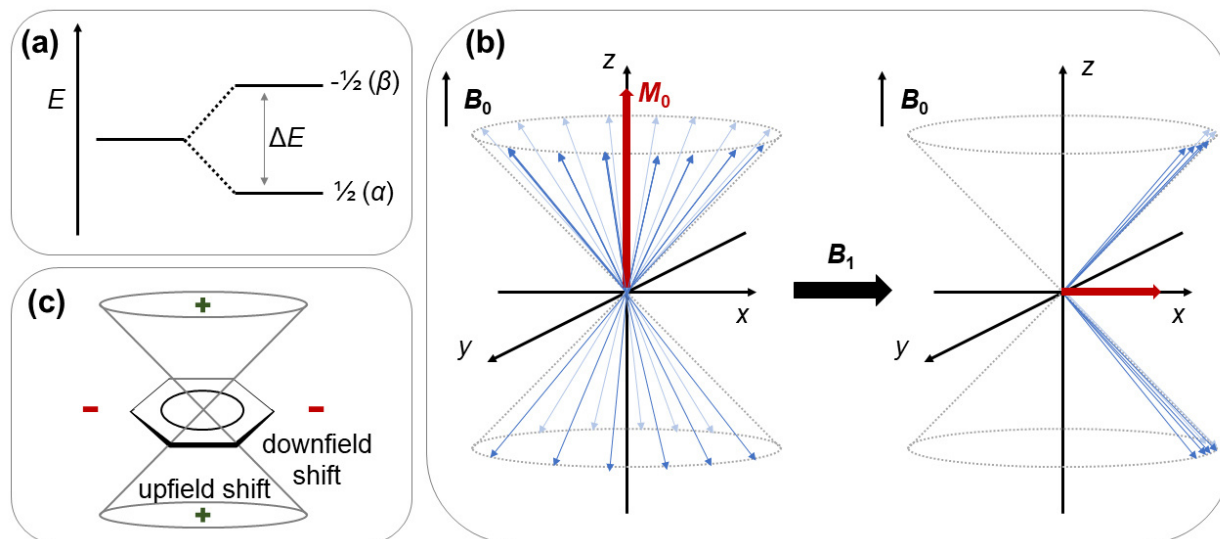


Figure 6: (a) Schematic energy level diagram depicting the two possible spin state for a nucleus with a magnetic quantum number of  $\frac{1}{2}$  when an external magnetic field  $B_0$  is applied. In the  $\alpha$  state, the magnetic moment of the nucleus is oriented parallel to  $B_0$ , whereas its orientation is antiparallel in the  $\beta$  state. (b) Vector model in NMR spectroscopy. Blue arrows schematically depict nuclear magnetic moments precessing in the external magnetic field.  $M_0$  represents the bulk magnetization vector at thermal equilibrium. Upon irradiation of the oscillating magnetic field  $B_1$ , nuclear magnetic moments precess in phase and the population difference between the  $\alpha$  and  $\beta$  state is altered, resulting in equal population of both states for the presented case. The red arrow corresponds to the bulk magnetization vector. (c) Schematic effect aromatic moieties have on the  $^1\text{H}$ -NMR chemical shift of neighbouring protons. Adapted from Guo et al.<sup>143</sup>

A loss in phase coherence over time occurs, because individual nuclei experience slightly different magnetic fields and therefore precess with slightly different frequencies. The variation of local magnetic field strength is caused by moving electron clouds, which induce a magnetic field opposite to  $B_0$ , resulting in a shielding of atomic nuclei. Therefore, the observation of individual precession frequencies provides an idea about the local environment of atomic nuclei. Quantitatively, the effective frequency of precession  $\nu_{\text{eff}}$  depends on the shielding constant  $\sigma$ , which increases with increasing electron density around the nucleus according to eq (5):<sup>141</sup>

$$\nu_{\text{eff}} = \frac{\gamma}{2\pi} (1 - \sigma) |B_0| \quad (5)$$

The chemical shift, which is depicted on the  $x$ -axis of an NMR-spectrum and given by eq (6) therefore decreases with increasing shielding.

$$\delta = \frac{\nu_{\text{eff}} - \nu_{\text{ref}}}{\nu_{\text{ref}}} \quad (6)$$

In eq (6),  $\nu_{\text{ref}}$  is the precession frequency of a reference compound, e.g. tetramethylsilane.

Concerning the localization of additives in surfactant micelles, variations in the spectral position of surfactant or additive  $^1\text{H}$ -NMR resonances can be used to infer the position of the additive in the micelle. The incorporation of the additive into the micelle leads to alterations in the electron density around  $^1\text{H}$  nuclei close to the locus of solubilisation. Dependent on the chemical structure of both components and on additive position, this may result in shielding or de-shielding of these nuclei. Corresponding resonances are therefore shifted up- or downfield compared to their position in the spectrum of the pure component. Strong changes in the chemical shift are usually observed when strongly polar or charged functional groups or aromatic moieties are involved. Figure 6c displays the effect of an aromatic moiety on the chemical shift of neighbouring protons.<sup>143</sup>

A quantification of the extent to which chemical shifts of surfactant  $^1\text{H}$  nuclei change upon addition of another compound permits a first estimation on how deeply this compound penetrates into the surfactant micelle.<sup>61,143–149</sup> Furthermore, the orientation of an additive molecule within the surfactant micelle can potentially be inferred by comparing variations in the chemical shifts of additive  $^1\text{H}$  nuclei. Such an analysis was performed by Bachofer et al. who determined the localisation and orientation of substituted benzoate anions in cetyltrimethylammoniumbromide (CTAB) micelles.<sup>147</sup> Apart from an indication of additive localization,  $^1\text{H}$ -NMR spectroscopy may also provide an idea about the onset of morphological changes of additive-surfactant micelles due to peak broadening when micelles grow longer. However, morphological changes would need to be confirmed using scattering techniques or electron microscopy.<sup>61</sup>

A more reliable and complete picture can be obtained from Nuclear Overhauser Effect (NOE) spectroscopy. NOE spectroscopy permits to detect spatially proximal atomic nuclei based on through-space magnetic interactions (dipolar coupling), even if the considered nuclei are not connected through chemical bonds. In an NOE experiment, the resonance of one atomic nucleus is selectively saturated or inverted and the effect of this saturation on the intensity of other NMR resonances is observed.<sup>150</sup> The NMR resonances of nuclei within a distance of less than 5 Å - 6 Å to the saturated nucleus then exhibit either an intensity increase (positive NOE) or decrease (negative NOE).<sup>141,150</sup> Whether a positive or negative NOE is observed depends on the sign of the gyromagnetic ratio of participating spins and on the motional properties of the molecule.<sup>150</sup> The intensity change is caused by the emergence of cross-relaxation pathways, which cause the transfer of nuclear spin polarization between the saturated and the observed nucleus. These

cross-relaxation pathways are referred to as the zero-quantum transition ( $W_0$ ), which is favoured by slowly tumbling molecules and as the double-quantum transition ( $W_2$ ), which is favoured by rapidly tumbling molecules. If the  $W_0$  transition is favoured, negative NOEs are observed, whereas a dominating  $W_2$  relaxation results in positive NOEs.<sup>150</sup> The evaluation of the NOE sign therefore provides an idea of whether the observed molecule or assembly tumbles slowly or rapidly in solution, which indicates the molecular or assembly size. However, for molecules showing intermediate tumbling rates, it is possible that the NOE becomes zero.<sup>150,151</sup> This is the case if both cross-relaxation pathways are equally prominent ( $W_2 = W_0$ ). Zero NOE due to tumbling of molecules in the intermediate range can be circumvented by measuring NOEs in the rotating frame.<sup>150</sup> The rotating frame NOE (ROE) remains positive for all tumbling rates.

In practice, NOE spectroscopy (NOESY) and ROE spectroscopy (ROESY) experiments yield 2-dimensional spectra. Cross peaks indicate the presence of an NOE. Therefore, spatial correlations are directly detected by the identification of such cross peaks.

As NOESY experiments permit the direct detection of spatial proximity, this technique was heavily used for the localization of additives in surfactant micelles and in surface active block-copolymers.<sup>62,152–157</sup>

However, the interpretation of NMR-spectra is sometimes ambiguous, as it may not always be possible to resolve the required spectroscopic features. The overlap of additive  $^1\text{H-NMR}$  resonances with surfactant  $^1\text{H-NMR}$  resonances represents a frequently encountered problem.<sup>62,145,157</sup> Furthermore, the interpretation of changes of the chemical shift caused by additive-surfactant interaction might be difficult.<sup>143,152,158</sup> In addition to that, NOESY signals are highly sensitive to the separation between two nuclei.<sup>150</sup> This could implicate the absence of NOESY signals even though an additive is located close to the micelle-water interface.<sup>152,157</sup> Finally,  $^1\text{H-NMR}$  spectroscopy and NOESY do not provide direct information on the morphology of an additive-surfactant micelle. Fortunately, this can be made accessible by suitable scattering techniques.

**Small-angle neutron scattering:** Small-angle scattering (SAS) permits the elucidation of the shape and organization of assemblies on length scales smaller than 100 nm. It provides ensemble average information on the irradiated volume, which may be an advantage over microscopy techniques (Figure 7a).

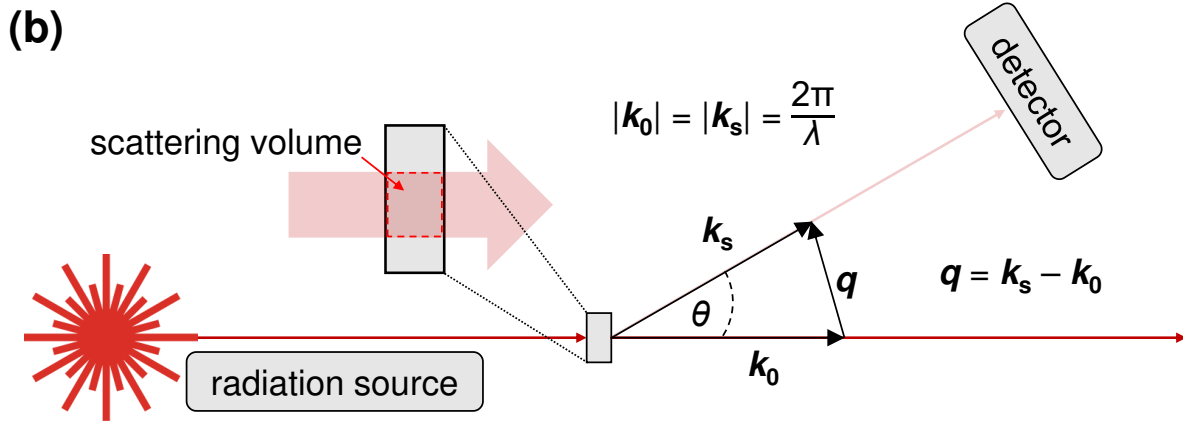
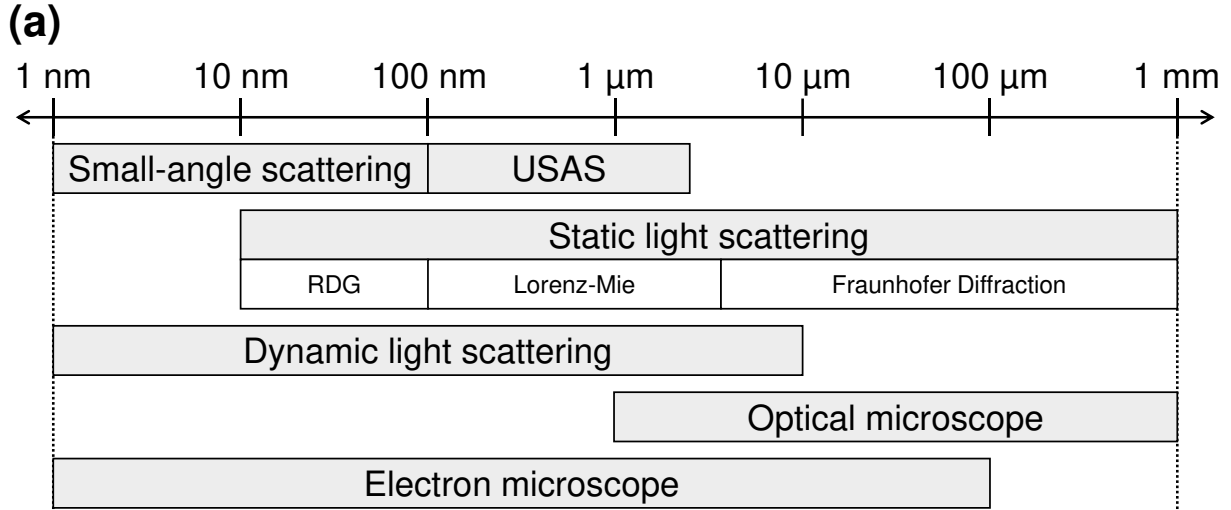


Figure 7: (a) Size ranges accessible with scattering and microscopy techniques. USAS = Ultra-small-angle scattering, RDG = Rayleigh-Debye-Gans.<sup>159</sup> (b) Setup of a scattering experiment.

During scattering experiments, the sample is irradiated and the intensity of the scattered radiation recorded as a function of the scattering vector  $\mathbf{q}$  (Figure 7b):<sup>159,160</sup>

$$q = |\mathbf{q}| = \frac{4\pi}{\lambda} n_m \cdot \sin\left(\frac{\theta}{2}\right) \quad (7)$$

In eq (7),  $\lambda$  is the wavelength of the incident radiation,  $\theta$  the scattering angle defined in Figure 7b and  $n_m$  the refractive index of the dispersion medium for the case of static light scattering (SLS). For neutrons and X-Rays,  $n_m \approx 1$ . Figure 7 shows how  $\mathbf{q}$  is calculated from the wave vectors of the incident ( $\mathbf{k}_0$ ) and the scattered ( $\mathbf{k}_s$ ) beam.

The  $q$ -dependency of the scattered intensity  $I_q$  is a function of the shape and distribution of scattering particles in solution.<sup>161,162</sup> The shape of a scattering particle is described by the single particle form factor  $P(q)$ , which arises from the interference of waves scattered from the same particle.<sup>162</sup> Theoretical form factors were calculated for various particle geometries, which permits

the deduction of the morphology of probed assemblies by comparison of experimental and theoretical scattering curves. Interparticle interferences are described by the structure factor  $S(q)$ . They arise through interparticle ordering, which is caused by the existence of non-negligible interparticle interactions. The structure factor can be neglected for highly dilute solutions.<sup>159,160</sup> Accordingly, the scattered intensity is described by the following equation:<sup>159,162</sup>

$$I_q(q, c_m) = c_m K M_p P(q) S(q) + BG_{\text{incoh}} \quad (8)$$

In eq (8)  $c_m$  [ $\text{g cm}^{-3}$ ] is the mass concentration of the particles,  $K$  [ $\text{cm}^2 \text{mol g}^{-2}$ ] the “contrast factor”,  $M_p$  [ $\text{g mol}^{-1}$ ] the molar mass of the scattering particle or assembly and  $BG_{\text{incoh}}$  the constant background signal arising from incoherent scattering. The single particle form factor  $P(q)$  approaches 1 for  $q \rightarrow 0$  and the structure factor  $S(q)$  approaches 1 for negligible interparticle interactions. If  $S(q) \approx 1$ , i.e. in very dilute systems, the scattering curve can be described by the Guinier approximation for small  $q$ .<sup>159,163</sup>

$$P(q) \approx \exp\left(-\frac{q^2 R_g^2}{3}\right) \quad (9)$$

Eq (9) is valid for  $qR_g < 1$  with  $R_g$  being the radius of gyration of the scattering particle.

The contrast factor  $K$  depends on the refractive index increment for SLS, on electron density differences for SAXS and on scattering length density differences for SANS.<sup>159</sup> Scattering length densities are calculated from nuclear scattering lengths, which depend on the type of nucleus and do not systematically vary with atomic number.<sup>164</sup> They are furthermore isotope specific permitting the variation of the contrast  $K$  by isotopic substitution, which is not possible in SAXS.<sup>164</sup> Eq (10) provides the definition of  $K$  for SANS.

$$K = \frac{(\rho_2 - \rho_1)^2 V_{m,2}^2}{M_2^2 N_A} \quad (10)$$

In eq (10), the subscript “1” indicates the solvent and the subscript “2” indicates the elementary scattering unit of the scatterer, which could be a monomer if the term “scatterer” denotes a polymer or a single surfactant molecule in case of surfactant micelles. Therefore,  $\rho_1$  [ $\text{cm}^{-2}$ ] is the scattering length density of the solvent and  $\rho_2$  [ $\text{cm}^{-2}$ ] the scattering length density of the elementary scattering unit.  $V_{m,2}$  [ $\text{cm}^3 \text{mol}^{-1}$ ] is the partial molar volume of the elementary scattering unit,  $M_2$  [ $\text{g mol}^{-1}$ ] its molar mass and  $N_A$  Avogadro’s number. The scattering length density  $\rho_i$  of a molecule  $i$  can be calculated from the coherent scattering lengths  $b_j$  of the constituting atoms, their respective number  $n_j$  and the partial molar volume  $V_{m,i}$  of the molecule.<sup>159</sup>

$$\rho_i = \frac{\sum_j n_j b_j}{V_{m,i}} = \frac{b_i}{V_{m,i}} \quad (11)$$

In eq (11),  $b_i$  is the scattering length of the molecule.

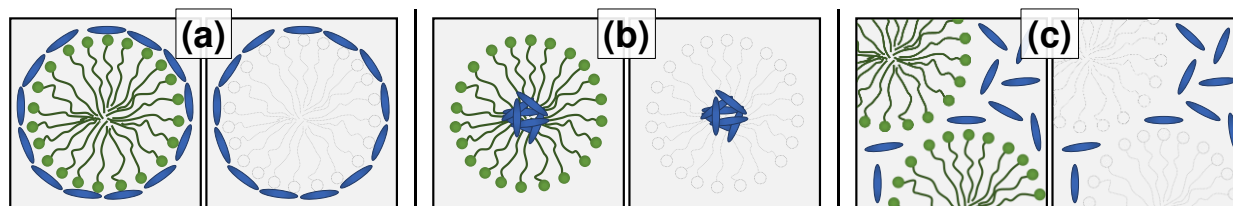


Figure 8: Schematic representation of the contrast matching principle for solution containing surfactant micelles (green) and dye molecules (blue). (a), (b) and (c) depict different possibilities for the assembly between dye and surfactant micelles. The left picture always represents the full contrast case, whereas the surfactant is contrast matched to the solvent in the right picture.

SANS contrast variation is an invaluable tool for studying multicomponent systems. It permits to eliminate the contrast between certain components of the system so that only the scattering signal arising due to structures formed by the component of interest is observed. If the scattering contrast between two components is completely eliminated, these components are designated “contrast-matched”. The principle of contrast matching is illustrated in Figure 8 for the example of dye-surfactant solutions. Figure 8a, b and c indicate possible assembly situations in dye-surfactant solutions. In each case, the left image shows the “full contrast” case where both, dye and surfactant exhibit non-zero contrast to the solvent. The image to the right displays the “surfactant matched” case, where the scattering contrast between the surfactant and the solvent was eliminated by isotopic substitution. As a result, only the scattering signal arising due to scattering of the dye is observed. Contrast matching represents a specific case of contrast variation. However, in some cases a variation of contrast conditions without achieving zero contrast suffices to answer a given research question. In this case, a global analysis of SANS curves obtained from the same system at different contrasts is frequently performed. A common way to execute contrast variation in aqueous systems is the variation of the solvent  $H_2O/D_2O$  ratio. As hydrogen and deuterium strongly differ in their scattering lengths, a wide range of contrasts is made available by this approach, which suffices for most soft matter systems. An alternative way to perform contrast variation is the use of selectively deuterated scatterers or scatterers, where other elements were isotopically substituted.

SANS contrast variation was successfully employed to study micellar solutions and other systems containing amphiphilic molecules. Investigations exploiting this technique range from investigations on the morphology of pure surfactant<sup>121,165,166</sup> or block-copolymer micelles<sup>167–169</sup>



and mixed micellar systems<sup>170–175</sup> to surfactant-stabilized emulsions.<sup>176–178</sup> However, only few examples for the application of SANS contrast variation for the localisation of additives in assemblies of amphiphilic molecules exist. Causse et al. localized tributylphosphate in the core of PEO-PPO-PEO block copolymers by eliminating the scattering contrast between the polymer and the solvent upon preparation of the solvent with a suitable H<sub>2</sub>O/D<sub>2</sub>O mixture.<sup>179</sup> As completely deuterated tributylphosphate was used for this investigation, the contrast difference between the PEO block, the PPO block and the solvent was rendered negligible compared to the high contrast between the deuterated tributylphosphate and the solvent. Garg et al. found, that cholesterol does not form stable nanodomains in phospholipid vesicles by contrast matching solvent and phospholipid.<sup>180</sup> Zhang et al. investigated the co-assembly of the protein Hydrophobin with the cationic surfactant CTAB, the anionic surfactant sodiumdodecylsulphate (SDS) or the non-ionic surfactant C<sub>12</sub>E<sub>6</sub>.<sup>181</sup> They recorded SANS curves from solutions containing the hydrogenated Hydrophobin and either the hydrogenated or deuterated surfactant in H<sub>2</sub>O or D<sub>2</sub>O as a solvent. However, no contrast matching was performed. Considering SANS curves collected under varying contrast conditions, Zhang et al. located the protein in the outer shell of all globular surfactant micelles. Finally, Penfold et al. located small fragrance molecules in micelles of the non-ionic surfactant C<sub>12</sub>E<sub>12</sub>.<sup>182</sup> Similar to Zhang et al, Penfold et al. did not perform precise contrast matching, but recorded SANS curves at varying contrast conditions, employing completely hydrogenated and alkyl-chain deuterated C<sub>12</sub>E<sub>12</sub>. This strategy permitted the localization of rather hydrophobic molecules in the core of the surfactant micelle. The more hydrophilic phenyl ethanol, however, was not unambiguously located with this technique and its location assumed to be on the hydrophilic/hydrophobic interface of the surfactant micelle based on comparison to literature.

The latter two studies could have benefited from precise contrast matching between the surfactant and the surrounding solvent. Observing only additive scattering could have given access to the precise additive solubilisation locus.

To summarize this section, SANS contrast variation is a powerful technique to determine the distribution of individual components in a multicomponent system while simultaneously obtaining information on overall assembly structure. Even though valuable information can already be obtained without contrast matching, contrast matching should be preferred as it results in a more straightforward interpretation of scattering curves and more precise information on the system.

Despite its efficiency for the elucidation of the morphology of assembling systems, SANS contrast variation suffers from limited accessibility. Firstly, SANS experiments need to be performed at a neutron facility. Secondly, deuterated material needs to be available in sufficient quality and quantity for SANS experiments. This is a minor problem if SANS contrast variation can be performed by variation of the H<sub>2</sub>O/D<sub>2</sub>O ratio of an aqueous solvent, but may require elaborate synthesis procedures if one of the assembling molecules is to be deuterated. Lastly, the interpretation of SANS curves obtained at different contrast conditions may be hampered by isotope effects, which strongly depend on the system. For determining the extent of these effects, additional small-angle X-Ray scattering (SAXS) measurements could be necessary.

### **1.5. Objective of the thesis**

The objective of this dissertation is the investigation of the self-assembly of the three hair dyes shown in Figure 2 and their co-assembly with different surfactants. The investigation addresses both, the morphology of co-assemblies and the determination of the distribution of dye molecules within these co-assemblies. For the latter, SANS contrast matching shall be established as a suitable method for the localisation of small additives in micelles of low molecular weight surfactant.

The efficiency of hair dyeing may be hampered by dye self-assembly, which reduces the rate of diffusion into the hair fibre. If a mixture of dyes is applied, differences in the penetration efficiency of different dyes lead to a distortion of the final hair colour compared to the initially anticipated colour shade of the dye mixture. It is therefore crucial to understand differences in the self-assembly of the dyes Yellow, Blue and Red (Figure 2), which are usually applied in a mixture.

Furthermore, knowledge about the interaction between dyes and other key components of the dyeing liquor is needed, as they compete with interactions between dye and the hair fibre. Hair dyeing formulations often contain surfactants, which creates the need to well understand dye-surfactant interactions. This understanding can be obtained by determining the preferential solubilisation locus of the dye in a surfactant micelle. Such an approach permits the elucidation of intermolecular interactions responsible for dye-surfactant co-assembly. It may furthermore reveal the mechanism of concentration-induced morphological transitions of dye-surfactant co-assemblies based on the concept of the packing parameter (eq (2)). This is valuable, because the morphology of dye-surfactant assemblies dictates macroscopic rheological properties of dye-surfactant solutions, which are relevant for their application to the hair.

Dyeing formulations and hair care products contain different types of surfactant. Therefore, the interaction between hair dyes and differently charged surfactants needs to be studied to reveal a more complete picture of interactions that govern the formation of dye-surfactant co-assemblies. From a fundamental perspective, the investigation of solutions containing a cationic surfactant and negatively charged dyes is interesting with respect to the formation of insoluble salts from the oppositely charged species. From an application perspective on the other hand, the interaction between dyes and anionic or non-ionic surfactant is of higher relevance.

Concerning the durability of the hair colour and the development of suitable hair care products, an understanding of the pH-dependent interaction between dye and surfactant is imperative. Hair dyeing is usually performed at alkaline pH, whereas shampoos often possess a slightly acidic pH between 4.5 and 6.<sup>183,184</sup> The phenol group of the dye molecules shown in Figure 2 is deprotonated during dyeing at alkaline pH, but mostly protonated at slightly acidic pH. A variation in solution pH therefore entails a variation of the polarity of the dye molecules. This behaviour permits to study systematically the solubilisation locus of dye molecules with different polarity but the same chemical constitution in micelles of a non-pH-responsive surfactant by variation of the solution pH. Such an experiment may reveal different morphologies for dye-surfactant co-assemblies at varying pH due to the localisation of dye in different parts of the surfactant micelle.

## 1.6. References

- (1) Chen, Z.; Lohr, A.; Saha-Möller, C. R.; Würthner, F. Self-Assembled  $\pi$ -Stacks of Functional Dyes in Solution: Structural and Thermodynamic Features. *Chem. Soc. Rev.* **2009**, *38* (2), 564–584. <https://doi.org/10.1039/B809359H>.
- (2) Bialas, D.; Kirchner, E.; Röhr, M. I. S.; Würthner, F. Perspectives in Dye Chemistry: A Rational Approach toward Functional Materials by Understanding the Aggregate State. *J. Am. Chem. Soc.* **2021**, *143* (12), 4500–4518. <https://doi.org/10.1021/jacs.0c13245>.
- (3) Heyne, Belinda. Self-Assembly of Organic Dyes in Supramolecular Aggregates. *Photochem. Photobiol. Sci.* **2016**, No. 15, 1103–1114. <https://doi.org/10.1039/c6pp00221h>.
- (4) Rohatgi, K. K. Absorption Spectra of the Dimers of Ionic Dyes. *Journal of Molecular Spectroscopy* **1968**, *27* (1), 545–548. [https://doi.org/10.1016/0022-2852\(68\)90061-1](https://doi.org/10.1016/0022-2852(68)90061-1).
- (5) Cuétara-Guadarrama, F.; Vonlanthen, M.; Sorroza-Martínez, K.; González-Méndez, I.; Rivera, E. Photoisomerizable Azobenzene Dyes Incorporated into Polymers and Dendrimers. Influence of the Molecular Aggregation on the Nonlinear Optical Properties. *Dyes and Pigments* **2021**, *194*, 109551. <https://doi.org/10.1016/j.dyepig.2021.109551>.

- (6) Shao, C.; Grüne, M.; Stolte, M.; Würthner, F. Perylene Bisimide Dimer Aggregates: Fundamental Insights into Self-Assembly by NMR and UV/Vis Spectroscopy. *Chemistry – A European Journal* **2012**, *18* (43), 13665–13677. <https://doi.org/10.1002/chem.201201661>.
- (7) Kasha, M. Energy Transfer Mechanisms and the Molecular Exciton Model for Molecular Aggregates. *Radiation Research* **1963**, *20* (1), 55–70. <https://doi.org/10.2307/3571331>.
- (8) Würthner, F.; Thalacker, C.; Diele, S.; Tschierske, C. Fluorescent J-Type Aggregates and Thermotropic Columnar Mesophases of Perylene Bisimide Dyes. *Chemistry – A European Journal* **2001**, *7* (10), 2245–2253. [https://doi.org/10.1002/1521-3765\(20010518\)7:10<2245::AID-CHEM2245>3.0.CO;2-W](https://doi.org/10.1002/1521-3765(20010518)7:10<2245::AID-CHEM2245>3.0.CO;2-W).
- (9) Hu, X.; Ritz, T.; Damjanović, A.; Autenrieth, F.; Schulten, K. Photosynthetic Apparatus of Purple Bacteria. *Quarterly Reviews of Biophysics* **2002**, *35* (1), 1–62. <https://doi.org/10.1017/S0033583501003754>.
- (10) Tamiaki, H. Supramolecular Structure in Extramembraneous Antennae of Green Photosynthetic Bacteria. *Coordination Chemistry Reviews* **1996**, *148*, 183–197. [https://doi.org/10.1016/0010-8545\(95\)01188-9](https://doi.org/10.1016/0010-8545(95)01188-9).
- (11) Balaban, T. S.; Tamiaki, H.; Holzwarth, A. R. Chlorins Programmed for Self-Assembly. In *Supramolecular Dye Chemistry*; Würthner, F., Ed.; Topics in Current Chemistry; Springer: Berlin, Heidelberg, 2005; pp 1–38. <https://doi.org/10.1007/b137480>.
- (12) Würthner, F.; Kaiser, T. E.; Saha-Möller, C. R. J-Aggregates: From Serendipitous Discovery to Supramolecular Engineering of Functional Dye Materials. *Angewandte Chemie International Edition* **2011**, *50* (15), 3376–3410. <https://doi.org/10.1002/anie.201002307>.
- (13) Shanker, G.; Hegde, G.; Rodriguez-Abreu, C. Self-Assembly of Thiocyanine Dyes in Water for the Synthesis of Active Hybrid Nanofibres. *Liquid Crystals* **2016**, *43* (4), 473–483. <https://doi.org/10.1080/02678292.2015.1118770>.
- (14) Würthner, F.; Saha-Möller, C. R.; Fimmel, B.; Ogi, S.; Leowanawat, P.; Schmidt, D. Perylene Bisimide Dye Assemblies as Archetype Functional Supramolecular Materials. *Chem. Rev.* **2016**, *116* (3), 962–1052. <https://doi.org/10.1021/acs.chemrev.5b00188>.
- (15) Hämisch, Benjamin. Establishment of a Model for Self-Assembly Processes in Biological Systems. Dissertation, University of Paderborn, Paderborn, 2022.
- (16) Atkins, P. W.; De Paula, J. *Atkins' Physical Chemistry*, 10th ed.; Oxford University Press: Oxford ; New York, 2014.
- (17) McRae, E. G.; Kasha, M. THE MOLECULAR EXCITON MODEL\*\*Work Supported in Part by a Contract between the Division of Biology and Medicine, U.S. Atomic Energy Commission, and the Florida State University. In *Physical Processes in Radiation Biology*;

- Augenstein, L., Mason, R., Rosenberg, B., Eds.; Academic Press, 1964; pp 23–42.  
<https://doi.org/10.1016/B978-1-4831-9824-8.50007-4>.
- (18) Kasha, M.; Rawls, H. R.; El-Bayoumi, M. A. The exciton model in molecular spectroscopy. *Pure and Applied Chemistry* **1965**, *11* (3–4), 371–392.  
<https://doi.org/10.1351/pac196511030371>.
- (19) Rosen, M. J. *Surfactants and Interfacial Phenomena*, 3rd ed.; Wiley-Interscience; John Wiley & Sons, Inc: Hoboken, New Jersey, USA, 2004.
- (20) Behr, A.; Agar, D. W.; Jörisen, J.; Vorholt, A. J. *Einführung in die Technische Chemie*, 2. Auflage.; Springer Spektrum: Berlin, 2016.
- (21) Raffa, P. Design and Synthesis of Low Molecular Weight and Polymeric Surfactants for Enhanced Oil Recovery. In *Surfactants in Upstream E&P*; Solling, T., Shahzad Kamal, M., Shakil Hussain, S. M., Eds.; Springer International Publishing: Cham, 2021; pp 3–37.  
[https://doi.org/10.1007/978-3-030-70026-3\\_1](https://doi.org/10.1007/978-3-030-70026-3_1).
- (22) Marques, E. F.; Silva, B. F. B. Surfactant Self-Assembly. In *Encyclopedia of Colloid and Interface Science*; Tadros, T., Ed.; Springer: Berlin, Heidelberg, 2013; pp 1202–1241.  
[https://doi.org/10.1007/978-3-642-20665-8\\_169](https://doi.org/10.1007/978-3-642-20665-8_169).
- (23) Intermolecular and Surface Forces. In *Intermolecular and Surface Forces (Third Edition)*; Israelachvili, J. N., Ed.; Academic Press: Boston, 2011; p iii. <https://doi.org/10.1016/B978-0-12-391927-4.10024-6>.
- (24) Nagarajan, R. Molecular Packing Parameter and Surfactant Self-Assembly: The Neglected Role of the Surfactant Tail. *Langmuir* **2002**, *18* (1), 31–38.  
<https://doi.org/10.1021/la010831y>.
- (25) Zaldivar, G.; Conda-Sheridan, M.; Tagliacuzzi, M. Molecular Basis for the Morphological Transitions of Surfactant Wormlike Micelles Triggered by Encapsulated Nonpolar Molecules. *Langmuir* **2021**, *37* (10), 3093–3103. <https://doi.org/10.1021/acs.langmuir.0c03421>.
- (26) *Self-Assembly: From Surfactants to Nanoparticles*, First edition.; Nagarajan, R., Ed.; Wiley series on surface and interfacial chemistry; Wiley: Hoboken, NJ, 2019.
- (27) Dreiss, C. A. Chapter 1 Wormlike Micelles: An Introduction. In *Wormlike Micelles: Advances in Systems, Characterisation and Applications*; Soft Matter Series; Royal Society of Chemistry, 2017; pp 1–8.
- (28) Magnus Bergström, L. Second CMC in Surfactant Micellar Systems. *Current Opinion in Colloid & Interface Science* **2016**, *22*, 46–50. <https://doi.org/10.1016/j.cocis.2016.02.008>.

- (29) Bulut, S.; Hamit, J.; Olsson, U.; Kato, T. On the Concentration-Induced Growth of Nonionic Wormlike Micelles. *Eur. Phys. J. E* **2008**, *27* (3), 261–273. <https://doi.org/10.1140/epje/i2008-10379-2>.
- (30) Schurtenberger, P.; Cavaco, C.; Tiberg, F.; Regev, O. Enormous Concentration-Induced Growth of Polymer-like Micelles. *Langmuir* **1996**, *12* (12), 2894–2899. <https://doi.org/10.1021/la9508248>.
- (31) Porte, G.; Poggi, Y.; Appell, J.; Maret, G. Large Micelles in Concentrated Solutions. The Second Critical Micellar Concentration. *J. Phys. Chem.* **1984**, *88* (23), 5713–5720. <https://doi.org/10.1021/j150667a051>.
- (32) Imae, T.; Ikeda, S. Sphere-Rod Transition of Micelles of Tetradecyltrimethylammonium Halides in Aqueous Sodium Halide Solutions and Flexibility and Entanglement of Long Rodlike Micelles. *J. Phys. Chem.* **1986**, *90* (21), 5216–5223. <https://doi.org/10.1021/j100412a065>.
- (33) Khoshnood, A.; Lukanov, B.; Firoozabadi, A. Temperature Effect on Micelle Formation: Molecular Thermodynamic Model Revisited. *Langmuir* **2016**, *32* (9), 2175–2183. <https://doi.org/10.1021/acs.langmuir.6b00039>.
- (34) Lindman, B.; Karlström, G. Nonionic Polymers and Surfactants: Temperature Anomalies Revisited. *Comptes Rendus Chimie* **2009**, *12* (1), 121–128. <https://doi.org/10.1016/j.crci.2008.06.017>.
- (35) Lindman, B.; Medronho, B.; Karlström, G. Clouding of Nonionic Surfactants. *Current Opinion in Colloid & Interface Science* **2016**, *22*, 23–29. <https://doi.org/10.1016/j.cocis.2016.01.005>.
- (36) Bernheim-Groswasser, A.; Wachtel, E.; Talmon, Y. Micellar Growth, Network Formation, and Criticality in Aqueous Solutions of the Nonionic Surfactant C12E5. *Langmuir* **2000**, *16* (9), 4131–4140. <https://doi.org/10.1021/la991231q>.
- (37) Dharaiya, N.; Patel, U.; Ray, D.; K. Aswal, V.; V. Sastry, N.; Bahadur, P. Different PH Triggered Aggregate Morphologies in Sodium Oleate–Cationic Surfactants Mixed Systems. *New Journal of Chemistry* **2017**, *41* (17), 9142–9151. <https://doi.org/10.1039/C6NJ03871A>.
- (38) Myers, D. *Surfactant Science and Technology*, Fourth edition.; John Wiley & Sons, Inc: Hoboken, NJ, 2020.
- (39) Cummins, P. G.; Staples, E.; Penfold, J.; Heenan, R. K. The Geometry of Micelles of the Poly(Oxyethylene) Nonionic Surfactants C16E6 and C16E8 in the Presence of Electrolyte. *Langmuir* **1989**, *5* (5), 1195–1199. <https://doi.org/10.1021/la00089a012>.

- (40) Lin, Z.; Scriven, L. E.; Davis, H. T. Cryogenic Electron Microscopy of Rodlike or Wormlike Micelles in Aqueous Solutions of Nonionic Surfactant Hexaethylene Glycol Mono-hexadecyl Ether. *Langmuir* **1992**, *8* (9), 2200–2205. <https://doi.org/10.1021/la00045a021>.
- (41) A. Dreiss, C. Wormlike Micelles: Where Do We Stand? Recent Developments, Linear Rheology and Scattering Techniques. *Soft Matter* **2007**, *3* (8), 956–970. <https://doi.org/10.1039/B705775J>.
- (42) Ikeda, S.; Ozeki, S.; Hayashi, S. Size and Shape of Charged Micelles of Ionic Surfactants in Aqueous Salt Solutions. *Biophysical Chemistry* **1980**, *11* (3), 417–423. [https://doi.org/10.1016/0301-4622\(80\)87016-5](https://doi.org/10.1016/0301-4622(80)87016-5).
- (43) Herzog, B.; Huber, K.; Rennie, A. R. Characterization of Worm-like Micelles Containing Solubilized Dye-Molecules by Light Scattering Techniques. *Journal of Colloid and Interface Science* **1994**, *164* (2), 370–381. <https://doi.org/10.1006/jcis.1994.1179>.
- (44) Candau, S. J.; Hirsch, E.; Zana, R.; Adam, M. Network Properties of Semidilute Aqueous KBr Solutions of Cetyltrimethylammonium Bromide. *Journal of Colloid and Interface Science* **1988**, *122* (2), 430–440. [https://doi.org/10.1016/0021-9797\(88\)90377-3](https://doi.org/10.1016/0021-9797(88)90377-3).
- (45) Aswal, V. K.; Goyal, P. S. Role of Counterion Distribution on the Structure of Micelles in Aqueous Salt Solutions: Small-Angle Neutron Scattering Study. *Chemical Physics Letters* **2002**, *357* (5), 491–497. [https://doi.org/10.1016/S0009-2614\(02\)00558-4](https://doi.org/10.1016/S0009-2614(02)00558-4).
- (46) Jensen, G. V.; Lund, R.; Gummel, J.; Narayanan, T.; Pedersen, J. S. Monitoring the Transition from Spherical to Polymer-like Surfactant Micelles Using Small-Angle X-Ray Scattering. *Angewandte Chemie* **2014**, *126* (43), 11708–11712. <https://doi.org/10.1002/ange.201406489>.
- (47) Bergström, L. M. A Theoretical Investigation of the Influence of the Second Critical Micelle Concentration on the Solubilization Capacity of Surfactant Micelles. *AIP Advances* **2018**, *8* (5), 055136. <https://doi.org/10.1063/1.5027062>.
- (48) Imae, T.; Abe, A.; Taguchi, Y.; Ikeda, S. Solubilization of a Water-Insoluble Dye in Aqueous Solutions of Dodecyltrimethylammonium Halides, and Its Relation to Micelle Size and Shape. *Journal of Colloid and Interface Science* **1986**, *109* (2), 567–575. [https://doi.org/10.1016/0021-9797\(86\)90338-3](https://doi.org/10.1016/0021-9797(86)90338-3).
- (49) Shiloach, A.; Blankshtein, D. Predicting Micellar Solution Properties of Binary Surfactant Mixtures. *Langmuir* **1998**, *14* (7), 1618–1636. <https://doi.org/10.1021/la971151r>.
- (50) Rehman, A.; Usman, M.; Bokhari, T. H.; Haq, A. ul; Saeed, M.; Rahman, H. M. A. U.; Siddiq, M.; Rasheed, A.; Nisa, M. U. The Application of Cationic-Nonionic Mixed Micellar Media for

- Enhanced Solubilization of Direct Brown 2 Dye. *Journal of Molecular Liquids* **2020**, *301*, 112408. <https://doi.org/10.1016/j.molliq.2019.112408>.
- (51) Noor, S.; Babar Taj, M. Mixed-Micellar Approach for Enhanced Dye Entrapment: A Spectroscopic Study. *Journal of Molecular Liquids* **2021**, 116701. <https://doi.org/10.1016/j.molliq.2021.116701>.
- (52) Bergström, M.; Pedersen, J. S. Formation of Tablet-Shaped and Ribbonlike Micelles in Mixtures of an Anionic and a Cationic Surfactant. *Langmuir* **1999**, *15* (7), 2250–2253. <https://doi.org/10.1021/la981495x>.
- (53) Schmölzer, St.; Gräbner, D.; Gradzielski, M.; Narayanan, T. Millisecond-Range Time-Resolved Small-Angle X-Ray Scattering Studies of Micellar Transformations. *Phys. Rev. Lett.* **2002**, *88* (25), 258301. <https://doi.org/10.1103/PhysRevLett.88.258301>.
- (54) Jensen, G. V.; Lund, R.; Narayanan, T.; Pedersen, J. S. Transformation from Globular to Cylindrical Mixed Micelles through Molecular Exchange That Induces Micelle Fusion. *J. Phys. Chem. Lett.* **2016**, *7* (11), 2039–2043. <https://doi.org/10.1021/acs.jpcllett.6b00767>.
- (55) Irshad, S.; Sultana, H.; Usman, M.; Ahmad, M.; Al-Hussain, S. A.; Zaki, M. E. A. Enhanced Solubilization and Encapsulation of Direct Dyes through Self-Assembled Single and Mixed Micellar Nanocarriers. *Environmental Technology & Innovation* **2023**, 103061. <https://doi.org/10.1016/j.eti.2023.103061>.
- (56) Mao, M.; Huang, J.; Zhu, B.; Yin, H.; Fu, H. The Structural Transition of Catanionic Vesicles Induced by Toluene. *Langmuir* **2002**, *18* (8), 3380–3382. <https://doi.org/10.1021/la011787p>.
- (57) Creatto, E. J.; Okasaki, F. B.; Cardoso, M. B.; Sabadini, E. Wormlike Micelles of CTAB with Phenols and with the Corresponding Phenolate Derivatives - When Hydrophobicity and Charge Drive the Coacervation. *Journal of Colloid and Interface Science* **2022**, *627*, 355–366. <https://doi.org/10.1016/j.jcis.2022.07.044>.
- (58) Caetano, W.; Gelamo, E. L.; Tabak, M.; Itri, R. Chlorpromazine and Sodium Dodecyl Sulfate Mixed Micelles Investigated by Small Angle X-Ray Scattering. *Journal of Colloid and Interface Science* **2002**, *248* (1), 149–157. <https://doi.org/10.1006/jcis.2001.8164>.
- (59) Hassan, P. A.; Fritz, G.; Kaler, E. W. Small Angle Neutron Scattering Study of Sodium Dodecyl Sulfate Micellar Growth Driven by Addition of a Hydrotropic Salt. *Journal of Colloid and Interface Science* **2003**, *257* (1), 154–162. [https://doi.org/10.1016/S0021-9797\(02\)00020-6](https://doi.org/10.1016/S0021-9797(02)00020-6).
- (60) Silva, K. N.; Novoa-Carballal, R.; Drechsler, M.; Müller, A. H. E.; Penott-Chang, E. K.; Müller, A. J. The Influence of Concentration and PH on the Structure and Rheology of Cationic



- Surfactant/Hydrotrope Structured Fluids. *Colloids and Surfaces A: Physicochemical and Engineering Aspects* **2016**, *489*, 311–321. <https://doi.org/10.1016/j.colsurfa.2015.10.054>.
- (61) Rajput, S. M.; Gangele, K.; Kumar, S.; Aswal, V. K.; Mata, J. P.; Malek, N. I.; Kailasa, S. K.; Poluri, K. M. Nano-Vehicles for Drug Delivery Using Low-Cost Cationic Surfactants: A Drug Induced Structural Transitions. *ChemistrySelect* **2018**, *3* (32), 9454–9463. <https://doi.org/10.1002/slct.201801111>.
- (62) Hu, X.; Gong, H.; Li, Z.; Ruane, S.; Liu, H.; Pambou, E.; Bawn, C.; King, S.; Ma, K.; Li, P.; Padia, F.; Bell, G.; Lu, J. R. What Happens When Pesticides Are Solubilized in Nonionic Surfactant Micelles. *Journal of Colloid and Interface Science* **2019**, *541*, 175–182. <https://doi.org/10.1016/j.jcis.2019.01.056>.
- (63) Törnblom, M.; Henriksson, U. Effect of Solubilization of Aliphatic Hydrocarbons on Size and Shape of Rodlike C16TABr Micelles Studied by 2H NMR Relaxation. *J. Phys. Chem. B* **1997**, *101* (31), 6028–6035. <https://doi.org/10.1021/jp970899f>.
- (64) Vikholm, I.; Douhéret, G.; Backlund, S.; Høiland, H. Shape Transitions in the Aqueous Phase of the System Hexadecyltrimethylammonium Bromide—Hexanol—Water. *Journal of Colloid and Interface Science* **1987**, *116* (2), 582–587. [https://doi.org/10.1016/0021-9797\(87\)90153-6](https://doi.org/10.1016/0021-9797(87)90153-6).
- (65) Taddese, T.; Anderson, R. L.; Bray, D. J.; Warren, P. B. Recent Advances in Particle-Based Simulation of Surfactants. *Current Opinion in Colloid & Interface Science* **2020**, *48*, 137–148. <https://doi.org/10.1016/j.cocis.2020.04.001>.
- (66) Swope, W. C.; Johnston, M. A.; Duff, A. I.; McDonagh, J. L.; Anderson, R. L.; Alva, G.; Tek, A. T.; Maschino, A. P. Challenge to Reconcile Experimental Micellar Properties of the CnEm Nonionic Surfactant Family. *J. Phys. Chem. B* **2019**, *123* (7), 1696–1707. <https://doi.org/10.1021/acs.jpcc.8b11568>.
- (67) Zueva, O. S.; Rukhlov, V. S.; Zuev, Y. F. Morphology of Ionic Micelles as Studied by Numerical Solution of the Poisson Equation. *ACS Omega* **2022**, *7* (7), 6174–6183. <https://doi.org/10.1021/acsomega.1c06665>.
- (68) Barni, E.; Savarino, P.; Viscardi, G. Dye-Surfactant Interactions and Their Applications. *Acc. Chem. Res.* **1991**, *24* (4), 98–103. <https://doi.org/10.1021/ar00004a002>.
- (69) Kert, M.; Simončič, B. Importance of dye-surfactant interactions in dyeing. *Tekstilec* **2007**, No. 50, 187–207.
- (70) Hanyak, M.; Darhuber, A. A.; Ren, M. Surfactant-Induced Delay of Leveling of Inkjet-Printed Patterns. *Journal of Applied Physics* **2011**, *109* (7), 074905. <https://doi.org/10.1063/1.3560770>.

- (71) Smith, J. E. Effect of Surface-Active Agents in Dyeing. *Ind. Eng. Chem.* **1939**, *31* (1), 40–43. <https://doi.org/10.1021/ie50349a009>.
- (72) Delaney, M.J. The Sorption of Acid Dyes and Nonionic Surfactants on Polyamide and Wool Substrates. Dissertation, University of New South Wales, 1970.
- (73) Datyner, A.; Delaney, M. J.; Jima, T. The Interaction between Acid Dyes and Nonionic Surfactants and Its Effect on Sorption and Diffusion Behavior: Part III: Diffusion of Dyes into Polyamide 6 Films. *Textile Research Journal* **1973**, *43* (1), 48–53. <https://doi.org/10.1177/004051757304300107>.
- (74) Sultana, H.; Usman, M.; Ghaffar, A.; Bokhari, T. H.; Mansha, A.; Yusuf, A. Sustainable Application of Ionic Flocculation Method for Textile Effluent Treatment. In *Sustainable Practices in the Textile Industry*; John Wiley & Sons, Ltd, 2021; pp 253–272. <https://doi.org/10.1002/9781119818915.ch10>.
- (75) Allègre, C.; Moulin, P.; Maisseu, M.; Charbit, F. Treatment and Reuse of Reactive Dyeing Effluents. *Journal of Membrane Science* **2006**, *269* (1), 15–34. <https://doi.org/10.1016/j.memsci.2005.06.014>.
- (76) Rashid, T. U.; Kabir, S. M. F.; Biswas, M. C.; Bhuiyan, M. A. R. Sustainable Wastewater Treatment via Dye–Surfactant Interaction: A Critical Review. *Ind. Eng. Chem. Res.* **2020**, *59* (21), 9719–9745. <https://doi.org/10.1021/acs.iecr.0c00676>.
- (77) Verma, Y. Acute Toxicity Assessment of Textile Dyes and Textile and Dye Industrial Effluents Using *Daphnia Magna* Bioassay. *Toxicol Ind Health* **2008**, *24* (7), 491–500. <https://doi.org/10.1177/0748233708095769>.
- (78) Carvalho Barros, G. K. G.; Duarte, L. J. N.; Melo, R. P. F.; Lopes, F. W. B.; Barros Neto, E. L. Ionic Dye Removal Using Solvent-Assisted Ionic Micellar Flocculation. *J Polym Environ* **2022**, *30*, 2534–2546. <https://doi.org/10.1007/s10924-021-02360-7>.
- (79) Purkait, M. K.; DasGupta, S.; De, S. Removal of Dye from Wastewater Using Micellar-Enhanced Ultrafiltration and Recovery of Surfactant. *Separation and Purification Technology* **2004**, *37* (1), 81–92. <https://doi.org/10.1016/j.seppur.2003.08.005>.
- (80) Moreno, M.; Mazur, L. P.; Weschenfelder, S. E.; Regis, R. J.; de Souza, R. A. F.; Marinho, B. A.; da Silva, A.; de Souza, S. M. A. G. U.; de Souza, A. A. U. Water and Wastewater Treatment by Micellar Enhanced Ultrafiltration – A Critical Review. *Journal of Water Process Engineering* **2022**, *46*, 102574. <https://doi.org/10.1016/j.jwpe.2022.102574>.
- (81) Schwarze, M. Micellar-Enhanced Ultrafiltration (MEUF) – State of the Art. *Environ. Sci.: Water Res. Technol.* **2017**, *3* (4), 598–624. <https://doi.org/10.1039/C6EW00324A>.

- (82) Ahmad, A. L.; Puasa, S. W.; Zulkali, M. M. D. Micellar-Enhanced Ultrafiltration for Removal of Reactive Dyes from an Aqueous Solution. *Desalination* **2006**, *191* (1), 153–161. <https://doi.org/10.1016/j.desal.2005.07.022>.
- (83) Schwarze, M.; Schaefer, L.; Chiappisi, L.; Gradzielski, M. Micellar Enhanced Ultrafiltration (MEUF) of Methylene Blue with Carboxylate Surfactants. *Separation and Purification Technology* **2018**, *199*, 20–26. <https://doi.org/10.1016/j.seppur.2018.01.043>.
- (84) Sultana, H.; Bokhari, T. H.; Usman, M. Adsorptive Micellar Flocculation (Surfactant-Based Phase Separation Technique): Theory and Applications. *Journal of Molecular Liquids* **2021**, *323*, 115001. <https://doi.org/10.1016/j.molliq.2020.115001>.
- (85) Demissie, H.; Lu, S.; Jiao, R.; Liu, L.; Xiang, Y.; Ritigala, T.; Ajibade, F. O.; Mihiranga, H. K. M.; An, G.; Wang, D. Advances in Micro Interfacial Phenomena of Adsorptive Micellar Flocculation: Principles and Application for Water Treatment. *Water Research* **2021**, *202*, 117414. <https://doi.org/10.1016/j.watres.2021.117414>.
- (86) Mukerjee, P.; Mysels, K. J. A Re-Evaluation of the Spectral Change Method of Determining Critical Micelle Concentration. *J. Am. Chem. Soc.* **1955**, *77* (11), 2937–2943. <https://doi.org/10.1021/ja01616a003>.
- (87) Reeves, R. L.; Kaiser, R. S.; Mark, H. W. The Nature of Species Giving Spectral Changes in an Azo Dye on Interaction with Cationic Surfactants below the Critical Micelle Concentration. *Journal of Colloid and Interface Science* **1973**, *45* (2), 396–405. [https://doi.org/10.1016/0021-9797\(73\)90277-4](https://doi.org/10.1016/0021-9797(73)90277-4).
- (88) Hayashi, M. Interactions of Surface Active Agents with Congo Red. *BCSJ* **1961**, *34* (1), 119–123. <https://doi.org/10.1246/bcsj.34.119>.
- (89) Hiskey, C. F.; Downey, T. A. The Colloid Error of Indicators. *J. Phys. Chem.* **1954**, *58* (10), 835–840. <https://doi.org/10.1021/j150520a009>.
- (90) Zakrevskyy, Y.; Stumpe, J.; Faul, C. F. J. A Supramolecular Approach to Optically Anisotropic Materials: Photosensitive Ionic Self-Assembly Complexes. *Advanced Materials* **2006**, *18* (16), 2133–2136. <https://doi.org/10.1002/adma.200600631>.
- (91) Faul, C. F. J.; Antonietti, M. Facile Synthesis of Optically Functional, Highly Organized Nanostructures: Dye–Surfactant Complexes. *Chemistry – A European Journal* **2002**, *8* (12), 2764–2768. [https://doi.org/10.1002/1521-3765\(20020617\)8:12<2764::AID-CHEM2764>3.0.CO;2-X](https://doi.org/10.1002/1521-3765(20020617)8:12<2764::AID-CHEM2764>3.0.CO;2-X).
- (92) Guan, Y.; Antonietti, M.; Faul, C. F. J. Ionic Self-Assembly of Dye–Surfactant Complexes: Influence of Tail Lengths and Dye Architecture on the Phase Morphology. *Langmuir* **2002**, *18* (15), 5939–5945. <https://doi.org/10.1021/la0257182>.

- (93) Cheng, X.; Peng, Y.; Gao, C.; Yan, Y.; Huang, J. Studying of 1-D Assemblies in Anionic Azo Dyes and Cationic Surfactants Mixed Systems. *Colloids and Surfaces A: Physicochemical and Engineering Aspects* **2013**, *422*, 10–18. <https://doi.org/10.1016/j.colsurfa.2012.12.062>.
- (94) Guan, Y.; Zakrevskyy, Y.; Stumpe, J.; Antonietti, M.; Faul, C. F. J. Perylenediimide-Surfactant Complexes: Thermotropic Liquid-Crystalline Materials via Ionic Self-Assembly. *Chem. Commun.* **2003**, No. 7, 894–895. <https://doi.org/10.1039/B211753C>.
- (95) Zakrevskyy, Y.; Faul, C. F. J.; Guan, Y.; Stumpe, J. Alignment of a Perylene-Based Ionic Self-Assembly Complex in Thermotropic and Lyotropic Liquid-Crystalline Phases. *Advanced Functional Materials* **2004**, *14* (9), 835–841. <https://doi.org/10.1002/adfm.200305194>.
- (96) Zakrevskyy, Y.; Stumpe, J.; Smarsly, B.; Faul, C. F. J. Photoinduction of Optical Anisotropy in an Azobenzene-Containing Ionic Self-Assembly Liquid-Crystalline Material. *Phys. Rev. E* **2007**, *75* (3), 031703. <https://doi.org/10.1103/PhysRevE.75.031703>.
- (97) Akpınar, E.; Topcu, G.; Reis, D.; Neto, A. M. F. Effect of the Anionic Azo Dye Sunset Yellow in Lyotropic Mixtures with Uniaxial and Biaxial Nematic Phases. *Journal of Molecular Liquids* **2020**, *318*, 114010. <https://doi.org/10.1016/j.molliq.2020.114010>.
- (98) Akpınar, E.; Uygur, N.; Ordu, O. D.; Reis, D.; Neto, A. M. F. Effect of the Surfactant Head-Group Size Dependence of the Dye-Surfactant Interactions on the Lyotropic Uniaxial to Biaxial Nematic Phase Transitions. *Journal of Molecular Liquids* **2021**, *332*, 115842. <https://doi.org/10.1016/j.molliq.2021.115842>.
- (99) Akpınar, E.; Uygur, N.; Topcu, G.; Lavrentovich, O. D.; Martins Figueiredo Neto, A. Gemini Surfactant Behavior of Conventional Surfactant Dodecyltrimethylammonium Bromide with Anionic Azo Dye Sunset Yellow in Aqueous Solutions. *Journal of Molecular Liquids* **2022**, 119556. <https://doi.org/10.1016/j.molliq.2022.119556>.
- (100) Garcia, M. E. D.; Sanz-Medel, A. Dye-Surfactant Interactions: A Review. *Talanta* **1986**, *33* (3), 255–264. [https://doi.org/10.1016/0039-9140\(86\)80060-1](https://doi.org/10.1016/0039-9140(86)80060-1).
- (101) Rehman, A.; Nisa, M. U.; Usman, M.; Ahmad, Z.; Bokhari, T. H.; Rahman, H. M. A. U.; Rasheed, A.; Kiran, L. Application of Cationic-Nonionic Surfactant Based Nanostructured Dye Carriers: Mixed Micellar Solubilization. *Journal of Molecular Liquids* **2021**, 115345. <https://doi.org/10.1016/j.molliq.2021.115345>.
- (102) Ghosh, D. C.; Sen, P. K.; Pal, B. Evidence of Formation of Dye–Surfactant Ion Pair Micelle in the Anionic Surfactant Mediated Alkaline Fading of Methyl Violet Carbocation. *International Journal of Chemical Kinetics* **2021**, *53* (11), 1228–1238. <https://doi.org/10.1002/kin.21528>.

- (103) Göktürk, S.; Keskin, G.; Talman, R. Y. C.; Çakır, N. Spectroscopic and Conductometric Studies on the Interactions of Thionine with Anionic and Nonionic Surfactants. *Coloration Technology* **2017**, *133* (5), 362–368. <https://doi.org/10.1111/cote.12284>.
- (104) Kurniasih, I. N.; Liang, H.; Mohr, P. C.; Khot, G.; Rabe, J. P.; Mohr, A. Nile Red Dye in Aqueous Surfactant and Micellar Solution. *Langmuir* **2015**, *31* (9), 2639–2648. <https://doi.org/10.1021/la504378m>.
- (105) Nazar, M. F.; Shah, S. S.; Khosa, M. A. Interaction of Azo Dye with Cationic Surfactant Under Different PH Conditions. *Journal of Surfactants and Detergents* **2010**, *13* (4), 529–537. <https://doi.org/10.1007/s11743-009-1177-8>.
- (106) Karukstis, K. K.; Savin, D. A.; Loftus, C. T.; D'Angelo, N. D. Spectroscopic Studies of the Interaction of Methyl Orange with Cationic Alkyltrimethylammonium Bromide Surfactants. *Journal of Colloid and Interface Science* **1998**, *203* (1), 157–163. <https://doi.org/10.1006/jcis.1998.5494>.
- (107) Mukerjee, Pasupati. Use of Ionic Dyes in Analysis of Ionic Surfactants and Other Ionic Organic Compounds. *Anal. Chem.* **1956**, *28* (5), 870–873. <https://doi.org/10.1021/ac60113a026>.
- (108) Saha, M.; Biswas, N.; Hussain, S. A.; Bhattacharjee, D. Micellar Effect of CTAB on Phenol Red Sodium Salt: A Model System May Be Used for Cell Membrane Study. *Materials Today: Proceedings* **2021**. <https://doi.org/10.1016/j.matpr.2020.10.1008>.
- (109) Piñeiro, L.; Novo, M.; Al-Soufi, W. Fluorescence Emission of Pyrene in Surfactant Solutions. *Advances in Colloid and Interface Science* **2015**, *215*, 1–12. <https://doi.org/10.1016/j.cis.2014.10.010>.
- (110) Robbins, C.R. Dyeing Human Hair. In *Chemical and Physical Behavior of Human Hair*; Springer Berlin Heidelberg: Berlin Heidelberg, 2012; pp 445–488.
- (111) Morel, O. J. X.; Christie, R. M. Current Trends in the Chemistry of Permanent Hair Dyeing. *Chem. Rev.* **2011**, *111* (4), 2537–2561. <https://doi.org/10.1021/cr1000145>.
- (112) Guerra-Tapia, A.; Gonzalez-Guerra, E. Hair Cosmetics: Dyes. *Actas Dermosifiliogr.* **2014**, *105* (9), 833–839.
- (113) Yun, K.; Ahn, C. Effect of Surfactant Type on the Dyeability and Color Resistance of Semi-Permanent Basic Hair Dye. *Fashion and Textiles* **2023**, *10* (1), 4. <https://doi.org/10.1186/s40691-022-00326-4>.
- (114) Kruś, S.; Majewski, S. Principles of Direct Hair Dyestuffs Selection. *HPCI-CONGRESS 2008 PROCEEDINGS* **2008**, 136–141.

- (115) Rageliene, L.; Treigiene, Rase; Musnickas, Juozas. Physical Properties of Human Hair Dyed Using Nonionic Surfactants. *Materials Science* **2009**, *15* (3), 277–282.
- (116) Buncel, E.; Rajagopal, S. Solvatochromism and Solvent Polarity Scales. *Acc. Chem. Res.* **1990**, *23* (7), 226–231. <https://doi.org/10.1021/ar00175a004>.
- (117) Alessandrini, Aurora; Piraccini, Bianca Maria. Essential of Hair Care Cosmetics. *Cosmetics* **2016**, No. 3, 34. <https://doi.org/10.3390/cosmetics3040034>.
- (118) Li, L.; Yang, Y.; Dong, J.; Li, X. Azobenzene Dye Induced Micelle to Vesicle Transition in Cationic Surfactant Aqueous Solutions. *Journal of Colloid and Interface Science* **2010**, *343* (2), 504–509. <https://doi.org/10.1016/j.jcis.2009.11.056>.
- (119) Kumar, S.; Naqvi, A. Z.; Kabir-ud-Din. Micellar Morphology in the Presence of Salts and Organic Additives. *Langmuir* **2000**, *16* (12), 5252–5256. <https://doi.org/10.1021/la991071i>.
- (120) Tehrani-Bagha, A. R.; Holmberg, K. Solubilization of Hydrophobic Dyes in Surfactant Solutions. *Materials* **2013**, *6* (2), 580–608. <https://doi.org/10.3390/ma6020580>.
- (121) Berr, S. S. Solvent Isotope Effects on Alkytrimethylammonium Bromide Micelles as a Function of Alkyl Chain Length. *J. Phys. Chem.* **1987**, *91* (18), 4760–4765. <https://doi.org/10.1021/j100302a024>.
- (122) He, M.; Zheng, W.; Wang, N.; Gao, H.; Ouyang, D.; Huang, Z. Molecular Dynamics Simulation of Drug Solubilization Behavior in Surfactant and Cosolvent Injections. *Pharmaceutics* **2022**, *14* (11), 2366. <https://doi.org/10.3390/pharmaceutics14112366>.
- (123) Lauth, G. J.; Kowalczyk, J. *Einführung in die Physik und Chemie der Grenzflächen und Kolloide*; Springer Berlin Heidelberg: Berlin, Heidelberg, 2016. <https://doi.org/10.1007/978-3-662-47018-3>.
- (124) Zana, R.; Yiv, S.; Strazielle, C.; Lianos, P. Effect of Alcohol on the Properties of Micellar Systems: I. Critical Micellization Concentration, Micelle Molecular Weight and Ionization Degree, and Solubility of Alcohols in Micellar Solutions. *Journal of Colloid and Interface Science* **1981**, *80* (1), 208–223. [https://doi.org/10.1016/0021-9797\(81\)90177-6](https://doi.org/10.1016/0021-9797(81)90177-6).
- (125) Candau, S.; Zana, R. Effect of Alcohols on the Properties of Micellar Systems: III. Elastic and Quasielastic Light Scattering Study. *Journal of Colloid and Interface Science* **1981**, *84* (1), 206–219. [https://doi.org/10.1016/0021-9797\(81\)90277-0](https://doi.org/10.1016/0021-9797(81)90277-0).
- (126) Hedin, N.; Sitnikov, R.; Furó, I.; Henriksson, U.; Regev, O. Shape Changes of C16TABr Micelles on Benzene Solubilization. *J. Phys. Chem. B* **1999**, *103* (44), 9631–9639. <https://doi.org/10.1021/jp991686o>.
- (127) Irshad, S.; Sultana, H.; Usman, M.; Saeed, M.; Akram, N.; Yusaf, A.; Rehman, A. Solubilization of Direct Dyes in Single and Mixed Surfactant System: A Comparative Study.

*Journal of Molecular Liquids* **2021**, *321*, 114201.  
<https://doi.org/10.1016/j.molliq.2020.114201>.

- (128) Zaldivar, G.; Perez Sirkin, Y. A.; Debais, G.; Fiora, M.; Missoni, L. L.; Gonzalez Solveyra, E.; Tagliazucchi, M. Molecular Theory: A Tool for Predicting the Outcome of Self-Assembly of Polymers, Nanoparticles, Amphiphiles, and Other Soft Materials. *ACS Omega* **2022**, *7* (43), 38109–38121. <https://doi.org/10.1021/acsomega.2c04785>.
- (129) Mchedlov-Petrosyan, N. O.; Farafonov, V. S.; Cheipesh, T. A.; Shekhovtsov, S. V.; Nerukh, D. A.; Lebed, A. V. In Search of an Optimal Acid-Base Indicator for Examining Surfactant Micelles: Spectrophotometric Studies and Molecular Dynamics Simulations. *Colloids and Surfaces A: Physicochemical and Engineering Aspects* **2019**, *565*, 97–107. <https://doi.org/10.1016/j.colsurfa.2018.12.048>.
- (130) Farafonov, V. S.; Lebed, A. V.; Mchedlov-Petrosyan, N. O. Computing PKa Shifts Using Traditional Molecular Dynamics: Example of Acid–Base Indicator Dyes in Organized Solutions. *J. Chem. Theory Comput.* **2020**, *16* (9), 5852–5865. <https://doi.org/10.1021/acs.jctc.0c00231>.
- (131) Farafonov, V.; Lebed, A.; Khimenko, N. L.; Mchedlov-Petrosyan, N. Molecular Dynamics Study of an Acid-Base Indicator Dye in Triton X-100 Non-Ionic Micelles. *Voprosy Khimii i Khimicheskoi Tekhnologii* **2020**, 97–103. <https://doi.org/10.32434/0321-4095-2019-128-1-97-103>.
- (132) Berendsen, H. J. C. Molecular Dynamics Simulations: The Limits and Beyond. In *Computational Molecular Dynamics: Challenges, Methods, Ideas*; Deuffhard, P., Hermans, J., Leimkuhler, B., Mark, A. E., Reich, S., Skeel, R. D., Eds.; Lecture Notes in Computational Science and Engineering; Springer: Berlin, Heidelberg, 1999; pp 3–36. [https://doi.org/10.1007/978-3-642-58360-5\\_1](https://doi.org/10.1007/978-3-642-58360-5_1).
- (133) Consta, S.; In Oh, M.; Kwan, V.; Malevanets, A. Strengths and Weaknesses of Molecular Simulations of Electrosprayed Droplets. *J. Am. Soc. Mass Spectrom.* **2018**, *29* (12), 2287–2296. <https://doi.org/10.1007/s13361-018-2039-2>.
- (134) Tokiwa, F. Solubilization Behavior of Sodium Dodecylpolyoxyethylene Sulfates in Relation to Their Polyoxyethylene Chain Lengths. *J. Phys. Chem.* **1968**, *72* (4), 1214–1217. <https://doi.org/10.1021/j100850a024>.
- (135) Heindl, A.; Strnad, J.; Kohler, H. H. Effect of Aromatic Solubilizates on the Shape of CTABr Micelles. *J. Phys. Chem.* **1993**, *97* (3), 742–746. <https://doi.org/10.1021/j100105a035>.
- (136) Simon, S. A.; McDaniel, R. V.; McIntosh, T. J. Interaction of Benzene with Micelles and Bilayers. *J. Phys. Chem.* **1982**, *86* (8), 1449–1456. <https://doi.org/10.1021/j100397a048>.

- (137) Choi, T.-S.; Shimizu, Y.; Shirai, H.; Hamada, K. Solubilization of Disperse Dyes in Cationic Gemini Surfactant Micelles. *Dyes and Pigments* **2000**, *45* (2), 145–152. [https://doi.org/10.1016/S0143-7208\(00\)00015-2](https://doi.org/10.1016/S0143-7208(00)00015-2).
- (138) Tehrani-Bagha, A. R.; Singh, R. G.; Holmberg, K. Solubilization of Two Organic Dyes by Cationic Ester-Containing Gemini Surfactants. *Journal of Colloid and Interface Science* **2012**, *376* (1), 112–118. <https://doi.org/10.1016/j.jcis.2012.02.016>.
- (139) Petcu, A. R.; Rogozea, E. A.; Lazar, C. A.; Olteanu, N. L.; Meghea, A.; Mihaly, M. Specific Interactions within Micelle Microenvironment in Different Charged Dye/Surfactant Systems. *Arabian Journal of Chemistry* **2016**, *9* (1), 9–17. <https://doi.org/10.1016/j.arabjc.2015.09.009>.
- (140) Claridge, T. D. W. Introducing High-Resolution NMR. In *High-Resolution NMR Techniques in Organic Chemistry*; Tetrahedron Organic Chemistry Series; Elsevier, 2009; Vol. 27, pp 11–34. [https://doi.org/10.1016/S1460-1567\(08\)10002-2](https://doi.org/10.1016/S1460-1567(08)10002-2).
- (141) Lambert, J. B. *Spektroskopie: Strukturaufklärung in der Organischen Chemie*; Pearson, Higher Education, 2012.
- (142) Edwards, D. J.; Jones, J. W.; Lozman, O.; Ormerod, A. P.; Sinyureva, M.; Tiddy, G. J. T. Chromonic Liquid Crystal Formation by Edicol Sunset Yellow. *J. Phys. Chem. B* **2008**, *112* (46), 14628–14636. <https://doi.org/10.1021/jp802758m>.
- (143) Guo, L. N.; Arnaud, I.; Petit-Ramel, M.; Gauthier, R.; Monnet, C.; LePerchec, P.; Chevalier, Y. Solution Behavior of Dye-Surfactant Associations. *Journal of Colloid and Interface Science* **1994**, *163* (2), 334–346. <https://doi.org/10.1006/jcis.1994.1112>.
- (144) Eriksson, J. C.; Gillberg, G. NMR-Studies of the Solubilisation of Aromatic Compounds in Cetyltrimethylammonium Bromide Solution II. *Acta Chem. Scand.* **20** *1966*, *20* (8), 2019–2027. <https://doi.org/10.3891/acta.chem.scand.20-2019>.
- (145) Patel, V.; Dharaiya, N.; Ray, D.; Aswal, V. K.; Bahadur, P. PH Controlled Size/Shape in CTAB Micelles with Solubilized Polar Additives: A Viscometry, Scattering and Spectral Evaluation. *Colloids and Surfaces A: Physicochemical and Engineering Aspects* **2014**, *455*, 67–75. <https://doi.org/10.1016/j.colsurfa.2014.04.025>.
- (146) Onoda-Yamamuro, N.; Yamamuro, O.; Tanaka, N.; Nomura, H. NMR and Neutron Scattering Studies on Spherical and Rod-like Micelles of Dodecyltrimethylammonium Bromide in Aqueous Sodium Salicylate Solutions. *Journal of Molecular Liquids* **2005**, *117* (1), 139–145. <https://doi.org/10.1016/j.molliq.2004.08.009>.



- (147) Bachofer, S. J.; Turbitt, R. M. The Orientational Binding of Substituted Benzoate Anions at the Cetyltrimethyl Ammonium Bromide Interface. *Journal of Colloid and Interface Science* **1990**, *135* (2), 325–334. [https://doi.org/10.1016/0021-9797\(90\)90003-7](https://doi.org/10.1016/0021-9797(90)90003-7).
- (148) Padsala, S.; Dharaiya, N.; Sastry, N. V.; Aswal, V. K.; Bahadur, P. Microstructural Morphologies of CTAB Micelles Modulated by Aromatic Acids. *RSC Adv.* **2016**, *6* (107), 105035–105045. <https://doi.org/10.1039/C6RA24271E>.
- (149) Sen, I. D.; Semwal, D.; Jayaram, R. V. Interaction of Imidazolium Based Ionic Liquids with Aqueous Triton X-100 Surfactant: Clouding, Fluorescence and NMR Studies. *Journal of Molecular Liquids* **2019**, *293*, 111481. <https://doi.org/10.1016/j.molliq.2019.111481>.
- (150) Claridge, T. D. W. Correlations through Space: The Nuclear Overhauser Effect. In *High-Resolution NMR Techniques in Organic Chemistry*; Tetrahedron Organic Chemistry Series; Elsevier, 2009; Vol. 27, pp 247–302. [https://doi.org/10.1016/S1460-1567\(08\)10008-3](https://doi.org/10.1016/S1460-1567(08)10008-3).
- (151) Renshaw, M. P.; Day, I. J. NMR Characterization of the Aggregation State of the Azo Dye Sunset Yellow in the Isotropic Phase. *J. Phys. Chem. B* **2010**, *114* (31), 10032–10038. <https://doi.org/10.1021/jp104356m>.
- (152) Sabatino, P.; Szczygiel, A.; Sinnaeve, D.; Hakimhashemi, M.; Saveyn, H.; Martins, J. C.; Van der Meer, P. NMR Study of the Influence of PH on Phenol Sorption in Cationic CTAB Micellar Solutions. *Colloids and Surfaces A: Physicochemical and Engineering Aspects* **2010**, *370* (1), 42–48. <https://doi.org/10.1016/j.colsurfa.2010.08.042>.
- (153) Parekh, P.; Singh, K.; Marangoni, D. G.; Aswal, V. K.; Bahadur, P. Solubilization of Aromatic Hydrocarbons in Ethylene Oxide-Propylene Oxide Triblock Micelles: Location of Solubilizate and Its Effect on Micelle Size from 2D NMR and Scattering Techniques. *Journal of Surfactants and Detergents* **2012**, *15* (1), 23–32. <https://doi.org/10.1007/s11743-011-1268-1>.
- (154) Kaur, G.; Chiappisi, L.; Prévost, S.; Schweins, R.; Gradzielski, M.; Mehta, S. K. Probing the Microstructure of Nonionic Microemulsions with Ethyl Oleate by Viscosity, ROESY, DLS, SANS, and Cyclic Voltammetry. *Langmuir* **2012**, *28* (29), 10640–10652. <https://doi.org/10.1021/la300540d>.
- (155) Dharaiya, N.; Bahadur, P.; Singh, K.; Marangoni, D. G.; Bahadur, P. Light Scattering and NMR Studies of Triton X-100 Micelles in the Presence of Short Chain Alcohols and Ethoxylates. *Colloids and Surfaces A: Physicochemical and Engineering Aspects* **2013**, *436*, 252–259. <https://doi.org/10.1016/j.colsurfa.2013.06.014>.
- (156) Pan, A.; Sil, P.; Dutta, S.; Das, P. K.; Bhattacharya, S. C.; Rakshit, A. K.; Aswal, V. K.; Moulik, S. P. Micellization of Cetyltrimethylammonium Bromide: Effect of Small Chain Bola

- Electrolytes. *J. Phys. Chem. B* **2014**, *118* (11), 3041–3052. <https://doi.org/10.1021/jp4108427>.
- (157) Valero, M.; Castiglione, F.; Mele, A.; da Silva, M. A.; Grillo, I.; González-Gaitano, G.; Dreiss, C. A. Competitive and Synergistic Interactions between Polymer Micelles, Drugs, and Cyclodextrins: The Importance of Drug Solubilization Locus. *Langmuir* **2016**, *32* (49), 13174–13186. <https://doi.org/10.1021/acs.langmuir.6b03367>.
- (158) Chaghi, R.; de Ménorval, L.-C.; Charnay, C.; Derrien, G.; Zajac, J. Interactions of Phenol with Cationic Micelles of Hexadecyltrimethylammonium Bromide Studied by Titration Calorimetry, Conductimetry, and <sup>1</sup>H NMR in the Range of Low Additive and Surfactant Concentrations. *Journal of Colloid and Interface Science* **2008**, *326* (1), 227–234. <https://doi.org/10.1016/j.jcis.2008.07.035>.
- (159) *Neutrons, X-Rays, and Light: Scattering Methods Applied to Soft Condensed Matter*, 1st ed.; Lindner, P., Zemb, T., Eds.; North-Holland delta series; Elsevier: Amsterdam ; Boston, 2002.
- (160) Schärftl, W. *Light Scattering from Polymer Solutions and Nanoparticle Dispersions*; Springer Laboratory; Springer Berlin Heidelberg: Berlin, Heidelberg, 2007. <https://doi.org/10.1007/978-3-540-71951-9>.
- (161) Glatter, O.; Kratky, O.; Kratky, H. C. *Small Angle X-Ray Scattering*; Academic Press, 1982.
- (162) Grillo, I. Small-Angle Neutron Scattering and Applications in Soft Condensed Matter. In *Soft Matter Characterization*; Borsali, R., Pecora, R., Eds.; Springer Netherlands: Dordrecht, 2008; pp 723–782. [https://doi.org/10.1007/978-1-4020-4465-6\\_13](https://doi.org/10.1007/978-1-4020-4465-6_13).
- (163) Guinier, A.; Fournet, G. *Small-Angle Scattering of X-Rays*, 1st ed.; Structure of Matter Series; John Wiley & Sons, Inc: New York, London, 1955.
- (164) Sivia, D. S. *Elementary Scattering Theory. For X-Ray and Neutron Users*; Oxford University Press: Oxford ; New York, 2011.
- (165) Manet, S.; Cuvier, A.-S.; Valotteau, C.; Fadda, G. C.; Perez, J.; Karakas, E.; Abel, S.; Baccile, N. Structure of Bolaamphiphile Sophorolipid Micelles Characterized with SAXS, SANS, and MD Simulations. *J. Phys. Chem. B* **2015**, *119* (41), 13113–13133. <https://doi.org/10.1021/acs.jpcc.5b05374>.
- (166) Tabony, J. Structure of the Polar Head Layer and Water Penetration in a Cationic Micelle. *Molecular Physics* **1984**, *51* (4), 975–989. <https://doi.org/10.1080/00268978400100641>.
- (167) Pedersen, J. S.; Hamley, I. W.; Ryu, C. Y.; Lodge, T. P. Contrast Variation Small-Angle Neutron Scattering Study of the Structure of Block Copolymer Micelles in a Slightly Selective

- Solvent at Semidilute Concentrations. *Macromolecules* **2000**, *33* (2), 542–550. <https://doi.org/10.1021/ma990740w>.
- (168) Pedersen, J. S.; Svaneborg, C.; Almdal, K.; Hamley, I. W.; Young, R. N. A Small-Angle Neutron and X-Ray Contrast Variation Scattering Study of the Structure of Block Copolymer Micelles: Corona Shape and Excluded Volume Interactions. *Macromolecules* **2003**, *36* (2), 416–433. <https://doi.org/10.1021/ma0204913>.
- (169) Carl, N.; Prévost, S.; Schweins, R.; Huber, K. Contrast Variation of Micelles Composed of Ca<sup>2+</sup> and Block Copolymers of Two Negatively Charged Polyelectrolytes. *Colloid and Polymer Science* **2020**, *298* (7), 663–679. <https://doi.org/10.1007/s00396-019-04596-1>.
- (170) Hayter, B.; Hayoun, M.; Zemb, T. Neutron Scattering Study of Pentanol Solubilization in Sodium Octanoate Micelles. *Colloid & Polymer Sci* **1984**, *262* (10), 798–803. <https://doi.org/10.1007/BF01451710>.
- (171) Brasher, L. L.; Kaler, E. W. A Small-Angle Neutron Scattering (SANS) Contrast Variation Investigation of Aggregate Composition in Catanionic Surfactant Mixtures. *Langmuir* **1996**, *12* (26), 6270–6276. <https://doi.org/10.1021/la960493e>.
- (172) Almgren, M.; Garamus, V. M.; Asakawa, T.; Jiang, N. Contrast Variation SANS Investigation of Composition Distributions in Mixed Surfactant Micelles. *J. Phys. Chem. B* **2007**, *111* (25), 7133–7141. <https://doi.org/10.1021/jp070271x>.
- (173) Croce, V.; Cosgrove, T.; Dreiss, C. A.; Maitland, G.; Hughes, T. Mixed Spherical and Wormlike Micelles: A Contrast-Matching Study by Small-Angle Neutron Scattering. *Langmuir* **2004**, *20* (23), 9978–9982. <https://doi.org/10.1021/la048355+>.
- (174) Kancharla, S.; Bedrov, D.; Tsianou, M.; Alexandridis, P. Structure and Composition of Mixed Micelles Formed by Nonionic Block Copolymers and Ionic Surfactants in Water Determined by Small-Angle Neutron Scattering with Contrast Variation. *Journal of Colloid and Interface Science* **2022**, *609*, 456–468. <https://doi.org/10.1016/j.jcis.2021.10.176>.
- (175) Schmutzler, Tilo; Schindler, Torben; Schmiele, Martin; Appavou, Marie-Sousai; Lages, Sebastian; Kriele, Armin; Gilles, Ralph; Unruh, Tobias. The Influence of N-Hexanol on the Morphology and Composition of CTAB Micelles. *Colloids and Surfaces A* **2018**, *543*, 56–63. <https://doi.org/10.1016/j.colsurfa.2017.12.039>.
- (176) Grillo, I.; Levitz, P.; Zemb, Th. SANS Structural Determination of a Nonionic Surfactant Layer Adsorbed on Clay Particles. *Eur. Phys. J. B* **1999**, *10* (1), 29–34. <https://doi.org/10.1007/s100510050826>.
- (177) Jestin, J.; Simon, S.; Zupancic, L.; Barré, L. A Small Angle Neutron Scattering Study of the Adsorbed Asphaltene Layer in Water-in-Hydrocarbon Emulsions: Structural Description

- Related to Stability. *Langmuir* **2007**, *23* (21), 10471–10478. <https://doi.org/10.1021/la701193f>.
- (178) Endo, H.; Mihailescu, M.; Monkenbusch, M.; Allgaier, J.; Gompper, G.; Richter, D.; Jakobs, B.; Sottmann, T.; Strey, R.; Grillo, I. Effect of Amphiphilic Block Copolymers on the Structure and Phase Behavior of Oil–Water-Surfactant Mixtures. *J. Chem. Phys.* **2001**, *115* (1), 580–600. <https://doi.org/10.1063/1.1377881>.
- (179) Causse, J.; Oberdisse, J.; Jestin, J.; Lagerge, S. Small-Angle Neutron Scattering Study of Solubilization of Tributyl Phosphate in Aqueous Solutions of L64 Pluronic Triblock Copolymers. *Langmuir* **2010**, *26* (20), 15745–15753. <https://doi.org/10.1021/la1021164>.
- (180) Garg, S.; Castro-Roman, F.; Porcar, L.; Butler, P.; Bautista, P. J.; Krzyzanowski, N.; Perez-Salas, U. Cholesterol Solubility Limit in Lipid Membranes Probed by Small Angle Neutron Scattering and MD Simulations. *Soft Matter* **2014**, *10* (46), 9313–9317. <https://doi.org/10.1039/C4SM01219D>.
- (181) Zhang, X. L.; Penfold, J.; Thomas, R. K.; Tucker, I. M.; Petkov, J. T.; Bent, J.; Cox, A.; Grillo, I. Self-Assembly of Hydrophobin and Hydrophobin/Surfactant Mixtures in Aqueous Solution. *Langmuir* **2011**, *27* (17), 10514–10522. <https://doi.org/10.1021/la2020226>.
- (182) Penfold, J.; Tucker, I.; Green, A.; Grainger, D.; Jones, C.; Ford, G.; Roberts, C.; Hubbard, J.; Petkov, J.; Thomas, R. K.; Grillo, I. Impact of Model Perfumes on Surfactant and Mixed Surfactant Self-Assembly. *Langmuir* **2008**, *24* (21), 12209–12220. <https://doi.org/10.1021/la801662g>.
- (183) Harrison, S.; Sinclair, R. Hair Colouring, Permanent Styling and Hair Structure. *Journal of Cosmetic Dermatology* **2004**, No. 2, 180–185. <https://doi.org/10.1111/j.1473-2130.2004.00064.x>.
- (184) Klein, Ken. Shampoo Formulation: The Basics. *Cosmetics & Toiletries magazine* **2004**, *119* (5), 64–68.

## Chapter 2

### Synopsis

This dissertation includes three publications and one manuscript in preparation. The first two publications (Chapter 4 and Chapter 5) compare the self-assembly of the three direct dyes shown in Chapter 1 (Figure 2) and their co-assembly with the cationic surfactant dodecyltrimethylammoniumbromide (DTAB). The third publication and the manuscript in preparation (Chapter 6 and Chapter 7 respectively) provide a deeper understanding of the impact of the type of surfactant on the co-assembly with an anionic dye. To this end, the dye Blue is mixed with either the cationic surfactant DTAB or the non-ionic surfactant pentaethyleneglycolmonododecylether ( $C_{12}E_5$ ). Investigations on the co-assembly between the anionic dyes and anionic surfactants are restricted to the conditions of few preliminary experiments only, which include SANS curves from solutions containing Blue and sodiumdodecylsulphate (SDS) under alkaline conditions and light scattering experiments on solutions of Yellow and SDS. Due to the absence of interesting morphological transitions, no further SANS experiments were performed.

The pH-dependency of dye-surfactant co-assembly is studied on the example of Blue and  $C_{12}E_5$  in Chapter 7. The use of a non-ionic surfactant for studying pH-dependent interactions facilitates the design of experiments, because the self-assembly of  $C_{12}E_5$  does not depend on pH and the impact of small variations in ionic strength, which are introduced by pH-adjustment, is negligible. This would not necessarily be the case for micelles of ionic surfactants, which are usually highly responsive to changes in the ionic strength of the solution.<sup>1,2</sup>

#### 2.1 Dye self-assembly

The three dyes Yellow, Blue and Red shown in Figure 2 of Chapter 1 are used for the preparation of commercial dyeing formulations for direct dyeing, i.e. directly applying the molecules to the substrate.<sup>3</sup> For such an application the predictability of the final hair colour is important, which can be hampered by differences in the diffusion properties of constituent dye molecules. Therefore, it is crucial to study factors influencing the penetration of dye into a substrate fibre and to elucidate differences among dye molecules that are usually applied in a mixture. One of the most significant factors is dye self-aggregation.<sup>4,5</sup>

The dyes Yellow, Blue and Red all possess a 3-chloro-4-hydroxyphenylazo sub-unit as a common structural feature, and could therefore be expected to exhibit similar self-aggregation properties

in solution. However, the opposite is shown in Chapter 4, where strong differences in the self-aggregation of the three dyes are detected under the given solution conditions (Figure 1). The consideration of solvent composition and temperature is important, because dye solubility may vary as a function of these conditions.<sup>6</sup>

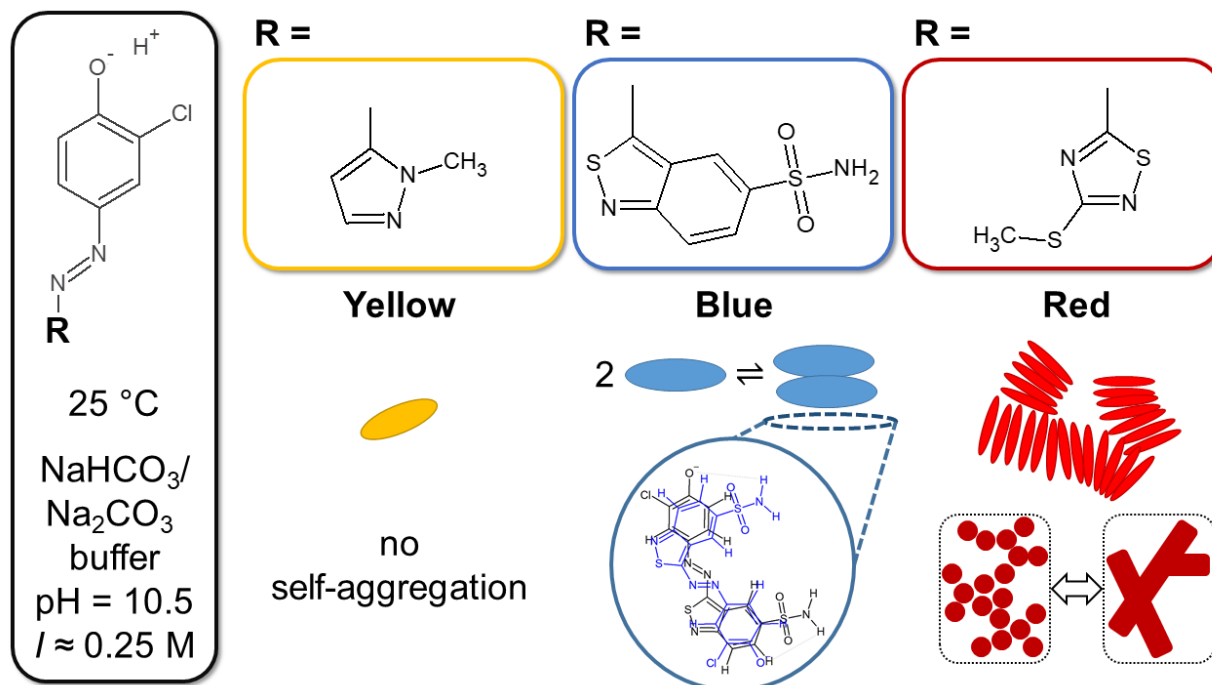


Figure 1: Overview on the self-assembly behaviour of the three direct dyes Yellow, Blue and Red in a  $\text{NaHCO}_3/\text{Na}_2\text{CO}_3$  buffer (pH = 10.5,  $I \approx 0.25$  M) at 25 °C. Adapted graphical abstract of Chapter 4.

Hair dyeing is usually performed at alkaline pH, leading to the deprotonation of the phenolic hydroxyl group of all three dyes, which renders them water soluble.<sup>7,8</sup> For this reason, an aqueous  $\text{NaHCO}_3/\text{Na}_2\text{CO}_3$  buffer with pH = 10.5 was chosen as a suitable solvent for the investigation on dye self-aggregation (Chapter 4) and for all other investigations, which did not consider pH-dependent behaviour (Chapter 5 and Chapter 6).

UV/vis spectroscopic investigations on the validity of Beer-Lambert's law in solutions containing dye at varying concentration provided a first insight into dye solubility and self-aggregation. Solutions of the dye Yellow follow Beer-Lambert's law up to a solubility limit of  $[\text{Yellow}] = 11$  mM, where visually observable precipitation occurs. This observation points towards molecular solubility of Yellow up to its solubility limit and was confirmed by the absence of a correlation function in dynamic light scattering experiments on corresponding solutions. The formation of soluble aggregates of Yellow is likely hampered by the impossibility to form  $\pi$ -stacks.  $\pi$ - $\pi$ -stacking between the aromatic phenolate groups is hindered by electrostatic repulsion between

the deprotonated hydroxyl groups of two molecules, whereas steric repulsion due to methyl-substitution inhibits  $\pi$ - $\pi$ -stacking between the pyrazole moieties.

For the dyes Blue and Red, UV/vis-spectroscopy suggested the formation of soluble aggregates due to a systematic deviation from Beer-Lambert's law at higher concentrations, but did not permit the detection of a solubility threshold up to a dye concentration of 25 mM.

Concentration-dependent UV/vis spectra of the dye Blue exhibit an isosbestic point. This enabled the quantitative evaluation of these spectra, assuming the self-aggregation of Blue into dimers (Figure 1). The dimerization constant of the underlying dimerization equilibrium was calculated to  $K_D = (728 \pm 8) \text{ L mol}^{-1}$ . The absorption spectrum of the dimer was calculated and evaluated according to exciton theory, leading to information on the geometry of Blue self-aggregation: In the model of non-parallel transition dipoles, Blue molecules form H-aggregates with a twist angle between their molecular polarization axes of  $42^\circ$  and an interplanar spacing of  $5.2 \text{ \AA}$ . The formation of dimers was confirmed by SANS, whereas ROESY confirmed the orientation of two Blue molecules within the dimer.  $\pi$ - $\pi$  stacking and the formation of hydrogen bonds between the phenolate oxygen and hydrogen atoms of the sulphonamide group are attractive driving forces for self-aggregation with the latter having a directing effect on the geometry of the assembly. Furthermore, electrostatic repulsion between negatively charged phenolate groups may be a second reason for the observed orientation of Blue molecules within the aggregate. The formation of larger aggregates could be inhibited by electrostatic repulsion and due to spatial requirements of the sulphonamide group.

The self-aggregation of Red is more complicated. Small-angle neutron scattering showed the formation of fractal-like aggregates, which are likely formed by short cylindrical segments. These segments consist of  $\pi$ - $\pi$  stacked Red molecules.  $\pi$ - $\pi$ -stacking is assumed to occur between 1,2,4-thiadiazole heterocyclic moieties. Compared to the pyrazole moiety in Yellow, this heterocycle is not directly substituted with a methyl group, but with a methanethiol group. The intermediate sulphur atom may introduce flexibility into the substituent, which compensates the effect of steric repulsion between  $\pi$ -stacked heterocycles.

To conclude, even though Yellow, Blue and Red possess a congruent 3-chloro-4-hydroxy-phenylazo moiety, they exhibit significantly different self-assembly properties. Yellow does not aggregate at all, Blue dimerizes and Red forms large aggregates. This observation is interesting from a fundamental point of view as well as with respect to applications because aggregation is undesirable in hair dyeing formulations.

## 2.2 Co-assembly between dye and surfactant

To reduce problems arising due to dye self-aggregation and to achieve desirable rheological properties, dyeing liquors often contain various additives such as salt, small organic molecules and surfactants.<sup>5</sup> Notably surfactants take up various functions in a dyeing bath. They act as wetting or antifoaming agents, slow down the absorption of the dye and, most importantly, increase solubility.<sup>9</sup> It is therefore crucial to not only investigate dye self-aggregation behaviour, but also to understand the interaction between dye molecules and surfactant in solution.

**Co-assembly between dye and the cationic surfactant DTAB:** Chapter 5 and Chapter 6 deal with the assembly between the direct dyes and the cationic surfactant DTAB. Electrostatic interactions between the negatively charged dye and the positively charged dodecyltrimethylammonium cation lead to phase separation of dye-DTAB solutions. Chapter 5 provides a comparative study on the stoichiometry of underlying interactions, whereas Chapter 6 presents a detailed investigation on morphological transitions including macroscopic phase separation.

In a first step, concentration-dependent phase diagrams of dye-DTAB solutions were recorded. Throughout almost the entire probed concentration range, phase separation occurs above a constant dye:DTAB ratio for all dyes (Table 1). This ratio is indicative of the binding stoichiometry between dye and DTAB in the coacervate phase for Yellow or for the solid precipitate for Blue and Red. The solid precipitate formed between Blue and DTAB was studied using wide-angle X-ray scattering (WAXS). Several diffraction peaks are visible in the WAXS curves, pointing towards crystalline ordering within the solid complexes.

In a second step, the interaction between dye and DTAB in the 1-phase region was probed. UV/vis spectroscopic investigations on solutions containing a given concentration of Blue, but varying concentrations of DTAB permitted deductions on the stoichiometry of dye-DTAB binding by assuming the following association equilibrium:



In eq (1), “Dye” refers to one dye molecule and “S” to one DTAB molecule. Eq (1) formally describes the co-assembly of one dye molecule with  $m$  DTAB molecules in equilibrium with monomeric dye and monomeric surfactant. This model well includes the possibility of  $\text{DyeS}_m$  assembling further, i.e. into larger co-assemblies with the same stoichiometry of  $\text{DyeS}_m$ . From UV/vis-spectroscopic analysis, equilibrium constants and stoichiometries 1: $m$  for dye:DTAB binding were obtained. The latter are compared to stoichiometries obtained from analysis of the



phase transition threshold in Table 1. The stoichiometry of dye:DTAB binding in solution decreases from 1:2 for Yellow over 1:3 for Blue to 1:4 for Red. The same relative trend was found for the stoichiometry of dye:DTAB binding in the 2-phase region by evaluation of corresponding phase diagrams.

The differences between Yellow, Blue and Red in their binding with DTAB demonstrate, that the one-fold negative charge of all dye molecules is not the only factor determining their interaction with the oppositely charged surfactant DTAB. Differences could be related to different steric requirements of the dyes, which affect the packing between dye molecules and DTAB. However, the packing of dye and DTAB molecules was not systematically investigated in the present dissertation.

Table 1: Phase separation and stoichiometry of dye-DTAB binding in the 2-phase region, which was obtained from an evaluation of the phase diagram and comparison to the stoichiometry of dye-DTAB association in solution. An aqueous NaHCO<sub>3</sub>/Na<sub>2</sub>CO<sub>3</sub> buffer (pH = 10.5, *I* ≈ 0.25 M) served as the solvent.

	Yellow	Blue	Red
Phase separation type	liquid/liquid	solid/liquid	solid/liquid
Stoichiometry at phase transition threshold Dye:DTAB	1:1.67	1:2.56	1:2.94
Stoichiometry of dye-DTAB association in solution Dye:DTAB	1:2	1:3	1:4

SANS on dye-DTAB solutions revealed the unidimensional growth of DTAB-micelles from an oblate, ellipsoidal shape to cylindrical micelles upon addition of dye. This growth is observed independent of which dye molecule is added, but its extent depends on the dye and its concentration. Figure 2 provides an overview on the length of dye-DTAB co-assemblies as a function of their composition. In all cases, micelles grow when the phase transition threshold is approached. In solutions of Blue and DTAB, the formation of wormlike micelles is observed close to the phase transition threshold. It is furthermore visible from Figure 2, that at any given DTAB concentration, micelles formed between Yellow and DTAB are the smallest, whereas the largest micelles are formed from Red and DTAB. The lengths of micelles therefore inversely correlate with binding stoichiometries given in Table 1.

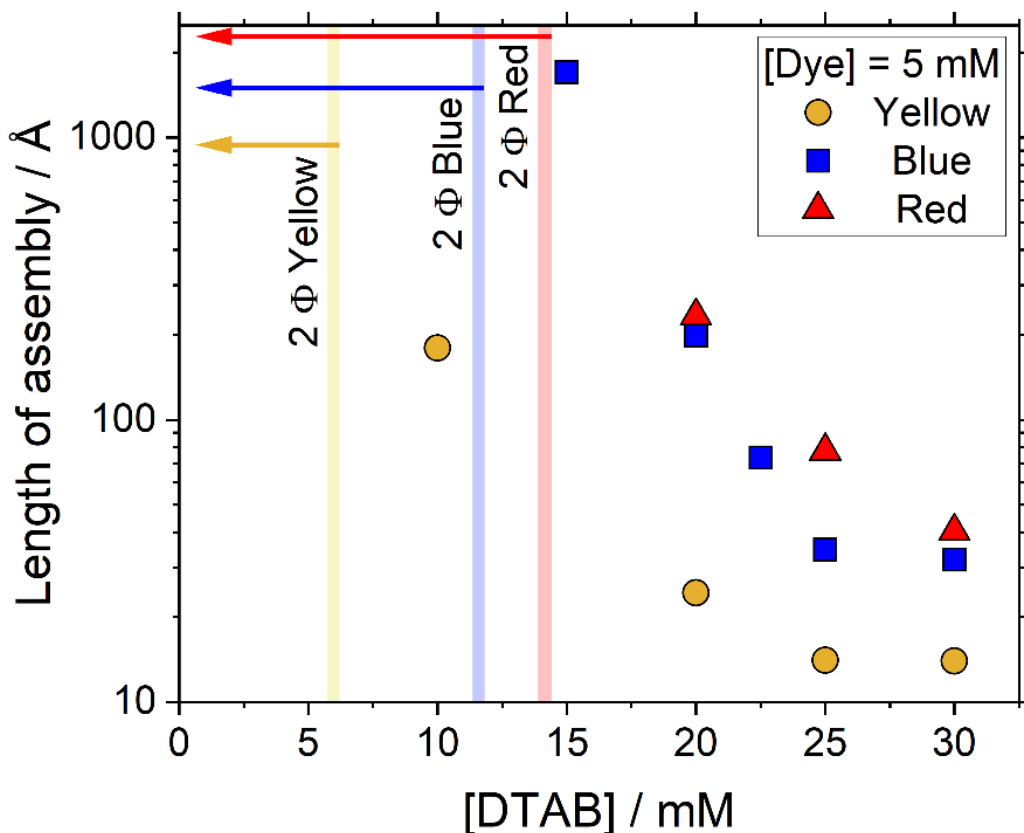


Figure 2: Length of dye-DTAB micelles determined by form factor fitting to experimental SANS curves from corresponding solutions. The dye concentration was  $[Dye] = 5 \text{ mM}$  in all cases. An aqueous  $\text{NaHCO}_3/\text{Na}_2\text{CO}_3$  buffer ( $\text{pD} = 10.7 \text{ mM}$ ,  $I \approx 0.25 \text{ M}$ ) prepared in  $\text{D}_2\text{O}$  served as a solvent. Measurements were performed at  $25 \text{ }^\circ\text{C}$ . Phase transition thresholds are indicated for each dye by a vertical line with a colour, which corresponds to the colour of the dye and symbol.

The reason for micellar growth close to the phase transition threshold is elucidated in Chapter 6 on the example of Blue-DTAB co-assemblies. For this purpose, Blue was located in DTAB micelles using a combination of SANS contrast matching and NOESY. The complementarity of both techniques permitted the unambiguous localization of the dye Blue in the outer- or head group region of DTAB micelles (Figure 3). Blue interacts with positively charged DTAB head groups and with up to the 4<sup>th</sup> methylene group of the neighbouring  $\text{C}_{12}$  alkyl chain. Based on the comparison of chemical shift changes in the  $^1\text{H-NMR}$  spectrum of Blue upon DTAB addition, the orientation of Blue in the DTAB head group layer was deduced and is displayed in Figure 3.

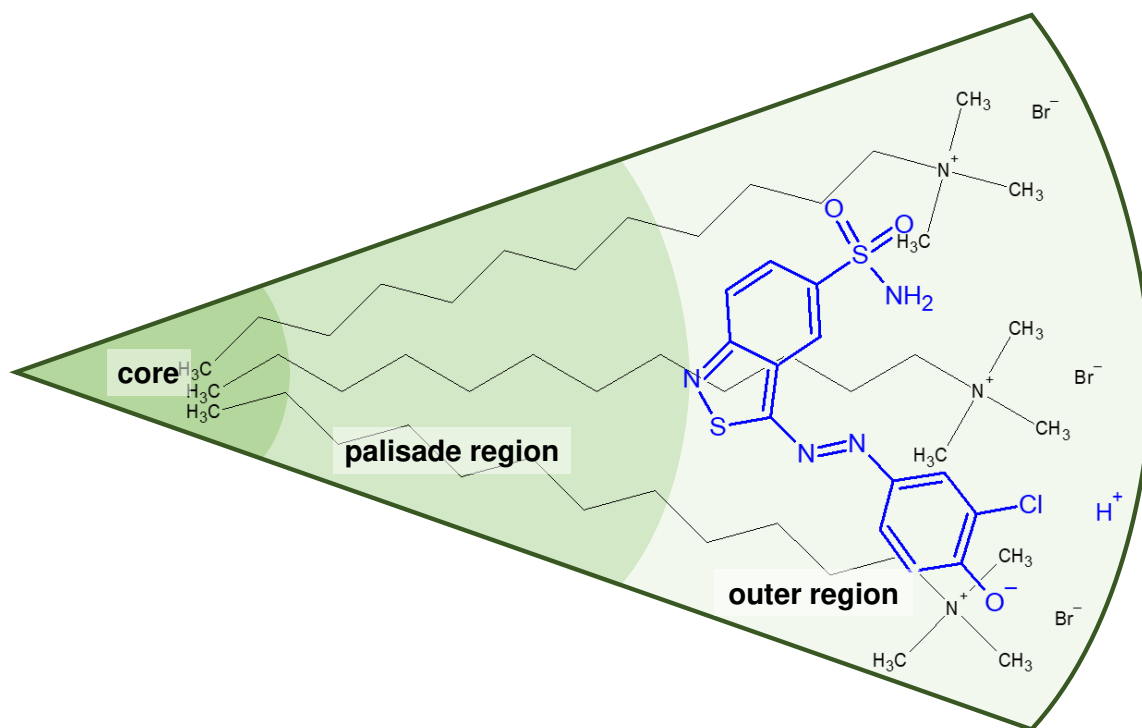


Figure 3: Location of the dye Blue in DTAB micelles deduced from SANS contrast variation and NOESY and its orientation deduced from  $^1\text{H-NMR}$  spectroscopy.

Following the localization of Blue close to the DTAB head group, the uniaxial growth of Blue-DTAB co-assemblies from ellipsoidal over cylindrical to wormlike structures is easily explained using the concept of the critical packing parameter  $P$  (Figure 4): Micellar growth, which correlates with an increase of the packing parameter, can be caused by: (1) A reduction in the effective surface area per DTAB molecule or (2) an increase of the DTAB hydrophobic chain volume. Following the localisation of Blue close to the surfactant head group, an increase in the DTAB hydrophobic chain volume upon addition of Blue may be ruled out as the principal cause for the ellipsoid-to-cylinder transition. Therefore, Blue addition must cause a reduction of the effective surface area per DTAB molecule. This likely results from a partial neutralisation of the positive DTAB head group charge upon interaction with negatively charged Blue, which overcompensates an increase in the DTAB head group size due to inclusion of the Blue molecule.

A similar mechanism is expected to cause morphological transitions observed in solutions containing Yellow and DTAB or Red and DTAB. However, the orientation and packing of these dyes within the DTAB outer layer might be different, causing binding stoichiometries to vary and morphological transitions to occur to a different extent.

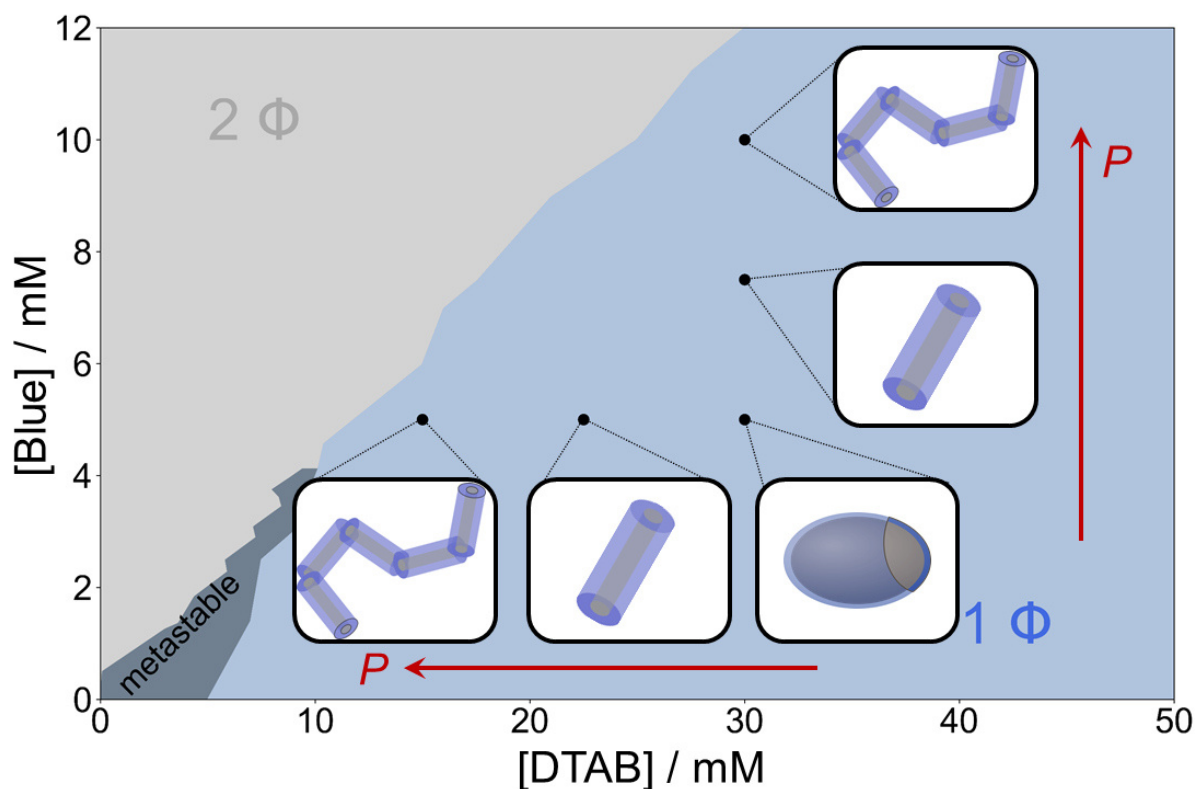


Figure 4: Composition-dependent morphology of Blue-DTAB co-assemblies in an alkaline  $\text{NaHCO}_3/\text{Na}_2\text{CO}_3$  buffer ( $\text{pD} = 10.7$ ,  $I \approx 0.25 \text{ M}$ ) prepared in  $\text{D}_2\text{O}$  at a temperature of  $25^\circ\text{C}$ . The blue shell in images representing assembly morphology indicate the location of Blue in the outer layer of DTAB micelles. Red arrows signal an increase of the critical packing parameter ( $P$ ).

It is worth mentioning, that the formation of wormlike micelles in solutions of Blue and DTAB was unambiguously confirmed with cryogenic transmission electron microscopy (cryo-TEM) images. Furthermore, the rheological behaviour of Blue-DTAB solutions was probed, showing an increase in solution viscosity close to the phase transition threshold, which is characteristic for the formation of wormlike micelles and their entanglement.

Apart from providing more detailed insights on the assembly between Blue and DTAB, Chapter 6 serves the additional purpose to demonstrate the feasibility of SANS contrast matching for the localization of small organic molecules in surfactant micelles. As discussed in the introduction, SANS contrast matching was previously performed on systems containing polymeric surfactants. For the localization of small organic solutes in micelles of low molecular weight surfactant, however, mostly contrast variation without precise contrast matching was done up until now.<sup>10,11</sup> In the present approach, the scattering contrast between DTAB micelles and the solvent was precisely eliminated, so that a  $q$ -dependency of the scattering signal solely arose from Blue. This approach facilitates data analysis by permitting the direct evaluation of the scattering signal with form factors of Blue assemblies in surfactant solutions without having to consider superimposed

form factors of surfactant micelles. Such an analysis is displayed in Figure 5. Here, SANS curves of solutions containing Blue and the contrast-matched DTAB are shown. Contrast matching was achieved by preparing a mixture of  $d_{25}$ - and  $d_{34}$ -DTAB, which had the same scattering length density as the solvent. SANS curves were analysed with either the form factor model of a hollow cylinder or the form factor model of a hollow ellipsoid. In both cases, Blue was assumed to form the shell of these core-shell structures. The dimensions obtained for their cross-sections were compared to cross-section dimensions obtained from analysing corresponding full-contrast SANS curves, i.e. SANS curves of samples with the same composition except that completely hydrogenated DTAB was used instead of the contrast-matching mixture of  $d_{25}$ - and  $d_{34}$ -DTAB. Core radii obtained for the core-shell structures were only slightly smaller than cross section radii obtained from the analysis of full contrast data, which confirmed the localization of Blue close to the DTAB head group in Blue-DTAB co-assemblies.

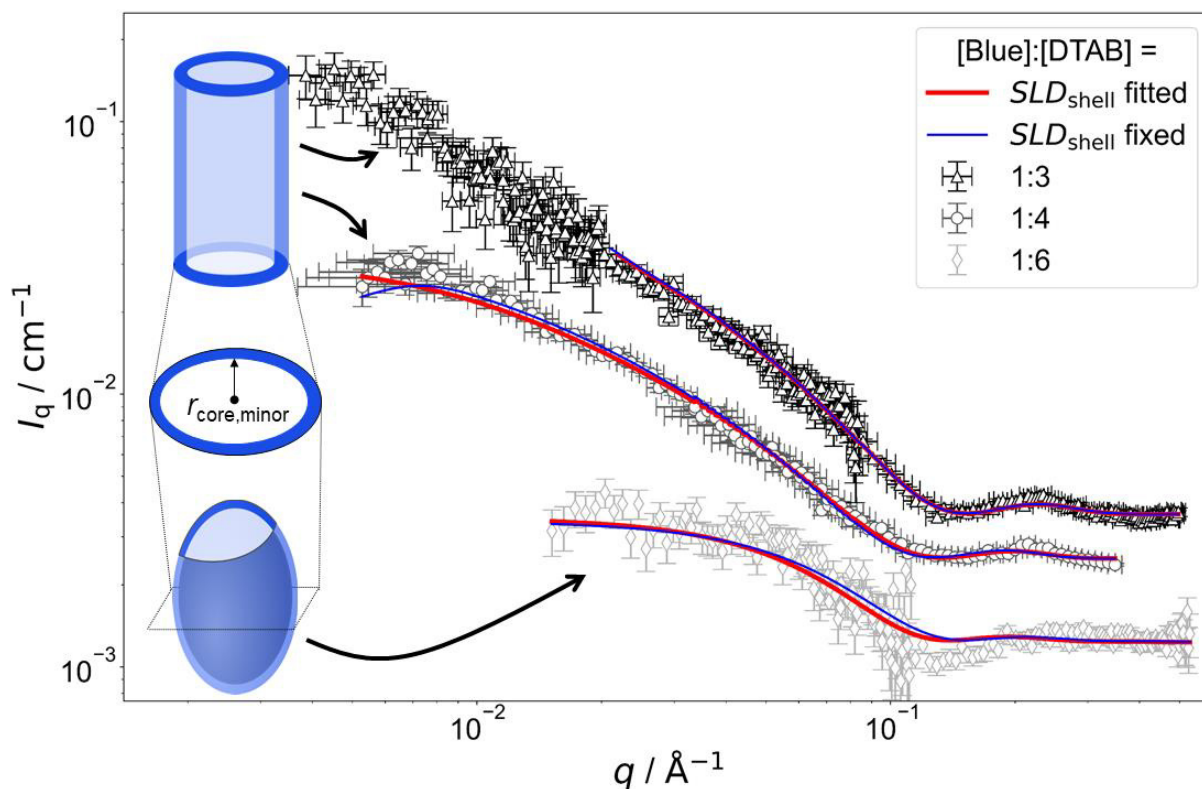


Figure 5: SANS curves of samples containing the contrast-matched surfactant DTAB at a concentration of 30 mM and variable concentrations of Blue. Samples were prepared in a  $\text{NaHCO}_3/\text{Na}_2\text{CO}_3$  buffer ( $\text{pD} = 10.7$ ,  $l \approx 0.25 \text{ M}$ ) in  $\text{D}_2\text{O}$  and measurements performed at a sample temperature of 25 °C. SANS curves were fitted with form factor models for the displayed core-shell structures. The red line displays a fit for which the scattering length density ( $SLD$ ) of the shell was fixed to the  $SLD$  of the one-fold deprotonated Blue. The blue line displays a fit for which the  $SLD$  of the shell was fitted.

**Co-assembly between dye and the non-ionic surfactant C<sub>12</sub>E<sub>5</sub>:** Non-ionic surfactants with polyethyleneglycol head group are frequently used in cosmetic formulations due to their mildness and low toxicity.<sup>12,13</sup> The objective of the last chapter is therefore to study the interaction between hair dye and a non-ionic surfactant. Instead of comparing the interaction of three different dyes with the non-ionic surfactant C<sub>12</sub>E<sub>5</sub>, only the interaction between Blue and the surfactant is considered and the behaviour of Blue-C<sub>12</sub>E<sub>5</sub> solutions compared at different pH. The pH-dependent behaviour is interesting, because hair dyeing is usually performed at alkaline pH, whereas shampoos often possess a slightly acidic pH between 4.5 and 6.<sup>7,12</sup> It was mentioned before, that the phenolic hydroxyl group of Blue can be deprotonated. At sufficiently high pH, the sulphonamide group is deprotonated as well, resulting in the formation of two-fold negatively charged Blue (Blue<sup>2-</sup>).

As the distinction between differently charged Blue species is important in Chapter 7, protonated Blue is denoted as BlueH, one-fold deprotonated Blue is denoted as Blue<sup>-</sup> and two-fold deprotonated Blue is denoted as Blue<sup>2-</sup> in the remaining part of Section 2.2. The term “Blue” is solely used, when it is not referred to a specific state of deprotonation. Furthermore it should be noted, that all investigations for Chapter 7 were performed in D<sub>2</sub>O. Therefore, rather than referring to solution pH, it is referred to solution pD.

Aqueous solutions of C<sub>12</sub>E<sub>5</sub> phase separate into a surfactant-rich and a surfactant-poor phase at a given temperature. This temperature depends on the composition of a C<sub>12</sub>E<sub>5</sub>-containing solution and is termed "clouding temperature" (CT) in Chapter 7. The CT of a 25 mM solution of C<sub>12</sub>E<sub>5</sub> in an isotonic NaCl solution in D<sub>2</sub>O does not depend on the pD of the solution. However, the CT of such solutions varies upon addition of Blue: It is decreased upon addition of the uncharged BlueH, but increased upon addition of Blue<sup>-</sup> and Blue<sup>2-</sup> at pD = 9 and pD = 13 as shown in Figure 6.

Chapter 7 aims to understand mechanisms that result into the observed CT behaviour of Blue-C<sub>12</sub>E<sub>5</sub> solutions.

For this purpose, SANS experiments were performed in a first step to obtain information on morphological transition and on inter-micellar interactions upon variation of sample composition: In C<sub>12</sub>E<sub>5</sub> solutions, a rapprochement to the CT can already be detected in the one-phase region due to the appearance of concentration fluctuations, which result from attractive interactions between surfactant micelles. In Chapter 7, the correlation length ( $\xi$ ) of such concentration fluctuations is used as a measure to compare the extent of attractive interactions between micelles for different samples. Importantly, correlation lengths and hence attractive interactions

are shown to decrease with increasing distance from the CT of the sample. This observation is made for all samples, independent of their composition and CT.

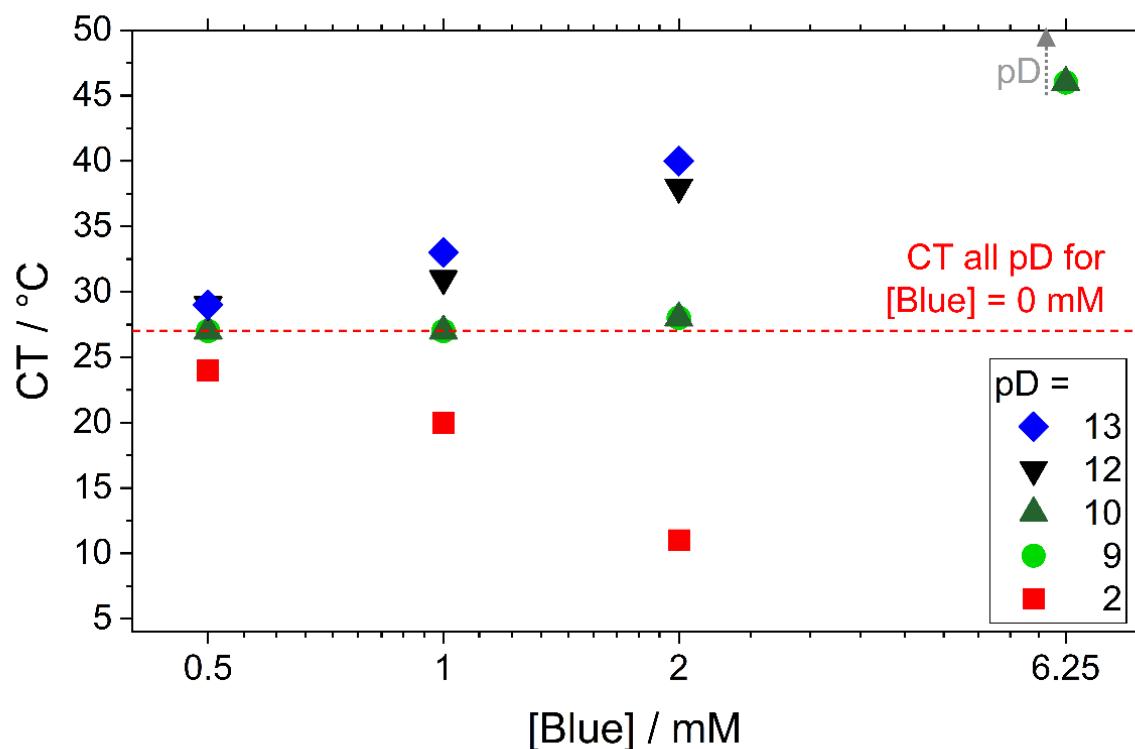


Figure 6: CTs of solutions containing the surfactant  $C_{12}E_5$  at a concentration of 25 mM and varying concentrations of Blue at different pD. CTs were detected in a temperature interval of  $4\text{ }^{\circ}\text{C} \leq \text{CT} \leq 50\text{ }^{\circ}\text{C}$ . At pD = 2, the completely protonated BlueH is present, at pD = 9 and pD = 10 the one-fold deprotonated  $\text{Blue}^-$  is present in high excess, at pD = 12 a mixture of  $\text{Blue}^-$  and  $\text{Blue}^{2-}$  exists and at pD = 13 the two-fold deprotonated  $\text{Blue}^{2-}$  is present in high excess. An isotonic NaCl solution ( $I = 0.154\text{ M}$ ) in  $D_2O$  was used as the solvent. The horizontal line shows the CT of the pure  $C_{12}E_5$  solution, which is independent of solution pD. The grey arrow indicates, that the CTs of solutions containing  $[\text{Blue}] = 6.25$  at  $\text{pD} \geq 12$  lay outside the detected temperature range.

At a given temperature of  $10\text{ }^{\circ}\text{C}$  it was found, that the addition of BlueH (pD = 2) to a 25 mM  $C_{12}E_5$  solution increases attractive inter micellar-interactions, because  $\xi$  increased. Conversely, the addition of  $\text{Blue}^-$  (pD = 9) or  $\text{Blue}^{2-}$  (pD = 13) decreases attractive inter-micellar interactions. At high enough concentrations of  $\text{Blue}^{2-}$ , the emergence of repulsive inter-micellar interactions was found from fits to full contrast SANS data.

To elucidate mechanisms, which lead to an in- or decrease of attractive inter micellar interactions upon addition of BlueH,  $\text{Blue}^-$  or  $\text{Blue}^{2-}$ , these molecules were located in  $C_{12}E_5$  micelles. For this purpose, a combination of NMR spectroscopy and SANS contrast variation was used.

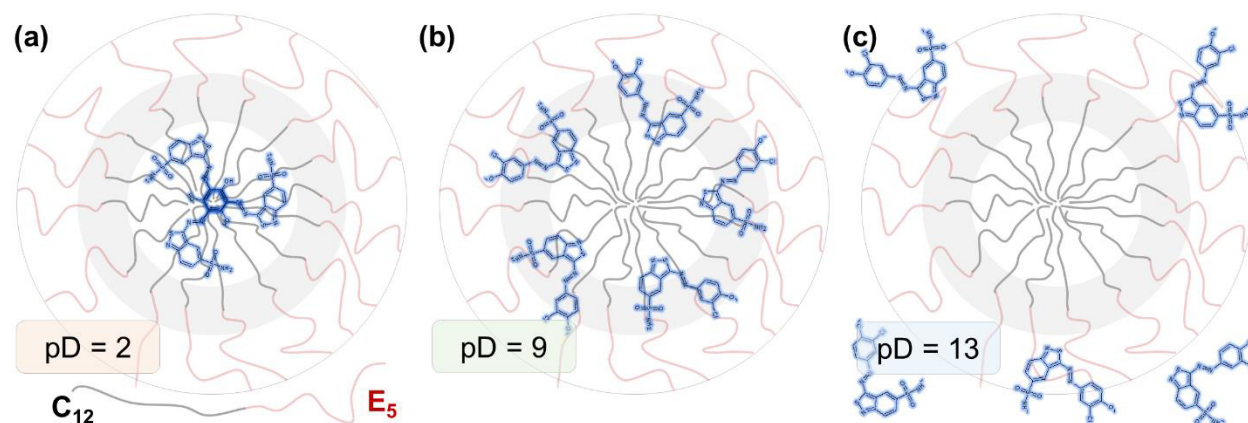


Figure 7: Schematic localization of (a) BlueH, (b) Blue<sup>-</sup> or (c) Blue<sup>2-</sup> in the cross section of C<sub>12</sub>E<sub>5</sub> micelles. Grey lines represent the hydrophobic alkyl chain (C<sub>12</sub>) and red lines represent the hydrophilic pentaethyleneglycol head group (E<sub>5</sub>). The palisade layer is highlighted in grey.

Figure 7 schematically displays the results of this investigation: The uncharged BlueH is mostly dissolved in the hydrophobic core of C<sub>12</sub>E<sub>5</sub> micelles. This increases the hydrophobic chain volume of the C<sub>12</sub>E<sub>5</sub> surfactant which, according to the packing parameter  $P$ , increases the packing of C<sub>12</sub>E<sub>5</sub> molecules in BlueH-C<sub>12</sub>E<sub>5</sub> co-assemblies. The denser packing of C<sub>12</sub>E<sub>5</sub> molecules reduces head group hydration, as less space is available for water molecules in the pentaethyleneglycol head group. A reduction in head group hydration decreases the water solubility of C<sub>12</sub>E<sub>5</sub> micelles, which is associated with an increase in attractive interactions between these micelles and a concomitant decrease in the CT of such solutions.

In contrast to BlueH, the charged molecules Blue<sup>-</sup> and Blue<sup>2-</sup> are well soluble in water. Addition of either species to a C<sub>12</sub>E<sub>5</sub> solution therefore increases the water solubility of Blue-C<sub>12</sub>E<sub>5</sub> micelles, because Blue<sup>-</sup> and Blue<sup>2-</sup> favourably interact with both, the surfactant pentaethyleneglycol head group and water. In addition to that, the interaction between Blue<sup>-</sup> or Blue<sup>2-</sup> with the surfactant introduces charges into the surfactant micelles, which could lead to electrostatic repulsion between them. This effect was not unambiguously visible at pD = 9 under the observed conditions, because Blue<sup>-</sup> is mostly buried in the palisade region of the C<sub>12</sub>E<sub>5</sub> micelle. This leads to a decay of the electrostatic surface potential of the palisade layer to the level of the actual surface layer of the micelle. Nevertheless, a decrease in attractive micellar interactions visible by a decrease of  $\xi$  was unambiguously observed and explains the increase in the CT of C<sub>12</sub>E<sub>5</sub> solution upon addition of Blue<sup>-</sup>. For high enough concentrations of Blue<sup>2-</sup> at pD = 13, repulsive inter-micellar interactions and subsequent long-range ordering were detected. This is not only related to the higher charge of Blue<sup>2-</sup> compared to Blue<sup>-</sup>, but also to its localization in the outer layer close to the surface of C<sub>12</sub>E<sub>5</sub> micelles. This behaviour is consistent with the observation, that



the CT increase is highest at  $pD = 13$ . It should be mentioned, that at  $pD = 13$  not all  $\text{Blue}^{2-}$  molecules interact with  $\text{C}_{12}\text{E}_5$ , meaning that molecularly dissolved  $\text{Blue}^{2-}$  molecules coexist with  $\text{Blue}^{2-}$  molecules that interact with the head group of micellized  $\text{C}_{12}\text{E}_5$  surfactant.

Finally, it is noted, that variations in the type and magnitude of inter-micellar interactions are almost always accompanied by a change in the size or even the morphology of surfactant micelles. The reason for this is, that the same forces that lead to alterations of inter micellar interactions change the effective surface area of surfactant head groups, which influences their packing. An increasing effective surface area due to increasing repulsive interactions between surfactant head groups therefore leads to a shrinking of surfactant micelles.

Just as Chapter 6, Chapter 7 does not solely serve the purpose of understanding dye-surfactant interactions, but is also designed to demonstrate the applicability of SANS contrast matching for the localization of Blue in micelles of yet another surfactant. However, information obtained in Chapter 7 are less clear than the results obtained in Chapter 6. The main reason for this is, that no strong dominant contribution, which directs dye-surfactant interactions exists. Therefore, Blue molecules are distributed throughout the entire surfactant micelle rather than having a single, well-defined solubilisation locus. It is outlined in Chapter 6, that the electrostatic attraction between the negatively charged  $\text{Blue}^-$  and the cationic surfactant DTAB leads to  $\text{Blue}^-$  having a strong preference to interact with the positively charged DTAB head group. As  $\text{C}_{12}\text{E}_5$  carries no charge, no such contribution exists in the Blue- $\text{C}_{12}\text{E}_5$  system. Nevertheless, dependent on its state of deprotonation, Blue still shows a preferential solubilisation locus within such micelles. However, given the distribution of Blue throughout the entire micelle and the solvent, it is more difficult to discern form factor oscillations that emerge from an assembly of Blue in its preferential locus of solubilisation. This is particularly difficult in case of high surfactant excess. Furthermore, the interpretation of SANS curves becomes more complicated, if more than one type of assembly exists. Chapter 7 therefore reveals limitations of the SANS contrast matching method for the localization of small molecules in surfactant micelles. Even though the complementary use of NMR-spectroscopy may help to reduce ambiguities, it does not necessarily provide sufficient information to compensate the limitations of the contrast matching technique. This problem is particularly pronounced, if the solute is distributed throughout the entire surfactant micelle and NOESY cross peaks are observed for almost all resonances.

## 2.3 Outlook

The self-assembly of three direct dyes, their co-assembly with the cationic surfactant DTAB and the pH-dependent co-assembly of one of these dyes with the non-ionic surfactant C<sub>12</sub>E<sub>5</sub> is explored in the present dissertation. Its relevance for future investigations is outlined in the following.

In Chapter 5, the phase separation of solutions containing dye and the cationic surfactant DTAB is discussed. This phase separation differs for the three investigated dyes in that the dye:DTAB ratio above which phase separation occurs varies with the dye. Further differences are that solutions of Yellow and DTAB phase separate into two liquid phases, whereas solutions of Red or Blue and DTAB show liquid-solid phase separation. In the latter case, the solid corresponds to a precipitate with crystalline appearance. The observation of clearly discernible diffraction peaks by powder diffraction experiments (Figure 8) proved the crystallinity of Blue-DTAB complexes. Further powder diffraction experiments could be performed for Red-DTAB complexes and the diffraction pattern be interpreted quantitatively. This would permit the elucidation of the structure and packing of crystalline dye-DTAB complexes and potentially provide an explanation for observed stoichiometries of phase separation. Additional SANS or small-angle X-Ray scattering experiments on both phases of the Yellow-DTAB 2-phase region may help to elucidate why no solid complexes are formed between Yellow and DTAB and potentially permit the detection of a liquid crystalline phase.<sup>14</sup> In a second step or in an attempt to permit a more unambiguous interpretation of powder diffraction data on the two-phase region, the assembly between the dyes and cationic surfactants with longer alkyl chains such as tetradecyltrimethylammoniumbromide (TTAB) or cetyltrimethylammoniumbromide (CTAB) could be studied.

In Chapter 5 it is furthermore mentioned, that dye-induced micelles can be formed in the 1-phase region of dye-DTAB solutions which contain DTAB at a concentration lower than its critical micelle concentration (cmc). Dye addition therefore acts as a trigger for the formation of dye-DTAB co-assemblies from solutions containing DTAB in its molecularly dissolved form. This behaviour could be exploited in experiments, which address the kinetics of dye-surfactant co-assembly formation from solutions of the molecularly dissolved species.

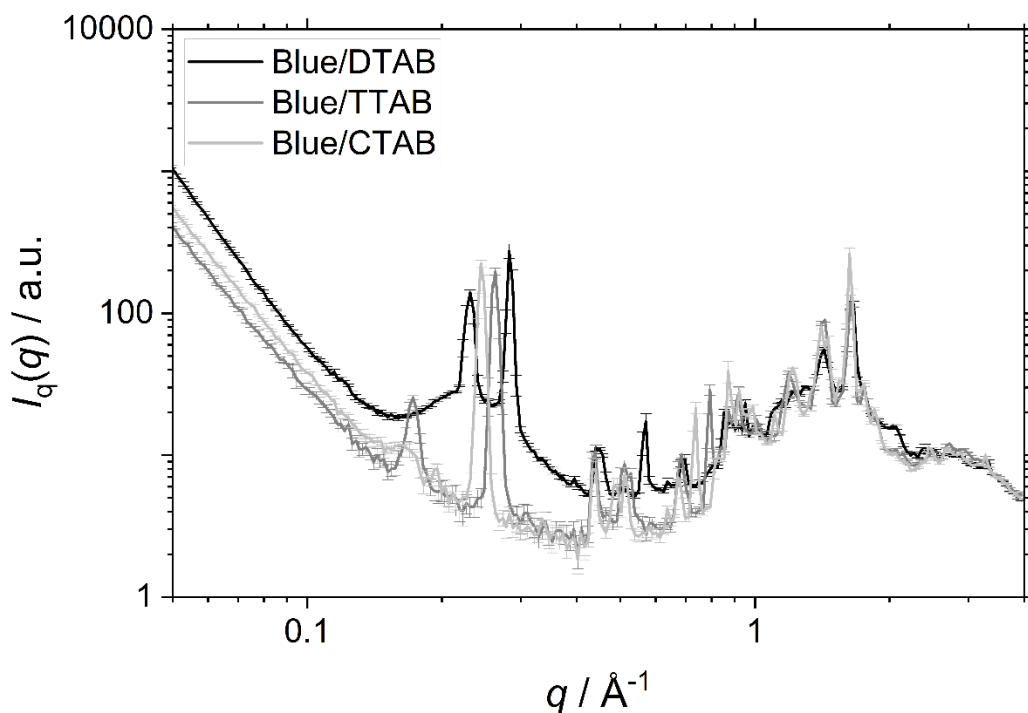


Figure 8: Wide-angle X-Ray scattering (powder diffraction) of solid complexes formed between the anionic dye Blue and cationic alkyltrimethylammoniumbromide surfactants with varying length of their hydrophobic alkyl chain ( $C_n$ ): DTAB ( $n = 12$ ), TTAB ( $n = 14$ ), CTAB ( $n = 16$ ).

In Chapter 7 the following question is raised: Do cylindrical micelles of the non-ionic surfactant  $C_{12}E_5$  coexist with spherical micelles? It is hardly possible to answer this question with scattering techniques, as these provide ensemble averaged information on the system. The size distribution of  $C_{12}E_5$  micelles is too broad for making accessible a clear distinction between two types of micelles based on the analysis of intensity correlation functions from dynamic light scattering. Furthermore, the existence of critical scattering and the broad size distribution of  $C_{12}E_5$  micelles hampers the interpretation of SANS curves in terms of the co-existence of two types of micelles. The only technique, which could provide an answer to such questions is cryo-TEM. Bernheim-Groswasser et al.<sup>15</sup> demonstrated the feasibility of cryo-TEM for the investigation of micelles formed by  $C_{12}E_5$ . Dependent on concentration and temperature, they observed the coexistence of cylindrical and spherical micelles or branched networks of cylindrical micelles in aqueous solutions of the  $C_{12}E_5$  surfactant.<sup>15</sup> Assuming the co-existence of spherical and cylindrical micelles in solutions containing Blue and  $C_{12}E_5$ , it would be interesting to find out whether Blue only penetrates into cylindrical micelles, only into spherical micelles or into both types of  $C_{12}E_5$  micelles. It was not possible to unambiguously answer this question with SANS contrast variation. Energy-filtered cryo-TEM, which permits to map the distribution of elements in the detected sample area would be necessary for that purpose. In such an experiment, the distribution of

sulphur or nitrogen could be mapped in the detected area and compared to the bright field image or carbon distribution in the same area.<sup>16</sup> Sulphur and nitrogen are specific to Blue. For this reason, this approach would permit the detection of whether Blue only participates in the formation of one or of all types of C<sub>12</sub>E<sub>5</sub> micelles.

Another future investigation could focus on the interaction of the three direct dyes with substrates. The quality of dyeing does not only depend on the solution behaviour of the direct dyes, but also on their affinity to the substrate and their diffusion within the substrate. Furthermore, self-aggregation of dye within the substrate could reduce its diffusion out of the substrate during washing procedures. This is particularly relevant for the durability of the hair colour. Furthermore, the comparison between the three dyes that are usually applied as a mixture is important, because they could be washed out to a different extent based on differences in their affinity to the substrate and on differences in self-aggregation within the substrate. This would lead to an undesired alteration of the substrate colour upon washing. Experiments could include small-angle scattering on dyed substrates.

Finally, investigations on dye-surfactant mixtures and investigations on dye-substrate interactions could be combined in experiments on the absorption of dye into the substrate from surfactant-containing dyeing solutions. Investigations on the kinetics of dye absorption into a substrate are performed by determining the dye concentration in substrates that were dyed for different times under the same solution conditions. This type of investigation is highly relevant for hair dyeing applications, because a sufficient amount of dye needs to penetrate into the hair fibre within time scales that are reasonable for a visit to the hairdresser.

## 2.4 References

- (1) Bergstrom, M.; Pedersen, J. Structure of Pure SDS and DTAB Micelles in Brine Determined by Small-Angle Neutron Scattering (SANS). *PHYS CHEM CHEM PHYS* **1999**, *1*, 4437–4446. <https://doi.org/10.1039/a903469b>.
- (2) Rosen, M. J. *Surfactants and Interfacial Phenomena*, 3rd ed.; Wiley-Interscience; John Wiley & Sons, Inc: Hoboken, New Jersey, USA, 2004.
- (3) Hartmann, H.; Pratt, D. M. Kosmetikindustrie: Henna und Heteroaromatisches. *Nachrichten aus der Chemie* **2022**, *70* (2), 26–28. <https://doi.org/10.1002/nadc.20224121433>.
- (4) Hunger, K.; Mischke, P.; Rieper, W.; Zhang, S. Azo Dyes, 3. Direct (Substantive) Dyes. In *Ullmann's Encyclopedia of Industrial Chemistry*; John Wiley & Sons, Ltd, 2018; pp 1–14. [https://doi.org/10.1002/14356007.o03\\_o07.pub2](https://doi.org/10.1002/14356007.o03_o07.pub2).

- (5) Hassan, M. M.; Bhagvandas, M. Sustainable Low Liquor Ratio Dyeing of Wool with Acid Dyes: Effect of Auxiliaries on Agglomeration of Dye Molecules in a Dyebath and Dyeing Uniformity. *Journal of Cleaner Production* **2017**, *152*, 464–473. <https://doi.org/10.1016/j.jclepro.2017.03.139>.
- (6) Doostdar, Mahnaz. Investigation of Dyestuff Aggregation via Static and Dynamic Light Scattering and Ultraviolet Spectroscopy. Dissertation, University of Paderborn, Paderborn, 2022. <http://digital.ub.uni-paderborn.de/hs/6634182> (accessed 2023-04-26).
- (7) Harrison, S.; Sinclair, R. Hair Colouring, Permanent Styling and Hair Structure. *Journal of Cosmetic Dermatology* **2004**, No. 2, 180–185. <https://doi.org/10.1111/j.1473-2130.2004.00064.x>.
- (8) Morel, O. J. X.; Christie, R. M. Current Trends in the Chemistry of Permanent Hair Dyeing. *Chem. Rev.* **2011**, *111* (4), 2537–2561. <https://doi.org/10.1021/cr1000145>.
- (9) Kert, M.; Simončič, B. Importance of dye-surfactant interactions in dyeing. *Tekstilec* **2007**, No. 50, 187–207.
- (10) Penfold, J.; Tucker, I.; Green, A.; Grainger, D.; Jones, C.; Ford, G.; Roberts, C.; Hubbard, J.; Petkov, J.; Thomas, R. K.; Grillo, I. Impact of Model Perfumes on Surfactant and Mixed Surfactant Self-Assembly. *Langmuir* **2008**, *24* (21), 12209–12220. <https://doi.org/10.1021/la801662g>.
- (11) Zhang, X. L.; Penfold, J.; Thomas, R. K.; Tucker, I. M.; Petkov, J. T.; Bent, J.; Cox, A.; Grillo, I. Self-Assembly of Hydrophobin and Hydrophobin/Surfactant Mixtures in Aqueous Solution. *Langmuir* **2011**, *27* (17), 10514–10522. <https://doi.org/10.1021/la2020226>.
- (12) Klein, Ken. Shampoo Formulation: The Basics. *Cosmetics & Toiletries magazine* **2004**, *119* (5), 64–68.
- (13) Fiume, M. M.; Heldreth, B.; Bergfeld, W. F.; Belsito, D. V.; Hill, R. A.; Klaassen, C. D.; Liebler, D.; Marks, J. G.; Shank, R. C.; Slaga, T. J.; Snyder, P. W.; Andersen, F. A. Safety Assessment of Alkyl PEG Ethers as Used in Cosmetics. *Int J Toxicol* **2012**, *31* (5\_suppl), 169S-244S. <https://doi.org/10.1177/1091581812444141>.
- (14) Guan, Y.; Antonietti, M.; Faul. Ionic Self-Assembly of Dye–Surfactant Complexes: Influence of Tail Lengths and Dye Architecture on the Phase Morphology. *Langmuir* **2002**, *18* (15), 5939–5945. <https://doi.org/10.1021/la0257182>.
- (15) Bernheim-Groswasser, A.; Wachtel, E.; Talmon, Y. Micellar Growth, Network Formation, and Criticality in Aqueous Solutions of the Nonionic Surfactant C12E5. *Langmuir* **2000**, *16* (9), 4131–4140. <https://doi.org/10.1021/la991231q>.

- (16) Weiss, A.-V.; Koch, M.; Schneider, M. Combining Cryo-TEM and Energy-Filtered TEM for Imaging Organic Core-Shell Nanoparticles and Defining the Polymer Distribution. *International Journal of Pharmaceutics* **2019**, *570*, 118650. <https://doi.org/10.1016/j.ijpharm.2019.118650>.

## Chapter 3

### Co-authors' contribution

This dissertation consists of three publications (Chapter 4, Chapter 5 and Chapter 6) and one manuscript in preparation (Chapter 7).

Wenke Müller authored all of these chapters and is fully responsible for all parts of the work not addressed here.

**Prof. Dr. Klaus Huber** and **Dr. Bernd Nöcker** contributed to the discussion and interpretation of results and to writing (all chapters).

**Dr. Ralf Schweins** provided help for SANS measurements at the Institute Laue-Langevin (Grenoble, France) and contributed to the discussion and interpretation of results and to writing (all chapters).

**Dr. Hans Egold** recorded the NMR-data shown in Chapter 4 and Chapter 6 and contributed to the discussion and interpretation of NMR-data and to editing Chapter 4 and Chapter 6.

**Dr. Joachim Kohlbrecher** provided help for the SANS measurements at the Paul Scherrer Institute (Villigen, Switzerland) shown in Chapter 5.

**Dr. Glen J Smales** recorded the wide-angle X-ray scattering (WAXS) data shown in Chapter 5 and contributed to the discussion and interpretation of WAXS data and to editing Chapter 5.

**Dr. Yvonne Hannappel** recorded the cryo-TEM images shown in Chapter 6.

**Weronika Sroka** performed valuable preliminary experiments for Chapter 7, which facilitated the choice of sample compositions.

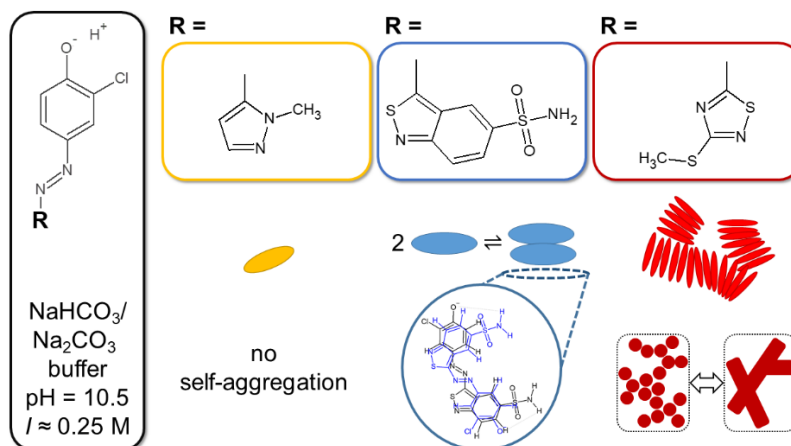
**Dr. Jia-Fei Poon** performed the synthesis of (partly) deuterated surfactants used in Chapter 7.

## Chapter 4

# Comparative study of the self-assembly behaviour of 3-chloro-4-hydroxy-phenylazo dyes

### Abstract

The complexity of intermolecular interactions and the difficulty to predict assembly behaviour solely based on chemical constitution was demonstrated by studying the self-assembly of three one-fold negatively charged 3-chloro-4-hydroxy-phenylazo dyes (Yellow, Blue and Red). Dye self-assembly was investigated using UV/vis- and NMR-spectroscopy, light- and small-angle neutron scattering. Significant differences between the three dyes were observed. While Yellow does not self-assemble, Red assembles into higher-order aggregates and Blue forms well-defined H-aggregate dimers with a dimerization constant of  $K_D = (728 \pm 8) \text{ L mol}^{-1}$ . Differences between dyes were suggested to emerge from variations in the propensity to form  $\pi$ - $\pi$ -interactions due to electrostatic repulsion, sterical constraints and hydrogen-bonding interactions





This chapter corresponds to: Müller, Wenke; Schweins, Ralf; Nöcker, Bernd; Egold, Hans; Huber, Klaus. Comparative Study of the Self-Assembly Behaviour of 3-Chloro-4-Hydroxy-Phenylazo Dyes. *Soft Matter* **2023**, *19* (24), 4579–4587. <https://doi.org/10.1039/D3SM00500C> published by the Royal Society of Chemistry.

## 4.1 Introduction

Dye molecules were subject to scientific investigations for decades in order to respond to the needs from industries in the field of textile- or paper dyeing. The replacement of natural dyes by synthetic dyes permitted the fine-tuning of dye properties by variation of chemical functionalities.<sup>1-3</sup> Apart from traditional dye research, the use of dyes as functional materials, e.g. in dye-sensitized solar cells or organic light-emitting diodes (OLEDs), received increasing attention over the past 20 years.<sup>4-6</sup> Contrary to traditional dye research, where it often sufficed to consider molecular structure – molecular property relationships, the design of functional materials requires understanding dye-dye intermolecular interactions, which impacts properties such as absorption, solid-state fluorescence and electron transport in the solid state material.<sup>4,7</sup>

A possibility to reduce the complexity of a system whilst getting valuable insight into intermolecular interactions affecting the solid-state system is to consider the self-assembly of dye molecules in solution, as they constitute an intermediate between the monomeric dye and the solid-state material.<sup>4,7</sup> Furthermore, the investigation of dye self-assembly in solution may be helpful to understand and mimic biological systems within which dye molecules assemble to fulfil specific tasks like the assembly of chlorophylls in photosynthetic organisms.<sup>4,8-11</sup>

$\pi$ - $\pi$ -interactions are considered as one of the major driving forces for dye self-aggregation in solution.<sup>12</sup> Depending on chemical constitution of the dye and geometrical constraints, other intermolecular interactions such as Coulomb forces, hydrophobic effect and dispersion forces or hydrogen bonding may additionally influence self-assembly.<sup>13</sup> Owing to the amount and complexity of possible intermolecular interactions, the prediction of dye self-assembly structure was reported to be difficult if no distinct dominant contribution exists.<sup>12</sup>

Herein we report investigations confirming the difficulty to predict dye self-assembly structure solely based on the chemical constitution of the dye. For this purpose, the self-assembly behaviour of three azo dyes with one congruent structural sub-unit (Figure 1) is investigated by means of UV/vis-spectroscopy, scattering methods and NMR-spectroscopy. Self-assembly structures are elucidated and analogies and differences discussed.

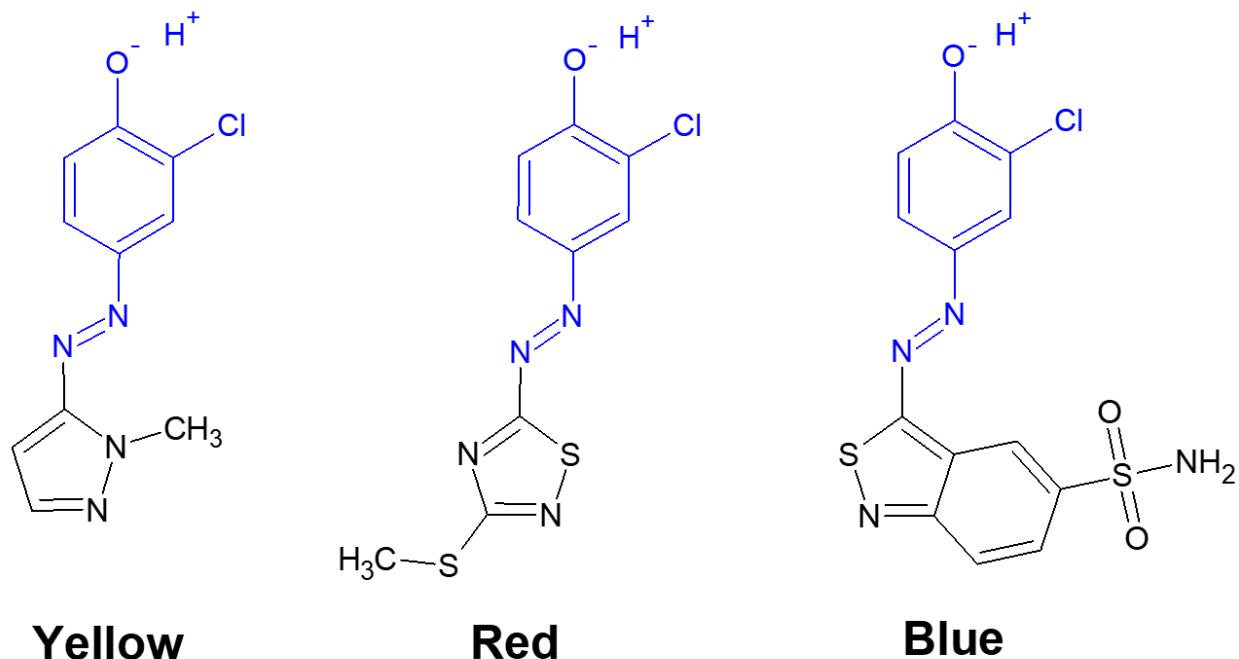


Figure 1: Chemical structure of three azo dyes with their common structural sub-unit marked in blue. At alkaline pH such as pH = 10.5, the phenolate group is deprotonated in all cases.

## 4.2 Experimental

**Chemicals and sample preparation.** Three azo dyes Yellow (HC Yellow 16,  $\geq 99\%$ ), Blue (HC Blue 18,  $\geq 99.8\%$ ) and Red (HC Red 18,  $\geq 99\%$ ) were provided by KAO GmbH, Germany. The buffer salts sodium carbonate  $\text{Na}_2\text{CO}_3$  ( $\geq 99.8\%$ ) and sodium bicarbonate  $\text{NaHCO}_3$  ( $\geq 99.7\%$ ) were obtained from Sigma Aldrich Chemie GmbH, Germany. MilliQ water was used to prepare the  $\text{NaHCO}_3/\text{Na}_2\text{CO}_3$  buffer solutions (pH = 10.5, ionic strength  $I \approx 0.25\text{ M}$ ) for UV/vis-spectroscopy and light scattering samples.  $\text{D}_2\text{O}$  was used to prepare the  $\text{NaHCO}_3/\text{Na}_2\text{CO}_3$  buffer solutions (pD = 10.7, ionic strength  $I \approx 0.25\text{ M}$ ) for NMR and small-angle neutron scattering samples.  $\text{D}_2\text{O}$  (99.90% D) was obtained from Eurisotop, France. Chemicals were used without further purification. Samples were prepared from stock solutions, followed by a minimum equilibration time of 20 h at room temperature prior to analysis.

**UV/vis spectroscopy.** UV/vis spectra were recorded using a V-630 spectrometer from Jasco. Hellma quartz glass cuvettes with optical path lengths ranging from 0.01 cm to 1 cm were used for this purpose. The spectrometer was equipped with a thermostat to guarantee a constant measurement temperature of 25 °C.

**Small-angle neutron scattering.** Samples for small-angle neutron scattering (SANS) measurements were obtained by dissolving the respective dye in a  $\text{NaHCO}_3/\text{Na}_2\text{CO}_3$  buffer in  $\text{D}_2\text{O}$  (pD = 10.7, ionic strength  $I \approx 0.25$  M). The solution was subsequently filtered (MACHEREY-NAGEL, CHROMAFIL Xtra H-PTFE syringe filters, pore size  $0.2 \mu\text{m}$ ) into a dust-free sample vial and equilibrated for a minimum of 20 h at room temperature.

SANS was performed at the small-angle neutron scattering instrument D11 at the Institut Laue-Langevin (Grenoble, France). Different setups were used: (1) Samples containing the dye Blue were measured at three sample-to-detector distances (28 m collimation 28 m), (8 m collimation 8 m), (1.7 m collimation 4.0 m) at a neutron wavelength of  $6 \text{ \AA}$  to cover a  $q$ -range of  $0.002 \text{ \AA}^{-1}$  to  $0.5 \text{ \AA}^{-1}$ . A circular neutron beam with a diameter of 15 mm was used. (2) The sample containing  $[\text{Red}]_{\text{tot}} = 10 \text{ mM}$  was measured at three sample-to-detector distances (38 m collimation 40.5 m), (10.5 m collimation 10.5 m), (1.7 m collimation 2.5 m) at a neutron wavelength of  $6 \text{ \AA}$  to cover a  $q$ -range of  $0.0014 \text{ \AA}^{-1}$  to  $0.5 \text{ \AA}^{-1}$ . A circular neutron beam with a diameter of 14 mm was used. (3) The sample containing  $[\text{Red}]_{\text{tot}} \approx 5 \text{ mM}$  was measured at three sample-to-detector distances (38.0 m collimation 40.5 m), (10.5 m collimation 10.5 m), (2.5 m collimation 2.5 m) at a neutron wavelength of  $6 \text{ \AA}$  to cover a  $q$ -range of  $0.0014 \text{ \AA}^{-1}$  to  $0.5 \text{ \AA}^{-1}$ . A circular neutron beam with a diameter of 14 mm was used.

Neutrons were detected with a  $^3\text{He}$ -detector (Reuter-Stokes multi-tube detector consisting of 256 tubes with a tube diameter of 8 mm and a pixel size of  $8 \text{ mm} \times 4 \text{ mm}$ ), detector images azimuthally averaged, corrected to the transmission of the direct beam and scaled to absolute intensity using the Mantid software.<sup>14,15</sup> Solvent scattering and empty cell scattering were subtracted from the scattering curves.<sup>16</sup> SANS data were collected at a sample temperature of  $25 \text{ }^\circ\text{C}$ .

**NMR-spectroscopy.** Samples for NMR-spectroscopy were obtained by dissolving the respective dye in a  $\text{NaHCO}_3/\text{Na}_2\text{CO}_3$  buffer in  $\text{D}_2\text{O}$  (pD = 10.7, ionic strength  $I \approx 0.25$  M). The solution was subsequently filtered (MACHEREY-NAGEL, CHROMAFIL Xtra H-PTFE syringe filters, pore size  $0.2 \mu\text{m}$ ) into the NMR-tube.  $^1\text{H}$ -NMR- and 2-dimensional rotating frame nuclear overhauser effect spectroscopy- (EASY ROESY) spectra were recorded with a NMR Ascent 700 spectrometer (700 MHz) equipped with a cryogenic probe with  $z$ -gradient at 298 K. The ROESY field strength was 5000 Hz. The magnetization was locked

at an angle of 45 ° off the z-axis which ensures suppression of TOCSY artefacts. Chemical shifts were referenced to residual HDO.<sup>17</sup>

### 4.3 Discussion

In the aqueous NaHCO<sub>3</sub>/Na<sub>2</sub>CO<sub>3</sub> buffer (pH = 10.5, ionic strength  $I \approx 0.25$  M), which was used as a solvent, the three azo dyes shown in Figure 1 are present in their phenolate form in all cases, as the phenolic hydroxyl group common to all dyes is deprotonated. Figure 2 compares the absorption spectra of all three dyes at a concentration of 5 mM. In the following, a brief overview of UV/vis spectroscopic observations will be given for all three dyes, followed by a detailed discussion of some specifically interesting features.

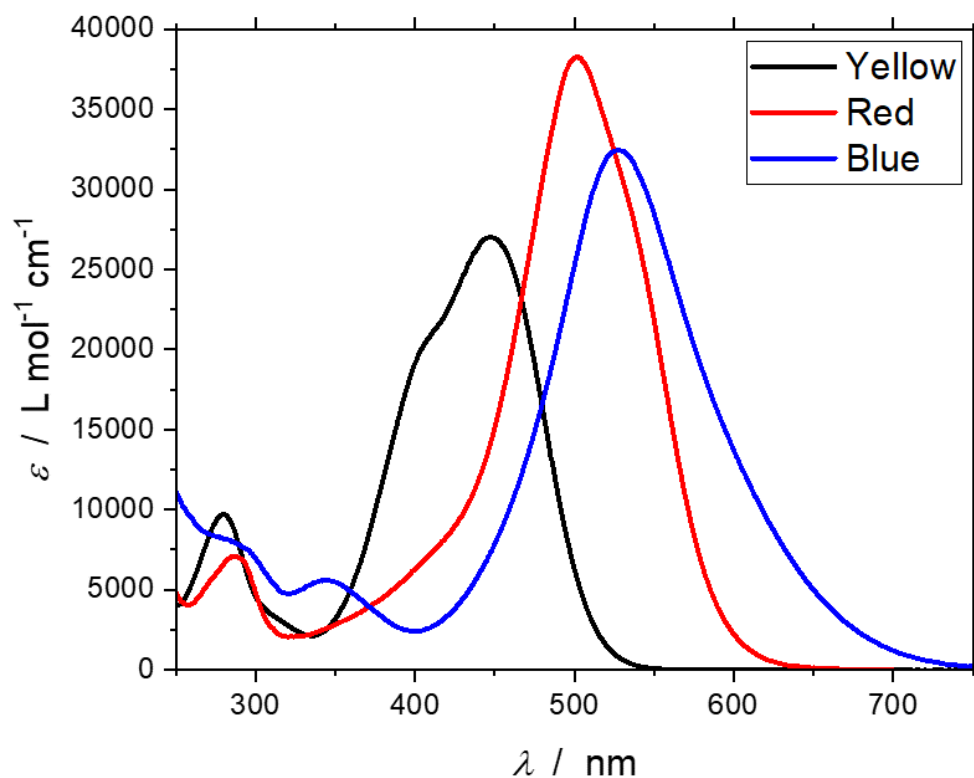


Figure 2: UV/vis spectra of the three investigated dyes at a concentration of 5 mM and pH = 10.5 in an aqueous NaHCO<sub>3</sub>/Na<sub>2</sub>CO<sub>3</sub> buffer ( $I \approx 0.25$  M) at 25 °C. At the given pH all dye molecules are present in their phenolate form.

First insights into dye solubility and self-aggregation can be obtained from UV/vis spectroscopy: In case the dye is soluble on a molecular level and does not self-aggregate, Beer-Lambert law (eq (1)) is fulfilled at each wavelength of the absorption spectrum.

$$A = \log\left(\frac{I_0}{I}\right) = [\text{Dye}]_{\text{tot}} \cdot d \cdot \epsilon \quad (1)$$

In eq (1),  $[\text{Dye}]_{\text{tot}}$  is the total molar concentration of dye in the sample,  $d$  is the optical path length and  $\epsilon$  is the molar extinction coefficient. To facilitate discussion, the absorbance divided by optical path length  $A_d$  will be referred to as “Absorbance”.

$$A_d = \frac{A}{d} = [\text{Dye}]_{\text{tot}} \cdot \epsilon \quad (2)$$

In case the dye does not self-aggregate,  $A_d$  is expected to linearly increase with  $[\text{Dye}]_{\text{tot}}$ .<sup>18</sup> For the reported systems this is only the case for the dye Yellow up until its solubility limit of  $[\text{Yellow}]_{\text{tot}} = 11$  mM. Corresponding investigations are displayed in the supplementary information (SI), Figure SI1. Dynamic and static light scattering confirm the absence of self-aggregation in solutions of Yellow (Figures SI3 and SI4). Opposed to Yellow, UV/vis absorption spectra of Blue and Red significantly change with increasing  $[\text{Dye}]_{\text{tot}}$ . In both cases, the main absorption maximum experiences a blue-shift with increasing concentration of dye, which points towards H-aggregation (face-to-face-aggregation).<sup>12,18,19</sup> Furthermore, a solubility limit as observed for Yellow was not observed for Blue and Red in the investigated concentration range of up to 25 mM (Figure SI1). Hence, the observed spectral changes are typical for the formation of soluble aggregates and will be discussed for Blue and Red separately.

**Self-assembly of Blue.** Concentration-induced changes in the absorption spectrum of Blue were attributed to dimer formation: Figure 3 shows UV/vis absorption spectra of solutions containing different concentrations of Blue.

Increasing  $[\text{Blue}]_{\text{tot}}$  leads to a shift of the absorption maximum to lower wavelengths and a decrease in the maximum molar extinction coefficient  $\epsilon_{\text{max}}$ . In addition to that, an isosbestic point at  $\lambda_{\text{isosbestic}} = (655 \pm 2)$  nm and  $\epsilon_{\text{isosbestic}} = (4350 \pm 110)$  L mol<sup>-1</sup> cm<sup>-1</sup> is observed. This is characteristic of only two species contributing to the total sample absorption.<sup>12,20</sup> Even though absorption spectra do not directly provide information on aggregation number, it is reasonable to assume an equilibrium between a monomeric dye molecule M and a dimer D.



[M] and [D] are molar equilibrium concentrations of the monomer and the dimer.  $K_D$  is the dimerization constant. Assuming that both, the monomer and the dimer contribute to the absorbance of the solution,  $A_d$  can be calculated at each wavelength  $\lambda$ .

$$A_d(\lambda) = [M] \cdot \epsilon_M(\lambda) + [D] \cdot \epsilon_D(\lambda) \quad (4)$$

$\epsilon_M(\lambda)$  and  $\epsilon_D(\lambda)$  are monomer and dimer molar extinction coefficients at wavelength  $\lambda$ . The total molar concentration of Blue  $[\text{Blue}]_{\text{tot}}$  is calculated as shown in eq (5).

$$[\text{Blue}]_{\text{tot}} = [M] + 2 \cdot [D] \quad (5)$$

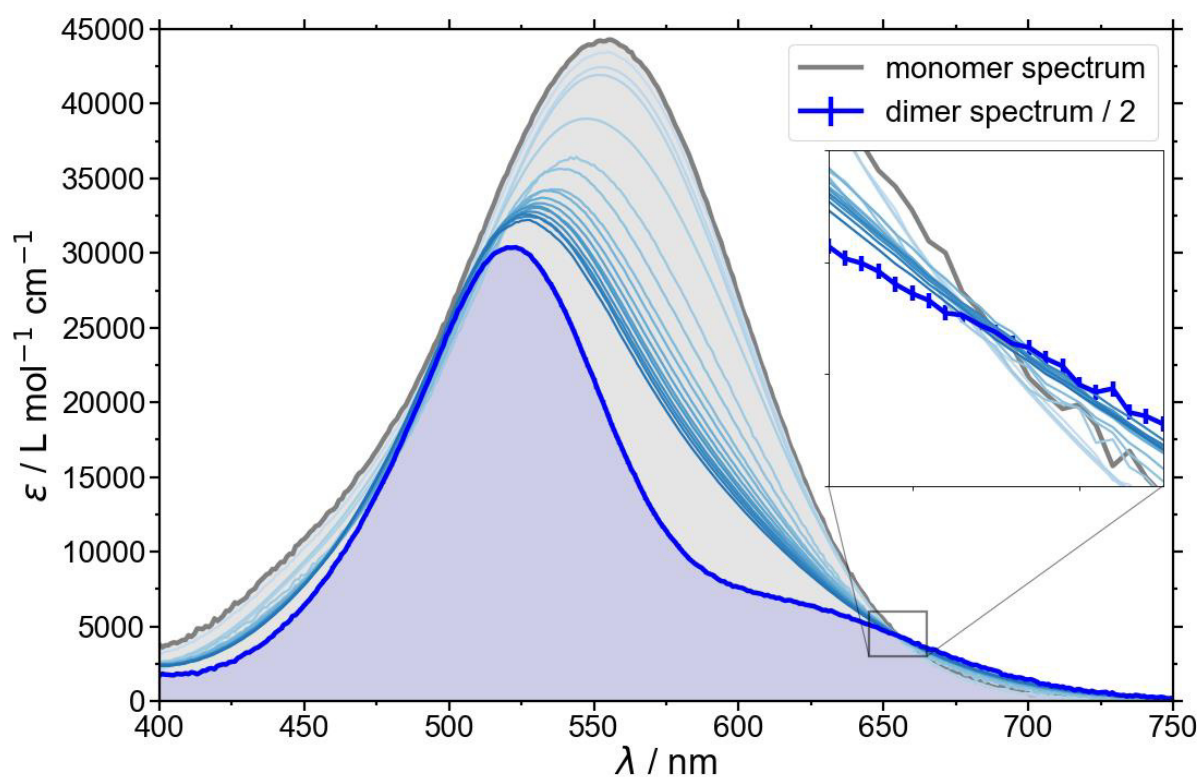


Figure 3: Spectra of Blue recorded at 25 °C in buffer solution at different concentrations. The arrow indicates an increase in  $[\text{Blue}]_{\text{tot}}$  from 0.01 mM to 6 mM. The monomer spectrum was recorded at  $[\text{Blue}]_{\text{tot}} = 5 \mu\text{M}$ . The dimer spectrum results from fitting. It was divided by 2 to refer to the concentration of monomer. The inset magnifies the region around the isosbestic point.

Inserting eq (3) and (5) into (4) permits the calculation of  $A_d$  from  $[\text{Blue}]_{\text{tot}}$  at any given wavelength, once the molar extinction coefficients of monomer and dimer and the dimerization constant  $K_D$  are known (eq (6)).<sup>20–22</sup>

$$\begin{aligned}
A_d(\lambda) = & \epsilon_M(\lambda) \left( \frac{-1 \pm \sqrt{1 + 8 K_D \cdot [\text{Blue}]_{\text{tot}}}}{4 K_D} \right) \\
& + \epsilon_D(\lambda) \left( \frac{[\text{Blue}]_{\text{tot}}}{2} - \frac{-1 \pm \sqrt{1 + 8 K_D \cdot [\text{Blue}]_{\text{tot}}}}{8 K_D} \right)
\end{aligned}
\tag{6}$$

The molar extinction coefficient of the monomer  $\epsilon_M(\lambda)$  was retrieved from a measurement at a very low concentration of Blue  $[\text{Blue}]_{\text{tot}} = 5 \mu\text{M}$ . Eq (6) was fitted to spectroscopic data  $A_d(\lambda) = f([\text{Blue}]_{\text{tot}})$  to obtain the dimer molar extinction coefficient  $\epsilon_D(\lambda)$  for each wavelength. In addition to that, the dimerization constant  $K_D$  was fitted as a global parameter, independent of the wavelength. The analysis was performed at wavelengths ranging from 400 nm to 750 nm with a resolution of  $\Delta\lambda = 1$  nm. The least squares algorithm implemented in the `scipy.optimize.leastsq` method of the Python SciPy module was used for the optimization of fit parameters.<sup>23</sup> The source code can be found in the SI. From that optimization, a dimerization constant of  $K_D = (728 \pm 8) \text{ L mol}^{-1}$  was obtained with  $\chi_{\text{red}}^2 = 0.35$ . The dimer spectrum is shown in Figure 3. In this graph, the dimer molar extinction coefficient was divided by 2 to refer to dye monomer concentration and hence visualize the expected change in sample spectra more clearly.

The dimer spectrum in Figure 3 shows two clearly discernible peaks with absorption maxima at energies higher and lower than that of the monomer. This can be explained by exciton theory where the first excited energy state of the monomer splits into two due to dipole-dipole interaction in case the transition dipole moments of the two monomers are aligned in a face-to-face mode (H-aggregation).<sup>24</sup> The transition with the higher energy is based on an in-phase oscillation of the two transition dipole moments and the transition with the lower energy is attributed to an out-of-phase oscillation of the two transition dipole moments.<sup>24</sup> In this context, the change in dye absorption spectrum permits insight into dimer geometry.<sup>19,25</sup> Quantitative analysis of the Blue dimer spectrum was performed and geometrical parameters of the dimer calculated. This calculation and the model are discussed in detail in the SI. It was found, that the transition dipole moments of two interacting molecules are twisted by an angle of  $\alpha = 42^\circ$ . The two transition dipole moments show no inclination, meaning that the centres of two molecules are stacked on top of each other. The interplanar spacing  $R$  between those centres was determined to be  $R = 5.2 \text{ \AA}$  in the model of non-parallel transition dipoles.



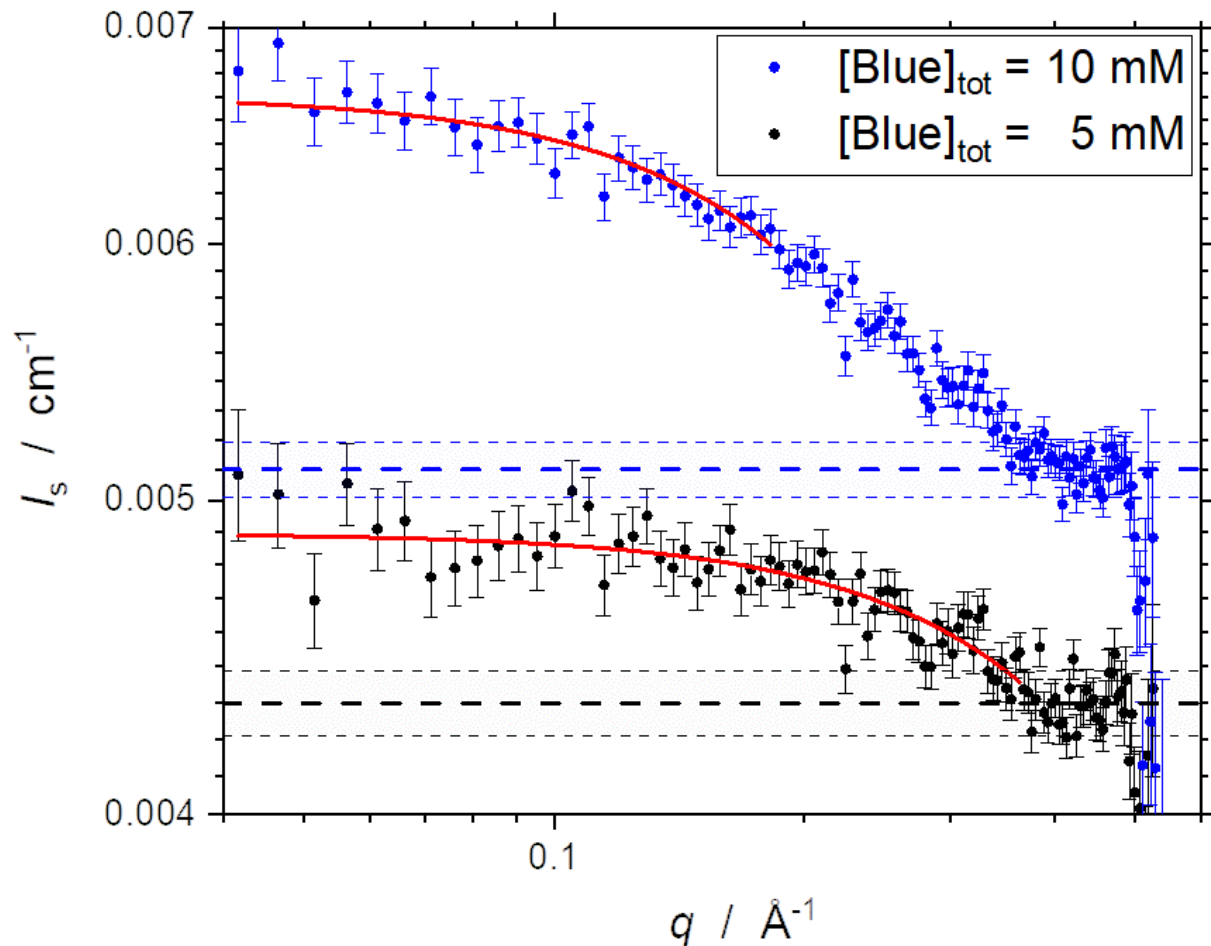


Figure 4: SANS curves of two solutions of Blue and corresponding Guinier analysis (red lines). The incoherent background is displayed as dashed line with its error indicated as the light-blue or light-grey region.

SANS was carried out on two solutions of Blue (Figure 4). The sample containing  $[\text{Blue}]_{\text{tot}} = 5 \text{ mM}$  shows a lower scattering intensity  $I_s$  than the sample with  $[\text{Blue}]_{\text{tot}} = 10 \text{ mM}$ . Furthermore, the scattering intensity declines at higher values of the modulus of the scattering vector  $q$  for  $[\text{Blue}]_{\text{tot}} = 5 \text{ mM}$ . These observations point towards a lower mass and smaller size of assemblies in the sample with  $[\text{Blue}]_{\text{tot}} = 5 \text{ mM}$ .

Guinier analysis was performed to obtain forward scattering intensities  $I_0$  and the average radius of gyration of the scatterers  $R_g$  according to eq (7).<sup>26</sup>

$$\ln(I_s) = \ln(I_0) - \frac{R_g^2}{3} \cdot q \quad (7)$$

$R_g$  obtained for both samples are summarized in Table 1. Linearized Guinier plots can be found in the SI (Figure SI8). From  $I_0$  the coherent forward scattering intensity  $I_{0,\text{coherent}}$  is

obtained by subtracting the incoherent background  $BG_{\text{incoherent}}$ . The value for the incoherent background was determined by averaging  $I_s$  in the high- $q$  range of the scattering curve which is displayed as dashed line in Figure 4. The weight-averaged molar mass of the scatterers  $M_w$  can then be determined from  $I_{0,\text{coherent}}$  with eq (8).<sup>16</sup>

$$I_{0,\text{coherent}} = I_0 - BG_{\text{incoherent}} = c \cdot K \cdot M_w \quad (8)$$

$$K \left[ \frac{\text{cm}^2 \text{ mol}}{\text{g}^2} \right] = \frac{(\rho_s - \rho_{\text{solv}})^2 \cdot V_{\text{m,s}}^2}{M_s^2 \cdot N_A} \quad (9)$$

$c$  is the mass concentration of the solute Blue,  $\rho_s$  and  $\rho_{\text{solv}}$  the scattering length densities of the elementary scattering units of solute and solvent respectively,  $V_{\text{m,s}}$  is the molar volume of the elementary scattering unit of the solute and  $M_s$  its molar mass.  $N_A$  is Avogadro's number. These parameters and results from analysis of absolute forward scattering intensities are summarized in Table 1.

Table 1: Parameters for absolute analysis of SANS forward scattering intensity of Blue solutions and comparison to calculations from known dimerization constant.

Parameter	[Blue] <sub>tot</sub> = 5 mM	[Blue] <sub>tot</sub> = 10 mM
$c$ [ $10^{-3} \text{ g cm}^{-3}$ ]	$1.85 \pm 0.02$	$3.70 \pm 0.03$
$\rho_s$ [ $\text{cm}^{-2}$ ]		$3.004 \cdot 10^{10}$
$\rho_{\text{solv}}$ [ $\text{cm}^{-2}$ ]		$6.376 \cdot 10^{10}$
$V_{\text{m,s}}$ [ $\text{cm}^3 \text{ mol}^{-1}$ ]		246.31
$M_s$ [ $\text{g mol}^{-1}$ ]		368.82
SANS	[Blue] <sub>tot</sub> = 5 mM	[Blue] <sub>tot</sub> = 10 mM
$I_{0,\text{coherent}}$ [ $10^{-3} \text{ cm}^{-1}$ ]	$0.6 \pm 0.1$	$1.6 \pm 0.1$
$M_w$ [ $\text{g mol}^{-1}$ ]	$362 \pm 97$	$502 \pm 47$
$R_g$ [ $\text{\AA}$ ]	$1.6 \pm 0.1$	$3.1 \pm 0.1$
$K_D = 728 \text{ L mol}^{-1}$	[Blue] <sub>tot</sub> = 5 mM	[Blue] <sub>tot</sub> = 10 mM
[M] [mM]	$1.54 \pm 0.02$	$2.30 \pm 0.02$
[D] [mM]	$1.73 \pm 0.01$	$3.85 \pm 0.01$
$M_w(K_D)$ [ $\text{g mol}^{-1}$ ]	$624 \pm 1$	$653 \pm 1$

The weight average molar mass of the scatterer is furthermore compared to the theoretical weight average molar mass of a mixture of Blue monomers and dimers according to the dimerization equilibrium described by eq (3) with the calculated dimerization constant of

$K_D = (728 \pm 8) \text{ L mol}^{-1}$ . Knowing the total molar dye concentration, the molar concentrations of Blue monomer [M] and Blue dimer [D] are obtained by combining eq (3) and (5).  $M_w(K_D)$  is then obtained from:

$$M_w(K_D) = \frac{[M] \cdot M_s^2 + [D] \cdot (2M_s)^2}{[M] \cdot M_s + [D] \cdot 2M_s} \quad (10)$$

As the elementary scattering unit corresponds to one Blue molecule,  $M_s$  is the molar mass of Blue.

From Table 1, several observations are made: (1) According to Guinier analysis,  $M_w$  and  $R_g$  of scatterers in the sample containing  $[\text{Blue}]_{\text{tot}} = 10 \text{ mM}$  are higher than  $M_w$  and  $R_g$  of scatterers in the sample containing  $[\text{Blue}]_{\text{tot}} = 5 \text{ mM}$ . This is consistent with the assumption of concentration-induced aggregation. (2) Due to the extremely low scattering intensities from the dye solutions and concomitant poor statistics, errors in  $M_w$  from SANS are high in this case. (3)  $M_w$  from SANS does not directly compare to  $M_w(K_D)$  from the experiments presented here. This could be due to the high error in  $M_w$ , low values of  $M_w$  and uncertainty in scattering contrast.<sup>27</sup> It should, however, be noted that  $M_w$  from SANS is smaller than  $M_w(K_D)$  in both cases, rendering the possibility of aggregates of more than two monomers unlikely. (4) The radius of gyration of the scatterers at either concentration is very small. Considering the model of a homogeneous cylinder,  $R_g = 4 \text{ \AA}$  was estimated for the dimer considering its chemical structure and results from exciton analysis. The calculation is outlined in the SI.  $R_g = 4 \text{ \AA}$  is not significantly higher than the experimentally determined  $R_g$  from SANS for the sample with  $[\text{Blue}]_{\text{tot}} = 10 \text{ mM}$ . A direct comparison of this theoretical value to the experimental ones is difficult, as each solution contains a mixture of monomer and dimer and the homogeneous cylinder model is only an approximation. Nevertheless it shows that the interplanar spacing  $R = 5.2 \text{ \AA}$  obtained by exciton theory is within an acceptable size range.

Information on the cause for dimer formation in solutions of Blue may be obtained by elucidating how Blue molecules assemble within the dimeric aggregate. For this purpose, ROESY (rotating frame nuclear overhauser effect spectroscopy) has been used to evaluate correlations through space. This type of NOE (nuclear overhauser effect) spectroscopy permits to study the spatial proximity of protons up to a distance of about  $5 \text{ \AA}$ .<sup>28</sup> In contrast to the more frequently performed NOESY (nuclear overhauser effect

spectroscopy), ROESY cross peak signals are always positive and do not vanish if the molecule or assembly exhibits a medium tumbling rate.<sup>29,30</sup> Figure 5 displays the ROESY spectrum of a solution containing  $[\text{Blue}]_{\text{tot}} = 10 \text{ mM}$ . Cross peaks for signals  $a'-b'$  and  $d'-e'$  are expected due to the chemical structure of Blue. However, cross peaks are also observed between signals  $a'-e'$ ,  $b'-f'$  and  $c'-f'$ . They exhibit much weaker intensities than the cross peaks mentioned before, which is likely caused by a greater distance between corresponding protons. These cross peaks are therefore related to the proximity of protons of two different molecules.

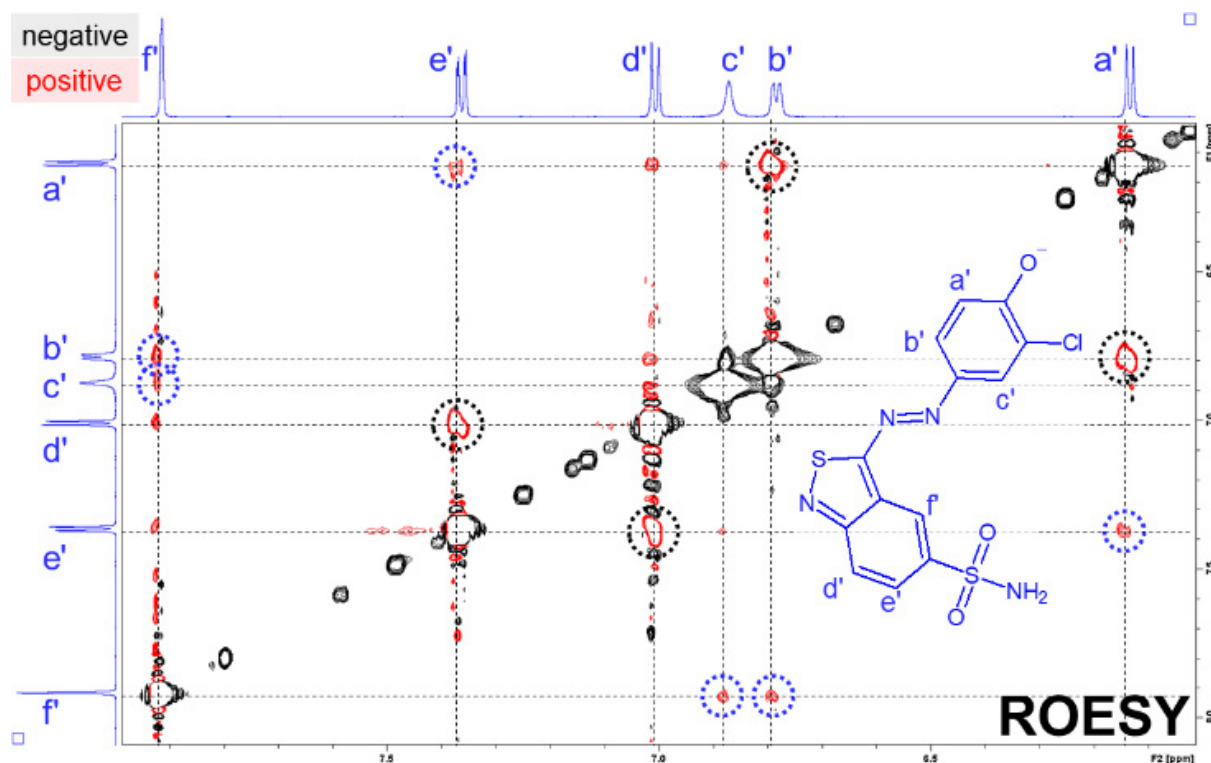


Figure 5: ROESY spectrum of a solution containing  $[\text{Blue}]_{\text{tot}} = 10 \text{ mM}$  in a  $\text{NaHCO}_3/\text{Na}_2\text{CO}_3$  buffer with  $\text{pD} = 10.7$  and  $I \approx 0.25 \text{ M}$  prepared in  $\text{D}_2\text{O}$ . Cross-peaks arising due to the proximity of protons as expected by chemical structure are encircled in black. Cross peaks arising due to intermolecular proximity of protons are encircled in Blue.

Figure 6(B) displays the structure of the Blue dimer, which explains cross peaks that were observed in the ROESY spectrum and is chemically meaningful. For readability, observed intermolecular NOE couplings are marked on two aligned but displaced chemical structures of Blue in Figure 6(A). In terms of intermolecular interactions, three major driving forces leading to the observed self-assembly are expected: (1) Electrostatic repulsion between negatively charged phenolate groups, (2)  $\pi$ - $\pi$  stacking of aromatic moieties and (3) hydrogen bonding interactions between the phenolate oxygen atom and hydrogen atoms from the sulphonamide groups.

The formation of assemblies with higher aggregation numbers may be hindered by steric requirements of the sulphonamide group and resulting packing constraints as well as electrostatic repulsion between nearby phenolate groups, which supports the assumption of dimer formation.

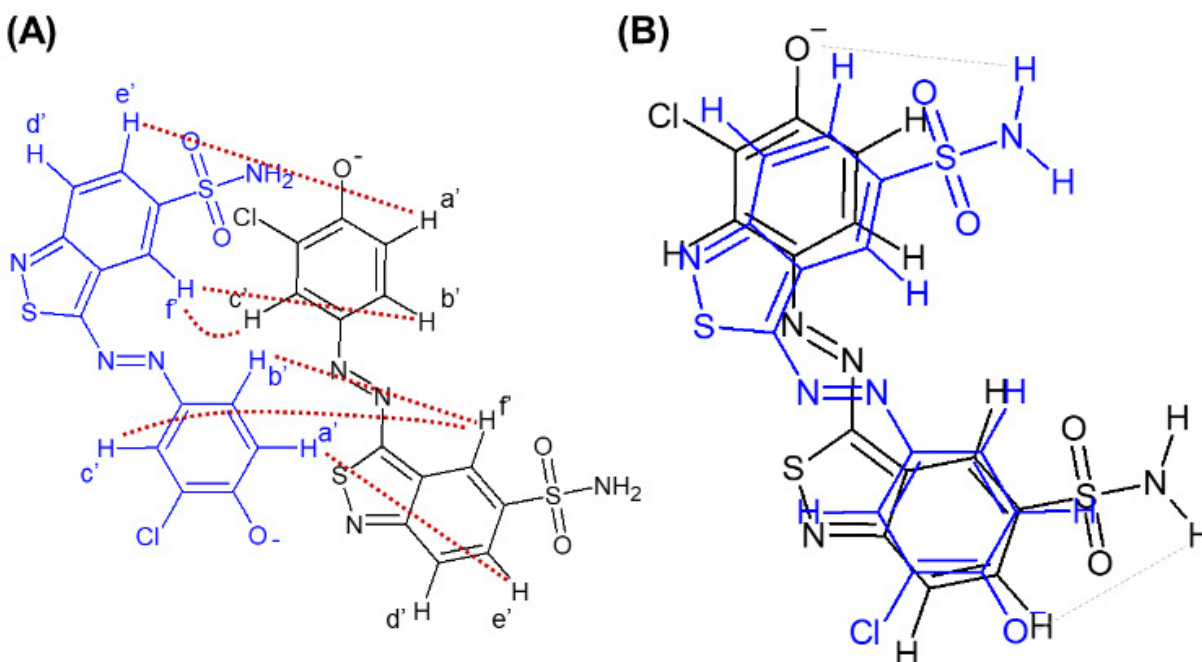


Figure 6: (A) Chemical structure of two molecules of Blue aligned as expected in the dimeric assembly but displaced for visibility. Protons are labelled according to the peak assignment in the ROESY spectrum (Figure 5). Observed intermolecular NOE coupling is indicated by red dotted lines. (B) Structure of the Blue dimer. Grey, dotted lines indicate potential hydrogen bonding interactions.

The dimer structure shown in Figure 6(B) is relatively symmetrical, indicating that protons from both molecules participating in dimer formation experience similar chemical environments, which leads to narrow  $^1\text{H-NMR}$  signals.<sup>28</sup> Furthermore, the proposed structure complies with results from preceding analysis of UV/vis spectra according to exciton theory: Within the model of non-planar transition dipoles a tilt angle  $\alpha = 42^\circ$  between two molecular planes was found, which agrees with the proposed structure as these planes are not given a direction and  $\alpha < 90^\circ$ .<sup>19</sup> Furthermore, an interplanar spacing of  $R = 5.2 \text{ \AA}$  does not rule out the occurrence of a NOE between interacting Blue molecules.

To conclude this section, the self-assembly of Blue in an aqueous  $\text{NaHCO}_3/\text{Na}_2\text{CO}_3$  buffer with  $\text{pH} = 10.5$  and  $I \approx 0.25 \text{ M}$  was elucidated using UV/vis-spectroscopy, SANS and NMR-spectroscopy. Concentration-dependent UV/vis spectra pointed towards dimer

formation and H-aggregation of Blue molecules with a dimerization constant of  $K_D = (728 \pm 8) \text{ L mol}^{-1}$ . SANS confirmed concentration-induced aggregation while proving higher-than-dimer aggregation unlikely. Dimer geometry was elucidated with the help of NMR-spectroscopy and the quantitative analysis of UV/vis spectra according to exciton theory, suggesting  $\pi$ - $\pi$ - and hydrogen bonding interactions as the most relevant attractive forces. Conversely, electrostatic repulsion between phenolate groups and steric requirements of the sulphonamide group potentially inhibit the formation of higher-order aggregates.

**Self-assembly of Red.** The absorption spectra of the dye Red are affected by concentration induced self-aggregation (Figure 7). An increase in concentration leads to a shift of the absorption maximum to lower wavelengths. However, no well-defined isosbestic point exists, suggesting more than two absorbing species contributing to the overall spectrum. Therefore, we abstained from an attempt to decompose the spectra into contributions from components.

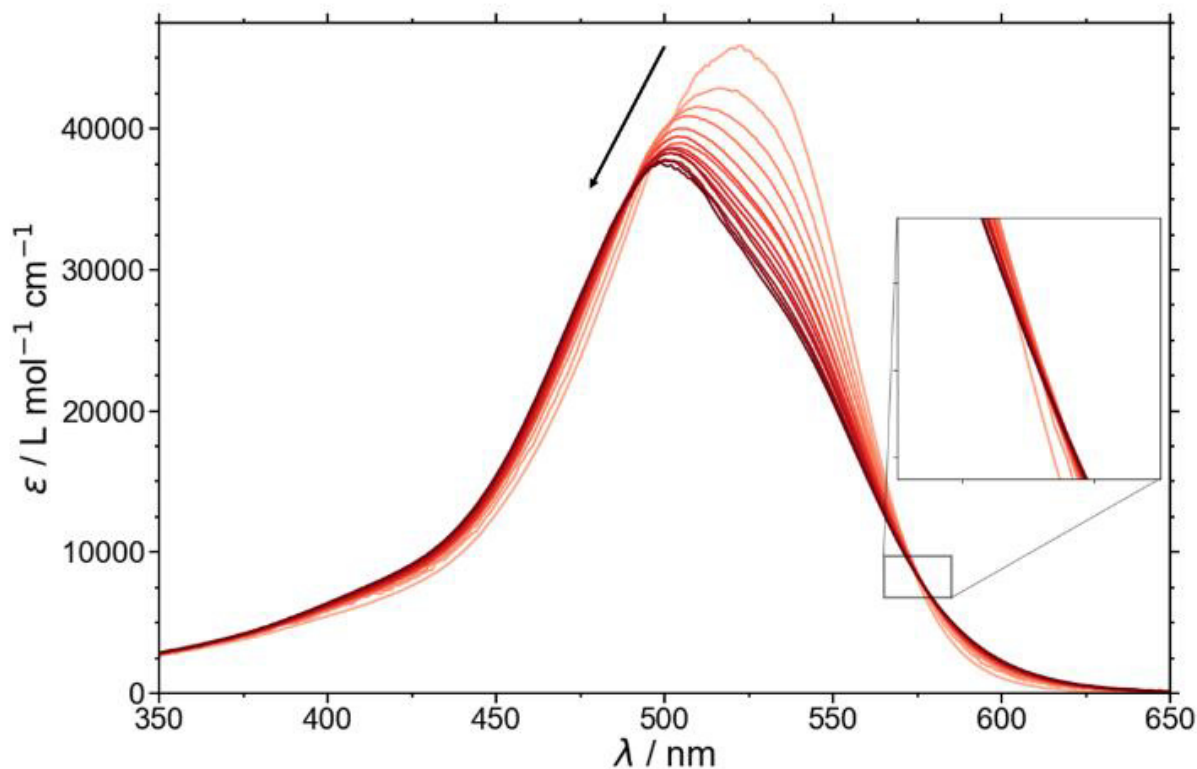


Figure 7: Spectra of Red recorded at 25 °C in buffer solution at different concentrations. The arrow indicates an increase in  $[\text{Red}]_{\text{tot}}$  from 0.02 mM to 6 mM. The inset shows a region where an isosbestic point could be assumed but does not exist.

SANS was performed on solutions of Red (Figure 8), one solution containing  $[\text{Red}]_{\text{tot}} = 10$  mM and the other one containing Red at an approximate concentration of  $[\text{Red}]_{\text{tot}} \approx 5$  mM. The concentration of Red in the latter sample was obtained by comparing forward scattering intensities of both SANS curves, as the sample with  $[\text{Red}]_{\text{tot}} \approx 5$  mM was intended to contain a higher concentration of Red, but was filtered too soon after its preparation when the dye was not yet completely dissolved, resulting into a loss of material. Details can be found in the SI (Figure SI10). For both curves, two Guinier shoulders are discernible at  $q < 0.003 \text{ \AA}^{-1}$  and  $q > 0.05 \text{ \AA}^{-1}$ . This likely results from scattering of at least two morphological features: A small structure, showing a Guinier-plateau in the high- $q$  region at  $q > 0.05 \text{ \AA}^{-1}$  and a large structure, causing the scattering intensity in the mid- and low- $q$  region to rise.

The radius of gyration of the species contributing to the scattering signal in the high- $q$  region was determined to  $8.5 \text{ \AA}$  by model-independent Guinier analysis for both curves. Furthermore, the SANS curves were described using the sum of a fractal form factor and a Guinier fit.<sup>31</sup> The fractal model describes the mid- and low- $q$  region and is characterized by the radius of spherical building blocks,  $R_{\text{block}}$ , its scattering length density  $\rho_{\text{block}}$ , the fractal dimension  $D_f$  and the cluster correlation length  $L_{\text{corr}}$ , which represents the total fractal cluster size.  $R_{\text{block}} = (9 \pm 1) \text{ \AA}$  was found to be similar to  $R_g = 8.5 \text{ \AA}$  obtained for the small species. The sum of a fractal model and a Guinier fit describes both SANS curves sufficiently well. Both curves can be described using identical geometrical parameters and fractal dimension when permitting the scaling of the fractal and the Guinier contribution to be different. Size parameters are given in the caption of Figure 8 and are summarized in the SI (Table SI2).

Aside from reproducing the scattering pattern of true fractals, the fractal form factor model can often be used for hierarchically structured aggregates, which cannot be further specified in terms of a more specific form factor model such as sphere, ellipsoid or cylinder without introducing a large number of fitting parameters, e.g. concerning polydispersity.<sup>32–34</sup> The fractal model has been successfully applied for instance in asphaltene research, where asphaltene molecules in a nonpolar solvent are assumed to aggregate in a three-step hierarchy from core aggregates due to  $\pi$ - $\pi$ -stacking of molecules, over medium aggregates, which are secondary aggregates of core aggregates, to fractal aggregates.<sup>35</sup>

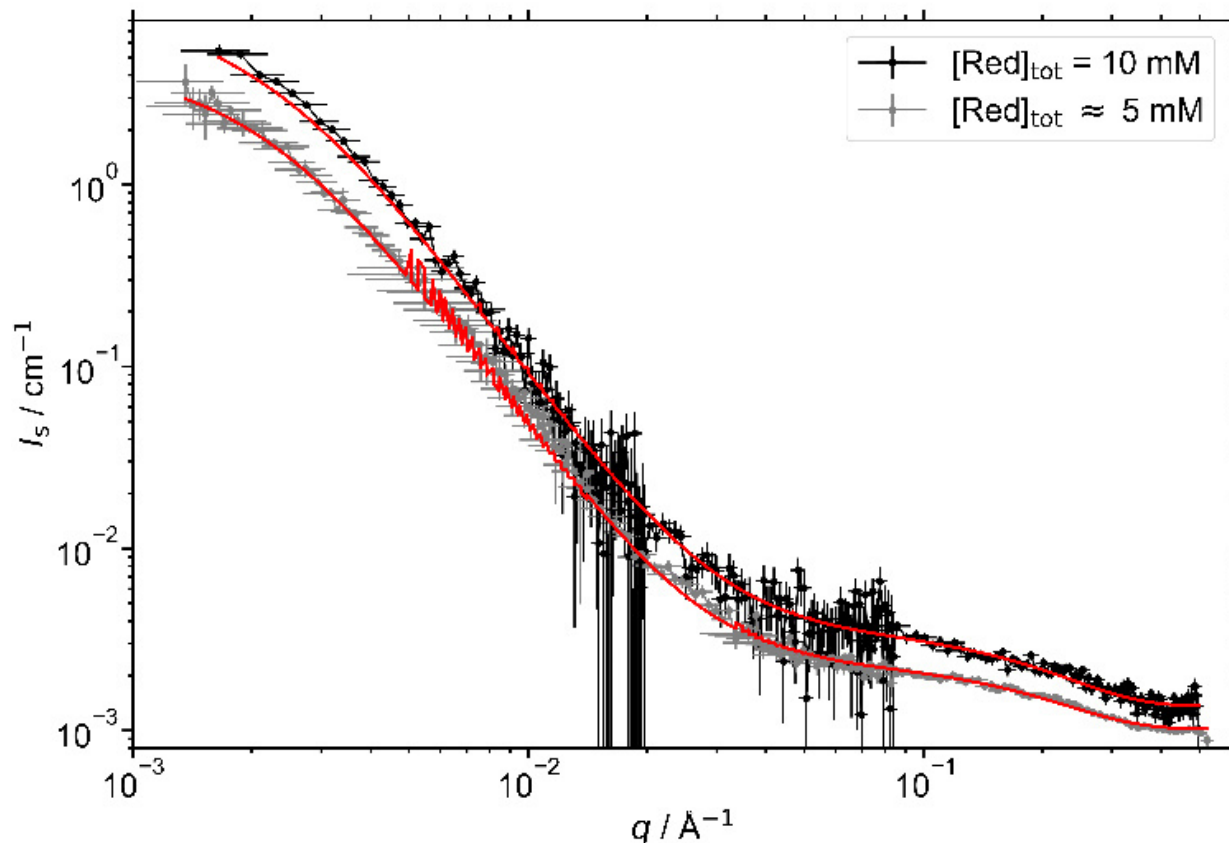


Figure 8: SANS data of two solutions of Red in buffer and at 25 °C. The form factor fit corresponding to the contribution of a Guinier fit ( $R_g = 8.5 \text{ \AA}$ ) with a fractal structure ( $D_f = 2.66 \pm 0.03$ ,  $L_{\text{corr}} = (437 \pm 10) \text{ \AA}$ ,  $R_{\text{block}} = (9 \pm 1) \text{ \AA}$ ) is shown as a red line.<sup>31</sup> Both displayed fits only differ by scaling factors.  $\chi_{\text{red}}^2$  ( $[\text{Red}]_{\text{tot}} = 10 \text{ mM}$ ) = 1.52,  $\chi_{\text{red}}^2$  ( $[\text{Red}]_{\text{tot}} \approx 5 \text{ mM}$ ) = 3.31.

Concerning the dye Red, the assumption of  $\pi$ - $\pi$ -stacking interactions leads to cylinders as the first choice to describe SANS curves of corresponding solutions.<sup>4</sup> However, an apparent scaling of  $I_s \propto q^{-2.66}$  instead of  $I_s \propto q^{-1}$  in the low- to mid- $q$  region contradicts the presence of simple, non-interacting cylinders.<sup>36</sup> Furthermore, the Kratky plot of corresponding SANS curves (Figure SI11) shows an initial maximum and in the Holtzer plot (Figure SI12) a minimum is visible before reaching a plateau in the high- $q$  region. Both observations point towards a structure, which is more compact than a random coil polymer chain.<sup>36</sup> However, these observations do not rule out the existence of cylinders as a structural feature, particularly because a  $I_s \propto q^{-1}$  dependency is observed in the mid- to high- $q$  region. A possible explanation could be branching of these cylinders.<sup>37,38</sup> A more in-depth discussion is given in the SI. The presence of at least two structural levels is therefore likely to occur and visualized in Figure 9. Herein, the formation of cylinder-like aggregates induced by  $\pi$ - $\pi$ -stacking of Red is the onset of the aggregation. These  $\pi$ -stacks may elongate to cylindrical aggregates, which could show branching. Alternatively,



further assembly of short cylinder segments may lead to fractal aggregates. The cluster correlation length in the fractal model would correspond to the overall size of the branched cylinder aggregate and the thickness (or size) of the building units in the fractal model would reproduce the cylinder cross section in the branched cylinder picture.

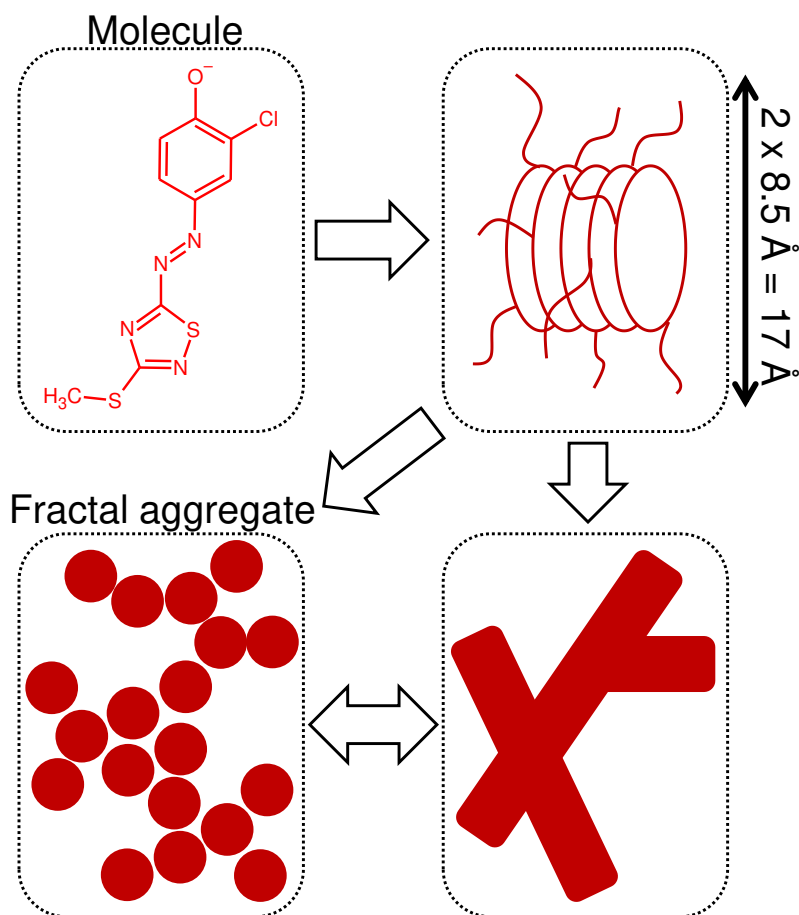


Figure 9: Potential hierarchy in the aggregation of Red. The image and theory were adapted from considerations regarding the aggregation of asphaltenes in *n*-heptane according to Tanaka et al.<sup>35</sup>

Figure 10 shows the  $^1\text{H-NMR}$  spectrum of a 10 mM solution of Red. In addition to that, it was attempted to obtain an idea about spatial proximity of protons belonging to different Red molecules using ROESY (Figure SI15). However, no cross peaks were observed in the ROESY spectrum. As not even the a-b cross peak expected from chemical structure of the Red molecule was visible, the absence of observable spatial correlations in the ROESY spectrum was attributed to the extreme peak broadening of signals b and c. Peak broadening is often a sign of aggregation arising from increased spin-spin relaxation rates due to slower molecular motion in aggregates.<sup>39,40</sup> This is a rather frequently observed

phenomenon for systems exhibiting  $\pi$ - $\pi$ -stacking, like dye molecules in solution.<sup>30,41,42</sup> Nevertheless it is remarkable, that signals a and d are not as strongly line broadened as signals b and c, which could result from corresponding protons experiencing a smaller variety of chemical environments and protons of type d potentially tumbling faster leading to the observation of an average chemical shift.<sup>43</sup> Following these observations, protons b and c are likely located closer to the structural sub-unit leading to intermolecular aggregation of Red, which results in a greater variety of chemical environments and rigidity, whereas protons of type a and d are located further away from that part of the molecule. Considering that  $\pi$ - $\pi$ -stacking interactions between 1,2,4-oxadiazole moieties were shown of great relevance for the aggregation of molecules containing such a heterocycle, it is likely that the aggregation of Red molecules results from  $\pi$ - $\pi$ -stacking interactions between the similar 1,2,4-thiadiazole heterocyclic moieties.<sup>44</sup> This aligns well with the assumption of electrostatic repulsion between phenolate groups, as these are free to point towards opposite directions when  $\pi$ - $\pi$ -stacking occurs on the 1,2,4-thiadiazole aromatic sub-unit.

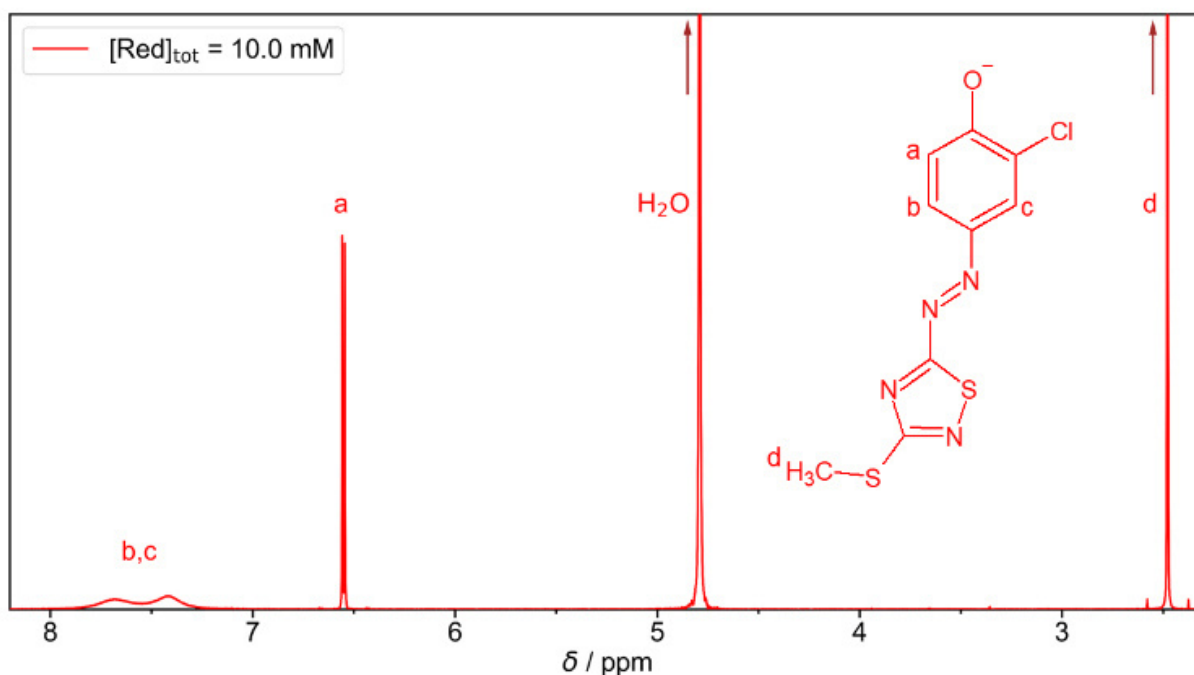


Figure 10:  $^1\text{H-NMR}$  spectrum of a solution containing Red at  $[\text{Red}]_{\text{tot}} = 10 \text{ mM}$  in a  $\text{NaHCO}_3/\text{Na}_2\text{CO}_3$  buffer ( $\text{pD} = 10.7$ ,  $I \approx 0.25 \text{ M}$ ) prepared in  $\text{D}_2\text{O}$ .

To conclude, the self-assembly of Red in an aqueous  $\text{NaHCO}_3/\text{Na}_2\text{CO}_3$  buffer with  $\text{pH} = 10.5$  and  $I \approx 0.25 \text{ M}$  commences with a cylindrical arrangement of Red monomers. NMR spectroscopic investigations suggest  $\pi$ - $\pi$ -stacking between the 1,2,4-thiadiazole

sub-units of different Red molecules to be the main reason for this arrangement. The cylinders probably elongate and eventually branch. The SANS curves of the resulting aggregates can be reproduced by a simplified fractal model.

#### 4.4 Conclusions

Three 3-chloro-4-hydroxy-phenylazo dyes, each of them carrying a negative charge due to deprotonation of the phenolic hydroxyl group at alkaline pH, were shown to significantly differ in their self-assembly behaviour. This confirms the complexity of intermolecular interactions and the difficulty to predict assembly behaviour of molecules just from their chemical structure.

Unlike to Blue and Red, the dye Yellow does not self-assemble. In addition to that, Yellow shows a solubility limit of 11 mM in the aqueous buffer used as a solvent, which was not observed for the other dyes. The lack of Yellow self-aggregation can be attributed to the impossibility to form intermolecular  $\pi$ - $\pi$ -stacking interactions.  $\pi$ - $\pi$ -stacking between phenolate groups is likely hindered by electrostatic repulsion between the deprotonated hydroxyl groups. Furthermore,  $\pi$ - $\pi$ -stacking between pyrazole sub-units might be hindered by steric constraints due to the substitution of one nitrogen atom with a methyl group.

The self-assembly of Blue and Red can be followed using UV/vis spectroscopy. Blue was observed to form dimers with a dimerization constant of  $K_D = (728 \pm 8) \text{ L mol}^{-1}$ . With the calculated dimer spectrum, H-aggregation of Blue molecules is revealed. Their aggregation geometry calculated with exciton theory, yields a twist angle of transition dipole moments of  $\alpha = 42^\circ$  and an interplanar spacing of 5.2 Å in the model of non-parallel transition dipoles. Driving forces for self-aggregation include  $\pi$ - $\pi$ -stacking, electrostatic repulsion between phenolate groups and likely hydrogen bonding between the phenolate oxygen and hydrogen atoms of the sulphonamide group. Steric effects due to spatial requirements of the sulphonamide group and electrostatic repulsion between phenolate groups pointing towards the same direction could hinder the formation of larger aggregates.

The self-aggregation of Red is more complex than that of Blue. The absence of an isosbestic point in concentration-dependent UV/vis spectra suggests the presence of multiple aggregate species. SANS revealed an average aggregate size of at least 400 Å. Self-aggregation of Red likely occurs due to  $\pi$ - $\pi$ -stacking of the 1,2,4-thiadiazole sub-unit,

leading to cylindrical building blocks which are able to form larger aggregate structures, most likely via branching.

Following these investigations, it becomes evident, that assembly properties cannot easily be predicted based on structural similarities. Rather, assembly morphology is directed by a subtle balance of intermolecular interactions and steric effects, which can be influenced dramatically by minor constitutional changes. Therefore, care has to be taken when expecting similar behaviour from molecules with similar chemical functionalities.

**Author Contributions:** Conceptualization: WM, RS, BN, KH, experimental: WM, RS, HE, analysis: WM with contributions from RS, HE, KH, BN, writing: WM, editing: WM, RS, BN, KH, HE, funding acquisition: RS, BN, KH

**Conflicts of interest:** There are no conflicts to declare.

**Acknowledgements:** The authors thank the Institut Laue-Langevin for the provision of internal beamtime (<https://doi.ill.fr/10.5291/ILL-DATA.INTER-557>). The authors gratefully acknowledge the use of the Partnership for Soft Condensed Matter (PSCM) facilities. W.M. acknowledges funding for a Ph.D. scholarship from the European Union's Horizon 2020 research and innovation programme under the Marie Skłodowska-Curie grant agreement No 847439 within the InnovaXN framework (Project number XN2019-ILL23).

## 4.5 Supporting information

### 4.5.1 Experimental

**UV/vis spectroscopy.** UV/vis spectra were recorded using a V-630 spectrometer from Jasco. Hellma quartz glass cuvettes with optical path lengths ranging from 0.01 cm to 1 cm were used for this purpose. The spectrometer was equipped with a thermostat to guarantee a constant measurement temperature of 25 °C. Samples showing precipitation were filtered prior to measurement (MACHEREY-NAGEL, CHROMAFIL Xtra H-PTFE syringe filters, pore size 0.2 µm).

**Light Scattering.** Light scattering measurements of solutions containing the dye Yellow were performed on an ALV 5000E compact goniometer system using a HeNe laser at a wavelength of 632.8 nm. Light scattering measurements were performed at 13 angles ranging from 30 ° to 150 °. To determine the absolute scattering intensity in terms of the Rayleigh ratio  $RR$  of the sample, the solvent scattering  $I_{\text{solvent}}$  was subtracted from the scattering intensity of the sample  $I_{\text{sample}}$  and the resulting signal normalized to the scattering intensity  $I_{\text{toluene}}$  arising from toluene with  $RR_{\text{toluene}}$  being the Rayleigh ratio of toluene at the given angle.

$$RR = \frac{I_{\text{sample}} - I_{\text{solvent}}}{I_{\text{toluene}}} \cdot RR_{\text{toluene}} \quad (\text{SI11})$$

An aqueous  $\text{NaHCO}_3/\text{Na}_2\text{CO}_3$  buffer (pH = 10.5, ionic strength  $I \approx 0.25$  M) was used as the solvent. Measurements were performed at 25 °C. Cylindrical cuvettes with a 1 cm inner diameter were used. Samples were filtered prior to measurement (MACHEREY-NAGEL, CHROMAFIL Xtra H-PTFE syringe filters, pore size 0.2 µm).

Light scattering measurements of solutions containing the dye Red were performed on an ALV CGS-3 Compact Goniometer System (ALV GmbH, Langen, FRG) using a HeNe laser at a wavelength of 632.8 nm. Light scattering measurements and data treatment were performed analogous to the above-mentioned procedure. For the creation of a Zimm plot, the contrast factor  $K$  was calculated according to:<sup>26</sup>

$$K = \frac{4 \cdot \pi^2}{\lambda_0^4 \cdot N_A} \cdot n_m^2 \cdot \left( \frac{dn}{dc_m} \right)^2 \quad (\text{SI12})$$

Where  $\lambda_0 = 632.8$  nm is the laser wavelength,  $N_A$  Avogadro's number,  $n_m$  the refractive index of the solvent and  $\left( \frac{dn}{dc_m} \right)$  the refractive index increment. The refractive index increment of solutions of Red in an aqueous  $\text{NaHCO}_3/\text{Na}_2\text{CO}_3$  buffer with pH = 10.5 and  $I \approx 0.25$  M was determined using a differential refractometer (Typ DR-3 from SLS Systemtechnik, Denzlingen, Germany) which is equipped with a diode laser (wavelength: 635 nm).

**Small-angle neutron scattering.** Samples for small-angle neutron scattering (SANS) measurements were obtained by dissolving the dye Red in a  $\text{NaHCO}_3/\text{Na}_2\text{CO}_3$  buffer in  $\text{D}_2\text{O}$  (pD = 10.7, ionic strength  $I \approx 0.25$  M). The solution was subsequently filtered (MACHEREY-NAGEL, CHROMAFIL Xtra H-PTFE syringe filters, pore size  $0.2 \mu\text{m}$ ) into a dust-free sample vial and equilibrated for a minimum of 20 h at room temperature.

SANS was performed at the small-angle neutron scattering instrument D11 at the Institut Laue-Langevin (Grenoble, France). Different setups were used: (2) The sample containing  $[\text{Red}]_{\text{tot}} = 10$  mM was measured at three sample-to-detector distances (38.0 m collimation 40.5 m), (10.5 m collimation 10.5 m), (1.7 m collimation 2.5 m) at a neutron wavelength of  $6 \text{ \AA}$  to cover a  $q$ -range of  $0.0014 \text{ \AA}^{-1}$  to  $0.5 \text{ \AA}^{-1}$ . A circular neutron beam with a diameter of 14 mm was used. (3) The sample containing  $[\text{Red}]_{\text{tot}} \approx 5$  mM was measured at three sample-to-detector distances (38.0 m collimation 40.5 m), (10.5 m collimation 10.5 m), (2.5 m collimation 2.5 m) at a neutron wavelength of  $6 \text{ \AA}$  to cover a  $q$ -range of  $0.0014 \text{ \AA}^{-1}$  to  $0.5 \text{ \AA}^{-1}$ . A circular neutron beam with a diameter of 14 mm was used.

Neutrons were detected with a  $^3\text{He}$ -detector (Reuter-Stokes multi-tube detector consisting of 256 tubes with a tube diameter of 8 mm and a pixel size of  $8 \text{ mm} \times 4 \text{ mm}$ ), detector images azimuthally averaged, corrected to the transmission of the direct beam and scaled to absolute intensity using the Mantid software.<sup>14,15</sup> Solvent scattering and empty cell scattering were subtracted from the scattering curves.<sup>16</sup> SANS data were collected at a sample temperature of  $25 \text{ }^\circ\text{C}$ .

**NMR-spectroscopy.** Samples for NMR-spectroscopy were obtained by dissolving the dye Red in a  $\text{NaHCO}_3/\text{Na}_2\text{CO}_3$  buffer in  $\text{D}_2\text{O}$  (pD=10.7, ionic strength  $I \approx 0.25$  M). The solution was subsequently filtered (MACHEREY-NAGEL, CHROMAFIL Xtra H-PTFE syringe filters, pore size  $0.2 \mu\text{m}$ ) into the NMR-tube. 2-dimensional rotating frame nuclear overhauser effect spectroscopy-(EASY ROESY) spectra were recorded with a NMR Ascent 700 spectrometer (700 MHz) equipped with a cryogenic probe with z-gradient at 298 K. The ROESY field strength was 5000 Hz. The magnetization was locked at an angle of  $45^\circ$  off the z-axis which ensures suppression of TOCSY artefacts. Chemical shifts were referenced to residual HDO.<sup>17</sup>

#### 4.5.2 Results and discussion

**Solubility of three dyes.** The solubility of Yellow, Blue and Red in the aqueous  $\text{NaHCO}_3/\text{Na}_2\text{CO}_3$  buffer (pH = 10.5, ionic strength  $I \approx 0.25$  M) at  $25 \text{ }^\circ\text{C}$  was studied by means of UV/vis spectroscopy. In the absence of precipitation and at a wavelength where self-aggregation does

not have an effect on dye absorption, the molar extinction coefficient does not depend on dye concentration. Therefore, a plot of sample absorbance divided by path-length ( $A_d$ ) vs dye concentration  $[Dye]_{tot}$  should result in a linear relationship. Figure S11 shows these plots for all three dyes.

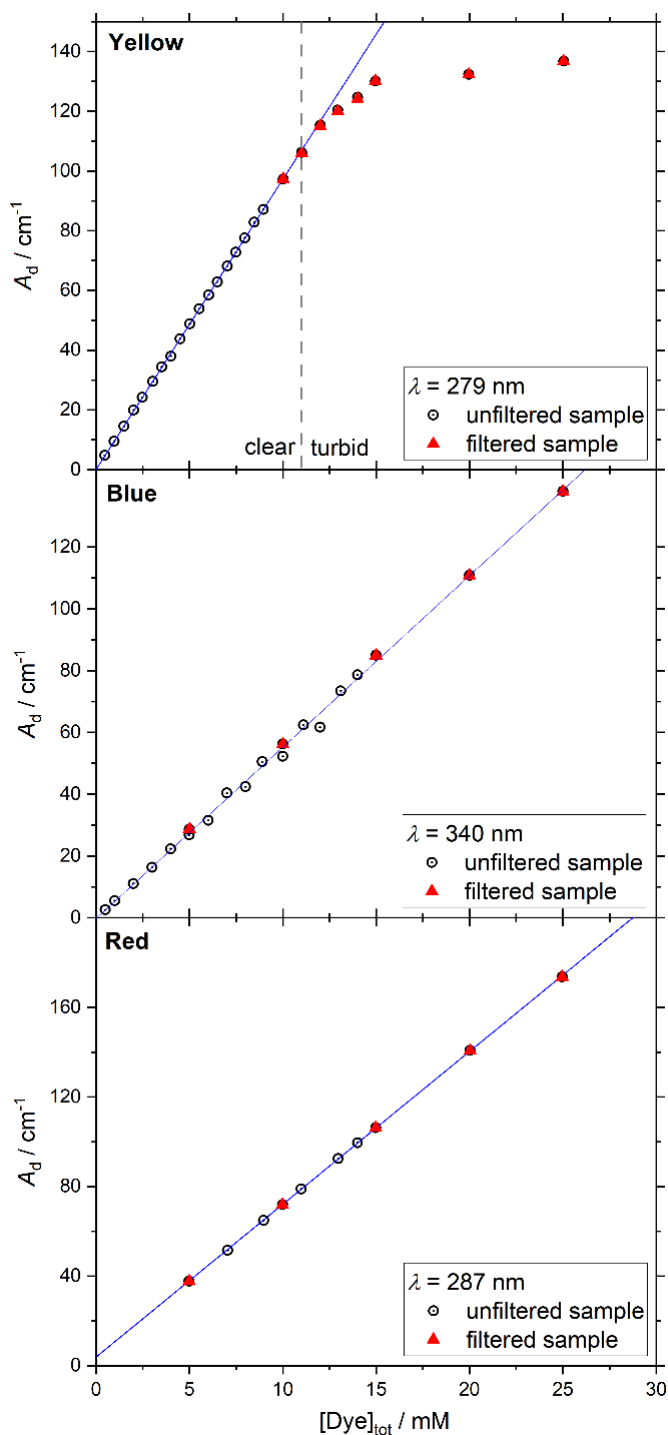


Figure S11: Solubility of dyes in an aqueous  $\text{NaHCO}_3/\text{Na}_2\text{CO}_3$  buffer at 25 °C investigated with UV/vis spectroscopy. Spectra were recorded the day after sample preparation.

Spectra of Yellow do not depend on concentration. For Red and Blue,  $A_d$  was evaluated at a wavelength, where dye absorption is not influenced by its self-aggregation. This wavelength corresponds to the position of an absorption maximum at lower wavelengths compared to the main peak.  $A_d$  of filtered and unfiltered samples were compared. Filtration was done on a sample basis and for samples visually showing phase separation. Filters with a pore size of 0.2  $\mu\text{m}$  were used (MACHEREY-NAGEL, CHROMAFIL Xtra H-PTFE syringe filters). Within the observed concentration range, only the dye Yellow shows a solubility limit at  $[\text{Yellow}]_{\text{tot}} = 11 \text{ mM}$ , which is observed visually and by a deviation from Beer-Lambert law. Solutions containing Blue and Red do not show this solubility limit within the observed timeframe, i.e. one day after sample preparation.

**Solubility of Yellow.** Figure S12 shows UV/vis absorption spectra of the dye Yellow at various concentrations. Different to Blue and Red, the absorption spectrum of Yellow does not change with concentration. This points towards an absence of concentration-induced aggregation in the  $\text{NaHCO}_3/\text{Na}_2\text{CO}_3$ -buffer.

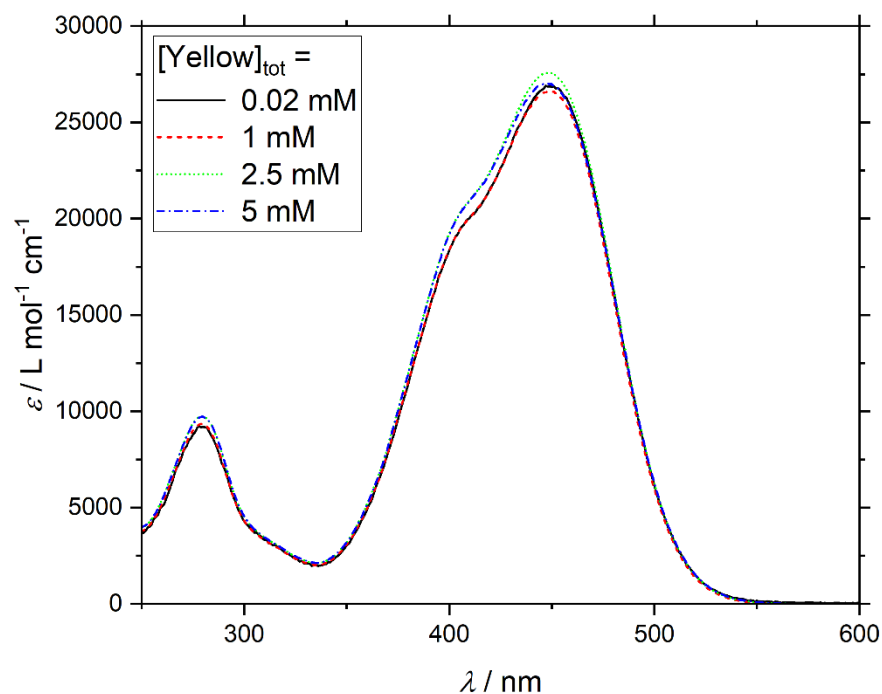


Figure S12: UV/vis absorption spectra of the dye Yellow recorded at four different concentrations in an aqueous  $\text{NaHCO}_3/\text{Na}_2\text{CO}_3$  buffer at 25  $^\circ\text{C}$ .



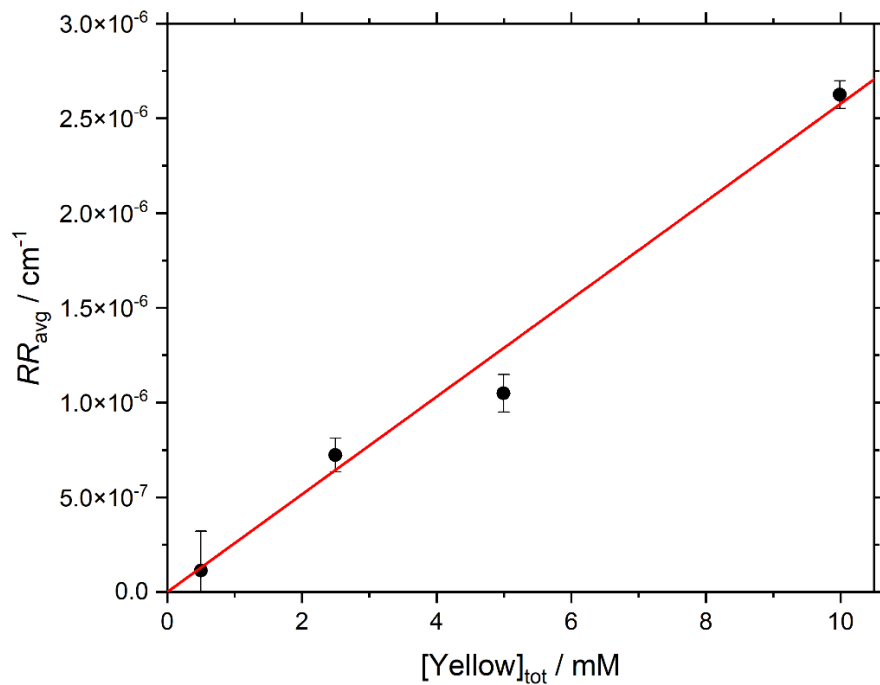


Figure S13: Rayleigh ratio of samples containing Yellow at various concentrations in the NaHCO<sub>3</sub>/Na<sub>2</sub>CO<sub>3</sub> buffer at 25 °C. The Rayleigh ratio was obtained by SLS and averaged over all angles due to the absence of an angular dependency. The red line displays a linear fit to the data.

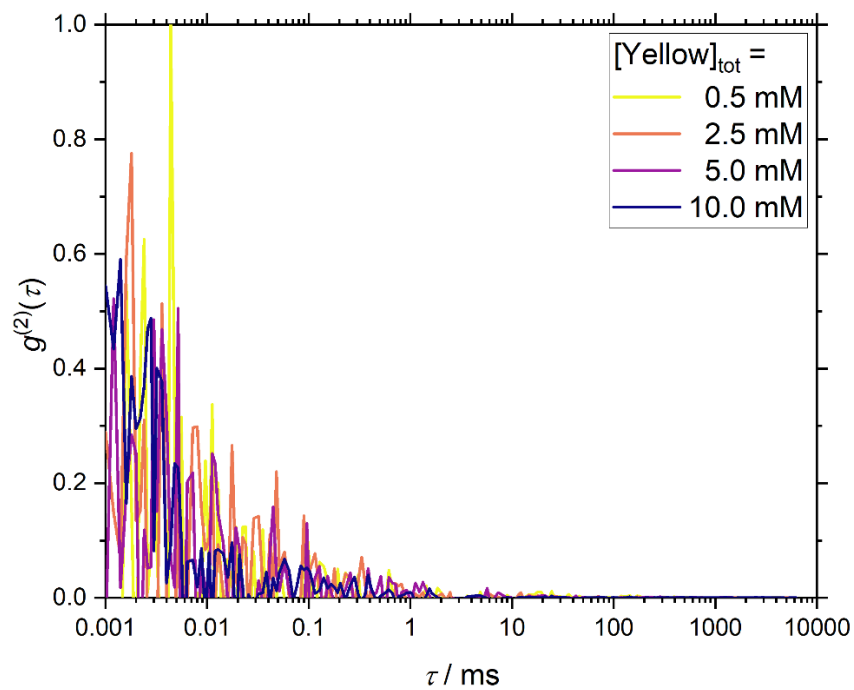


Figure S14: DLS intensity correlation functions  $g^{(2)}(\tau)$  of samples containing varying concentrations of Yellow in the NaHCO<sub>3</sub>/Na<sub>2</sub>CO<sub>3</sub> buffer at 25 °C.

Absence of self-aggregation of Yellow was confirmed by light scattering. Combined static and dynamic light scattering (SLS and DLS) was performed on solutions containing between 0.5 mM and 10 mM of Yellow. First of all,  $RR$  detected by SLS did not depend on the scattering angle. Therefore,  $RR$  obtained at different measurement angles were averaged to yield  $RR_{\text{avg}}$  and plotted against the concentration of Yellow in the corresponding sample. The resulting linear relationship between  $RR_{\text{avg}}$  and  $[\text{Yellow}]_{\text{tot}}$  is shown in Figure S13 and confirms the absence of concentration-induced aggregation. The absence of a correlation function in DLS-measurements (Figure S14) confirms the absence of aggregates.

**Application of exciton theory to determine Blue dimer geometry.** The dimer spectrum of Blue shows two clearly discernible peaks with absorption maxima at energies higher and lower than that of the monomer. This can be explained by exciton theory:<sup>24</sup> Upon dimerization, the first excited energy state of the monomer splits into two due to dipole-dipole interaction between the two interacting molecules.<sup>18,24,45,46</sup> For quantitative calculations, the ground state of the monomer is assumed to remain unaffected during dimerization.<sup>45</sup> The dimer splitting depends on transition dipole moments and on dimer geometry.<sup>46</sup> As the planar character of the mostly aromatic molecule Blue suggests  $\pi$ -stacking as one of the preferred types of intermolecular interactions, two possible dimer geometries depicted in Figure S15 were further investigated: The model of coplanar inclined transition dipoles (Figure S15(A)) and the model of non-planar transition dipoles (Figure S15(B)).<sup>19</sup>

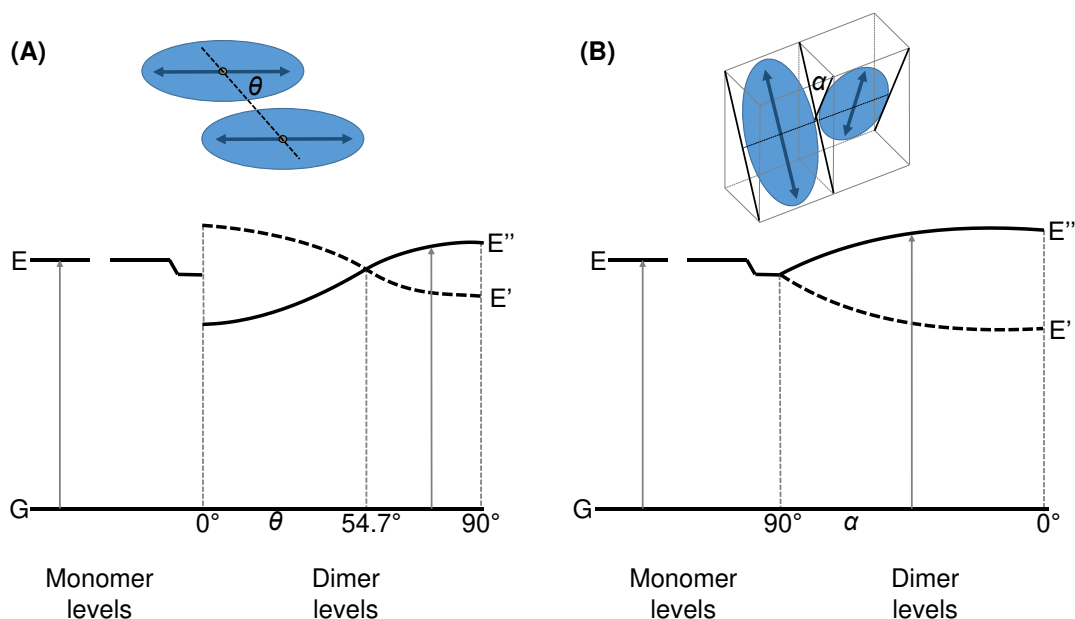


Figure S15: (A) Schematic and exciton band energy diagram for a molecular dimer with coplanar transition dipoles. (B) Schematic and exciton band energy diagram for a molecular dimer with non-planar transition dipoles and an angle  $\alpha$  between molecular planes. The schemes were adopted from Kasha et al.<sup>19</sup>

Both geometries are simple and permit simultaneous H-band and J-band absorption with the blue-shifted H-band showing a larger intensity than the red-shifted J-band.<sup>45</sup> The asymmetry of functional groups in the molecule Blue may lead to deviations from a precisely coplanar arrangement of transition dipole moments. Nevertheless, both geometries are assumed to be reasonable enough to calculate structural features of the dimer.

Within the model of coplanar inclined transition dipoles (Figure SI5(A)) the angle  $\theta$  made by the polarization axes of the unit molecule with the line of molecular centers and the interplanar spacing  $R$  can be calculated according to:<sup>19,45</sup>

$$\theta = \arctan\left(\frac{f_H^2}{f_J^2}\right) \quad (\text{SI13})$$

$$R = \left(\frac{2.14 \cdot 10^{10} \cdot f_M \cdot (1 - 3 \cos^2 \theta)}{\tilde{\nu}_M \cdot \Delta\tilde{\nu}_{H,J}}\right)^{\frac{1}{3}} \quad \text{in } [\text{\AA}] \quad (\text{SI14})$$

$f_J$ ,  $f_H$  and  $f_M$  are the oscillator strengths of the J-band, the H-band and the monomer respectively.  $\tilde{\nu}_M$  is the absorbance maximum position of the monomer in [ $\text{cm}^{-1}$ ] and  $\Delta\tilde{\nu}_{H,J} = \tilde{\nu}_H - \tilde{\nu}_J$  the dimer splitting in [ $\text{cm}^{-1}$ ].

Assuming the model of non-planar transition dipoles (Figure SI5(B)), the angle  $\theta$  is considered to be zero and an angle  $\alpha$  describes the torsion between two molecular planes. This difference in geometry also needs to be considered when calculating the interplanar spacing  $R$ .<sup>20,25,45</sup>

$$\alpha = 2 \cdot \arctan \sqrt{\frac{f_J}{f_H}} \quad (\text{SI15})$$

$$R = \left(\frac{2.14 \cdot 10^{10} \cdot f_M \cdot \cos \alpha}{\tilde{\nu}_M \cdot \Delta\tilde{\nu}_{H,J}}\right)^{\frac{1}{3}} \quad \text{in } [\text{\AA}] \quad (\text{SI16})$$

The oscillator strength  $f$  of any transition can be calculated from the area under the respective band according to:<sup>47</sup>

$$f = 4.32 \cdot 10^{-9} \frac{\text{mol cm}^2}{\text{L}} \int_{\text{band}} \epsilon \, d\tilde{\nu} \quad (\text{SI17})$$

Where  $\epsilon$  is the molar extinction coefficient in [ $\text{L mol}^{-1} \text{cm}^{-1}$ ] and  $\tilde{\nu}$  the wavenumber in [ $\text{cm}^{-1}$ ].

To obtain oscillator strengths  $f$  and absorption maximum positions of relevant transitions, monomer- and dimer-spectrum were described with Gauss-functions. This can be justified by various spectral line broadening effects such as interaction between absorbing species and solvent, Doppler broadening and limitations on resolution.<sup>48</sup>

The monomer spectrum exhibits a weak vibrational fine structure. To obtain the fundamental mode of vibronic transitions  $\Delta\tilde{\nu}_{\text{vib}}$ , the fourth derivative of the spectrum was calculated to make possible a more precise localization of transitions contributing to the monomer spectrum (Figure SI6).<sup>20</sup>

Four components with their maxima being separated by  $\Delta\tilde{\nu}_{\text{vib}} = (1578 \pm 185) \text{ cm}^{-1}$  were resolved. This likely corresponds to the fundamental mode of a single vibronic progression according to:

$$\tilde{\nu}_{M,i} = \tilde{\nu}_M + i \cdot \Delta\tilde{\nu}_{\text{vib}} \quad i=1, 2, 3, \dots \quad (\text{SI18})$$

The value  $\Delta\tilde{\nu}_{\text{vib}}$  determined for the fundamental mode is reasonable, as fundamental modes of aromatic compounds typically lie around  $1400 \text{ cm}^{-1}$ .<sup>49</sup> Following this analysis, the monomer spectrum was best described with one vibrational progression, taking into account four bands with Gaussian line shape and fixed positions as obtained by derivative analysis in Figure SI16. Therefore, the molar extinction coefficient of the monomer  $\epsilon_M(\tilde{\nu})$  as a function of wavenumber  $\tilde{\nu}$  was described by the following equation:

$$\epsilon_M(\tilde{\nu}) = \frac{A_M}{w_M \cdot \sqrt{\frac{\pi}{2}}} \exp\left[-\frac{2 \cdot (\tilde{\nu} - \tilde{\nu}_M)^2}{w_M^2}\right] + \sum_{i=1}^3 \frac{A_{M,i}}{w_{M,i} \cdot \sqrt{\frac{\pi}{2}}} \exp\left[-\frac{2 \cdot (\tilde{\nu} - \tilde{\nu}_{M,i})^2}{w_{M,i}^2}\right] \quad (\text{SI19})$$

$A_M$  and  $A_{M,i}$  correspond to the area under the respective Gauss function and therefore directly replace the integral in equation (SI17).  $w_M$  and  $w_{M,i}$  describe peak width and correspond to double the standard deviation from the peak maximum.  $\tilde{\nu}_M$  and  $\tilde{\nu}_{M,i}$  denote peak positions and were kept constant following equation (1). Fitted Gaussian bands are shown in Figure SI7(A) and the calculated oscillator strength  $f_M$  is given in Table SI1.

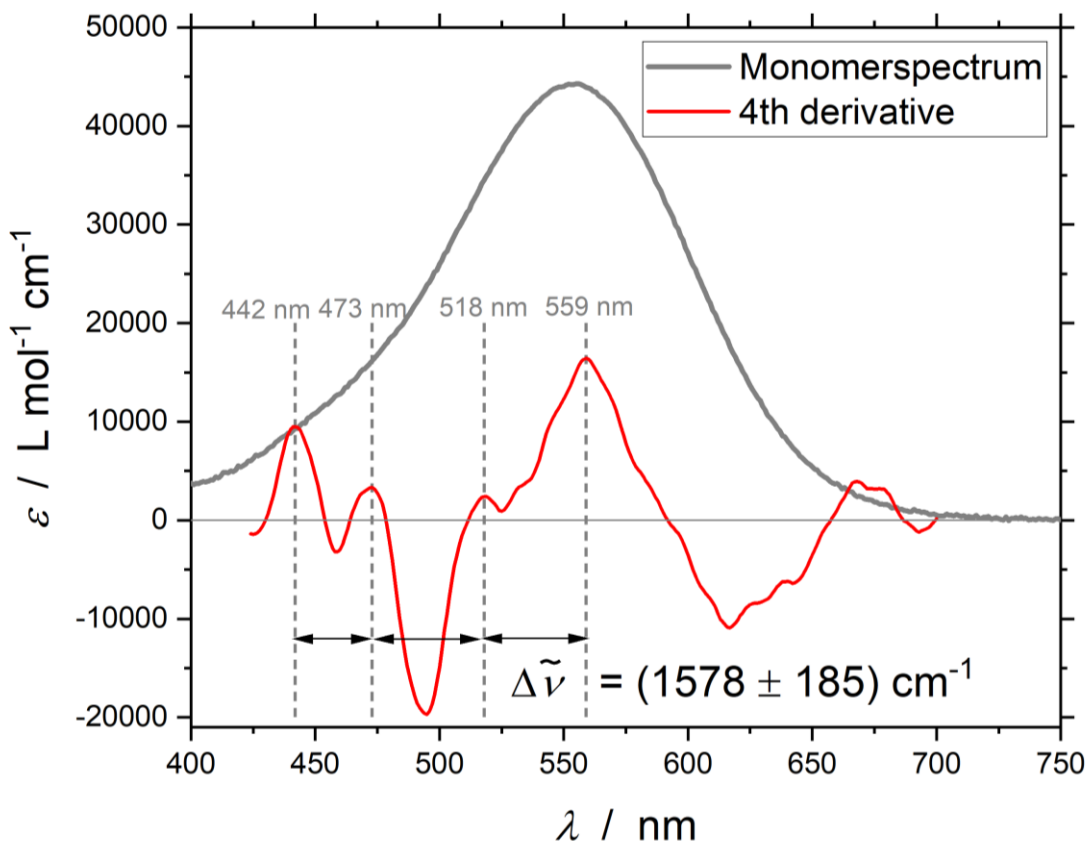


Figure SI6: Monomerspectrum of Blue recorded at  $[\text{Blue}]_{\text{tot}} = 5 \mu\text{M}$  (grey line) and its 4<sup>th</sup> derivative (red line).

A similar analysis was carried out to describe the dimer spectrum with Gauss functions, taking into account the J-band and the H-band. As the dimer spectrum does not show a distinct vibrational fine structure, the same fundamental vibrational mode  $\Delta\tilde{\nu}_{\text{vib}} = (1578 \pm 185) \text{ cm}^{-1}$  as for the monomer spectrum was assumed for the vibronic progression of the H-band. Due to its comparably small intensity, a vibronic progression of the J-band was not considered.<sup>20</sup> Therefore, keeping peak positions constant, the dimer spectrum was best described with six Gaussian bands:  $\tilde{\nu}_J = 15868 \text{ cm}^{-1}$ ,  $\tilde{\nu}_H = 17889 \text{ cm}^{-1}$  and:

$$\tilde{\nu}_{H,i} = \tilde{\nu}_H + i \cdot \Delta\tilde{\nu}_{\text{vib}} \quad i = 1, 2, 3, \dots \quad (\text{SI20})$$

$$\begin{aligned} \epsilon_D(\tilde{\nu}) = & \frac{A_J}{w_J \cdot \sqrt{\frac{\pi}{2}}} \exp\left[\frac{-2 \cdot (\tilde{\nu} - \tilde{\nu}_J)^2}{w_J^2}\right] + \frac{A_H}{w_H \cdot \sqrt{\frac{\pi}{2}}} \exp\left[\frac{-2 \cdot (\tilde{\nu} - \tilde{\nu}_H)^2}{w_H^2}\right] \\ & + \sum_{i=1}^4 \frac{A_{H,i}}{w_{H,i} \cdot \sqrt{\frac{\pi}{2}}} \exp\left[\frac{-2 \cdot (\tilde{\nu} - \tilde{\nu}_{H,i})^2}{w_{H,i}^2}\right] \end{aligned} \quad (\text{SI21})$$

The result is visualized in Figure SI7(B). Inserting  $A_J$  and  $A_H$  as the integral in equation (SI17), oscillator strengths  $f_J$  and  $f_H$  of the respective bands were obtained (Table SI1).

Applying equations (SI13) and (SI14) for the calculation of parameters describing the dimer geometry of coplanar inclined transition dipoles leads to an inclination angle  $\theta = 89^\circ$ . This is very close to  $\theta = 90^\circ$ , i.e. the absence of inclination, and confirms the presence of H-aggregated dimers. In addition to that it strengthens an analysis according to the dimer geometry of non-planar transition dipoles without inclination. Within this model, a tilt angle  $\alpha = 42^\circ$  and an interplanar spacing  $R = 5.2 \text{ \AA}$  was obtained, which is comparable to  $R = 5.7 \text{ \AA}$  obtained within the previous model. These values are reasonable. In literature, values between  $3.4 \text{ \AA}$  and  $8.3 \text{ \AA}$  were reported for the interplanar spacing between dye molecules containing aromatic units.<sup>20,25,50</sup>

Table SI1: Peak positions and oscillator strengths of transitions into the vibrational ground state of excited electronic state(s) for the monomer and the dimer of Blue. Results from analysis according to exciton theory are shown.

Monomerspectrum	
$\tilde{\nu}_M [\text{cm}^{-1}]$	17 889
Fundamental mode $\Delta\tilde{\nu}_{\text{vib}} [\text{cm}^{-1}]$	$1\,578 \pm 185$
$f_M$	0.51
Dimerspectrum	
$\tilde{\nu}_J [\text{cm}^{-1}]$	15 868
$f_J$	0.11
$\tilde{\nu}_H [\text{cm}^{-1}]$	19 125
$f_H$	0.73
Dimer splitting $\Delta\tilde{\nu}_{H,J} [\text{cm}^{-1}]$	3 257
Exciton Model: Coplanar inclined transition dipoles	
Inclination angle $\theta [^\circ]$	89
Interplanar spacing $R [\text{\AA}]$	5.7
Exciton Model: Non-planar transition dipoles	
Tilt angle $\alpha [^\circ]$	42
Interplanar spacing $R [\text{\AA}]$	5.2

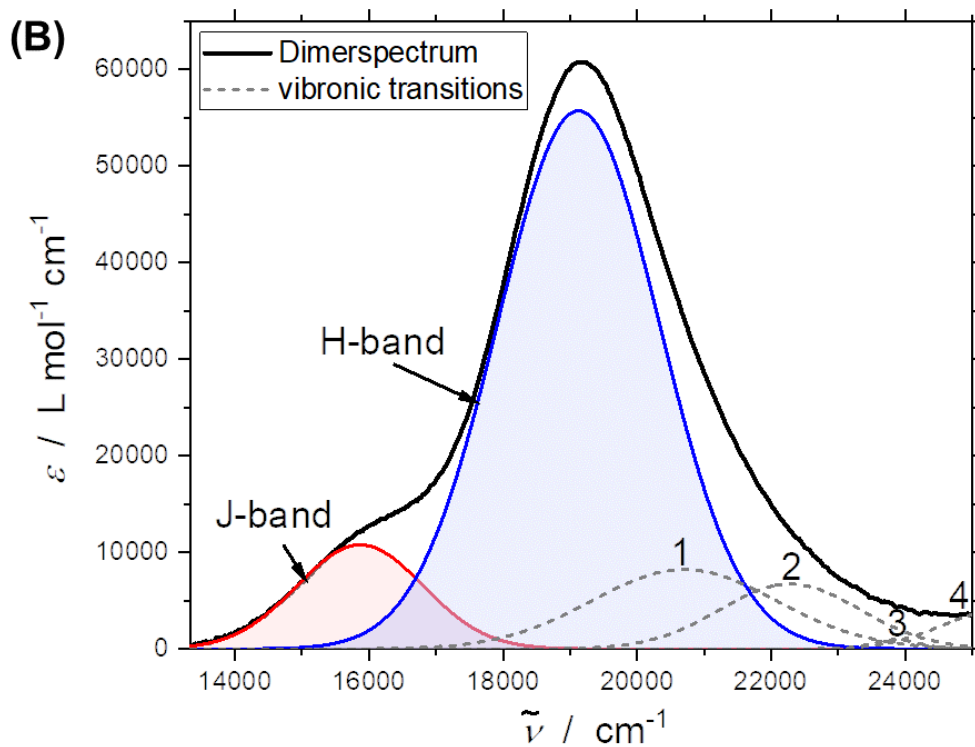
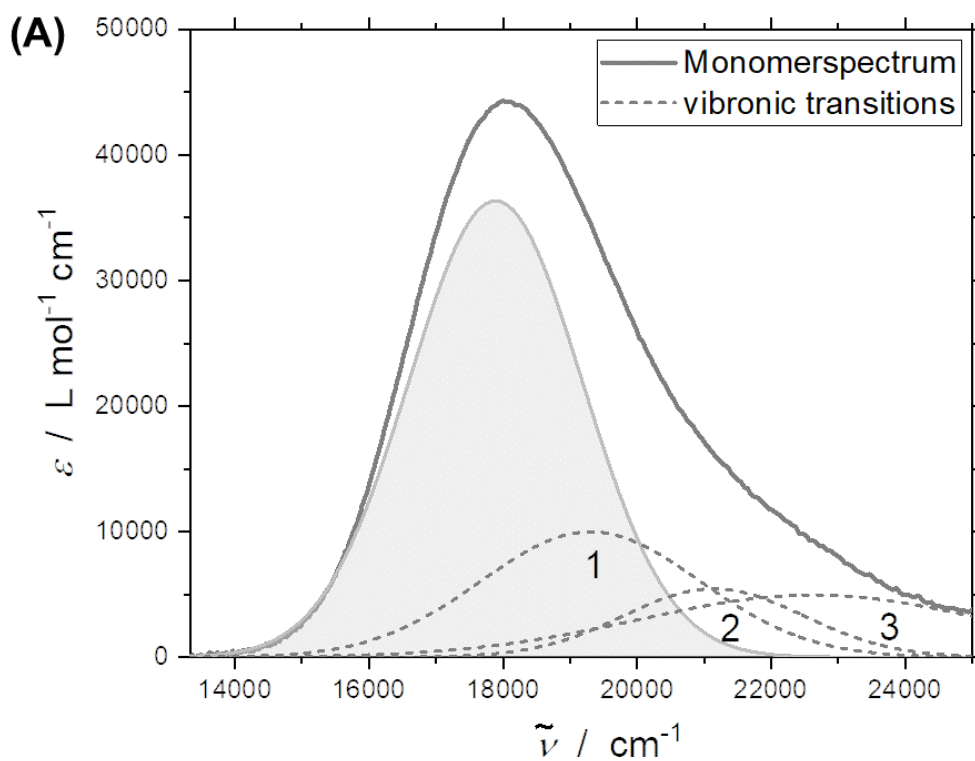


Figure S17: (A) Monomer spectrum of Blue recorded at  $[\text{Blue}]_{\text{tot}} = 5 \mu\text{M}$  (grey line) and underlying Gaussian bands. (B) Dimer spectrum of Blue (black line) and underlying Gaussian bands.

## Guinier analysis of SANS curves of Blue solutions

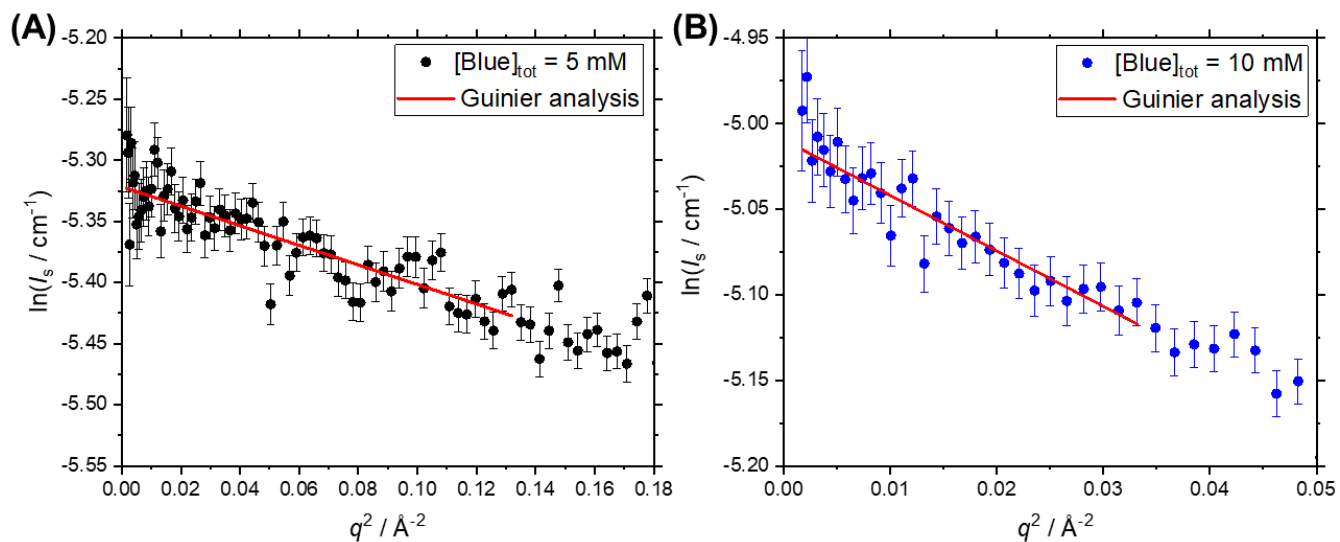


Figure S18: Guinier analysis of linearized SANS curves of solutions containing (A)  $[\text{Blue}]_{\text{tot}} = 5\text{ mM}$  and (B)  $[\text{Blue}]_{\text{tot}} = 10\text{ mM}$  in an  $\text{NaHCO}_3/\text{Na}_2\text{CO}_3$  buffer with  $\text{pD} = 10.7$  and  $I \approx 0.25\text{ M}$  prepared in  $\text{D}_2\text{O}$ . Results were given in Table 1 in the main text.

**Theoretical calculation of radius of gyration of Blue dimer.** The radius of gyration  $R_g$  of a homogeneous cylinder can be calculated according to the following equation:<sup>51</sup>

$$R_g^2 = \frac{b^2}{2} + \frac{L^2}{12} \quad (\text{SI22})$$

$b$  is the radius and  $L$  the length of the cylinder. Even though a dimer consisting of two Blue molecules is likely not correctly described with a homogeneous cylinder model, it gives a first approximation of its radius of gyration. The cylinder radius was assumed to be half the distance between the negatively charged oxygen ion of the alkoxide group and the carbon atom in position 7 of the aromatic 2,1-benzothiazole subunit:  $b = 0.5 \cdot 10.5\text{ \AA} = 5.25\text{ \AA}$ . The cylinder length was assumed to correspond to the interplanar spacing between two transition dipole moments:  $L = R = 5.2\text{ \AA}$  determined by exciton theory. This yields  $R_g \approx 4\text{ \AA}$ .



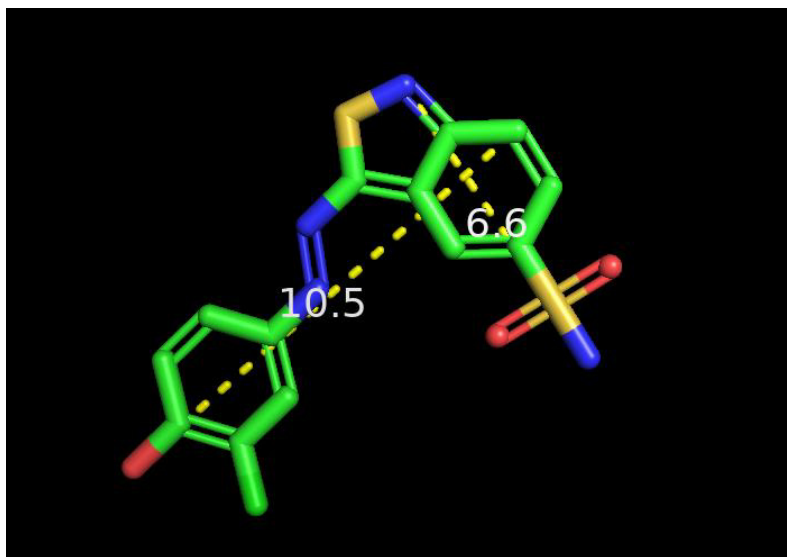


Figure S19: Chemical structure of dissociated Blue, not including hydrogen atoms, and distances between some atoms generated with the software PyMOL.<sup>52</sup> Distances are given in Å.

**Red self-aggregation.** SANS curves of two solutions of Red were shown in Figure 8 in the main text. One solution contained  $[\text{Red}]_{\text{tot}} = 10$  mM and the other one was intended to contain  $[\text{Red}]_{\text{tot}} = 15$  mM. The latter was filtered too soon after its preparation, resulting in a loss of Red which was not completely dissolved and therefore a reduction of dye concentration to  $[\text{Red}]_{\text{tot}} < 10$  mM. This is visible by a lower incoherent background for this sample compared to the one containing  $[\text{Red}]_{\text{tot}} = 10$  mM. In order to obtain an idea about the actual dye concentration in this sample, its SANS forward scattering intensity  $I_0$  was compared to that of the sample with  $[\text{Red}]_{\text{tot}} = 10$  mM,  $I_0$  being determined by Guinier analysis. The corresponding analysis is shown in Figure S110 with results given in the caption. As  $I_0$  of the sample with unknown Red concentration was determined to be approximately half the forward scattering intensity of the sample with  $[\text{Red}]_{\text{tot}} = 10$  mM, its concentration is approximated to be  $[\text{Red}]_{\text{tot}} \approx 5$  mM. Not precisely knowing the concentration of Red does not pose a big problem as no absolute analysis of scattering intensities was performed here. Both SANS curves of solutions of Red displayed in the main text (Figure 8) show similar slopes and features and the radii of gyration obtained by Guinier analysis in the high- $q$ -region are almost identical (Table S12). Therefore, the same model was applied to fit both SANS curves simultaneously, permitting the incoherent background and volume fractions to differ. Results from form factor fitting with the sum of a fractal form factor and a Guinier fit are given in Table S12.<sup>31</sup> The fractal describes the mid- and low- $q$  region and is characterized by the radius of spherical building blocks,  $R_{\text{block}}$ , its scattering length density  $\rho_{\text{block}}$ , the fractal dimension  $D_f$  and the cluster correlation length  $L_{\text{corr}}$ , which represents the total fractal

cluster size.  $\phi_{\text{block}}$  is the volume fraction of spherical building blocks. As size parameters were kept constant, fits only differ in scaling of the Guinier and the fractal contribution.

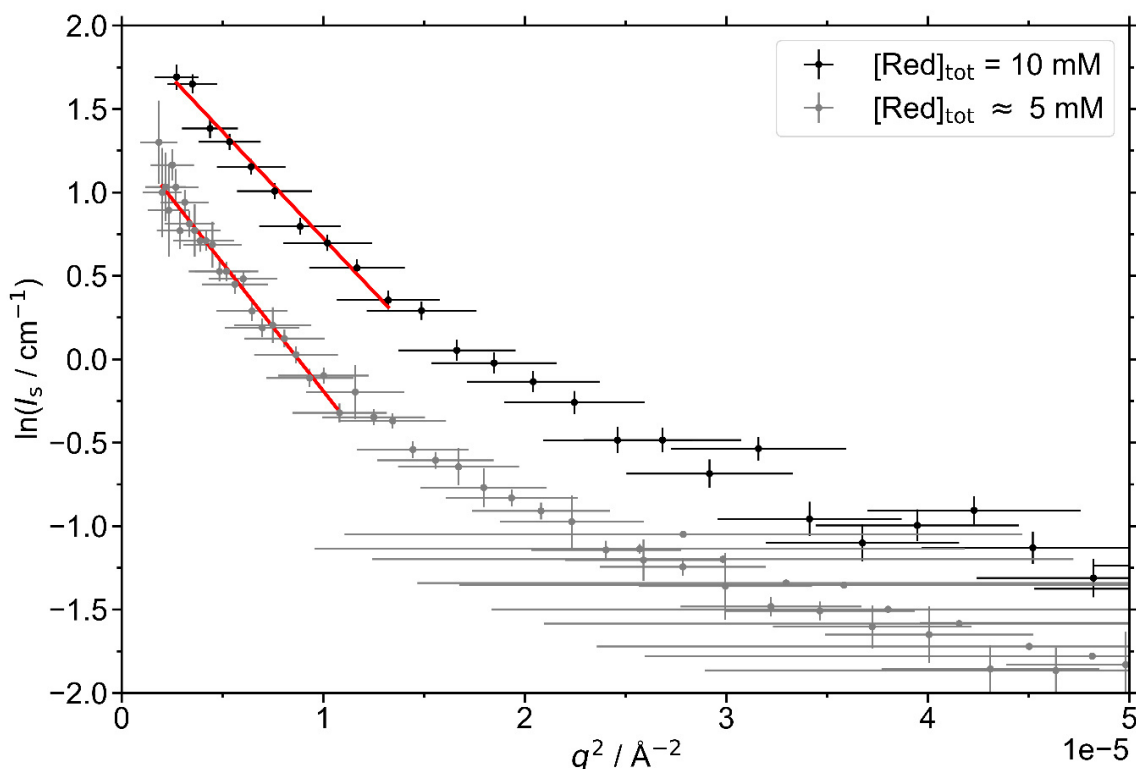


Figure S110: Guinier analysis and linearized SANS curves of solutions containing Red at a concentration of 10 mM and approximately 5 mM. Solutions were prepared in a  $\text{NaHCO}_3/\text{Na}_2\text{CO}_3$  buffer in  $\text{D}_2\text{O}$  with  $\text{pD} = 10.7$  and  $I \approx 0.25 \text{ M}$ . Results of Guinier analysis for  $[\text{Red}]_{\text{tot}} = 10 \text{ mM}$ :  $l_0 = (7.4 \pm 0.3) \text{ cm}^{-1}$ ,  $R_g = (620 \pm 13) \text{ \AA}$ , for  $[\text{Red}]_{\text{tot}} \approx 5 \text{ mM}$ :  $l_0 = (3.8 \pm 0.2) \text{ cm}^{-1}$ ,  $R_g = (679 \pm 13) \text{ \AA}$ .

An alternative to describing the recorded SANS curves with a fractal form factor could be the sum of a star form factor and the form factor of a smaller species, which would exist in equilibrium and act as a building block for the larger structure. Considering  $\pi$ - $\pi$ -stacking interactions to be of major relevance to the aggregation of Red, the presence of cylindrical core aggregates is likely. However, the use of only a cylinder model to describe recorded SANS curves is not plausible due to several characteristics of the curve: First of all, a  $I_s \propto q^{-2.66}$  slope is observed in the low- to mid- $q$  region. Second of all, the Kratky plot of the curves (Figure S11(A)) shows an initial maximum before an approximately linear increase of the curve is observed. Third of all, a minimum can be seen in the Holtzer plot (Figure S12(A)) before a plateau value is reached. The plateau value is characteristic for rod-like aggregates.<sup>53</sup> Both, the maximum in the Kratky plot and the minimum in the Holtzer plot point towards a rather compact structure, which could result from branching and network formation due to overlap of the cylindrical core aggregates.<sup>37,38</sup> A possibility to describe

branching points would be the application of a form factor model for stars, which considers the existence of specific star centres.<sup>38,54</sup> Huber et al. performed Monte Carlo calculations to determine such form factors for star-branched polymers. The Kratky- and Holtzer plot of example form factors for polymer stars of different sizes, the size being indicated by the number of bonds  $n_B$ , are shown in Figure SI11(B) and Figure SI12(B) respectively.<sup>38</sup> These form factors show similar features in the Kratky- and Holtzer-plot compared to the curves recorded from solutions of Red: Firstly, the initial maximum in the Kratky plot is well present and secondly, a minimum can be observed in the Holtzer plot before a plateau value is reached. Considering branching due to the overlap of cylindrical core aggregates of Red, the sum of a star form factor and the form factor of a cylinder could therefore be a reasonable model to describe the observed SANS curves from Red solutions.

Table SI2: SANS analysis of two solutions of Red. A form factor consisting of additive contributions from a Guinier-fit and a fractal model was used.<sup>31</sup>

Guinier Analysis, high- $q$	[Red] <sub>tot</sub> = 10 mM	[Red] <sub>tot</sub> ≈ 5 mM
$R_g$ [Å]	$8.7 \pm 0.2$	$8.5 \pm 0.1$
Fit: Guinier + Fractal	[Red] <sub>tot</sub> = 10 mM	[Red] <sub>tot</sub> ≈ 5 mM
$BG_{\text{incoherent}}$ [cm <sup>-1</sup> ]	0.001357 (fixed)	0.001015 (fixed)
Scale (Guinier)	$0.0019 \pm 0.0003$	$0.00120 \pm 0.00007$
$R_g$ (Guinier) [Å]		8.5 (fixed)
Scale (Fractal)	$0.009 \pm 0.001$	$0.0043 \pm 0.0005$
$R_{\text{block}}$ [Å]		$9 \pm 1$
$D_f$		$2.66 \pm 0.03$
$L_{\text{corr}}$ [Å]		$437 \pm 10$
$\phi_{\text{block}}$		0.0022 (fixed)
$\rho_{\text{block}}$ [10 <sup>-6</sup> Å <sup>-2</sup> ]		2.642 (fixed)
$\rho_{\text{solv}}$ [10 <sup>-6</sup> Å <sup>-2</sup> ]		6.376 (fixed)
$\chi_{\text{red}}^2$	1.5175	3.3116

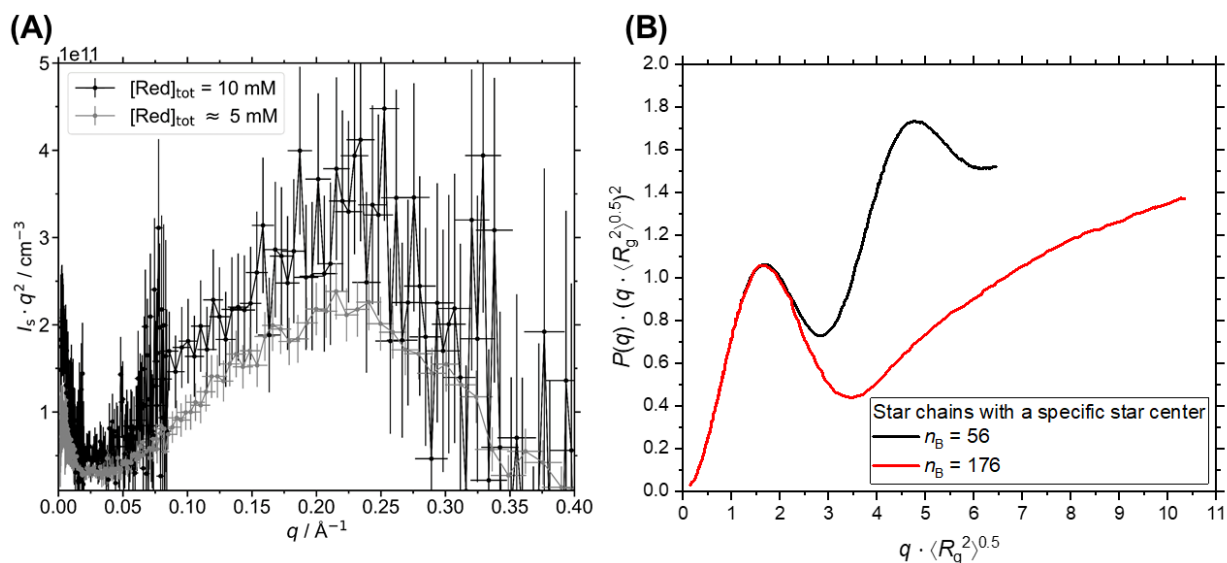


Figure S111: (A) Kratky plot of SANS curves from solutions containing Red at a concentration of 10 mM and 5 mM. Solutions were prepared in a  $\text{NaHCO}_3/\text{Na}_2\text{CO}_3$  buffer in  $\text{D}_2\text{O}$  with  $\text{pD} = 10.7$  and  $l \approx 0.25$  M. (B) Kratky plot of a form factor model for star polymer chains with a specific star center as calculated by Huber et al.<sup>38</sup> The size of the polymer is indicated by the number of bonds,  $n_B$ .  $R_g$  is the radius of gyration and  $P(q)$  the form factor.

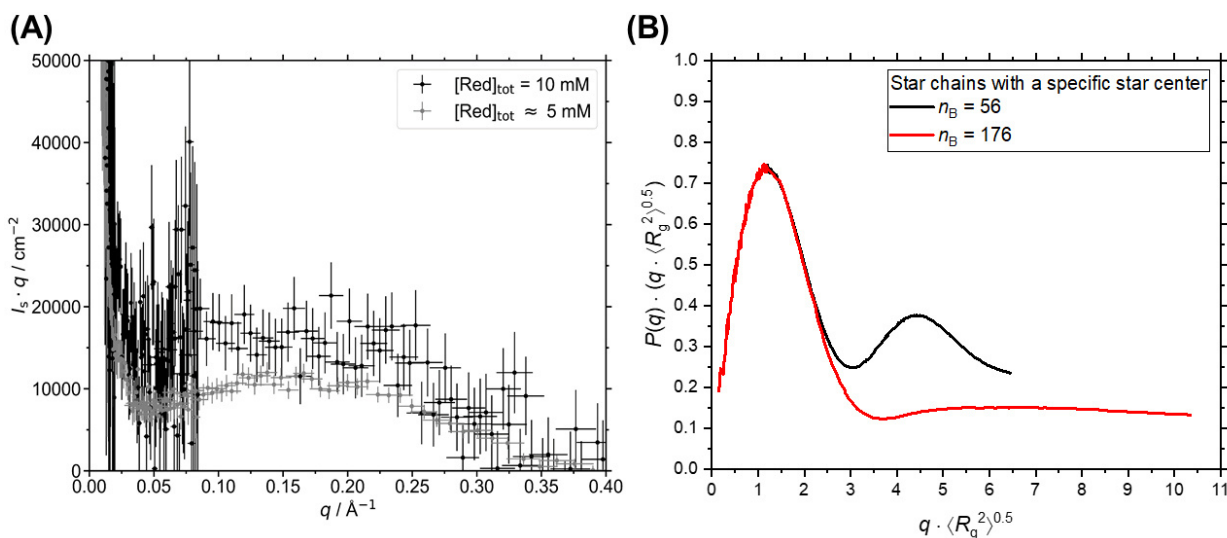


Figure S112: (A) Holtzer plot of SANS curves from solutions containing Red at a concentration of 10 mM and 5 mM. Solutions were prepared in a  $\text{NaHCO}_3/\text{Na}_2\text{CO}_3$  buffer in  $\text{D}_2\text{O}$  with  $\text{pD} = 10.7$  and  $l \approx 0.25$  M. (B) Holtzer plot of a form factor model for star polymer chains with a specific star center as calculated by Huber et al.<sup>38</sup> The size of the polymer is indicated by the number of bonds,  $n_B$ .  $R_g$  is the radius of gyration and  $P(q)$  the form factor.

To extend the available  $q$ -range and to confirm findings from SANS measurements, it was attempted to perform light scattering measurements on solutions of Red. However, data quality and the available concentration range is strongly reduced by absorption of the dye Red at the wavelength of  $\lambda = 632.8$  nm available for light scattering measurements (Figure S113(A)). Therefore, only a short qualitative discussion of light scattering data obtained from solutions containing  $[\text{Red}]_{\text{tot}} = 0.5$  mM and  $[\text{Red}]_{\text{tot}} = 1$  mM is given here. A Zimm-plot of static light

scattering data is displayed in Figure S113(B) and shows a strong angular dependency of the scattered intensity, which confirms the existence of rather large assemblies like it was already shown by SANS. Furthermore, the presence of aggregates is confirmed by the existence of a correlation function from dynamic light scattering measurements. This is shown exemplarily for two angles in Figure S14. Theoretically, the intensity correlation function  $g^{(2)}(\tau)$  should approach a value of 0.33 for low correlation times  $\tau$ , which is specific to the setup of the light scattering device. However, data quality is hampered by the absorption of the dye Red and it was therefore abstained from quantitative analysis.

Figure S115 shows the ROESY spectrum of a 10 mM solution of Red. No cross peaks are observed, which is likely due to the strong peak broadening of signals b and c.

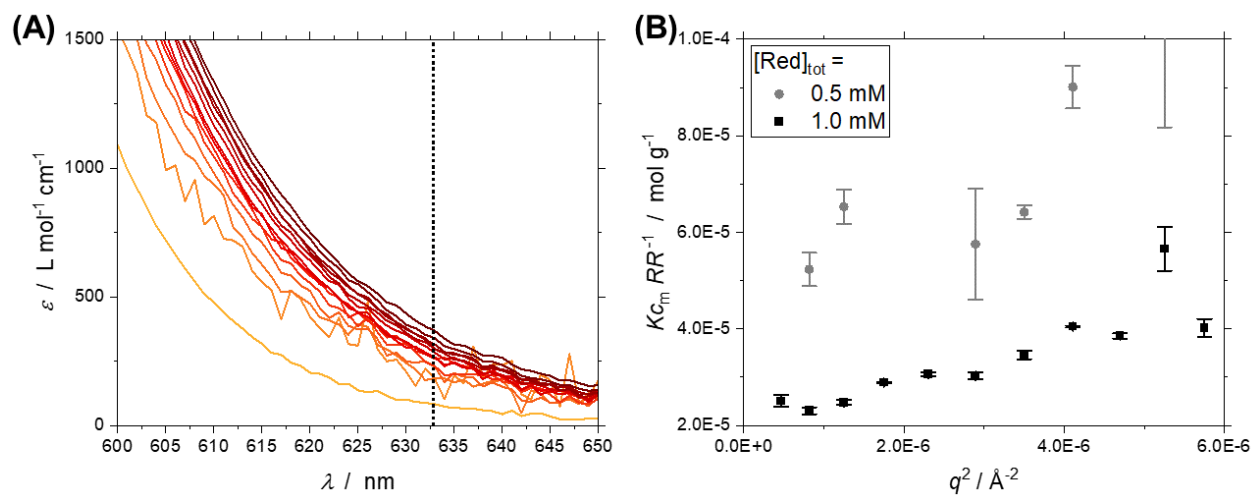


Figure S113: (A) Section of UV/vis absorption spectra from solutions of Red containing  $0.02 \text{ mM} < [\text{Red}]_{\text{tot}} < 6 \text{ mM}$  (yellow to dark red lines). The wavelength, at which light scattering measurements can be performed is indicated by a vertical, dotted line. (B) Apparent Zimm plot of Rayleigh ratios resulting from static light scattering on solutions containing either  $[\text{Red}]_{\text{tot}} = 0.5 \text{ mM}$  or  $[\text{Red}]_{\text{tot}} = 1.0 \text{ mM}$  in a  $\text{NaHCO}_3/\text{Na}_2\text{CO}_3$  buffer with  $\text{pH} = 10.5$  and  $I \approx 0.25 \text{ M}$  prepared in  $\text{H}_2\text{O}$ . Rayleigh ratios were not corrected for absorption.  $K$  was calculated based on the following values:  $\lambda_0 = 632.8 \text{ nm}$ ,  $n_m = 1.3326$ ,  $\left(\frac{dn}{dc_m}\right) = 0.000339 \text{ mL mg}^{-1}$ .  $c_m$  is the mass concentration of the solute.

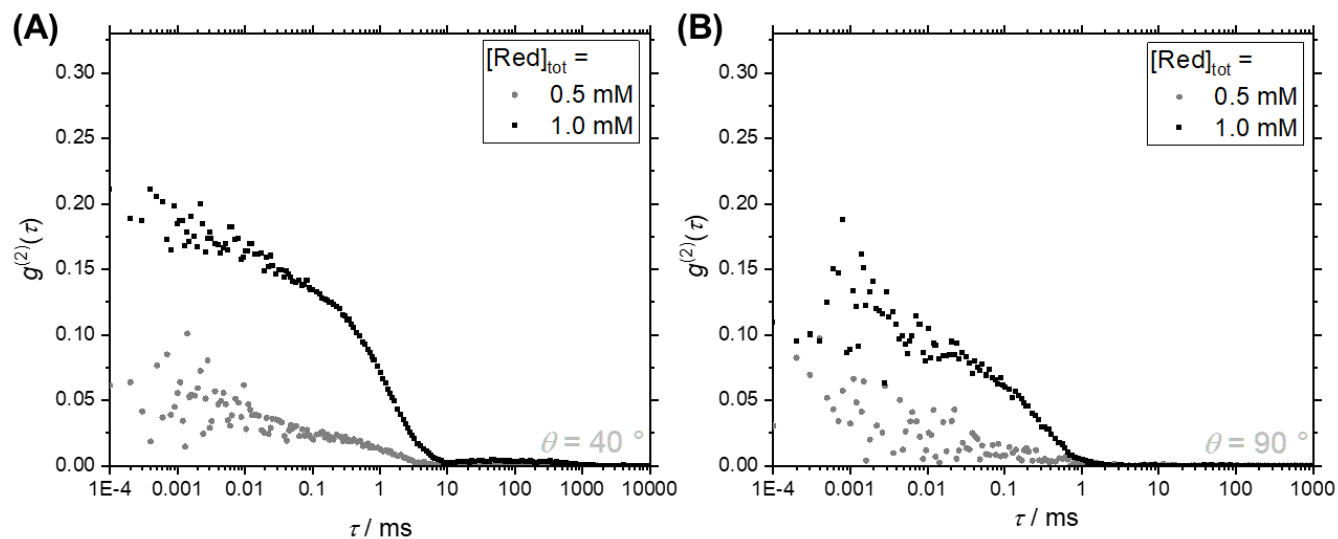


Figure S14: Intensity correlation functions  $g^{(2)}(\tau)$  of solutions of Red in an aqueous  $\text{NaHCO}_3/\text{Na}_2\text{CO}_3$  buffer (pH = 10.5,  $I \approx 0.25 \text{ M}$ ) from dynamic light scattering. (A) Measurement at a scattering angle of  $40^\circ$ , (B) Measurement at a scattering angle of  $90^\circ$ .

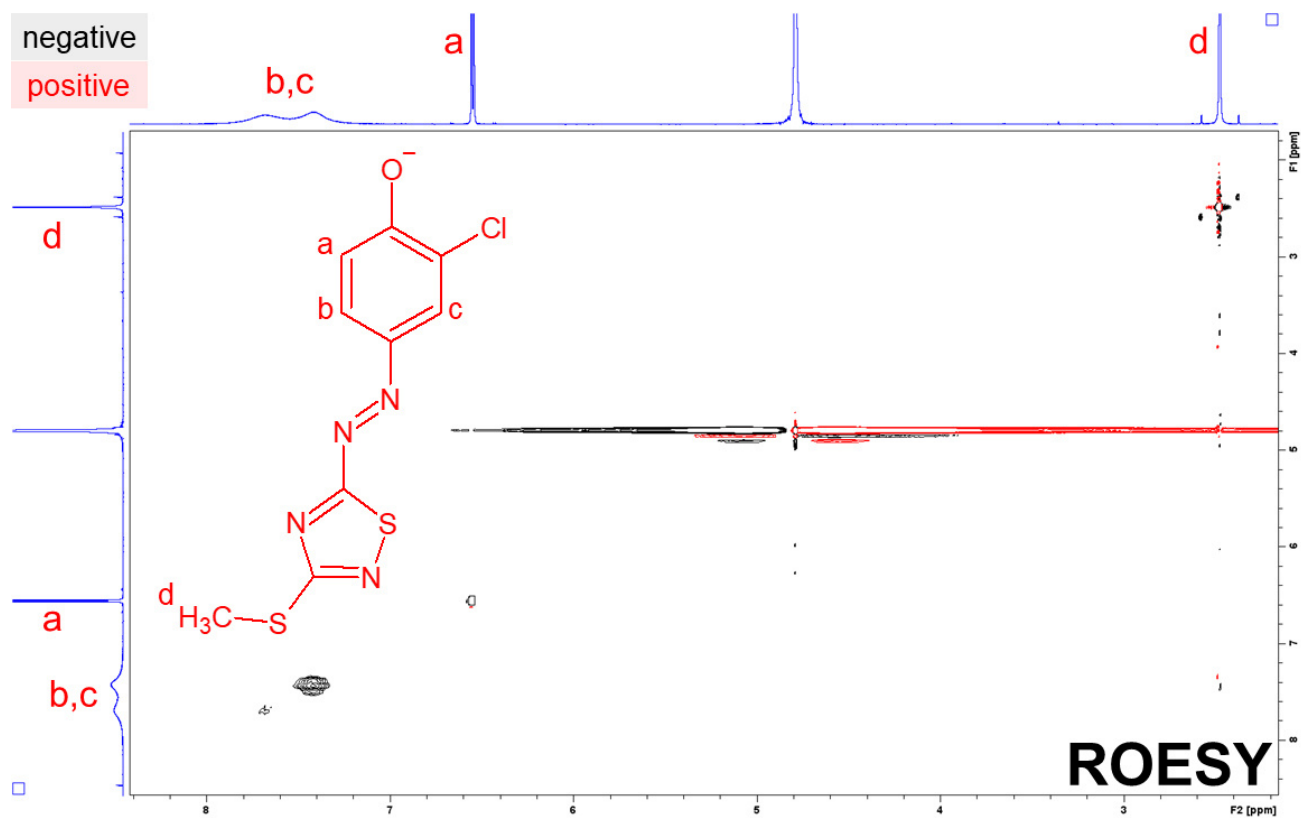


Figure S15: ROESY spectrum of a solution containing  $[\text{Red}]_{\text{tot}} = 10 \text{ mM}$  in an  $\text{NaHCO}_3/\text{Na}_2\text{CO}_3$  buffer (pD = 10.7,  $I \approx 0.25 \text{ M}$ ) prepared in  $\text{D}_2\text{O}$ . Negative peaks are shown in black, whereas peaks with positive intensities are shown in red.

### Source Code: Determination of Blue dimer spectrum (Python 3)

```
import numpy as np
from scipy.optimize import leastsq

#conc = 1-dimensional array containing concentrations of Blue
#A_exp = 1-dimensional array with length of conc,
#    contains experimental values of absorbance at respective concentration
#spectra = 2-dimensional array with number of lines corresponding to number of
#    wavelengths and number of columns corresponding to number of concentrations,
#    contains experimental data
#p = array containing initial guess of parameters
#K_in = initial guess of dimerization constant
#e_list = array containing initial guess of dimer spectrum
#    (spectrum of sample with highest concentration of Blue used)
#wavelengthlist = array containing wavelengths

p = np.concatenate((K_in,e_list))

def A_red_theo(conc,e_M,KD,e_D):
    A_red = np.zeros(len(conc))
    for i,ctot in enumerate(conc):
        A_red[i] = (e_D*(ctot/2-(np.sqrt(1+8*KD*ctot) - 1)/(8*KD))+e_M*(np.sqrt(1+8*KD*ctot)-1)/(4*KD))
    return A_red

def err_loc(conc,A_exp,e_M,KD,e_D):
    return np.subtract(A_exp,A_red_theo(conc,e_M,KD,e_D))

def err_glob(p,conc,spectra):
    errors = np.zeros([0])
    KD = p[0]
    for i,l in enumerate(wavelengthlist):
        e_M = monomer_E[i] #molar extinction coefficient of monomer at given wavelength
        A_exp = spectra[i]
        e_D = p[i+1]
        errors = np.concatenate((errors, err_loc(conc,A_exp,e_M,KD,e_D)))
    return(errors)

popt, pcov, infodict, errmsg, success = leastsq(err_glob,p,args = (conc, spectra),full_output=1)
residuals = err_glob(popt,conc,spectra)
squaredresiduals = np.square(residuals)
chisqu = np.sum(squaredresiduals)
redchisqu = chisqu/(len(residuals)-len(p))
KD = pop[0]
errKD = np.sqrt(pcov[0][0]*redchisqu)
dimerspectrum = np.zeros([len(wavelengthlist),3])
for i,(par,dev) in enumerate(zip(popt,np.diagonal(pcov))):
    if i == 0:
        pass
    else:
        dimerspectrum[i-1,0] = wavelengthlist[i-1]
        dimerspectrum[i-1,1] = par
        dimerspectrum[i-1,2] = np.sqrt(dev*redchisqu)
    pass
```

## 4.6 References

- (1) Bechtold, T.; Mahmud-Ali, A.; Mussak, R. Natural Dyes for Textile Dyeing: A Comparison of Methods to Assess the Quality of Canadian Golden Rod Plant Material. *Dyes and Pigments* **2007**, *75* (2), 287–293. <https://doi.org/10.1016/j.dyepig.2006.06.004>.
- (2) ElGuesmi, N.; Farghaly, Thoraya. A.; Khormi, A. Y.; Shaaban, M. R.; Katin, K. P.; Kaya, S. Synthesis and Spectral Properties of Novel Series of Fluorene-Based Azo Dyes Containing Thiazole Scaffold: Studying of the Solvent and Substituent Effect on Absorption Spectra. *Journal of Molecular Structure* **2023**, *1271*, 134002. <https://doi.org/10.1016/j.molstruc.2022.134002>.
- (3) Jiang, H.; Zhang, L.; Cai, J.; Ren, J.; Cui, Z.; Chen, W. Quinoidal Bithiophene as Disperse Dye: Substituent Effect on Dyeing Performance. *Dyes and Pigments* **2018**, *151*, 363–371. <https://doi.org/10.1016/j.dyepig.2018.01.017>.
- (4) Bialas, D.; Kirchner, E.; Röhr, M. I. S.; Würthner, F. Perspectives in Dye Chemistry: A Rational Approach toward Functional Materials by Understanding the Aggregate State. *J. Am. Chem. Soc.* **2021**, *143* (12), 4500–4518. <https://doi.org/10.1021/jacs.0c13245>.
- (5) Hagfeldt, A.; Boschloo, G.; Sun, L.; Kloo, L.; Pettersson, H. Dye-Sensitized Solar Cells. *Chem. Rev.* **2010**, *110* (11), 6595–6663. <https://doi.org/10.1021/cr900356p>.
- (6) Chou, P.-T.; Chi, Y. Phosphorescent Dyes for Organic Light-Emitting Diodes. *Chemistry – A European Journal* **2007**, *13* (2), 380–395. <https://doi.org/10.1002/chem.200601272>.
- (7) Würthner, F.; Saha-Möller, C. R.; Fimmel, B.; Ogi, S.; Leowanawat, P.; Schmidt, D. Perylene Bisimide Dye Assemblies as Archetype Functional Supramolecular Materials. *Chem. Rev.* **2016**, *116* (3), 962–1052. <https://doi.org/10.1021/acs.chemrev.5b00188>.
- (8) Hu, X.; Ritz, T.; Damjanović, A.; Autenrieth, F.; Schulten, K. Photosynthetic Apparatus of Purple Bacteria. *Quarterly Reviews of Biophysics* **2002**, *35* (1), 1–62. <https://doi.org/10.1017/S0033583501003754>.
- (9) Hu, X.; Damjanović, A.; Ritz, T.; Schulten, K. Architecture and Mechanism of the Light-Harvesting Apparatus of Purple Bacteria. *Proc Natl Acad Sci U S A* **1998**, *95* (11), 5935–5941.
- (10) Tamiaki, H. Supramolecular Structure in Extramembraneous Antennae of Green Photosynthetic Bacteria. *Coordination Chemistry Reviews* **1996**, *148*, 183–197. [https://doi.org/10.1016/0010-8545\(95\)01188-9](https://doi.org/10.1016/0010-8545(95)01188-9).
- (11) Balaban, T. S.; Tamiaki, H.; Holzwarth, A. R. Chlorins Programmed for Self-Assembly. In *Supramolecular Dye Chemistry*; Würthner, F., Ed.; Topics in Current Chemistry; Springer: Berlin, Heidelberg, 2005; pp 1–38. <https://doi.org/10.1007/b137480>.



- (12) Chen, Z.; Lohr, A.; Saha-Möller, C. R.; Würthner, F. Self-Assembled  $\pi$ -Stacks of Functional Dyes in Solution: Structural and Thermodynamic Features. *Chem. Soc. Rev.* **2009**, *38* (2), 564–584. <https://doi.org/10.1039/B809359H>.
- (13) Faul, C. f. j.; Antonietti, M. Ionic Self-Assembly: Facile Synthesis of Supramolecular Materials. *Advanced Materials* **2003**, *15* (9), 673–683. <https://doi.org/10.1002/adma.200300379>.
- (14) Mantid Project. Mantid (2013): Manipulation and Analysis Toolkit for Instrument Data. <http://dx.doi.org/10.5286/SOFTWARE/MANTID>.
- (15) Arnold, O.; Bilheux, J. C.; Borreguero, J. M.; Buts, A.; Campbell, S. I.; Chapon, L.; Doucet, M.; Draper, N.; Ferraz Leal, R.; Gigg, M. A.; Lynch, V. E.; Markvardsen, A.; Mikkelsen, D. J.; Mikkelsen, R. L.; Miller, R.; Palmen, K.; Parker, P.; Passos, G.; Perring, T. G.; Peterson, P. F.; Ren, S.; Reuter, M. A.; Savici, A. T.; Taylor, J. W.; Taylor, R. J.; Tolchenov, R.; Zhou, W.; Zikovsky, J. Mantid—Data Analysis and Visualization Package for Neutron Scattering and  $\mu$  SR Experiments. *Nuclear Instruments and Methods in Physics Research Section A: Accelerators, Spectrometers, Detectors and Associated Equipment* **2014**, *764*, 156–166. <https://doi.org/10.1016/j.nima.2014.07.029>.
- (16) *Neutrons, X-Rays, and Light: Scattering Methods Applied to Soft Condensed Matter*, 1st ed.; Lindner, P., Zemb, T., Eds.; North-Holland delta series; Elsevier: Amsterdam ; Boston, 2002.
- (17) Gottlieb, H. E.; Kotlyar, V.; Nudelman, A. NMR Chemical Shifts of Common Laboratory Solvents as Trace Impurities. *J. Org. Chem.* **1997**, *62* (21), 7512–7515. <https://doi.org/10.1021/jo971176v>.
- (18) Cuétara-Guadarrama, F.; Vonlanthen, M.; Sorroza-Martínez, K.; González-Méndez, I.; Rivera, E. Photoisomerizable Azobenzene Dyes Incorporated into Polymers and Dendrimers. Influence of the Molecular Aggregation on the Nonlinear Optical Properties. *Dyes and Pigments* **2021**, *194*, 109551. <https://doi.org/10.1016/j.dyepig.2021.109551>.
- (19) Kasha, M.; Rawls, H. R.; El-Bayoumi, M. A. The exciton model in molecular spectroscopy. *Pure and Applied Chemistry* **1965**, *11* (3–4), 371–392. <https://doi.org/10.1351/pac196511030371>.
- (20) Neumann, B.; Huber, K.; Pollmann, P. A Comparative Experimental Study of the Aggregation of Acid Red 266 in Aqueous Solution by Use of  $^{19}\text{F}$ -NMR, UV/Vis Spectroscopy and Static Light Scattering. *Phys. Chem. Chem. Phys.* **2000**, *2* (16), 3687–3695. <https://doi.org/10.1039/B004172F>.

- (21) Horng, M.-L.; Quitevis, E. L. Visible Absorption Spectroscopy and Structure of Cyanine Dimers in Aqueous Solution: An Experiment for Physical Chemistry. *J. Chem. Educ.* **2000**, *77* (5), 637. <https://doi.org/10.1021/ed077p637>.
- (22) Sabaté, R.; Gallardo, M.; de la Maza, A.; Estelrich, J. A Spectroscopy Study of the Interaction of Pinacyanol with N-Dodecyltrimethylammonium Bromide Micelles. *Langmuir* **2001**, *17* (21), 6433–6437. <https://doi.org/10.1021/la010463y>.
- (23) Virtanen, P.; Gommers, R.; Oliphant, T. E.; Haberland, M.; Reddy, T.; Cournapeau, D.; Burovski, E.; Peterson, P.; Weckesser, W.; Bright, J.; van der Walt, S. J.; Brett, M.; Wilson, J.; Millman, K. J.; Mayorov, N.; Nelson, A. R. J.; Jones, E.; Kern, R.; Larson, E.; Carey, C. J.; Polat, İ.; Feng, Y.; Moore, E. W.; VanderPlas, J.; Laxalde, D.; Perktold, J.; Cimrman, R.; Henriksen, I.; Quintero, E. A.; Harris, C. R.; Archibald, A. M.; Ribeiro, A. H.; Pedregosa, F.; van Mulbregt, P. SciPy 1.0: Fundamental Algorithms for Scientific Computing in Python. *Nat Methods* **2020**, *17* (3), 261–272. <https://doi.org/10.1038/s41592-019-0686-2>.
- (24) Kasha, M. Energy Transfer Mechanisms and the Molecular Exciton Model for Molecular Aggregates. *Radiation Research* **1963**, *20* (1), 55–70. <https://doi.org/10.2307/3571331>.
- (25) Rohatgi, K. K. Absorption Spectra of the Dimers of Ionic Dyes. *Journal of Molecular Spectroscopy* **1968**, *27* (1), 545–548. [https://doi.org/10.1016/0022-2852\(68\)90061-1](https://doi.org/10.1016/0022-2852(68)90061-1).
- (26) Schärftl, W. *Light Scattering from Polymer Solutions and Nanoparticle Dispersions*; Springer Laboratory; Springer Berlin Heidelberg: Berlin, Heidelberg, 2007. <https://doi.org/10.1007/978-3-540-71951-9>.
- (27) Rubinson, K. A.; Stanley, C.; Krueger, S. Small-Angle Neutron Scattering and the Errors in Protein Structures That Arise from Uncorrected Background and Intermolecular Interactions. *J Appl Cryst* **2008**, *41* (2), 456–465. <https://doi.org/10.1107/S0021889808004950>.
- (28) Lambert, J. B. *Spektroskopie: Strukturaufklärung in der Organischen Chemie*; Pearson, Higher Education, 2012.
- (29) Claridge, T. D. W. Correlations through Space: The Nuclear Overhauser Effect. In *High-Resolution NMR Techniques in Organic Chemistry*; Tetrahedron Organic Chemistry Series; Elsevier, 2009; Vol. 27, pp 247–302. [https://doi.org/10.1016/S1460-1567\(08\)10008-3](https://doi.org/10.1016/S1460-1567(08)10008-3).
- (30) Renshaw, M. P.; Day, I. J. NMR Characterization of the Aggregation State of the Azo Dye Sunset Yellow in the Isotropic Phase. *J. Phys. Chem. B* **2010**, *114* (31), 10032–10038. <https://doi.org/10.1021/jp104356m>.

- (31) Teixeira, J. Small-Angle Scattering by Fractal Systems. *J Appl Cryst* **1988**, *21* (6), 781–785. <https://doi.org/10.1107/S0021889888000263>.
- (32) Hoepfner, M. P.; Vilas Bôas Fávero, C.; Haji-Akbari, N.; Fogler, H. S. The Fractal Aggregation of Asphaltenes. *Langmuir* **2013**, *29* (28), 8799–8808. <https://doi.org/10.1021/la401406k>.
- (33) Eyssautier, J.; Levitz, P.; Espinat, D.; Jestin, J.; Gummel, J.; Grillo, I.; Barré, L. Insight into Asphaltene Nanoaggregate Structure Inferred by Small Angle Neutron and X-Ray Scattering. *J. Phys. Chem. B* **2011**, *115* (21), 6827–6837. <https://doi.org/10.1021/jp111468d>.
- (34) Gawrys, K. L.; Blankenship, G. A.; Kilpatrick, P. K. Solvent Entrainment in and Flocculation of Asphaltenic Aggregates Probed by Small-Angle Neutron Scattering. *Langmuir* **2006**, *22* (10), 4487–4497. <https://doi.org/10.1021/la052509j>.
- (35) Tanaka, R.; Sato, E.; Hunt, J. E.; Winans, R. E.; Sato, S.; Takanohashi, T. Characterization of Asphaltene Aggregates Using X-Ray Diffraction and Small-Angle X-Ray Scattering. *Energy Fuels* **2004**, *18* (4), 1118–1125. <https://doi.org/10.1021/ef034082z>.
- (36) Pedersen, J. S. Analysis of Small-Angle Scattering Data from Colloids and Polymer Solutions: Modeling and Least-Squares Fitting. *Advances in Colloid and Interface Science* **1997**, *70*, 171–210. [https://doi.org/10.1016/S0001-8686\(97\)00312-6](https://doi.org/10.1016/S0001-8686(97)00312-6).
- (37) Huber, K.; Burchard, W. Scattering Behavior of Wormlike Star Macromolecules. *Macromolecules* **1989**, *22* (8), 3332–3336. <https://doi.org/10.1021/ma00198a024>.
- (38) Huber, K.; Burchard, W.; Bantle, S.; Fetters, L. J. Monte Carlo Calculations in Comparison to Neutron Scattering Studies: 3. On the Structure of 12-Arm Star Molecules. *Polymer* **1987**, *28* (12), 1997–2003. [https://doi.org/10.1016/0032-3861\(87\)90032-2](https://doi.org/10.1016/0032-3861(87)90032-2).
- (39) Edwards, D. J.; Jones, J. W.; Lozman, O.; Ormerod, A. P.; Sinyureva, M.; Tiddy, G. J. T. Chromonic Liquid Crystal Formation by Edicol Sunset Yellow. *J. Phys. Chem. B* **2008**, *112* (46), 14628–14636. <https://doi.org/10.1021/jp802758m>.
- (40) Shao, C.; Grüne, M.; Stolte, M.; Würthner, F. Perylene Bisimide Dimer Aggregates: Fundamental Insights into Self-Assembly by NMR and UV/Vis Spectroscopy. *Chemistry – A European Journal* **2012**, *18* (43), 13665–13677. <https://doi.org/10.1002/chem.201201661>.
- (41) Ahrens, M. J.; Sinks, L. E.; Rybtchinski, B.; Liu, W.; Jones, B. A.; Giaimo, J. M.; Gusev, A. V.; Goshe, A. J.; Tiede, D. M.; Wasielewski, M. R. Self-Assembly of Supramolecular Light-Harvesting Arrays from Covalent Multi-Chromophore Perylene-3,4:9,10-Bis(Dicarboximide)

- Building Blocks. *J. Am. Chem. Soc.* **2004**, *126* (26), 8284–8294.  
<https://doi.org/10.1021/ja039820c>.
- (42) Ahrens, M. J.; Kelley, R. F.; Dance, Z. E. X.; Wasielewski, M. R. Photoinduced Charge Separation in Self-Assembled Cofacial Pentamers of Zinc-5,10,15,20-Tetrakis(Perylenediimide)Porphyrin. *Phys. Chem. Chem. Phys.* **2007**, *9* (12), 1469–1478.  
<https://doi.org/10.1039/B617876F>.
- (43) Furó, I. NMR Spectroscopy of Micelles and Related Systems. *Journal of Molecular Liquids* **2005**, *117* (1), 117–137. <https://doi.org/10.1016/j.molliq.2004.08.010>.
- (44) Baykov, S. V.; Mikherdov, A. S.; Novikov, A. S.; Geyl, K. K.; Tarasenko, M. V.; Gureev, M. A.; Boyarskiy, V. P.  $\pi$ - $\pi$  Noncovalent Interaction Involving 1,2,4- and 1,3,4-Oxadiazole Systems: The Combined Experimental, Theoretical, and Database Study. *Molecules* **2021**, *26* (18), 5672. <https://doi.org/10.3390/molecules26185672>.
- (45) Monahan, A. R.; Blossey, D. F. Aggregation of Arylazonaphthols. I. Dimerization of Bonadur Red in Aqueous and Methanolic Systems. *J. Phys. Chem.* **1970**, *74* (23), 4014–4021. <https://doi.org/10.1021/j100717a002>.
- (46) McRae, E. G.; Kasha, M. THE MOLECULAR EXCITON MODEL \*\*Work Supported in Part by a Contract between the Division of Biology and Medicine, U.S. Atomic Energy Commission, and the Florida State University. In *Physical Processes in Radiation Biology*; Augenstein, L., Mason, R., Rosenberg, B., Eds.; Academic Press, 1964; pp 23–42.  
<https://doi.org/10.1016/B978-1-4831-9824-8.50007-4>.
- (47) Belay, A. Measurement of Integrated Absorption Cross-Section, Oscillator Strength and Number Density of Caffeine in Coffee Beans by Integrated Absorption Coefficient Technique. *Food Chemistry* **2010**, *121* (2), 585–590.  
<https://doi.org/10.1016/j.foodchem.2009.12.052>.
- (48) Atkins, P. W.; De Paula, J. *Atkins' Physical Chemistry*, 10th ed.; Oxford University Press: Oxford; New York, 2014.
- (49) McCoy, E. F.; Ross, I. G. Electronic States of Aromatic Hydrocarbons: The Franck-Condon Principle and Geometries in Excited States. *Aust. J. Chem.* **1962**, *15* (4), 573–590.  
<https://doi.org/10.1071/ch9620573>.
- (50) Tiddy, G. J. T.; Mateer, D. L.; Ormerod, A. P.; Harrison, W. J.; Edwards, D. J. Highly Ordered Aggregates in Dilute Dye-Water Systems. *Langmuir* **1995**, *11* (2), 390–393.  
<https://doi.org/10.1021/la00002a002>.

- (51) Livsey, I. Neutron Scattering from Concentric Cylinders. Intraparticle Interference Function and Radius of Gyration. *J. Chem. Soc., Faraday Trans. 2* **1987**, *83* (8), 1445–1452. <https://doi.org/10.1039/F29878301445>.
- (52) Schrödinger LCC. PyMOL Molecular Graphics System, Version 1.2r3pre. <https://pymol.org/2/>.
- (53) Denkinger, P.; Burchard, W. Determination of Chain Stiffness and Polydispersity from Static Light-Scattering. *Journal of Polymer Science Part B: Polymer Physics* **1991**, *29* (5), 589–600. <https://doi.org/10.1002/polb.1991.090290508>.
- (54) Huber, K.; Burchard, W.; Bantle, S.; Fetters, L. J. Monte Carlo Calculations in Comparison to Neutron Scattering Studies: 2. Global Dimensions of 12-Arm Stars. *Polymer* **1987**, *28* (12), 1990–1996. [https://doi.org/10.1016/0032-3861\(87\)90031-0](https://doi.org/10.1016/0032-3861(87)90031-0).

## 4.7 Appendix

In the following, Figure 3 and Figure 7 are reproduced and the concentrations of measured dye solutions are specified.

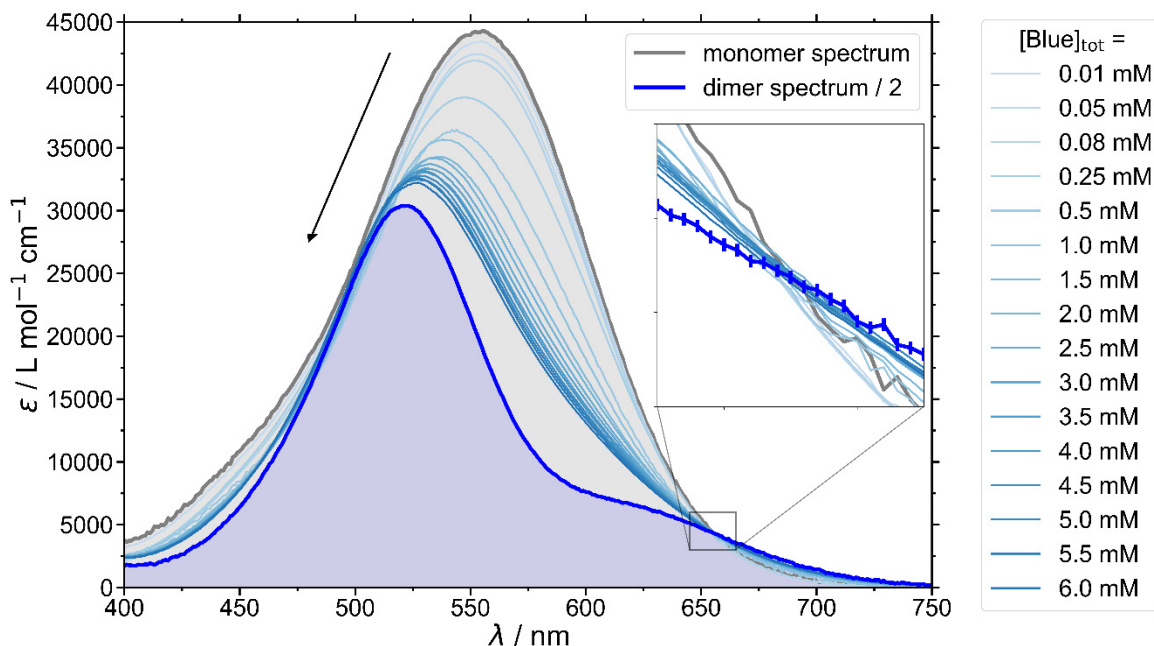


Figure 3: Spectra of Blue recorded at 25 °C in buffer solution at specified concentrations. The arrow indicates an increase in  $[\text{Blue}]_{\text{tot}}$  from 0.01 mM to 6 mM. The monomer spectrum was recorded at  $[\text{Blue}]_{\text{tot}} = 5 \mu\text{M}$ . The dimer spectrum results from fitting. It was divided by 2 to refer to the concentration of monomer. The inset magnifies the region around the isosbestic point.

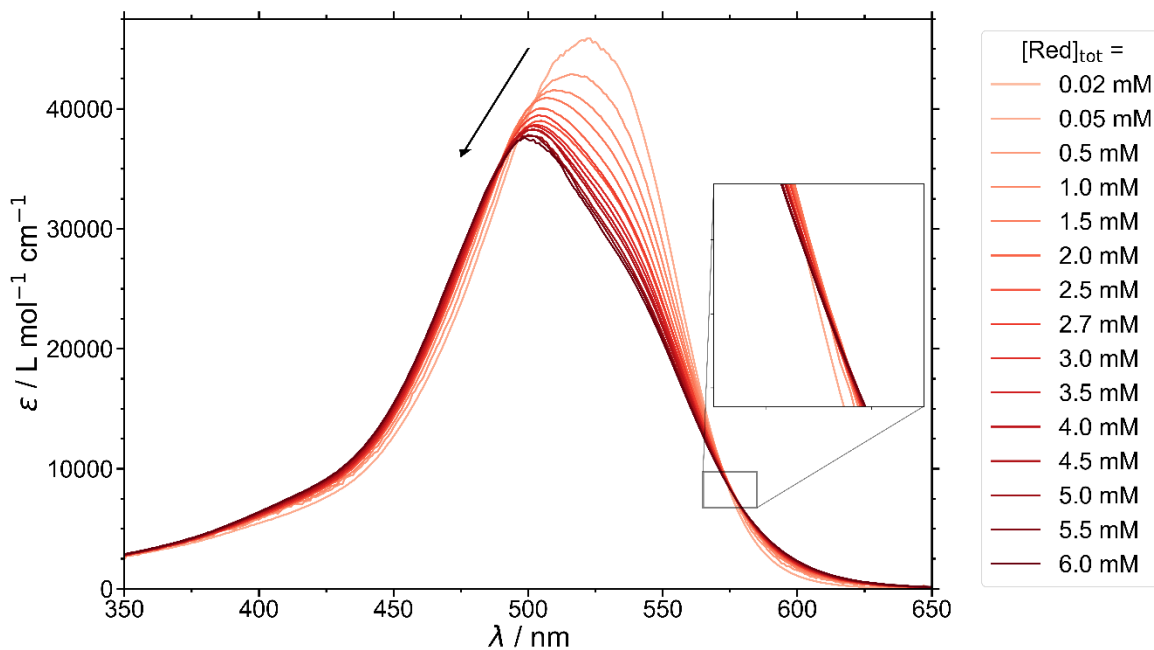


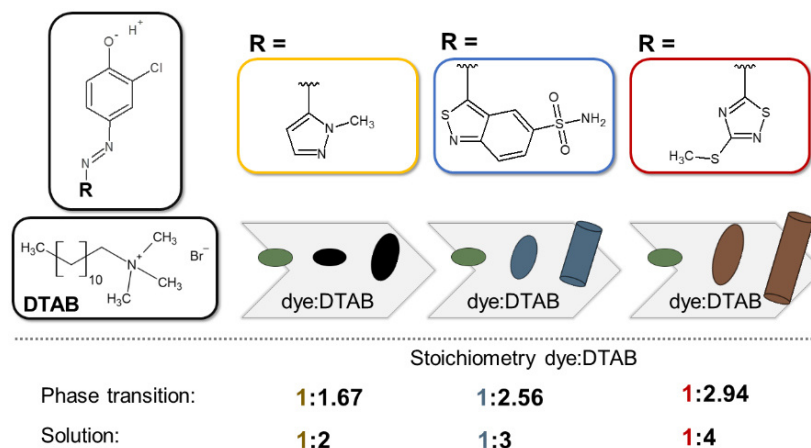
Figure 7: Spectra of Red recorded at 25 °C in buffer solution at specified concentrations. The inset shows a region where an isosbestic point could be assumed but does not exist.

## Chapter 5

# Comparative study of the co-assembly behaviour of 3-chloro-4-hydroxy-phenylazo dyes with DTAB

### Abstract

The co-assembly of three one-fold negatively charged 3-chloro-4-hydroxy-phenylazo dyes (Yellow, Blue and Red) with the cationic surfactant dodecyltrimethylammoniumbromide (DTAB) was studied to probe dye-DTAB binding stoichiometry and assembly morphology. For each dye, phase separation was observed above a given dye:DTAB ratio with the ratio depending on the dye. While Yellow and DTAB showed liquid/liquid phase separation above Yellow:DTAB = 1:1.67, crystalline dye-DTAB complexes were observed for Blue-DTAB and Red-DTAB above Blue:DTAB = 1:2.56 and Red:DTAB = 1:2.94 respectively. In homogeneous solution, UV/vis spectroscopic investigations suggest stoichiometries of Yellow:DTAB = 1:2, Blue:DTAB = 1:3 and Red:DTAB = 1:4. It was concluded, that Yellow exhibits the highest dye:DTAB binding stoichiometry in both, dye-surfactant complexes in the 2-phase region and in solution, whereas the lowest dye:DTAB binding stoichiometry was observed for Red-DTAB in both cases. The observed stoichiometries are inversely correlated to the impact dye addition has on the morphology of DTAB micelles. Generally, addition of dye to DTAB micelles leads to a reduction in spontaneous curvature of these micelles and to the formation of triaxial ellipsoidal or cylindrical micelles from oblate ellipsoidal DTAB micelles. At a DTAB concentration of 30 mM and a dye concentration of 5 mM, this effect was most pronounced for Red and least pronounced for Yellow, whilst Blue showed an intermediate effect.



This chapter corresponds to: Müller, Wenke; Schweins, Ralf; Nöcker, Bernd; Kohlbrecher, Joachim; Smales, Glen J.; Huber, Klaus. Comparative Study of the Co-Assembly Behaviour of 3-Chloro-4-Hydroxy-Phenylazo Dyes with DTAB. *Soft Matter* **2023**, *19* (24), 4588–4598. <https://doi.org/10.1039/D3SM00501A> published by the Royal Society of Chemistry.



## 5.1 Introduction

Non-covalent intermolecular interactions, leading to self- and co-assembly, are pivotal to life. They enable structures and functions ranging from cell membranes over metabolic processes to the DNA double helix. Inspired by nature, scientists are trying to exploit the spontaneous assembly of one or more components for the creation of functional materials, which could be used in regenerative medicine<sup>1,2</sup>, as carrier systems<sup>3,4</sup>, for solar cells<sup>5</sup>, as sensors<sup>6,7</sup> or in photonics<sup>8,9</sup>.

The complexity of intermolecular interactions exacerbates the prediction of assembly behaviour by simple models, as not only forces like van der Waals-, dipole-dipole-, electrostatic- or  $\pi$ - $\pi$ -interactions play a role, but other phenomena such as entropic effects, repulsive interactions, cooperativity and external forces might need to be considered.<sup>10</sup> This highlights the necessity of comprehensive investigations of co- and self-assembling systems to obtain a better understanding of their fundamental principles as well as the system specific features that govern assembly structures and properties.

Polyelectrolytes are a typical family of building blocks for self-assembly processes in aqueous systems, while also being a simple model system for biological building units.<sup>11–13</sup> One reason for this is that assembly of linear polyelectrolytes or dendrimers can be triggered by oppositely charged counter ions. To give but an example, specific counter ion binding of  $\text{Ca}^{2+}$  was used to induce micellization of a block-copolyelectrolyte.<sup>14</sup> Morphological changes of polyelectrolyte micelles in solution can also be triggered by the addition of charged amphiphilic molecules, which is interesting for the design of well-defined nanostructures.<sup>15</sup> In a recent example it was shown, that the addition of ionic surfactants to an amphoteric diblock-copolyelectrolyte resulted in the formation of core-shell complexes, with an internal crystalline core structure and either positive or negative surface charge, dependent on the charge of the surfactant.<sup>16</sup> Moreover, like the addition of inorganic counter ions or amphiphilic molecules, the introduction of charged dye molecules into polyelectrolyte systems yields supramolecular structures. These structures may be responsive to light as a trigger for morphological changes.<sup>17</sup> This was, among others, shown in a recent example where assembly morphology between oppositely charged polyelectrolyte and azo dye was controlled by a change in N=N-bond configuration, demonstrating the complexity of underlying intermolecular interactions.<sup>18</sup> Due to the interest in light-switchability, the interaction between dye molecules and polyelectrolytes has been studied for a long time, revealing that such systems form well-

defined supramolecular nanoparticles of adjustable size, based on electrostatic assembly with various azo dyes.<sup>19</sup> Furthermore, the assembly morphology was shown to not only depend on structural features of the dye, but also on its self-assembly behaviour.<sup>20</sup>

The use of polymeric building blocks does, however, come along with some drawbacks. Apart from challenges arising due to availability of some polymers in sufficient purity at the needed degree of polymerization and dispersity, pathways in polymer assembly are frequently subjected to kinetic limitations.<sup>21–23</sup> Substituting polyelectrolytes with low molecular weight surfactants that assemble into micelles could be a pathway to circumvent such problems while obtaining assemblies with interesting and well-defined properties. To give an example, the Faul group observed the formation of highly ordered complexes between azo dye and oppositely charged surfactant molecules.<sup>24</sup> Some of these complexes showed pleochroism.<sup>25</sup> Considering the defined and regular shape of charged dye molecules and their potential to not only interact electrostatically, but also to form  $\pi$ - $\pi$ -interactions makes them an interesting system for studying intermolecular interactions.<sup>26</sup>

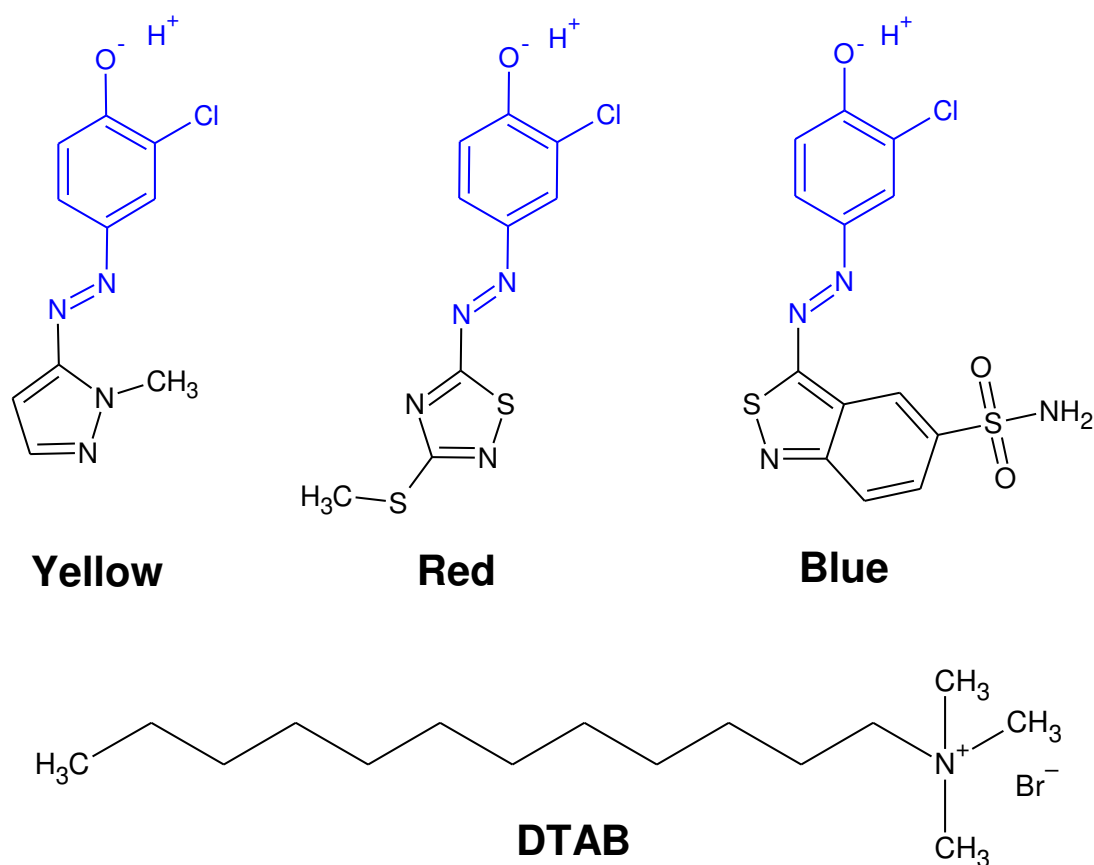


Figure 1: Chemical structure of three azo dyes with their common structural sub-unit marked in blue and of the cationic surfactant DTAB. At alkaline pH such as pH = 10.5, the phenolic hydroxyl group is deprotonated in all cases.

Herein we report investigations on the stoichiometry of dye-surfactant binding between the positively charged surfactant dodecyltrimethylammoniumbromide (DTAB) and three negatively charged azo dyes (Figure 1). The stoichiometry of dye-surfactant binding in solution is compared to the stoichiometry of dye-surfactant binding in solid complexes as obtained from the corresponding phase diagrams. Furthermore, differences in the morphology of dye-DTAB micelles were elucidated with small-angle neutron scattering (SANS).

## 5.2 Experimental

**Chemicals and sample preparation.** Three azo dyes Yellow (HC Yellow 16,  $\geq 99\%$ ), Blue (HC Blue 18,  $\geq 99.8\%$ ) and Red (HC Red 18,  $\geq 99\%$ ) were provided by KAO GmbH, Germany. Completely hydrogenated dodecyltrimethylammoniumbromide (DTAB, 99%) was obtained from abcr GmbH, Germany. Completely deuterated dodecyltrimethylammoniumbromide ( $d^{34}$ -DTAB, 99% isotopic purity) was obtained from INNOVACHEM SAS, France. Tail-deuterated dodecyltrimethylammoniumbromide ( $d^{25}$ -DTAB, 99.1% isotopic purity) was obtained from C/D/N Isotopes Inc., Canada. The buffer salts sodium carbonate  $\text{Na}_2\text{CO}_3$  ( $\geq 99.8\%$ ) and sodium bicarbonate  $\text{NaHCO}_3$  ( $\geq 99.7\%$ ) were obtained from Sigma Aldrich Chemie GmbH, Germany. MilliQ water was used to prepare the  $\text{NaHCO}_3/\text{Na}_2\text{CO}_3$  buffer solutions (pH = 10.5, ionic strength  $I \approx 0.25$  M) for UV/vis-spectroscopy and light scattering samples.  $\text{D}_2\text{O}$  was used to prepare the  $\text{NaHCO}_3/\text{Na}_2\text{CO}_3$  buffer solutions (pD = 10.7, ionic strength  $I \approx 0.25$  M) for small-angle neutron scattering samples.  $\text{D}_2\text{O}$  (99.90% D) was obtained from Eurisotop, France. Chemicals were used without further purification. Samples were prepared from stock solutions, followed by a minimum equilibration time of 20 h at room temperature prior to analysis.

**Phase diagrams.** Phase diagrams were established by stepwise addition of a dye stock solution to a DTAB solution.  $\text{NaHCO}_3/\text{Na}_2\text{CO}_3$  buffer solution (pH = 10.5, ionic strength  $I \approx 0.25$  M) was prepared in  $\text{H}_2\text{O}$  and used as a solvent in all cases. Dye stock solutions contained dye molar concentrations of 10 mM, 15 mM and 15 mM for Yellow, Blue and Red respectively. The concentration of the employed DTAB stock solution was chosen according to the desired sample composition. After each addition of dye stock solution, the sample was vortexed for approximately 30 s and its visual appearance observed immediately. Phase diagrams were established at room temperature ( $\approx 22$  °C). Longer timescales were not systematically investigated. It should, however, be noted that at low

DTAB-concentrations (below its critical micelle concentration of 9 mM) some initially stable samples showed precipitation after 24 h.

**UV/vis spectroscopy.** UV/vis spectra of solutions containing dye and DTAB were recorded with a Lambda-19 spectrometer from Perkin Elmer. A Hellma quartz glass cuvette with an optical path length of 0.01 cm was used. The spectrometer was equipped with a thermostat to guarantee a constant measurement temperature of 25 °C. Samples showing precipitation were filtered prior to measurement (MACHEREY-NAGEL, CHROMAFIL Xtra H-PTFE syringe filters, pore size 0.2  $\mu\text{m}$ ).

**Small-angle neutron scattering.** Samples for small-angle neutron scattering (SANS) measurements were obtained by mixing the solvent, a dye stock solution and a stock solution containing DTAB at appropriate ratios. The solvent was a  $\text{NaHCO}_3/\text{Na}_2\text{CO}_3$  buffer in  $\text{D}_2\text{O}$  (pD = 10.7, ionic strength  $I \approx 0.25$  M). The sample containing [Blue] = 5 mM and [DTAB] = 30 mM represents an exception to this procedure, as it was initially prepared for another project. For this sample, the solvent, a dye stock solution and a stock solution containing  $\text{d}^{25}$ -DTAB and  $\text{d}^{34}$ -DTAB at a ratio of 46:54 (v/v) were mixed at appropriate ratios. The solvent was a  $\text{NaHCO}_3/\text{Na}_2\text{CO}_3$  buffer prepared in a mixture of  $\text{H}_2\text{O}:\text{D}_2\text{O} = 50:50$  (v/v) (pH/D = 10.5, ionic strength  $I \approx 0.25$  M). The resulting SANS curve of this sample and its fit were scaled by a factor of 3.6 in Figure 5 to account for the difference in contrast.

After their preparation, sample solutions were filtered (MACHEREY-NAGEL, CHROMAFIL Xtra H-PTFE syringe filters, pore size 0.2  $\mu\text{m}$ ) into a dust-free sample vial and equilibrated for a minimum of 20 h at room temperature.

SANS measurements were performed at the instrument D11 at the Institut Laue-Langevin (ILL, Grenoble, France) and at the instrument SANS-I at the Paul Scherrer Institute (PSI, Villigen, Switzerland).

At the ILL, different setups were used: (1) The sample containing no dye and  $[\text{DTAB}]_{\text{tot}} = 30$  mM and the sample containing  $[\text{Blue}]_{\text{tot}} = 5$  mM and  $[\text{DTAB}]_{\text{tot}} = 30$  mM were measured at three sample-to-detector distances (28 m collimation 28 m), (8 m collimation 8 m), (1.7 m collimation 4.0 m) at a neutron wavelength of 6  $\text{\AA}$  to cover a  $q$ -range of 0.002  $\text{\AA}^{-1}$  to 0.5  $\text{\AA}^{-1}$ . A circular neutron beam with a diameter of 15 mm was used. (2) All samples containing Red were measured at three sample-to-detector distances (38.0 m collimation 40.5 m), (10.5 m collimation 10.5 m), (2.5 m collimation 2.5 m) at a neutron wavelength of 6  $\text{\AA}$  to cover a  $q$ -range of 0.0014  $\text{\AA}^{-1}$  to 0.5  $\text{\AA}^{-1}$ . A circular neutron beam with a diameter of 14 mm was used. Neutrons were detected with a  $^3\text{He}$ -detector

(Reuter-Stokes multi-tube detector consisting of 256 tubes with a tube diameter of 8 mm and a pixel size of 8 mm x 4 mm), detector images azimuthally averaged, corrected to the transmission of the direct beam and scaled to absolute intensity using the Mantid software.<sup>27,28</sup> Solvent scattering and empty cell scattering were subtracted from the scattering curves.<sup>29</sup> SANS data were collected at a sample temperature of 25 °C.

The sample containing [Blue]<sub>tot</sub> = 5 mM and [DTAB]<sub>tot</sub> = 20 mM and all samples containing Yellow were measured at the PSI SANS-I instrument. The measurements were performed at 3 sample-to-detector distances (18.0 m collimation 18.0 m), (6.0 m collimation 6.0 m), (1.6 m collimation 6.0 m) at a wavelength of 6 Å to cover a  $q$ -range of 0.003 Å<sup>-1</sup> to 0.4 Å<sup>-1</sup>. A circular neutron beam with a diameter of 14 mm was used. Neutrons were detected with a 2D MWPC CERCA <sup>3</sup>He-detector with 128 x 128 elements of 7.5 x 7.5 mm<sup>2</sup>. Detector images were corrected for pixel efficiency using scattering from a water sample which also served as a secondary standard, corrected for transmission and azimuthally averaged using the BerSANS software.<sup>30</sup> Solvent scattering and empty cell scattering were subtracted from the scattering curves.<sup>29</sup> SANS data were collected at a sample temperature of 25 °C.

Data analysis was performed with the SasView small angle scattering analysis software. In all cases, the solvent scattering length density was fixed to the known value and the assembly volume fraction was calculated based on known sample composition and partial molar volumes of each component, assuming that all molecules take part in assembly formation. This yielded an estimation of the assembly volume fraction, which was fixed to the calculated value during fitting to avoid over parameterization. The scattering length density (*SLD*) of the assembly was fitted. Molar volumes and complete parameter sets can be found in the supporting information (SI).

### 5.3 Discussion

**Phase diagrams.** Adding dye to a solution of the cationic surfactant DTAB leads to a concentration-dependency of solution stability. This is visualized by phase diagrams shown in Figure 2. In all cases, a homogeneous solution was obtained for sufficient surfactant excess and denoted as 1-phase region in each phase diagram. Phase separation and concomitant entry into a 2-phase region was observed at different dye:DTAB ratios for each dye and will be discussed in the following. Within the selected concentration region, the correlation between the dye concentration [Dye]<sub>tot</sub> and DTAB

concentration  $[\text{DTAB}]_{\text{tot}}$  where phase separation occurs can be described by a linear relationship (eq (1)).

$$[\text{Dye}]_{\text{tot}} = A \cdot [\text{DTAB}]_{\text{tot}} + B \quad (1)$$

In case of Yellow and DTAB a liquid/liquid phase separation is observed. Combining either Blue or Red with the cationic surfactant DTAB gives rise to the formation of solid complexes above a threshold ratio of dye and DTAB concentration. The formation of such solid dye-surfactant complexes, from oppositely charged species, was described previously for various systems.<sup>24,25,31,32</sup>

Determining the phase transition threshold line according to eq (1) indicates the stoichiometry of dye-surfactant complex formation within the observed concentration range ( $2 \text{ mM} \leq [\text{DTAB}]_{\text{tot}} \leq 30 \text{ mM}$ ). This was done by a linear fit to the compositions of samples containing the highest concentration of dye still being within the 1-phase region. Data points used for fitting are highlighted in the corresponding phase diagrams.

For Yellow and DTAB,  $A = 0.60$  and  $B = 1.29 \text{ mM}$  suggests a stoichiometry of  $[\text{Yellow}]_{\text{tot}}:[\text{DTAB}]_{\text{tot}} = 1:1.67$  for an entry into the 2-phase region. At low DTAB concentration, a deviation from this linearity was observed and not included into the linear fit. This is not unexpected, as the 1-phase region should extend to  $[\text{Yellow}]_{\text{tot}} = 11 \text{ mM}$ , i.e. the solubility limit of Yellow in the absence of DTAB.<sup>33</sup> As Blue and Red show a very high solubility ( $> 25 \text{ mM}$ ) in the present buffer system and the absence of DTAB, a similar deviation at low DTAB concentration is expected for both of them.<sup>33</sup> It was, however, not observed in the investigated DTAB concentration range and likely happens at even lower DTAB concentrations.

The phase diagram of Blue and DTAB shows a defined phase transition. In the 2-phase region precipitates with crystalline appearance are formed. This suggests high ordering of the complexes, which was confirmed by wide-angle X-Ray scattering (WAXS) measurements shown in the SI (Figure SI3). From a linear fit based on eq (1) a stoichiometry of  $[\text{Blue}]_{\text{tot}}:[\text{DTAB}]_{\text{tot}} = 1:2.56$  was determined.

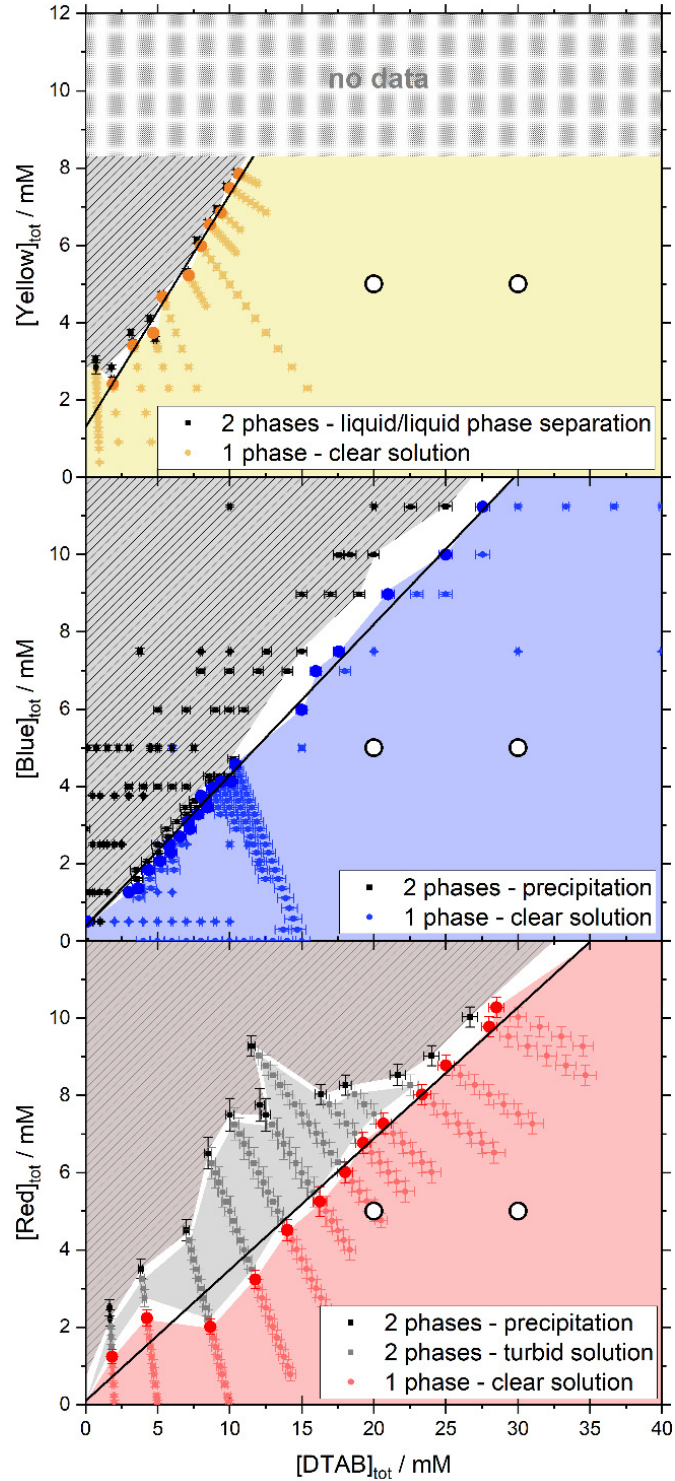


Figure 2: Concentration-dependent phase behaviour and linear fit of phase transition threshold line (eq (1)) for Yellow ( $A = 0.60$ ,  $B = 1.29$  mM), Blue ( $A = 0.39$ ,  $B = 0.38$  mM) and Red ( $A = 0.34$ ,  $B = 0.09$  mM) in combination with DTAB. The phase transition threshold line was obtained from fitting to the sample compositions marked with bold points in the 1-phase region. All phase diagrams were observed 30 s after mixing and at room temperature. The solvent was an aqueous  $\text{NaHCO}_3/\text{Na}_2\text{CO}_3$ -buffer in all cases. In the Yellow/DTAB diagram, dye concentrations higher than 8 mM were not accessible, as the Yellow stock solution used for sample preparation would have exceeded the solubility limit of Yellow. White circles ( $\circ$ ) display the composition of samples which were investigated with SANS.

The phase transition threshold between the 1- and 2-phase region is less defined for Red and DTAB. Within the reported observation time of 30 s, two different 2-phase-regions were observed, one appearing as a turbid solution, likely due to liquid/liquid phase separation, and the other one showing unambiguous precipitation of crystalline Red-DTAB-complexes. A linear fit based on eq (1) was performed to obtain information on the transition from the 1-phase-region into the 2-phase-region, independent of the appearance of the 2-phase-region. It yielded a stoichiometry for Red-DTAB complex formation of  $[\text{Red}]_{\text{tot}}:[\text{DTAB}]_{\text{tot}} = 1:2.94$ . It should be noted that not all samples containing dye and DTAB in the 1-phase-region were long-term stable. Some samples close to the precipitation threshold were stable within the observation time of 30 s, but precipitated after 1 h to 1 day. This occurred more frequently at  $[\text{DTAB}]_{\text{tot}}$  below the critical micelle concentration of DTAB.

To conclude this section, the excess of DTAB molecules needed to enter the soluble 1-phase-region differs for all three dyes and increases from 1.67 for Yellow over 2.56 for Blue to 2.94 for Red. The formation of dye-surfactant complexes with a defined stoichiometry is observed in most of the investigated DTAB concentration range.

**UV/vis-spectroscopy.** Dye-surfactant aggregation is commonly studied by means of UV/vis-spectroscopy and various models were developed to quantitatively evaluate dye-surfactant interaction.<sup>32,34–37</sup> These models rely on a change in dye absorption upon addition of surfactant, which is explained by the interaction between dye and surfactant causing a polarity change in the microenvironment of the dye.<sup>34,38</sup> For the dyes Yellow, Blue and Red a bathochromic shift of their absorption maximum and an increase in its extinction upon successive addition of DTAB in the 1-phase region was observed (Figure 3). It should be pointed out, that for a given dye concentration the 1-phase region only exists at sufficiently high DTAB concentrations (Figure 2). At low DTAB concentrations, the 2-phase region occurs due to liquid/liquid phase separation or precipitation of dye-DTAB complexes. Therefore, Figure 3 only shows absorption spectra of dye-DTAB solutions in the 1-phase region in comparison to the absorption spectrum of the solution of pure dye. The total dye concentration was  $[\text{Dye}]_{\text{tot}} = 2.5 \text{ mM}$  in all cases. The value  $A_d$  designating the  $y$ -axis of all spectra corresponds to the absorbance  $A$  of the sample divided by the optical path length  $d$ . The optical path length was  $d = 0.01 \text{ cm}$  in all cases. In the present work,  $A_d$  was used consistently in place of  $A$  in order to simplify calculations and mathematical expressions by not having to consider the path length.  $[\text{Dye}]_{\text{tot}} = 2.5 \text{ mM}$  was chosen to provide a dye concentration high enough to obtain a



reasonable scattering signal during contrast variation SANS experiments, which will be reported more extensively in a follow-up publication. At the same time it is low enough to permit the recording of UV/vis spectra in a cuvette with 0.01 cm path length while not significantly exceeding a maximum absorbance of  $A = 1$ .

As visible from Figure 3, bathochromic shifts of absorption maxima of  $\Delta\lambda_{\max} = 11$  nm,  $\Delta\lambda_{\max} = 34$  nm and  $\Delta\lambda_{\max} = 24$  nm were observed for Yellow, Blue and Red between a solution containing only dye and a solution containing dye and  $[\text{DTAB}]_{\text{tot}} = 90$  mM. These values signal a bathochromic shift significant enough to perform quantitative evaluation of recorded UV/vis-spectra with respect to an underlying dye-surfactant association equilibrium. For this purpose, dye absorbance was monitored as a function of DTAB concentration at a given wavelength. For Yellow, this wavelength was chosen to  $\lambda = 460$  nm, for Blue to  $\lambda = 565$  nm and for Red to  $\lambda = 528$  nm. These wavelengths are indicated in Figure 3 by a red, vertical line for each dye. They correspond to the wavelength of maximum absorbance in the sample with highest surfactant excess.  $[\text{Dye}]_{\text{tot}}$  was kept constant at 2.5 mM while varying DTAB concentration between  $0 \text{ mM} < [\text{DTAB}]_{\text{tot}} < 90$  mM.

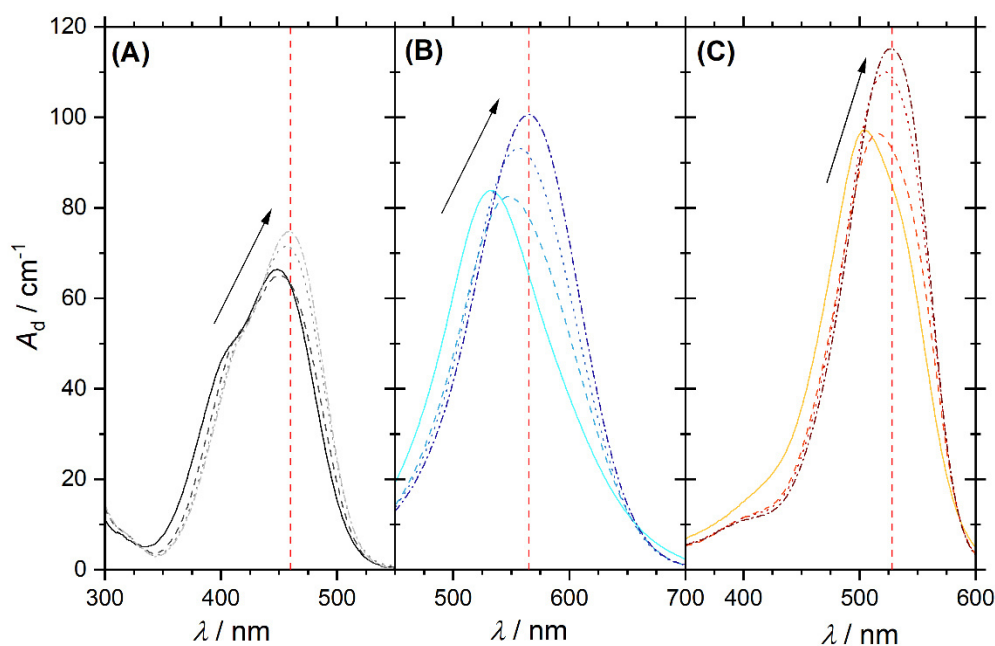


Figure 3: Spectra of solutions containing dye (solid line) or dye and DTAB in the homogeneous 1-phase region (dotted/dashed lines). The arrows indicate an increase in DTAB concentration from 0 mM to 90 mM. The red, vertical lines indicate the wavelength at which quantitative analysis was performed.  $[\text{Dye}]_{\text{tot}} = 2.5$  mM in all cases. (A) Yellow, (B) Blue, (C) Red. At any wavelength,  $A_d$  corresponds to the absorbance at that wavelength divided by optical path length  $A_d = A/d$  with  $d = 0.01$  cm.

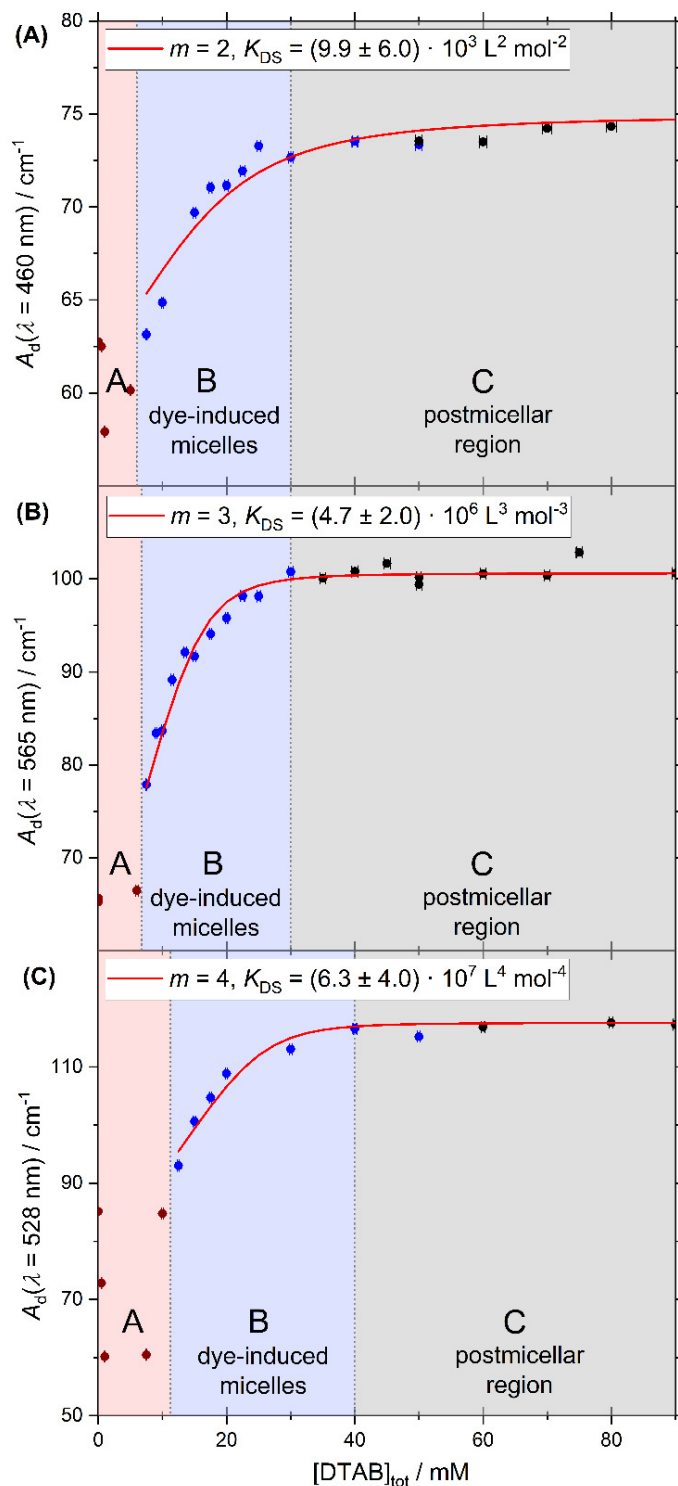


Figure 4: Absorption of dye solutions with  $[Dye]_{tot} = 2.5$  mM containing different concentrations of DTAB. Phase-separating samples are indicated by red dots, blue and black dots indicate stable samples in the 1-phase region. Blue data points were used to calculate  $K_{DS}$ . The red line displays the applied dye-surfactant association model assuming a stoichiometry of 1: $m$  for dye:DTAB binding and the given  $K_{DS}$ . (A) Yellow,  $A_d(\lambda = 460$  nm), (B) Blue,  $A_d(\lambda = 565$  nm), (C) Red,  $A_d(\lambda = 528$  nm).  $A_d(\lambda = x$  nm) corresponds to the absorbance at wavelength  $x$  divided by optical path length  $A_d = A/d$  with  $d = 0.01$  cm.

Figure 4 shows the development of  $A_d$  as a function of  $[\text{DTAB}]_{\text{tot}}$  at  $[\text{Dye}]_{\text{tot}} = 2.5 \text{ mM}$  for all three dyes at wavelengths indicated in Figure 3 by the red lines. Figure 4 permits the distinction of three surfactant concentration regions commonly referred to when observing the aggregation between oppositely charged dye and surfactant:<sup>32,36,39</sup>

Region A: Formation of dye-surfactant ion pairs. This corresponds to the 2-phase region in the phase diagrams, where the precipitation of dye-surfactant complexes leads to a strong decrease in absorbance, as precipitation and filtration of corresponding samples before measurement removes part of the dye.

Region B: Dye-induced micelles.<sup>32,39</sup> The region of dye-induced micelles was identified as the DTAB concentration region, where the spectrum of the dye is still sensitive to DTAB concentration changes.<sup>32</sup> Part of it lays below the critical micelle concentration (cmc) of pure DTAB, which was determined to be 9 mM in the present buffer system at 25 °C. In a following paper it will be shown, that micelles are indeed formed in the entire region B.

Region C: Postmicellar region. This region is identified by an absence of change in dye absorption upon further addition of DTAB.<sup>32</sup> It lays above DTAB cmc. Ghosh et al. referred to the aggregates in this region as dye-embedded micelles.<sup>39</sup> In view of the fact that the dyes and DTAB carry opposite charges, the location of dyes close to the positively charged DTAB head groups is likely. Therefore, the term "dye-embedded micelles" may not be the most accurate description of aggregates in this case. Nevertheless, the excess of surfactant in the post micellar region causes most of the dye molecules to interact with surfactant molecules in corresponding aggregates rather than not interacting with surfactant.

Within the last 70 years, various models were developed for the quantitative evaluation of equilibrium constants from UV/vis-spectroscopic data.<sup>40–42</sup> In the case of solute-surfactant association it is possible to either assume a thermodynamic equilibrium between a solute molecule and  $m$  surfactant molecules or between one solute molecule and one surfactant micelle. The latter gives rise to the well-known Benesi-Hildebrand equation frequently used in case of high surfactant excess.<sup>32,34,36,43</sup> In the current system, however, the application of a dye-micelle equilibrium model is not suitable as (1) surfactant concentrations studied are too low to assume surfactant excess and (2) some of the studied surfactant concentrations lay below the cmc of DTAB without the dye. Therefore, an equilibrium between one dye molecule (Dye) and  $m$  free surfactant molecules (S) on one side and the complex  $\text{DyeS}_m$  on the other side is considered, assuming that micelle formation does only occur due to the interaction between dye and surfactant.



The assumption of a 1: $m$  rather than a 1:1 stoichiometry for dye-surfactant association in solution is reasonable considering observed stoichiometries for dye-surfactant binding determined in eq (1) for the solid dye-surfactant complex. The equilibrium- or dye-surfactant association constant  $K_{\text{DS}}$  for eq (2) can be written as:

$$K_{\text{DS}} = \frac{[\text{DyeS}_m]}{[\text{Dye}] \cdot [\text{S}]^m} \quad (3)$$

$[\text{DyeS}_m]$ ,  $[\text{Dye}]$  and  $[\text{S}]$  denote molar equilibrium concentrations of the dye-surfactant complex, dye monomer and surfactant monomer. Our model based on eq (2) is fully compatible with the choice of  $[\text{Dye}]_{\text{tot}} = 2.5 \text{ mM}$ . The model formally describes the co-assembly of one dye molecule with  $m$  surfactant molecules in equilibrium with monomeric dye and monomeric surfactant. This feature well includes the possibility of mixed micelles with the same stoichiometry as  $\text{DyeS}_m$ . In other words, if this co-assembly triggers micelle formation it is automatically included.

It is emphasized that preliminary self-assembly equilibria of dye molecules are neglected. Indeed, previous studies on the self-assembly of the three dyes showed, that Blue self-assembles to dimers and Red to fractal-like aggregates, whereas Yellow remains molecularly dissolved in their pure solution without surfactant.<sup>33</sup> However, self-assembly was suggested to be mainly driven by  $\pi$ - $\pi$ -stacking and hydrogen bonding interactions, which are generally weaker than the strong electrostatic attraction between oppositely charged dye- and surfactant molecules.<sup>26</sup> Therefore, dye-dye complexes are considered to be easily broken apart within dye-DTAB mixed micelles due to strong electrostatic interaction between negatively charged dye molecules and cationic surfactant molecules. An observation confirming preferential binding between dye and DTAB molecules is the precipitation of solid dye-DTAB complexes at small surfactant concentrations (2-phase region, Figure 2).

Taking total molar concentrations of the dye monomer  $[\text{Dye}]_{\text{tot}}$  and the surfactant  $[\text{S}]_{\text{tot}} = [\text{DTAB}]_{\text{tot}}$  into account, equation (3) can be written as:

$$K_{\text{DS}} = \frac{[\text{DyeS}_m]}{([\text{Dye}]_{\text{tot}} - [\text{DyeS}_m]) \cdot ([\text{S}]_{\text{tot}} - m [\text{DyeS}_m])^m} \quad (4)$$

Assuming that only the dye and the dye-surfactant complex [DyeS<sub>m</sub>] absorb at the relevant wavelength (indicated by the red vertical lines of Figure 3) and assuming the validity of Beer-Lambert Law for both species, the absorbance of a sample can be expressed as:

$$A_d = \epsilon_{\text{Dye}} \cdot [\text{Dye}] + \epsilon_{\text{DS}_m} \cdot [\text{DyeS}_m] \quad (5)$$

With  $[\text{Dye}] = [\text{Dye}]_{\text{tot}} - [\text{DyeS}_m]$  and with  $A_{d,0} = \epsilon_{\text{Dye}} \cdot [\text{Dye}]_{\text{tot}}$ , eq (6) as an expression for  $[\text{DyeS}_m]$  is revealed:

$$[\text{DyeS}_m] = \frac{A_d - A_{d,0}}{\epsilon_{\text{DS}_m} - \epsilon_{\text{Dye}}} \quad (6)$$

$\epsilon_{\text{Dye}}$  and  $\epsilon_{\text{DS}_m}$  are the molar extinction coefficients of the dye and the dye-surfactant complex respectively. Assuming a stoichiometry  $m$ , a value  $K_{\text{DS}}$  can therefore be calculated from each data pair  $A_d = f([\text{S}]_{\text{tot}})$  by substituting eq (6) into eq (4).  $A_{d,0}$  and  $\epsilon_{\text{Dye}}$  are known from the absorption spectrum of pure dye, whereas  $\epsilon_{\text{DS}_m}$  was obtained from the sample with maximum surfactant excess, located in the postmicellar region where dye absorption does not change upon further addition of surfactant.

Model fits were carried out with six stoichiometries. For a given stoichiometry  $m$ ,  $K_{\text{DS}}$  was determined from the  $A_d = f([\text{S}]_{\text{tot}})$  data pair of  $N$  samples mostly located in the region of dye-induced micelles and indicated as blue data points in Figure 4. The average of all  $K_{\text{DS}}$  obtained for this stoichiometry  $m$  was then taken and used to calculate the theoretical absorbance  $A_{d,\text{theo}}$  for each of the  $N$  samples. The deviation of  $A_{d,\text{theo}}$  from the recorded absorbance  $A_d$  of the respective sample yielded the  $\chi_{\text{red}}^2$  value defined by eq (7).

$$\chi_{\text{red}}^2 = \frac{\sum_{i=1}^N (A_{d,i} - A_{d,\text{theo},i})^2}{N} \quad (7)$$

This procedure was performed for six stoichiometries. Corresponding  $\chi_{\text{red}}^2$  values are reported in Table 1 for each dye. Due to the absence of specific spectral features signalling a build-up and disassembly or modification of soluble dye-surfactant complexes DyeS<sub>m</sub> at a 1: $m$  ratio, it was not possible to employ a more straightforward analysis technique to obtain information on the stoichiometry of dye-surfactant binding.<sup>44</sup> Furthermore, as discussed earlier, the application of a previously reported analysis technique assuming 1:1 stoichiometry of dye-surfactant binding in the region of dye-induced micelles (B, Figure 4) would have been unreasonable.<sup>45</sup> Therefore, strategy to obtain information on

stoichiometry  $m$  and association  $K_{DS}$  of dye-surfactant binding, presented here, is considered to be most suitable for the system under consideration.

Table 1: Evaluation of the stoichiometry of the dye-surfactant association equilibrium with  $\chi_{red}^2$  defined by eq (7) as criterium.

Dye:	Yellow	Blue	Red
Data interval:	$7.5 \text{ mM} \leq [S]_{tot} \leq 50 \text{ mM}$	$7.5 \text{ mM} \leq [S]_{tot} \leq 25 \text{ mM}$	$12.5 \text{ mM} \leq [S]_{tot} \leq 55 \text{ mM}$
$m$	$\chi_{red}^2$	$\chi_{red}^2$	$\chi_{red}^2$
1	29.78	145.97	44.53
2	<b>1.64</b>	137.88	11.26
3	51.28	<b>2.22</b>	4.64
4	66.02	378.88	<b>3.35</b>
5	71.83	626.11	4.02
6	74.03	608.56	5.19

The data are best described by a stoichiometry  $m$  at which the lowest  $\chi_{red}^2$  is obtained. This stoichiometry, together with the corresponding dye-surfactant association constant  $K_{DS}$  is summarized in Table 2.  $A_{d,theo} = f([S]_{tot})$  based on these values is displayed in Figure 4 as a red curve. Experimental data points are reasonably well described by these curves so that the model can be considered to be a relatively good approximation under the given conditions.

Association constants  $K_{DS}$  obtained by this procedure suffer from considerable uncertainties. However, information about their order of magnitude is obtained. In addition to that, all  $K_{DS}$  lay well above 1, which means that dye-surfactant complex formation is strongly favoured.

It is remarkable that the stoichiometry of dye:DTAB binding decreases from 1:2 for Yellow over 1:3 for Blue to 1:4 for Red. The same trend was established for the stoichiometry of dye:DTAB binding from evaluation of the phase transition threshold line in the phase diagrams (Figure 2). In addition to that, the number of DTAB molecules aggregating with one dye molecule in the homogeneous 1-phase region is always higher than that obtained from the analysis of the phase transition threshold in the phase diagram. This is consistent with the assumption that soluble  $DyeS_m$  aggregates are only formed below a certain dye:DTAB threshold ratio.

Table 2: Stoichiometry and association constants for the association equilibrium of dye-surfactant complexes.

Dye	Yellow	Blue	Red
$m$	2	3	4
$K_{DS}(m)$ [ $L^m \text{ mol}^{-m}$ ]	$(9.9 \pm 6.0) \cdot 10^3$	$(4.7 \pm 2.0) \cdot 10^6$	$(6.3 \pm 4.0) \cdot 10^7$
$\chi_{\text{red}}^2$	1.64	2.22	3.35

**Small-angle neutron scattering.** SANS studies were performed on samples which, according to their dye:DTAB ratio, lay within the region of dye-induced micelles. The impact of adding different dye molecules at a concentration of  $[\text{Dye}]_{\text{tot}} = 5 \text{ mM}$  on the morphology of DTAB micelles was studied. Figure 5 displays SANS curves from solutions containing  $[\text{Dye}]_{\text{tot}} = 5 \text{ mM}$  and  $[\text{DTAB}]_{\text{tot}} = 30 \text{ mM}$  in comparison to the SANS curve of pure DTAB at that concentration. The latter was described with the form factor model of an oblate ellipsoid including a structure factor derived by Hayter and Penfold to consider inter-micellar interaction.<sup>46,47</sup> The choice of this model was based on work by Bergström and Pedersen whom investigated the morphology of DTAB micelles in brine solution.<sup>48</sup> The use of such a structure factor significantly improved quality of the fit, even though no obvious correlation peak is visible in the dilute solution of DTAB (Figure 5), which also contains a rather high concentration of buffer salt (ionic strength  $I \approx 0.25 \text{ M}$ ).

For the description of SANS curves originating from solutions containing both, dye and DTAB, no structure factor was used, as the anionic dye is assumed to interact with the positively charged DTAB head group, which leads to charge screening and reduces medium- to long-range ordering caused by electrostatic interactions.<sup>49</sup> The SANS curve of Yellow was well described using the form factor of an oblate ellipsoid with dimensions similar to the pure DTAB micelle (Table 3).

For the description of SANS curves emerging from solutions of Blue with DTAB and Red with DTAB, the assumption of a more anisometric micellar morphology became necessary. This was realized by moving to a triaxial ellipsoid model to fit the data.<sup>50</sup> Resulting geometrical dimensions are displayed in Table 3. Interestingly, the two smaller radii of each triaxial ellipsoid are similar to the polar and equatorial radius  $r_p$  and  $r_{eq}$  of oblate ellipsoidal DTAB micelles. This points towards an one-dimensional growth of DTAB micelles upon addition of dye, like it is frequently observed for cationic surfactant micelles upon addition of salt or hydrotrope.<sup>51–53</sup>

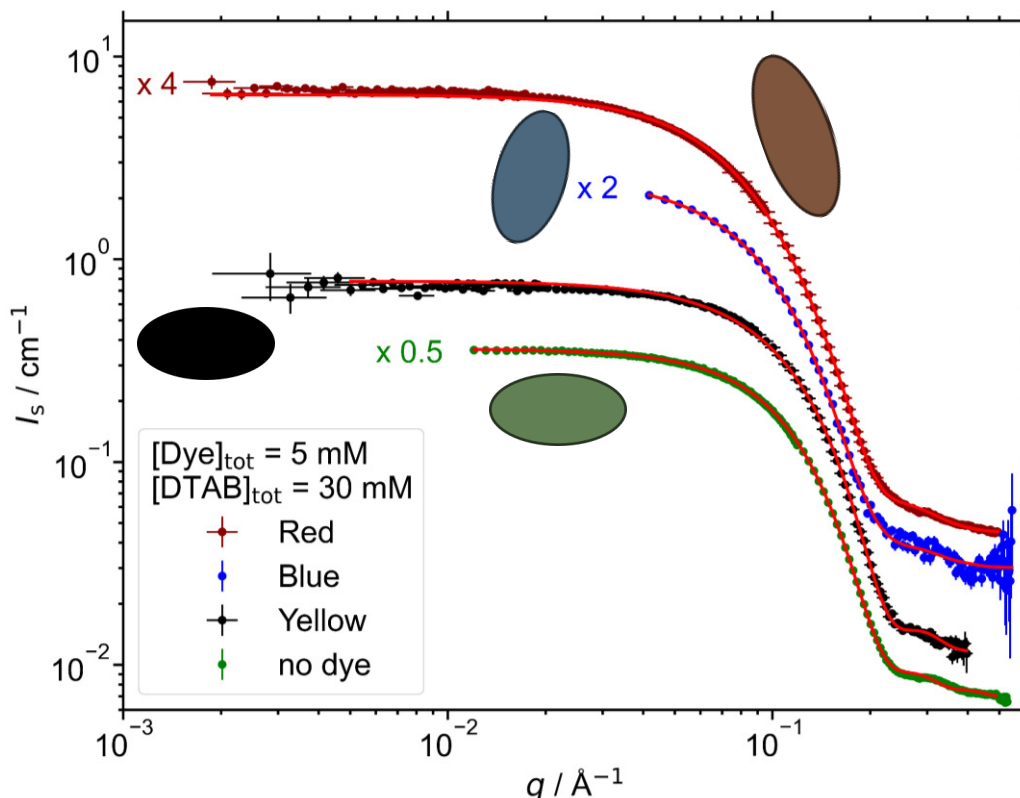


Figure 5: SANS curves of solutions containing  $[\text{Dye}]_{\text{tot}} = 5 \text{ mM}$  and  $[\text{DTAB}]_{\text{tot}} = 30 \text{ mM}$  and a solution containing DTAB at a concentration of  $30 \text{ mM}$  without dye. Samples were prepared in a  $\text{NaHCO}_3/\text{Na}_2\text{CO}_3$  buffer ( $\text{pD} = 10.7$ ,  $I \approx 0.25 \text{ M}$ ) in  $\text{D}_2\text{O}$  except for the sample containing Blue, where the buffer was dissolved in a mixture of  $\text{H}_2\text{O}$  and  $\text{D}_2\text{O}$  (50:50, v/v). Fits are shown as red lines. The form factor models are sketched next to the corresponding curve.

Table 3: Model parameters from form factor fits to SANS curves resulting from solutions containing dye at a concentration of  $[\text{Dye}]_{\text{tot}} = 5 \text{ mM}$  and DTAB at a concentration of  $[\text{DTAB}]_{\text{tot}} = 30 \text{ mM}$ . Samples were prepared in an aqueous  $\text{NaHCO}_3/\text{Na}_2\text{CO}_3$  buffer ( $\text{pD} = 10.7$ ,  $I \approx 0.25 \text{ M}$ ) in  $\text{D}_2\text{O}$  except for the sample containing Blue where the buffer was prepared in a  $\text{H}_2\text{O}/\text{D}_2\text{O}$  mixture (50:50 v/v) as described in the experimental part. For fitting the SANS curve emerging from a pure DTAB solution, the product of an oblate ellipsoidal form factor and a structure factor by Hayter and Penfold was used.<sup>46,47</sup> In the case of the form factor model of a triaxial ellipsoid, the length parameter is equivalent to the longest radius.

Dye	Model	Cross Section		Length
		$r_{\text{minor}} / \text{Å}$	$r_{\text{major}} / \text{Å}$	$L / \text{Å}$
no dye	Oblate ellipsoid*	$r_{\text{eq}} = 22.357 \pm 0.009$		$r_{\text{p}} = 14.048 \pm 0.008$
Yellow	Oblate ellipsoid	$r_{\text{eq}} = 21.73 \pm 0.04$		$r_{\text{p}} = 13.98 \pm 0.06$
Blue	Triaxial ellipsoid	$15.3 \pm 0.2$	$22.0 \pm 0.3$	$32.0 \pm 0.3$
Red	Triaxial ellipsoid	$15.93 \pm 0.02$	$22.32 \pm 0.03$	$40.31 \pm 0.04$

\*Oblate ellipsoid x structure factor; Symbols:  $r_{\text{p}}$  – polar radius,  $r_{\text{eq}}$  – equatorial radius,  $r_{\text{minor}}$  – minor cross section radius,  $r_{\text{major}}$  – major cross section radius,  $L$  – length.



Moving on to a DTAB concentration of  $[\text{DTAB}]_{\text{tot}} = 20 \text{ mM}$  while remaining at  $[\text{Dye}]_{\text{tot}} = 5 \text{ mM}$ , micelle morphologies were found to become more anisometric compared to  $[\text{DTAB}]_{\text{tot}} = 30 \text{ mM}$  (Figure 6). This is in agreement with literature. A decrease in the spontaneous curvature of surfactant micelles was frequently observed upon hydrotrope addition.<sup>53–55</sup> This was also the case for the addition of dye molecules to surfactant systems, with the morphology of assemblies depending on the system in use.<sup>56–58</sup>

In the present work, the SANS curve from a solution of Yellow and DTAB was described with the form factor model of a triaxial ellipsoid, whereas SANS curves from solutions of Blue or Red and DTAB were described with the form factor model of a cylinder with elliptical cross section.<sup>46</sup> The corresponding fit parameters can be found in Table 4. Micelles of Blue or Red and DTAB are very polydisperse in length, which makes sense considering the underlying dynamic equilibrium present in micellar surfactant solutions.<sup>59</sup> To fit the data, the ratio between the root-mean-square deviation from the average length ( $\sigma$ ) and the average length ( $L_{\text{avg}}$ ) was set to  $\sigma/L_{\text{avg}} = 0.95$  for Blue-DTAB micelles according to a strategy employed by Bergström and Pedersen who observed polydisperse mixed micelles formed from sodiumdodecylsulphate and DTAB.<sup>60</sup> It was intended to use the same  $\sigma/L_{\text{avg}}$  for the SANS curve emerging from the corresponding Red-DTAB solution. However, the data was better described using  $\sigma/L_{\text{avg}} = 0.5$ . Strikingly, the dimensions of the elliptical cylinder cross section remain very similar to  $r_{\text{eq}}$  and  $r_{\text{p}}$  found for DTAB micelles at  $[\text{DTAB}]_{\text{tot}} = 30 \text{ mM}$  (Table 4). This confirms the assumption of an unidimensional growth of these micelles upon increase of the dye:DTAB ratio from 1:6 to 1:4.

The differences in the morphologies of dye-DTAB micelles observed for the different dyes correlate with the stoichiometries found for dye-DTAB binding from the phase transition threshold as well as in solution. This can easily be related to the SANS sample composition relative to the phase transition threshold in the concentration-dependent phase diagrams of Figure 2. For the dye Red, the sample compositions investigated with SANS, i.e.  $[\text{Dye}]_{\text{tot}} = 5 \text{ mM}$  and  $[\text{DTAB}]_{\text{tot}} = 20 \text{ mM}$  or  $30 \text{ mM}$  lay much closer to its phase transition threshold than for Blue or Yellow. Conversely, the phase transition threshold in the phase diagram of Yellow and DTAB is the farthest away from these sample compositions. The micelles formed between  $[\text{Yellow}]_{\text{tot}} = 5 \text{ mM}$  and  $[\text{DTAB}]_{\text{tot}} = 30 \text{ mM}$  are about the same size as pure DTAB micelles, indicating that the composition of this sample presumably lays close to the post-micellar region, where assembly morphology is determined by DTAB micelles due to their excess presence. Furthermore, it is logical to assume a DTAB excess

at a Yellow:DTAB ratio of 1:6, considering that Yellow and DTAB interact at a stoichiometry of 1:2 (Table 2).

To conclude, the morphology of dye-surfactant micelles depends on the dye added to the solution. The magnitude of observed deviations from the morphology of pure DTAB micelles at a given sample composition inversely correlates with dye:DTAB binding stoichiometries found at the phase transition threshold as well as in solution. The one-dimensional growth of DTAB micelles upon dye addition was strongest for the addition of Red, which binds to DTAB at a stoichiometry of Red:DTAB = 1:4 in solution, medium for the addition of Blue with a stoichiometry of Blue:DTAB = 1:3 and weakest for Yellow with a stoichiometry of Yellow:DTAB = 1:2. A general increase in micellar anisometry when increasing the dye:DTAB ratio from 1:6 to 1:4, i.e. when moving closer to the phase transition threshold from the side of DTAB excess, was observed for all dyes.

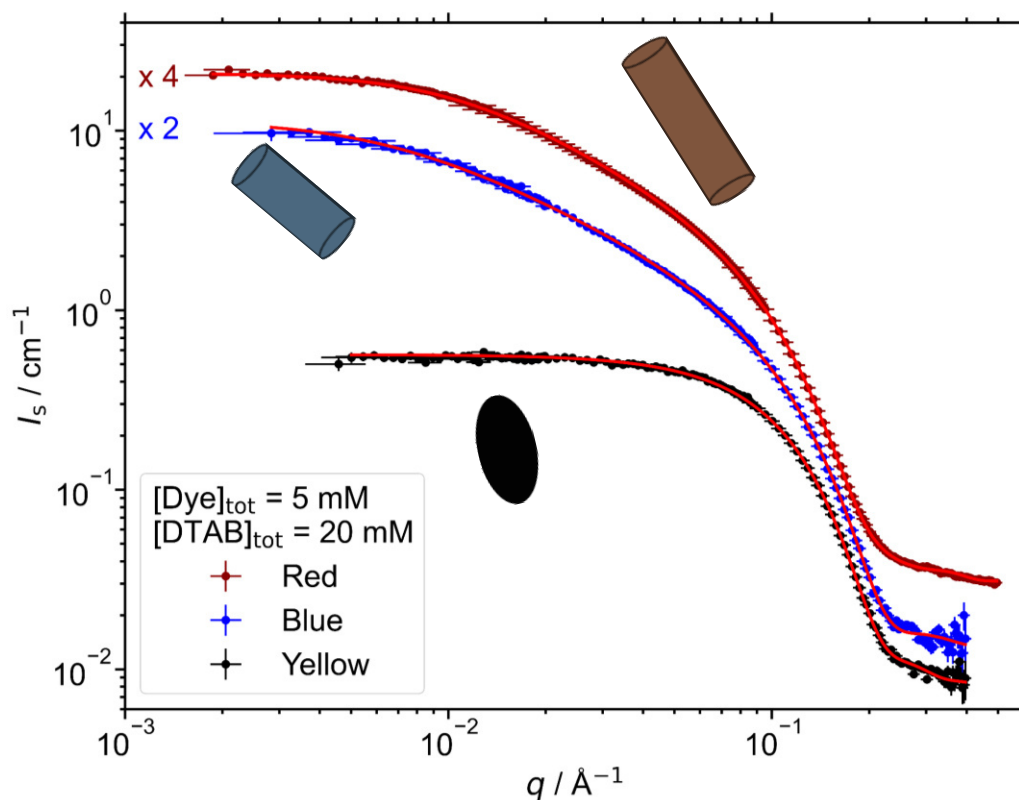


Figure 6: SANS curves of solutions containing  $[\text{Dye}]_{\text{tot}} = 5 \text{ mM}$  and  $[\text{DTAB}]_{\text{tot}} = 20 \text{ mM}$ . Samples were prepared in an  $\text{NaHCO}_3/\text{Na}_2\text{CO}_3$  buffer ( $\text{pD} = 10.7$ ,  $I \approx 0.25 \text{ M}$ ) in  $\text{D}_2\text{O}$ . Fits are shown as red lines. The form factor models are sketched next to the corresponding curve.

Table 4: Model parameters from form factor fits to SANS curves resulting from solutions containing dye at a concentration of  $[\text{Dye}]_{\text{tot}} = 5 \text{ mM}$  and DTAB at a concentration of  $[\text{DTAB}]_{\text{tot}} = 20 \text{ mM}$ . Samples were prepared in an aqueous  $\text{NaHCO}_3/\text{Na}_2\text{CO}_3$  buffer ( $\text{pD} = 10.7$ ,  $I \approx 0.25 \text{ M}$ ) in  $\text{D}_2\text{O}$ . In the case of the form factor model of a triaxial ellipsoid, the length parameter is equivalent to the longest radius.

Dye	Model	Cross Section		Length
		$r_{\text{minor}} / \text{\AA}$	$r_{\text{major}} / \text{\AA}$	$L / \text{\AA}$
Yellow	Triaxial ellipsoid	$13.8 \pm 0.2$	$21.6 \pm 0.6$	$24.4 \pm 0.6$
Blue	Cylinder with elliptical cross section	$13.1 \pm 0.2$	$19.6 \pm 0.4$	$L = 199 \pm 3$ $\sigma/L_{\text{avg}} = 0.95$
Red	Cylinder with elliptical cross section	$14.19 \pm 0.02$	$23.64 \pm 0.05$	$L = 233.5 \pm 0.7$ $\sigma/L_{\text{avg}} = 0.5$

Symbols:  $\sigma/L_{\text{avg}}$  - ratio of the root-mean-square deviation from the average length and the average length

## 5.4 Conclusions

Three 3-chloro-4-hydroxy-phenylazo dyes, each of them carrying a negative charge due to deprotonation of the phenolic hydroxyl group at alkaline pH, were shown to differ in the stoichiometry of their co-assembly with the cationic surfactant DTAB.

For all dyes, phase separation of dye-DTAB solutions was observed above a given dye:DTAB ratio with the ratio depending on the dye. It was observed to decrease from Yellow (1:1.67) over Blue (1:2.56) to Red (1:2.94) and gives an indication of the stoichiometry of dye-DTAB binding in the coacervate phase for Yellow or the solid precipitate for Blue and Red.

Furthermore, the stoichiometry of dye-DTAB binding in solution, i.e. the 1-phase region, was studied using UV/vis spectroscopy. Stoichiometries of 1:2, 1:3 and 1:4 were found for Yellow, Blue and Red with DTAB respectively. The lower dye:DTAB ratios obtained in homogeneous solution as compared to the ratios at the respective phase transition threshold can nicely be reconciled with a larger amount of DTAB molecules required for the solubilisation of dye compared to that of the formation of solid complexes.

Furthermore, the morphology of dye-DTAB micelles was studied using SANS. DTAB micelles show an uniaxial growth upon dye addition with its extend being dependent upon the dye and being inversely correlated to dye:DTAB binding stoichiometry at a set total concentration of dye and DTAB. This was attributed to a sample composition being closer to the postmicellar region if the dye:DTAB binding stoichiometry is high, e.g. Yellow:DTAB = 1:2, or closer to the phase transition threshold or region of dye-surfactant ion pair formation for a low binding stoichiometry, e.g. Red:DTAB = 1:4. A sample being close to

the postmicellar region indicates surfactant excess, which leads to micellar morphology being largely determined by the morphology of surfactant micelles.

Following the presented investigations, differences in the co-assembly behaviour of three structurally similar azo dyes with DTAB were elucidated. Differences in co-assembly morphology were related to the stoichiometry of dye-DTAB binding. It becomes clear, that even structurally similar molecules can show significant differences in their interaction with a surfactant.

**Author Contributions:** Conceptualization: WM, RS, BN, KH, experimental: WM, RS, GS, JK, analysis: WM with contributions from RS, GS, KH, BN, writing: WM, editing: RS, BN, KH, GS, funding acquisition: RS, BN, KH

**Conflicts of interest:** There are no conflicts to declare.

**Acknowledgements:** The authors thank the Institut Laue-Langevin for the provision of internal beamtime (<https://doi.ill.fr/10.5291/ILL-DATA.INTER-557>). The authors thank the Paul Scherrer Institut for the provision of internal beamtime (Proposal 20221454). The authors gratefully acknowledge the use of the Partnership for Soft Condensed Matter (PSCM) facilities. The authors acknowledge the Bundesanstalt für Materialforschung und –prüfung (BAM) for measurements at the MOUSE SAXS-instrument. W.M. acknowledges funding for a Ph.D. scholarship from the European Union’s Horizon 2020 research and innovation programme under the Marie Skłodowska-Curie grant agreement No 847439 within the InnovaXN framework (Project number XN2019-ILL23). This work benefited from the use of the SasView application, originally developed under NSF award DMR-0520547. SasView contains code developed with funding from the European Union’s Horizon 2020 research and innovation programme under the SINE2020 project, grant agreement No 654000.

## 5.5 Supporting information

### 5.5.1 Experimental

**Chemicals.** Tetradecyltrimethylammoniumbromide ( $\geq 99\%$ ) and Cetyltrimethylammoniumbromide (BioXtra,  $\geq 99\%$ ) were obtained from Sigma Aldrich and used as received without further purification.

**Phase diagrams.** Phase diagrams were established by stepwise addition of a Blue stock solution to a surfactant solution.  $\text{NaHCO}_3/\text{Na}_2\text{CO}_3$  buffer solution ( $\text{pH} = 10.5$ , ionic strength  $I \approx 0.25\text{ M}$ ) was used as a solvent in all cases. The stock solution contained Blue at a molar concentration of  $15\text{ mM}$ . The concentration of the surfactant solution was chosen according to the desired sample composition. After each addition of dye stock solution, the sample was vortexed for approximately  $30\text{ s}$  and its visual appearance observed immediately. Phase diagrams were established at room temperature ( $\approx 22\text{ }^\circ\text{C}$ ). It should be noted that at low surfactant-concentrations (below  $\approx 9\text{ mM}$ ) some initially stable samples showed precipitation after  $1\text{ h} - 24\text{ h}$ .

**UV/vis spectroscopy.** UV/vis spectra of solutions containing dye and DTAB were recorded with a Lambda-19 spectrometer from Perkin Elmer. A Hellma quartz glass cuvette with an optical path length of  $0.01\text{ cm}$  was used. The spectrometer was equipped with a thermostat to guarantee a constant measurement temperature of  $25\text{ }^\circ\text{C}$ . Samples showing precipitation were filtered prior to measurement (MACHEREY-NAGEL, CHROMAFIL Xtra H-PTFE syringe filters, pore size  $0.2\text{ }\mu\text{m}$ ).

**Wide-angle X-ray scattering.** Wide-angle X-ray scattering (WAXS) was performed on the powder samples of Blue-surfactant precipitates. Data was collected with the MOUSE SAXS/WAXS instrument located at the Bundesanstalt für Materialforschung und –prüfung (BAM, Germany).<sup>61</sup> X-rays were generated from a microfocus X-ray tube, followed by multilayer optics to parallelize and monochromatize the X-ray beams ( $\text{Cu K}\alpha$ ,  $\lambda = 0.154\text{ \AA}$ ). The scattered radiation was detected using an *in-vacuum* Eiger 1M detector (Dectris, Switzerland), which was placed at multiple distances between  $55 - 2307\text{ mm}$  from the sample. The resulting data has been processed to an absolute intensity scale using the DAWN software package in a standardized complete 2D correction pipeline with uncertainty propagation.<sup>62,63</sup>

Powder samples were prepared by isolation of Blue-surfactant complexes from a phase-separated sample. For this purpose, a stock solution of Blue was added to a stock solution of surfactant to obtain a sample with  $[\text{Blue}]_{\text{tot}} = 10\text{ mM}$  and  $[\text{S}]_{\text{tot}} = 20\text{ mM}$ . An aqueous  $\text{NaHCO}_3/\text{Na}_2\text{CO}_3$  buffer ( $\text{pH} = 10.5$ , ionic strength  $I \approx 0.25\text{ M}$ ) was used as the solvent in

all cases. The resulting sample showed phase separation and precipitation of solid dye-surfactant complexes. The samples were equilibrated for 24 h at room temperature while gently mixing on a roller mixer. Afterwards, the sample was centrifuged and the liquid supernatant decanted. The solid residue was subsequently suspended in MilliQ-water, centrifuged and the liquid decanted again. This washing procedure was repeated two times to remove the buffer salts. The solid remainder was then dried in vacuo at room temperature.

**Density.** Density measurements were performed using an Anton-Paar Density Meter (DMA 4500 M) requiring a sample volume of 1 mL. Density measurements were performed to be able to calculate apparent molar volumes  $V_m(c)$  of solutions of Blue and Red. For this purpose, five solutions containing Blue concentrations between 1 mM ( $0.37 \text{ g L}^{-1}$ ) and 20 mM ( $7.39 \text{ g L}^{-1}$ ) and eight solutions containing Red concentrations between 0.5 mM ( $0.14 \text{ g L}^{-1}$ ) and 10 mM ( $2.87 \text{ g L}^{-1}$ ) were prepared in an  $\text{NaHCO}_3/\text{Na}_2\text{CO}_3$  buffer ( $\text{pD} = 10.7$ ,  $I \approx 0.25$ ) in 100 %  $\text{D}_2\text{O}$ . The densities of these solutions as well as of the buffer were measured after equilibrating the temperature of each sample to 25 °C. This yielded sample densities ( $\rho$ ) as well as the density of the solvent ( $\rho_0$ ).

### 5.5.2 Influence of DTAB addition on dye absorption

Figure SI1 shows the change in position of the absorption maximum of all three dyes upon addition of various concentrations of DTAB.

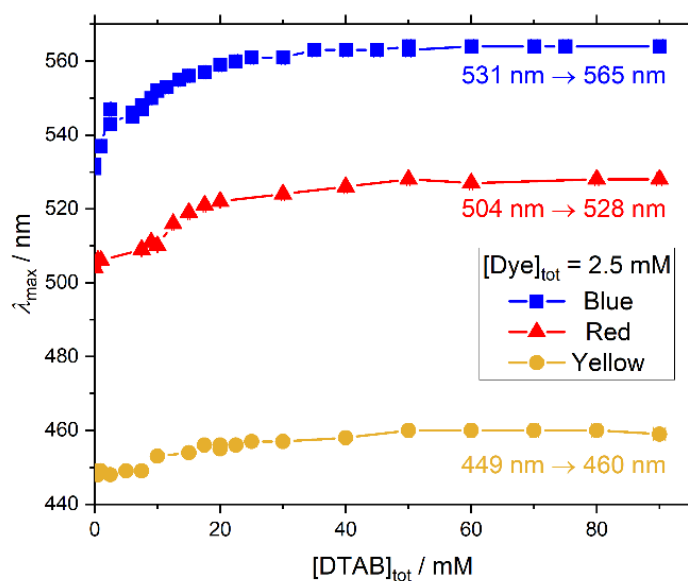


Figure SI1: Extent of change in the position of the dye absorption maximum upon addition of DTAB in  $\text{NaHCO}_3/\text{Na}_2\text{CO}_3$  buffer at 25 °C.

### 5.5.3 Solid dye-surfactant complexes between Blue and cationic surfactants with different chain lengths

#### Phase diagrams.

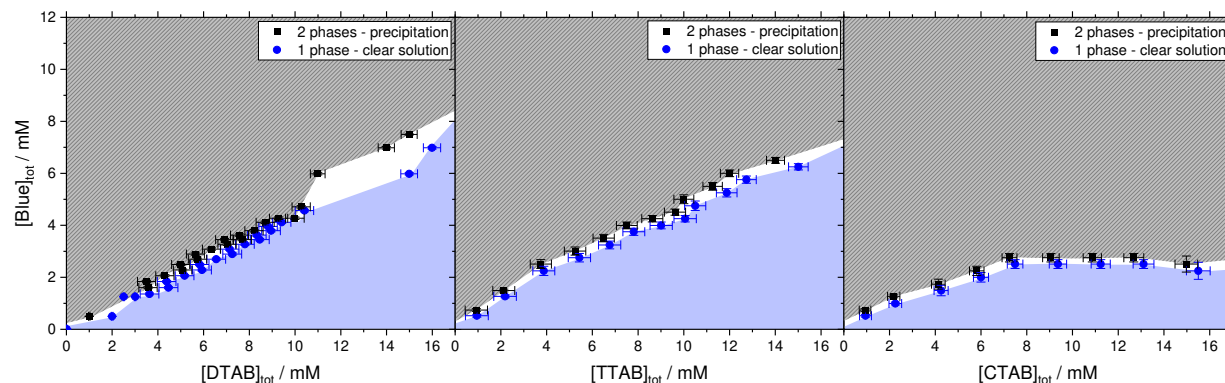


Figure S12: Concentration-dependent phase behaviour of solutions of Blue in combination with cationic trimethylammoniumbromide surfactants. From left to right with increasing alkyl chain length  $C_n$ : Dodecyltrimethylammoniumbromide (DTAB,  $C_{12}$ ), Tetradecyltrimethylammoniumbromide (TTAB,  $C_{14}$ ), Cetyltrimethylammoniumbromide (CTAB,  $C_{16}$ ). An aqueous  $\text{NaHCO}_3/\text{Na}_2\text{CO}_3$  buffer ( $\text{pH} = 10.5$ ,  $I \approx 0.25 \text{ M}$ ) was used as a solvent at all times. Phase diagrams were established at room temperature ( $\approx 22 \text{ }^\circ\text{C}$ ).

**Wide-angle X-ray scattering.** Precipitates formed between the dye Blue and the cationic surfactant DTAB in the 2-phase region of the phase diagram were isolated and analysed by X-ray scattering on the powder sample. The corresponding powder WAXS-curve is shown in Figure S13 as a black line and displays clearly discernible diffraction peaks.

This points towards crystalline ordering within the Blue-DTAB precipitates. To facilitate the assignment of peaks to structural features of the crystalline precipitates, WAXS curves were also recorded for complexes formed between the dye Blue and the surfactants tetradecyltrimethylammoniumbromide (TTAB) and cetyltrimethylammoniumbromide (CTAB). All three surfactants have the same head group and only show a variation in the length of their hydrophobic tail. This variation is reflected in the WAXS-pattern of solid dye-surfactant complexes. The position of the second diffraction peak is shifted from  $q = 0.282 \text{ \AA}^{-1}$  (DTAB) to  $q = 0.244 \text{ \AA}^{-1}$  (CTAB) with increasing chain length. Due to the reciprocal relation between the value of  $q$  and real-space length scales this is consistent with the length of the hydrophobic tail. Apart from this trend some reflections overlay, suggesting similar structural features independent of surfactant hydrophobic chain length. It was abstained from a more detailed investigation of the structure of Blue-surfactant complexes. A lamellar structure was suggested for similar systems by the Faul group.<sup>24</sup> This is not unlikely for the present system, but needs to be confirmed.

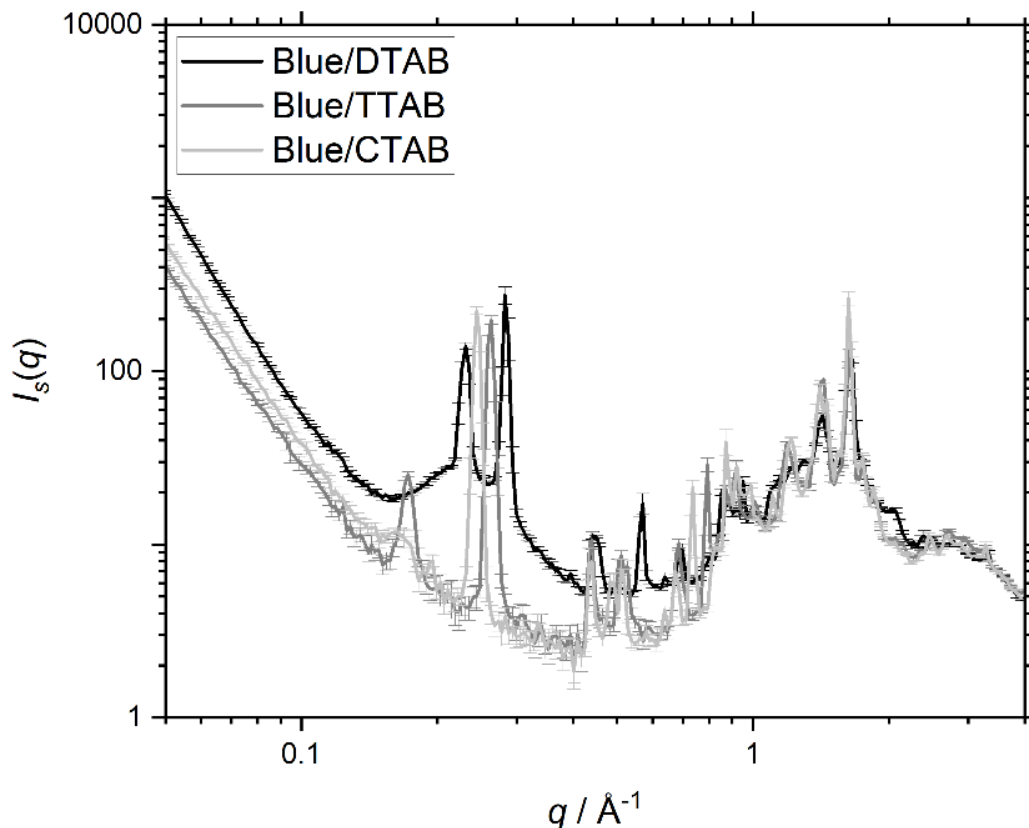


Figure S13: WAXS-curves of solid complexes between the anionic dye Blue and cationic surfactants with varying hydrophobic alkyl chain lengths  $C_n$ : DTAB ( $C_{12}$ ), TTAB ( $C_{14}$ ), CTAB ( $C_{16}$ ).

#### 5.5.4 Analysis of small-angle neutron scattering curves.

For the analysis of SANS data, the volume fraction of dye-surfactant assemblies in solution was calculated from the known concentration of dye and surfactant as well as their molar volumes. It was assumed that all dye- and surfactant molecules in the sample take part in assembly formation and that their molar volumes do not change upon interaction. Although both assumptions might not be true due to the existence of a critical micelle concentration, the presence of free molecules up to this concentration and volume compression or expansion effects upon aggregation, it is a useful strategy to reduce the number of parameters that have to be fitted. As the scattering length density ( $SLD$ ) of the overall assembly was fitted and not used for the interpretation of data, the use of slightly incorrect volume fraction should not devalue size parameters obtained from fitting.

**Molar volume.** Table S11 summarizes molar volumes used for the calculation of aggregate volume fractions. Molar volumes of Blue and Red were determined by measuring the densities of solutions containing the respective dye at various concentrations  $c$ . Details on density measurements can be found in the experimental part. A  $\text{NaHCO}_3/\text{Na}_2\text{CO}_3$  buffer



(pD = 10.7,  $I \approx 0.25$  M) prepared in D<sub>2</sub>O was used as a solvent in all cases. Measurements were performed at 25 °C. Apparent molar volumes  $V_m(c)$  were calculated according to the following equation:<sup>64</sup>

$$V_m(c) = \frac{1000 \cdot (\rho_0 - \rho)}{c \cdot \rho} + \frac{M}{\rho} \quad (\text{SI1})$$

$\rho_0$  is the density of the solvent,  $\rho$  the density of the solution and  $M$  the molar mass of the solute. Extrapolation of  $V_m(c)$  to  $c = 0$  yields the molar volume  $V_m = V_m(c \rightarrow 0)$ . As in the presented cases of Blue and Red apparent molar volumes  $V_m(c)$  did not depend on sample concentration, their average was calculated to obtain  $V_m$ . The molar volume of Yellow was not measured and assumed to correspond to the molar volume of Red.

Table SI1: Molar volumes of several compounds at 25 °C.

Compound	Molar volume $V_m / \text{cm}^3 \text{mol}^{-1}$
Yellow <sup>*</sup>	213.1
Blue	246.3
Red	213.1
DTAB <sup>**</sup>	302.7

<sup>\*</sup>Assumed to have the same molar volume as Red. <sup>\*\*</sup>Calculated from molar volumes of methyl-, methylene-, and trimethylammonium groups as well as the molar volume of Br<sup>-</sup> employed and reported in literature assuming additivity of molar volumes.<sup>65-67</sup>

## SANS fit parameters.

Table SI2: Model parameters from form factor fits to SANS curves resulting from solutions containing dye at a concentration of  $[\text{Dye}]_{\text{tot}} = 5 \text{ mM}$  and DTAB at a concentration of  $[\text{DTAB}]_{\text{tot}} = 30 \text{ mM}$ . Samples were prepared in an aqueous  $\text{NaHCO}_3/\text{Na}_2\text{CO}_3$  buffer ( $\text{pD} = 10.7$ ,  $I \approx 0.25 \text{ M}$ ) in  $\text{D}_2\text{O}$  except for the sample containing Blue. For the sample containing Blue the buffer was prepared in a  $\text{H}_2\text{O}/\text{D}_2\text{O}$  mixture (50:50 v/v) as described in the experimental part in the main document. For fitting the SANS curve emerging from a pure DTAB solution, the product of an oblate ellipsoidal form factor and a structure factor by Hayter and Penfold was used.<sup>46,47</sup> The scattering length density of the solvent was set to a fixed value of  $6.376 \cdot 10^{-6} \text{ \AA}^{-2}$  in all cases except for the sample containing Blue, where the solvent was prepared in a  $\text{H}_2\text{O}/\text{D}_2\text{O}$  mixture (50:50 v/v) and it was set to  $2.918 \cdot 10^{-6} \text{ \AA}^{-2}$ . In the case of the form factor model of a triaxial ellipsoid, the length parameter is equivalent to the longest radius.

Dye	Model	Cross Section		Length	<i>SLD</i>	$\varphi$	$\chi^2$
		$r_{\text{minor}} / \text{\AA}$	$r_{\text{major}} / \text{\AA}$	$L / \text{\AA}$	$10^{-6} \text{ \AA}^{-2}$		
	Oblate						
no dye	ellipsoid x structure factor	$r_{\text{eq}} = 22.357 \pm 0.009$		$r_{\text{p}} = 14.048 \pm 0.008$	$-0.11 \pm 0.04$	0.00635	12.667
Yellow	Oblate ellipsoid	$r_{\text{eq}} = 21.73 \pm 0.04$		$r_{\text{p}} = 13.98 \pm 0.06$	$1.136 \pm 0.006$	0.01014	5.5788
Blue	Triaxial ellipsoid	$15.3 \pm 0.2$	$22.0 \pm 0.3$	$32.0 \pm 0.3$	$5.778 \pm 0.004$	0.01031	1.3194
Red	Triaxial ellipsoid	$15.93 \pm 0.02$	$22.32 \pm 0.03$	$40.31 \pm 0.04$	$1.239 \pm 0.001$	0.01015	18.64

$r_{\text{p}}$  – polar radius,  $r_{\text{eq}}$  – equatorial radius,  $r_{\text{minor}}$  – minor cross section radius,  $r_{\text{major}}$  – major cross section radius,  $L$  – length, *SLD* – scattering length density of the scatterer,  $\varphi$  – scatterer volume fraction; Parameters for calculating the structure factor in a solution of DTAB without dye: Micellar charge: 15, temperature: 298.15 K, salt concentration =  $I \approx 0.25 \text{ M}$ , dielectric constant: 78.06<sup>68</sup>

Table SI3: Model parameters from form factor fits to SANS curves resulting from solutions containing dye at a concentration of  $[\text{Dye}]_{\text{tot}} = 5 \text{ mM}$  and DTAB at a concentration of  $[\text{DTAB}]_{\text{tot}} = 20 \text{ mM}$ . Samples were prepared in an aqueous  $\text{NaHCO}_3/\text{Na}_2\text{CO}_3$  buffer ( $\text{pD} = 10.7$ ,  $I \approx 0.25 \text{ M}$ ) in  $\text{D}_2\text{O}$ . The scattering length density of the solvent was set to a fixed value of  $6.376 \cdot 10^{-6} \text{ \AA}^{-2}$  in all cases. In the case of the form factor model of a triaxial ellipsoid, the length parameter is equivalent to the longest radius.

Dye	Model	Cross Section		Length	$SLD$ $10^{-6} \text{ \AA}^{-2}$	$\varphi$	$\chi^2$
		$r_{\text{minor}} / \text{ \AA}$	$r_{\text{major}} / \text{ \AA}$	$L / \text{ \AA}$			
Yellow	Triaxial ellipsoid	$13.8 \pm 0.2$	$21.6 \pm 0.6$	$24.4 \pm 0.6$	$1.312 \pm 0.008$	0.00712	1.5499
Blue	Cylinder with elliptical cross section	$13.1 \pm 0.2$	$19.6 \pm 0.4$	$L = 199 \pm 3$ $\sigma/L_{\text{avg}} = 0.95$	$1.323 \pm 0.006$	0.00729	2.0759
Red	Cylinder with elliptical cross section	$14.19 \pm 0.02$	$23.64 \pm 0.05$	$L = 233.5 \pm 0.7$ $\sigma/L_{\text{avg}} = 0.5$	$1.493 \pm 0.001$	0.00713	7.2001

$r_p$  – polar radius,  $r_{\text{eq}}$  – equatorial radius,  $r_{\text{minor}}$  – minor cross section radius,  $r_{\text{major}}$  – major cross section radius,  $L$  – length,  $\sigma/L_{\text{avg}}$  - ratio between the root-mean-square deviation from the average length and the average length,  $SLD$  – scattering length density of the scatterer,  $\varphi$  – scatterer volume fraction

## 5.6 References

- (1) Silva, G. A.; Czeisler, C.; Niece, K. L.; Beniash, E.; Harrington, D. A.; Kessler, J. A.; Stupp, S. I. Selective Differentiation of Neural Progenitor Cells by High-Epitope Density Nanofibers. *Science* **2004**, *303* (5662), 1352–1355. <https://doi.org/10.1126/science.1093783>.
- (2) Rajangam, K.; Behanna, H. A.; Hui, M. J.; Han, X.; Hulvat, J. F.; Lomasney, J. W.; Stupp, S. I. Heparin Binding Nanostructures to Promote Growth of Blood Vessels. *Nano Lett.* **2006**, *6* (9), 2086–2090. <https://doi.org/10.1021/nl0613555>.
- (3) Zhou, S.; Burger, C.; Chu, B.; Sawamura, M.; Nagahama, N.; Togano, M.; Hackler, U. E.; Isobe, H.; Nakamura, E. Spherical Bilayer Vesicles of Fullerene-Based Surfactants in Water: A Laser Light Scattering Study. *Science* **2001**, *291* (5510), 1944–1947. <https://doi.org/10.1126/science.291.5510.1944>.
- (4) Discher, D. E.; Eisenberg, A. Polymer Vesicles. *Science* **2002**, *297* (5583), 967–973. <https://doi.org/10.1126/science.1074972>.
- (5) Schenning, A. P. H. J.; v. Herrikhuyzen, J.; Jonkheijm, P.; Chen, Z.; Würthner, F.; Meijer, E. W. Photoinduced Electron Transfer in Hydrogen-Bonded Oligo(p-Phenylene Vinylene)–Perylene Bisimide Chiral Assemblies. *J. Am. Chem. Soc.* **2002**, *124* (35), 10252–10253. <https://doi.org/10.1021/ja020378s>.
- (6) Shipway, A. N.; Katz, E.; Willner, I. Nanoparticle Arrays on Surfaces for Electronic, Optical, and Sensor Applications. *ChemPhysChem* **2000**, *1* (1), 18–52. [https://doi.org/10.1002/1439-7641\(20000804\)1:1<18::AID-CPHC18>3.0.CO;2-L](https://doi.org/10.1002/1439-7641(20000804)1:1<18::AID-CPHC18>3.0.CO;2-L).
- (7) Velev, O. D.; Kaler, E. W. In Situ Assembly of Colloidal Particles into Miniaturized Biosensors. *Langmuir* **1999**, *15* (11), 3693–3698. <https://doi.org/10.1021/la981729c>.
- (8) Norris, D. J.; Vlasov, Yu. A. Chemical Approaches to Three-Dimensional Semiconductor Photonic Crystals. *Advanced Materials* **2001**, *13* (6), 371–376. [https://doi.org/10.1002/1521-4095\(200103\)13:6<371::AID-ADMA371>3.0.CO;2-K](https://doi.org/10.1002/1521-4095(200103)13:6<371::AID-ADMA371>3.0.CO;2-K).
- (9) Velev, O. D.; Kaler, E. W. Structured Porous Materials via Colloidal Crystal Templating: From Inorganic Oxides to Metals. *Advanced Materials* **2000**, *12* (7), 531–534. [https://doi.org/10.1002/\(SICI\)1521-4095\(200004\)12:7<531::AID-ADMA531>3.0.CO;2-S](https://doi.org/10.1002/(SICI)1521-4095(200004)12:7<531::AID-ADMA531>3.0.CO;2-S).
- (10) Palmer, L. C.; Velichko, Y. S.; Olvera de la Cruz, M.; Stupp, S. I. Supramolecular Self-Assembly Codes for Functional Structures. *Philosophical Transactions of the Royal Society A: Mathematical, Physical and Engineering Sciences* **2007**, *365* (1855), 1417–1433. <https://doi.org/10.1098/rsta.2007.2024>.
- (11) Rubinstein, M.; A. Papoian, G. Polyelectrolytes in Biology and Soft Matter. *Soft Matter* **2012**, *8* (36), 9265–9267. <https://doi.org/10.1039/C2SM90104H>.

- (12) Kwon, H. J.; Gong, J. P. Negatively Charged Polyelectrolyte Gels as Bio-Tissue Model System and for Biomedical Application. *Current Opinion in Colloid & Interface Science* **2006**, *11* (6), 345–350. <https://doi.org/10.1016/j.cocis.2006.09.006>.
- (13) Du, G.; Belić, D.; Del Giudice, A.; Alfredsson, V.; Carnerup, A. M.; Zhu, K.; Nyström, B.; Wang, Y.; Galantini, L.; Schillén, K. Condensed Supramolecular Helices: The Twisted Sisters of DNA. *Angewandte Chemie* **2022**, *134* (4), e202113279. <https://doi.org/10.1002/ange.202113279>.
- (14) Carl, N.; Prévost, S.; Schweins, R.; Huber, K. Ion-Selective Binding as a New Trigger for Micellization of Block Copolyelectrolytes with Two Anionic Blocks. *Soft Matter* **2019**, *15* (41), 8266–8271. <https://doi.org/10.1039/C9SM01138B>.
- (15) Antonietti, M.; Conrad, J.; Thuenemann, A. Polyelectrolyte-Surfactant Complexes: A New Type of Solid, Mesomorphous Material. *Macromolecules* **1994**, *27* (21), 6007–6011. <https://doi.org/10.1021/ma00099a011>.
- (16) Trindade, S. G.; Piculell, L.; Loh, W. Versatile Diblock Polyampholytes Can Form Two Types of Charged and Internally Structured Core–Shell Particles by Complexation with Cationic or Anionic Surfactants. *Langmuir* **2022**, *38* (9), 2906–2918. <https://doi.org/10.1021/acs.langmuir.1c03322>.
- (17) Willerich, I.; Gröhn, F. Photoswitchable Nanoassemblies by Electrostatic Self-Assembly. *Angewandte Chemie International Edition* **2010**, *49* (44), 8104–8108. <https://doi.org/10.1002/anie.201003271>.
- (18) Carl, N.; Müller, W.; Schweins, R.; Huber, K. Controlling Self-Assembly with Light and Temperature. *Langmuir* **2020**, *36* (1), 223–231. <https://doi.org/10.1021/acs.langmuir.9b03040>.
- (19) Zika, A.; Agarwal, M.; Schweins, R.; Gröhn, F. Joining Two Switches in One Nano-Object: Photoacidity and Photoisomerization in Electrostatic Self-Assembly. *Chemistry – A European Journal* **2022**, *29* (10), e202203373. <https://doi.org/10.1002/chem.202203373>.
- (20) Willerich, I.; Gröhn, F. Molecular Structure Encodes Nanoscale Assemblies: Understanding Driving Forces in Electrostatic Self-Assembly. *J. Am. Chem. Soc.* **2011**, *133* (50), 20341–20356. <https://doi.org/10.1021/ja207565m>.
- (21) Kanai, S.; Muthukumar, M. Phase Separation Kinetics of Polyelectrolyte Solutions. *J. Chem. Phys.* **2007**, *127* (24), 244908. <https://doi.org/10.1063/1.2806299>.
- (22) Fares, H. M.; Schlenoff, J. B. Diffusion of Sites versus Polymers in Polyelectrolyte Complexes and Multilayers. *J. Am. Chem. Soc.* **2017**, *139* (41), 14656–14667. <https://doi.org/10.1021/jacs.7b07905>.

- (23) Kolman, K.; Poggi, G.; Baglioni, M.; Chelazzi, D.; Baglioni, P.; Persson, M.; Holmberg, K.; Bordes, R. PH-Controlled Assembly of Polyelectrolyte Layers on Silica Nanoparticles in Concentrated Suspension. *Journal of Colloid and Interface Science* **2022**, *615*, 265–272. <https://doi.org/10.1016/j.jcis.2022.01.120>.
- (24) Guan, Y.; Antonietti, M.; Faul, C. F. J. Ionic Self-Assembly of Dye–Surfactant Complexes: Influence of Tail Lengths and Dye Architecture on the Phase Morphology. *Langmuir* **2002**, *18* (15), 5939–5945. <https://doi.org/10.1021/la0257182>.
- (25) Faul, C. F. J.; Antonietti, M. Facile Synthesis of Optically Functional, Highly Organized Nanostructures: Dye–Surfactant Complexes. *Chemistry – A European Journal* **2002**, *8* (12), 2764–2768. [https://doi.org/10.1002/1521-3765\(20020617\)8:12<2764::AID-CHEM2764>3.0.CO;2-X](https://doi.org/10.1002/1521-3765(20020617)8:12<2764::AID-CHEM2764>3.0.CO;2-X).
- (26) Faul, C. f. j.; Antonietti, M. Ionic Self-Assembly: Facile Synthesis of Supramolecular Materials. *Advanced Materials* **2003**, *15* (9), 673–683. <https://doi.org/10.1002/adma.200300379>.
- (27) Mantid Project. Mantid (2013): Manipulation and Analysis Toolkit for Instrument Data. <http://dx.doi.org/10.5286/SOFTWARE/MANTID>.
- (28) Arnold, O.; Bilheux, J. C.; Borreguero, J. M.; Buts, A.; Campbell, S. I.; Chapon, L.; Doucet, M.; Draper, N.; Ferraz Leal, R.; Gigg, M. A.; Lynch, V. E.; Markvardsen, A.; Mikkelsen, D. J.; Mikkelsen, R. L.; Miller, R.; Palmen, K.; Parker, P.; Passos, G.; Perring, T. G.; Peterson, P. F.; Ren, S.; Reuter, M. A.; Savici, A. T.; Taylor, J. W.; Taylor, R. J.; Tolchenov, R.; Zhou, W.; Zikovsky, J. Mantid—Data Analysis and Visualization Package for Neutron Scattering and  $\mu$ SR Experiments. *Nuclear Instruments and Methods in Physics Research Section A: Accelerators, Spectrometers, Detectors and Associated Equipment* **2014**, *764*, 156–166. <https://doi.org/10.1016/j.nima.2014.07.029>.
- (29) *Neutrons, X-Rays, and Light: Scattering Methods Applied to Soft Condensed Matter*, 1st ed.; Lindner, P., Zemb, T., Eds.; North-Holland delta series; Elsevier: Amsterdam ; Boston, 2002.
- (30) Keiderling, U. The New ‘BerSANS-PC’ Software for Reduction and Treatment of Small Angle Neutron Scattering Data. *Appl Phys A* **2002**, *74* (1), s1455–s1457. <https://doi.org/10.1007/s003390201561>.
- (31) Carvalho Barros, G. K. G.; Duarte, L. J. N.; Melo, R. P. F.; Lopes, F. W. B.; Barros Neto, E. L. Ionic Dye Removal Using Solvent-Assisted Ionic Micellar Flocculation. *J Polym Environ* **2022**, *30*, 2534–2546. <https://doi.org/10.1007/s10924-021-02360-7>.

- (32) Owoyomi, O.; Junaid, O. Z.; Olaoye, O. E. Spectroscopic Investigation of the Interaction between Crystal-Violet and Sodium Dodecanoylsarcosinate. *Physics and Chemistry of Liquids* **2021**, *60* (1), 129–140. <https://doi.org/10.1080/00319104.2021.1916929>.
- (33) Müller, Wenke; Schweins, Ralf; Nöcker, Bernd; Egold, Hans; Huber, Klaus. Comparative Study of the Self-Assembly Behaviour of 3-Chloro-4-Hydroxy-Phenylazo Dyes. *Soft Matter* **2023**, *19* (24), 4579–4587. <https://doi.org/10.1039/D3SM00500C>.
- (34) Sabaté, R.; Gallardo, M.; de la Maza, A.; Estelrich, J. A Spectroscopy Study of the Interaction of Pinacyanol with N-Dodecyltrimethylammonium Bromide Micelles. *Langmuir* **2001**, *17* (21), 6433–6437. <https://doi.org/10.1021/la010463y>.
- (35) Shah, S. S.; Shah, S. W. H.; Naeem, K. Surfactant–Dye Aggregates. In *Encyclopedia of Surface and Colloid Science, Third Edition*; Taylor & Francis, 2015; pp 7141–7149. <https://doi.org/10.1081/E-ESCS3-120000001>.
- (36) Shah, P.; Kumari Jha, S.; Bhattarai, A. Spectrophotometric Study of the Sodium Dodecyl Sulfate in the Presence of Methylene Blue in the Methanol–Water Mixed Solvent System. *Journal of Molecular Liquids* **2021**, *340*, 117200. <https://doi.org/10.1016/j.molliq.2021.117200>.
- (37) Dutta, R. K.; Bhat, S. N. Association of Neutral Red with Micelles and Its Effect on the PKa. *Can. J. Chem.* **1993**, *71* (11), 1785–1791. <https://doi.org/10.1139/v93-221>.
- (38) Rehman, A.; Nisa, M. U.; Usman, M.; Ahmad, Z.; Bokhari, T. H.; Rahman, H. M. A. U.; Rasheed, A.; Kiran, L. Application of Cationic-Nonionic Surfactant Based Nanostructured Dye Carriers: Mixed Micellar Solubilization. *Journal of Molecular Liquids* **2021**, 115345. <https://doi.org/10.1016/j.molliq.2021.115345>.
- (39) Ghosh, D. C.; Sen, P. K.; Pal, B. Evidence of Formation of Dye–Surfactant Ion Pair Micelle in the Anionic Surfactant Mediated Alkaline Fading of Methyl Violet Carbocation. *International Journal of Chemical Kinetics* **2021**, *53* (11), 1228–1238. <https://doi.org/10.1002/kin.21528>.
- (40) Rose, N. J.; Drago, R. S. Molecular Addition Compounds of Iodine. I. An Absolute Method for the Spectroscopic Determination of Equilibrium Constants. *J. Am. Chem. Soc.* **1959**, *81* (23), 6138–6141. <https://doi.org/10.1021/ja01532a009>.
- (41) Seal, B. K.; Mukherjee, A. K.; Mukherjee, D. C. An Alternative Method of Solving the Rose-Drage Equation for the Determination of Equilibrium Constants of Molecular Complexes. *BCSJ* **1979**, *52* (7), 2088–2090. <https://doi.org/10.1246/bcsj.52.2088>.

- (42) Benesi, H. A.; Hildebrand, J. H. A Spectrophotometric Investigation of the Interaction of Iodine with Aromatic Hydrocarbons. *J. Am. Chem. Soc.* **1949**, *71* (8), 2703–2707. <https://doi.org/10.1021/ja01176a030>.
- (43) Perussi, J. R.; Yushmanov, V. E.; Monte, S. C.; Imasato, H.; Tabak, M. Interaction of Primaquine and Chloroquine with Ionic Micelles as Studied by <sup>1</sup>H NMR and Electronic Absorption Spectroscopy. *Physiol Chem Phys Med NMR* **1995**, *27* (1), 1–15.
- (44) Karukstis, K. K.; Savin, D. A.; Loftus, C. T.; D'Angelo, N. D. Spectroscopic Studies of the Interaction of Methyl Orange with Cationic Alkyltrimethylammonium Bromide Surfactants. *Journal of Colloid and Interface Science* **1998**, *203* (1), 157–163. <https://doi.org/10.1006/jcis.1998.5494>.
- (45) Bielska, M.; Sobczyńska, A.; Prochaska, K. Dye–Surfactant Interaction in Aqueous Solutions. *Dyes and Pigments* **2009**, *80* (2), 201–205. <https://doi.org/10.1016/j.dyepig.2008.05.009>.
- (46) Feigin, L. A.; Svergun, D. I. *Structure Analysis by Small-Angle X-Ray and Neutron Scattering*; Springer US, 1987. <https://doi.org/10.1007/978-1-4757-6624-0>.
- (47) Hayter, J. B.; Penfold, J. An Analytic Structure Factor for Macroion Solutions. *Molecular Physics* **1981**, *42* (1), 109–118. <https://doi.org/10.1080/00268978100100091>.
- (48) Bergstrom, M.; Pedersen, J. Structure of Pure SDS and DTAB Micelles in Brine Determined by Small-Angle Neutron Scattering (SANS). *PHYS CHEM CHEM PHYS* **1999**, *1*, 4437–4446. <https://doi.org/10.1039/a903469b>.
- (49) Hassan, P. A.; Fritz, G.; Kaler, E. W. Small Angle Neutron Scattering Study of Sodium Dodecyl Sulfate Micellar Growth Driven by Addition of a Hydrotropic Salt. *Journal of Colloid and Interface Science* **2003**, *257* (1), 154–162. [https://doi.org/10.1016/S0021-9797\(02\)00020-6](https://doi.org/10.1016/S0021-9797(02)00020-6).
- (50) Finnigan, J. A.; Jacobs, D. J. Light Scattering by Ellipsoidal Particles in Solution. *J. Phys. D: Appl. Phys.* **1971**, *4* (1), 72. <https://doi.org/10.1088/0022-3727/4/1/310>.
- (51) A. Dreiss, C. Wormlike Micelles: Where Do We Stand? Recent Developments, Linear Rheology and Scattering Techniques. *Soft Matter* **2007**, *3* (8), 956–970. <https://doi.org/10.1039/B705775J>.
- (52) Quirion, F.; Magid, L. J. Growth and Counterion Binding of Cetyltrimethylammonium Bromide Aggregates at 25 °C: A Neutron and Light Scattering Study. *J. Phys. Chem.* **1986**, *90* (21), 5435–5441. <https://doi.org/10.1021/j100412a108>.
- (53) Onoda-Yamamuro, N.; Yamamuro, O.; Tanaka, N.; Nomura, H. NMR and Neutron Scattering Studies on Spherical and Rod-like Micelles of Dodecyltrimethylammonium



- Bromide in Aqueous Sodium Salicylate Solutions. *Journal of Molecular Liquids* **2005**, *117* (1), 139–145. <https://doi.org/10.1016/j.molliq.2004.08.009>.
- (54) Dreiss, C. A. Chapter 1 Wormlike Micelles: An Introduction. In *Wormlike Micelles: Advances in Systems, Characterisation and Applications*; Soft Matter Series; Royal Society of Chemistry, 2017; pp 1–8.
- (55) Creatto, E. J.; Okasaki, F. B.; Cardoso, M. B.; Sabadini, E. Wormlike Micelles of CTAB with Phenols and with the Corresponding Phenolate Derivatives - When Hydrophobicity and Charge Drive the Coacervation. *Journal of Colloid and Interface Science* **2022**, *627*, 355–366. <https://doi.org/10.1016/j.jcis.2022.07.044>.
- (56) Wang, D.; Long, P.; Dong, R.; Hao, J. Self-Assembly in the Mixtures of Surfactant and Dye Molecule Controlled via Temperature and  $\beta$ -Cyclodextrin Recognition. *Langmuir* **2012**, *28* (40), 14155–14163. <https://doi.org/10.1021/la3030028>.
- (57) Li, L.; Yang, Y.; Dong, J.; Li, X. Azobenzene Dye Induced Micelle to Vesicle Transition in Cationic Surfactant Aqueous Solutions. *Journal of Colloid and Interface Science* **2010**, *343* (2), 504–509. <https://doi.org/10.1016/j.jcis.2009.11.056>.
- (58) Kutz, A.; Mariani, G.; Gröhn, F. Ionic Dye–Surfactant Nanoassemblies: Interplay of Electrostatics, Hydrophobic Effect, and  $\pi$ – $\pi$  Stacking. *Colloid Polym Sci* **2016**, *294* (3), 591–606. <https://doi.org/10.1007/s00396-015-3814-2>.
- (59) Patist, A.; Oh, S. G.; Leung, R.; Shah, D. O. Kinetics of Micellization: Its Significance to Technological Processes. *Colloids and Surfaces A: Physicochemical and Engineering Aspects* **2001**, *176* (1), 3–16. [https://doi.org/10.1016/S0927-7757\(00\)00610-5](https://doi.org/10.1016/S0927-7757(00)00610-5).
- (60) Bergström, M.; Pedersen, J. S. Formation of Tablet-Shaped and Ribbonlike Micelles in Mixtures of an Anionic and a Cationic Surfactant. *Langmuir* **1999**, *15* (7), 2250–2253. <https://doi.org/10.1021/la981495x>.
- (61) Smales, G. J.; Pauw, B. R. The MOUSE Project: A Meticulous Approach for Obtaining Traceable, Wide-Range X-Ray Scattering Information. *J. Inst.* **2021**, *16* (06), P06034. <https://doi.org/10.1088/1748-0221/16/06/P06034>.
- (62) Filik, J.; Ashton, A. W.; Chang, P. C. Y.; Chater, P. A.; Day, S. J.; Drakopoulos, M.; Gerring, M. W.; Hart, M. L.; Magdysyuk, O. V.; Michalik, S.; Smith, A.; Tang, C. C.; Terrill, N. J.; Wharmby, M. T.; Wilhelm, H. Processing Two-Dimensional X-Ray Diffraction and Small-Angle Scattering Data in DAWN 2. *J Appl Cryst* **2017**, *50* (3), 959–966. <https://doi.org/10.1107/S1600576717004708>.

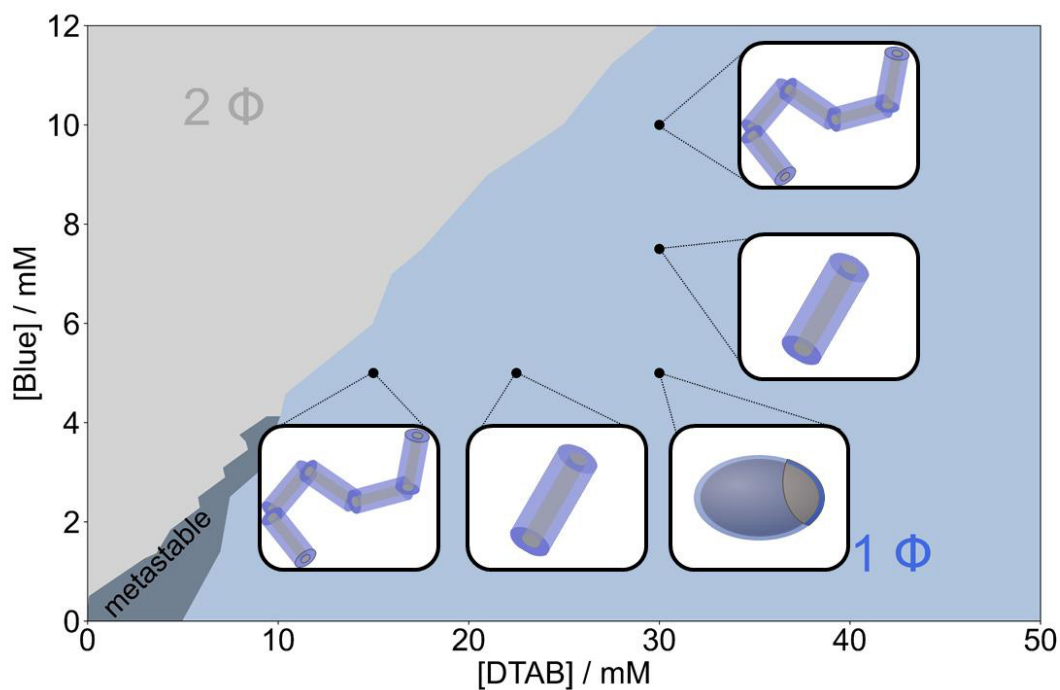
- (63) Pauw, B. R.; Smith, A. J.; Snow, T.; Terrill, N. J.; Thünemann, A. F. The Modular Small-Angle X-Ray Scattering Data Correction Sequence. *J Appl Cryst* **2017**, *50* (6), 1800–1811. <https://doi.org/10.1107/S1600576717015096>.
- (64) Garland, C. W.; Nibler, J. W.; Shoemaker, D. P. *Experiments in Physical Chemistry*, 8th ed.; McGraw-Hill Higher Education: Boston, 2009.
- (65) Berr, S. S. Solvent Isotope Effects on Alkytrimethylammonium Bromide Micelles as a Function of Alkyl Chain Length. *J. Phys. Chem.* **1987**, *91* (18), 4760–4765. <https://doi.org/10.1021/j100302a024>.
- (66) Hayter, J. B.; Penfold, J. Determination of Micelle Structure and Charge by Neutron Small-Angle Scattering. *Colloid & Polymer Sci* **1983**, *261* (12), 1022–1030. <https://doi.org/10.1007/BF01421709>.
- (67) Marcus, Y. *Ion Properties*; Marcel Dekker: New York, 1997.
- (68) Vidulich, G. A.; Evans, D. F.; Kay, R. L. The Dielectric Constant of Water and Heavy Water between 0 and 40 Degree. *J. Phys. Chem.* **1967**, *71* (3), 656–662. <https://doi.org/10.1021/j100862a028>.

## Chapter 6

# SANS contrast matching for the unambiguous localization of anionic dye in cationic surfactant micelles

### Abstract

Contrast variation in small-angle neutron scattering (SANS) was successfully applied to localize the anionic azo dye Blue in co-assemblies with the cationic surfactant dodecyltrimethylammoniumbromide (DTAB). For this purpose, the scattering contrast between DTAB and the aqueous solvent was eliminated by SANS contrast matching, leaving only the scattering signal from Blue to be detected. Results obtained by contrast matching were confirmed by NOESY NMR-spectroscopy, showing that Blue interacts with the positively charged DTAB head groups and with up to the 4<sup>th</sup> neighbouring methylene group of the DTAB C<sub>12</sub>-alkyl chain. Its localization in the outer layer of the Blue-DTAB co-assembly explains the uniaxial growth of spheroidal DTAB micelles to wormlike micelles with increasing [Blue]:[DTAB] ratio from 0:1 to 1:3. This is in line with the concept of the packing parameter for amphiphilic substances.



This chapter corresponds to: Müller, Wenke; Schweins, Ralf; Nöcker, Bernd; Egold, Hans; Hannappel, Yvonne; Huber, Klaus. SANS contrast matching for the unambiguous localization of anionic dye in cationic surfactant micelles. Accepted with revisions by the journal *Nanoscale Advances* (Royal Society of Chemistry). Resubmitted version, 28.08.2023.

## 6.1 Introduction

Systems capable of interacting with and responding to their environment are interesting for the design of sensor applications or molecular switches.<sup>1</sup> For instance, systems of wormlike micelles (WLMs) were found to respond to various triggers, by forming cross-linked networks of these micelles. Such a response results in a viscosity increase of the solution as directly observable parameter.<sup>2-4</sup> Depending on the system, responsivity to composition, pH, ionic strength, temperature, redox reactions, light and even CO<sub>2</sub> may be achieved.<sup>2,5-11</sup> WLMs are frequently formed by small amphiphilic surfactant molecules upon concentration increase or addition of inorganic salt, another surfactant or hydrotropic solutes.<sup>4,9,10,12-14</sup> This provides a versatile, simple and huge toolbox for stimuli-responsive systems.<sup>2</sup> Given the variety of possible components of WLM-forming systems, it is important to fundamentally understand intermolecular interactions leading to observable responses. Responsivity to pH, redox conditions or irradiation is frequently achieved by the interaction of surfactant micelles with a compound sensitive to corresponding changes.<sup>2,7,15,16</sup> In order to understand the mechanism of responsivity to permit systematic improvement or rational design of similar systems, the localization of such a compound within the surfactant micelle needs to be known.

It is possible to obtain information on the localization of a compound in a surfactant micelle using nuclear magnetic resonance (NMR)-spectroscopy. Use of the 2-dimensional Nuclear Overhauser Effect spectroscopy (NOESY) is particularly helpful in this regard, as it provides information on spatial proximity.<sup>17,18</sup> In some cases, however, an unambiguous localization of a solute in a co-assembly is not possible with NOESY due to overlap of resonances or ambiguity in peak assignment.<sup>5,19</sup> Furthermore, NOESY does not provide information on the morphology of the co-assemblies.

Small-angle neutron scattering (SANS) permits the elucidation of assembly morphology while also providing the possibility to locate an added compound within that assembly using contrast variation. This technique can either be used in combination with NOESY to confirm and extend findings, but may also be applied as stand-alone-method.

SANS contrast variation was previously employed to explain morphological transitions of mixed surfactant micelles upon variation of the ratio between both surfactants by identifying their mutual arrangement in the mixed micellar assembly.<sup>20,21</sup> It was furthermore successfully used to locate the protein hydrophobin in the outer shell of its co-assemblies with either ionic or non-ionic surfactant and to identify its folding state.<sup>22</sup> Penfold et al. located small organic fragrance

molecules in micelles formed by the non-ionic surfactant dodecaethylene glycol monododecyl ether (C<sub>12</sub>E<sub>12</sub>) by recording SANS curves under different contrast conditions.<sup>23</sup> However, Penfold et al. did not perform contrast matching, resulting in ambiguity concerning the solubilisation locus of phenyl ethanol.

Herein, the value and feasibility of SANS contrast matching for the localization of an organic azo dye in micelles of a low molecular weight surfactant is demonstrated. The SANS experiments are complemented by NMR experiments and the results jointly discussed.

WLM formation of the cationic surfactant dodecyltrimethylammoniumbromide (DTAB) and the anionic azo dye Blue (Figure 1) was studied as a model system. The interaction between oppositely charged azo dyes and surfactants has received attention as their manifold intermolecular interactions render them as promising building blocks in colloidal chemistry.<sup>14,24,25</sup> Apart from hydrophobic and electrostatic interactions,  $\pi$ - $\pi$  stacking of the dye was suggested to have a template-effect on assembly morphology.<sup>26</sup> The co-assembly of Blue and DTAB was studied in an aqueous NaHCO<sub>3</sub>/Na<sub>2</sub>CO<sub>3</sub> buffer with pH = 10.5 and ionic strength  $I \approx 0.25$  M.

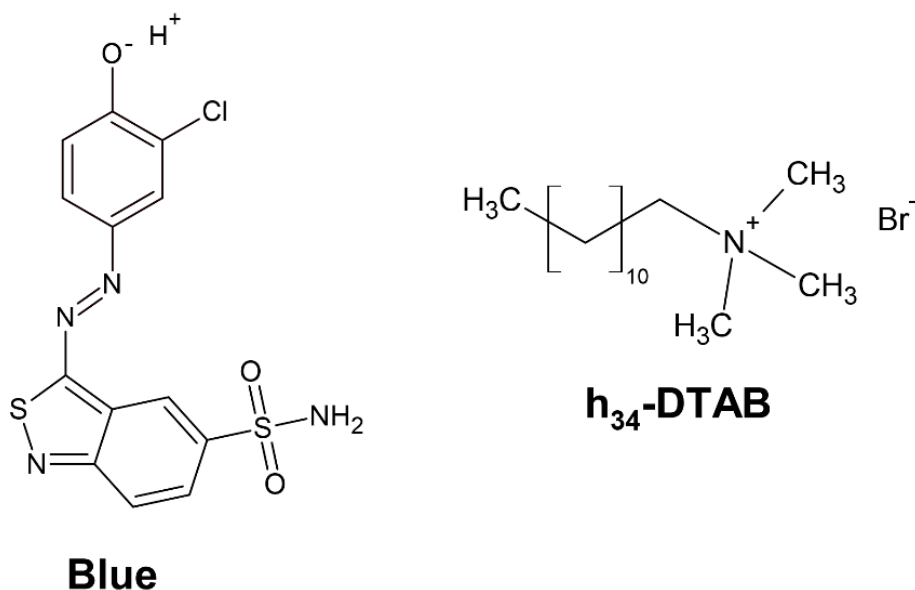


Figure 1: Chemical structure of 3-(3-chloro-4-hydroxy-phenylazo)benzo[c]isothiazole-5-sulfonamide (Blue) and of completely hydrogenated dodecyltrimethylammoniumbromide (h<sub>34</sub>-DTAB). In the aqueous, alkaline NaHCO<sub>3</sub>/Na<sub>2</sub>CO<sub>3</sub> buffer system (pH = 10.5 or pD = 10.7,  $I \approx 0.25$  M) used as a solvent in this work, the phenolic hydroxyl group of Blue is deprotonated.

## 6.2 Experimental

**Chemicals and sample preparation.** Blue (HC Blue 18,  $\geq 99.8$  %) was provided by KAO GmbH, Germany. Hydrogenated dodecyltrimethylammoniumbromide (h<sub>34</sub>-DTAB, 99 %) was obtained

from abcr GmbH, Germany. Completely deuterated dodecyltrimethylammoniumbromide ( $d_{34}$ -DTAB, 99 % isotopic purity) was obtained from INNOVACHEM SAS, France. Tail-deuterated dodecyltrimethylammoniumbromide ( $d_{25}$ -DTAB, 99.1 % isotopic purity) was obtained from C/D/N Isotopes Inc., Canada. The buffer salts sodium carbonate  $\text{Na}_2\text{CO}_3$  ( $\geq 99.8$  %) and sodium bicarbonate  $\text{NaHCO}_3$  ( $\geq 99.7$  %) were obtained from Sigma Aldrich Chemie GmbH, Germany. MilliQ water was used to prepare the  $\text{NaHCO}_3/\text{Na}_2\text{CO}_3$  buffer solutions ( $\text{pH} = 10.5$ , ionic strength  $I \approx 0.25$  M) for samples for viscosity measurements, Cryo-TEM measurements and determination of the phase diagram by visual inspection.  $\text{D}_2\text{O}$  was used to prepare the  $\text{NaHCO}_3/\text{Na}_2\text{CO}_3$  buffer solutions ( $\text{pD} = 10.7$ , ionic strength  $I \approx 0.25$  M) for SANS and NMR samples. A mixture of 50 vol%  $\text{H}_2\text{O}$  and 50 vol%  $\text{D}_2\text{O}$  was used to prepare the  $\text{NaHCO}_3/\text{Na}_2\text{CO}_3$  buffer solutions ( $\text{pH} = 10.5$ , ionic strength  $I \approx 0.25$  M) for the SANS sample containing Blue at a concentration of  $[\text{Blue}] = 5$  mM and  $h_{34}$ -DTAB at a concentration of  $[h_{34}\text{-DTAB}] = 30$  mM. In all cases, the buffer contained  $\text{NaHCO}_3$  at a concentration of 0.021 M and  $\text{Na}_2\text{CO}_3$  at a concentration of 0.079 M, which resulted in the given ionic strength ( $I \approx 0.25$  M) and  $\text{pH} = 10.5$  ( $\text{pD} = 10.7$ ).  $\text{D}_2\text{O}$  (99.90 % D) was obtained from Eurisotop, France or Sigma Aldrich Chemie GmbH, Germany. Chemicals were used without further purification. Samples were prepared from stock solutions, followed by a minimum equilibration time of 20 h at room temperature prior to analysis.

**Phase diagram.** The phase diagram was established by stepwise addition of a 15 mM stock solution of Blue to solutions containing  $h_{34}$ -DTAB at different concentrations, depending on the concentration range to be probed.  $\text{NaHCO}_3/\text{Na}_2\text{CO}_3$  buffer solution ( $\text{pH} = 10.5$ , ionic strength  $I \approx 0.25$  M) was prepared with MilliQ water and used as a solvent in all cases. After each addition of dye stock solution, the sample was vortexed for approximately 30 s and its visual appearance recorded immediately. Some samples were kept and visually inspected after 24 h to investigate long-term stability. Phase diagrams were established at room temperature ( $\approx 22$  °C).

**Cryo-TEM.** The cryo-transmission electron microscopy (Cryo-TEM) measurements were performed on a JEOL JEM-2200FS electron microscope (JEOL, Freising, Germany) operating at 200 kV acceleration voltage and equipped with an “OneView” CMOS camera (Gatan, Pleasanton, CA, USA). 3  $\mu\text{L}$  of a sample containing Blue at a concentration of 10 mM and DTAB at a concentration of 30 mM in an aqueous  $\text{NaHCO}_3/\text{Na}_2\text{CO}_3$  buffer ( $\text{pH} = 10.5$ , ionic strength  $I \approx 0.25$  M) were deposited on the surface of a lacey carbon film coated grid (200 Mesh, Cu, Science Services GmbH, Munich, Germany) and vitrified by a Leica blotting and plunging device operating at room temperature (Leica EM GP, Leica Mikrosysteme Vertrieb GmbH, Wetzlar, Germany). The samples were plunged into liquid ethane, which was cooled with liquid nitrogen to

achieve sufficiently fast cooling and freezing without formation of ice crystals. Afterwards the sample was transferred into a cryo transfer and tomography holder (Fischione, Model 2550, E.A. Fischione Instruments, Pittsburgh, PA, USA). The images captured were afterwards processed with a digital imaging processing program (Digital Micrograph®, Version 3.21, GMS 3, Gatan, Pleasanton, CA, USA).

**Viscosity.** The kinematic viscosities  $\nu$  of solutions containing Blue and h<sub>34</sub>-DTAB in an aqueous NaHCO<sub>3</sub>/Na<sub>2</sub>CO<sub>3</sub> buffer (pH = 10.5, ionic strength  $I \approx 0.25$  M) were determined using an Ubbelohde viscometer (Type 52710/l Schott, viscometer constant  $K = 0.00933$  mm<sup>2</sup> s<sup>-2</sup>). Viscosity measurements were performed at 25 °C. The kinematic viscosity was obtained by multiplying the viscometer constant  $K$  by the time  $t$  the solution needed to drop from the first to the second mark of the Ubbelohde viscometer:  $\nu = K \cdot t$ .

**Small-angle neutron scattering.** After their preparation from stock solutions, SANS samples were filtered (MACHEREY-NAGEL, CHROMAFIL Xtra H-PTFE syringe filters, pore size 0.2 μm) into dust-free sample vials and equilibrated for a minimum of 20 h at room temperature.

In a first step, contrast matching of a d<sub>25</sub>-DTAB/d<sub>34</sub>-DTAB mixture to the NaHCO<sub>3</sub>/Na<sub>2</sub>CO<sub>3</sub> buffer prepared in 100 % D<sub>2</sub>O was performed. For this purpose, four solutions containing a total DTAB concentration of 30 mM but varying proportions of d<sub>25</sub>-DTAB and d<sub>34</sub>-DTAB were prepared and their SANS-curves recorded. Square roots of resulting forward scattering intensities  $\sqrt{I_{q,0}}$  were plotted against the volume fraction of d<sub>25</sub>-DTAB contained in the sample and the match composition of d<sub>25</sub>-DTAB:d<sub>34</sub>-DTAB determined to 46:54 (v/v) by linear extrapolation towards  $\sqrt{I_{q,0}} = 0$ . This match composition was experimentally confirmed by recording the SANS curve of a corresponding solution, which is shown in the SI (Figure SI2). “DTAB-matched” samples with eliminated scattering contrast between DTAB and the solvent were therefore always prepared with a 46:54 (v/v) mixture of d<sub>25</sub>-DTAB:d<sub>34</sub>-DTAB in a NaHCO<sub>3</sub>/Na<sub>2</sub>CO<sub>3</sub> buffer in 100 % D<sub>2</sub>O.

In a second step, “full contrast” SANS curves were recorded, where Blue and DTAB show non-zero contrast relative to the solvent. In the first set of experiments, full contrast SANS curves were obtained by dissolving the above-mentioned 46:54 mixture of d<sub>25</sub>-DTAB and d<sub>34</sub>-DTAB in a NaHCO<sub>3</sub>/Na<sub>2</sub>CO<sub>3</sub> buffer with a mixture of 50 vol% H<sub>2</sub>O and 50 vol% D<sub>2</sub>O instead of 100 vol% D<sub>2</sub>O. This only concerns the sample containing Blue at a concentration of [Blue] = 5 mM and DTAB at a concentration of [DTAB] = 30 mM. In all other cases, full contrast was achieved by dissolving 100% h<sub>34</sub>-DTAB in a NaHCO<sub>3</sub>/Na<sub>2</sub>CO<sub>3</sub> buffer with 100 vol% D<sub>2</sub>O. To permit comparison between



full contrast SANS curves of the sample with [Blue] = 5 mM and [DTAB] = 30 mM to all other full contrast SANS curves, this SANS curve and corresponding fits were multiplied with a scaling factor  $f$  for display. The scaling factor is intended to account for scattering length density ( $SLD$ ) differences and was estimated according to theoretical  $SLD$  differences to:

$$f = (SLD_{h_{34}\text{-DTAB}} - SLD_{100\% \text{ D}_2\text{O solvent}})^2 / (SLD_{\text{matched DTAB}} - SLD_{50\% \text{ D}_2\text{O solvent}})^2 \quad (1)$$

$$= [(-0.224 - 6.376) \cdot 10^{-6} \text{Å}^{-2}]^2 / [(6.376 - 2.918) \cdot 10^{-6} \text{Å}^{-2}]^2 \approx 3.6$$

In eq (1)  $SLD_{h_{34}\text{-DTAB}}$  is the theoretical  $SLD$  of  $h_{34}$ -DTAB and  $SLD_{\text{matched DTAB}}$  the  $SLD$  of the mixture of  $d_{25}$ -DTAB and  $d_{34}$ -DTAB (46:54).  $SLD_{100\% \text{ D}_2\text{O solvent}}$  is the  $SLD$  of the solvent containing 100 vol%  $D_2O$ .  $SLD_{50\% \text{ D}_2\text{O solvent}}$  is the  $SLD$  of the solvent consisting of 50 vol%  $H_2O$  and 50 vol%  $D_2O$ . This scaling was solely done for plotting the full contrast SANS curve of the sample with [Blue] = 5 mM and [DTAB] = 30 mM for comparison to full contrast SANS curves of other samples obtained under different  $SLD$  conditions. Fitting was performed with the unscaled data.

In a third step, SANS curves of “DTAB-matched” samples were recorded, where the scattering contrast of DTAB relative to the solvent is zero but Blue shows a scattering contrast with the respective solvent. For this purpose, the above-described mixture of 46:54 (v/v) mixture of  $d_{25}$ -DTAB: $d_{34}$ -DTAB in a  $NaHCO_3/Na_2CO_3$  buffer in 100 %  $D_2O$  was used.

SANS was performed at the small-angle neutron scattering instrument D11 at the Institut Laue-Langevin (Grenoble, France). Different setups were used: (1) Identification of the match point and the measurement of the full contrast and the DTAB-matched sample containing [Blue] = 5 mM and [DTAB] = 30 mM were carried out at three sample-to-detector distances (28 m, collimation 28 m), (8 m, collimation 8 m), (1.7 m, collimation 4.0 m) at a neutron wavelength of 6 Å to cover a  $q$ -range of 0.002 Å<sup>-1</sup> to 0.5 Å<sup>-1</sup>. A circular neutron beam with a diameter of 15 mm was used. (2) Full contrast and DTAB-matched samples containing [Blue]:[DTAB] at a ratio of 1:3 were measured at three sample-to-detector distances (38.0 m, collimation 40.5 m), (10.5 m, collimation 10.5 m), (1.7 m, collimation 2.5 m) at a neutron wavelength of 6 Å to cover a  $q$ -range of 0.0014 Å<sup>-1</sup> to 0.5 Å<sup>-1</sup>. A circular neutron beam with a diameter of 14 mm was used. (3) Full contrast and DTAB-matched samples containing [Blue]:[DTAB] at a ratio of 1:4 or 1:4.5 were measured at three sample-to-detector distances (38.0 m, collimation 40.5 m), (10.5 m, collimation 10.5 m), (2.5 m, collimation 2.5 m) at a neutron wavelength of 6 Å to cover a  $q$ -range of 0.0014 Å<sup>-1</sup> to 0.5 Å<sup>-1</sup>. A circular neutron beam with a diameter of 14 mm was used. Neutrons were detected with a <sup>3</sup>He-detector (Reuter-Stokes multi-tube detector consisting of 256 tubes with a tube diameter of 8 mm

and a pixel size of 8 mm x 4 mm), detector images azimuthally averaged, corrected to the transmission of the direct beam and scaled to absolute intensity using the Mantid software.<sup>27,28</sup> Empty cell and solvent scattering were subtracted from the scattering curves.<sup>29</sup> SANS data were collected at a sample temperature of 25 °C.

**NMR-spectroscopy.** Samples for NMR-spectroscopy were prepared from stock solutions. A NaHCO<sub>3</sub>/Na<sub>2</sub>CO<sub>3</sub> buffer (pD = 10.7, ionic strength  $I \approx 0.25$  M) prepared in D<sub>2</sub>O was used as a solvent in all cases. Sample solutions were filtered (MACHEREY-NAGEL, CHROMAFIL Xtra H-PTFE syringe filters, pore size 0.2 μm) into the NMR-tube. <sup>1</sup>H-NMR and Nuclear Overhauser Effect spectroscopy (NOESY) spectra were recorded with a NMR Ascent 700 spectrometer (700 MHz) equipped with a cryogenic probe with z-gradient at 298 K. <sup>1</sup>H-NMR chemical shifts were referenced to residual HDO.<sup>30</sup>

### 6.3 Data analysis

The absolute scattering intensity  $I_q$  arising from particles with a volume  $V_{\text{part}}$  and a volume fraction of  $\phi = N \cdot V_{\text{part}} / V_{\text{tot}}$  with  $N$  being the number of particles and  $V_{\text{tot}}$  the total sample volume is generally described by the following equation:<sup>29</sup>

$$I_q = K \cdot \phi \cdot V_{\text{part}} \cdot P(q) \cdot S(q) + B_{\text{incoh}} \quad (2)$$

$K$  is the contrast factor and  $P(q)$  is the particle form factor, which describes  $q$ -dependent modulations in scattered intensity caused by interferences between neutron waves scattered from the same particle. It is therefore determined by particle geometry. For small  $q$  it approaches  $P(q \rightarrow 0) = 1$ .<sup>29</sup>  $S(q)$  denotes the structure factor which arises due to spatial ordering of different particles. In case of negligible inter-particle interactions and ordering, e.g. in sufficiently dilute solutions,  $S(q)$  tends to one.<sup>29</sup>  $B_{\text{incoh}}$  is a background signal arising due to incoherent scattering and is therefore termed “incoherent background”. Scattering contrast is caused by differences in  $SLD$  between the particle and the solvent. In case of a simple system, where the particles possess a constant  $SLD_1$  which is homogeneously distributed throughout the whole particle, and the solvent possesses a homogeneous  $SLD_{\text{solv}}$ ,  $K$  depends on their difference according to:<sup>29</sup>

$$K = (SLD_1 - SLD_{\text{solv}})^2 \quad (3)$$

For SANS data presented in this work, the particle form factor used to describe an experimental SANS curve was chosen based on: (1) preliminary information on the system, (2) characteristic features of the SANS-curves, (3) fit quality and (4) morphological transitions expected from

existing models and similar systems. The SasView small-angle scattering analysis software with implemented form- and structure factor models was used for analysis of experimental SANS curves in most cases.<sup>31</sup> For generating and fitting the form factor model of a triaxial ellipsoidal shell, the SASfit software package was used.<sup>32</sup> For form factor fits, the volume fraction of scattering particles was derived from the known molar concentration of scatterers and their partial molar volumes. For this purpose, it was assumed that all Blue- and DTAB-molecules, which are present in solution, participate in micelle formation. Partial molar volumes are displayed in the Supporting Information (SI, Table SI1).  $SLD_1$ ,  $B_{\text{incoh}}$  and size parameters were fitted. For form factor fitting of core-shell structures two fit strategies were used: In a first approach, the  $SLD$  of the shell was kept constant. In a second approach it was fitted. Details regarding this procedure can be found in the discussion. The consideration of a structure factor was only necessary for fitting SANS curves from pure DTAB micelles in the absence of Blue. In all other cases no relevant inter-particle ordering was observed.

## 6.4 Results and discussion

### 6.4.1 Phase diagram and viscosity

Figure 2(a) shows the concentration-dependent phase diagram of solutions containing Blue and DTAB at room temperature. Phase separation of homogeneous solutions into a liquid and a solid phase occurs within 30 s after mixing once a certain Blue:DTAB ratio is exceeded.<sup>33</sup> The solid phase was observed to be a crystalline precipitate corresponding to highly ordered Blue-DTAB complexes, which are likely caused by lamellar assembly of both components.<sup>24,33</sup>

To understand phenomena leading to phase separation, the viscosity of samples in the 1-phase region was investigated. Figure 2(b) and Figure 2(c) show the development of the kinematic viscosity  $\nu$  of Blue-DTAB solutions at a constant concentration of Blue ( $[\text{Blue}]$ ) as a function of DTAB concentration ( $[\text{DTAB}]$ ) and at a constant concentration of DTAB as a function of  $[\text{Blue}]$  respectively. Both figures show that the kinematic viscosity of samples increases with increasing Blue:DTAB ratio, i.e. upon approaching the phase transition threshold. This increase is not linear but rises with proximity to the 2-phase region. Considering existing literature, similar trends were observed for the change in solution zero shear viscosity  $\eta_0$  upon addition of hydrotrope to surfactant solutions and are often related to morphological changes in the sample.<sup>9,14</sup> The observation of a viscosity increase when approaching the phase transition threshold points towards the formation of WLMs, their entanglement and network formation.<sup>3,9,34,35</sup>

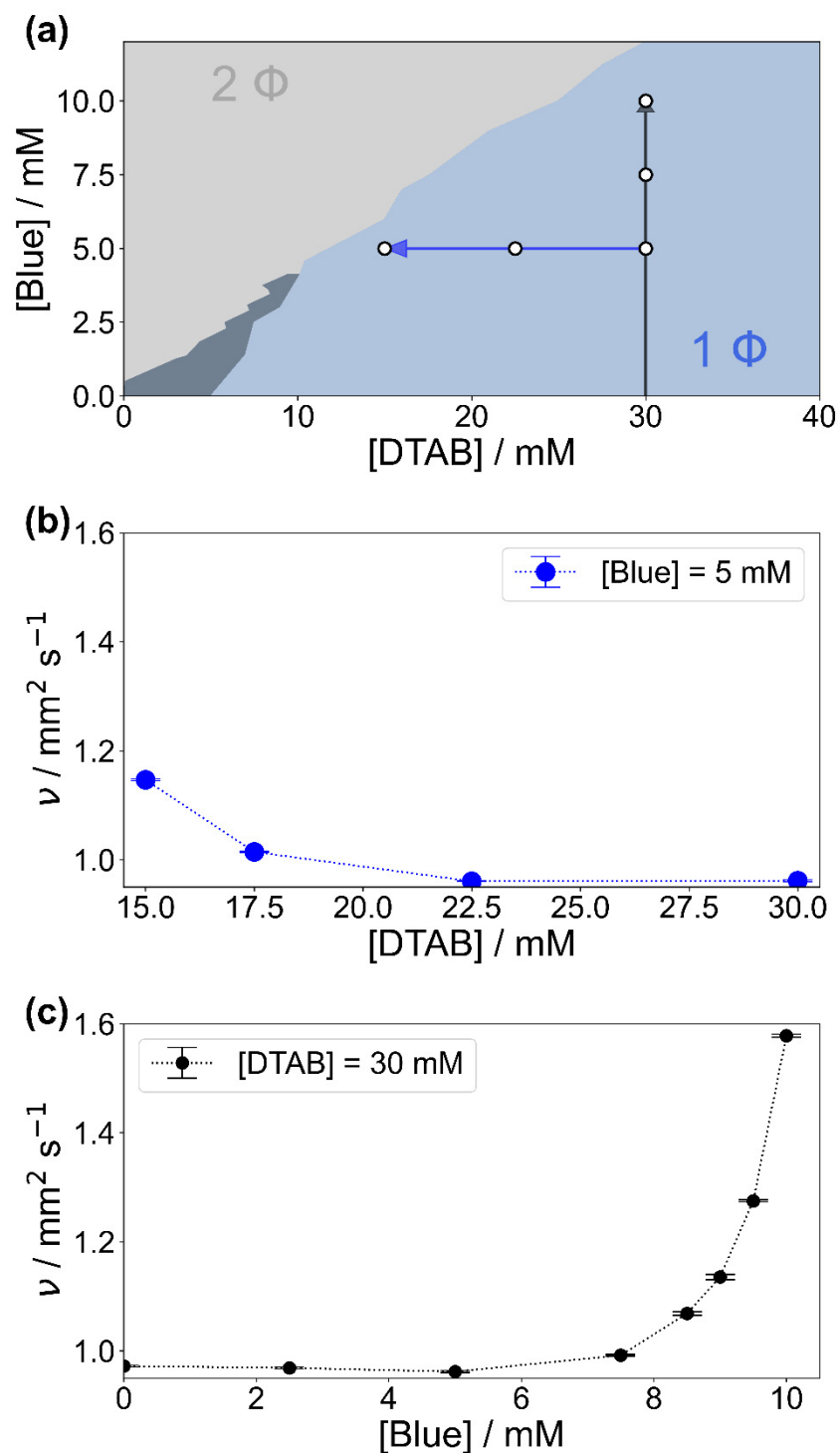


Figure 2: (a) Phase diagram of solutions containing Blue and DTAB in a  $\text{NaHCO}_3/\text{Na}_2\text{CO}_3$  buffer with  $\text{pH} = 10.5$  and ionic strength  $I \approx 0.25 \text{ M}$  at room temperature. The light blue  $1 \Phi$  region covers stable solutions. The dark slate grey area denotes a metastable region within which samples are stable for 30 s after mixing but precipitate within 1 h to 24 h. In the  $2 \Phi$  region phase separation occurs due to the formation of solid Blue-DTAB complexes. Arrows indicate an increase of the kinematic viscosity of samples at  $25 \text{ }^\circ\text{C}$  according to (b) and (c). White circles denote the composition of samples studied by SANS. (b) Kinematic viscosity of solutions containing [Blue] = 5 mM and varying concentrations of DTAB at  $25 \text{ }^\circ\text{C}$ . (c) Kinematic viscosity of solutions containing [DTAB] = 30 mM and varying concentrations of Blue at  $25 \text{ }^\circ\text{C}$ .

WLM formation from cationic surfactants is a frequently observed phenomenon and can be induced by various triggers.<sup>4</sup> These include the addition of salt or hydrotropes such as phenol and phenolate derivatives or the addition of negatively charged azo dyes.<sup>9,10,12,14</sup> For this reason, the presence of WLMs in solutions of the negatively charged azo dye Blue and the positively charged surfactant DTAB close to the phase transition threshold was strongly expected.

A confirmation of WLMs was obtained from cryo-transmission electron microscopy (cryo-TEM) images of a solution containing [Blue] = 10 mM and [DTAB] = 30 mM. Two images of the same solution at different locations are shown in Figure 3. Thin, entangled WLMs with lengths of several hundred nanometers are clearly visible.

The formation of WLMs is likely caused by successive growth upon addition of Blue to DTAB. To investigate this mechanism further and to obtain ensemble-average information on the morphology of Blue-DTAB assemblies in solution, SANS was performed on samples with compositions indicated by white dots in Figure 2(a).

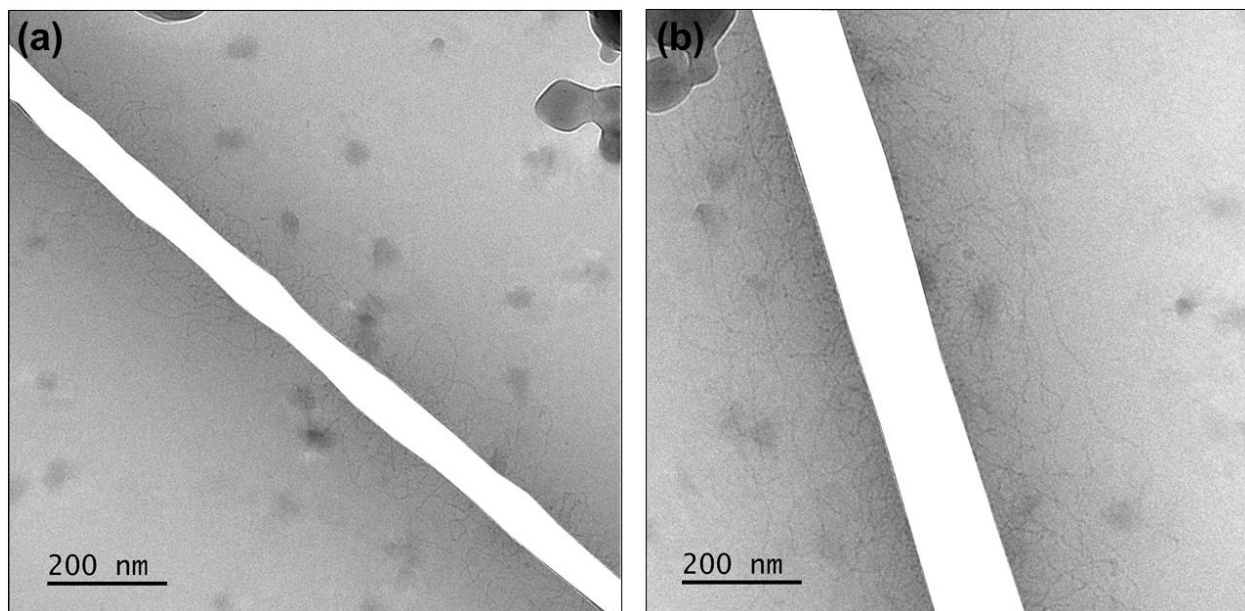


Figure 3: Cryo-TEM images of a solution containing [Blue] = 10 mM and [DTAB] = 30 mM in an aqueous  $\text{NaHCO}_3/\text{Na}_2\text{CO}_3$  buffer with  $\text{pH} = 10.5$  and  $I \approx 0.25$  M. Dark spots correspond to ice crystals. The mesh of the grid used as sample holder was masked. Original cryo-TEM images can be found in the SI (Figure S11).

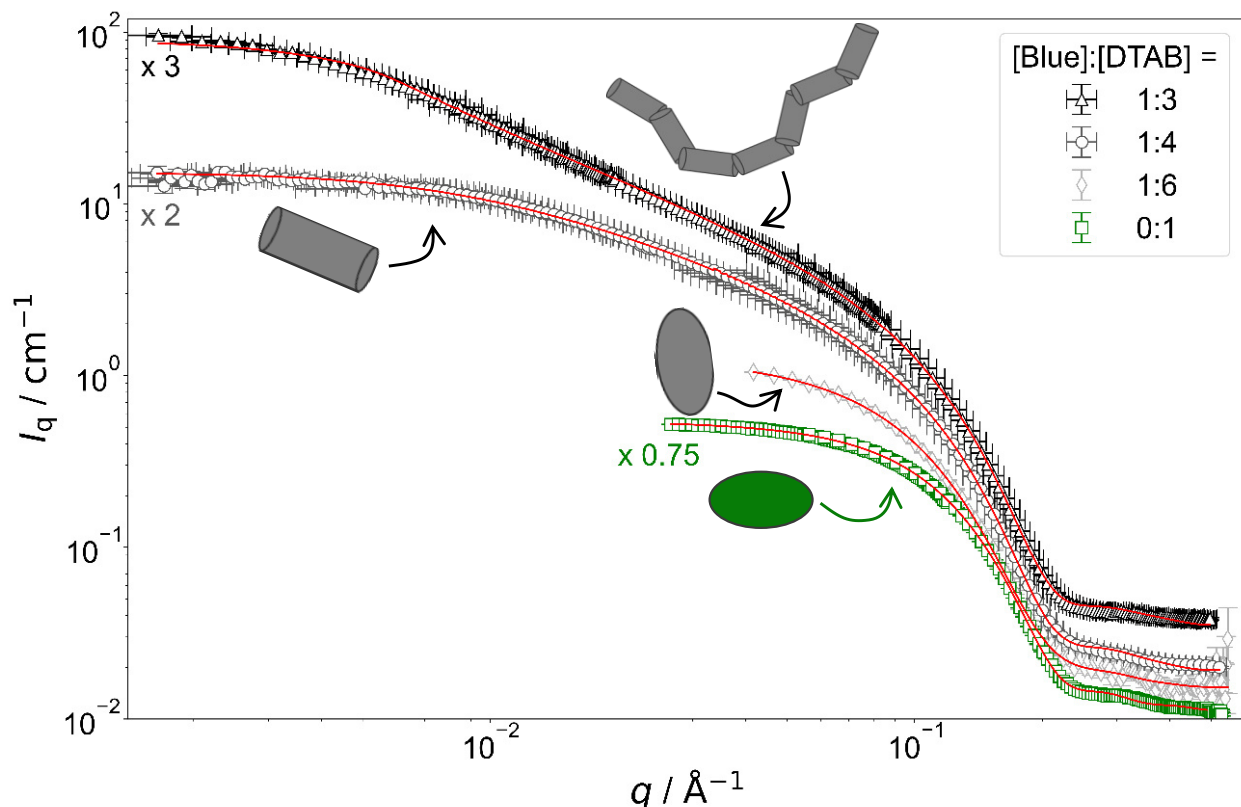


Figure 4: Full contrast SANS curves of solutions containing [DTAB] = 30 mM and varying concentrations of Blue in an aqueous  $\text{NaHCO}_3/\text{Na}_2\text{CO}_3$  buffer with  $\text{pD} = 10.7$  and ionic strength  $I \approx 0.25$ . Red lines display form factor fits according to the model of flexible cylinders with elliptical cross section<sup>36</sup> for [Blue]:[DTAB] = 1:3, cylinders with elliptical cross section<sup>37</sup> for [Blue]:[DTAB] = 1:4, triaxial ellipsoids<sup>38</sup> for [Blue]:[DTAB] = 1:6 and oblate spheroids<sup>37</sup> including a structure factor according to Hayter and Penfold in the rescaled mean spherical approximation<sup>39-41</sup> for [Blue] = 0 mM.

#### 6.4.2 Small-angle neutron scattering

Figure 4 shows full contrast SANS curves obtained from solutions containing [DTAB] = 30 mM and different concentrations of Blue. Similarly, Figure 5 shows full contrast SANS curves obtained from solutions containing a constant concentration of [Blue] = 5 mM and varying concentrations of DTAB. First assessments of SANS curves will consider the molar ratio between Blue and DTAB ([Blue]:[DTAB]). From both figures a shift of the Guinier plateau to lower values of the magnitude of the scattering vector  $q$  with increasing [Blue]:[DTAB] is evident. This indicates an increase in the radius of gyration of the scatterers and therefore an increase in assembly size.<sup>42</sup> Furthermore, the appearance of a power law of  $I_q \sim q^{-1}$  in the mid- $q$  region with increasing [Blue]:[DTAB] suggests a morphological transition from spherical to cylindrical structures.<sup>7,43,44</sup> The SANS curves of samples containing Blue and DTAB at a molar ratio of 1:3 furthermore show a crossover region between  $I_q \sim q^{-1}$  and a power law  $I_q \sim q^{-x}$  with an exponent  $x > 1$ . This likely results from the appearance of flexibility upon elongation of the cylindrical structures. A power law behaviour of  $I_q \sim q^{-2}$  is characteristic for the random walk configuration ( $\theta$  solvents) and  $I_q \sim q^{-5/3}$  is

characteristic for SANS curves from polymer chains in the self-avoiding random walk configuration (good solvents).<sup>36,44</sup> Once length scales probed by  $q$  approach the persistence length of those chains, a transition to  $I_q \sim q^{-1}$  is observed.<sup>36</sup> At higher  $q$ , a  $I_q \sim q^{-4}$  decay is observed for all [Blue]:[DTAB] ratios due to the finite cross section of all micelles.<sup>4,36</sup>

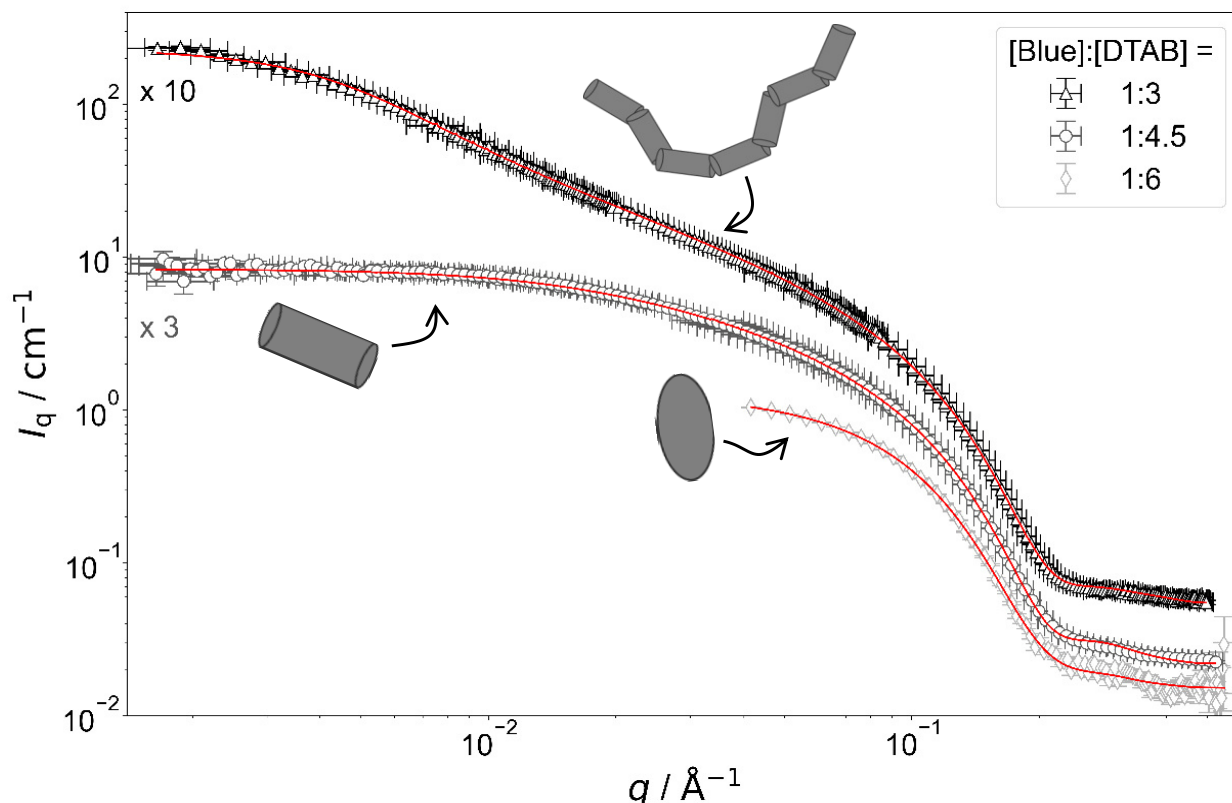


Figure 5: Full contrast SANS-curves of solutions containing [Blue] = 5 mM and varying concentrations of DTAB in an aqueous  $\text{NaHCO}_3/\text{Na}_2\text{CO}_3$  buffer with  $\text{pD} = 10.7$  and ionic strength  $I \approx 0.25$ . Red lines display form factor fits according to the model of flexible cylinders with elliptical cross section<sup>36</sup> for [Blue]:[DTAB] = 1:3, cylinders with elliptical cross section<sup>37</sup> for [Blue]:[DTAB] = 1:4.5 and triaxial ellipsoids<sup>38</sup> for [Blue]:[DTAB] = 1:6. The latter is also shown in Figure 4 and is displayed here for reference.

To quantitatively estimate the size of Blue-DTAB assemblies, SANS curves were fitted with appropriate form factor models suggested by the previous qualitative discussion. The scattering length density  $SLD_1$  of Blue-DTAB co-assemblies was fitted to account for  $SLD$  changes, which are introduced by a variation in the composition of such assemblies through variation of sample composition. The  $SLD$  of the solvent was kept constant and the volume fraction of scatterers was calculated as indicated in the section on data analysis. Fitted  $SLDs$  (Supporting information, Table SI6) are reasonable for the investigated system and will not be discussed further. Form factor models and resulting size parameters are displayed in Table 1 and will be discussed in the following.

Table 1: Size parameters obtained from fitting full contrast SANS curves of solutions containing Blue and DTAB at varying concentrations in an aqueous NaHCO<sub>3</sub>/Na<sub>2</sub>CO<sub>3</sub> buffer with pD = 10.7 and  $I \approx 0.25$  M at 25 °C. SANS curves and fits are visualized in Figure 4 and Figure 5. Except for the DTAB solution without Blue, no structure factor was used during fitting. For fitting the SANS curve from the 30 mM DTAB solution, a structure factor according to Hayter and Penfold in the rescaled mean spherical approximation was used.<sup>39–41</sup>

[Blue] mM	[DTAB] mM	Form factor model	Cross section radii		Length
			$r_{\text{minor}}$ Å	$r_{\text{major}}$ Å	$L$ Å
0	30	Spheroid <sup>37</sup> (oblate) <sup>I</sup>	14.048 ± 0.008	22.357 ± 0.009	
5	30	Ellipsoid <sup>38</sup> (triaxial) <sup>II</sup>	15.3 ± 0.2	22.0 ± 0.3	32.0 ± 0.3
7.5	30	Cylinder with elliptical cross section <sup>37,III</sup>	14.336 ± 0.009	21.19 ± 0.04	$\bar{L} = 148 \pm 1$ $\sigma/\bar{L} = 0.95$
10	30	Flexible cylinder with elliptical cross section <sup>36,IV</sup>	14.046 ± 0.008	21.15 ± 0.04	$L = 1000 \pm 6$ $l_p = 300 \pm 3$
5	22.5	Cylinder with elliptical cross section <sup>37,III</sup>	14.78 ± 0.02	21.21 ± 0.06	$\bar{L} = 73.4 \pm 2$ $\sigma/\bar{L} = 0.95$
5	15	Flexible cylinder with elliptical cross section <sup>36,IV</sup>	13.92 ± 0.02	21.19 ± 0.07	$L = 1705 \pm 12$ $l_p = 209 \pm 1$

<sup>I</sup>For an oblate spheroid  $r_{\text{minor}}$  corresponds to the polar radius and  $r_{\text{major}}$  to the equatorial radius. <sup>II</sup>For a triaxial ellipsoid  $r_{\text{minor}}$ ,  $r_{\text{major}}$  and  $L$  correspond to the radii of three semi-axes with  $r_{\text{minor}} < r_{\text{major}} < L$ . <sup>III</sup>A Schulz distribution in cylinder length was assumed.  $\bar{L}$  is the number-average cylinder length and  $\sigma$  its root-mean-square deviation. <sup>IV</sup>For a flexible cylinder,  $L$  denotes the contour length and  $l_p$  its persistence length.

**DTAB micelles:** The size and structure of pure DTAB micelles in various solvents was reported in previous literature. Bergström and Pedersen studied the structure of DTAB micelles in aqueous NaBr solutions at 40 °C using SANS.<sup>39</sup> Dependent on the ionic strength of the solvent, SANS curves were best described using either the form factor of an oblate spheroid or a triaxial ellipsoid form factor considering intermicellar interactions with a structure factor according to Hayter and Penfold in the rescaled mean spherical approximation.<sup>40,41</sup> The formation of oblate spheroidal micelles with a polar radius of 14 Å and an equatorial radius of 24 Å in a 0.2 M NaBr solution was suggested. As this solvent ionic strength of  $I = 0.2$  M is similar to the ionic strength  $I \approx 0.25$  M of the NaHCO<sub>3</sub>/Na<sub>2</sub>CO<sub>3</sub> buffer used as a solvent in the present work, the same form factor model was used to fit the SANS curve resulting from a 30 mM DTAB solution (Figure 4). Micelles with a polar radius of 14 Å and an equatorial radius of 22 Å were found, which is comparable to Bergström’s and Pedersen’s results.



The use of a structure factor significantly improved the fit quality for the SANS curve from pure DTAB solution, even though no obvious correlation peak was observed. The absence of a distinct correlation peak results from screening of the surface charges of DTAB micelles by buffer salt.<sup>45–47</sup> SANS curves from solutions containing Blue and DTAB also did not show a correlation peak. In addition to that, these SANS curves were sufficiently well described using only a form factor and no structure factor, which indicates negligible intermicellar interactions and ordering. This likely results from further screening of DTAB head group charges due to electrostatic interactions with the oppositely charged dye molecule.<sup>47</sup>

**Ellipsoidal Blue-DTAB micelles:** The SANS curve of the sample containing [Blue] = 5 mM and [DTAB] = 30 mM (ratio 1:6) is well described using the form factor of a triaxial ellipsoid. This resembles observations of Bergström and Pedersen who showed that with increasing ionic strength of the solution by NaBr addition, oblate spheroidal micelles turn into triaxial ellipsoids.<sup>39</sup> However, the main reason for the morphological transition observed here is likely not the increase of solution ionic strength by ~ 2 % upon addition of 0.005 M of the acid Blue to the buffer with  $I \approx 0.25$  M. The adsorption of Blue on the micellar surface or even insertion into the micelle close to the surfactant head group results in more efficient screening of micellar surface charges and is a more plausible explanation for the observed behaviour.<sup>4,47</sup> Furthermore, form factor fits (Table 1) indicate a strong similarity between the radius of the smallest semi-axis of Blue-DTAB triaxial ellipsoidal micelles ( $r_{\text{minor}} = 15.3 \text{ \AA}$ ) and of the polar radius of oblate spheroidal DTAB micelles ( $r_{\text{minor}} = 14.0 \text{ \AA}$ ) as well as the radius of the medium semi axis of the Blue-DTAB triaxial ellipsoidal micelles ( $r_{\text{major}} = 22.0 \text{ \AA}$ ) and the equatorial radius of DTAB micelles ( $r_{\text{major}} = 22.4 \text{ \AA}$ ). This could point towards an uniaxial growth of these micelles.<sup>4</sup>

**Cylindrical Blue-DTAB micelles:** SANS curves of samples containing [Blue] = 5 mM with [DTAB] = 22.5 mM (ratio 1:4.5) and [Blue] = 7.5 mM with [DTAB] = 30 mM (ratio 1:4) are well described using either the form factor of a cylinder with elliptical cross section or the form factor of a cylinder with circular, polydisperse cross section. The application of the model of a cylinder with elliptical cross section resulted in a better fit of experimental data. Furthermore, resulting cross section radii agree well with the minor and the medium semi-axes ( $r_{\text{minor}}$  and  $r_{\text{major}}$ ) of Blue-DTAB triaxial ellipsoidal micelles ([Blue] = 5 mM, [DTAB] = 30 mM, Table 1). Therefore, cylindrical Blue-DTAB assemblies likely exhibit an elliptical cross section. This assessment is supported by several sources in which micellar growth by hydrotrope or surfactant addition was studied.<sup>4,13,47</sup> Among them, Bergström and Pedersen used a form factor model with elliptical cross section to describe mixed micelles of DTAB and sodium dodecyl sulfate (SDS).<sup>13</sup> Furthermore,

Hassan et al. suggested that the polydispersity obtained for the circular cross-section radius of cylindrical hydrotrope-SDS micelles likely results from an effective elliptical cross section of those micelles.<sup>47</sup> Whereas cross section radii of Blue-DTAB assemblies remain approximately similar for all sample compositions (Table 1), cylinder lengths vary and show pronounced polydispersity. This is not unlikely and was already observed by Bergström and Pedersen for DTAB-SDS mixed micelles with similar morphologies.<sup>13</sup> They considered the polydispersity in cylinder length by assuming a broad Schulz distribution. A similar strategy was applied for fitting SANS curves from Blue-DTAB solutions with the form factor model of cylinders with elliptical cross section. Herein, the length of cylindrical micelles was assumed to be distributed according to a Schulz distribution. Its relative standard deviation  $\sigma/\bar{L}$  was fixed to  $\sigma/\bar{L} = 0.95$ , where  $\bar{L}$  is the number averaged contour length and  $\sigma$  the standard deviation of the number frequency. The resulting fit parameters are displayed in Table 1 with fits being shown in Figure 4 and Figure 5.

The length of cylindrical assemblies increases from 73.4 Å to 148 Å when decreasing the excess of DTAB from [Blue]:[DTAB] = 1:4.5 to [Blue]:[DTAB] = 1:4. Decrease of the DTAB excess to [Blue]:[DTAB] = 1:3 leads to further growth of cylindrical micelles and appearance of flexibility. Therefore, SANS curves of corresponding samples were described using a form factor model for flexible cylinders with elliptical cross section (Figure 4 and Figure 5).<sup>36</sup> The appearance of almost identical cross section radii for all samples containing Blue and DTAB (Table 1) independent of length and applied form factor model confirms that micelles generally grow in only one dimension, leaving the elliptical cross section unaltered.<sup>4</sup>

#### 6.4.3 Packing parameter

The mechanism of the above-described morphological transition of DTAB micelles beginning with oblate spheroidal micelles via triaxial ellipsoidal micelles and rod-like cylinders to WLMs upon addition of Blue is easily explained by the concept of the packing parameter  $P$  for amphiphilic molecules:<sup>48</sup>

$$P = \frac{v}{a_0 l_c} \quad (4)$$

In eq (4)  $v$  is the volume of the hydrophobic chain of the amphiphilic molecule,  $l_c$  its length and  $a_0$  the effective head group area occupied per molecule at the hydrocarbon-water interface.<sup>48</sup> The packing parameter can be used to predict an assembly morphology based on these geometrical considerations. As shown in Figure 6(a), low values ( $P < \frac{1}{3}$ ) imply spherical micelles, values of

$\frac{1}{3} < P < \frac{1}{2}$  point towards ellipsoidal micelles and for packing parameters around  $P \approx \frac{1}{2}$  the formation of cylindrical or rod-like micelles is favoured. Further increase results in the formation of various interconnected structures ( $\frac{1}{2} < P < 1$ ), vesicles and extended bilayers ( $P \approx 1$ ).<sup>48</sup> This sequence of assembly morphologies goes along with a change in their spontaneous curvature from high for spherical aggregates to low for aggregates with locally flat interfaces such as bilayers.<sup>3</sup>

Based on the packing parameter it can be understood that intermolecular interactions between surfactant molecules and additives may change the morphology of surfactant micelles by changing the geometry of the amphiphile. In other words, the effective size of the hydrophobic and hydrophilic sections may be influenced by their rigidity and interactions such as hydrogen bonding or electrostatic interactions. Moreover, salt or hydrotrope addition usually reduces the effective head group size of ionic surfactant molecules due to charge screening and a concomitant reduction in electrostatic repulsion between head groups.<sup>3,4</sup>

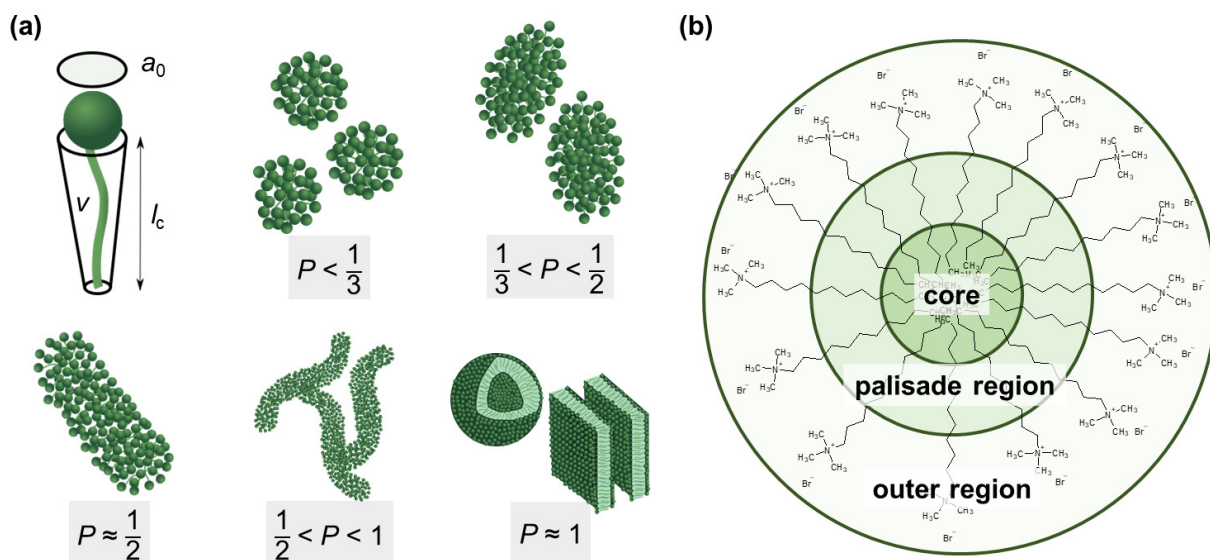


Figure 6: (a) Size parameters contributing to the packing parameter  $P$  of amphiphilic substances and schematic illustration of the relationship between the packing parameter and the morphology of assemblies.<sup>48</sup> Spheres represent the hydrophilic surfactant head group whereas the hydrophobic tail is described by a line. (b) Classification of different regions of a DTAB micelle in water according to their hydrophilicity.<sup>49,50</sup> The outer region consists of the positively charged DTAB head group and four neighbouring methylene groups, which are expected to interact with the surrounding water according to SANS investigations on pure DTAB micelles by Berr et al.<sup>50</sup>

Accordingly, the observed morphological transitions in solutions of Blue and DTAB can be reconciled with a reduction in DTAB head group size  $a_0$  due to shielding of electrostatic repulsion between positively charged DTAB head groups by negatively charged molecules of Blue. The

reduction in  $a_0$  due to shielding of electrostatic repulsions must overcompensate an eventual increase of DTAB head group size caused by the geometrical inclusion of Blue into the head group layer to result in a net decrease of  $a_0$ . This decrease of  $a_0$  leads to an increase of the packing parameter and explains the morphological transition from ellipsoidal to wormlike micelles upon successive addition of Blue. In addition to that, an increase of  $P$  can also be achieved if parts of the Blue molecules would contribute to the volume  $v$  of the hydrophobic surfactant chain. This would require a penetration of Blue into the palisade layer or core of the DTAB micelle. As Blue molecules carry a charge opposite to that of the DTAB head group and are well water soluble, they are expected to remain on the surface or outer layer of the micelle, rendering the reduction of effective head group size by charge screening the most likely reason for micellar growth. To confirm this hypothesis, it is necessary to locate Blue within the Blue-DTAB micelle. For this purpose, a combination of SANS contrast matching and NMR spectroscopy was used.

#### 6.4.4 Localization of Blue in Blue-DTAB micelles by means of contrast matching

SANS contrast matching gives access to one component of the mixed Blue-DTAB micelle by eliminating the contrast of the other component relative to the surrounding medium upon isotopic substitution. Within the investigations presented here, the contrast of DTAB relative to the aqueous solvent, i.e.  $\text{NaHCO}_3/\text{Na}_2\text{CO}_3$  buffer prepared in  $\text{D}_2\text{O}$ , was eliminated by using deuterated  $\text{d}_{25}$ -DTAB and  $\text{d}_{34}$ -DTAB at a volume ratio of 46:54, which corresponds to the experimental match composition.

Figure 7 shows SANS curves of solutions containing 30 mM DTAB and varying concentrations of Blue with DTAB being matched to the solvent. As a consequence, only scattering from Blue is observed. SANS curves from corresponding samples, based on the scattering from Blue and DTAB (full contrast), were shown in Figure 4 and discussed before. Analogously, Figure 8 and Figure 5 show SANS curves from samples containing 5 mM Blue and varying concentrations of DTAB in DTAB-matched and full contrast mode respectively.

The form factor models used to describe experimental data are visually indicated next to the respective SANS curve in Figure 7 and Figure 8. Core-shell models were used in all cases with the scattering length density ( $SLD$ ) of the core corresponding to the  $SLD$  of the solvent. This  $SLD$  was fixed to its theoretical value ( $6.376 \cdot 10^{-6} \text{ \AA}^{-2}$ ) during fits. Two fitting strategies were employed: In a first attempt, the  $SLD$  of the shell was fixed to  $SLD_{\text{shell}} = 3.028 \cdot 10^{-6} \text{ \AA}^{-2}$ . This is the  $SLD$  of the one-fold deprotonated Blue based on its elemental composition and on the experimentally determined partial molar volume. In a second attempt the  $SLD$  of the shell was fitted. This permits

a less dense shell of Blue due to hydration and proximity of the hydrophilic head groups of DTAB. For this reason, the latter strategy is more realistic and resulted into a similar or slightly better fit quality in most cases.<sup>50</sup> However, results have to be evaluated with care as size parameters, such as shell thickness, depend on the  $SLD$ .<sup>52</sup>

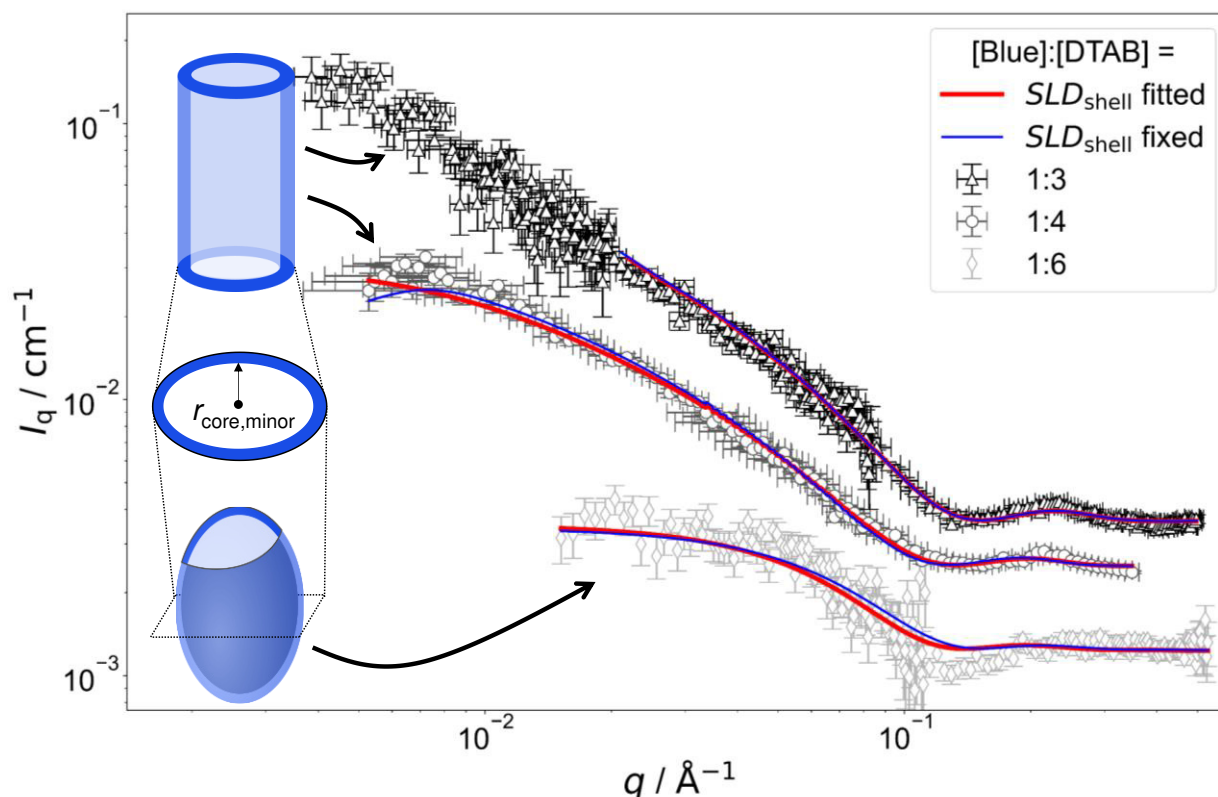


Figure 7: SANS curves of solutions containing 30 mM DTAB and varying concentrations of Blue with DTAB being a mixture of 46 vol%  $d_{25}$ -DTAB and 54 vol%  $d_{34}$ -DTAB corresponding to its experimental match composition. This means that the  $SLD$  of the surfactant mixture is the same as the  $SLD$  of the solvent, eliminating the contrast between the surfactant and the solvent. The solvent is a  $\text{NaHCO}_3/\text{Na}_2\text{CO}_3$  buffer ( $\text{pD} = 10.7$ ,  $l \approx 0.25$  M) prepared in 100 vol%  $\text{D}_2\text{O}$ . Measurements were performed at 25 °C. Red and blue lines display form factor fits according to the model of core-shell cylinders with elliptical cross section<sup>51</sup> for [Blue]:[DTAB] ratios of 1:3 and 1:4 or the model of a triaxial core-shell ellipsoid for a [Blue]:[DTAB] ratio of 1:6. The fit displayed as red line was obtained when the  $SLD$  of the shell was fitted whereas the fit displayed as blue line was obtained while fixing the shell  $SLD$ .

Fitted curves are displayed together with experimental data in Figure 7 and Figure 8. Results related to the assembly cross section are displayed in Table 2. To reduce the number of fit parameters, parameters related to length and cross section anisometry were fixed to values obtained from fitting to corresponding full contrast data. The following details shall be explicitly outlined: Owing to poor data quality in the low- $q$  region, SANS curves containing [Blue]:[DTAB] = 1:3 for contrast matched DTAB were described using the form factor model of a rigid core-shell cylinder rather than a flexible core-shell cylinder. This does not depreciate the

analysis, as the scattering signal in the evaluated high- $q$  range does not carry information on flexibility of the overall assembly. Furthermore, information on overall assembly size were obtained from full contrast measurements. In addition to that, the evaluation of cross section dimensions should not be hampered by not considering low- $q$  scattering. Therefore, lengths of core-shell cylinders used to describe SANS curves from DTAB contrast matched samples were fixed to values obtained from fitting corresponding full contrast SANS curves. Precise values can be found in the Supporting Information (Table SI6). In addition to the length parameter, the cross section anisotropy of assemblies formed in DTAB contrast matched samples was fixed to the anisotropy obtained from fitting full contrast SANS curves by fixing the ratio between the major and the minor core radius of the core-shell model ( $r_{\text{core,major}}/r_{\text{core,minor}}$ ) to the ratio between  $r_{\text{major}}$  and  $r_{\text{minor}}$  of the respective full contrast model (Table 1). All parameters are summarized in the Supporting Information (Table SI6).

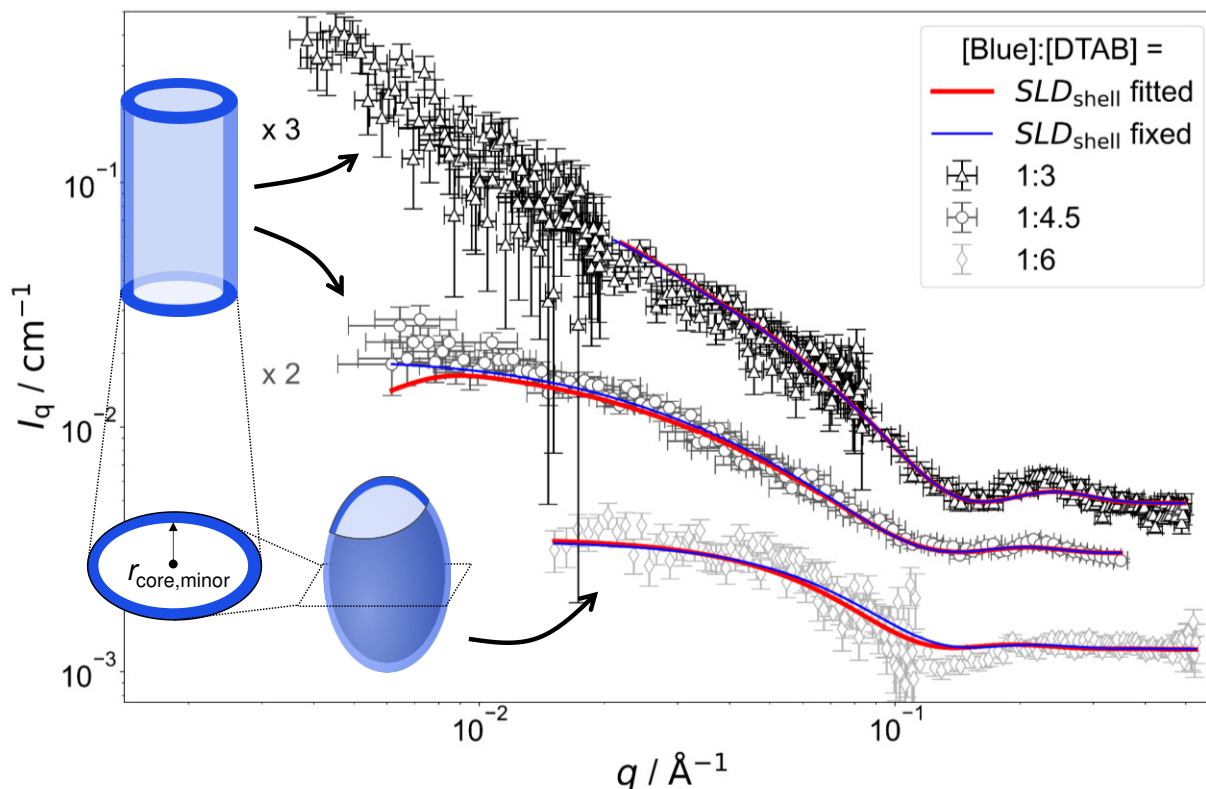


Figure 8: SANS curves of solutions containing 5 mM Blue and varying concentration of DTAB with DTAB being a mixture of 46 vol%  $d_{25}$ -DTAB and 54 vol%  $d_{34}$ -DTAB corresponding to its experimental match composition. This means that the  $SLD$  of the surfactant mixture is the same as the  $SLD$  of the solvent, eliminating the contrast between the surfactant and the solvent. The solvent is a  $\text{NaHCO}_3/\text{Na}_2\text{CO}_3$  buffer ( $\text{pD} = 10.7$ ,  $I \approx 0.25$  M) prepared in 100 vol%  $\text{D}_2\text{O}$ . Measurements were performed at 25 °C. Red and blue lines display form factor fits according to the model of core-shell cylinders with elliptical cross section<sup>51</sup> for [Blue]:[DTAB] ratios of 1:3 and 1:4 or the model of a triaxial core-shell ellipsoid for a [Blue]:[DTAB] ratio of 1:6. The fit displayed as red line was obtained when the  $SLD$  of the shell was fitted whereas the fit displayed as blue line was obtained while fixing the shell  $SLD$ .

As many size parameters were adapted from fits to full contrast SANS curves, only the minor core radius  $r_{\text{core,minor}}$ , the shell thickness ( $th$ ) and, dependent on the employed strategy,  $SLD_{\text{shell}}$  needed to be fitted. To this end, two strategies were applied. In one strategy,  $SLD_{\text{shell}}$  was fixed and in the other strategy,  $SLD_{\text{shell}}$  was fitted. Table 2 displays only these parameters in comparison to  $r_{\text{minor}}$  obtained for the elliptical cross section from fitting full contrast SANS curves.

Table 2: Cross section size parameters of core-shell structures obtained from fitting SANS-curves from DTAB contrast matched solutions in comparison to the minor cross section radius  $r_{\text{minor}}$  obtained from fitting full contrast SANS-curves with a model assuming a homogenous  $SLD$  distribution. The radius of the shortest semi-axis of the triaxial ellipsoid form factor is given for the sample with [Blue] = 5 mM and [DTAB] = 30 mM and the minor radius of the elliptical cross section of the elliptical cylinder form factor in all other cases. The  $SLD$  of the core is equal to that of the solvent with  $SLD_{\text{core}} = SLD_{\text{solvent}} = 6.376 \cdot 10^{-6} \text{ \AA}^{-2}$  for DTAB contrast matched structures.

[Blue] mM	[DTAB] mM	Full contrast	DTAB contrast matched $SLD_{\text{shell}} =$ $3.028 \cdot 10^{-6} \text{ \AA}^{-2}$		DTAB contrast matched $SLD_{\text{shell}}$ fitted		
		$r_{\text{minor}}$ $\text{\AA}$	$r_{\text{core,minor}}$ $\text{\AA}$	$th$ $\text{\AA}$	$r_{\text{core,minor}}$ $\text{\AA}$	$th$ $\text{\AA}$	$SLD_{\text{shell}}$ $10^{-6} \text{ \AA}^{-2}$
5	30	$15.3 \pm 0.2$	$14.4 \pm 0.6$	$1.6 \pm 0.02$	$14.4 \pm 0.6$	$4.7 \pm 0.9$	$5.4 \pm 0.2$
7.5	30	$14.336 \pm 0.009$	$15.7 \pm 0.2$	$0.874 \pm 0.004$	$14.5 \pm 0.2$	$2.1 \pm 0.4$	$5.0 \pm 0.2$
10	30	$14.046 \pm 0.008$	$12.6 \pm 0.2$	$1.28 \pm 0.02$	$12.0 \pm 0.8$	$2.4 \pm 1.2$	$4.5 \pm 0.3$
5	22.5	$14.78 \pm 0.02$	$14.7 \pm 0.3$	$0.748 \pm 0.006$	$13.3 \pm 0.4$	$3.3 \pm 0.5$	$5.6 \pm 0.2$
5	15	$13.92 \pm 0.02$	$11.7 \pm 0.3$	$1.41 \pm 0.02$	$10.9 \pm 0.5$	$3.5 \pm 0.8$	$4.9 \pm 0.3$

$r_{\text{minor}}$  – minor radius of the elliptical cross section obtained from fitting full-contrast SANS curves,  $r_{\text{core,minor}}$  – minor radius of the elliptical cross section of the core obtained from fitting SANS-curves of samples, where DTAB was contrast matched, with a core-shell model,  $th$  – shell thickness,  $SLD_{\text{shell}}$  – scattering length density of the shell

Comparing the results of both fitting strategies based on core-shell structures leads to two main observations: (1) Shell thicknesses  $th$  are larger when  $SLD_{\text{shell}}$  was fitted and (2) fitted  $SLD_{\text{shell}}$  are higher than the  $SLD$  of negatively charged Blue, leading to lower contrast relative to the solvent. Both observations are easily explained by considering that the shell does not solely consist of a dense layer of Blue, but also solvent molecules and head groups from the SLD-matched DTAB. This leads to an increase in  $SLD$  and, as shell thickness and  $SLD$  correlate, a thicker shell.<sup>52</sup> As fitting the  $SLD_{\text{shell}}$  resulted in more realistic thicknesses ( $> 1 \text{ \AA}$ ) compared to fitting with the  $SLD_{\text{shell}}$  being kept constant, further discussion will be based on the fits where  $SLD_{\text{shell}}$  was fitted.

From Table 2 it can be seen, that the cross section core radius of the core-shell structure  $r_{\text{core,minor}}$  is smaller than  $r_{\text{minor}}$  from analysis of full contrast curves in most cases except for the sample with [Blue] = 7.5 mM and [DTAB] = 30 mM. However,  $r_{\text{core,minor}}$  and  $r_{\text{minor}}$  agree within uncertainty of the values for this sample. The relation  $r_{\text{core,minor}} < r_{\text{minor}}$  implies that the “shell” containing Blue molecules extends into the DTAB micelle. Furthermore, the sum of  $r_{\text{core,minor}}$  and  $th$ , corresponding to the total minor radius of the elliptical cross section for the core-shell structure, is similar and systematically bigger than  $r_{\text{minor}}$  for all samples. The relation  $r_{\text{minor}} < r_{\text{core,minor}} + th$  implies that the shell likely ranges into the surrounding medium. Core radii and shell thicknesses vary only insignificantly with varying sample composition and therefore do not allow to discern any trends concerning the penetration depth of Blue into the DTAB micelle as a function of [Blue]:[DTAB] ratio.

As a major result, SANS based on contrast matching successfully demonstrates that Blue molecules are located close to the DTAB head groups in the Blue-DTAB co-assembly. From the presented results it is reasonable to further conclude that at least a part of the Blue molecules are localized next to the positively charged DTAB head groups.

#### 6.4.5 NMR-spectroscopy

**<sup>1</sup>H-NMR spectroscopy.** NMR experiments were performed to further investigate intermolecular interactions between Blue and DTAB in solution. Figure 9 shows resonance signals of DTAB in solutions containing [DTAB] = 30 mM and varying amounts of Blue. The <sup>1</sup>H-NMR spectrum of pure DTAB is shown in green, along with the peak assignment.<sup>53</sup> Peaks are narrow even though [DTAB] = 30 mM lays far above the cmc of 9 mM in the present solvent, where monomeric DTAB molecules and micellar aggregates exist in equilibrium. Narrow peaks for this system suggest rather loosely coupled DTAB molecules with a high degree of relative thermal mobility.<sup>54</sup> From Figure 9 it is visible that successive addition of Blue to a DTAB solution leads to an upfield shift of resonances associated with protons close to the DTAB head group (a,b,c,d) and splitting of the resonance signal of protons of type e, presumably due to slightly different shielding of these protons.<sup>55,56</sup> The methyl group f experiences a small downfield shift. The upfield shift of most proton resonances is mostly caused by an increase in electron density upon addition of the negatively charged Blue. This results into shielding of protons close to the negative charge towards the external magnetic field.<sup>17,57,58</sup> Furthermore, the ring current of aromatic moieties of the Blue molecule could affect the chemical shift of neighbouring protons. Depending on the localisation of these protons relative to the aromatic moiety, shielding or de-shielding can occur.<sup>59</sup> However, the contribution of such ring current effects to changes in the chemical shift of DTAB



proton resonances is assumed to be exceeded by the shielding due to the negative charge of Blue. Depending on the localisation of DTAB protons relative to the negatively charged phenolate group of Blue, some DTAB protons may experience stronger shielding and therefore a more pronounced upfield shift compared to others. This phenomenon may permit deductions on the localisation of Blue in DTAB micelles. To give an example, protons of type a or b experience a stronger change in their chemical shift upon Blue insertion than protons of type f, indicating that the negative charge of Blue is likely to be in direct proximity of type a or type b protons.<sup>17,58</sup> Furthermore, the insertion of Blue causes a variation in electron density experienced by different protons of type e, resulting into splitting of the corresponding proton resonance.

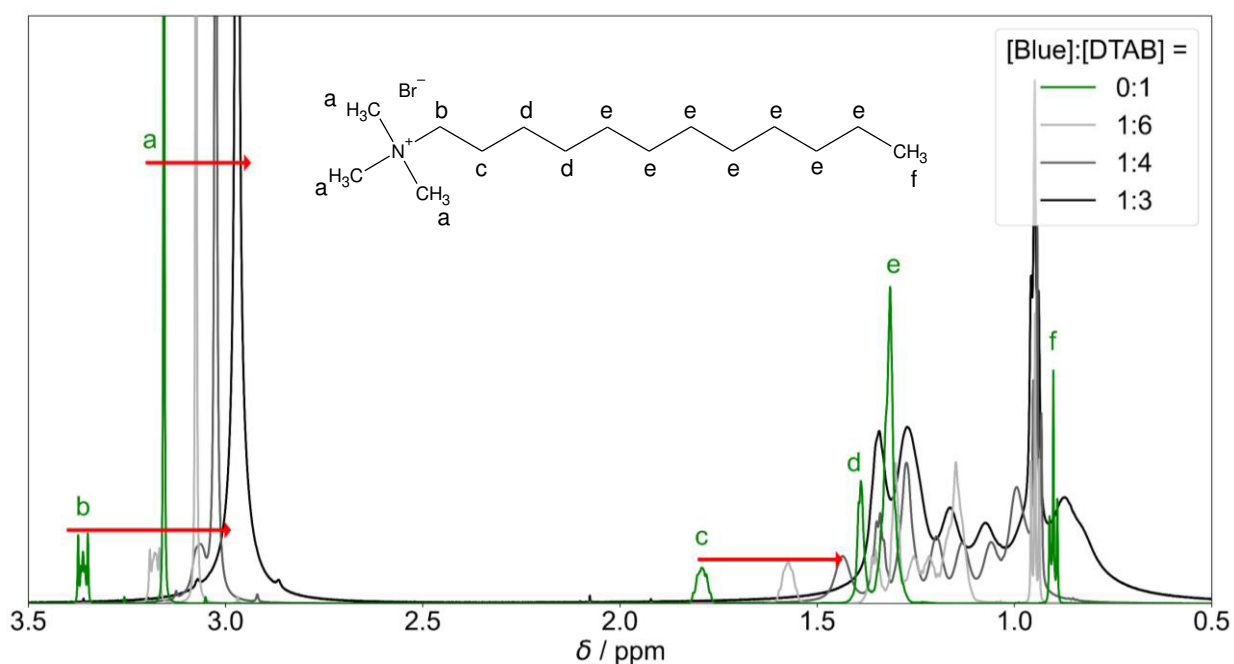


Figure 9:  $^1\text{H}$ -NMR resonances of DTAB protons in solutions containing  $[\text{DTAB}] = 30 \text{ mM}$  and varying concentrations of Blue. The green curve corresponds to the  $^1\text{H}$ -NMR spectrum of DTAB in the absence of Blue. Solutions were prepared in an  $\text{NaHCO}_3/\text{Na}_2\text{CO}_3$  buffer ( $\text{pD} = 10.7$ ,  $I \approx 0.25 \text{ M}$ ) in  $\text{D}_2\text{O}$ . Red arrows indicate alterations in chemical shift of resonances a, b and c with increasing concentration of Blue.

The continuous upfield shift of NMR resonances with increasing  $[\text{Blue}]:[\text{DTAB}]$  ratio can be understood considering an equilibrium of multiple DTAB states with protons experiencing different local magnetic environments and therefore exhibiting different chemical shifts. Given a sufficiently fast exchange between these states, a single time-averaged spectrum is obtained.<sup>53,55–57</sup> Increasing the  $[\text{Blue}]:[\text{DTAB}]$  ratio increases the fraction of DTAB molecules interacting with Blue and therefore the weighting of corresponding resonances for the time-averaged NMR spectrum, resulting into an upfield shift of time-averaged signals.

Apart from an upfield shift of most DTAB resonances, the addition of Blue results in peak broadening. This may be caused by two effects: (1) A penetration of Blue into the DTAB micelle likely decreases the mobility of DTAB molecules, favouring spin-spin relaxation and leading to peak broadening. (2) The formation of cylindrical micelles and micellar growth with increasing Blue:DTAB ratio results in a slowing of the end-over-end tumbling motion of rod-like micelles in the isotropic micellar phase. This causes a broadening of their proton resonances.<sup>53,58,60</sup> The observations are therefore consistent with the previously made observations of aggregate growth with increasing dye-to-surfactant ratio.

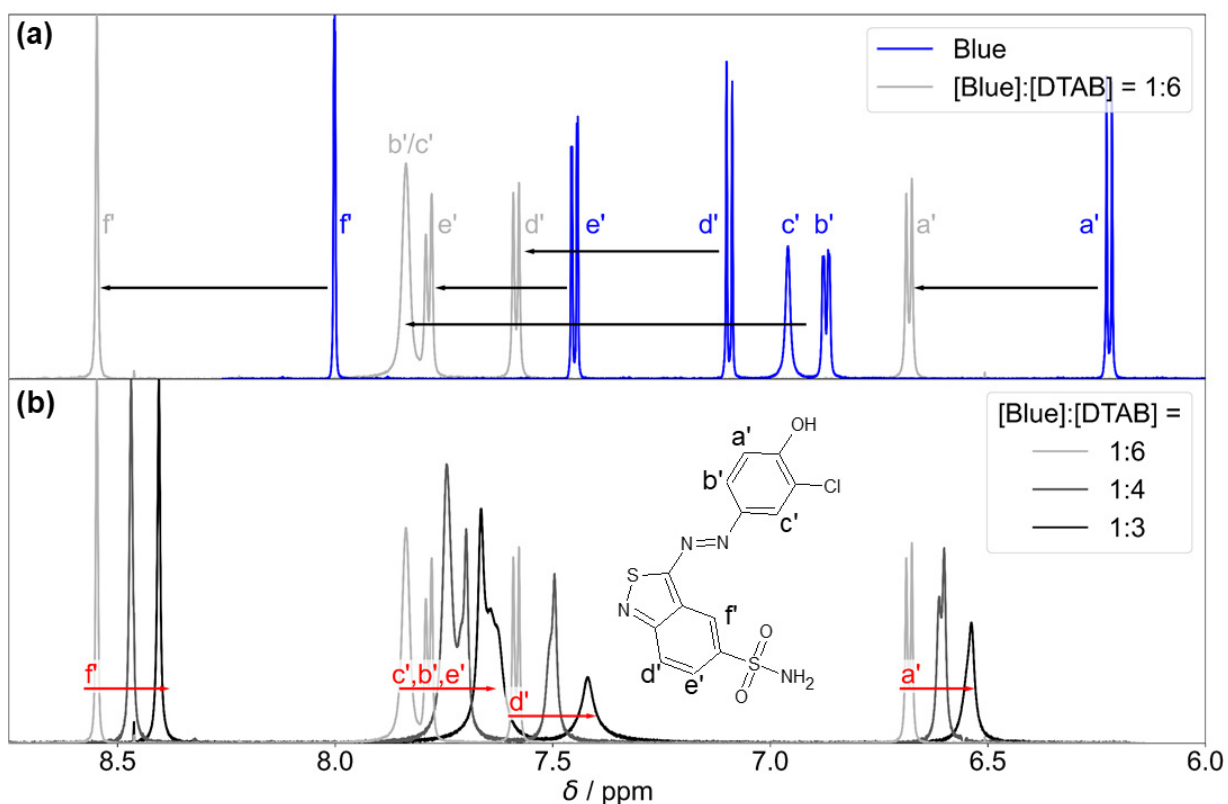


Figure 10: (a) <sup>1</sup>H-NMR spectrum of Blue in its pure solution with [Blue] = 10 mM (blue line) compared to the <sup>1</sup>H-NMR spectrum of Blue in presence of a 6-fold excess of DTAB (light grey line) with [Blue] = 5 mM and [DTAB] = 30 mM. Black arrows indicate alterations in the chemical shift of Blue proton resonances upon addition of DTAB. Resonances are labelled according to the designation of protons shown next to the chemical structure of Blue in (b). (b) <sup>1</sup>H-NMR resonances of Blue in solutions containing [DTAB] = 30 mM and varying concentrations of Blue. Red arrows indicate alterations in <sup>1</sup>H chemical shifts of Blue proton resonances in solutions containing DTAB and Blue with increasing concentration of Blue at constant DTAB concentration. Solutions were prepared in a NaHCO<sub>3</sub>/Na<sub>2</sub>CO<sub>3</sub> buffer (pD = 10.7, I ≈ 0.25 M) in D<sub>2</sub>O.

Figure 10(a) shows the <sup>1</sup>H-NMR spectrum of Blue in the absence and in presence of DTAB. First and foremost, an obvious downfield shift of Blue proton resonances upon addition of DTAB is observed. This is likely caused by electrostatic interactions between Blue and DTAB and corresponding proximity of the positively charged DTAB head group to Blue, which results in a

removal of electron density and subsequent de-shielding of Blue proton resonances upon DTAB addition.<sup>17</sup>

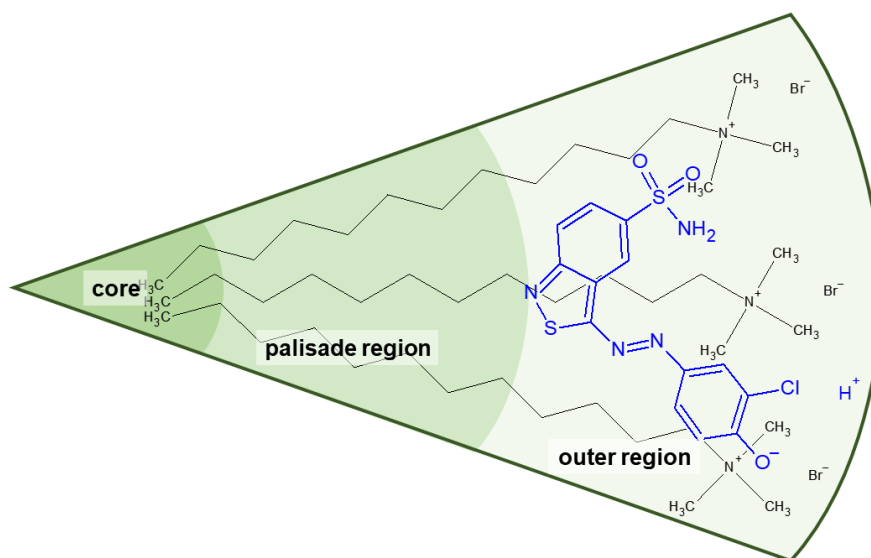


Figure 11: Suggested orientation of Blue in DTAB micelles according to the evaluation of DTAB-induced changes in chemical shifts of Blue proton resonances. The location was inferred from SANS contrast variation and evaluation of NOESY spectra.

Preliminary information on the orientation of Blue in DTAB micelles can be obtained by comparing the extent of downfield shifts observed for proton resonances from the two aromatic subunits of Blue upon addition of DTAB to a solution of pure Blue (Figure 10(a)).<sup>58</sup> The observed downfield shift is highest for resonances from protons b' and c' in meta-position to the phenolate group of the phenolic sub-unit with  $\Delta\sigma$  of 0.97 ppm and 0.88 ppm for the sample containing [Blue]:[DTAB] = 1:6 compared to pure Blue. The signal position of proton a' is affected less with  $\Delta\sigma = 0.46$  ppm, which is likely due to the delocalization of the negative phenolate charge into its ortho- rather than meta- position based on structural resonance formula.<sup>61</sup> Therefore, a' is likely less affected by the de-shielding effect caused by the proximity of the positively charged DTAB head group than b' and c'. Proton resonances of the benzothiazole aromatic sub-unit were affected less leading to  $\Delta\sigma = 0.49$  ppm, 0.33 ppm and 0.55 ppm for d', e' and f' respectively when comparing chemical shifts from the <sup>1</sup>H-NMR spectrum of the sample with [Blue]:[DTAB] = 1:6 to pure Blue. Considering the stronger de-shielding for resonances of phenolic protons b' and c', the phenolate subunit is likely located closer to the positively charged DTAB head group than the benzothiazole subunit (Figure 11). This is reasonable considering electrostatic attractions between the positively charged DTAB head group and the negatively charged phenolate.

Furthermore, the mildly hydrophobic benzothiazole sub-unit is expected to penetrate into the DTAB micelle rather than protruding into the aqueous solvent. This hypothesis is examined by NOESY in one of the following sections.

Figure 10(b) shows  $^1\text{H-NMR}$  resonance signals of Blue in solutions containing DTAB at a constant concentration of  $[\text{DTAB}] = 30 \text{ mM}$  and varying concentrations of Blue. With increasing  $[\text{Blue}]:[\text{DTAB}]$  molar ratio, an upfield shift of all Blue proton resonances is observed. Two possible explanations for this observation exist, which are not mutually exclusive: At higher  $[\text{Blue}]:[\text{DTAB}]$  ratios more negatively charged Blue molecules are expected to interact with the positively charged DTAB head groups. This results into a higher density of Blue molecules in the DTAB head group region and subsequent increase in electron density. Therefore, the shielding of Blue protons located in that region successively increases with increasing concentration of Blue. Another explanation is related to the dynamic equilibrium present in micellar solutions: A  $^1\text{H-NMR}$  spectrum represents the time-average spectrum of all states of Blue present in solution given that the exchange between these states is fast enough.<sup>53,55–57</sup> Therefore, an alternative possibility to explain resonance shifts would be a change in the molar ratio between these states with varying sample composition. Assuming the simplest case of two states of Blue, one interacting with DTAB and the other one being free in solution, the chemical shift of the time-averaged signal ( $\sigma$ ) can be calculated from eq (5).<sup>55</sup>

$$\sigma = \sigma_{\text{mic}} \cdot x_{\text{mic}} + \sigma_{\text{free}} \cdot (1 - x_{\text{mic}}) \quad (5)$$

In eq (5)  $\sigma_{\text{free}}$  is the chemical shift of a proton resonance of Blue in the free state, not interacting with DTAB (Figure 10(a), blue line) and  $x_{\text{mic}}$  is the mole fraction of Blue interacting with DTAB. Furthermore,  $\sigma_{\text{mic}}$  is the chemical shift of a proton resonance of Blue interacting with DTAB, assuming that  $\sigma_{\text{mic}}$  does not change with varying  $[\text{Blue}]:[\text{DTAB}]$  ratio. However, as mentioned above, a change of  $\sigma_{\text{mic}}$  with an increasing number of Blue molecules interacting with DTAB micelles is possible. It is likely that both effects, variations in  $x_{\text{mic}}$  and changes in  $\sigma_{\text{mic}}$  contribute to changes in the chemical shift of Blue proton resonances with varying  $[\text{Blue}]:[\text{DTAB}]$  ratio.

Previous UV/vis spectroscopic investigations on the presented system indeed showed that the mole fraction of Blue molecules interacting with DTAB changes significantly from 0.95 for  $[\text{Blue}]:[\text{DTAB}] = 1:6$  over 0.85 for  $[\text{Blue}]:[\text{DTAB}] = 1:4$  to 0.73 for  $[\text{Blue}]:[\text{DTAB}] = 1:3$ . These values were calculated from the Blue-DTAB association constant of  $K = (4.7 \pm 2) \cdot 10^6 \text{ L}^3 \text{ mol}^{-3}$

for a stoichiometry of [Blue]:[DTAB] = 1:3.<sup>33</sup> Accordingly, with decreasing DTAB excess, the fraction of Blue molecules interacting with DTAB micelles decreases.

**NOESY.** Spatial proximity of protons up to a distance of about 5 Å can be studied by observing the Nuclear Overhauser Effect (NOE) with 2-dimensional NMR-spectroscopy by recording NOESY spectra.<sup>17</sup> Figure 12 shows a relevant section of NOESY spectra from solutions containing [DTAB] = 30 mM and varying concentrations of Blue. As discussed above, <sup>1</sup>H resonances are shifted relative to each other due to variation in the fraction of Blue interacting with DTAB, which makes it possible to display all three NOESY spectra in the same graph. Intensities of cross peaks are negative in all cases, which means that the zero-quantum transition  $W_0$  dominates over the double-quantum transition  $W_2$  causing the NOE.<sup>17,18</sup> This points towards the presence of large aggregates.

Several cross peaks are visible and can be distinguished into (1) cross peaks between resonances of Blue, (2) cross peaks between resonances of DTAB and (3) cross peaks between resonances of Blue and resonances of DTAB. Cross peaks between resonances of Blue suggest spatial proximity among Blue molecules within Blue-DTAB co-assemblies. This proximity could be promoted by the formation of intermolecular  $\pi$ - $\pi$ -stacking interactions between aromatic moieties of Blue. Such a mechanism was previously suggested for the interaction between oppositely charged dye and surfactant and would promote the formation of elongated, cylindrical assembly structures.<sup>26</sup> Cross peaks between resonances of DTAB were not analysed due to strong overlap. Cross peaks between resonances of Blue and resonances of DTAB carry valuable information on the penetration of Blue into the DTAB micelle and are therefore discussed in the following.

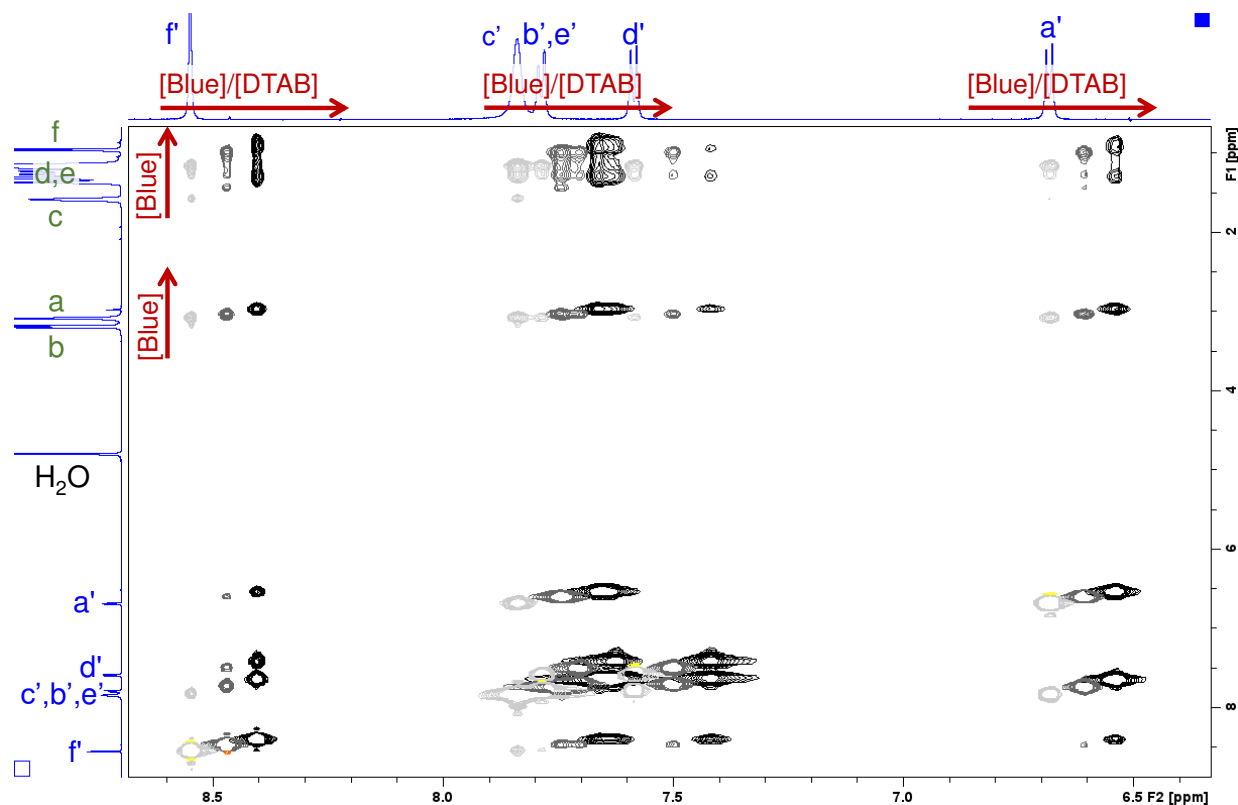


Figure 12: Section of NOESY spectra recorded from solutions containing [DTAB] = 30 mM and varying concentrations of Blue. The solvent is a  $\text{NaHCO}_3/\text{Na}_2\text{CO}_3$  buffer ( $\text{pD} = 10.7$ ,  $I \approx 0.25$  M) prepared in  $\text{D}_2\text{O}$ . Negative peaks are displayed in light grey, dark grey and black for samples containing [Blue] = 5 mM, 7.5 mM and 10 mM respectively. Positive peaks are displayed in yellow, orange and red for samples containing [Blue] = 5 mM, 7.5 mM and 10 mM respectively. Chemical shifts in the  $^1\text{H}$ -NMR spectrum induced by the increase of Blue concentration are indicated by red arrows. The  $^1\text{H}$ -NMR spectra of the sample containing [Blue] = 5 mM and [DTAB] = 30 mM are displayed on the side. Peak assignment was adopted from Figure 9 and Figure 10. The complete NOESY spectrum is shown in the SI (Figure S19).

Figure 12 clearly shows several cross peaks between resonances of Blue and resonances of DTAB. Based on previous discussions, cross peaks between proton resonances arising from the DTAB trimethylammoniumhead group (a) and its geminal methylene group (b) and all Blue proton resonances are expected due to electrostatic interaction between the Blue and the DTAB head group. Furthermore, cross peaks are observed between all Blue proton resonances and the resonance arising from the methylene group in  $\beta$ -position to the ammonium ion (c). This is reasonable according to investigations made by Berr et al., where the structure of DTAB micelles was studied using SANS contrast variation and who found, that the first four methylene groups of the DTAB alkyl chain are part of the hydrated shell of the DTAB micelle.<sup>50</sup> For this reason, cross peaks should also be observed between Blue proton resonances and resonances of DTAB protons of type d. Unfortunately, an unambiguous assignment of DTAB alkyl chain resonances to corresponding protons is not possible due to peak broadening and shifts induced by the addition of Blue to DTAB solution. However, all Blue proton resonances show one or two additional cross

peaks with resonances from protons in the DTAB alkyl chain. Due to the strongly upfield shifted spectrum of DTAB in Blue-DTAB solutions compared to pure DTAB solution, these cross peaks are attributed to the spatial proximity of Blue-protons and the four DTAB protons of type d. As discussed before, the strong upfield shift of these resonances results from an increase in electron density and subsequent shielding of proton resonances due to the interaction of DTAB with negatively charged Blue.<sup>17</sup> Finally, the observation of cross peaks between DTAB proton resonances and all Blue proton resonances confirms the penetration of Blue molecules into DTAB micelles rather than a part of the Blue molecules sticking out of the micelles (Figure 11).

To summarize results from the NMR-spectroscopic study, Blue was found to penetrate into the hydrated part of the DTAB-micelle, which corresponds to the Stern layer or outer region (Figure 11).<sup>49,50</sup> This outer region includes the trimethylammonium head group and the first four methylene groups of the DTAB alkyl chain.<sup>50</sup> The shift of all <sup>1</sup>H-NMR resonance signals upon variation of the [Blue]:[DTAB] ratio is likely caused by two effects: (1) The existence of various states of Blue and DTAB, i.e. Blue molecules interacting with DTAB micelles and Blue molecules being dissolved as single molecules in solution, generates a time-average resonance due to fast exchange between these two states. This resonance shifts with an increasing or decreasing fraction of Blue molecules interacting with DTAB. (2) A change in Blue- and DTAB-resonances due to continuous shielding or de-shielding effects upon variation of the composition of Blue-DTAB micelles.

## 6.5 Conclusion

The co-assembly of the azo dye Blue and the cationic surfactant DTAB in an alkaline NaHCO<sub>3</sub>/Na<sub>2</sub>CO<sub>3</sub> buffer with ionic strength of  $I = 0.25$  M was investigated in detail. Small-angle neutron scattering clearly showed that addition of Blue in successive steps induces a uniaxial growth of pure, oblate spheroidal DTAB micelles to prolate ellipsoidal micelles and further on to cylinders and WLMs.

Using SANS contrast matching, Blue was observed to be located close to the DTAB head groups in all cases. These results were confirmed and extended by 2-dimensional NOESY. NOE dipolar coupling occurs between protons of Blue and DTAB alkyl chain protons up to the 4<sup>th</sup> methylene group, thereby showing that the penetration boundary of Blue molecules reaches the inner boundary of the outer layer (Figure 6). Furthermore, <sup>1</sup>H-NMR spectroscopy shed light on the orientation of Blue in the DTAB micelle by the change of chemical shift of Blue proton resonances

upon addition of DTAB: According to this observation, the phenolate group of Blue is expected to be located closer to the DTAB head group than the benzoisothiazole aromatic subunit.

The localization of Blue in the DTAB micelle reveals the reason for micellar growth upon addition of Blue. Micellar growth, which correlates with an increase of the packing parameter, can be caused by: (1) A reduction in the effective surface area per DTAB molecule or (2) an increase of the DTAB hydrophobic chain volume. Following the localisation of Blue close to the surfactant head group, an increase in the DTAB hydrophobic chain volume upon addition of Blue may be ruled out as the principal cause for the ellipsoid-to-cylinder transition. Therefore, Blue addition must cause a reduction of the effective surface area per DTAB molecule. This is likely caused by partial neutralisation of the positive DTAB head group charge upon interaction with negatively charged Blue, which overcompensates an increase in the DTAB head group size due to inclusion of the Blue molecule.

The complementary use of SANS contrast matching and NMR-spectroscopy is powerful for the localization of solutes in surfactant micelles. Not only does each method reveal a set of highly relevant information, but also does their complementarity reduce doubts in data interpretation, which could be caused by ambiguities of results obtained by just one method. As the feasibility of performing SANS contrast matching experiments for the localization of solutes in small surfactant micelles was demonstrated, such use may be particularly helpful in systems, where NMR peak assignment is hampered by peak overlap or unexpected changes in chemical shifts.

**Acknowledgement.** This work benefited from the use of the SasView application, originally developed under NSF award DMR-0520547. SasView contains code developed with funding from the European Union's Horizon 2020 research and innovation programme under the SINE2020 project, grant agreement No 654000. This work benefited from the use of the SASfit software package developed by Joachim Kohlbrecher and Ingo Bressler with copyright to the Paul Scherrer Institut (PSI).<sup>32</sup> The authors thank the Institut Laue-Langevin for the provision of internal beamtime (<https://doi.ill.fr/10.5291/ILL-DATA.INTER-557>). The authors gratefully acknowledge the use of the Partnership for Soft Condensed Matter (PSCM) facilities. W.M. acknowledges funding for a Ph.D. scholarship from the European Union's Horizon 2020 research and innovation programme under the Marie Skłodowska-Curie grant agreement No 847439 within the InnovaXN framework (Project number XN2019-ILL23). The authors thank Gisela Jünnemann-Held for collecting viscosity data.



## 6.6 Supporting information

### 6.6.1 Experimental

**Density and partial molar volumes.** Density measurements were performed using an Anton-Paar Density Meter (DMA 4500 M) requiring a sample volume of 1 mL. Density measurements were performed to make the calculation of partial molar volumes  $V_m(c)$  of Blue in buffer possible. For this purpose, five solutions containing Blue concentrations between 1 mM (0.37 g L<sup>-1</sup>) and 20 mM (7.39 g L<sup>-1</sup>) were prepared in an NaHCO<sub>3</sub>/Na<sub>2</sub>CO<sub>3</sub> buffer (pD = 10.7,  $I \approx 0.25$ ) in 100 % D<sub>2</sub>O. The densities of these solutions as well as of the buffer were measured after equilibrating the temperature of each sample to 25 °C. This yielded sample densities ( $\rho$ ) and the density of the buffer corresponding to the solvent ( $\rho_0$ ).

First, the partial molar volume of Blue in each of the measured solutions was calculated according to eq (SI1).<sup>62</sup>

$$V_m(c) = \frac{1000 \cdot (\rho_0 - \rho)}{c \cdot \rho} + \frac{M}{\rho} \quad (\text{SI1})$$

In eq (SI1)  $c$  is the mass concentration of Blue and  $M$  its molar mass. In the present case, partial molar volumes  $V_m(c)$  did not depend on  $c$ . Therefore, the average of all determined  $V_m(c)$  was calculated to obtain the partial molar volume of Blue. Further partial molar volumes were obtained from literature. Table SI1 summarizes partial molar volumes used for the calculation of scattering length densities ( $SLD$ ) of assembly components and of assembly volume fractions, the latter being required as an input parameter in SasView.

**Viscosity.** The kinematic viscosity  $\nu$  of a NaHCO<sub>3</sub>/Na<sub>2</sub>CO<sub>3</sub> buffer (pD = 10.7,  $I \approx 0.25$  M) in D<sub>2</sub>O was determined using an Ubbelohde viscosimeter. (Type 52710/I Schott, viscosimeter constant  $K = 0.009433 \text{ mm}^2 \text{ s}^{-2}$ ). Viscosity measurements were performed at 25 °C. For calculating the dynamic viscosity  $\eta$ , the experimentally determined buffer density of  $\rho_0 = 1.11437 \text{ g cm}^{-3}$  at a temperature of 25 °C was used:

$$\eta = \nu \cdot \rho_0 \quad (\text{SI2})$$

**Dynamic light scattering.** Light scattering measurements were performed on an ALV CGS-3 Compact Goniometer System (ALV GmbH, Langen, FRG) using a HeNe laser at a wavelength of 632.8 nm. Measurements were performed using cylindrical quartz glass cuvettes with an inner diameter of 1 cm. The temperature of the the sample in the toluene bath was controlled using a thermostat and set to 25 °C. Intensity correlation functions ( $g^{(2)}(\tau)$ ) resulting from dynamic light

scattering (DLS) were fitted with a mono exponential model according to the revised method of cumulants, which permits the inclusion of longer correlation times into the analysis as compared to the traditional method of cumulants.<sup>63</sup> An expansion up to the second cumulant was considered:

$$g^{(2)}(\tau) = B + \beta \cdot \exp(-2\Gamma\tau) \cdot \left(1 + \frac{\mu_2}{2!} \cdot \tau^2\right)^2 \quad (\text{SI3})$$

$B$  is commonly referred to as baseline or the long-time value of  $g^{(2)}(\tau)$ ,  $\beta$  is a factor that depends on experimental geometry,  $\Gamma$  is the decay rate,  $\mu_2$  is the second-order cumulant and  $\tau$  is the correlation time. An apparent diffusion coefficient  $D_{\text{app}}$ , which potentially depends on the scattering angle, can be calculated from the decay rate:<sup>63</sup>

$$\Gamma = D_{\text{app}} \cdot q^2 \quad (\text{SI4})$$

$q$  is the magnitude of the scattering vector, which is calculated from the scattering angle. If  $D_{\text{app}}$  shows an observable  $q$ -dependency, the diffusion coefficient  $D$  is then obtained from the intercept in a linear fit according to the dynamic Zimm equation:<sup>42</sup>

$$D_{\text{app}}(q^2) = D \cdot (1 + K \cdot q^2) \quad (\text{SI5})$$

where  $D$  is the diffusion coefficient of the particle and  $K$  a factor depending on sample polydispersity, particle morphology and size. If the sample consists of monodisperse spheres,  $K = 0$  and  $D_{\text{app}}(q) = D$ .

The hydrodynamic radius  $R_h$  of the particles or assemblies in solution is obtained from the Stokes-Einstein-equation:<sup>42</sup>

$$R_h = \frac{k_B \cdot T}{6 \cdot \pi \cdot \eta \cdot D} \quad (\text{SI6})$$

Where  $k_B$  is Boltzmann's constant,  $T$  the temperature and  $\eta$  the dynamic viscosity of the solvent.

In the presented work, dynamic light scattering experiments were performed on solutions containing differently deuterated species of DTAB at a concentration of  $[\text{DTAB}] = 30 \text{ mM}$  in a  $\text{NaHCO}_3/\text{Na}_2\text{CO}_3$  buffer ( $\text{pD} = 10.7$ ,  $I \approx 0.25 \text{ M}$ ) in  $\text{D}_2\text{O}$ . The viscosity of the buffer was measured according to the above-described procedure and amounts to  $\eta = (1.157 \pm 0.002) \text{ cP}$  at a temperature of  $25 \text{ }^\circ\text{C}$ .

### 6.6.2 Scattering length densities

For the analysis of small-angle neutron scattering curves with form factor models, the volume fraction of the Blue-DTAB co-assembly was fixed to a value calculated from known partial molar volumes  $V_m$  and concentrations of assembling molecules. For this purpose, it was assumed that partial molar volumes estimated for the components remain unchanged while being incorporated into the assemblies and that all molecules participate in assembly formation, ignoring the existence of monomeric molecules below the critical micelle concentration ( $cmc$ ) of these molecules. Given the neglect of the  $cmc$  and considering that molar volumes are likely to be slightly altered upon assembly formation, the presented strategy results in an estimation rather than a precise calculation of volume fractions. Nevertheless, it is good enough to facilitate reduction of the number of parameters during fitting, which by no means lowers the validity of the obtained size parameters. Above all, the scattering length density ( $SLD$ ) was fitted in most cases.

Table SI1 summarizes partial molar volumes used for the calculation of assembly volume fractions and theoretical  $SLDs$  of molecules and structural units. The scattering length density  $SLD$  of a molecule can be calculated from the coherent scattering lengths  $b_j$  of its constituting atoms, their respective number  $n_j$  and the partial molar volume of the molecule  $V_m$  according to eq (SI7):<sup>29</sup>

$$SLD = N_A \cdot \frac{\sum_j n_j \cdot b_j}{V_m} \quad (\text{SI7})$$

In eq (SI7)  $N_A$  is Avogadro's number in [ $\text{mol}^{-1}$ ], the partial molar volume  $V_m$  is given in [ $\text{cm}^3 \text{mol}^{-1}$ ] and scattering lengths  $b_j$  are given in [ $\text{cm}$ ].

Table S11: Partial molar volumes and scattering length densities of molecules and structural building blocks. Additivity of partial molar volumes was assumed. Concentration of buffer salts in the solvent:  $[\text{NaHCO}_3] = 0.0214 \text{ mol L}^{-1}$ ,  $[\text{Na}_2\text{CO}_3] = 0.0786 \text{ mol L}^{-1}$ .

Molecule or structural units	$V_m$ $\text{cm}^3 \text{ mol}^{-1}$	$SLD$ $10^{-6} \text{ \AA}^{-2}$
BlueH ( $\text{C}_{13}\text{H}_9\text{ClN}_4\text{O}_3\text{S}_2$ )	246.31 <sup>I</sup>	3.004
Blue (deprotonated, $\text{C}_{13}\text{H}_8\text{ClN}_4\text{O}_3\text{S}_2$ )	218.58 <sup>II</sup>	3.028
CH <sub>3</sub>	32.70 <sup>50</sup>	-0.842
CD <sub>3</sub>	32.70 <sup>III</sup>	4.910
CH <sub>2</sub>	16.20 <sup>50</sup>	-0.309
CD <sub>2</sub>	16.20 <sup>50</sup>	7.430
N(CH <sub>3</sub> ) <sub>3</sub> Br	91.81 <sup>IV,64,65</sup>	0.160
N(CD <sub>3</sub> ) <sub>3</sub> Br	91.81 <sup>III</sup>	6.306
h <sub>34</sub> -DTAB ( $\text{C}_{15}\text{H}_{34}\text{BrN}$ )	302.70 <sup>IV</sup>	-0.224
d <sub>34</sub> -DTAB ( $\text{C}_{15}\text{D}_{34}\text{BrN}$ )	302.70 <sup>IV</sup>	6.817
CH <sub>3</sub> (CH <sub>2</sub> ) <sub>11</sub>	210.89 <sup>IV</sup>	-0.392
CD <sub>3</sub> (CD <sub>2</sub> ) <sub>11</sub>	210.89 <sup>IV</sup>	7.040
H <sub>2</sub> O	18.07 <sup>66</sup>	-0.558
D <sub>2</sub> O	18.13 <sup>66</sup>	6.358
NaHCO <sub>3</sub> /Na <sub>2</sub> CO <sub>3</sub> buffer in 100 vol% D <sub>2</sub> O	18.04 <sup>V,65</sup>	6.376 <sup>VI</sup>
NaHCO <sub>3</sub> /Na <sub>2</sub> CO <sub>3</sub> buffer in 50 vol% D <sub>2</sub> O and 50 vol% H <sub>2</sub> O		2.918 <sup>VII</sup>
NaHCO <sub>3</sub> /Na <sub>2</sub> CO <sub>3</sub> buffer in 100 vol% H <sub>2</sub> O	17.98 <sup>V,65</sup>	-0.540 <sup>VI</sup>

<sup>I</sup>Measured, <sup>II</sup>Calculated from measured data and  $V_m(\text{H}^+) = -5.5 \text{ cm}^3 \text{ mol}^{-1}$  following additivity principles.<sup>65,67</sup>, <sup>III</sup>Assumed to be the same as for the hydrogenated species., <sup>IV</sup>Calculated assuming additivity of molar volumes., <sup>V</sup>Calculated assuming additivity of molar volumes and considering buffer composition., <sup>VI</sup>Calculated considering buffer composition., <sup>VII</sup>Calculated considering  $SLDs$  of buffers containing 100 vol% D<sub>2</sub>O and 100 vol% H<sub>2</sub>O.

### 6.6.3 Cryo transmission electron microscopy

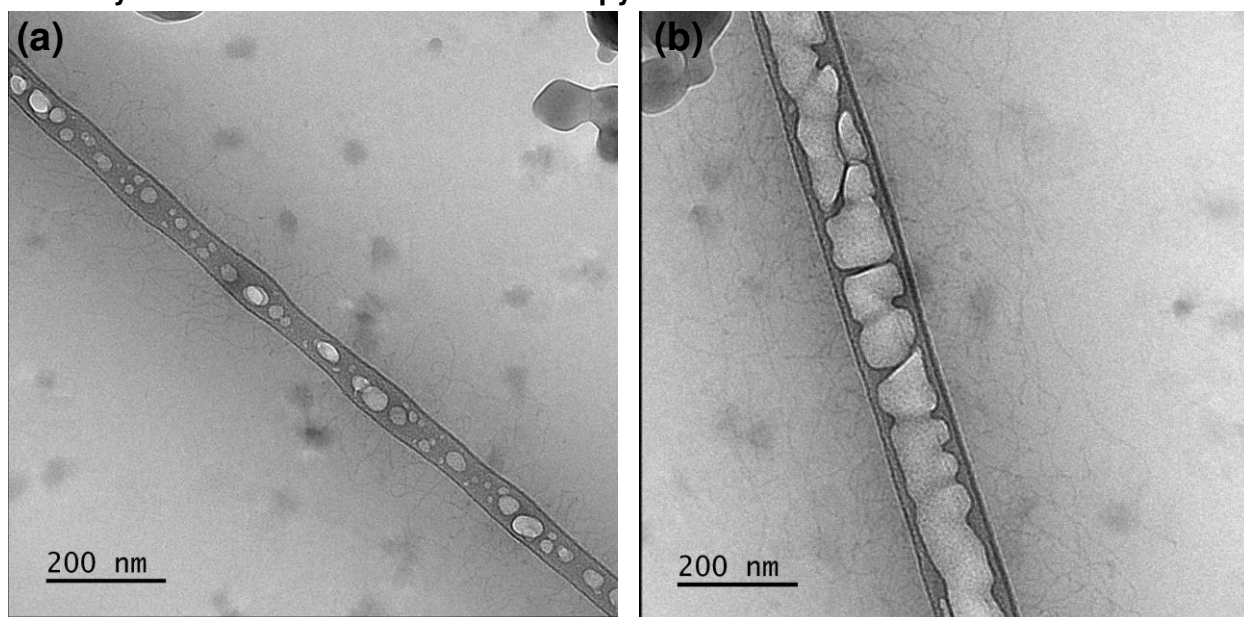


Figure S11: Cryo TEM images of a solution containing [Blue] = 10 mM and [DTAB] = 30 mM in an aqueous  $\text{NaHCO}_3/\text{Na}_2\text{CO}_3$  buffer with  $\text{pH} = 10.5$  and  $I \approx 0.25$  M.

### 6.6.4 Small-angle neutron scattering and assembly structure

**Pure DTAB micelles.** The size of pure DTAB micelles in the applied  $\text{NaHCO}_3/\text{Na}_2\text{CO}_3$  buffer ( $\text{pD} = 10.7$ ,  $I \approx 0.25$  M) in  $\text{D}_2\text{O}$  at  $25^\circ\text{C}$  was studied by recording SANS curves from solutions of three differently deuterated DTAB species, i.e.  $h_{34}$ -DTAB,  $d_{34}$ -DTAB and  $d_{25}$ -DTAB, with a total DTAB concentration of  $[\text{DTAB}] = 30$  mM (Figure S12).

Furthermore, a SANS curve was recorded from a solution containing DTAB with a concentration of  $[\text{DTAB}] = 30$  mM and at match composition (46 vol%  $d_{25}$ -DTAB and 54 vol%  $d_{34}$ -DTAB) and is also shown in Figure S12. The curve is lacking any  $q$ -dependence and thus confirms successful matching of the  $SLD$  of the DTAB mixture to the  $SLD$  of the solvent.

SANS curves from the other three samples were described using the product of a form- and a structure factor, as the use of a structure factor improved the fit in the low  $q$  regime. In all cases, a structure factor derived by Hayter and Penfold was used assuming a micellar charge of 15.<sup>40,41</sup> The assumption of a micellar charge of 15 resulted in a better fit compared to the assumption of a micellar charge of 10, 20, 30 or 50. It is emphasized, that the choice of a micellar charge within this range does not affect the resulting fit parameters ( $r_{\text{eq}}$  and  $r_{\text{p}}$ ), as these parameters agree when rounded to the nearest integer (investigation not shown). The salt concentration was set to the ionic strength of the buffer (0.25 M) and the  $\text{D}_2\text{O}$  dielectric constant was set to 78.06 considering the measurement temperature of  $25^\circ\text{C}$ .<sup>68</sup>

For describing SANS curves emerging from solutions of  $h_{34}$ -DTAB and  $d_{34}$ -DTAB, the form factor model of an oblate spheroid with homogeneously distributed scattering length density ( $SLD$ ) was used.<sup>37</sup> For describing the SANS curve emerging from a solution of  $d_{25}$ -DTAB, a core-shell structure was employed.<sup>69</sup> Results from form factor fitting are displayed in Table SI2. The structure of DTAB micelles was previously studied in NaBr solutions, corresponding either to oblate spheroids of revolution or to triaxial ellipsoids depending on the ionic strength of the solution.<sup>39</sup> The results from this reference agree with the dimensions of the DTAB micelles displayed in Table SI2.<sup>39</sup>

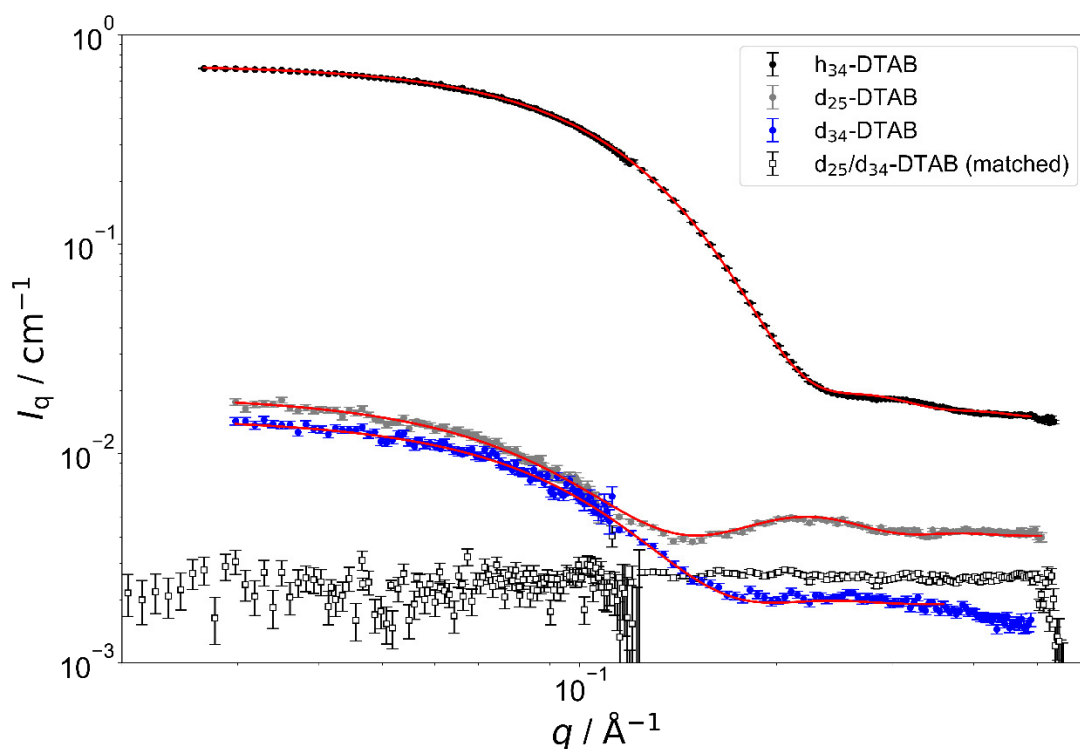


Figure SI2: SANS curves of solutions containing 30 mM DTAB with different degrees of deuteration in a  $\text{NaHCO}_3/\text{Na}_2\text{CO}_3$  buffer with  $\text{pD} = 10.7$  and ionic strength  $I \approx 0.25$  M.  $\text{D}_2\text{O}$  was used to prepare the buffer. From a solution containing 46 vol%  $d_{25}$ -DTAB and 54 vol%  $d_{34}$ -DTAB no  $q$ -dependent scattering is observed ( $\square$ ). Fits are shown as red lines and correspond to the product of the form factor of an oblate spheroid with a structure factor derived by Hayter and Penfold for  $h_{34}$ -DTAB and  $d_{34}$ -DTAB.<sup>40,41</sup> For  $d_{25}$ -DTAB, the product of the form factor of an oblate core-shell spheroid with the same structure factor was used.

However, Table SI2 reveals discrepancies between the radii of  $h_{34}$ -DTAB micelles and the radii of  $d_{34}$ -DTAB or  $d_{25}$ -DTAB micelles, obtained from form factor fits to corresponding SANS curves. A first attempt to explain these differences could be based on the occurrence of “isotope effects”, i.e. different sizes of micelles being caused by different degrees of deuteration of the surfactant. Such effects were previously observed for alkyltrimethylammoniumbromide surfactants when changing solvent composition in terms of  $\text{H}_2\text{O}/\text{D}_2\text{O}$  ratio in the solvent.<sup>50,70</sup> Conversely, the use of

differently deuterated species in the same solvent was previously not suspected to result in observable differences of assembly size and structure.<sup>71</sup> Furthermore, DLS data collected before the neutron experiment on the very same solutions do not suggest a change in size of DTAB micelles when varying its isotopic composition from h<sub>34</sub>-DTAB over d<sub>25</sub>-DTAB to d<sub>34</sub>-DTAB. Correlation functions of solutions containing [DTAB] = 30 mM in the NaHCO<sub>3</sub>/Na<sub>2</sub>CO<sub>3</sub> buffer in D<sub>2</sub>O overlap at all angles and are shown exemplarily for three angles in Figure SI3. Furthermore, fitting the correlation function with a single-exponential decay according to a revised method of cumulants (eq (SI3)) resulted in similar apparent diffusion coefficients  $D_{app}$  for solutions of all DTAB-species and at all probed angles (Figure SI4).<sup>63</sup> Finally, Table SI3 shows hydrodynamic radii  $R_h$  obtained for each DTAB-species. Apparent differences lay within the range of the error and micelles of h<sub>34</sub>-DTAB, d<sub>25</sub>-DTAB and d<sub>34</sub>-DTAB are therefore of the same size according to dynamic light scattering measurements. In addition to the hydrodynamic radii  $R_h$  of DTAB micelles, Table SI3 also shows radii of gyration obtained from linearized Guinier analysis of corresponding SANS curves (Figure SI5). Radii of gyration also agree within experimental uncertainty, with an average value of  $R_g = 15.8 \text{ \AA}$  and a maximum deviation of  $\Delta R_g = 1.7 \text{ \AA}$ .

Table SI2: Parameters resulting from fitting SANS curves of solutions containing differently deuterated DTAB species in an NaHCO<sub>3</sub>/Na<sub>2</sub>CO<sub>3</sub> buffer (pD = 10.7,  $I \approx 0.25 \text{ M}$ ) in D<sub>2</sub>O and at a concentration of [DTAB] = 30 mM. The scattering length density of the solvent  $SLD_{solvent}$  was fixed to  $6.376 \cdot 10^{-6} \text{ \AA}^{-2}$ . For fitting SANS curves from solutions of h<sub>34</sub>-DTAB or d<sub>34</sub>-DTAB, the form factor model of an oblate spheroid was used. For fitting the SANS curve from a solution of d<sub>25</sub>-DTAB, the form factor model of a core-shell oblate spheroid was used.

Surfactant	$r_{eq}$ Å	$r_p$ Å	$SLD$ $10^{-6} \text{ \AA}^{-2}$	$\chi^2$		
h <sub>34</sub> -DTAB	$22.357 \pm 0.009$	$14.048 \pm 0.008$	$-0.11 \pm 0.04$	12.667		
d <sub>34</sub> -DTAB	$25.6 \pm 0.7$	$19.3 \pm 1.0$	$7.1 \pm 0.2$	1.4089		
	$th$ Å	$r_{core,eq}$ Å	$r_{core,p}$ Å	$SLD_{core}$ $10^{-6} \text{ \AA}^{-2}$	$SLD_{shell}$ $10^{-6} \text{ \AA}^{-2}$	$\chi^2$
d <sub>25</sub> -DTAB	$7.1 \pm 0.8$	$17.5 \pm 0.6$	$11.9 \pm 1$	$6.80 \pm 0.08$	$5.1 \pm 0.3$	1.6331

$r_{eq}$  – equatorial radius,  $r_p$  – polar radius,  $SLD$  – scattering length density of scatterer,  $\chi^2$  – chi square parameter divided by the number of datapoints,  $th$  – shell thickness,  $r_{core,eq}$  – equatorial radius of the core,  $r_{core,p}$  – polar radius of the core,  $SLD_{core}$  – scattering length density of the core,  $SLD_{shell}$  – scattering length density of the shell

It was previously suggested that small differences in scattering contrast ( $\Delta SLD < 2 \cdot 10^{-6} \text{ \AA}^{-2}$ ) do not permit an accurate size determination, referring to the thickness of the shell in a core-shell structure.<sup>72</sup> Considering the small difference in the scattering length densities ( $SLDs$ ) between the solvent (NaHCO<sub>3</sub>/Na<sub>2</sub>CO<sub>3</sub> buffer in 100 vol% D<sub>2</sub>O) and the trimethylammoniumbromide head

group  $N(\text{CD}_3)_3\text{Br}$  (Table SI1) of the  $d_{34}$ -DTAB molecule, this could be the case for  $d_{34}$ -DTAB. To verify this assumption, experiments with solvents containing varying  $\text{H}_2\text{O}/\text{D}_2\text{O}$  ratios would need to be performed and compared to isotope effects caused by the use of different solvents with small-angle X-ray scattering. Here, we abstained from such an analysis and the differences were attributed to uncertainties in the  $SLD$  values. This is backed by DLS investigations, which reveal the same hydrodynamic radius  $R_h$  for  $h_{34}$ -DTAB,  $d_{25}$ -DTAB and  $d_{34}$ -DTAB micelles thus discarding isotope effects. Furthermore, the dimensions of the  $h_{34}$ -DTAB micelle were used for further evaluation and discussion, as the highest SANS scattering contrast between surfactant micelle and solvent is obtained in this sample.

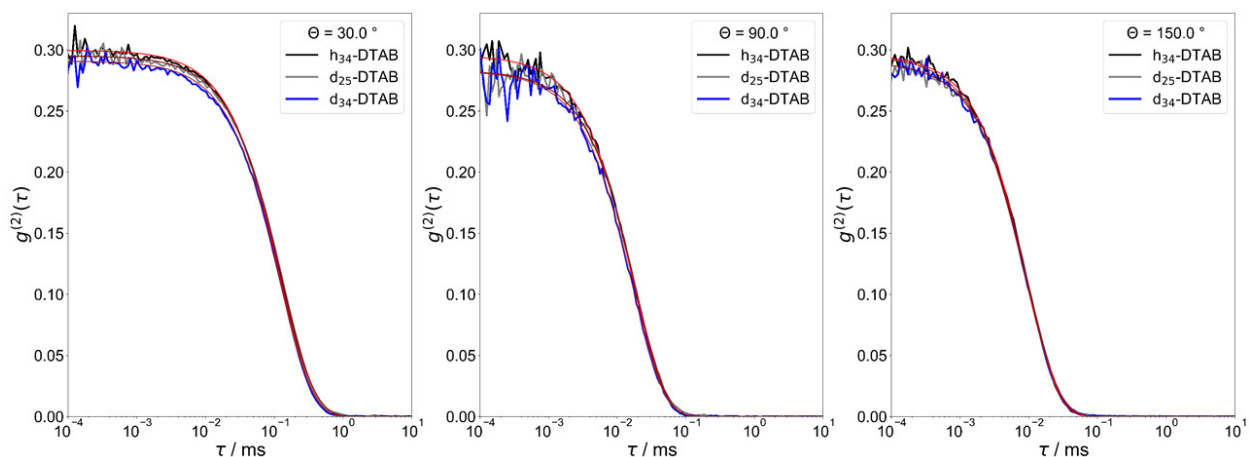


Figure SI3: Intensity correlation functions  $g^{(2)}(\tau)$  obtained from DLS measurements with solutions containing  $h_{34}$ -DTAB,  $d_{25}$ -DTAB or  $d_{34}$ -DTAB at a concentration of  $[\text{DTAB}] = 30 \text{ mM}$  in a  $\text{NaHCO}_3/\text{Na}_2\text{CO}_3$  buffer ( $\text{pD} = 10.7$ ,  $I \approx 0.25 \text{ M}$ ) in  $\text{D}_2\text{O}$ . Mono exponential fits according to the revised method of cumulants eq (SI3) are shown in red ( $h_{34}$ -DTAB), dark red ( $d_{25}$ -DTAB) or brown ( $d_{34}$ -DTAB). Measurement angles  $\Theta$  are indicated.  $\tau$  is the correlation time. Due to device-specific configurations, a maximum  $g^{(2)}(\tau)$  of 0.33 is expected.



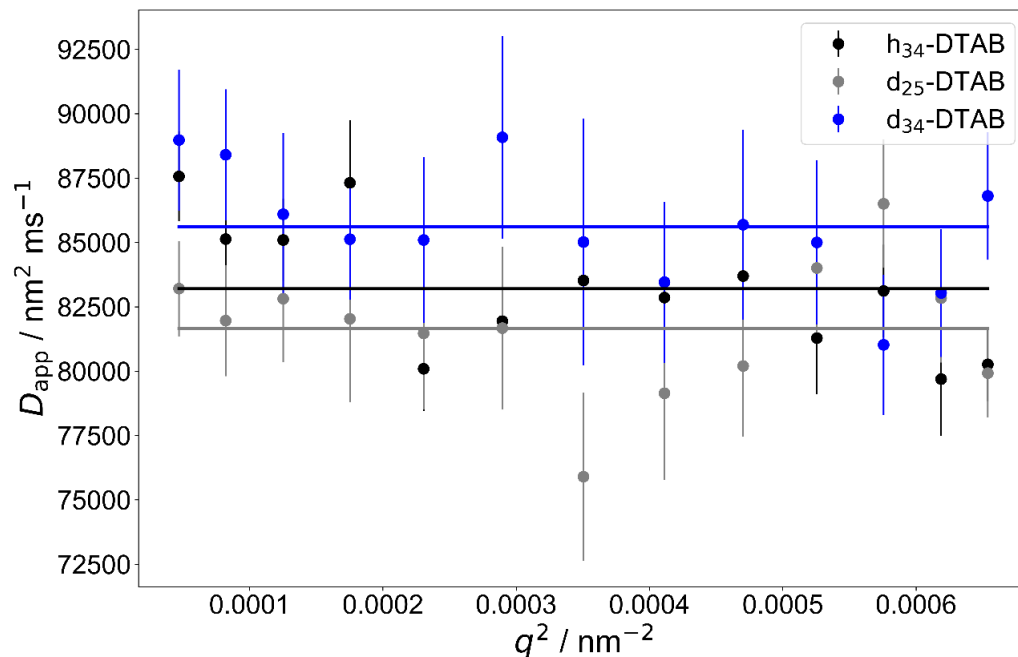


Figure S14: Apparent diffusion coefficient obtained for DTAB micelles from mono exponential fitting of intensity correlation functions from DLS measurements at different angles according to a revised method of cumulants.<sup>63</sup> Correlation functions were obtained from solutions containing [DTAB] = 30 mM in a NaHCO<sub>3</sub>/Na<sub>2</sub>CO<sub>3</sub> buffer (pD = 10.7,  $I \approx 0.25$  M) in D<sub>2</sub>O. As no angular dependency was observed, horizontal lines indicate the average of all  $D_{app}$  for each DTAB species (black: h<sub>34</sub>-DTAB, grey: d<sub>25</sub>-DTAB, blue: d<sub>34</sub>-DTAB).

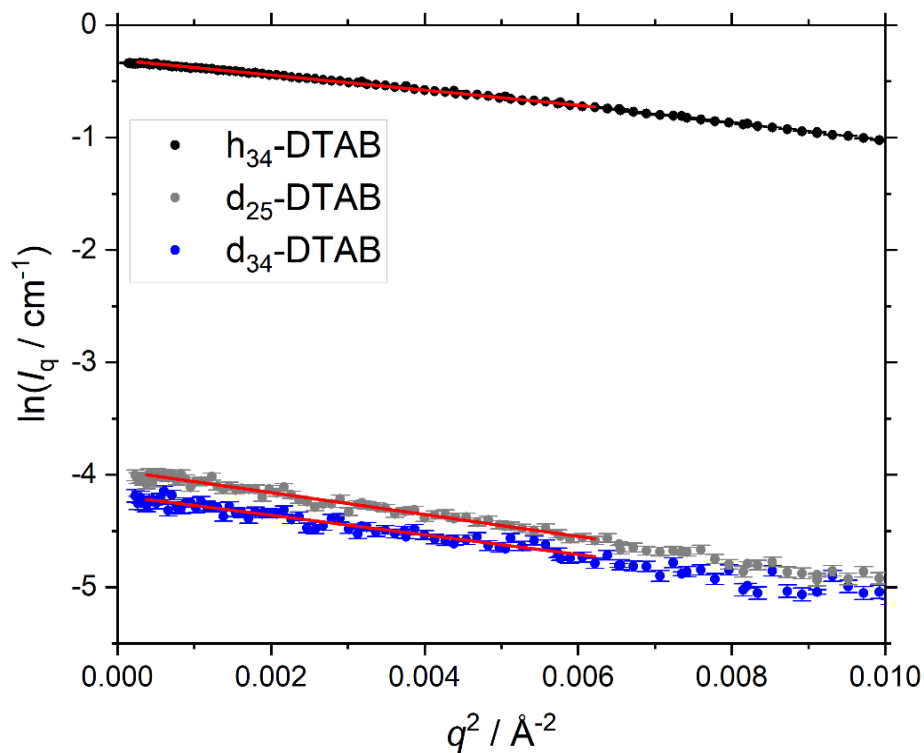


Figure S15: Linearized Guinier plot and Guinier fits (red lines) of SANS curves of solutions containing of [DTAB] = 30 mM in a NaHCO<sub>3</sub>/Na<sub>2</sub>CO<sub>3</sub> buffer (pD = 10.7,  $I \approx 0.25$  M) in D<sub>2</sub>O. The colour code has the same meaning as in Figure S12.

Table SI3: Diffusion coefficient  $D$ , hydrodynamic radius  $R_h$ , radius of gyration  $R_g$  and  $R_g/R_h$  of micelles of differently deuterated DTAB species at a concentration of  $[DTAB] = 30$  mM in a  $\text{NaHCO}_3/\text{Na}_2\text{CO}_3$  buffer ( $\text{pD} = 10.7$ ,  $I \approx 0.25$  M) in  $\text{D}_2\text{O}$ . Diffusion coefficients were obtained by averaging apparent diffusion coefficients  $D_{\text{app}}$  obtained at different measurements angles. Their errors correspond to the standard deviation of  $D_{\text{app}}$ . Apparent diffusion coefficients are shown as a function of  $q$  in Figure SI4. Radii of gyration were obtained from a linearized Guinier analysis shown in Figure SI5.

Surfactant	$D$ $\text{nm}^2 \text{ms}^{-1}$	$R_h$ $\text{\AA}$	$R_g$ $\text{\AA}$	$R_g/R_h$
$\text{h}_{34}$ -DTAB	$8.3 \pm 0.3$	$22.7 \pm 0.8$	$14.18 \pm 0.04$	$0.62 \pm 0.03$
$\text{d}_{25}$ -DTAB	$8.2 \pm 0.3$	$23.1 \pm 0.8$	$17.1 \pm 0.3$	$0.74 \pm 0.05$
$\text{d}_{34}$ -DTAB	$8.6 \pm 0.3$	$22.0 \pm 0.7$	$16.2 \pm 0.3$	$0.74 \pm 0.05$

**Wormlike micelles and dependency on absolute concentration.** Figure SI6 shows SANS curves of solutions containing Blue and DTAB with a molar ratio of  $[\text{Blue}]:[\text{DTAB}] = 1:3$  at different absolute concentrations. The inset shows the Holtzer plot of the same curves. Three features shall be outlined in detail. (1) A significant scattering signal due to the formation of micellar assemblies is observed from a sample containing  $[\text{Blue}] = 2.5$  mM and  $[\text{DTAB}] = 7.5$  mM.  $[\text{DTAB}] = 7.5$  mM lays below the critical micelle concentration (cmc) of pure DTAB (9 mM in the employed buffer system), which shows that the addition of Blue lowers the cmc of pure DTAB. This was reported in a previous publication and is commonly observed for the addition of solute to surfactant systems.<sup>33,73</sup> (2) All SANS curves are well described with the form factor model of a flexible cylinder with elliptical cross section with cross section dimensions  $r_{\text{minor}}$  and  $r_{\text{major}}$  remaining almost constant for all samples (Table SI4). In addition to a form factor fit according to this model, Figure SI6 also shows form factor fits of the same curves using the form factor model of a flexible cylinder with circular cross section and polydispersity in the cross section radius. This polydispersity was considered by a number-weighted Schulz distribution of the cross section radius and the relative standard deviation of the number average cross section radius was fixed to  $\sigma/\bar{r} = 0.14$ . As visible from Figure SI6 at  $q > 0.2 \text{ \AA}^{-1}$ , SANS curves are better described with an elliptical rather than a polydisperse circular cross section. In order to well describe the SANS curves using a circular cross section, the polydispersity of the radius would have to be increased, which is less reasonable for the presented system, as the defined hydrophobic chain length and head group size of DTAB molecules does not permit a strong variation in cross section dimensions. (3) The flexibility of wormlike micelles formed from Blue and DTAB is confirmed by a distinct maximum in the Holtzer plot of experimental SANS curves (inset in Figure SI6), which

verifies that the contour length  $L$  of these micelles exceeds their persistence length  $l_p$ .<sup>4</sup> Considering the dynamic equilibrium in micellar solutions and the length polydispersity found for cylindrical Blue-DTAB micelles (Table 1, main document), a size distribution of the contour length  $L$  of flexible cylinders is likely.<sup>74</sup> However, to avoid overparameterization of the fit, this was not considered in the analysis shown in Figure SI6, leading to a systematic deviation of the employed form factor model from the data towards lower forward scattering intensities in the low- $q$  region. Results from fitting the form factor of a flexible cylinder with elliptical cross section to the four experimental SANS curves are shown in Table SI4.

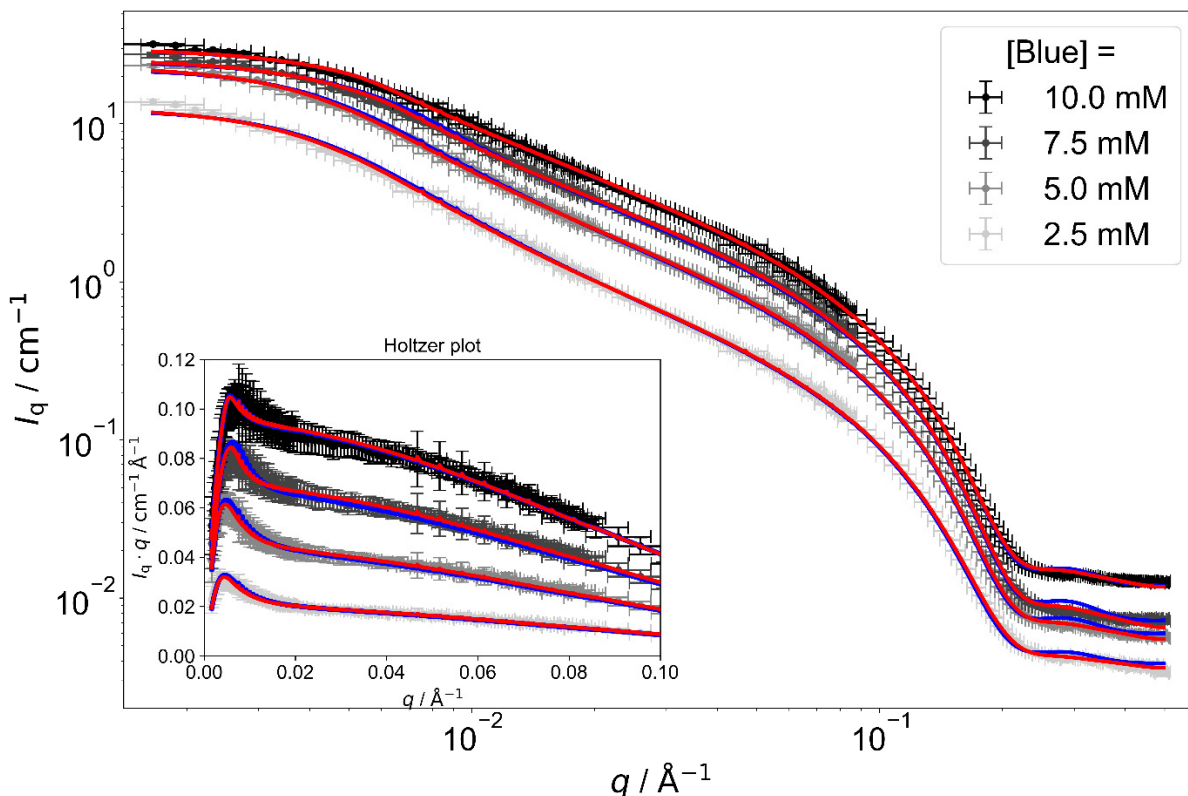


Figure SI6: Full contrast SANS curves from solutions containing Blue and DTAB at a molar ratio of [Blue]:[DTAB] = 1:3 with absolute concentrations of Blue given in the legend. Solutions were prepared in a  $\text{NaHCO}_3/\text{Na}_2\text{CO}_3$  buffer ( $\text{pD} = 10.7$ ,  $l \approx 0.25 \text{ M}$ ) in  $\text{D}_2\text{O}$ . The inset shows the Holtzer plot of experimental SANS curves including model fits. Red curves correspond to fits according to the form factor model of a flexible cylinder with elliptical cross section. Blue curves correspond to fits according to the form factor model of a flexible cylinder with circular cross section and set relative standard deviation of the cross section radius ( $\sigma/\bar{r} = 0.14$ ) considering a number-weighted Schulz distribution of the cross section radius. Fit parameters can be found in Table SI6. Reduced  $\chi^2$  values are compared in Table SI5.

Table SI4: Parameters from fitting the form factor model of flexible cylinders with elliptical cross section to full contrast SANS-curves of solutions containing Blue and DTAB at a molar ratio of 1:3 in an aqueous NaHCO<sub>3</sub>/Na<sub>2</sub>CO<sub>3</sub> buffer with pD = 10.7 and  $l \approx 0.25$  M. Corresponding fits are shown as red curves in Figure SI6 and Figure SI7.

[Blue]	[DTAB]	Cross section		$L_{\text{contour}}$ Å	$l_p$ Å	$SLD$ $10^{-6} \text{Å}^{-2}$	Red. $\chi^2$
		$r_{\text{minor}}$ Å	$r_{\text{major}}$ Å				
2.5	7.5	13.79 $\pm 0.03$	21.2 $\pm$ 2	2049 $\pm 25$	170 $\pm$ 1	2.289 $\pm 0.006$	2.0045
5	15	13.92 $\pm 0.02$	21.19 $\pm 0.07$	1705 $\pm 12$	209 $\pm$ 1	2.113 $\pm 0.004$	2.7727
7.5	22.5	13.99 $\pm 0.01$	21.22 $\pm 0.04$	1184 $\pm$ 8	257 $\pm$ 2	2.001 $\pm 0.003$	8.4383
10	30	14.05 $\pm 0.01$	21.15 $\pm 0.04$	1000 $\pm$ 6	300 $\pm$ 3	1.910 $\pm 0.002$	12.326
Average		<b>13.94</b>	<b>21.18</b>		<b>234</b>		

It can be seen, that an increase in absolute concentration results in a decrease of the contour length and absolute scattering length density of the assembly ( $SLD$ ), whereas the persistence length  $l_p$  apparently increases. As  $L$  is not significantly larger than  $l_p$ , the value obtained for  $l_p$  likely contains a relatively high error and it is not clear whether the observed trend for  $l_p$  is real or an artefact from the applied fitting procedure. For this reason, a separate form factor fit was performed, where  $l_p$  was kept constant to the average of  $l_p$  for all four samples. Furthermore, the cross section dimension of the flexible elliptical cylinder was kept constant in the second fit, so that only  $L$  and the  $SLD$  of the assembly were varied. Polydispersity of the contour length needed to be introduced to describe the low- $q$  region well. Resulting fits are compared to the model fits already shown in Figure SI6 in Figure SI7.

As anticipated, introduction of a polydispersity for  $L$  improved the fit in the low- $q$  region. However, overall fit quality was slightly worse compared to the initial fit for two of the four SANS curves, which can be seen from Table SI5 by comparing corresponding reduced  $\chi^2$  parameters. This likely results from keeping  $l_p$  constant. Nevertheless, parameters resulting from the described analysis are displayed in Figure SI8.

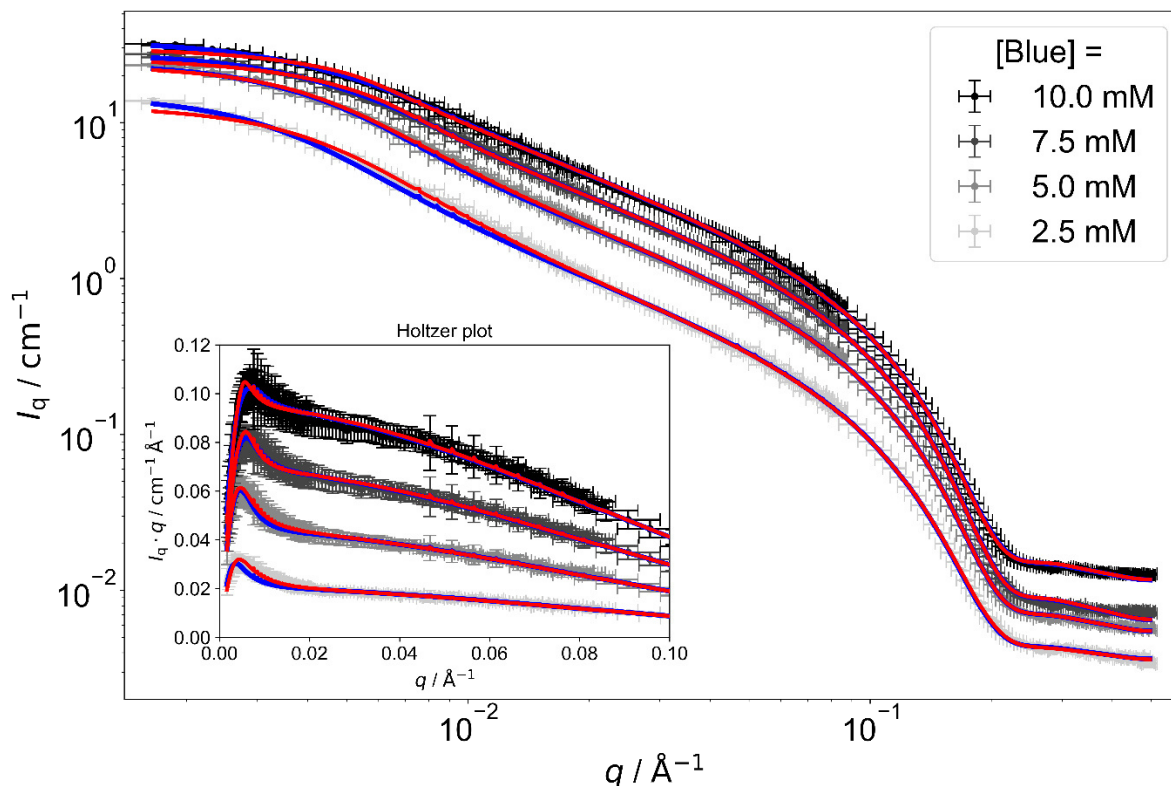


Figure S17: Full contrast SANS-curves from solutions containing Blue and DTAB at a molar ratio of [Blue]:[DTAB] = 1:3 with absolute concentrations of Blue given in the legend. Solutions were prepared in a  $\text{NaHCO}_3/\text{Na}_2\text{CO}_3$  buffer ( $\text{pD} = 10.7$ ,  $I \approx 0.25$  M) in  $\text{D}_2\text{O}$ . The inset shows the Holtzer plot of experimental SANS curves including model fits. Red curves correspond to fits according to the form factor model of a flexible cylinder with elliptical cross section, which was employed first. Corresponding parameters were given in Table S14. Blue lines display form factor fits according to the same model where the persistence length  $l_p$  was kept constant and a number-weighted Schulz distribution of the contour length  $L$  was assumed. Fit parameters are visualized in Figure S18 and reduced  $\chi^2$  values compared in Table S15.

Analogous to the initial analysis, a decrease in contour length and  $SLD$  is observed when increasing the absolute concentration of Blue and DTAB at constant molar ratio. The consistency of observed trends for both fitting procedures permits the following conclusive interpretation of these results. An increase in absolute concentration results in a shortening of wormlike micelles formed from Blue and DTAB, increasing the relative amount of cylinder end caps in the system and therefore the spontaneous curvature of Blue-DTAB assemblies. An increase of the spontaneous curvature of assemblies with increasing total concentration was previously reported in literature: Bergström and Pedersen observed that an increase in the absolute concentration of mixed DTAB/SDS micelles resulted in a decrease of micelle size, which was caused by an increase in spontaneous curvature of the assemblies.<sup>13</sup> Similarly, Verma et al. observed the increase of the spontaneous curvature of cetyltrimethylammoniumbromide/sodium salicylate bilayer structures which transformed to wormlike micelles at higher absolute concentrations.<sup>75</sup>

According to references 13 and 75, the increase in the spontaneous curvature of assemblies with increasing absolute concentration is easily explained by an increase of DTAB-concentration within dye-surfactant micelles upon increasing total concentration. The discrepancy between the overall DTAB content of the solution and the amount of DTAB in the Blue-surfactant co-assembly is caused by a cmc, which keeps some DTAB molecules as free monomers in bulk solution. The concentration of free monomer corresponds to the cmc of DTAB in the given system. Considering a constant concentration of free monomer this means that at higher absolute DTAB concentrations the ratio between the number of DTAB molecules participating in micelle formation and the number of monomeric DTAB molecules is higher compared to lower absolute DTAB concentrations. Therefore, higher absolute concentrations lead to a higher percentage of DTAB molecules participating in micelle formation, which leads to a decrease in the contour length. This assumption is reinforced by the observation of a decreasing *SLD* of Blue-DTAB assemblies with higher absolute concentrations, indicating that the *SLD* of the co-assembly gets closer to the *SLD* of DTAB or of the dodecyltrimethylammonium cation  $\text{DTA}^+$ , which is given in Figure SI8.

Table SI5: Comparison of reduced  $\chi^2$  values for different fits to SANS curves of samples containing Blue and DTAB at a molar ratio of 1:3 in a  $\text{NaHCO}_3/\text{Na}_2\text{CO}_3$  buffer (pD = 10.7,  $I \approx 0.25$  M) in  $\text{D}_2\text{O}$ .

[Blue]	[DTAB]	Flexible cylinder with elliptical cross section Red. $\chi^2$	Flexible cylinder with circular cross section and $\sigma/\bar{r} = 0.14$ Red. $\chi^2$	Flexible cylinder with elliptical cross section and $l_p = 234 \text{ \AA}$ Red. $\chi^2$
2.5	7.5	2.00	12.12	6.60
5	15	2.78	40.13	4.35
7.5	22.5	8.44	88.01	7.67
10	30	12.33	17.20	12.35

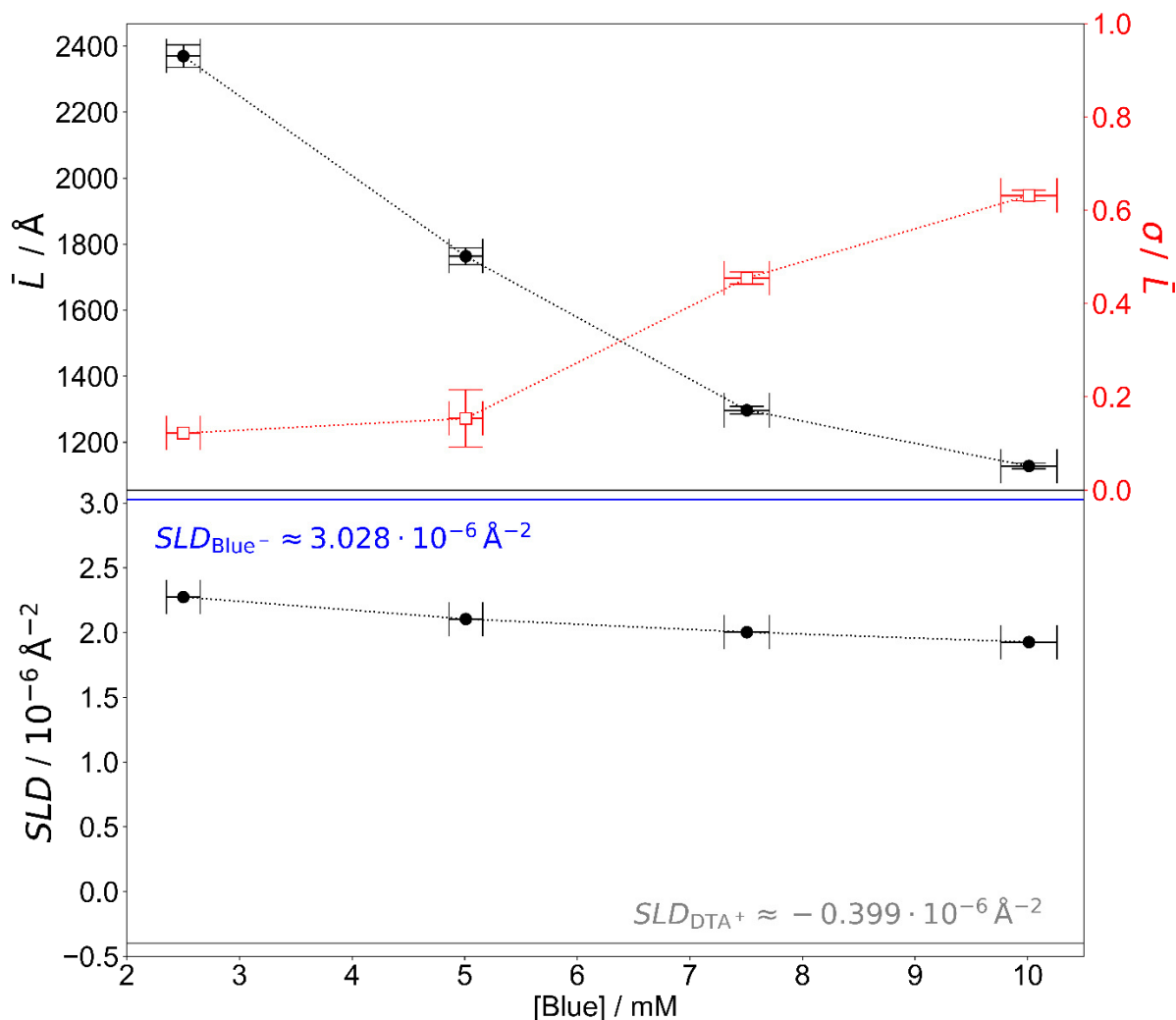


Figure S18: Parameters resulting from fitting the form factor model of flexible cylinders with elliptical cross section to SANS curves of samples containing Blue and DTAB at a molar ratio of 1:3. The persistence length  $l_p = 234 \text{Å}$  and dimensions of the cylinder cross section ( $r_{\text{minor}} = 13.94 \text{Å}$ ,  $r_{\text{major}} = 21.18 \text{Å}$ ) were kept constant (Table SI4). The number average contour length  $\bar{L}$ , the relative standard deviation of the number-average contour length assuming a Schulz distribution ( $\sigma/\bar{L}$ ) as well as the  $SLD$  of the assembly were fitted. Fits are shown as blue curves in Figure SI7. Reduced  $\chi^2$ -values can be found in Table SI5.

To conclude this section, the formation of wormlike micelles with elliptical cross section was observed for samples containing Blue and DTAB at a molar ratio of [Blue]:[DTAB] = 1:3. The cross section dimensions were observed to be similar for all samples. An increase in absolute concentration resulted in shortening of the wormlike micelles, which is easily explained by an increase of the [DTAB]:[Blue] ratio in the Blue-DTAB assemblies at higher absolute concentrations and a concomitant reduction in spontaneous curvature of the assembly.

Table S16: Complete parameter sets from form factor fitting of experimental SANS curves. The reduced  $\chi^2$  parameter is displayed. The scattering length density of the solvent was fixed to  $SLD_{\text{solvent}} = 6.376 \cdot 10^{-6} \text{ \AA}^{-2}$  for all samples except for the sample containing [Blue] = 5 mM and [DTAB] = 30 mM in the full contrast measurement, where  $SLD_{\text{solvent}}$  was fixed to  $2.918 \cdot 10^{-6} \text{ \AA}^{-2}$  according to solvent composition. Fits assuming an elliptical assembly cross section are compared to fits assuming a circular assembly cross section with fixed relative standard deviation of the cross section radius ( $\sigma/\bar{r} = 0.14$ ). A number-weighted Schulz distribution of the cross section radius was assumed, hence  $\bar{r}$  corresponds to the number average cross section radius. Polydispersity in the cross section radius was not considered for fitting SANS curves from samples within which the  $SLD$  of DTAB was matched to  $SLD_{\text{solvent}}$  to avoid over parameterization. In cases where the form factor model of a cylinder was used, a number-weighted Schulz distribution of cylinder length with a relative standard deviation of  $\sigma/\bar{L} = 0.95$  was assumed with  $L$  being the number-average cylinder length. In cases, where the form factor model of a triaxial ellipsoid was used, the following relation between radii of the three semi-axes was respected:  $r_{\text{core,minor}} < r_{\text{core,major}} < r_{\text{core,L}}$  for full contrast SANS curves and  $r_{\text{core,minor}} < r_{\text{core,major}} < r_{\text{core,L}}$  for DTAB matched SANS curves. In core-shell models  $th$  is the shell thickness.

[Blue] mM	[DTAB] mM	Elliptical cross section					Circular cross section						
		Mode/Model	$r_{\text{minor}}$ $\text{\AA}$	$r_{\text{major}}$ $\text{\AA}$	Length $\text{\AA}$	$SLD$ $10^{-6} \text{ \AA}^{-2}$	Red. $\chi^2$	Mode/Model	$r$ $\text{\AA}$	$\sigma/\bar{r}$	Length $\text{\AA}$	$SLD$ $10^{-6} \text{ \AA}^{-2}$	Red. $\chi^2$
5	30	<b>Full contrast/</b> Triaxial ellipsoid	$15.3 \pm 0.2$	$22.0 \pm 0.3$	$32 \pm 0.3$	$5.778 \pm 0.004$	1.319	<b>Full contrast/</b> Ellipsoid	$\bar{r} = 17.5 \pm 0.2$	$\sigma/\bar{r} = 0.14$ (fixed)	$31.8 \pm 0.0.6$	$5.78 \pm 0.02$	1.259
		<b>DTAB matched/</b> Triaxial core-shell ellipsoid	$r_{\text{core,minor}} = 14.4$ $th = 4.7 \pm 0.9$	$r_{\text{core,major}} = 20.7$ $th = 4.7 \pm 0.9$	$r_{\text{core,L}} = 30$ (fixed)	$5.4 \pm 0.2$	1.424	<b>DTAB matched/</b> Core-shell ellipsoid	$r_{\text{core}} = 19.8 \pm 0.7$ $th = 1.4 \pm 1.1$	-	$r_{\text{core,L}} = 34 \pm 2$ $th = 1.4 \pm 1.1$	$5.1 \pm 0.4$	1.350
		<b>DTAB matched/</b> Triaxial core-shell ellipsoid	$r_{\text{core,minor}} = 14.4$ $th = 1.59 \pm 0.02$	$r_{\text{core,major}} = 20.7$ $th = 1.59 \pm 0.02$	$r_{\text{core,L}} = 30$ (fixed)	$3.028$ (fixed)	1.563	<b>DTAB matched/</b> Core-shell ellipsoid	$r_{\text{core}} = 20.3 \pm 0.4$ $th = 0.512 \pm 0.008$	-	$r_{\text{core,L}} = 34.5 \pm 0.7$ $th = 0.512 \pm 0.008$	$3.028$ (fixed)	1.342
5	22.5	<b>Full contrast/</b> Elliptical cylinder	$14.78 \pm 0.02$	$21.21 \pm 0.06$	$\bar{L} = 73.4 \pm 2$ $\sigma/\bar{L} = 0.95$	$1.135 \pm 0.001$	16.20	<b>Full contrast/</b> Cylinder	$\bar{r} = 16.891 \pm 0.005$	$\sigma/\bar{r} = 0.14$ (fixed)	$\bar{L} = 74.5 \pm 0.2$ $\sigma/\bar{L} = 0.95$	$1.130 \pm 0.001$	18.62
		<b>DTAB matched/</b> Elliptical core-shell cylinder	$r_{\text{core,minor}} = 13.4 \pm 0.4$ $th = 3.3 \pm 0.5$	$r_{\text{core,major}} = 19.2 \pm 0.5$ $th = 3.3 \pm 0.5$	$\bar{L} = 73$ $\sigma/\bar{L} = 0.95$ (fixed)	$5.6 \pm 0.2$	1.963	<b>DTAB matched/</b> Core-shell cylinder	$r_{\text{core}} = 17.1 \pm 0.6$ $th = 3.6 \pm 0.7$	-	$\bar{L} = 74.5$ $\sigma/\bar{L} = 0.95$ (fixed)	$5.34 \pm 0.08$	4.468
		<b>DTAB matched/</b> Elliptical core-shell cylinder	$r_{\text{core,minor}} = 14.7 \pm 0.3$ $th = 0.748 \pm 0.006$	$r_{\text{core,major}} = 21.2 \pm 0.4$ $th = 0.748 \pm 0.006$	$\bar{L} = 73$ $\sigma/\bar{L} = 0.95$ (fixed)	$3.028$ (fixed)	1.768	<b>DTAB matched/</b> Core-shell cylinder	$r_{\text{core}} = 17.5 \pm 0.3$ $th = 0.333 \pm 0.005$	-	$\bar{L} = 74.5$ $\sigma/\bar{L} = 0.95$ (fixed)	$3.028$ (fixed)	1.627



7.5	30	<p><b>Full contrast/</b> Elliptical cylinder  <math>14.336 \pm 0.009</math></p> <p><b>DTAB matched/</b> Elliptical core-shell cylinder  <math>r_{\text{core,minor}} = 14.5 \pm 0.2</math>  <math>th = 2.1 \pm 0.4</math></p> <p><b>DTAB matched/</b> Elliptical core-shell cylinder  <math>r_{\text{core,minor}} = 15.7 \pm 0.2</math>  <math>th = 0.874 \pm 0.004</math></p>	$21.19 \pm 0.04$ $r_{\text{core,major}} = 21.4 \pm 0.3$ $th = 2.1 \pm 0.4$ $r_{\text{core,major}} = 23.3 \pm 0.2$ $th = 0.874 \pm 0.004$	$\bar{L} = 148 \pm 1$ $\sigma\bar{L} = 0.95$ $\bar{L} = 148$ $\sigma\bar{L} = 0.95$ (fixed) $\bar{L} = 148$ $\sigma\bar{L} = 0.95$ (fixed)	$1.059 \pm 0.001$ $5.0 \pm 0.2$ $3.028$ (fixed)	$15.71$ $2.717$ $8.189$	<p><b>Full contrast/</b> Cylinder  <math>\bar{r} = 16.621 \pm 0.003</math>  <math>\sigma\bar{r} = 0.14</math> (fixed)  <math>L = 151.0 \pm 0.4</math>  <math>\sigma\bar{L} = 0.95</math></p> <p><b>DTAB matched/</b> core-shell cylinder  <math>r_{\text{core}} = 16.9 \pm 0.3</math>  <math>th = 4.0 \pm 0.4</math>  <math>\bar{L} = 151</math>  <math>\sigma\bar{L} = 0.95</math> (fixed)</p> <p><b>DTAB matched/</b> core-shell cylinder  <math>r_{\text{core}} = 18.6 \pm 0.2</math>  <math>th = 0.573 \pm 0.004</math>  <math>\bar{L} = 151</math>  <math>\sigma\bar{L} = 0.95</math> (fixed)</p>	$1.061 \pm 0.001$ $5.34 \pm 0.06$ $3.028$ (fixed) $3.028$ (fixed)	$20.43$ $8.276$ $8.245$
2.5	7.5	<p><b>Full contrast/</b> Elliptical flexible cylinder  <math>13.79 \pm 0.03</math></p> <p><b>DTAB matched/</b> Elliptical core-shell cylinder  <math>r_{\text{core,minor}} = 10.3 \pm 0.6</math>  <math>th = 4.1 \pm 1.0</math></p> <p><b>DTAB matched/</b> Elliptical core-shell cylinder  <math>r_{\text{core,minor}} = 11.5 \pm 0.4</math>  <math>th = 1.43 \pm 0.03</math></p>	$21.2 \pm 2$ $r_{\text{core,major}} = 15.6 \pm 0.9$ $th = 4.1 \pm 1.0$ $r_{\text{core,major}} = 17.4 \pm 0.5$ $th = 1.43 \pm 0.03$	$L = 2049 \pm 25$ $l_p = 170 \pm 1$ $L = l_p = 170$ (fixed) $L = l_p = 170$ (fixed)	$2.289 \pm 0.006$ $5.1 \pm 0.4$ $3.028$ (fixed)	$2.005$ $2.009$ $1.708$	<p><b>Full contrast/</b> Flexible cylinder  <math>\bar{r} = 17.108 \pm 0.009</math>  <math>\sigma\bar{r} = 0.14</math> (fixed)  <math>L = 2057 \pm 22</math>  <math>l_p = 153 \pm 2</math></p> <p><b>DTAB matched/</b> Core-shell cylinder  <math>r_{\text{core}} = 11.6 \pm 1.2</math>  <math>th = 4.7 \pm 0.5</math>  <math>L = l_p = 153</math> (fixed)</p> <p><b>DTAB matched/</b> Core-shell cylinder  <math>r_{\text{core}} = 14.0 \pm 0.4</math>  <math>th = 1.03 \pm 0.03</math>  <math>L = l_p = 153</math> (fixed)</p>	$1.406 \pm 0.003$ $4.8 \pm 0.2$ $3.028$ (fixed) $3.028$ (fixed)	$12.12$ $1.717$ $1.612$
5	15	<p><b>Full contrast/</b> Elliptical flexible cylinder  <math>13.92 \pm 0.02</math></p> <p><b>DTAB matched/</b> Elliptical core-shell cylinder  <math>r_{\text{core,minor}} = 10.9 \pm 0.5</math>  <math>th = 3.5 \pm 0.8</math></p> <p><b>DTAB matched/</b> Elliptical core-shell cylinder  <math>r_{\text{core,minor}} = 11.7 \pm 0.3</math>  <math>th = 1.41 \pm 0.02</math></p>	$21.19 \pm 0.07$ $r_{\text{core,major}} = 16.5 \pm 0.7$ $th = 3.5 \pm 0.8$ $r_{\text{core,major}} = 17.8 \pm 0.4$ $th = 1.41 \pm 0.02$	$L = 1705 \pm 12$ $l_p = 209 \pm 1$ $L = l_p = 209$ (fixed) $L = l_p = 209$ (fixed)	$2.113 \pm 0.004$ $4.9 \pm 0.3$ $3.028$ (fixed)	$2.773$ $1.143$ $2.066$	<p><b>Full contrast/</b> Flexible cylinder  <math>\bar{r} = 17.091 \pm 0.006</math>  <math>\sigma\bar{r} = 0.14</math> (fixed)  <math>L = 1714 \pm 14</math>  <math>l_p = 178 \pm 2</math></p> <p><b>DTAB matched/</b> Core-shell cylinder  <math>r_{\text{core}} = 12.6 \pm 0.8</math>  <math>th = 4.9 \pm 0.4</math>  <math>L = l_p = 178</math> (fixed)</p> <p><b>DTAB matched/</b> Core-shell cylinder  <math>r_{\text{core}} = 14.6 \pm 0.3</math>  <math>th = 0.97 \pm 0.02</math>  <math>L = l_p = 178</math> (fixed)</p>	$1.199 \pm 0.002$ $4.93 \pm 0.07$ $3.028$ (fixed) $3.028$ (fixed)	$40.13$ $2.182$ $1.947$

7.5	22.5	<p><b>Full contrast/</b> Elliptical flexible cylinder</p> <p><math>r_{\text{core,minor}} = 13.99 \pm 0.01</math></p> <p><math>r_{\text{core,major}} = 21.22 \pm 0.04</math></p> <p><math>L = 1184 \pm 8</math> <math>l_p = 257 \pm 2</math></p>	<p><b>Full contrast/</b> Flexible cylinder</p> <p><math>\bar{r} = 17.074 \pm 0.004</math></p> <p><math>\sigma/\bar{r} = 0.14</math> (fixed)</p> <p><math>L = 1200 \pm 7</math> <math>l_p = 214 \pm 2</math></p>	<p>88.01</p> <p>1.067 <math>\pm 0.002</math></p>
		<p><b>DTAB matched/</b> Elliptical core-shell cylinder</p> <p><math>r_{\text{core,minor}} = 11.1 \pm 0.5</math> <math>th = 4.0 \pm 0.8</math></p> <p><math>r_{\text{core,major}} = 16.9 \pm 0.7</math> <math>th = 4.0 \pm 0.8</math></p> <p><math>L = l_p = 257</math> (fixed)</p>	<p><b>DTAB matched/</b> Core-shell cylinder</p> <p><math>r_{\text{core}} = 13.3 \pm 0.7</math> <math>th = 5.0 \pm 0.5</math></p> <p><math>L = l_p = 214</math> (fixed)</p>	<p>1.311</p> <p>5.10 <math>\pm 0.06</math></p>
		<p><b>DTAB matched/</b> Elliptical core-shell cylinder</p> <p><math>r_{\text{core,minor}} = 12.3 \pm 0.3</math> <math>th = 1.22 \pm 0.02</math></p> <p><math>r_{\text{core,major}} = 18.7 \pm 0.4</math> <math>th = 1.22 \pm 0.02</math></p> <p><math>L = l_p = 257</math> (fixed)</p>	<p><b>DTAB matched/</b> Core-shell cylinder</p> <p><math>r_{\text{core}} = 15.6 \pm 0.3</math> <math>th = 0.70 \pm 0.02</math></p> <p><math>L = l_p = 214</math> (fixed)</p>	<p>1.130</p> <p>3.028 (fixed)</p>
10	30	<p><b>Full contrast/</b> Elliptical flexible cylinder</p> <p><math>r_{\text{core,minor}} = 14.05 \pm 0.01</math></p> <p><math>r_{\text{core,major}} = 21.15 \pm 0.04</math></p> <p><math>L = 1000 \pm 6</math> <math>l_p = 300 \pm 3</math></p>	<p><b>Full contrast/</b> Flexible cylinder</p> <p><math>\bar{r} = 17.039 \pm 0.004</math></p> <p><math>\sigma/\bar{r} = 0.14</math> (fixed)</p> <p><math>L = 1002 \pm 6</math> <math>l_p = 293 \pm 3</math></p>	<p>17.20</p> <p>0.899 <math>\pm 0.002</math></p>
		<p><b>DTAB matched/</b> Elliptical core-shell cylinder</p> <p><math>r_{\text{core,minor}} = 12.0 \pm 0.8</math> <math>th = 2.4 \pm 1.2</math></p> <p><math>r_{\text{core,major}} = 18.3 \pm 1.2</math> <math>th = 2.4 \pm 1.2</math></p> <p><math>L = l_p = 300</math> (fixed)</p>	<p><b>DTAB matched/</b> Core-shell cylinder</p> <p><math>r_{\text{core}} = 13.7 \pm 0.5</math> <math>th = 4.7 \pm 0.4</math></p> <p><math>L = l_p = 293</math> (fixed)</p>	<p>1.926</p> <p>5.02 <math>\pm 0.05</math></p>
		<p><b>DTAB matched/</b> Elliptical core-shell cylinder</p> <p><math>r_{\text{core,minor}} = 12.6 \pm 0.2</math> <math>th = 1.28 \pm 0.02</math></p> <p><math>r_{\text{core,major}} = 19.1 \pm 0.2</math> <math>th = 1.28 \pm 0.02</math></p> <p><math>L = l_p = 300</math> (fixed)</p>	<p><b>DTAB matched/</b> Core-shell cylinder</p> <p><math>r_{\text{core}} = 15.6 \pm 0.2</math> <math>th = 0.761 \pm 0.006</math></p> <p><math>L = l_p = 293</math> (fixed)</p>	<p>1.967</p> <p>3.028 (fixed)</p>

## 6.6.5 NOESY Spectrum

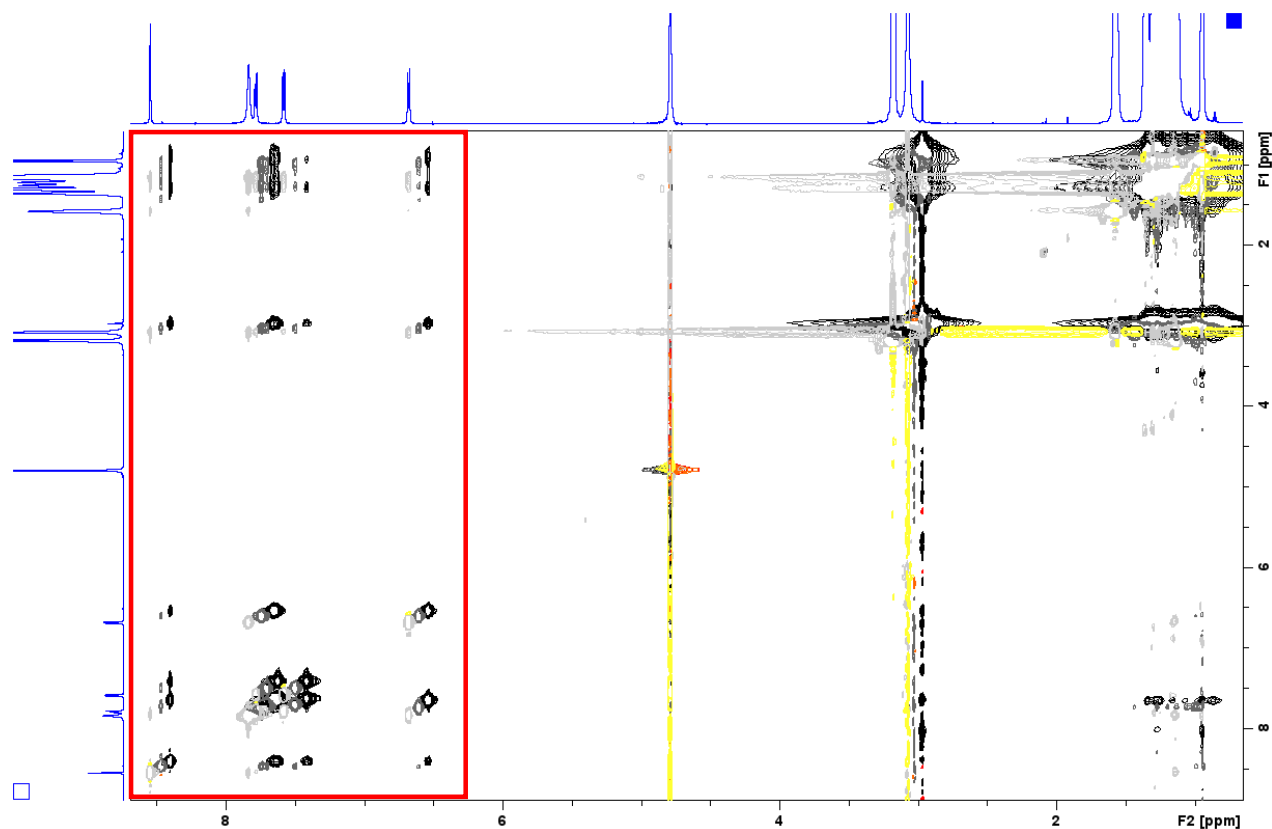


Figure S19: NOESY spectra of solutions containing [DTAB] = 30 mM and varying concentrations of Blue. The solvent is a  $\text{NaHCO}_3/\text{Na}_2\text{CO}_3$  buffer ( $\text{pD} = 10.7$ ,  $I \approx 0.25 \text{ M}$ ) prepared in  $\text{D}_2\text{O}$ . Negative peaks are displayed in light grey, dark grey and black for samples containing [Blue] = 5 mM, 7.5 mM and 10 mM respectively. Positive peaks are displayed in yellow, orange and red for samples containing [Blue] = 5 mM, 7.5 mM and 10 mM respectively. The red square marks the section shown in Figure 11 in the main document. The  $^1\text{H}$ -NMR spectra of the sample containing [Blue] = 5 mM and [DTAB] = 30 mM are displayed on the sides. Addition of Blue to a solution with constant DTAB concentration causes an upfield shift of some DTAB resonances, going along with peak broadening. Furthermore, an increase of the [Blue]:[DTAB] molar ratio causes an upfield shift of all Blue resonances. Therefore, peak positions in the NOESY spectrum depend on [Blue].

## 6.7 References

- (1) Stuart, M. A. C.; Huck, W. T. S.; Genzer, J.; Müller, M.; Ober, C.; Stamm, M.; Sukhorukov, G. B.; Szleifer, I.; Tsukruk, V. V.; Urban, M.; Winnik, F.; Zauscher, S.; Luzinov, I.; Minko, S. Emerging Applications of Stimuli-Responsive Polymer Materials. *Nature Mater* **2010**, *9* (2), 101–113. <https://doi.org/10.1038/nmat2614>.
- (2) Feng, Y.; Chu, Z.; Dreiss, C. A. Chapter 6: Stimulus-Responsive Wormlike Micelles. In *Wormlike Micelles*; 2017; pp 121–170. <https://doi.org/10.1039/9781782629788-00121>.

- (3) Dreiss, C. A. Chapter 1 Wormlike Micelles: An Introduction. In *Wormlike Micelles: Advances in Systems, Characterisation and Applications*; Soft Matter Series; Royal Society of Chemistry, 2017; pp 1–8.
- (4) A. Dreiss, C. Wormlike Micelles: Where Do We Stand? Recent Developments, Linear Rheology and Scattering Techniques. *Soft Matter* **2007**, *3* (8), 956–970. <https://doi.org/10.1039/B705775J>.
- (5) Hu, X.; Gong, H.; Li, Z.; Ruane, S.; Liu, H.; Pambou, E.; Bawn, C.; King, S.; Ma, K.; Li, P.; Padia, F.; Bell, G.; Lu, J. R. What Happens When Pesticides Are Solubilized in Nonionic Surfactant Micelles. *Journal of Colloid and Interface Science* **2019**, *541*, 175–182. <https://doi.org/10.1016/j.jcis.2019.01.056>.
- (6) Caetano, W.; Gelamo, E. L.; Tabak, M.; Itri, R. Chlorpromazine and Sodium Dodecyl Sulfate Mixed Micelles Investigated by Small Angle X-Ray Scattering. *Journal of Colloid and Interface Science* **2002**, *248* (1), 149–157. <https://doi.org/10.1006/jcis.2001.8164>.
- (7) Umeasiegbu, C. D.; Balakotaiah, V.; Krishnamoorti, R. PH-Induced Re-Entrant Microstructural Transitions in Cationic Surfactant–Hydrotrope Mixtures. *Langmuir* **2016**, *32* (3), 655–663. <https://doi.org/10.1021/acs.langmuir.5b02211>.
- (8) Silva, K. N.; Novoa-Carballal, R.; Drechsler, M.; Müller, A. H. E.; Penott-Chang, E. K.; Müller, A. J. The Influence of Concentration and PH on the Structure and Rheology of Cationic Surfactant/Hydrotrope Structured Fluids. *Colloids and Surfaces A: Physicochemical and Engineering Aspects* **2016**, *489*, 311–321. <https://doi.org/10.1016/j.colsurfa.2015.10.054>.
- (9) Creatto, E. J.; Okasaki, F. B.; Cardoso, M. B.; Sabadini, E. Wormlike Micelles of CTAB with Phenols and with the Corresponding Phenolate Derivatives - When Hydrophobicity and Charge Drive the Coacervation. *Journal of Colloid and Interface Science* **2022**, *627*, 355–366. <https://doi.org/10.1016/j.jcis.2022.07.044>.
- (10) Quirion, F.; Magid, L. J. Growth and Counterion Binding of Cetyltrimethylammonium Bromide Aggregates at 25 °C: A Neutron and Light Scattering Study. *J. Phys. Chem.* **1986**, *90* (21), 5435–5441. <https://doi.org/10.1021/j100412a108>.
- (11) Zhang, Y.; Chu, Z.; Dreiss, C. A.; Wang, Y.; Fei, C.; Feng, Y. Smart Wormlike Micelles Switched by CO<sub>2</sub> and Air. *Soft Matter* **2013**, *9* (27), 6217–6221. <https://doi.org/10.1039/C3SM50913C>.
- (12) Candau, S. J.; Hirsch, E.; Zana, R.; Adam, M. Network Properties of Semidilute Aqueous KBr Solutions of Cetyltrimethylammonium Bromide. *Journal of Colloid and Interface Science* **1988**, *122* (2), 430–440. [https://doi.org/10.1016/0021-9797\(88\)90377-3](https://doi.org/10.1016/0021-9797(88)90377-3).

- (13) Bergström, M.; Pedersen, J. S. Formation of Tablet-Shaped and Ribbonlike Micelles in Mixtures of an Anionic and a Cationic Surfactant. *Langmuir* **1999**, *15* (7), 2250–2253. <https://doi.org/10.1021/la981495x>.
- (14) Li, L.; Yang, Y.; Dong, J.; Li, X. Azobenzene Dye Induced Micelle to Vesicle Transition in Cationic Surfactant Aqueous Solutions. *Journal of Colloid and Interface Science* **2010**, *343* (2), 504–509. <https://doi.org/10.1016/j.jcis.2009.11.056>.
- (15) Zhang, Y.; Kong, W.; Wang, C.; An, P.; Fang, Y.; Feng, Y.; Qin, Z.; Liu, X. Switching Wormlike Micelles of Selenium-Containing Surfactant Using Redox Reaction. *Soft Matter* **2015**, *11* (38), 7469–7473. <https://doi.org/10.1039/C5SM01515D>.
- (16) Lin, Y.; Cheng, X.; Qiao, Y.; Yu, C.; Li, Z.; Yan, Y.; Huang, J. Creation of Photo-Modulated Multi-State and Multi-Scale Molecular Assemblies via Binary-State Molecular Switch. *Soft Matter* **2010**, *6* (5), 902–908. <https://doi.org/10.1039/B916721H>.
- (17) Lambert, J. B. *Spektroskopie: Strukturaufklärung in der Organischen Chemie*; Pearson, Higher Education, 2012.
- (18) Claridge, T. D. W. Correlations through Space: The Nuclear Overhauser Effect. In *High-Resolution NMR Techniques in Organic Chemistry*; Tetrahedron Organic Chemistry Series; Elsevier, 2009; Vol. 27, pp 247–302. [https://doi.org/10.1016/S1460-1567\(08\)10008-3](https://doi.org/10.1016/S1460-1567(08)10008-3).
- (19) Valero, M.; Castiglione, F.; Mele, A.; da Silva, M. A.; Grillo, I.; González-Gaitano, G.; Dreiss, C. A. Competitive and Synergistic Interactions between Polymer Micelles, Drugs, and Cyclodextrins: The Importance of Drug Solubilization Locus. *Langmuir* **2016**, *32* (49), 13174–13186. <https://doi.org/10.1021/acs.langmuir.6b03367>.
- (20) Croce, V.; Cosgrove, T.; Dreiss, C. A.; Maitland, G.; Hughes, T. Mixed Spherical and Wormlike Micelles: A Contrast-Matching Study by Small-Angle Neutron Scattering. *Langmuir* **2004**, *20* (23), 9978–9982. <https://doi.org/10.1021/la048355+>.
- (21) Brasher, L. L.; Kaler, E. W. A Small-Angle Neutron Scattering (SANS) Contrast Variation Investigation of Aggregate Composition in Catanionic Surfactant Mixtures. *Langmuir* **1996**, *12* (26), 6270–6276. <https://doi.org/10.1021/la960493e>.
- (22) Zhang, X. L.; Penfold, J.; Thomas, R. K.; Tucker, I. M.; Petkov, J. T.; Bent, J.; Cox, A.; Grillo, I. Self-Assembly of Hydrophobin and Hydrophobin/Surfactant Mixtures in Aqueous Solution. *Langmuir* **2011**, *27* (17), 10514–10522. <https://doi.org/10.1021/la2020226>.
- (23) Penfold, J.; Tucker, I.; Green, A.; Grainger, D.; Jones, C.; Ford, G.; Roberts, C.; Hubbard, J.; Petkov, J.; Thomas, R. K.; Grillo, I. Impact of Model Perfumes on Surfactant and Mixed

- Surfactant Self-Assembly. *Langmuir* **2008**, *24* (21), 12209–12220. <https://doi.org/10.1021/la801662g>.
- (24) Guan, Y.; Antonietti, M.; Faul, C. F. J. Ionic Self-Assembly of Dye–Surfactant Complexes: Influence of Tail Lengths and Dye Architecture on the Phase Morphology. *Langmuir* **2002**, *18* (15), 5939–5945. <https://doi.org/10.1021/la0257182>.
- (25) Faul, C. F. J.; Antonietti, M. Facile Synthesis of Optically Functional, Highly Organized Nanostructures: Dye–Surfactant Complexes. *Chemistry – A European Journal* **2002**, *8* (12), 2764–2768. [https://doi.org/10.1002/1521-3765\(20020617\)8:12<2764::AID-CHEM2764>3.0.CO;2-X](https://doi.org/10.1002/1521-3765(20020617)8:12<2764::AID-CHEM2764>3.0.CO;2-X).
- (26) Kutz, A.; Mariani, G.; Gröhn, F. Ionic Dye–Surfactant Nanoassemblies: Interplay of Electrostatics, Hydrophobic Effect, and  $\pi$ – $\pi$  Stacking. *Colloid Polym Sci* **2016**, *294* (3), 591–606. <https://doi.org/10.1007/s00396-015-3814-2>.
- (27) Mantid Project. Mantid (2013): Manipulation and Analysis Toolkit for Instrument Data. <http://dx.doi.org/10.5286/SOFTWARE/MANTID>.
- (28) Arnold, O.; Bilheux, J. C.; Borreguero, J. M.; Buts, A.; Campbell, S. I.; Chapon, L.; Doucet, M.; Draper, N.; Ferraz Leal, R.; Gigg, M. A.; Lynch, V. E.; Markvardsen, A.; Mikkelsen, D. J.; Mikkelsen, R. L.; Miller, R.; Palmen, K.; Parker, P.; Passos, G.; Perring, T. G.; Peterson, P. F.; Ren, S.; Reuter, M. A.; Savici, A. T.; Taylor, J. W.; Taylor, R. J.; Tolchenov, R.; Zhou, W.; Zikovsky, J. Mantid—Data Analysis and Visualization Package for Neutron Scattering and  $\mu$  SR Experiments. *Nuclear Instruments and Methods in Physics Research Section A: Accelerators, Spectrometers, Detectors and Associated Equipment* **2014**, *764*, 156–166. <https://doi.org/10.1016/j.nima.2014.07.029>.
- (29) *Neutrons, X-Rays, and Light: Scattering Methods Applied to Soft Condensed Matter*, 1st ed.; Lindner, P., Zemb, T., Eds.; North-Holland delta series; Elsevier: Amsterdam ; Boston, 2002.
- (30) Gottlieb, H. E.; Kotlyar, V.; Nudelman, A. NMR Chemical Shifts of Common Laboratory Solvents as Trace Impurities. *J. Org. Chem.* **1997**, *62* (21), 7512–7515. <https://doi.org/10.1021/jo971176v>.
- (31) SasView. *SasView*. <https://sasview.github.io/> (accessed 2023-01-11).
- (32) Breßler, I.; Kohlbrecher, J.; Thünemann, A. F. SASfit: A Tool for Small-Angle Scattering Data Analysis Using a Library of Analytical Expressions. *J Appl Cryst* **2015**, *48* (5), 1587–1598. <https://doi.org/10.1107/S1600576715016544>.

- (33) Müller, W.; Schweins, R.; Nöcker, B.; Kohlbrecher, Joachim; Smales, G. J.; Huber, K. Comparative Study of the Co-Assembly Behaviour of 3-Chloro-4 Hydroxy-Phenylazo Dyes with DTAB. *Soft Matter* **2023**, *19* (24), 4588–4598. <https://doi.org/10.1039/D3SM00501A>.
- (34) Rehage, H.; Hoffmann, H. Rheological Properties of Viscoelastic Surfactant Systems. *J. Phys. Chem.* **1988**, *92* (16), 4712–4719. <https://doi.org/10.1021/j100327a031>.
- (35) Hoffmann, H. Viscoelastic Surfactant Solutions. In *Structure and Flow in Surfactant Solutions*; ACS Symposium Series; American Chemical Society, 1994; Vol. 578, pp 2–31. <https://doi.org/10.1021/bk-1994-0578.ch001>.
- (36) Pedersen, J. S.; Schurtenberger, P. Scattering Functions of Semiflexible Polymers with and without Excluded Volume Effects. *Macromolecules* **1996**, *29* (23), 7602–7612. <https://doi.org/10.1021/ma9607630>.
- (37) Feigin, L. A.; Svergun, D. I. *Structure Analysis by Small-Angle X-Ray and Neutron Scattering*; Springer US, 1987. <https://doi.org/10.1007/978-1-4757-6624-0>.
- (38) Finnigan, J. A.; Jacobs, D. J. Light Scattering by Ellipsoidal Particles in Solution. *J. Phys. D: Appl. Phys.* **1971**, *4* (1), 72. <https://doi.org/10.1088/0022-3727/4/1/310>.
- (39) Bergström, M.; Pedersen, J. Structure of Pure SDS and DTAB Micelles in Brine Determined by Small-Angle Neutron Scattering (SANS). *PHYS CHEM CHEM PHYS* **1999**, *1*, 4437–4446. <https://doi.org/10.1039/a903469b>.
- (40) Hayter, J. B.; Penfold, J. An Analytic Structure Factor for Macroion Solutions. *Molecular Physics* **1981**, *42* (1), 109–118. <https://doi.org/10.1080/00268978100100091>.
- (41) Hansen, J.-P.; Hayter, J. B. A Rescaled MSA Structure Factor for Dilute Charged Colloidal Dispersions. *Molecular Physics* **1982**, *46* (3), 651–656. <https://doi.org/10.1080/00268978200101471>.
- (42) Schärfl, W. *Light Scattering from Polymer Solutions and Nanoparticle Dispersions*; Springer Laboratory; Springer Berlin Heidelberg: Berlin, Heidelberg, 2007. <https://doi.org/10.1007/978-3-540-71951-9>.
- (43) Glatter, O.; Kratky, O.; Kratky, H. C. *Small Angle X-Ray Scattering*; Academic Press, 1982.
- (44) Pedersen, J. S. Analysis of Small-Angle Scattering Data from Colloids and Polymer Solutions: Modeling and Least-Squares Fitting. *Advances in Colloid and Interface Science* **1997**, *70*, 171–210. [https://doi.org/10.1016/S0001-8686\(97\)00312-6](https://doi.org/10.1016/S0001-8686(97)00312-6).
- (45) Aswal, V. K.; Goyal, P. S. Role of Counterion Distribution on the Structure of Micelles in Aqueous Salt Solutions: Small-Angle Neutron Scattering Study. *Chemical Physics Letters* **2002**, *357* (5), 491–497. [https://doi.org/10.1016/S0009-2614\(02\)00558-4](https://doi.org/10.1016/S0009-2614(02)00558-4).

- (46) Behrens, M. A.; Lopez, M.; Kjøniksen, A.-L.; Zhu, K.; Nyström, B.; Pedersen, J. S. Structure and Interactions of Charged Triblock Copolymers Studied by Small-Angle X-Ray Scattering: Dependence on Temperature and Charge Screening. *Langmuir* **2012**, *28* (2), 1105–1114. <https://doi.org/10.1021/la202841q>.
- (47) Hassan, P. A.; Fritz, G.; Kaler, E. W. Small Angle Neutron Scattering Study of Sodium Dodecyl Sulfate Micellar Growth Driven by Addition of a Hydrotropic Salt. *Journal of Colloid and Interface Science* **2003**, *257* (1), 154–162. [https://doi.org/10.1016/S0021-9797\(02\)00020-6](https://doi.org/10.1016/S0021-9797(02)00020-6).
- (48) Intermolecular and Surface Forces. In *Intermolecular and Surface Forces (Third Edition)*; Israelachvili, J. N., Ed.; Academic Press: Boston, 2011; p iii. <https://doi.org/10.1016/B978-0-12-391927-4.10024-6>.
- (49) Tehrani-Bagha, A. R.; Holmberg, K. Solubilization of Hydrophobic Dyes in Surfactant Solutions. *Materials* **2013**, *6* (2), 580–608. <https://doi.org/10.3390/ma6020580>.
- (50) Berr, S. S. Solvent Isotope Effects on Alkytrimethylammonium Bromide Micelles as a Function of Alkyl Chain Length. *J. Phys. Chem.* **1987**, *91* (18), 4760–4765. <https://doi.org/10.1021/j100302a024>.
- (51) Onsager, L. The Effects of Shape on the Interaction of Colloidal Particles. *Annals of the New York Academy of Sciences* **1949**, *51* (4), 627–659. <https://doi.org/10.1111/j.1749-6632.1949.tb27296.x>.
- (52) Livsey, I. Neutron Scattering from Concentric Cylinders. Intraparticle Interference Function and Radius of Gyration. *J. Chem. Soc., Faraday Trans. 2* **1987**, *83* (8), 1445–1452. <https://doi.org/10.1039/F29878301445>.
- (53) Onoda-Yamamuro, N.; Yamamuro, O.; Tanaka, N.; Nomura, H. NMR and Neutron Scattering Studies on Spherical and Rod-like Micelles of Dodecyltrimethylammonium Bromide in Aqueous Sodium Salicylate Solutions. *Journal of Molecular Liquids* **2005**, *117* (1), 139–145. <https://doi.org/10.1016/j.molliq.2004.08.009>.
- (54) Eriksson, J. C.; Gillberg, G. NMR-Studies of the Solubilisation of Aromatic Compounds in Cethyltrimethylammonium Bromide Solution II. *Acta Chem. Scand.* **1966**, *20* (8), 2019–2027. <https://doi.org/10.3891/acta.chem.scand.20-2019>.
- (55) Furó, I. NMR Spectroscopy of Micelles and Related Systems. *Journal of Molecular Liquids* **2005**, *117* (1), 117–137. <https://doi.org/10.1016/j.molliq.2004.08.010>.



- (56) Wilson, L. D.; Verrall, R. E. A  $^1\text{H}$  NMR Study of Cyclodextrin - Hydrocarbon Surfactant Inclusion Complexes in Aqueous Solutions. *Can. J. Chem.* **1998**, *76* (1), 25–34. <https://doi.org/10.1139/v97-208>.
- (57) Shikata, T.; Hirata, H.; Kotaka, T. Micelle Formation of Detergent Molecules in Aqueous Media. 2. Role of Free Salicylate Ions on Viscoelastic Properties of Aqueous Cetyltrimethylammonium Bromide-Sodium Salicylate Solutions. *Langmuir* **1988**, *4* (2), 354–359. <https://doi.org/10.1021/la00080a019>.
- (58) Bachofer, S. J.; Turbitt, R. M. The Orientational Binding of Substituted Benzoate Anions at the Cetyltrimethyl Ammonium Bromide Interface. *Journal of Colloid and Interface Science* **1990**, *135* (2), 325–334. [https://doi.org/10.1016/0021-9797\(90\)90003-7](https://doi.org/10.1016/0021-9797(90)90003-7).
- (59) Guo, L. N.; Arnaud, I.; Petit-Ramel, M.; Gauthier, R.; Monnet, C.; LePerchec, P.; Chevalier, Y. Solution Behavior of Dye-Surfactant Associations. *Journal of Colloid and Interface Science* **1994**, *163* (2), 334–346. <https://doi.org/10.1006/jcis.1994.1112>.
- (60) Olsson, U.; Soederman, O.; Guering, P. Characterization of Micellar Aggregates in Viscoelastic Surfactant Solutions. A Nuclear Magnetic Resonance and Light Scattering Study. *J. Phys. Chem.* **1986**, *90* (21), 5223–5232. <https://doi.org/10.1021/j100412a066>.
- (61) Carey, F. A.; Sundberg, R. J. *Advanced Organic Chemistry Part A: Structure and Mechanisms*, 5th ed.; Advanced Organic Chemistry; Springer: New York, 2007; Vol. A. <https://doi.org/10.1007/978-0-387-44899-2>.
- (62) Garland, C. W.; Nibler, J. W.; Shoemaker, D. P. *Experiments in Physical Chemistry*, 8th ed.; McGraw-Hill Higher Education: Boston, 2009.
- (63) Frisken, B. J. Revisiting the Method of Cumulants for the Analysis of Dynamic Light-Scattering Data. *Appl. Opt.* **2001**, *40* (24), 4087–4091. <https://doi.org/10.1364/AO.40.004087>.
- (64) Hayter, J. B.; Penfold, J. Determination of Micelle Structure and Charge by Neutron Small-Angle Scattering. *Colloid & Polymer Sci* **1983**, *261* (12), 1022–1030. <https://doi.org/10.1007/BF01421709>.
- (65) Marcus, Y. *Ion Properties*; Marcel Dekker: New York, 1997.
- (66) Lide, D. R. *CRC Handbook of Chemistry and Physics*; CRC Press: Boca Raton, FL, 2005.
- (67) Conway, B. E. The Evaluation and Use of Properties of Individual Ions in Solution. *J Solution Chem* **1978**, *7* (10), 721–770. <https://doi.org/10.1007/BF00643580>.
- (68) Vidulich, G. A.; Evans, D. F.; Kay, R. L. The Dielectric Constant of Water and Heavy Water between 0 and 40 Degree. *J. Phys. Chem.* **1967**, *71* (3), 656–662. <https://doi.org/10.1021/j100862a028>.

- (69) Kotlarchyk, M.; Chen, S. Analysis of Small Angle Neutron Scattering Spectra from Polydisperse Interacting Colloids. *J. Chem. Phys.* **1983**, *79* (5), 2461–2469. <https://doi.org/10.1063/1.446055>.
- (70) Berr, S. S.; Caponetti, E.; Johnson, J. S. Jr.; Jones, R. R. M.; Magid, L. J. Small-Angle Neutron Scattering from Hexadecyltrimethylammonium Bromide Micelles in Aqueous Solutions. *J. Phys. Chem.* **1986**, *90* (22), 5766–5770. <https://doi.org/10.1021/j100280a059>.
- (71) Zana, R.; Picot, C.; Duplessix, R. Effect of Alcohol on the Properties of Micellar Systems. V. Small Angle Neutron Scattering Study. *Journal of Colloid and Interface Science* **1983**, *93* (1), 43–53. [https://doi.org/10.1016/0021-9797\(83\)90382-X](https://doi.org/10.1016/0021-9797(83)90382-X).
- (72) Tabony, J. Structure of the Polar Head Layer and Water Penetration in a Cationic Micelle. *Molecular Physics* **1984**, *51* (4), 975–989. <https://doi.org/10.1080/00268978400100641>.
- (73) Rosen, M. J. *Surfactants and Interfacial Phenomena*, 3rd ed.; Wiley-Interscience; John Wiley & Sons, Inc: Hoboken, New Jersey, USA, 2004.
- (74) Patist, A.; Oh, S. G.; Leung, R.; Shah, D. O. Kinetics of Micellization: Its Significance to Technological Processes. *Colloids and Surfaces A: Physicochemical and Engineering Aspects* **2001**, *176* (1), 3–16. [https://doi.org/10.1016/S0927-7757\(00\)00610-5](https://doi.org/10.1016/S0927-7757(00)00610-5).
- (75) Verma, G.; Kumar, S.; Schweins, R.; K. Aswal, V.; A. Hassan, P. Transition from Long Micelles to Flat Bilayers Driven by Release of Hydrotropes in Mixed Micelles. *Soft Matter* **2013**, *9* (17), 4544–4552. <https://doi.org/10.1039/C3SM27913H>.

## Chapter 7

# Impact of dye polarity on mixed dye-nonionic surfactant micelles: Micelle morphology and spatial dye distribution

---

### Abstract

The temperature-induced clouding of  $C_{12}E_5$  solutions in  $D_2O$  was rendered pD-dependent upon addition of the pD-responsive molecule Blue. At pD = 2, the completely protonated and therefore uncharged BlueH lowers the clouding temperature (CT) of  $C_{12}E_5$  solutions, which is partly attributed to its preferential localization in the micellar core. The solubilisation of BlueH in the micellar core causes an increase in the hydrophobic chain volume of the  $C_{12}E_5$  surfactant, which, according to the concept of the critical packing parameter, results in a denser packing of  $C_{12}E_5$  molecules in BlueH/ $C_{12}E_5$  co-assemblies. This reduces the available space for water molecules in the pentaethyleneglycol head group, which results in dehydration of the head group and subsequent decrease of its water solubility. At pD = 9, the one-fold negatively charged Blue<sup>-</sup> was found to be located in the palisade- and outer region of  $C_{12}E_5$  micelles and at pD = 13, the two fold negatively charged Blue<sup>2-</sup> is located in the outer region close to the surface of  $C_{12}E_5$  micelles. In both cases, the addition of increasing concentrations of Blue increased the CT of  $C_{12}E_5$  solutions. This was attributed to both substances causing a higher water solubility of the pentaethyleneglycol head groups and the introduction of repulsive electrostatic interactions between micelles. At high concentrations of Blue<sup>2-</sup>, repulsive interactions were found to outweigh attractive interactions between  $C_{12}E_5$  micelles, which explains the concomitant strong increase of the CT. It was furthermore shown that the correlation length of concentration fluctuations, which appear due to attractive interactions between micelles close to the liquid/liquid phase separation threshold, was independent of sample composition. It depended solely on the temperature-distance of the sample to its CT. Furthermore, Blue/ $C_{12}E_5$  micelles were proven to shrink with increasing temperature-distance to the CT.

---

This chapter corresponds to a manuscript in preparation.

Authors: Müller, Wenke; Sroka, Weronika; Schweins, Ralf; Nöcker, Bernd; Poon, Jia-Fei; Huber, Klaus

Preliminary title: Impact of additive polarity on mixed additive-nonionic surfactant micelles: Micelle morphology and spatial additive distribution.

## 7.1 Introduction

Alkyl ethoxylate surfactants  $C_nE_m$  with  $n$  alkyl chain carbon atoms and  $m$  ethylene glycol (EG) groups are an integral part of industrial and personal consumer products.<sup>1-3</sup> A common feature of these surfactants in aqueous solution is the occurrence of a temperature, at which the solution phase separates into a surfactant-rich and a surfactant-poor phase.<sup>3,4</sup> This temperature is termed "clouding temperature" (CT) and corresponds to the boundary between the monophasic and biphasic regions forming a binodal curve with a lower critical solution temperature (LCST).<sup>5</sup>

Several attempts were made to relate the clouding phenomenon to the molecular structure of  $C_nE_m$  molecules by considering the hydrophilic-lipophilic balance and theoretical models for the prediction of CTs were developed.<sup>3,6,7</sup> Generally, the CT of  $C_nE_m$  solutions increases with increasing hydrophilicity, i.e. with an increasing number of EG groups  $m$  at constant alkyl chain length and decreases with increasing fraction of the hydrophobic part, i.e. with increasing alkyl chain length  $n$  if  $m$  is kept constant.<sup>3,7-9</sup> Due to the interest in morphological transitions of micelles up to the point of phase separation,  $C_nE_m$  solutions were intensively investigated with scattering techniques throughout the last decades.<sup>6,10-13</sup> Scattering curves were interpreted assuming a combination of micellar growth and attractive interactions between individual  $C_nE_m$  micelles.<sup>12,13</sup>

Industrial formulations do not solely consist of pure  $C_nE_m$  solutions, but contain other ingredients such as inorganic salt, polymers, alcohols, co-surfactants and other additives. As such additives may interfere with both, micellar growth and interactions between  $C_nE_m$  micelles, they often cause a change in the CT of  $C_nE_m$  solutions.<sup>14</sup> Corti et al. suggested, that morphological transitions of  $C_nE_m$  micelles upon additive addition may be similar to morphological transitions observed upon temperature change, as both factors change the temperature-distance of a sample with given  $C_nE_m$  concentration to its CT.<sup>11</sup>

Addition of inorganic electrolytes, simple alcohols or other nonionic surfactants can raise or lower the CT of  $C_nE_m$  solutions.<sup>9,14-16</sup> Ionic surfactants strongly raise the CT in the absence of electrolyte, but may cause a CT decrease if electrolyte is present.<sup>14,17</sup>

Additive-induced CT variations are frequently discussed in terms of the polarity or hydrophilicity of the additive. Polar additives that interact favourably with both, EG and water will increase the CT, whereas nonpolar or hydrophobic additives will decrease the CT of  $C_nE_m$  solutions.<sup>14</sup>

Vicente et al. recently investigated the impact of surface-active ionic liquids on the CT of Tergitol surfactant solutions.<sup>5</sup> In accord with previously observed trends, they noticed a CT increase upon

addition of comparably hydrophilic ionic liquids, but a decrease for hydrophobic ones. They furthermore identified the critical packing parameter (*CPP*) of surface active ionic liquids as an additional indicator of whether the addition of the ionic liquid increases or decreases the CT of Tergitol solutions. To give an example, bulky surface active ionic liquids ( $CPP \geq 1$ ) are expected to decrease the CT by promoting the formation of bilayer aggregates.<sup>5</sup> Sen et al. found, that the CT of solutions containing Triton X-100 and imidazolium-based ionic liquids increases, when the length of the hydrophobic alkyl chain attached to the imidazolium moiety increases.<sup>18</sup> This observation represents an apparent discrepancy to the general assumption that an additive-caused increase of hydrophobicity lowers the CT. However, in the case described by Sen et al.<sup>18</sup>, the CT increase upon addition of more hydrophobic ionic liquids is explained by mixed micelle formation once the alkyl chain becomes sufficiently long.

The above-mentioned examples demonstrate, that steric effects interfere with a proper assessment of the influence of additive polarity on the CT of  $C_nE_m$  solutions, when additives with variable polarity and differing chemical constitution are compared. The impact of variable chemical constitutions with the resulting steric effects can be separated from the influence of polarity if polarity could be varied in one and the same additive. Such a variation in the polarity can be achieved with an acidic additive by pH (pD) variation triggering protonation or deprotonation. Figure 1 displays the acid/base equilibrium of the azo dye Blue, which is suitable for that purpose. Importantly, Blue possesses two  $pK_A$  values between pD = 0 and pD = 14 and therefore makes three different additive polarities accessible. This approach is further facilitated by the insensitivity of  $C_nE_m$  surfactant micelles to solution pH.

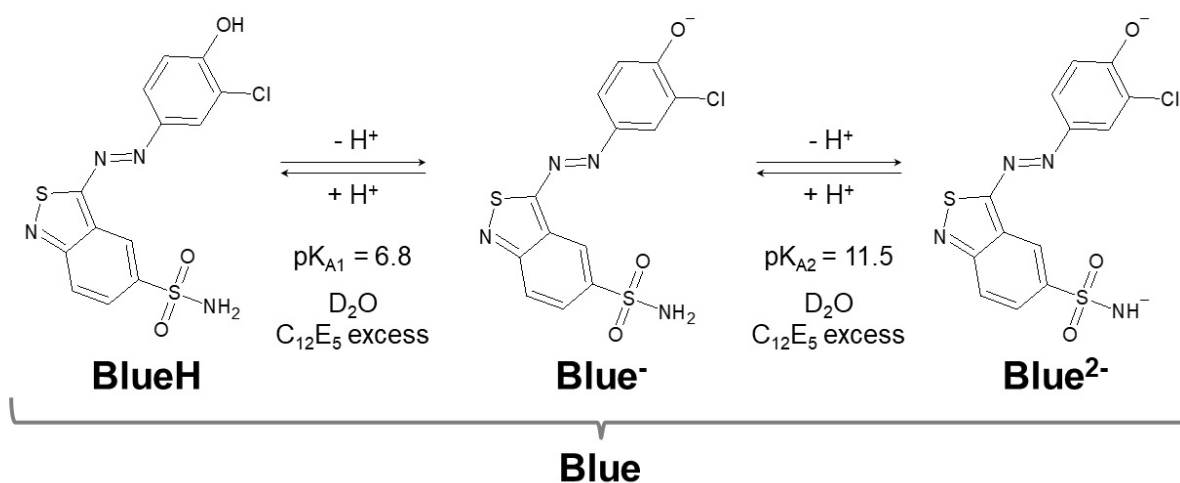


Figure 1: Acid/base equilibria of Blue. Displayed  $pK_A$  values were measured for an excess of  $C_{12}E_5$  in an isotonic solution of NaCl in  $D_2O$  at room temperature (22 °C). Discussions will therefore solely be based on pD values.

Accordingly, the objective of the present work is to fundamentally understand the effect of additive polarity, free of any steric effects, on the additive-surfactant interactions leading to variations in the CT of such solutions and in the morphology of the co-micelles in such solutions. The objective is followed by addressing two aspects: The first aspect deals with the impact of Blue on the phase behaviour and the morphology of Blue/ $C_{12}E_5$  co-assemblies. The second aspect addresses the spatial distribution of Blue within the co-assembly at variable pD. For the investigation of the latter, NMR-spectroscopy and contrast matching small-angle neutron scattering (SANS) were used.

## 7.2 Experimental

**Chemicals and sample preparation.** Blue (HC Blue 18,  $\geq 99.8\%$ ) was provided by KAO Germany GmbH, Germany. Hydrogenated pentaethyleneglycolmonododecylether ( $hC_{12}hE_5$ , BioXtra,  $\geq 98.0\%$  GC) was obtained from Sigma Aldrich Chemie GmbH, Germany.  $C_{12}E_5$  with statistical deuteration of the alkyl tail at a hydrogen:deuterium ratio of 9:91 and either hydrogenated ( $mC_{12}hE_5$ ) or deuterated ( $mC_{12}dE_5$ ) pentaethyleneglycol head group were synthesized by the DEMAX laboratory (ESS, Sweden) in order to be able to contrast match  $C_{12}E_5$  with  $D_2O$  (proposal number: 860178). NaCl (puriss. p. a.,  $\geq 99.5\%$ ) was obtained from Sigma Aldrich Chemie GmbH, Germany.  $D_2O$  (99.9 atom% D) was obtained from Sigma Aldrich Chemie GmbH, Germany. The 7.6 M DCl solution in  $D_2O$  (99 % D) used to prepare the DCl solution for pD-adjustment, was obtained from Euriso-top, France. The 40 wt% NaOD solution in  $D_2O$  (99.5 atom% D) used to prepare the NaOD solution for pD-adjustment, was obtained from Aldrich Chem. Co., US.

Figure 2a shows the  $C_{12}E_5$  surfactant employed in this research. As contrast matching in SANS was needed to localize Blue in  $C_{12}E_5$  micelles,  $C_{12}E_5$  was used in different degrees of deuteration. Therefore, Figure 2a also provides an overview of the employed isotopically substituted  $C_{12}E_5$  species. Figure 2b shows the classification of different regions in a surfactant micelle according to their polarity.<sup>19</sup>

Samples were prepared by mixing the alkaline solvent with stock solutions of Blue and  $C_{12}E_5$  at the required ratio and subsequently adjusting the pD. The solvent was prepared to contain NaCl at a concentration of 154 mM and NaOD at a concentration of 20 mM.  $D_2O$  was used to prepare the solvent in all cases. Stock solutions with  $[Blue] = 10\text{ mM}$  or  $[C_{12}E_5] = 75\text{ mM}$  were prepared by dissolving Blue or  $C_{12}E_5$  in the solvent and gentle mixing for 1 h to 2 h. Samples containing  $[Blue] = 12.5\text{ mM}$  were prepared by weighting the appropriate amount of Blue and subsequent addition of solvent and  $C_{12}E_5$  stock solution at the required ratio, followed by gentle mixing for 1 h

to 2 h. All other samples were prepared by mixing of stock solutions and solvent. Following this preparation, the pD of each sample was adjusted at room temperature (22 °C) using a ~1 M solution of NaOD in D<sub>2</sub>O and a ~1 M solution of DCI in D<sub>2</sub>O.

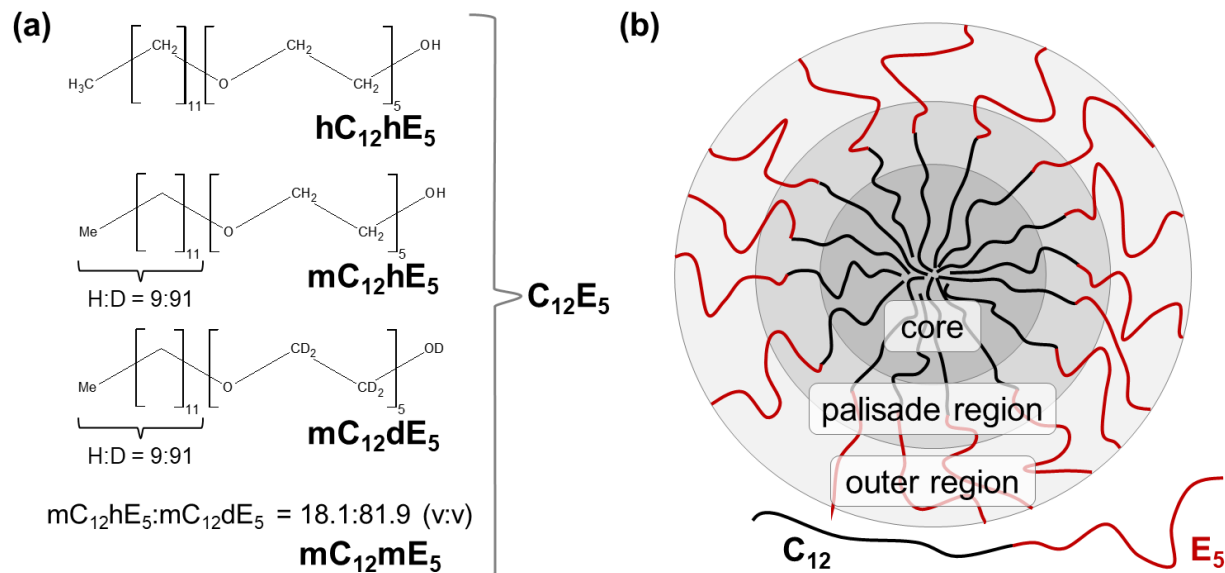


Figure 2: (a) Nonionic surfactant C<sub>12</sub>E<sub>5</sub> and isotopically substituted species used in the present work. H:D denotes the ratio of hydrogen to deuterium in the statistically deuterated alkyl chain. Me = methyl. (b) General classification of different regions in a surfactant micelle according to their polarity.<sup>19</sup>

Samples were stored at a temperature lower than measurement temperature (usually 4 °C to 7 °C) for a minimum of 24 h prior to measurement and equilibrated at measurement temperature for at least 1 h before measurement except for NMR-measurements, where the equilibration time was 15 min. Samples for NMR-spectroscopy were filtered (MACHEREY-NAGEL, CHROMAFIL Xtra H-PTFE syringe filters, pore size 0.2 µm) into NMR tubes at a temperature of 7 °C after an equilibration time of at least 4 h at that temperature and were subsequently stored for a minimum of 24 h at 7 °C. Samples for the match point determination with SANS were not filtered. However, the solvent used for preparing stock solutions as well as the DCI-solution used for pD adjustment were filtered (MACHEREY-NAGEL, CHROMAFIL Xtra H-PTFE syringe filters, pore size 0.2 µm). Samples for all other SANS experiments were not filtered either, but prepared from stock solutions, solvent, NaOD- and DCI solutions, which were filtered (MACHEREY-NAGEL, CHROMAFIL Xtra H-PTFE syringe filters, pore size 0.2 µm) at room temperature.

**Determination of phase diagrams.** For the determination of phase diagrams, samples were prepared as described above and stored at a temperature of 4 °C for 24 h before further analysis. Samples had a volume of 1.2 mL and were prepared in 4 mL glass vials. After equilibration, samples were placed in an incubator (model IL 68R, VWR, Belgium) and CTs ≥ 4 °C were



determined by equilibrating the sample for 1 h at a given temperature and subsequent visual determination of phase separation. Starting from 4 °C, sample temperature was increased in steps of 1 K up to a temperature of 50 °C, which corresponds to the maximum temperature of the used incubator model. The temperature, at which clouding occurs for a given sample composition is termed "clouding temperature" (CT) to avoid confusion with the cloud point defined by the ASTM standard test method ASTM D2024-09(2017)<sup>20</sup> for 1 wt% surfactant solutions.

**Small-angle neutron scattering.** Samples for small-angle neutron scattering (SANS) were prepared as described above. Three different SANS experiments were performed: (1) The first experiment corresponds to the match point determination experiment, which served to determine the ratio between mC<sub>12</sub>hE<sub>5</sub> and mC<sub>12</sub>dE<sub>5</sub> at which no form factor scattering is observed (match point). (2) In the second experiment, "full contrast" SANS curves were recorded from samples containing the completely hydrogenated surfactant hC<sub>12</sub>hE<sub>5</sub> and Blue. (3) In the third experiment, C<sub>12</sub>E<sub>5</sub>-matched SANS curves were recorded, where samples contained mC<sub>12</sub>hE<sub>5</sub> and mC<sub>12</sub>dE<sub>5</sub> at the match point determined in step 1 and Blue. As C<sub>12</sub>E<sub>5</sub> was matched out under these conditions, the *q*-dependent scattering signal only arose from Blue.

The match point determination experiment is outlined in detail in the supporting information (SI, section 7.8.1, sub-section "Determination of the SANS match point of C<sub>12</sub>E<sub>5</sub> in D<sub>2</sub>O") and yielded a volume ratio of  $\Phi(\text{mC}_{12}\text{hE}_5) : \Phi(\text{mC}_{12}\text{dE}_5) = 18.1:81.9$  (v:v) for the match point.

SANS was performed at the small-angle neutron scattering instrument D22 at the Institute Laue-Langevin (Grenoble, France). A circular neutron beam with a diameter of 13 mm and cuvettes with a path length of 2 mm were used. The D22 instrument possesses two detectors: The front detector, which was at a fixed distance of 1.4 m to the sample and a rear detector. Measurements were carried out at two sample-to-rear-detector distances: 4 m (collimation 4 m) and 17.6 m (collimation 17.6 m) at a neutron wavelength of 6 Å to cover a *q*-range of 0.0026 Å<sup>-1</sup> to 0.6424 Å<sup>-1</sup>. Neutrons were detected with two <sup>3</sup>He detectors (multi-tube detector consisting of vertically aligned Reuter-Stokes tubes, with 128 tubes for the rear and 96 tubes for the front detector, all with a diameter of 8 mm and a pixel size of 8 mm x 8 mm). Detector images were corrected to the transmission of the direct beam, scaled to absolute intensity and azimuthally averaged using the GRASP software.<sup>21</sup> Empty cell and solvent scattering were subtracted from the scattering curves.<sup>22</sup> SANS curves were fitted using the SASfit software package.<sup>23</sup>

**NMR spectroscopy.** Samples for NMR-spectroscopy were prepared, filtered and stored as described above. Samples were equilibrated in the NMR spectrometer at 10 °C for 15 min before

measurement.  $^1\text{H-NMR}$  and Nuclear Overhauser Effect (NOESY) spectra were recorded with a Bruker 600 MHz NMR spectrometer.  $^1\text{H-NMR}$  chemical shifts were referenced to residual HDO.<sup>24</sup>

### 7.3 Clouding temperatures of Blue/ $\text{C}_{12}\text{E}_5$ solutions

Figure 3 displays clouding temperatures of solutions containing Blue and the nonionic surfactant  $\text{hC}_{12}\text{hE}_5$  at variable Blue concentration in comparison to the CT of pure  $\text{hC}_{12}\text{hE}_5$  solutions for different solution pD. It is not clear, whether the determined CT lay on the binodal or spinodal curve of the phase diagram. However, the CTs shown in Figure 3 are comparable among themselves, because they were determined with the same method.

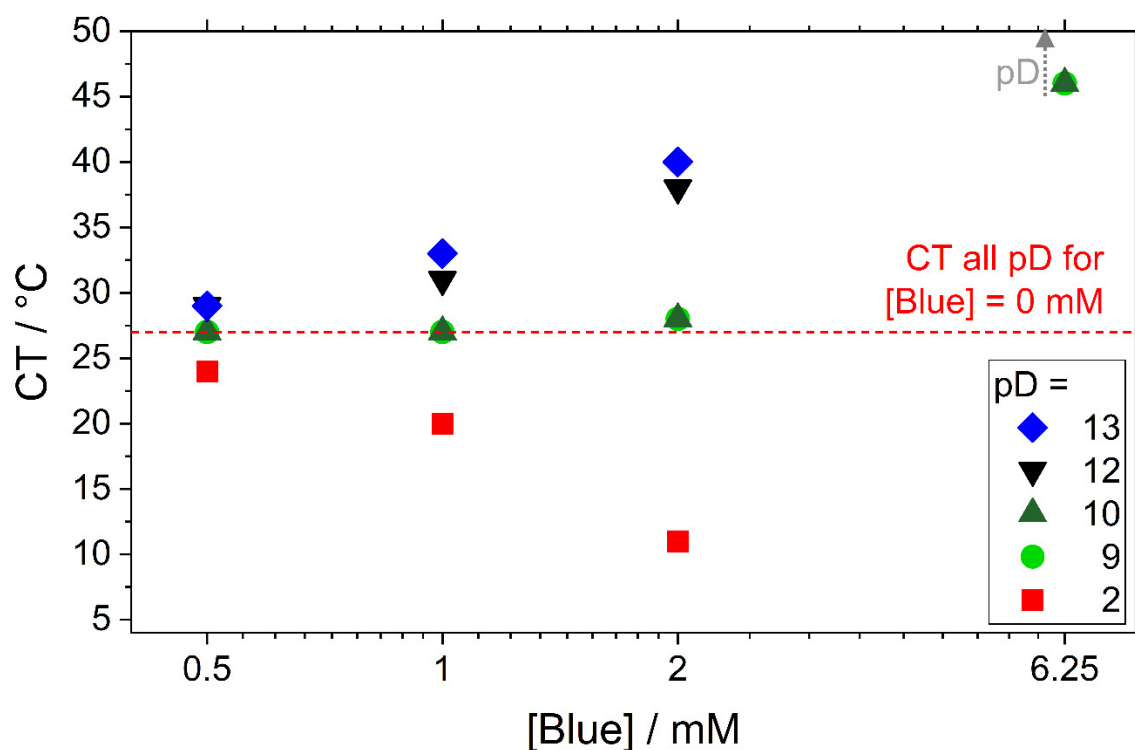


Figure 3: CTs of solutions containing the surfactant  $\text{hC}_{12}\text{hE}_5$  at a concentration of  $[\text{hC}_{12}\text{hE}_5] = 25 \text{ mM}$  and varying concentrations of Blue at different pD. An isotonic NaCl solution ( $I = 0.154 \text{ M}$ ) in  $\text{D}_2\text{O}$  served as the solvent. The pD was adjusted by addition of DCl or NaOD. For  $[\text{Blue}] = 12.5 \text{ mM}$ , solution CTs lay outside the observed temperature range, i.e. above  $50 \text{ }^\circ\text{C}$  for  $\text{pD} \geq 9$ . The same is true for  $[\text{Blue}] = 6.25 \text{ mM}$  at  $\text{pD} \geq 12$ . The latter observation is indicated by a grey, dotted arrow.  $\text{C}_{12}\text{E}_5$  solutions containing  $[\text{Blue}] \geq 6.25 \text{ mM}$  at  $\text{pD} = 2$  phase separated at all observed temperatures.

First and foremost, the CT of solutions containing only  $\text{hC}_{12}\text{hE}_5$  does not depend on solution pD. Changes in the CT of Blue- $\text{hC}_{12}\text{hE}_5$  solutions are therefore solely attributed to the presence of Blue at its given concentration and in its respective form ( $\text{BlueH}$ ,  $\text{Blue}^-$  or  $\text{Blue}^{2-}$ ) according to the pD of the solution. Table 1 provides an overview on dissociation states at variable pD based on

experimentally determined  $pK_A$  values. The determination of these  $pK_A$  values is outlined in the SI (section 7.8.1, sub-section "Determination of Blue acid dissociation constants").

Table 1: Position of the acid/base equilibrium shown in Figure 1 for different pD based on experimentally determined  $pK_A$  values. The determination of  $pK_A$  values is outlined in the SI (section 7.8.1) and was performed in an isotonic solution of NaCl in  $D_2O$  and at high  $C_{12E_5}$  excess at room temperature. The variable  $x$  denotes the mole fraction of each species in the acid/base equilibrium. Variations in that mole fraction, which could be induced through an experimental error of the pD to an extent of  $\pm 0.1$  are given as well.

pD	$x(\text{BlueH}) / \text{mol}\%$	$x(\text{Blue}^-) / \text{mol}\%$	$x(\text{Blue}^{2-}) / \text{mol}\%$
$2 \pm 0.1$	$100 \pm 0$	$0 \pm 0$	$0 \pm 0$
$9 \pm 0.1$	$0.3 \pm 0.1$	$99.5 \pm 0.2$	$0.2 \pm 0.1$
$10 \pm 0.1$	$0 \pm 0$	$96.9 \pm 0.8$	$3.1 \pm 0.8$
$12 \pm 0.1$	$0 \pm 0$	$24.0 \pm 5$	$76.0 \pm 5$
$13 \pm 0.1$	$0 \pm 0$	$3.1 \pm 0.8$	$96.9 \pm 0.8$

CTs shown in Figure 3 follow the trend expected for variations in additive polarity.<sup>14</sup> Addition of the rather nonpolar and poorly water soluble BlueH causes a significant decrease in the CT of  $C_{12E_5}$  solutions, which is already observed for a  $[\text{BlueH}]:[C_{12E_5}]$  ratio as low as 0.02:1, corresponding to the sample containing  $[\text{BlueH}] = 0.5 \text{ mM}$  in Figure 3.

At  $pD = 9$ , the CT is only slightly raised for low concentrations of Blue, but increases strongly for  $[\text{Blue}^-] = 6.25 \text{ mM}$ . It increases even more at higher concentrations of  $\text{Blue}^-$ , laying outside the observed temperature range for  $[\text{Blue}^-] = 12.5 \text{ mM}$ .

At  $pD = 13$ , Blue is two-fold deprotonated, which results in a greater increase of solution CT, even at low  $\text{Blue}^{2-}$  concentrations. As  $\text{Blue}^{2-}$  is expected to be more polar than  $\text{Blue}^-$ , the observed trend is consistent with the polarity hypothesis.<sup>14</sup>

At  $pD = 12$  a mixture of  $\text{Blue}^-$  and  $\text{Blue}^{2-}$  is present, resulting in an intermediate effect, which could be related to the  $\text{Blue}^-:\text{Blue}^{2-}$  ratio in such samples.

To conclude this section, the addition of the poorly water soluble BlueH to  $C_{12E_5}$  solution results in a reduction of their CT, whereas  $\text{Blue}^-$  and  $\text{Blue}^{2-}$  were observed to increase solution CT. With increasing  $[\text{Blue}]:[C_{12E_5}]$  ratio, the CT lowering or increase becomes more significant. Results are consistent with literature, which suggests an increase of the solubility of nonionic surfactant micelles and a concomitant CT increase upon addition of more polar additives.<sup>5,14</sup>

## 7.4 Morphology of C<sub>12</sub>E<sub>5</sub> surfactant micelles with and without Blue at variable pD

Small-angle scattering curves emerging from solutions of C<sub>n</sub>E<sub>m</sub> micelles frequently show a deviation from the anticipated form factor of rod-like aggregates in the regime of lower  $q$ . This can be attributed to the formation of wormlike micelles<sup>25–27</sup> and/or concentration fluctuations of the number density of micelles close to the phase transition threshold.<sup>11–13,28,29</sup> In the latter case, the scattering intensity in the low- $q$  regime can be described using the Ornstein-Zernike relation:<sup>11–13</sup>

$$C(q) = 1 + \frac{n_p k_B T \chi_T}{1 + q^2 \xi^2} = 1 + \frac{\kappa}{1 + q^2 \xi^2} \quad (1)$$

In eq (1),  $n_p$  is the number density of colloidal particles,  $k_B$  the Boltzmann constant,  $T$  the temperature,  $\chi_T$  the isothermal osmotic compressibility,  $q$  the modulus of the scattering vector and  $\xi$  the correlation length of local concentration fluctuations.

Based on cryogenic transmission electron microscopy (cryo-TEM) images, Bernheim-Groswasser et al.<sup>30</sup> suggested the coexistence of spherical and rather short wormlike micelles in C<sub>12</sub>E<sub>5</sub> solutions at temperatures sufficiently far away from the clouding temperature. In contrast to cryo-TEM, scattering techniques provide ensemble average information on a system. Scattering data on C<sub>n</sub>E<sub>m</sub> solutions were therefore mostly interpreted in terms of (polydisperse) cylinders rather than the coexistence of spherical and wormlike micelles.<sup>10,12,13</sup> To account for the deviation from the anticipated form factor of rod-like aggregates in the low- $q$  regime, a fluctuation scattering contribution according to eq (1) is often included in this approach.<sup>12,13,29</sup> As this does not permit to detect length changes of the overall wormlike assembly, a change in the cylinder length would therefore signal a variation in the ratio between spherical and wormlike micelles and/or a variation in the persistence length of wormlike micelles. Based on the analysis of cryo-TEM images, Bernheim-Groswasser et al.<sup>30</sup> furthermore suggested, that wormlike micelles interconnect close to the two-phase separation curve. This gives rise to the coexistence of concentrated and dilute networks of branched cylindrical micelles, which corroborates the assumption of fluctuation scattering close to the CT.<sup>30</sup> As both, wormlike micelles and concentration fluctuations cause a  $I(q) \sim q^{-2}$  dependency of the scattering intensity, it is not possible to discern whether an increase in the forward scattering intensity emerges from an increasing contour length of wormlike micelles or increasing correlation length of concentration fluctuations.<sup>31</sup> However, the consistent application of one of these models to a given set of scattering data may still reveal relevant trends in the investigated system.

The scattering intensity in a SANS experiment is described by the following equation:<sup>32,33</sup>

$$I_q(q) = N \cdot P(q) \cdot S(q) \quad (2)$$

In eq (2),  $N$  is the number density of scattering particles and  $P(q)$  the single particle form factor. In the presented case it reproduces the scattering cross section of that particle [ $\text{cm}^2$ ].<sup>32,33</sup>  $S(q)$  is the structure factor, which describes interparticle correlations. Structure factors were calculated for hard sphere potentials<sup>34,35</sup>, or spheres with attractive potentials (“Baxter” model)<sup>36</sup> and repulsive potentials (Hayter and Penfold).<sup>37</sup> Close to a liquid-liquid phase transition, the structure factor can be approximated by the Ornstein-Zernike expression  $C(q)$  (eq (1)).<sup>13,22</sup>

As the addition of Blue changes the CT of  $C_{12}E_5$  solutions, morphological transitions similar to temperature-induced transitions are expected for  $C_{12}E_5$  micelles. Therefore, SANS curves emerging from solutions of Blue and  $C_{12}E_5$  will be interpreted with models similar to models that were applied to describe the scattering from pure  $C_nE_m$  solutions. This means that concentration fluctuations of the number density of micelles are considered to contribute to the observed scattering signal while a cylindrical or spherical shape of Blue/ $C_{12}E_5$  micelles is assumed.<sup>13</sup>

For the analysis of SANS curves emerging from Blue/ $C_{12}E_5$  solutions, preliminary fits were first performed to assist a subsequent two-step fitting strategy.

Preliminary fits were performed on SANS curves of solutions containing  $[\text{Blue}] \leq 2 \text{ mM}$  at all pD. For this purpose, the form factor of end-capped core-shell cylinders including concentration fluctuations through the Ornstein-Zernike expression (eq (1)) was applied. The cylinder core length  $L_{\text{core}}$ , its shell thickness, scattering length densities and the parameters  $\kappa$  and  $\xi$  were fitted. Core lengths obtained from this approach were surprisingly similar and scattered around the average value of  $66 \text{ \AA}$  with a standard deviation of  $13 \text{ \AA}$ . The value of  $66 \text{ \AA}$  was therefore used as a starting point for further analysis.

Following the preliminary analysis, a two-step fitting strategy was applied: In the first step, cross section dimensions of Blue/ $C_{12}E_5$  assemblies upon assumption of a core-shell scattering length density profile were fitted. The core radius and its distribution obtained through step one were fixed in the second step, which served to investigate assembly size and fluctuation scattering parameters. In the following, both steps are discussed in detail.

**In the first step**, the average cross section of Blue/ $C_{12}E_5$  assemblies was analysed by only fitting the high- $q$  range ( $q > 0.045 \text{ \AA}^{-1}$ ) with form factors for core-shell assemblies. No structure factor

was considered here. Within this approach, the form factor model of a core-shell sphere and the form factor model of a core-shell cylinder were compared. Figure 4a displays the scattering length density difference ( $\Delta\eta$ ) profile, which was assumed for the cross section of these core-shell morphologies: The micellar core was assumed to possess a homogeneous scattering length density ( $\eta$ ), whereas the scattering length density difference between the micelle and the solvent was assumed to linearly decay towards the solvent in the shell region. The core radius  $r_{\text{core}}$  was furthermore assumed to be distributed according to a log-normal distribution. A log-normal distribution could account for small deviations in the assumed profile of  $\Delta\eta$  or polydispersity introduced by the coexistence of spherical and cylindrical micelles which possess different cross section dimensions.<sup>13,15</sup> Details on the choice of these models and on which model resulted in the best fit can be found in the SI (section 7.8.6, Table SI5).

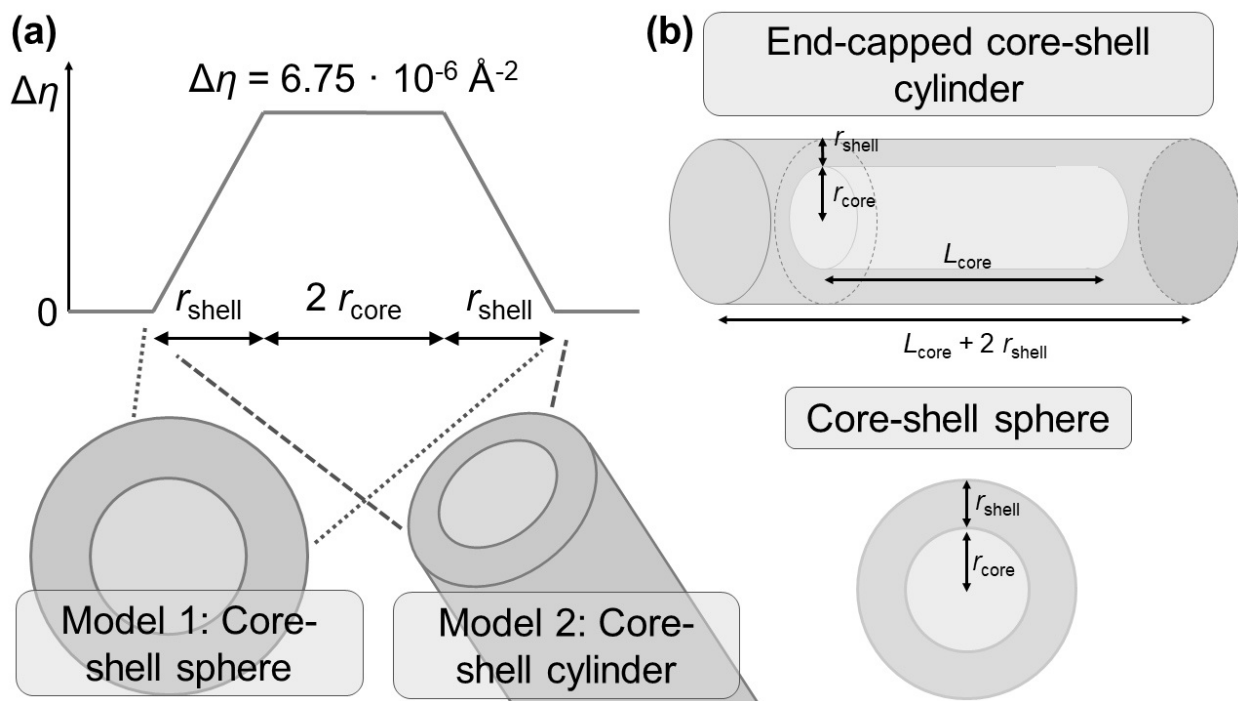


Figure 4: Schematic presentation of form factor models used for fitting (a) the high- $q$  range ( $q > 0.045 \text{ \AA}^{-1}$ ) and (b) the complete  $q$ -range of full contrast SANS curves emerging from solution containing Blue and  $\text{hC}_{12}\text{hE5}$ . (a) For fitting the high- $q$  range, the depicted scattering length density profile was assumed for the core-shell structure based on theoretical scattering length densities displayed in Table SI2 of the SI. (b) For fitting the entire  $q$ -range with the form factor of a core-shell structure, the core was assumed to possess the homogeneous scattering length density  $\eta_{\text{core}}$  and the shell was assumed to possess the homogeneous scattering length density  $\eta_{\text{shell}}$ .

Mean core radii ( $r_{\text{core}}$ ) were found to vary between  $12 \text{ \AA}$  and  $15 \text{ \AA}$  when the assumption of cylindrical micelles resulted in the best fit and between  $16 \text{ \AA}$  and  $17 \text{ \AA}$  when the SANS curve was best described upon assumption of spherical micelles (SI, section 7.8.6, Figure SI14). Standard deviations of  $r_{\text{core}}$ , which were calculated from the log-normal distribution, lay between  $2.5 \text{ \AA}$  and

4 Å in both cases. Shell thicknesses  $r_{\text{shell}}$  vary between 10 Å and 15 Å. None of these values show a systematic pD- or concentration dependency (SI, section 7.8.6, Figure SI14). The investigation of the micellar cross section was designed to provide dimensions of the micellar core, which were used in the subsequent analysis of the entire  $q$ -range.

**In the second step**, the whole  $q$ -range of full contrast SANS curves was analysed. For this purpose, form factors  $P(q)$  of end-capped core-shell cylinders with a core length  $L_{\text{core}}$  of either 20 Å, 40 Å, 66 Å, 100 Å or 200 Å and the form factor of a core-shell sphere (Figure 4b) were systematically applied to all experimental SANS curves. The choice of the intermediate value for  $L_{\text{core}}$  (66 Å) was based on the above-described preliminary analysis. The choice of the form factor for end-capped core-shell cylinders with flat ends rather than hemispherical end caps was based on its availability in common SANS analysis software (SasView, SASfit). Core dimensions were kept constant during fitting, because  $L_{\text{core}}$  was given and the core radius and its distribution were fixed to values that were obtained in the first step. Fluctuation scattering was included by substituting  $S(q)$  in eq (2) by the Ornstein-Zernike expression (eq. (1)).

The approach of keeping  $L_{\text{core}}$  constant was chosen to be able to compare correlation lengths of concentration fluctuations ( $\xi$ ) for different samples without having to consider the co-dependency of  $\xi$  and  $L_{\text{core}}$ . At the same time, it permits the comparison of different form factors, i.e. spheres or cylinders of different length, which enables deductions on micellar growth.

In all cases, the particle number density ( $N$ ) was estimated based on the core dimensions  $L_{\text{core}}$  and  $r_{\text{core}}$ : The quotient between the core volume and the partial molar volume of a C<sub>12</sub> alkyl chain ( $350.2 \text{ Å}^3$ )<sup>38</sup> provided an estimate for the micellar aggregation number. Assuming, that all C<sub>12</sub>E<sub>5</sub> molecules participate in assembly formation,  $N$  was then calculated from the known concentration of C<sub>12</sub>E<sub>5</sub> surfactant and the aggregation number. The shell thickness ( $r_{\text{shell}}$ ), scattering length densities of the core ( $\eta_{\text{core}}$ ) and the shell ( $\eta_{\text{shell}}$ ) and Ornstein-Zernike scattering parameters  $\kappa$  and  $\xi$  were fitted.

Figure 5 displays a representative set of SANS curves and fits with a selection of applied form factor models at variable pD corresponding to a variable polarity of Blue at [Blue] = 2 mM. All other SANS curves are shown in Figure SI15 to Figure SI18 in the SI (section 7.8.6).

Almost all fits with  $L_{\text{core}} \leq 100 \text{ Å}$  describe the low and mid- $q$  range ( $q < 0.134 \text{ Å}^{-1}$ ) of experimental SANS curves reasonably well. For this reason, fits were compared by means of the reduced  $\chi^2$  parameter at low- and mid- $q$  values ( $q < 0.134 \text{ Å}^{-1}$ ). This comparison is shown in the SI

(section 7.8.6, Table SI6). Following this analysis, Table 2 provides an overview on which form factor model best described the low- $q$  range of experimental SANS curves for each sample.

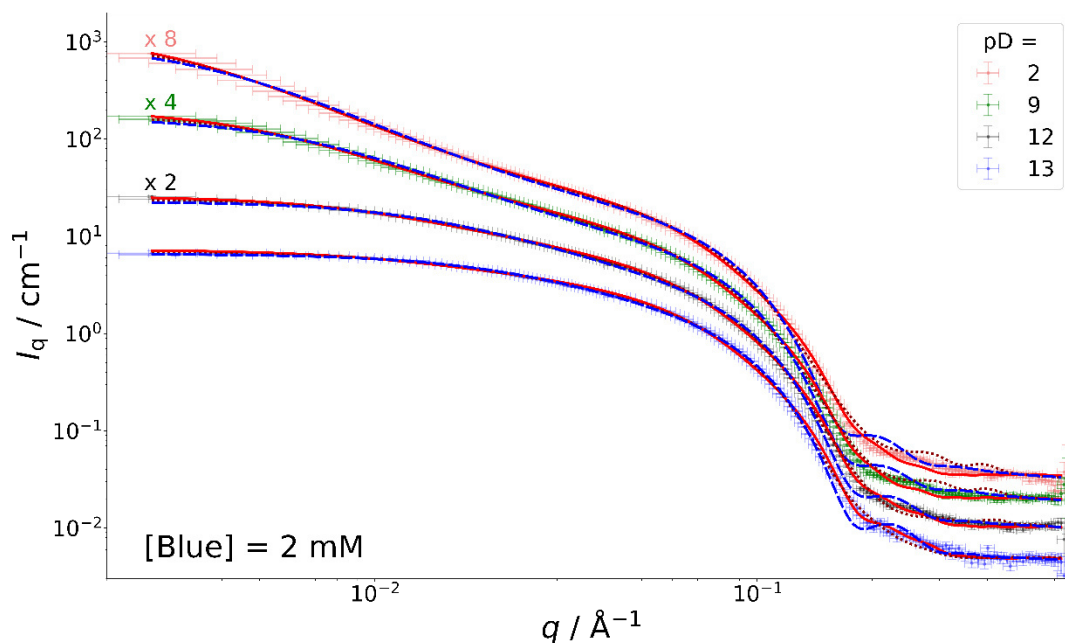


Figure 5: Full contrast SANS curves of solutions containing  $[\text{hC}_{12}\text{hE}_5] = 25 \text{ mM}$ , and  $[\text{Blue}] = 2 \text{ mM}$  at variable pD. An isotonic NaCl solution ( $I = 0.154 \text{ M}$ ) in  $\text{D}_2\text{O}$  served as the solvent. SANS curves were recorded at a sample temperature of  $10 \text{ }^\circ\text{C}$ . Red line (—): Fit with the form-factor of end-capped core-shell cylinders with a core length of  $L_{\text{core}} = 66 \text{ \AA}$  and Ornstein-Zernike scattering. Dark red dotted line (.....): Fit with the same model, but  $L_{\text{core}} = 40 \text{ \AA}$ . Blue dashed line (---): Fit with the form factor of core-shell spheres and Ornstein-Zernike scattering.

From Table 2, the shrinking of assembly size towards higher pD is clearly visible. Except for pD = 2, a decrease in assembly size is also observed when the Blue concentration is increased. The data of Table 2 indicate, that changes in solution conditions can cause shrinking or growth of micelles. Samples far away from the clouding temperature ( $\Delta T_{\text{CT}} > 20 \text{ K}$ ) tend to contain smaller micelles than samples closer to the CT, given that all measurements were performed at the same temperature and a variation in  $\Delta T_{\text{CT}}$  is caused by a shift of the clouding temperature.

SANS curves of samples containing  $[\text{Blue}] \geq 6.25 \text{ mM}$  and  $\text{pD} \geq 12$  could not be described with the above-discussed models. Ornstein-Zernike scattering was therefore neglected in a first attempt to describe experimental data with the form factor of a core-shell sphere. Corresponding fits are shown in the SI, Figure SI17 and Figure SI18. They were significantly improved upon inclusion of a structure factor derived from the hard sphere interaction potential.<sup>34,35</sup> The intermicellar distance was fitted and lays between  $68 \text{ \AA}$  and  $80 \text{ \AA}$ . This is larger than the mean diameter obtained for spherical micelles ( $2 \cdot [r_{\text{core}} + r_{\text{shell}}] \approx 58 \text{ \AA}$ ), which confirms the appearance of repulsive inter-micellar interactions in these samples.



Table 2: Form factor model which best reproduced the experimental full contrast SANS curve in the mid- and low- $q$  range ( $q < 0.134 \text{ \AA}^{-1}$ ) out of six applied models: Core-shell sphere or end-capped core-shell cylinder with a core length  $L_{\text{core}}$  of either 20  $\text{\AA}$ , 40  $\text{\AA}$ , 66  $\text{\AA}$ , 100  $\text{\AA}$  or 200  $\text{\AA}$ . Ornstein-Zernike scattering (eq (1)) was considered in all cases. SANS curves from samples with  $[\text{Blue}] \geq 6.25 \text{ mM}$  and  $pD \geq 12$  could not be described under the assumption of Ornstein-Zernike scattering. Here, the form factor of core-shell spheres needed to be combined with a structure factor taking into account repulsive hard sphere interactions. All samples contained  $\text{hC}_{12}\text{hE}_5$  at a concentration of  $[\text{hC}_{12}\text{hE}_5] = 25 \text{ mM}$ . An isotonic NaCl solution ( $I = 0.154 \text{ M}$ ) in  $\text{D}_2\text{O}$  served as the solvent. SANS curves were recorded at a sample temperature of 10 C.

	pD = 2	pD = 9	pD = 12	pD = 13
[Blue] = 0 mM	end-capped core-shell cylinder, $L_{\text{core}} = 66 \text{ \AA}$	end-capped core-shell cylinder, $L_{\text{core}} = 66 \text{ \AA}$	end-capped core-shell cylinder, $L_{\text{core}} = 66 \text{ \AA}$	end-capped core-shell cylinder, $L_{\text{core}} = 66 \text{ \AA}$
[Blue] = 1 mM	end-capped core-shell cylinder, $L_{\text{core}} = 66 \text{ \AA}$	end-capped core-shell cylinder, $L_{\text{core}} = 66 \text{ \AA}$	end-capped core-shell cylinder, $L_{\text{core}} = 40 \text{ \AA}$	end-capped core-shell cylinder, $L_{\text{core}} = 40 \text{ \AA}$
[Blue] = 2 mM	end-capped core-shell cylinder, $L_{\text{core}} = 66 \text{ \AA}$	end-capped core-shell cylinder, $L_{\text{core}} = 66 \text{ \AA}$	end-capped core-shell cylinder, $L_{\text{core}} = 40 \text{ \AA}$	end-capped core-shell cylinder, $L_{\text{core}} = 40 \text{ \AA}$
[Blue] = 6.25 mM	phase separated	end-capped core-shell cylinder, $L_{\text{core}} = 40 \text{ \AA}$	core-shell sphere, $r_{\text{core}} = 17.1 \text{ \AA}$ , hard sphere potential	core-shell sphere, $r_{\text{core}} = 16.3 \text{ \AA}$ , hard sphere potential
[Blue] = 12.5 mM	phase separated	end-capped core-shell cylinder, $L_{\text{core}} = 40 \text{ \AA}$	core-shell sphere, $r_{\text{core}} = 16.9 \text{ \AA}$ , hard sphere potential	core-shell sphere, $r_{\text{core}} = 16.5 \text{ \AA}$ , hard sphere potential

Figure 6a displays correlation lengths of concentration fluctuations ( $\xi$ ) obtained from above-described fits for the cases of core-shell cylinders with a core length of either 66  $\text{\AA}$  (solid symbols) or 40  $\text{\AA}$  (open symbols). Trends for  $\xi$  are similar for both core lengths.

At  $pD = 2$ ,  $\xi$  strongly increases with increasing concentration of Blue. This signals stronger attractive interactions between micelles when the system contains BlueH and is therefore consistent with the decrease of solution CT upon addition of BlueH.

At  $pD = 9$ ,  $pD = 12$  and  $pD = 13$ ,  $\xi$  decreases upon addition of [Blue]. This decrease in attractive interactions is more pronounced at  $pD \geq 12$ . Lack of  $\xi$  for  $[\text{Blue}] \geq 6.25 \text{ mM}$  signals the absence of concentration fluctuations. It was discussed above, that the respective samples ( $[\text{Blue}] \geq 6.25 \text{ mM}$  and  $pD \geq 12$ ) even show repulsive inter-micellar interactions.

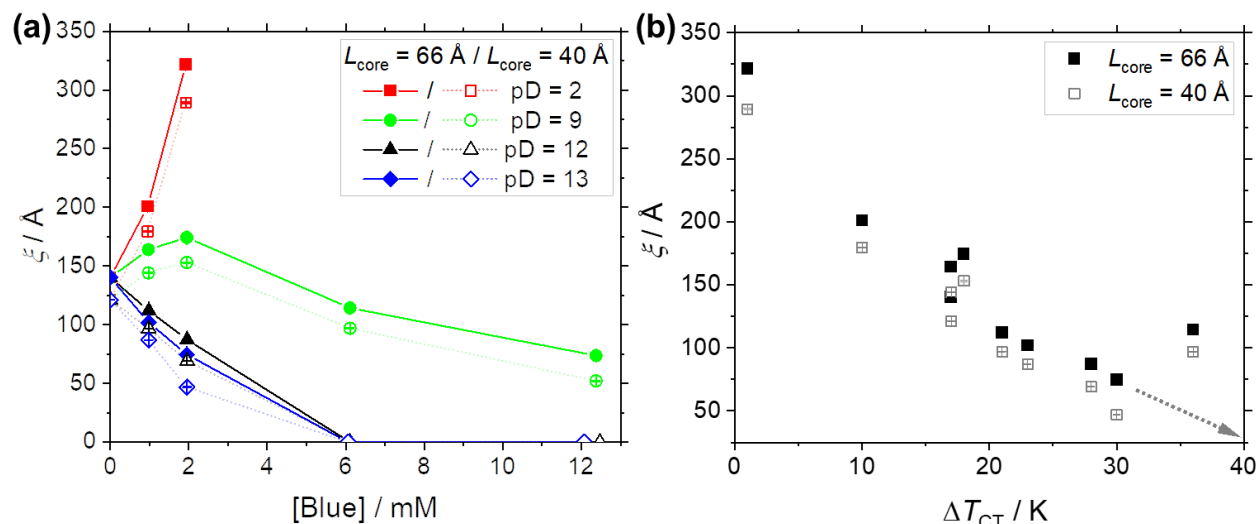


Figure 6: (a) Correlation length of concentration fluctuations  $\xi$  obtained from fitting full contrast SANS curves with the Ornstein-Zernike expression when assuming the form factor of end-capped core-shell cylinders with a core length of either  $L_{\text{core}} = 66$  Å or  $L_{\text{core}} = 40$  Å. Samples contained the indicated concentration of Blue at the given pD as well as  $\text{hC}_{12}\text{hE}_5$  at a concentration of  $[\text{hC}_{12}\text{hE}_5] = 25$  mM. An isotonic NaCl solution prepared in  $\text{D}_2\text{O}$  served as the solvent. SANS curves were recorded at a sample temperature of  $10$  °C. (b) The same values of  $\xi$  as a function of the temperature distance between the sample temperature and the CT of that sample, independent of sample composition. The grey, dotted arrow indicates, that no Ornstein-Zernike fluctuations were observed for most samples with  $\Delta T_{\text{CT}} > 40$  °C.

Figure 6b displays  $\xi$  as a function of the difference  $\Delta T_{\text{CT}}$  between the measurement temperature ( $10$  °C) and the CT of a given sample. Data obtained for all samples are displayed, independent of pD or Blue concentration. It is clearly seen that  $\xi$  decreases with the temperature distance from the CT, and does not depend on sample composition. As the measurement temperature was  $10$  °C and CTs were only observed up until  $50$  °C, the maximum observable  $\Delta T_{\text{CT}}$  amounts to  $40$  K. Data of five samples with  $\Delta T_{\text{CT}} > 40$  K are therefore not shown in the graph, but confirm the observed trend, as  $\xi = 52$  Å or  $74$  Å ( $L_{\text{core}} = 40$  Å or  $L_{\text{core}} = 66$  Å) for one sample and  $\xi = 0$  for the other four.

The analysis of SANS curves from samples containing  $\text{C}_{12}\text{E}_5$  at a constant concentration of  $[\text{C}_{12}\text{E}_5] = 25$  mM and a constant temperature of  $10$  °C confirmed, that the addition of Blue changes both, the size and inter-micellar interactions of  $\text{C}_{12}\text{E}_5$  micelles. Addition of BlueH significantly increases attractive interactions between micelles, whereas the addition of Blue<sup>-</sup> or Blue<sup>2-</sup> weakens inter-micellar attractions. This effect is more pronounced when Blue<sup>2-</sup> is added, which even induces the formation of micelles with repulsive inter-micellar interactions at  $[\text{Blue}^{2-}] \geq 6.25$  mM. In a summarizing analysis, the correlation length of concentration fluctuations as a measure for attractive inter-micellar interactions was shown to decrease with the temperature distance from the CT of a sample. This was observed upon comparison of data for all samples, independent of the added Blue species and its concentration. Concerning assembly size,

cylindrical C<sub>12</sub>E<sub>5</sub> micelles were shown to shrink upon addition of sufficient concentrations of Blue<sup>-</sup> or Blue<sup>2-</sup>, even resulting in the formation of spherical micelles in case of the latter. As SANS only permits the observation of ensemble average information, it is not clear whether the observed shrinking results from the continuous shrinking of the length of all cylindrical micelles or from a variation in the ratio between cylindrical and spherical assemblies.

## 7.5 Localization of Blue in C<sub>12</sub>E<sub>5</sub> micelles

**<sup>1</sup>H-NMR spectroscopy:** Changes in chemical shift and peak width of surfactant <sup>1</sup>H-resonances upon Blue addition provide first insights on the solubilisation locus of Blue in hC<sub>12</sub>hE<sub>5</sub> surfactant micelles.<sup>39–43</sup> Figure 7 shows the hC<sub>12</sub>hE<sub>5</sub> resonance region of <sup>1</sup>H-NMR spectra recorded from solutions containing Blue and hC<sub>12</sub>hE<sub>5</sub> in comparison to the spectrum of a pure hC<sub>12</sub>hE<sub>5</sub> solution. Resonances between 3.3 ppm and 3.5 ppm in the pure surfactant spectrum are assigned to protons of the pentaethyleneglycol head group. The most upfield shifted resonances belong to protons of the EG group closest to the hydrophobic core and the most downfield shifted resonances belong to protons of the EG group furthest away from the core.<sup>6,44</sup>

The first row in Figure 7 shows hC<sub>12</sub>hE<sub>5</sub> proton resonances of solutions containing [Blue] = 2 mM and [hC<sub>12</sub>hE<sub>5</sub>] = 25 mM for different pD. Analogously, the second row displays spectra recorded from solutions containing [Blue] = 12.5 mM and [hC<sub>12</sub>hE<sub>5</sub>] = 25 mM. The latter was not recorded for pD = 2 due to phase separation of the sample.

Addition of BlueH to a hC<sub>12</sub>hE<sub>5</sub> solution causes significant peak broadening of surfactant alkyl chain signals, which is not the case for resonances of the pentaethyleneglycol head group (Figure 7a). The latter furthermore show only a small variation in their chemical shift. Peak broadening of a multiproton resonance can be caused by the creation of differing microenvironments for these protons due to the spatial proximity of an additive. As the original peak was assigned to multiple protons, peak broadening due to splitting of resonances therefore signals the transition from protons experiencing a similar chemical environment to protons with different microenvironments. The significant peak broadening of the alkyl chain signal **b** in Figure 7a upon addition of BlueH points towards a localization of BlueH close to corresponding protons. Blue<sup>-</sup> and Blue<sup>2-</sup> induce less severe peak broadening of signal **b** compared to BlueH (Figure 7b and Figure 7c). They furthermore exert a smaller influence on the chemical shifts of signals **a**, **b** and **c**, signalling reduced penetration of these charged Blue species into the micellar core.

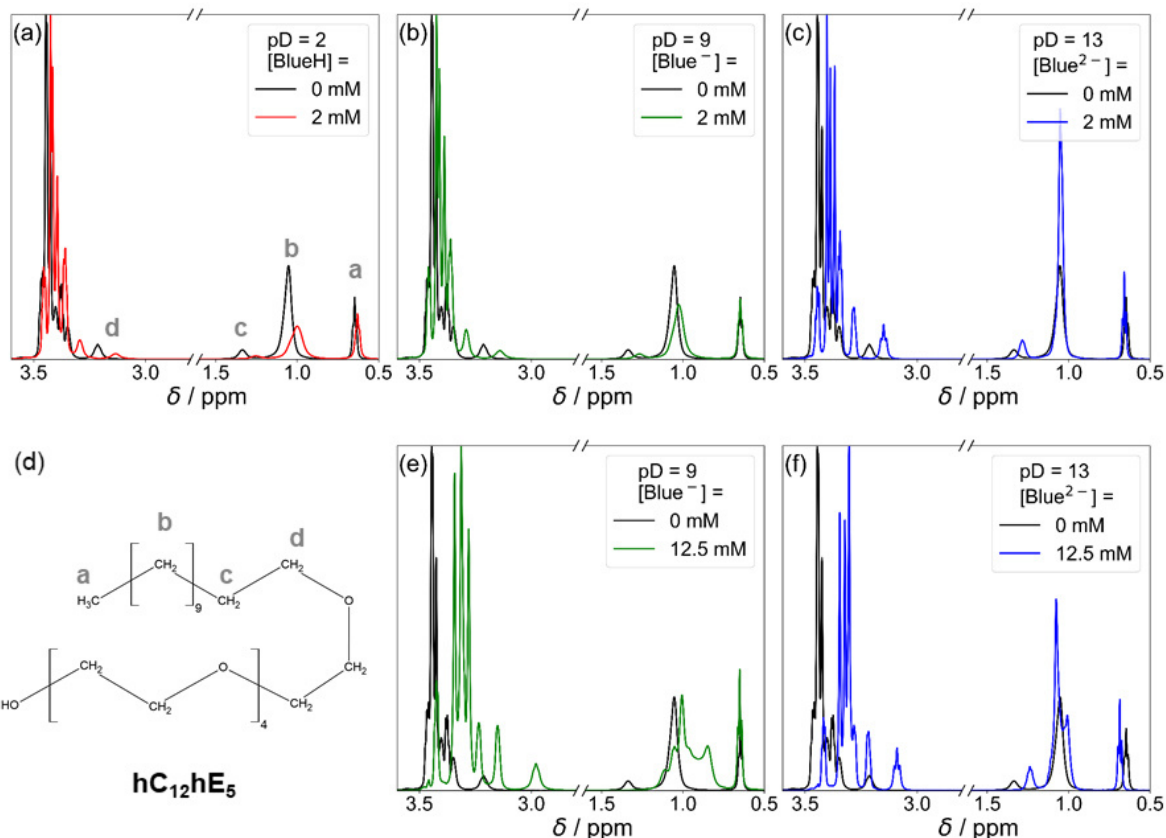


Figure 7:  $\text{hC}_{12}\text{hE}_5$  resonance region in  $^1\text{H}$ -NMR spectra of solutions containing Blue and  $[\text{hC}_{12}\text{hE}_5] = 25 \text{ mM}$  at variable Blue concentration and pD compared to the  $^1\text{H}$ -NMR spectrum of a pure surfactant solution (black line). An isotonic NaCl solution ( $I = 0.154 \text{ M}$ ) in  $\text{D}_2\text{O}$  served as the solvent. All measurements were performed at  $10^\circ\text{C}$ . Solutions containing  $[\text{Blue}] = 12.5 \text{ mM}$  and  $[\text{hC}_{12}\text{hE}_5] = 25 \text{ mM}$  phase separate at  $\text{pD} = 2$ , therefore no NMR-spectrum could be recorded for such a sample. (d) Displays the assignment of  $^1\text{H}$ -NMR resonances of the pure  $\text{hC}_{12}\text{hE}_5$  spectrum in (a) to protons of the  $\text{hC}_{12}\text{hE}_5$  molecule.<sup>6,40,45</sup> Resonances between 3.3 ppm and 3.5 ppm in the pure surfactant spectrum belong to protons of the pentaethyleneglycol head group ( $\text{E}_5$ ).<sup>6,40,45</sup>

Spectra recorded at higher Blue concentrations (Figure 7e and Figure 7f) reveal differences between  $\text{Blue}^-$  and  $\text{Blue}^{2-}$ : Adding  $\text{Blue}^-$  to a solution of  $\text{hC}_{12}\text{hE}_5$  causes significant peak broadening of signal **b**, whereas  $\text{Blue}^{2-}$  does not strongly affect the width of this resonance. This indicates that  $\text{Blue}^-$  has a higher affinity to the micellar core than  $\text{Blue}^{2-}$ . Resonances of the pentaethyleneglycol head group are significantly upfield shifted when either  $\text{Blue}^-$  or  $\text{Blue}^{2-}$  is added at a concentration of 12.5 mM. This can easily be explained by the shielding effect the negative charge of  $\text{Blue}^-$  or  $\text{Blue}^{2-}$  exerts on surrounding protons. The increased separation between pentaethyleneglycol resonances can be explained by the same argumentation as peak broadening.<sup>40</sup>

It needs to be kept in mind, that a time-averaged signal over all species in the sample solution is recorded.<sup>41,46</sup> Accordingly, it is not possible to decide whether chemical shift variations are caused by a change in the equilibrium ratio between  $\text{hC}_{12}\text{hE}_5$  micelles with Blue and  $\text{hC}_{12}\text{hE}_5$  micelles without Blue or by a continuous change in the electron density around all  $\text{hC}_{12}\text{hE}_5$  protons upon

addition of Blue. Considering the dynamic equilibrium of micellar surfactant solutions, both mechanisms likely influence surfactant  $^1\text{H}$ -resonances.<sup>46,47</sup>

**Nuclear Overhauser Effect spectroscopy:** Nuclear Overhauser Effect spectroscopy (NOESY) provides a less ambiguous picture of the spatial proximity between Blue and  $\text{hC}_{12}\text{hE}_5$  protons. Based on through-space magnetic interactions (dipolar coupling), proton pairs with an inter proton distance smaller than about 5 Å can be detected.<sup>48,49</sup> These proton pairs can directly be identified by assigning cross-peaks in the 2-dimensional NOESY spectrum. Figure 8a, b and c display a relevant section of NOESY spectra showing Blue- $\text{hC}_{12}\text{hE}_5$  cross peaks. These spectra were recorded from solutions containing Blue at a concentration of  $[\text{Blue}] = 2 \text{ mM}$  and  $\text{hC}_{12}\text{hE}_5$  at a concentration of  $[\text{hC}_{12}\text{hE}_5] = 25 \text{ mM}$  at variable pD.

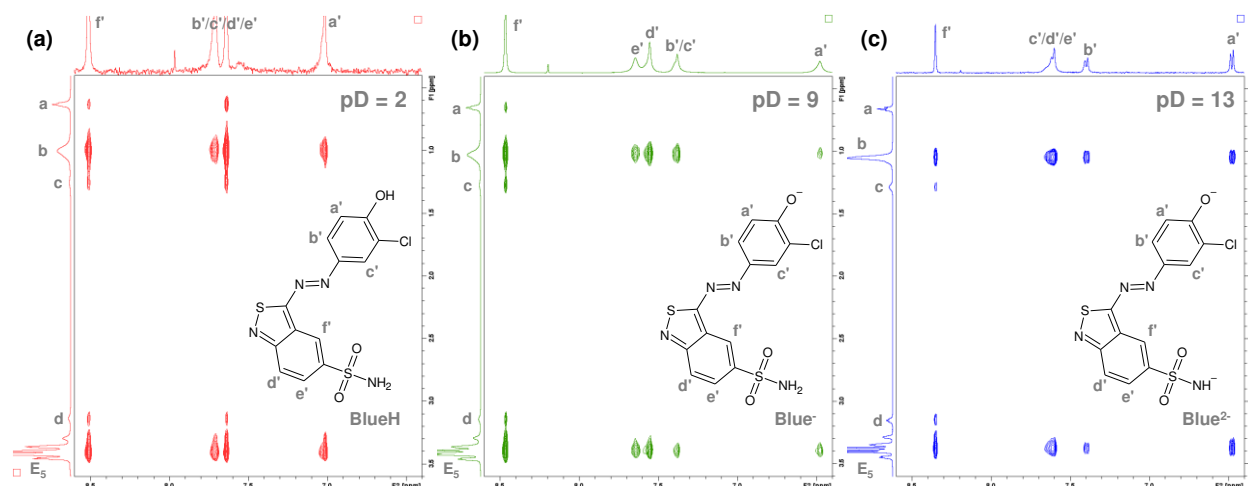


Figure 8: Section of NOESY spectra recorded from solutions containing Blue at a concentration of  $[\text{Blue}] = 2 \text{ mM}$  and  $\text{hC}_{12}\text{hE}_5$  at a concentration of  $[\text{hC}_{12}\text{hE}_5] = 25 \text{ mM}$ . An isotonic NaCl solution ( $I = 0.154 \text{ M}$ ) in  $\text{D}_2\text{O}$  served as the solvent. All measurements were performed at  $10 \text{ }^\circ\text{C}$ . (a), (b) and (c) correspond to spectra of samples with pD = 2, pD = 9 and pD = 13 respectively. The corresponding Blue species is shown in each spectrum to indicate peak assignment. The assignment of surfactant resonances is based on Figure 7d.

All spectra exhibit cross peaks between Blue proton resonances and proton resonances of the  $\text{hC}_{12}\text{hE}_5$  head group as well as between Blue proton resonances and proton resonances of methylene protons of the  $\text{hC}_{12}\text{hE}_5$  alkyl chain. Therefore, Blue neighbours surfactant head groups as well as hydrophobic methylene groups. Figure 8a furthermore shows discernible cross peaks between BlueH resonances and the terminal methyl group of the surfactant alkyl chain, which strengthens the hypothesis that BlueH penetrates deeply into the micellar core. The absence of cross peaks for some BlueH resonances is attributed to the broad peak width and low signal-to-noise ratio. For  $\text{Blue}^-$  and  $\text{Blue}^{2-}$  (Figure 8b and Figure 8c), no or negligible cross peaks with the resonance of the terminal  $\text{hC}_{12}\text{hE}_5$  methyl group occur. This remains the case for higher concentrations of  $\text{Blue}^-$  and  $\text{Blue}^{2-}$  (SI, section 7.8.7, Figure SI21).

Based on NMR-spectroscopic observations, the following conclusions are made: A distribution of all species of Blue between the hydrophilic  $C_{12}E_5$  head group and at least a part of the hydrophobic core region is expected. BlueH penetrates deeper into the hydrophobic core of  $C_{12}E_5$  micelles than  $Blue^-$  and  $Blue^{2-}$ . At high concentrations of  $Blue^-$  ( $[Blue^-] = 12.5 \text{ mM}$ ),  $Blue^-$  strongly affects alkyl chain  $^1H$ -NMR resonances of the surfactant, which signals that penetration brings  $Blue^-$  at least close to the aliphatic core.  $Blue^{2-}$  likely does not significantly penetrate into the micellar core, even at high concentration. Unfortunately, it cannot be distinguished whether chemical shift changes result from a shift in the ratio of different types of micelles (i.e. micelles loaded with Blue and micelles without Blue) or by a continuous variation of proton shielding in a single type of micelle. These mechanisms are not mutually exclusive. Complementary information on the spatial distribution of Blue in  $C_{12}E_5$  micelles is expected to be retrieved from SANS.

**SANS contrast matching:** Contrast matching the surfactant to the solvent in solutions of Blue and  $C_{12}E_5$  permits the detection of a  $q$ -dependent scattering signal, which arises from Blue only. Therefore, it is possible to directly observe the assembly of Blue in  $C_{12}E_5$  solutions. Such an investigation may permit the localisation of Blue in  $C_{12}E_5$  micelles.

Before discussing SANS curves from  $C_{12}E_5$ -matched samples at different pD, a few general remarks on their evaluation will be made: (1) The significance of SANS curves from samples containing a high excess of  $C_{12}E_5$ , i.e. samples which contain Blue at a concentration of either  $[Blue] = 1 \text{ mM}$  or  $[Blue] = 2 \text{ mM}$ , is strongly limited, because of the low Blue content of each micelle under these conditions. (2) If all micelles contain Blue and  $C_{12}E_5$  at a similar ratio, correlation lengths for concentration fluctuations in  $C_{12}E_5$  contrast matched samples should be similar to correlation lengths obtained from SANS curves of corresponding full contrast samples. (3) It was abstained from including any size distribution of Blue assemblies into the evaluation of  $C_{12}E_5$ -matched SANS curves. Even though the polydispersity of certain dimensions, e.g. the length of Blue assemblies, is possible, the inclusion of a distribution function would lead to over parameterization of fits to relatively noisy data.

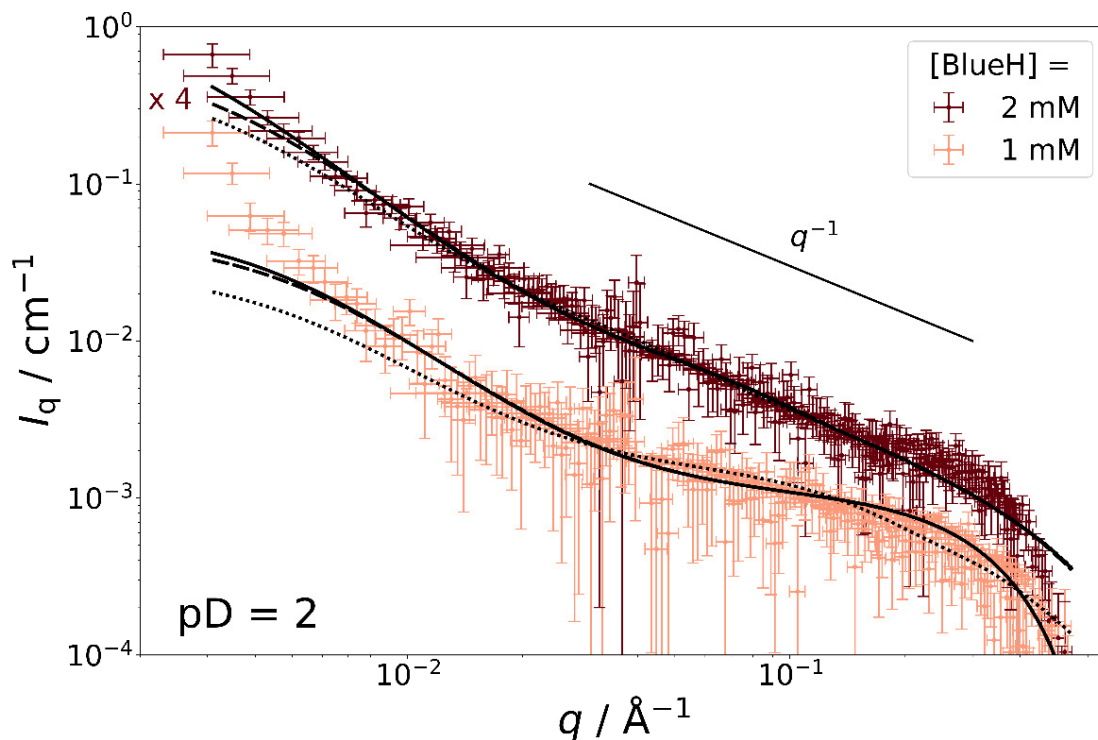


Figure 9:  $C_{12}E_5$ -matched SANS curves obtained from solutions with  $pD = 2$  containing  $[mC_{12}mE_5] = 25$  mM and BlueH at variable concentration in an isotonic NaCl solution prepared in  $D_2O$ . Measurements were performed at a sample temperature of  $10$  °C. Dotted line (.....): Fit with the form factor of a cylinder including Ornstein-Zernike scattering as a structure factor with  $\kappa$  and  $\xi$  obtained from the corresponding SANS full contrast measurement. Dashed line (---): Fit with the same model, but only  $\xi$  was kept constant according to the value obtained from the SANS full contrast measurement. Solid line (\_\_\_): Fit with the same model, but  $\xi$  was kept constant according to a value obtained from static light scattering. Precise parameters for each fit can be found in the SI, section 7.8.9, Table SI7.

Figure 9 displays SANS curves from solutions containing  $mC_{12}mE_5$  at a concentration of 25 mM and BlueH at a concentration of either 1 mM or 2 mM ( $pD = 2$ ). A  $I_q \sim q^{-1}$  slope is observed at  $q > 0.1 \text{ \AA}^{-1}$  for  $[BlueH] = 1$  mM and at  $q > 0.003 \text{ \AA}^{-1}$  for  $[BlueH] = 2$  mM. This observation points towards a rod-like arrangement of BlueH. Therefore, experimental SANS curves were fitted with a form factor for cylinders while including Ornstein-Zernike scattering (eq (1)) as  $S(q)$  according to:

$$I_q(q) = N \cdot P_{cylinder}(q) \cdot C(q) \quad (3)$$

The inclusion of Ornstein-Zernike scattering into the evaluation of SANS curves from solutions containing BlueH and  $C_{12}E_5$  at  $pD = 2$  is necessary, because the addition of BlueH increases the significance of attractive interactions between micelles. Figure 9 shows fits obtained upon assumption of correlation lengths ( $\xi$ ) that were determined with fits to full contrast SANS data (dotted and dashed curve) and upon assumption of  $\xi$  obtained from the evaluation of static light

scattering (SLS) data (solid curve). Better fits were obtained, when the scaling parameter  $\kappa$ , which relates to the isothermal osmotic compressibility, was varied (Figure 9 and SI, section 7.8.9, Table SI7). Larger values of  $\kappa$  were found in fits to C<sub>12</sub>E<sub>5</sub> matched data compared to the corresponding full contrast data. This discrepancy in  $\kappa$  could be caused by an inhomogeneous distribution of BlueH throughout the micelles, e.g. some C<sub>12</sub>E<sub>5</sub> micelles contain more and some contain less BlueH.

In all cases, cylindrical BlueH aggregates with a cross section radius of less than 6 Å were observed. Considering, that the length of a fully extended C<sub>12</sub> alkyl chain equals 16.7 Å<sup>50</sup> this means, that cylindrical domains formed by BlueH in C<sub>12</sub>E<sub>5</sub> solution can easily fit into the hydrophobic alkyl chain region of cylindrical C<sub>12</sub>E<sub>5</sub> micelles. This situation is schematically displayed in Table 3 and coherent with findings from the analysis of NMR spectra (Figure 7 and Figure 8), which indicate the interaction between BlueH and the hydrophobic C<sub>12</sub> alkyl chain of C<sub>12</sub>E<sub>5</sub>.

Figure 10 displays C<sub>12</sub>E<sub>5</sub> contrast-matched SANS curves from solutions containing mC<sub>12</sub>mC<sub>5</sub> at a concentration of 25 mM and variable concentrations of Blue<sup>-</sup> at pD = 9. Form factor oscillations that could be characteristic for a cylinder cross section become visible at  $q > 0.1 \text{ \AA}^{-1}$  for high concentrations of Blue<sup>-</sup> ( $\geq 6.25 \text{ mM}$ ).

The SANS curves shown in Figure 10 were fitted with the following model, which assumes the co-existence of cylindrical domains of Blue<sup>-</sup> with a core-shell structure ( $P_{\text{core-shell-cylinder}}$ ) and of molecularly dissolved Blue<sup>-</sup> or small oligomers thereof:

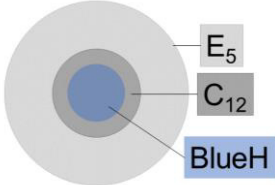
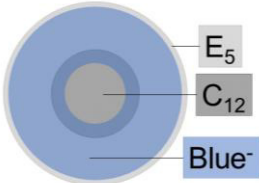
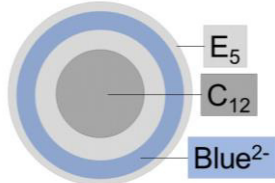
$$I_q(q) = N \cdot P_{\text{core-shell-cylinder}}(q) \cdot C(q) + I_{q,\text{Guinier}}(q) \quad (4)$$

$$I_{q,\text{Guinier}}(q) = A \cdot \exp\left(\frac{-R_g^2 \cdot q^2}{3}\right) \quad (5)$$

$I_{q,\text{Guinier}}(q)$  is a Guinier expression, which describes scattering from molecularly dissolved Blue<sup>-</sup> molecules (or small oligomers thereof) and accounts for the decay of the scattering intensity at  $q > 0.2 \text{ \AA}^{-1}$ . In eq (5),  $R_g$  is the radius of gyration and  $A$  the scaling factor or forward scattering intensity. By performing Guinier fits according to eq (5) to the  $q$ -range of  $q > 0.2 \text{ \AA}^{-1}$ , the value of  $R_g$  was identified to lay between 4.2 Å and 6.5 Å for all samples. It needs to be pointed out, that these values are not precise due to the low scattering intensity ( $I_q < 0.001 \text{ cm}^{-1}$ ) and the high signal-to-noise ratio in this  $q$ -range. Nevertheless, parameters from Guinier fits were kept constant in subsequent fits using eq (4).



Table 3: Form factor models for fitting SANS curves from C<sub>12</sub>E<sub>5</sub>-matched solutions with [mC<sub>12</sub>mE<sub>5</sub>] = 25 mM containing the indicated concentration of Blue in an isotonic NaCl solution in D<sub>2</sub>O at 10 °C and at the given pD. The contrast was fixed to a theoretical value of  $\Delta\eta = 3.358 \cdot 10^{-6} \text{ \AA}^{-2}$ . In case of core shell structures, the contrast of the core was fixed to  $\Delta\eta = 0$  and the contrast of the shell was fixed to  $\Delta\eta = 3.358 \cdot 10^{-6} \text{ \AA}^{-2}$ . The particle number density ( $N$ ) and cross section size parameters were fitted. Cross section size parameters, which resulted from such a fit to C<sub>12</sub>E<sub>5</sub> matched SANS curves are compared to cross section size parameters, which were obtained from fits to the high- $q$  region of corresponding full contrast SANS curves (step one of the two-step fitting strategy for full contrast SANS curves). Full contrast cross section dimensions describe a cylinder cross section in all cases except for samples with pD = 13 and [Blue<sup>2-</sup>]  $\geq$  6.25 mM, where  $r_{\text{core}}$  corresponds to the core radius and  $r_{\text{shell}}$  to the shell thickness of a core-shell sphere. In the full contrast case, the value of  $r_{\text{core}}$  corresponds to the mean core radius. In the C<sub>12</sub>E<sub>5</sub> matched case, no distribution of  $r_{\text{core}}$  was assumed. The value of  $r_{\text{cylinder}}$  corresponds to the radius of a homogeneous cylinder. All parameters can be found in the SI, section 7.8.9, Table SI7.

	pD = 2		pD = 9		pD = 13	
Model					<b>[Blue] <math>\leq</math> 2 mM:</b>	
C <sub>12</sub> E <sub>5</sub> matched	$I(q) = N \cdot P_{\text{cylinder}}(q) \cdot C(q)$		$I(q) = N \cdot P_{\text{core-shell-cylinder}}(q) \cdot C(q) + I_{q,\text{Guinier}}(q)$		$I(q) = N \cdot P_{\text{core-shell-cylinder}}(q) \cdot C(q) + I_{q,\text{Guinier}}(q)$	
					<b>[Blue] <math>\geq</math> 6.25 mM:</b>	
					$I(q) = N \cdot P_{\text{core-shell-sphere}}(q) + I_{q,\text{Guinier}}(q)$	
	Full contrast	C <sub>12</sub> E <sub>5</sub> matched	Full contrast	C <sub>12</sub> E <sub>5</sub> matched	Full contrast	C <sub>12</sub> E <sub>5</sub> matched
[Blue] = 1 mM	$r_{\text{core}} / \text{\AA}: 12.7 \pm 0.3$ $r_{\text{shell}} / \text{\AA}: 14.4 \pm 0.3$	$r_{\text{cylinder}} < 6 \text{ \AA}$	$r_{\text{core}} / \text{\AA}: 12.5 \pm 0.3$ $r_{\text{shell}} / \text{\AA}: 11.2 \pm 0.2$	$r_{\text{core}} / \text{\AA}: 7.4$ (fixed) $r_{\text{shell}} / \text{\AA}: 21 \pm 4$	$r_{\text{core}} / \text{\AA}: 13.7 \pm 0.2$ $r_{\text{shell}} / \text{\AA}: 12.0 \pm 0.3$	$r_{\text{core}} / \text{\AA}: 13 \pm 2$ $r_{\text{shell}} / \text{\AA}: 4.79 \pm 1.7$
[Blue] = 2 mM	$r_{\text{core}} / \text{\AA}: 13.3 \pm 0.3$ $r_{\text{shell}} / \text{\AA}: 13.6 \pm 0.3$	$r_{\text{cylinder}} < 6 \text{ \AA}$	$r_{\text{core}} / \text{\AA}: 12.4 \pm 0.3$ $r_{\text{shell}} / \text{\AA}: 14.5 \pm 0.3$	$r_{\text{core}} / \text{\AA}: 7.4$ (fixed) $r_{\text{shell}} / \text{\AA}: 19 \pm 2$	$r_{\text{core}} / \text{\AA}: 14.5 \pm 0.3$ $r_{\text{shell}} / \text{\AA}: 10.1 \pm 0.3$	$r_{\text{core}} / \text{\AA}: 13.6 \pm 0.7$ $r_{\text{shell}} / \text{\AA}: 4.79 \pm 1.7$
[Blue] = 6.25 mM	phase separated	phase separated	$r_{\text{core}} / \text{\AA}: 12.3 \pm 0.3$ $r_{\text{shell}} / \text{\AA}: 13.2 \pm 0.3$	$r_{\text{core}} / \text{\AA}: 7.9 \pm 0.3$ $r_{\text{shell}} / \text{\AA}: 17.6 \pm 0.2$	$r_{\text{core}} / \text{\AA}: 16.9 \pm 0.2$ $r_{\text{shell}} / \text{\AA}: 11.7 \pm 0.2$	$r_{\text{core}} / \text{\AA}: 21.1 \pm 0.4$ $r_{\text{shell}} / \text{\AA}: 4.79 \pm 1.7$
[Blue] = 12.5 mM	phase separated	phase separated	$r_{\text{core}} / \text{\AA}: 13.3 \pm 0.2$ $r_{\text{shell}} / \text{\AA}: 10.8 \pm 0.3$	$r_{\text{core}} / \text{\AA}: 6.9 \pm 0.4$ $r_{\text{shell}} / \text{\AA}: 16.2 \pm 0.3$	$r_{\text{core}} / \text{\AA}: 16.5 \pm 0.2$ $r_{\text{shell}} / \text{\AA}: 11.7 \pm 0.2$	$r_{\text{core}} / \text{\AA}: 17.2 \pm 0.3$ $r_{\text{shell}} / \text{\AA}: 4.79 \pm 1.7$
Cross section						

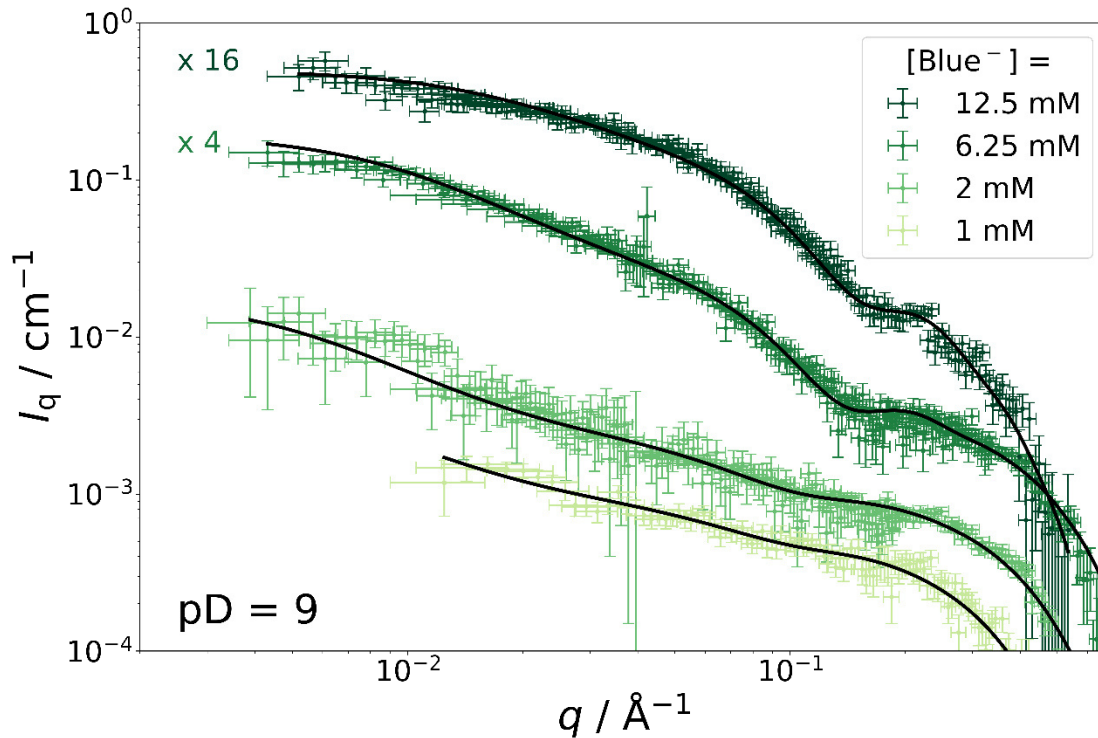


Figure 10:  $C_{12}E_5$ -matched SANS curves obtained from solutions with  $pD = 9$  containing  $[mC_{12}mE_5] = 25$  mM and  $Blue^-$  at variable concentration in an isotonic NaCl solution prepared in  $D_2O$ . Measurements were performed at a sample temperature of  $10$  °C. Solid line (—): Fit with the model described by eq (4). Parameter values for each fit can be found in the SI, section 7.8.9, Table SI7.

Scattering from cylindrical core-shell assemblies of  $Blue^-$  is described by the form factor  $P_{core-shell-cylinder}$  in eq (4), assuming that  $Blue^-$  makes up the shell. The length of these cylinders was fixed to  $66$  Å for  $[Blue^-] \leq 2$  mM and to  $40$  Å for  $[Blue^-] \geq 6.25$  mM, which corresponds to the core length of  $Blue^-/C_{12}E_5$  assemblies inferred from corresponding full contrast measurements (Table 2). The Ornstein-Zernike parameters  $\kappa$  and  $\xi$  were likewise fixed to values obtained from full contrast measurements. The contrast between the solvent and the core was set to  $\Delta\eta_{core} = 0$  and the contrast between the solvent and the shell was set to a value of  $\Delta\eta_{shell} = 3.358 \cdot 10^{-6} \text{ Å}^{-2}$ . The potential inaccuracy of this contrast is compensated by a variation of the particle number density ( $N$ ) during fitting. The described strategy left the particle number density  $N$  and the cross section dimension of the core-shell cylinder ( $r_{core}$  and  $r_{shell}$ ) to be identified. A simultaneous variation of these parameters during fitting of eq (4) to experimental SANS curves led to the cross section dimensions displayed in Table 3 for samples containing  $[Blue^-] \geq 6.25$  mM. For the analysis of SANS curves from samples containing  $[Blue^-] \leq 2$  mM,  $r_{core}$  was fixed to  $7.4$  Å, which corresponds to the average of the two  $r_{core}$  obtained from SANS curves of samples with  $[Blue^-] = 6.25$  mM and  $[Blue^-] = 12.5$  mM. This was done due to the high signal-to-noise ratio of

SANS curves from samples with  $[\text{Blue}^{2-}] \leq 2 \text{ mM}$  and only left  $N$  and  $r_{\text{shell}}$  to be fitted. The complete parameter set is summarized in the SI, section 7.8.9, Table SI7.

The core radius  $r_{\text{core}}$  obtained for the core-shell cylinders formed by  $\text{Blue}^{2-}$  is smaller than the length of a fully extended  $\text{C}_{12}$  alkyl chain ( $< 16.7 \text{ \AA}$ )<sup>50</sup> and smaller than the core radius found for  $\text{Blue}^{2-}/\text{C}_{12}\text{E}_5$  micelles through the analysis of full contrast SANS curves. Assuming, that  $\text{Blue}^{2-}$  assembles into core-shell cylindrical structures due to its interaction with parts of cylindrical  $\text{C}_{12}\text{E}_5$  micelles this means, that  $\text{Blue}^{2-}$  partially penetrates into the alkyl chain region. This is schematically depicted in Table 3. Furthermore, the sum  $r_{\text{core}} + r_{\text{shell}}$  obtained from analysis of full contrast and  $\text{C}_{12}\text{E}_5$ -matched SANS curves is similar, suggesting that  $\text{Blue}^{2-}$  is mainly located in the EG region. This is coherent with results from NMR-spectroscopic analysis, which suggests the interaction between  $\text{Blue}^{2-}$  and both, the alkyl part and the EG part of the  $\text{C}_{12}\text{E}_5$  surfactant.

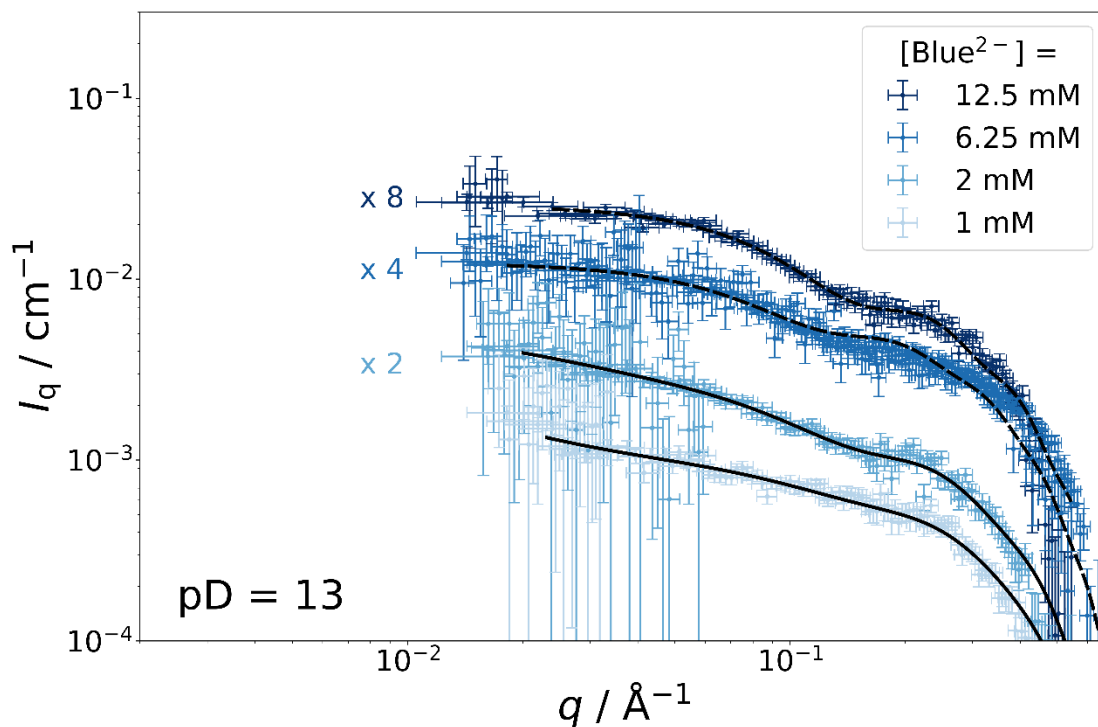


Figure 11:  $\text{C}_{12}\text{E}_5$ -matched SANS curves obtained from solutions with  $\text{pD} = 13$  containing  $[\text{mC}_{12}\text{mE}_5] = 25 \text{ mM}$  and  $\text{Blue}^{2-}$  at variable concentration in an isotonic  $\text{NaCl}$  solution prepared in  $\text{D}_2\text{O}$ . Measurements were performed at a sample temperature of  $10 \text{ }^\circ\text{C}$ . The scattering signal at  $q < 0.017 \text{ \AA}^{-1}$  was attributed to impurities in the sample and is therefore not shown (SI, section 7.8.8). Dashed lines (----) correspond to form factor fits according to eq (6). Solid lines (\_\_\_) correspond to form factor fits according to eq (4). Precise parameters for each fit can be found in the SI, section 7.8.9, Table SI7.

Figure 11 displays  $\text{C}_{12}\text{E}_5$  contrast-matched SANS curves from samples containing  $\text{mC}_{12}\text{mE}_5$  at a concentration of  $25 \text{ mM}$  and variable concentrations of  $\text{Blue}^{2-}$  ( $\text{pD} = 13$ ). Based on information

from NMR-spectroscopy, Blue<sup>2-</sup> is not expected to significantly penetrate into the micellar core, but to interact with the EG head group. This implies, that scattering from core-shell assemblies is observed in the C<sub>12</sub>E<sub>5</sub>-matched case, where the shell consists of Blue<sup>2-</sup> and the core shows no contrast ( $\Delta\eta = 0$ ) to the solvent. In addition to that, the presence of molecularly dissolved Blue<sup>2-</sup> molecules is expected, which causes a constant contribution to the overall scattering signal up until a decay of the scattering intensity at  $q > 0.2 \text{ \AA}^{-1}$ . Analogous to the evaluation of C<sub>12</sub>E<sub>5</sub>-matched SANS curves at pD = 9, the form factor  $P(q)$  that describes the inclusion of Blue molecules into C<sub>12</sub>E<sub>5</sub> micelles, was based on information from full contrast data (Table 2). According to Table 2, cylindrical assemblies with a core length of  $L_{\text{core}} = 40 \text{ \AA}$  are formed when Blue<sup>2-</sup> is added to a C<sub>12</sub>E<sub>5</sub> solution at a concentration of  $[\text{Blue}^{2-}] = 1 \text{ mM}$  or  $[\text{Blue}^{2-}] = 2 \text{ mM}$ . Therefore, eq (4) was applied to corresponding C<sub>12</sub>E<sub>5</sub>-matched curves displayed in Figure 11. At Blue<sup>2-</sup> concentrations of  $[\text{Blue}^{2-}] = 6.25 \text{ mM}$  or  $[\text{Blue}^{2-}] = 12.5 \text{ mM}$ , spherical Blue<sup>2-</sup>/C<sub>12</sub>E<sub>5</sub> co-assemblies were observed (Table 2). Ornstein-Zernike scattering did not need to be considered in these cases. Therefore, the following expression was applied to fit corresponding C<sub>12</sub>E<sub>5</sub>-matched SANS curves:

$$I_q(q) = N \cdot P_{\text{core-shell-sphere}}(q) + I_{q,\text{Guinier}}(q) \quad (6)$$

In eq (6),  $P_{\text{core-shell-sphere}}(q)$  is the form factor of a core-shell sphere and  $N$  the number density of core-shell particles.

Preliminary Guinier analysis of the high- $q$  region of all four SANS curves shown in Figure 11 according to eq (5) suggests an average  $R_g(\text{Blue}^{2-}) = 5.39 \text{ \AA}$ , which was kept constant during analysis with eq (4) or eq (6). Due to the low absolute scattering intensity and high signal-to-noise ratio of experimental SANS curves, this value of  $R_g$  is to be seen as an estimation.

For fitting eq (4) or eq (6) to SANS curves shown in Figure 11, values of the scattering contrast ( $\Delta\eta_{\text{core}} = 0$  and  $\Delta\eta_{\text{shell}} = 3.358 \cdot 10^{-6} \text{ \AA}^{-2}$ ) were fixed, but the number density of core-shell assemblies ( $N$ ) fitted to compensate for inaccuracies of the chosen scattering contrast.

For samples with  $[\text{Blue}^{2-}] \leq 2 \text{ mM}$ , eq (4) was used to describe experimental SANS curves. In this case, the cylinder length was fixed to  $40 \text{ \AA}$ , which corresponds to the core length of Blue<sup>2-</sup>/C<sub>12</sub>E<sub>5</sub> assemblies inferred from corresponding full contrast measurements (Table 2). The Ornstein-Zernike parameters were likewise fixed to values obtained from fits to full contrast SANS curves.

For all four SANS curves shown in Figure 11,  $r_{\text{shell}}$  was fitted globally to  $r_{\text{shell}} = 4.79 \text{ \AA}$  and  $r_{\text{core}}$  was fitted individually. Values of  $r_{\text{core}}$  are displayed in Table 3. Core radii ( $r_{\text{core}}$ ) obtained from the analysis of  $\text{C}_{12}\text{E}_5$ -matched SANS curves are similar to  $r_{\text{core}}$  obtained from the analysis of full contrast SANS curves in the cylinder case (eq (4)). In cases, where eq (6) was applied,  $r_{\text{core}}$  are larger than the length of a completely extended  $\text{C}_{12}$  alkyl chain ( $> 16.7 \text{ \AA}$ )<sup>50</sup> and larger than values of  $r_{\text{core}}$  obtained by the analysis of corresponding full contrast SANS curves. These observations point towards the preferential localization of  $\text{Blue}^{2-}$  molecules in the head-group region of  $\text{C}_{12}\text{E}_5$  micelles for all four cases. Based on the necessity to include a Guinier contribution to account for molecularly dissolved  $\text{Blue}^{2-}$  molecules,  $\text{Blue}^{2-}$  is expected to be distributed between the head group region of  $\text{C}_{12}\text{E}_5$  micelles and outside of the micelles.

To conclude this section, the evaluation of SANS curves from  $\text{C}_{12}\text{E}_5$  contrast-matched solutions in combination with the consideration of NMR-spectroscopic data provides valuable information on the interaction between Blue and  $\text{C}_{12}\text{E}_5$ .

Investigations at  $\text{pD} = 2$  were restricted to low concentrations of BlueH ( $\leq 2 \text{ mM}$ ) due to phase separation at higher concentrations. Analysis of  $\text{C}_{12}\text{E}_5$ -matched SANS curves suggests the presence of BlueH in cylindrical domains, which points towards the inclusion of BlueH into the hydrophobic core of  $\text{C}_{12}\text{E}_5$  micelles. At  $\text{pD} = 9$ ,  $\text{Blue}^-$  is expected to interact with the part of the hydrophobic  $\text{C}_{12}$  alkyl chain close to the pentaEG head group as well as with the pentaEG head group. This conclusion is based on cross section dimensions of the core-shell structure formed by  $\text{Blue}^-$  molecules, which are included into  $\text{C}_{12}\text{E}_5$  micelles and is in accord with NMR-spectroscopic results. A part of  $\text{Blue}^-$  is furthermore expected to be present outside of  $\text{C}_{12}\text{E}_5$  micelles. At  $\text{pD} = 13$ , geometrical considerations reveal the localisation of  $\text{Blue}^{2-}$  in the head group layer of  $\text{C}_{12}\text{E}_5$  micelles. In addition to that, a part of  $\text{Blue}^{2-}$  exists outside of  $\text{C}_{12}\text{E}_5$  micelles.

## 7.6 Discussion

The objective of this work is to fundamentally understand additive-caused variations in the morphology of hosting  $\text{C}_{12}\text{E}_5$  micelles and in the CT of  $\text{C}_{12}\text{E}_5$  solutions as a function of additive polarity. The pursuit of this objective requires the use of additives with different polarity but similar chemical structure. Only by means of such additives can varying steric requirements be excluded. We have identified the acid BlueH as a particularly suitable additive, which can be deprotonated up to two times. At  $\text{pD} = 2$ , BlueH is the neutral, non-dissociated acid. At  $\text{pD} = 9$ , the one-fold deprotonated  $\text{Blue}^-$  with intermediate polarity exists, whereas at  $\text{pD} = 13$  the two-fold deprotonated  $\text{Blue}^{2-}$  with the highest polarity is present. As the morphology of  $\text{C}_{12}\text{E}_5$  micelles in

pure  $C_{12}E_5$  solution and the CT of such solutions do not depend on solution pD, it was possible to vary the polarity of Blue by simply changing the pD of the solution.

Attractive inter-micellar interactions and the size of micelles grow when the CT of the solution is approached.<sup>12</sup> It was successfully demonstrated with Figure 6b, that the decisive property determining attractive inter-micellar forces is not the composition of the sample, but its temperature distance to the CT.<sup>11,12,28</sup> This means, that each change to the sample, which results in increasing attractive interactions between  $C_{12}E_5$  micelles, causes a lowering of the CT, moving the CT closer to the temperature of the sample. On the other hand, if attractive interactions are decreased or repulsive interactions are introduced, the CT of the system is increased, moving the CT further away from the temperature of the sample.

Increasing attractive interactions between  $C_{12}E_5$  micelles are associated with a loss in their water solubility, which is caused by dehydration of the pentaethyleneglycol head group.<sup>3,51</sup> Conversely, attractive interactions between  $C_{12}E_5$  micelles decrease when their water solubility is increased. In addition to that, repulsive interactions between  $C_{12}E_5$  micelles could be caused by their interaction with charged molecules. In the following, the impact of BlueH, Blue<sup>-</sup> or Blue<sup>2-</sup> on these interactions and on the CT of  $C_{12}E_5$  solutions will be jointly discussed and correlated to its corresponding localization in the  $C_{12}E_5$  micelle.

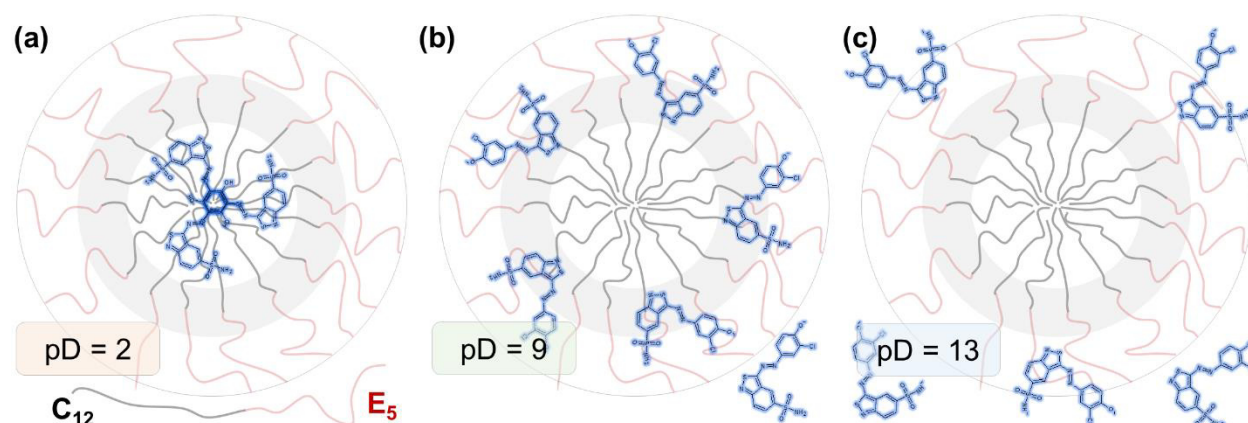


Figure 12: Schematic localization of (a) BlueH, (b) Blue<sup>-</sup> or (c) Blue<sup>2-</sup> in the cross section of  $C_{12}E_5$  micelles. Grey lines represent the hydrophobic alkyl chain ( $C_{12}$ ) and red lines represent the hydrophilic pentaethyleneglycol head group ( $E_5$ ). The palisade layer is highlighted in grey.

The uncharged molecule BlueH is poorly water soluble and a sufficiently high concentration of  $C_{12}E_5$  necessary to dissolve BlueH at concentrations such as 1 mM or 2 mM. This suggests preferential interactions between BlueH and the hydrophobic part of  $C_{12}E_5$ . NOESY revealed cross peaks between the resonance of protons belonging to the terminal methyl group of the  $C_{12}$  alkyl chain and resonances of BlueH, suggesting that at least some BlueH molecules interact with

the micellar core. Furthermore, a relatively strong upfield shift and peak broadening of resonances from C<sub>12</sub> alkyl chain protons were observed in the <sup>1</sup>H-NMR-spectrum of C<sub>12</sub>E<sub>5</sub> upon addition of BlueH.

The evaluation of SANS curves of C<sub>12</sub>E<sub>5</sub> contrast-matched samples suggests an incorporation of BlueH into the hydrophobic core of cylindrical C<sub>12</sub>E<sub>5</sub> micelles.

For explaining the reduction of the CT of C<sub>12</sub>E<sub>5</sub> solutions upon addition of BlueH, two effects need to be considered: (1) The water solubility of C<sub>12</sub>E<sub>5</sub> micelles decreases upon addition of the hydrophobic molecule BlueH.<sup>5</sup> (2) As BlueH preferentially interacts with the hydrophobic tail of C<sub>12</sub>E<sub>5</sub> molecules, it can be considered to alter the geometry of the surfactant, which determines surfactant packing. Surfactant packing is expressed by means of the critical packing parameter (*CPP*).<sup>52,53</sup>

$$CPP = \frac{v}{a_0 \cdot l_c} \quad (7)$$

In eq (7), *v* is the volume of the hydrophobic tail of the surfactant, *a*<sub>0</sub> its effective head group area and *l*<sub>c</sub> the length of the completely extended hydrophobic tail of the surfactant. In the following, *v*<sub>eff</sub>, *a*<sub>0,eff</sub> and *l*<sub>c,eff</sub> will be used to denote the same geometrical parameters if altered through the interaction of the surfactant molecule with an additive molecule. BlueH is located close to the hydrophobic tail of C<sub>12</sub>E<sub>5</sub> molecules, which potentially leads to an increase of the surfactant tail volume in the transversal direction. The effect of BlueH on *l*<sub>c</sub> is considered to be negligible, because the length of the C<sub>12</sub> chain exceeds the longest dimension of a BlueH molecule. An increase in *v*<sub>eff</sub> increases the *CPP*, which signals an increase in packing and promotes the preferential formation of cylindrical micelles or micellar growth. An increase in packing furthermore implies a reduction of space for water molecules in the hydrophilic surfactant head group and subsequent dehydration, which decreases water solubility.

The addition of Blue<sup>-</sup> to solutions of C<sub>12</sub>E<sub>5</sub> increases their CT if the concentration of Blue<sup>-</sup> is sufficiently high. NOESY suggests the distribution of Blue<sup>-</sup> throughout almost the entire C<sub>12</sub>E<sub>5</sub> micelle, because cross peaks between almost all C<sub>12</sub>E<sub>5</sub> proton resonances and Blue<sup>-</sup> proton resonances are observed. Even though Blue<sup>-</sup> may be distributed throughout C<sub>12</sub>E<sub>5</sub> micelles, it was possible to identify its preferential location in the palisade- and outer layer by evaluation of C<sub>12</sub>E<sub>5</sub> contrast-matched SANS curves (Figure 10). As Blue<sup>-</sup> is water soluble, its addition to solutions of C<sub>12</sub>E<sub>5</sub> increases the overall solubility of Blue<sup>-</sup>/C<sub>12</sub>E<sub>5</sub> co-assemblies compared to pure C<sub>12</sub>E<sub>5</sub> micelles.<sup>14</sup> A second factor, which increases water solubility and reduces attractive interactions

between  $C_{12}E_5$  micelles upon inclusion of  $Blue^-$  could be electrostatic repulsion, caused by the negative charge of  $Blue^-$ . However, this contribution is expected to be small for several reasons: (1)  $Blue^-$  is partly included into the palisade region of the micelle, which results in a decay of the electrostatic surface potential of the palisade layer to the level of the actual surface layer of the micelle. (2) The  $Na^+$  counter ion is likely located in close proximity to the negatively charged phenolate group, leading to charge screening already inside the surfactant head group region. (3) Electrostatic repulsion between micelles is screened by the NaCl salt ( $I = 154$  mM) present in solution. Therefore, inter-micellar interactions are likely not dominated by the electrostatic repulsion effect. This leads to net attractive interactions and is visible through the observation of Ornstein-Zernike scattering from samples with  $pD = 9$ . Nevertheless, the Ornstein-Zernike scattering contribution is significantly reduced compared to the pure surfactant system.

Similar to  $Blue^-$ , the two-fold negatively charged  $Blue^{2-}$  is hydrophilic and therefore increases the water solubility of  $C_{12}E_5$  micelles. The two negative charges suggest an even higher water solubility of  $Blue^{2-}$  compared to  $Blue^-$ . The localization of one charge on the phenolate- and one charge on the sulphonamide group do furthermore reduce the affinity of  $Blue^{2-}$  to interact with the hydrophobic  $C_{12}$  alkyl chains. This behaviour is confirmed by the small impact  $Blue^{2-}$  addition has on the chemical shift of alkyl chain proton resonances in their  $^1H$ -NMR spectrum.  $Blue^{2-}$  is expected to interact with the penta-EG head groups. As for  $Blue^-$ , such an interaction may also decrease inter-micellar attractions through the introduction of charges into the surfactant head group. As  $Blue^{2-}$  is likely located closer to the surface layer of the  $C_{12}E_5$  micelle and carries a higher charge than  $Blue^-$ , electrostatic repulsion between micelles is more relevant at  $pD = 13$  compared to  $pD = 9$ . Electrostatic repulsion even causes a net repulsive interaction between  $Blue^{2-}/C_{12}E_5$  micelles for  $[Blue^{2-}] \geq 6.25$  mM. This behaviour was demonstrated by the need to include a structure factor based on a repulsive hard sphere potential for fitting full contrast SANS curves of such solutions.

Increasing repulsive interactions between micelles go along with an increase in the effective surfactant head group size  $a_{0,eff}$ , because the same forces that cause repulsion between  $C_{12}E_5$  micelles, i.e. increasing head group hydration and electrostatic repulsion between head groups, cause an increase in  $a_{0,eff}$ .<sup>50,54</sup> As  $a_{0,eff}$  influences the packing of surfactant molecules according to eq (7), a change in micelle morphology with a change in inter-micellar interactions is inevitable. Repulsive interactions result in an increase of  $a_{0,eff}$ , which lowers the critical packing parameter, if the increase in  $a_{0,eff}$  is not compensated by an increase in  $v_{eff}$  due to the inclusion of the additive that causes repulsive interactions. A lowering of  $CPP$  causes the reduction of the size



of surfactant micelles and may even lead to a transition from cylindrical to spherical micelles. This phenomenon was in fact observed for the addition of increasing concentrations of either Blue<sup>-</sup> or Blue<sup>2-</sup> to a C<sub>12</sub>E<sub>5</sub> solution (Table 2). For the addition of Blue<sup>-</sup> only a shrinking of cylindrical surfactant micelles was found in the observed concentration range, whereas for the addition of Blue<sup>2-</sup> the formation of spherical micelles at high concentrations was confirmed. In both cases, the increase of  $a_{0,\text{eff}}$  through interaction of the Blue<sup>-</sup> or Blue<sup>2-</sup> molecule with the surfactant head group and through electrostatic repulsion between head groups outweighs the increase of the surfactant hydrophobic chain volume  $v_{\text{eff}}$ , caused by the inclusion of these molecules.

The question of whether spherical and cylindrical micelles co-exist and to which extent an incorporation of Blue, in its respective state of protonation, promotes spherical or cylindrical micelles, cannot be answered with the presented data. Cryo-TEM would be needed to prove the co-existence of two micelle morphologies in Blue/C<sub>12</sub>E<sub>5</sub> solutions.<sup>30</sup> For obtaining information on the distribution of Blue between these types of micelles, a contrast matching experiment analogous to the reported experiment but with significantly longer exposure times for a reduction in the signal-to-noise ratio could be performed. Alternatively, energy-filtered cryo-TEM could be used to map the distribution of sulphur or nitrogen in the detected area and compare it to the bright field image or the distribution of carbon in the same area.<sup>55</sup> As sulphur and nitrogen are specific to Blue, this would permit the detection of Blue with electron microscopy and therefore its distribution in the investigated area of the cryo-TEM image.

## 7.7 Conclusion

The clouding temperature (CT) of solutions containing the nonionic surfactant C<sub>12</sub>E<sub>5</sub> at a concentration of 25 mM in an isotonic NaCl solution in D<sub>2</sub>O is varied upon addition of sufficiently high concentrations of Blue. It decreases when BlueH is added at pD = 2, but increases when Blue<sup>-</sup> or Blue<sup>2-</sup> are added at pD = 9 or pD = 13 respectively. The CT alteration is greater when the additive Blue is added at higher concentration.

CT variations are related to variations in attractive inter-micellar interactions. Attractive inter-micellar interactions can lead to concentration fluctuations in systems that show liquid/liquid phase separation. The correlation length of concentration fluctuations ( $\xi$ ) was therefore used as a measure to compare the extent of attractive inter-micellar interactions.

It was confirmed, that the decisive criterion determining  $\xi$  is the temperature-distance of measurement conditions to the CT of the sample, which is determined by the sample composition.

It was therefore sufficient to study Blue/C<sub>12</sub>E<sub>5</sub> solutions at a temperature of 10 °C. The value of  $\xi$  increases when the CT of the system is approached upon variation of sample composition. Furthermore, at pD = 9 and pD = 13 an additional growth of Blue/C<sub>12</sub>E<sub>5</sub> micelles is observed with decreasing temperature-distance to the CT.

A combination of NMR-spectroscopy and SANS contrast matching sheds light on mechanisms that result into the observed behaviour: BlueH, which is present at pD = 2, carries no charge and is poorly water soluble, which leads to its preferential localisation in the hydrophobic core of C<sub>12</sub>E<sub>5</sub> micelles. BlueH reduces the water solubility of C<sub>12</sub>E<sub>5</sub> micelles due to its hydrophobicity. This behaviour is macroscopically observed through a reduced CT of BlueH/C<sub>12</sub>E<sub>5</sub> solutions compared to the CT of pure C<sub>12</sub>E<sub>5</sub> solutions.

At pD = 9 or pD = 13, the hydrophilic molecules Blue<sup>-</sup> or Blue<sup>2-</sup> are respectively present. Their addition to solutions of C<sub>12</sub>E<sub>5</sub> increases the water solubility of C<sub>12</sub>E<sub>5</sub> micelles. In addition to that, charges are introduced into the head groups of C<sub>12</sub>E<sub>5</sub> molecules due to the interaction of Blue<sup>-</sup> or Blue<sup>2-</sup> with the penta-EG part. This may lead to the electrostatic repulsion between head groups. Repulsive inter-micellar interactions were in fact observed at high concentrations of Blue<sup>2-</sup>.

**Acknowledgements.** The authors thank the ESS DEMAX platform for synthesizing and providing the deuterated surfactants mC<sub>12</sub>hE<sub>5</sub> and mC<sub>12</sub>dE<sub>5</sub> (Proposal number: 860178). This work benefited from the use of the SASfit software package developed by Joachim Kohlbrecher and Ingo Bressler with copyright to the Paul Scherrer Institut (PSI).<sup>23</sup> The authors thank the Institut Laue-Langevin for the provision of beamtime (<https://doi.ill.fr/10.5291/ILL-DATA.9-12-687>). The authors gratefully acknowledge the use of the Partnership for Soft Condensed Matter (PSCM) facilities. W.M. acknowledges funding for a Ph.D. scholarship from the European Union's Horizon 2020 research and innovation programme under the Marie Skłodowska-Curie grant agreement No 847439 within the InnovaXN framework (Project number XN2019-ILL23). This work used the platforms of the Grenoble Instruct-ERIC center (ISBG ; UAR 3518 CNRS-CEA-UGA-EMBL) within the Grenoble Partnership for Structural Biology (PSB), supported by FRISBI (ANR-10-INBS-0005-02) and GRAL, financed within the University Grenoble Alpes graduate school (Ecoles Universitaires de Recherche) CBH-EUR-GS (ANR-17-EURE-0003), and with financial support from the TGIR-RMN-THC Fr3050 CNRS.

## 7.8 Supporting Information

### 7.8.1. Experimental

**Light scattering.** Samples for light scattering were prepared by the same procedure as NMR- and SANS samples, which is described in the experimental section of the main document. Samples for light scattering were filtered (MACHEREY-NAGEL, CHROMAFIL Xtra H-PTFE syringe filters, pore size 0.2  $\mu\text{m}$ ) into tempered, dust-free cuvettes at a temperature of 7  $^{\circ}\text{C}$  after an equilibration time of at least 4 h at that temperature and subsequently stored for 24 h. Samples were equilibrated at measurement temperature for at least 1 h before measurement.

Light scattering measurements were performed on an ALV CGS-3 Compact Goniometer System (ALV GmbH, Langen, FRG) using a HeNe laser at a wavelength of 632.8 nm. Measurements were performed using cylindrical quartz glass cuvettes with an inner diameter of 1 cm. The temperature of the sample in the toluene bath was controlled using a thermostat set to 10  $^{\circ}\text{C}$ . Before measurement, samples were equilibrated at that temperature in the toluene bath for at least 1 h. For the evaluation of static light scattering (SLS) data, toluene was used as a standard.

**Determination of Blue acid dissociation constants.** The  $\text{pK}_{\text{A}}$  values of Blue could be determined by spectroscopic pD-titration, because the absorption spectrum of Blue is sensitive to pD-changes (Figure SI1). UV/vis spectra were recorded from solutions containing Blue at a concentration of  $[\text{Blue}] = 0.1 \text{ M}$  and  $\text{hC}_{12}\text{hE}_5$  at a concentration of  $[\text{hC}_{12}\text{hE}_5] = 12.5 \text{ mM}$ . Spectra were recorded at room temperature (22  $^{\circ}\text{C}$ ) using the Jasco V-630 UV-vis spectrophotometer. Samples were prepared and handled as described in the section on sample preparation in the main document. Added volumes of DCl and NaOD solution were noted to be able to precisely determine the concentration of Blue ( $[\text{Blue}]$ ) in each sample. This is needed for the calculation of the molar extinction coefficient  $\epsilon$  according to the Beer-Lambert law:<sup>56</sup>

$$\epsilon = \frac{A}{d \cdot [\text{Blue}]} \quad (\text{SI1})$$

In eq (SI1),  $A$  is the absorbance of the sample and  $d$  the optical path length, which was  $d = 0.1 \text{ cm}$  (Hellma QS cuvette) for the present experiment.

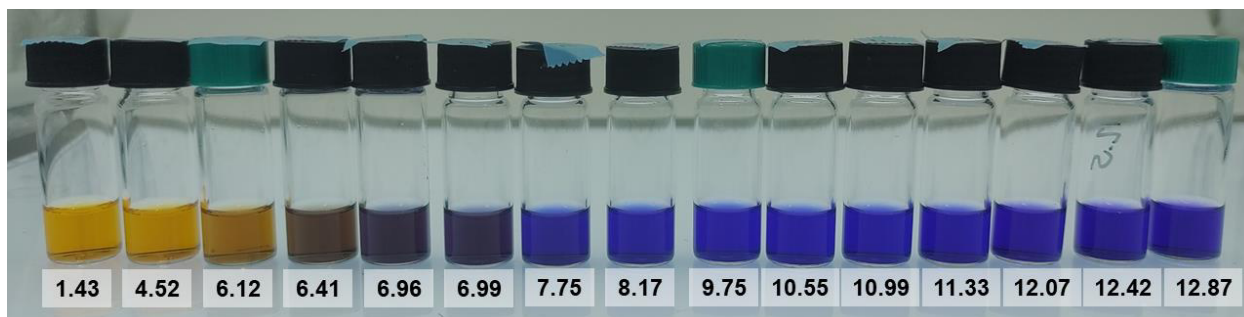


Figure S11: Photo of samples containing Blue at a concentration of  $[\text{Blue}] = 0.1 \text{ mM}$  and the surfactant  $\text{hC}_{12}\text{hE}_5$  at a concentration of  $[\text{hC}_{12}\text{hE}_5] = 12.5 \text{ mM}$  and at variable solution pD, which is indicated below each sample. An isotonic NaCl solution ( $I = 0.154 \text{ M}$ ) in  $\text{D}_2\text{O}$  served as the solvent. The pD of each solution was adjusted using  $1 \text{ M}$  solutions of DCl or NaOD. The photo was taken at room temperature ( $22 \text{ }^\circ\text{C}$ ).

Figure S12a shows the development of  $\epsilon$  at a wavelength of  $583 \text{ nm}$  as a function of solution pD. This wavelength corresponds to the wavelength of maximum absorbance ( $\lambda_{\text{max}}$ ) for solutions containing Blue in its one-fold deprotonated form ( $\text{Blue}^-$ ). A decrease in  $\epsilon(583 \text{ nm})$  therefore signals the protonation of Blue to form BlueH. From Figure S12a, the first  $\text{pK}_A$  ( $\text{pK}_{A1}$ ) describing the acid/base equilibrium between BlueH and  $\text{Blue}^-$  was obtained. This was done by determining the pD at which the ratio  $\text{BlueH}:\text{Blue}^-$  amounts to 1:1, which was detected by interpolating to the pD at which an average  $\epsilon(583 \text{ nm})$  is obtained with respect to  $\epsilon(583 \text{ nm})$  for BlueH and  $\epsilon(583 \text{ nm})$  for  $\text{Blue}^-$ . Following this analysis,  $\text{pK}_{A1}$  was determined to  $\text{pK}_{A1} = 6.8$ .

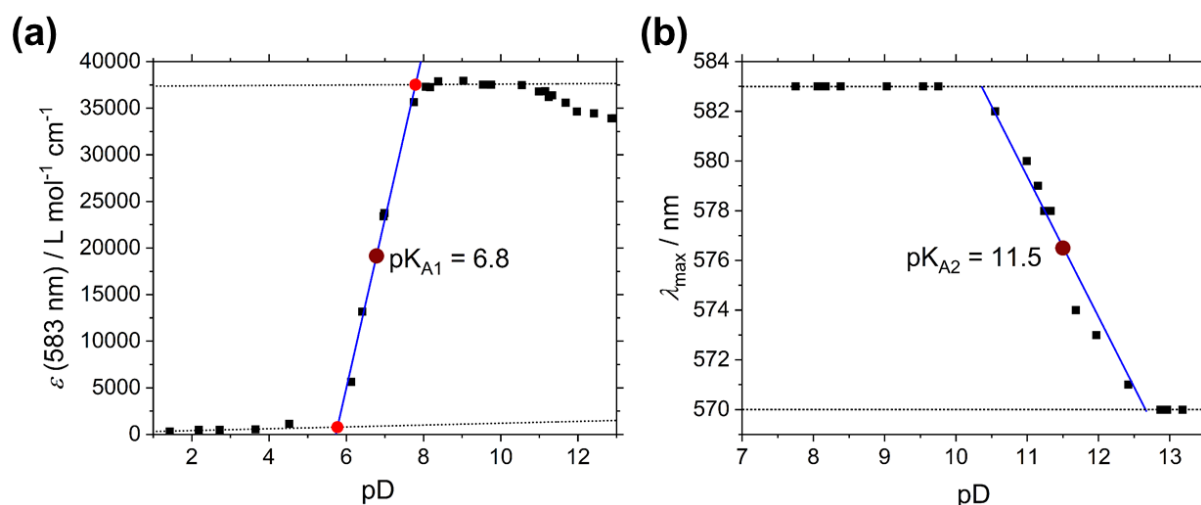


Figure S12: UV/vis spectroscopic pD-titration of samples containing  $[\text{Blue}] = 0.1 \text{ mM}$  and  $[\text{hC}_{12}\text{hE}_5] = 12.5 \text{ mM}$  at room temperature. An isotonic NaCl solution in  $\text{D}_2\text{O}$  was used as a solvent. The pD of each solution was adjusted using DCl and NaOD. (a) For the determination of  $\text{pK}_{A1}$ , the molar extinction coefficient at a wavelength of  $583 \text{ nm}$  was evaluated as a function of pD. (b) For the determination of  $\text{pK}_{A2}$ , the position of the absorption maximum ( $\lambda_{\text{max}}$ ) was evaluated as a function of pD.

Figure S12b shows the wavelength of maximum absorbance  $\lambda_{\text{max}}$  as a function of solution pD. The absorption maximum of  $\text{Blue}^-$  is red-shifted compared to the absorption maximum of  $\text{Blue}^{2-}$ . Therefore,  $\text{pK}_{A2}$ , which describes the acid/base equilibrium between  $\text{Blue}^-$  and  $\text{Blue}^{2-}$  was

identified as the pD, at which the UV/vis spectrum showed an average  $\lambda_{\max}$  by interpolation. From this analysis, pK<sub>A2</sub> was identified as pK<sub>A2</sub> = 11.5.

**Small-angle neutron scattering.** Samples for small-angle neutron scattering (SANS) were prepared as described in the main document. Three different SANS experiments were performed: (1) The first experiment served to determine the match point. The match point corresponds to the ratio between mC<sub>12</sub>hE<sub>5</sub> and mC<sub>12</sub>dE<sub>5</sub> at which no form factor scattering is observed. (2) In the second experiment, “full contrast” SANS curves were recorded from samples containing the completely hydrogenated surfactant hC<sub>12</sub>hE<sub>5</sub> and Blue. (3) In the third experiment, C<sub>12</sub>E<sub>5</sub>-matched SANS curves were recorded, where samples contained Blue and mC<sub>12</sub>hE<sub>5</sub> and mC<sub>12</sub>dE<sub>5</sub> at the match point determined in step 1. As C<sub>12</sub>E<sub>5</sub> is matched out under these conditions, the  $q$ -dependent scattering signal only arises from Blue.

In all cases, samples were equilibrated at the measurement temperature of 10 °C in the SANS cuvettes overnight. For match point determination and C<sub>12</sub>E<sub>5</sub>-matched experiments, 404-QS quartz cuvettes with a path length of 2 mm (Hellma, Müllheim, Germany) were used. For full contrast measurements, 404-QX quartz cuvettes with a path length of 2 mm (Hellma, Müllheim, Germany) were used.

**Determination of the SANS match point of C<sub>12</sub>E<sub>5</sub> in D<sub>2</sub>O.** Figure SI3 displays the result of the match point determination experiment. SANS curves of samples containing a total C<sub>12</sub>E<sub>5</sub> concentration of 25 mM but different volume fractions ( $\Phi$ ) of mC<sub>12</sub>hE<sub>5</sub> and mC<sub>12</sub>dE<sub>5</sub> with respect to the total C<sub>12</sub>E<sub>5</sub> concentration ( $\Phi(\text{mC}_{12}\text{hE}_5) = V(\text{mC}_{12}\text{hE}_5) / [V(\text{mC}_{12}\text{hE}_5) + V(\text{mC}_{12}\text{dE}_5)]$ ) were recorded at a sample temperature of 10 °C. The solvent was an isotonic NaCl solution in D<sub>2</sub>O with pD = 2. The square root of the scattering intensity observed at various values of the scattering vector ( $q$ ) or its negative was plotted as a function of  $\Phi(\text{mC}_{12}\text{hE}_5)$  (Figure SI3). For each  $q$ , a linear fit to  $\sqrt{I_q}$  and  $-\sqrt{I_q} = f[\Phi(\text{mC}_{12}\text{hE}_5)]$  was performed. Linear fits are shown as lines in Figure SI3. The value of  $\Phi(\text{mC}_{12}\text{hE}_5)$ , at which  $\sqrt{I_q} = 0$  and at which the linear fits intersect, was identified as the match point. It corresponds to a volume ratio of  $\Phi(\text{mC}_{12}\text{hE}_5) : \Phi(\text{mC}_{12}\text{dE}_5) = 18.1 : 81.9$ . This mixture is denoted as mC<sub>12</sub>mE<sub>5</sub> in the following and in the main document. Solutions containing mC<sub>12</sub>mE<sub>5</sub> were prepared by mixing stock solutions of mC<sub>12</sub>hE<sub>5</sub> and mC<sub>12</sub>dE<sub>5</sub> at the appropriate ratio. The success of contrast matching is demonstrated in Figure SI4, where the empty-cell subtracted SANS curve of a sample containing mC<sub>12</sub>mE<sub>5</sub> at a concentration of 25 mM is shown to be identical to solvent scattering and does not show form factor oscillations.

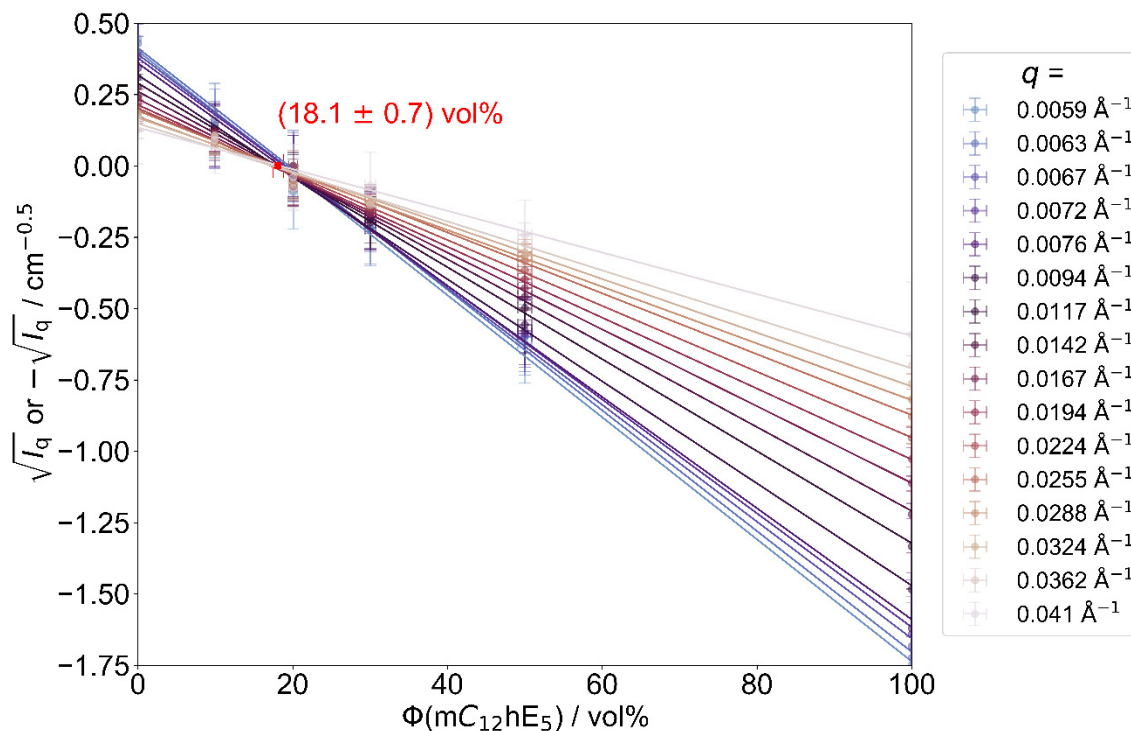


Figure SI3: Square root or its negative of the scattering intensity observed at the indicated value of the scattering vector ( $q$ ) for samples containing a total  $C_{12}E_5$  concentration of 25 mM, which is achieved by mixing 25 mM solutions of  $mC_{12}hE_5$  and  $mC_{12}dE_5$  at varying volume ratio. The volume fraction of  $mC_{12}hE_5$  in this mixture [ $\Phi(mC_{12}hE_5)$ ] is displayed on the x-axis for each sample. The volume fraction of  $mC_{12}hE_5$ , at which all linear fits to  $\sqrt{I_q}$  and  $-\sqrt{I_q} = f[\Phi(mC_{12}hE_5)]$  cross through  $\sqrt{I_q} = 0$  was identified as the match point. An isotonic NaCl solution in  $D_2O$  served as the solvent and the solution pD = 2 was adjusted by DCl addition. Investigations were performed at a sample temperature of 10 °C.

SANS was performed at the small-angle neutron scattering instrument D22 at the Institute Laue-Langevin (Grenoble, France). A circular neutron beam with a diameter of 13 mm and cuvettes with a path length of 2 mm were used. The D22 instrument possesses two detectors: The front detector, which was at a fixed distance of 1.4 m to the sample and a rear detector. Measurements were carried out at two sample-to-rear-detector distances: 4 m (collimation 4 m) and 17.6 m (collimation 17.6 m) at a neutron wavelength of 6 Å to cover a  $q$ -range of 0.0026 Å<sup>-1</sup> to 0.6424 Å<sup>-1</sup>. Neutrons were detected with two <sup>3</sup>He detectors (multi-tube detector consisting of vertically aligned Reuter-Stokes tubes, with 128 tubes for the rear and 96 tubes for the front detector, all with a diameter of 8 mm and a pixel size of 8 mm x 8 mm). Detector images were corrected to the transmission of the direct beam, scaled to absolute intensity and azimuthally averaged using the GRASP software.<sup>21</sup> Empty cell and solvent scattering were subtracted from the scattering curves.<sup>22</sup> SANS curves were fitted using the SASfit software package.<sup>23</sup>

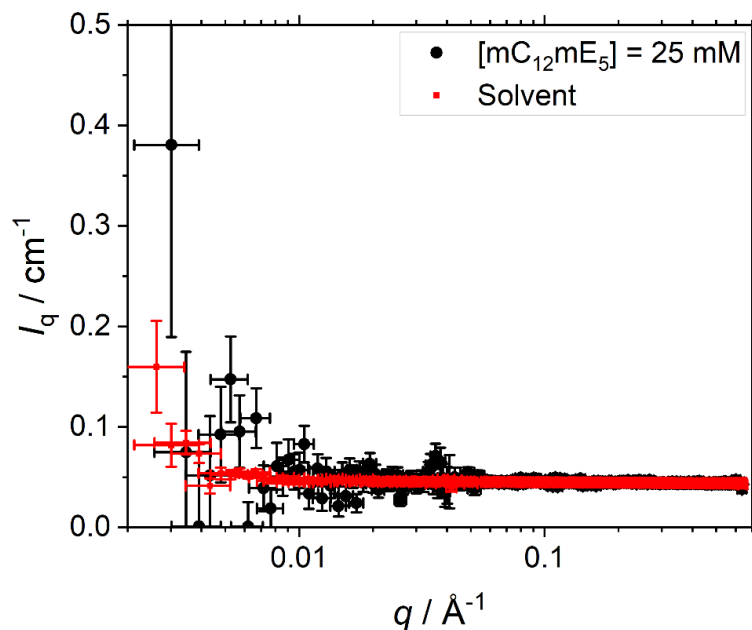


Figure S14: Empty cell subtracted SANS curves of the solvent (isotonic NaCl solution in D<sub>2</sub>O) and a solution containing mC<sub>12</sub>mE<sub>5</sub> at a concentration of 25 mM in the same solvent and at pD = 2. SANS curves were recorded at a sample temperature of 10 °C. Differences in the signal-to-noise ratio are attributed to differences in measurement times (solvent: 140 min at 17.6 m and 60 min at 4 m, mC<sub>12</sub>mE<sub>5</sub> solution: 20 min at 17.6 m and 10 min at 4 m with 17.6 m and 4 m being the sample-to-rear-detector distances).

## 7.8.2. Data evaluation

**Small-angle neutron scattering.** SANS curves were fitted with form factors and structure factors available in the SASfit software package (Version: 0.94.12, documentation from 09.01.2023).<sup>23,32</sup> In general, the  $q$ -dependency of the scattering intensity is described by the following equation:<sup>32,33</sup>

$$I_q(q) = N \cdot P(q) \cdot S(q) \quad (\text{S12})$$

In eq (S12),  $N$  is the number density of scattering particles and  $P(q)$  the single particle form factor, which describes the shape and contrast of a single particle. In the presented case, it returns the scattering cross section of that particle [cm<sup>2</sup>].<sup>32</sup>  $S(q)$  is the structure factor, which describes interparticle correlations and could be replaced by an Ornstein-Zernike expression in case of concentration fluctuations due to attractive interparticle interactions:<sup>13</sup>

$$C(q) = 1 + \frac{\kappa}{1 + q^2 \xi^2} \quad (\text{S13})$$

In eq (S13),  $\xi$  is the correlation length of concentration fluctuations and  $\kappa$  a scaling factor, which is proportional to the isothermal osmotic compressibility of interacting particles.<sup>13</sup>

A complete description of all form- and structure factors is provided in the SASfit user guide (“User guide for the SASfit software package”, version 0.94.12 from the 9<sup>th</sup> of January 2023).<sup>32</sup> Therefore it is abstained from a reproduction of mathematical expressions for form- and structure factors in

the current work. Alternatively, Table SI1 provides an overview of which SASfit models were used in this work.

Table SI1: Denotation of form- and structure factors used in this work compared to their name in the SASfit user guide.<sup>32</sup>

Denotation in the current work	Denotation in the SASfit user guide
<b>Form factors</b>	
<b>Form factors for fitting the entire <math>q</math>-range of full contrast SANS curves</b>	
Form factor of a core-shell sphere: $P_{\text{core-shell-sphere}}(q)$	Spherical Shell iii
Form factor of an end-capped core-shell cylinder with core length $L_{\text{core}}$ : $P_{\text{cap-core-shell-cylinder}}(q)$	CylShell2
<b>Form factors for fitting the entire <math>q</math>-range of <math>\text{C}_{12}\text{E}_5</math>-matched SANS curves</b>	
Form factor of a cylinder: $P_{\text{cylinder}}(q)$	Cylinder
Form factor of a sphere: $P_{\text{sphere}}(q)$	Sphere
Form factor of a core-shell cylinder with length $L$ (not end-capped) $P_{\text{core-shell-cylinder}}(q)$	CylShell1
Extended Guinier plateau: $I_{q,\text{Guinier}}(q)$	generalized Guinier law ( $\alpha = 0$ )
<b>Form factors for fitting the high-<math>q</math>-range of full contrast SANS curves (<math>q &gt; 0.045 \text{ \AA}^{-1}</math>)</b>	
Core-shell cylinder with linearly decaying shell contrast $P_{\text{core-linshell-cylinder}}(q)$	Pcs:linear shell cyl. · P'(Q): Rod
Core-shell sphere with linearly decaying shell contrast $P_{\text{core-linshell-sphere}}(q)$	LinShell
<b>Structure factors</b>	
Ornstein-Zernike expression $C(q)$	Critical Scattering
Hard sphere interactions	3D Hard Sphere (PY)



The following section provides information on how scattering length densities ( $\eta$ ) and the particle number density ( $N$ ) were used or determined during fitting:

For fitting the high- $q$  region of SANS curves ( $q > 0.045 \text{ \AA}^{-1}$ ) with the purpose of obtaining cross section dimensions and for fitting SANS curves of C<sub>12</sub>E<sub>5</sub>-matched solutions, scattering length density profiles were assumed according to values shown in Table SI2 and kept constant during fitting. The particle number density  $N$  was fitted in this approach.

For fitting the entire  $q$ -range,  $N$  was calculated and kept constant, whereas scattering length densities were fitted. Assemblies were assumed to possess a core-shell morphology in all cases. The micellar aggregation number was calculated by dividing the core volume of the assembly by the estimated partial molar volume of a C<sub>12</sub> alkyl chain ( $350.2 \text{ \AA}^3$ ).<sup>38</sup> Assuming, that all surfactant molecules participate in assembly formation,  $N$  was then calculated from the known concentration of the C<sub>12</sub>E<sub>5</sub> surfactant and the micellar aggregation number.

It should be mentioned, that scattering from molecularly dissolved C<sub>12</sub>E<sub>5</sub> molecules was not considered due to its low critical micelle concentration and a subsequent excess of micellized surfactant.

Table SI2: Scattering length densities used for the calculation of scattering length density profiles for form factor fitting.

Designation	Sum formula	Scattering length density $\eta / 10^{-6} \text{ \AA}^{-2}$
solvent	D <sub>2</sub> O	6.358
hC <sub>12</sub> (hydrogenated C <sub>12</sub> alkyl chain)	C <sub>12</sub> H <sub>25</sub>	-0.392
hE <sub>5</sub> (hydrogenated E <sub>5</sub> pentaethyleneglycol group)	C <sub>10</sub> H <sub>21</sub> O <sub>6</sub>	0.731
dE <sub>5</sub> (deuterated E <sub>5</sub> pentaethyleneglycol group)	C <sub>10</sub> D <sub>21</sub> O <sub>6</sub>	7.750
BlueH	C <sub>13</sub> H <sub>9</sub> ClN <sub>4</sub> O <sub>3</sub> S <sub>2</sub>	3.0

**Static light scattering.** The absolute intensity scattered by the sample at a given angle  $\theta$  is given by the Rayleigh ratio ( $R_\theta$ ) and calculated according to the following equation:<sup>57</sup>

$$R_\theta = \frac{I_\theta - I_{\text{solvent},\theta}}{I_{\text{toluene},\theta}} \cdot R_{\text{toluene}} \quad (\text{SI4})$$

In eq (SI4),  $I_\theta$  is the experimentally measured scattered intensity from the solution at the scattering angle  $\theta$ .  $I_{\text{solvent},\theta}$  and  $I_{\text{toluene},\theta}$  are the scattering intensities of the solvent and the standard toluene at the same angle and  $R_{\text{toluene}}$  the absolute scattering intensity of the standard toluene.

The  $q$ -dependency of the Rayleigh ratio was analysed under the assumption of fluctuation scattering and is described by the Ornstein-Zernike relation:<sup>11,28,58</sup>

$$R_\theta = \frac{R_0}{1 + q^2 \xi^2} \quad (\text{SI5})$$

In eq (SI5),  $R_0$  is the zero- or forward scattering intensity. It is related to the isothermal osmotic compressibility  $\chi_T$  according to:<sup>13,58</sup>

$$R_0 = AT \chi_T \quad (\text{SI6})$$

Where  $A$  is an instrumental constant and  $T$  the temperature. The validity of the Ornstein-Zernike relation can be verified by confirming a linear relation between the inverse of the scattered intensity ( $R_\theta^{-1}$ ) and the squared scattering vector  $q^2$  in an Ornstein-Zernike plot according to:<sup>58</sup>

$$\frac{1}{R_\theta} = \frac{1}{R_0} \cdot (1 + \xi^2 q^2) \quad (\text{SI7})$$

By extrapolation to  $q = 0$ , the forward scattering intensity ( $R_0$ ) and the correlation length of concentration fluctuations ( $\xi$ ) are easily obtained.

**Dynamic light scattering.** In a dynamic light scattering (DLS) experiment, the normalized intensity time autocorrelation function  $g^{(2)}(\tau)$  is measured as a function of the correlation time at given scattering vector  $q$ .<sup>57,59</sup> Cumulant analysis provides one tool to obtain the average decay rate ( $\bar{\Gamma}$ ) of  $g^{(2)}(\tau)$ , which relates to the apparent diffusion coefficient at a given angle ( $D_{\text{app}}$ ) according to:

$$\bar{\Gamma} = D_{\text{app}} \cdot q^2 \quad (\text{SI8})$$

Assuming a monomodal, but polydisperse distribution of  $\bar{\Gamma}$ ,  $g^{(2)}(\tau)$  can directly be fitted with the following expression:<sup>59</sup>

$$g^{(2)}(\tau) = B + \beta \exp(-2\bar{\Gamma}\tau) \left(1 + \frac{\mu_2}{2!} \tau^2\right)^2 \quad (\text{SI9})$$

In eq (SI9),  $\bar{\Gamma}$  is the average decay rate and  $\mu_2$  its variance. The variance of  $D_{\text{app}}$  is hence calculated as:

$$\text{Var}(D_{\text{app}}) = \left(\frac{1}{q^2}\right)^2 \cdot \mu_2 \quad (\text{SI10})$$

In cases, where no clear  $q$ -dependency of  $D_{\text{app}}$  was observed, the diffusion coefficient ( $D$ ) was obtained as an average of all  $D_{\text{app}}$ . The variance of  $D$  was obtained from error propagation as  $\text{Var}(D) = Z^{-2} \cdot \sum \text{Var}(D_{\text{app}})$  with  $Z$  being the number of averaged values. As each  $D_{\text{app}}$  was obtained from a separate fit, no covariance between  $D_{\text{app}}$  obtained at different angles was included. The standard deviation of the diffusion coefficient ( $SD(D)$ ) is the square root of its variance.

If  $D_{\text{app}}$  was observed to be dependent on  $q$ , the diffusion coefficient ( $D$ ) was obtained from extrapolation of  $D_{\text{app}}$  as a function of  $q^2$  to  $q = 0$ :<sup>57</sup>

$$D_{\text{app}}(q) = D \cdot \left(1 + K \cdot \langle R_g^2 \rangle_z q^2\right) \quad (\text{SI11})$$

In eq (SI11),  $\langle R_g^2 \rangle_z$  is the  $z$ -average radius of gyration of scattering particles and  $K$  depends on sample polydispersity as well as on the particle topology.<sup>57</sup>

An alternative approach to analyse dynamic light scattering data is to perform an inverse Laplace Transformation of the field autocorrelation function. The field-time autocorrelation function  $g^{(1)}(\tau)$  is related to the intensity-time autocorrelation function  $g^{(2)}(\tau)$  by the Siegert relation:<sup>57,59</sup>

$$g^{(2)}(\tau) = 1 + [g^{(2)}(\tau=0)] \cdot |g^{(1)}(\tau)|^2 \quad (\text{SI12})$$

One way to perform an inverse Laplace Transformation on  $g^{(1)}(\tau)$  is to use the constrained regularization method (CONTIN) developed by Provencher.<sup>58,60,61</sup> The CONTIN analysis is usually used to fit monomodal particle size distributions with a certain polydispersity. A distribution with multiple peaks would not correctly be fitted.<sup>61</sup>

The diffusion properties of the presented system depend on the motion of polydisperse C<sub>12</sub>E<sub>5</sub> micelles and on concentration fluctuations. Due to the similarity of micellar sizes and the correlation length of concentration fluctuations, a distinction between these two contributions is not possible with the performed experiments. Therefore,  $D$  was used to calculate an apparent distance  $R_a$  using the Stokes-Einstein equation:<sup>26,28</sup>

$$R_a = \frac{k_B T}{6\pi \eta D} \quad (\text{SI13})$$

In eq (SI13),  $k_B$  is the Boltzmann constant,  $T$  the temperature and  $\eta$  the viscosity of the solvent. The distance parameter  $R_a$  was used to compare relative differences of samples analysed within

this work, keeping in mind that an increase in  $R_a$  could signal an increase in particle size and/or in correlation length of concentration fluctuations ( $\xi$ ).

### 7.8.3. Dependence of $C_{12}E_5$ assembly on solution pD

Figure SI5 shows SANS curves recorded from solutions of  $hC_{12}hE_5$  at different pD. As these SANS curves are identical, they were fitted globally using the same size parameters (red, solid curve). Details concerning the fit are explained in section 7.4 of the main document and in section 7.8.6 of the SI. The identity of SANS curves from  $C_{12}E_5$  solutions with different pD proves, that the morphology of  $C_{12}E_5$  micelles does not depend on solution pD under the given conditions.

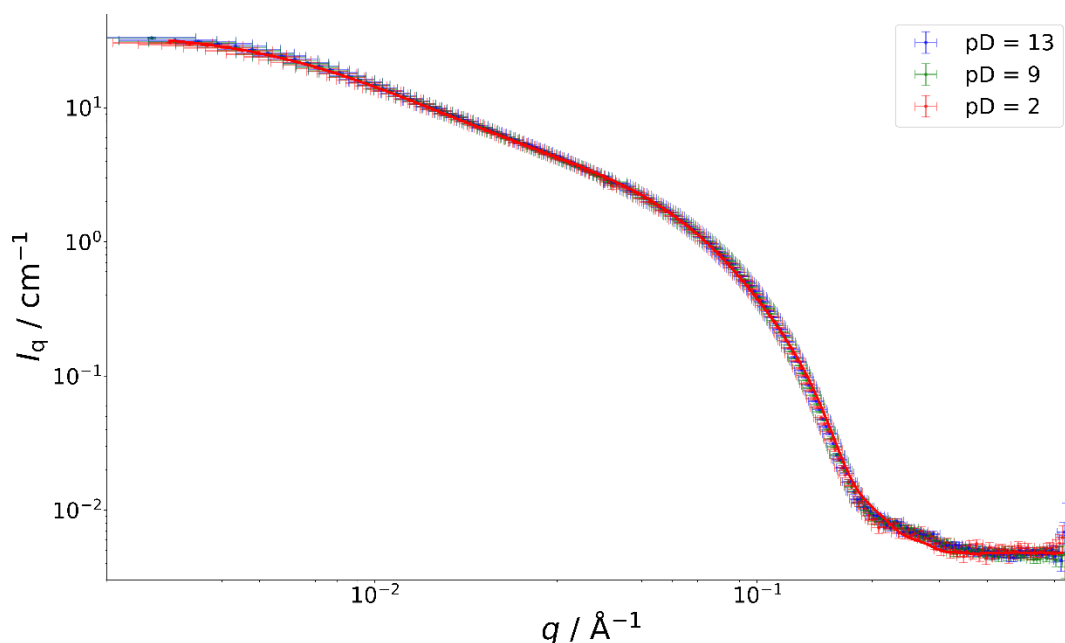


Figure SI5: Full contrast SANS curves of solutions containing  $[hC_{12}hE_5] = 25$  mM at the indicated pD. An isotonic NaCl solution in  $D_2O$  was used as the solvent and SANS curves were recorded at a sample temperature of  $10$  °C. The red line (—) displays a fit with the form factor model of end-capped core-shell cylinders with a core length of  $66$  Å including fluctuation scattering as a structure factor. Experimental SANS curves and the fit overlay.

### 7.8.4. Isotope effects

The right plot in Figure SI6 shows the clouding temperatures (CTs) of solutions in  $D_2O$  containing Blue at varying concentration and pD for samples prepared with  $mC_{12}mE_5$  at a concentration of  $[mC_{12}mE_5] = 25$  mM in comparison to samples containing  $hC_{12}hE_5$  with the same concentration (Figure SI6, left plot). Samples containing  $mC_{12}mE_5$ , which is a mixture of  $mC_{12}hE_5$  and  $mC_{12}dE_5$  at a volume ratio of 18.1:81.9, systematically show an elevated CT by  $6 - 7$ °K. This deviation is attributed to isotope effects. In literature, similar observations on the CT of  $C_nE_m$  systems were

reported when the H<sub>2</sub>O solvent was substituted for D<sub>2</sub>O, which resulted in an increase of the CT by about 3 – 5 K.<sup>13</sup> Nevertheless, clouding temperatures shown in Figure SI6 follow the same trend concerning their pD- and Blue concentration dependency, regardless of whether solutions containing hC<sub>12</sub>hE<sub>5</sub> or mC<sub>12</sub>mE<sub>5</sub> are observed.

According to literature and results reported in the main document (Figure 6b), a CT increase goes along with a reduction in the correlation length of concentration fluctuations ( $\xi$ ) and/or the size of micelles at a given temperature.<sup>11,12,28</sup> Therefore,  $\xi$  and the size of micelles are expected to be smaller for mC<sub>12</sub>mE<sub>5</sub> compared to hC<sub>12</sub>hE<sub>5</sub>. As mC<sub>12</sub>mE<sub>5</sub> is a mixture of mC<sub>12</sub>hE<sub>5</sub> and mC<sub>12</sub>dE<sub>5</sub>, its self-assembly and CT-properties likely lay between that of mC<sub>12</sub>hE<sub>5</sub> and mC<sub>12</sub>dE<sub>5</sub>. Therefore and to investigate trends as a function of the degree of deuteration of the surfactant, solutions of pure mC<sub>12</sub>hE<sub>5</sub> and pure mC<sub>12</sub>dE<sub>5</sub> were investigated and results compared to the behaviour hC<sub>12</sub>hE<sub>5</sub> in solution.

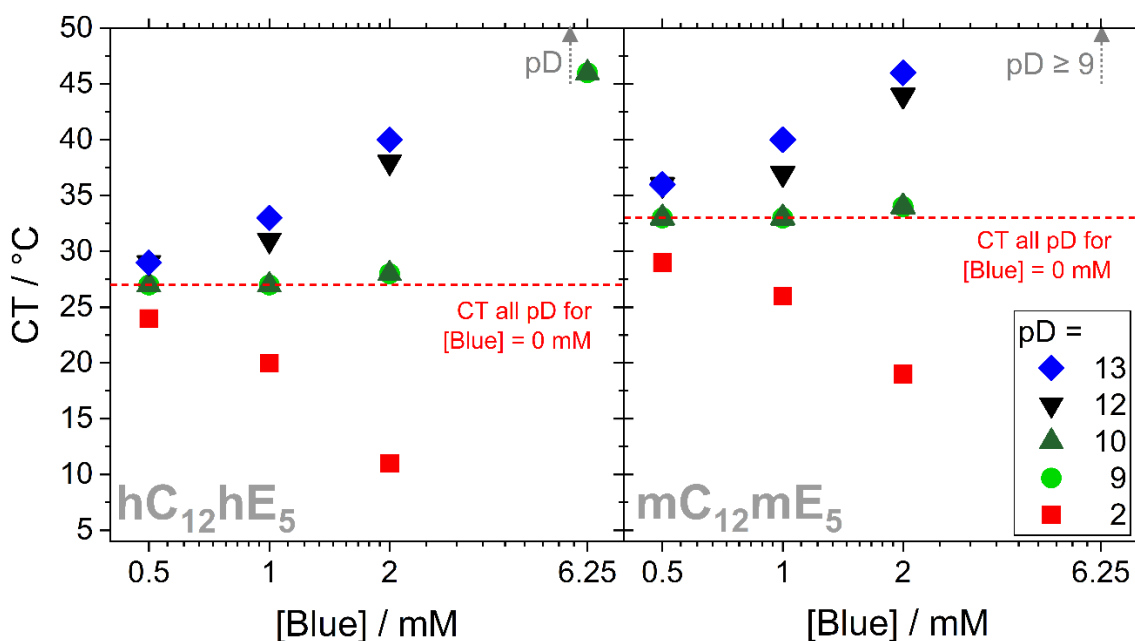


Figure SI6: CTs of solutions in D<sub>2</sub>O, containing either completely hydrogenated surfactant hC<sub>12</sub>hE<sub>5</sub> at a concentration of [hC<sub>12</sub>hE<sub>5</sub>] = 25 mM (left) or a mixture of mC<sub>12</sub>hE<sub>5</sub> and mC<sub>12</sub>dE<sub>5</sub> at match composition (mC<sub>12</sub>mE<sub>5</sub>) at a concentration of [mC<sub>12</sub>mE<sub>5</sub>] = 25 mM (right) at variable concentration of Blue and pD. An isotonic NaCl solution ( $I = 0.154$  M) in D<sub>2</sub>O was used as a solvent. The pD of each solution was adjusted with solutions of DCl and NaOD. Grey, dotted arrows indicate, that CTs of solutions containing [Blue] = 6.25 mM at pD  $\geq 12$  in the hC<sub>12</sub>hE<sub>5</sub> system and CTs of solutions containing [Blue] = 6.25 mM at pD  $\geq 9$  in the mC<sub>12</sub>mE<sub>5</sub> system lay above 50 °C. CTs of solutions containing [Blue] = 12.5 mM at pD  $\geq 9$  lay above 50 °C in all cases.

Figure SI7 shows DLS intensity correlation functions of samples containing either hC<sub>12</sub>hE<sub>5</sub>, mC<sub>12</sub>hE<sub>5</sub> or mC<sub>12</sub>dE<sub>5</sub> at a concentration of 25 mM. It is clearly visible, that the decay of  $g^{(2)}(\tau)$  is shifted to smaller correlation times for an increasing degree of deuteration, pointing towards

smaller micelles. Intensity correlation functions were fitted with the revised method of cumulants (eq (SI9)), which permitted to obtain an apparent diffusion coefficient  $D_{\text{app}}$  and its variance (eq (SI10)) for each angle. As  $D_{\text{app}}$  did not show a pronounced angular dependency, all values of  $D_{\text{app}}$  were averaged to obtain the diffusion coefficient  $D$ . Error propagation yielded the variance and therefore also the standard deviation ( $SD$ ) of  $D$ . The values of  $D$  and  $SD(D)$ , together with an apparent distance calculated according to eq (SI13) and its standard deviation are displayed in Table SI3. The standard deviations of  $D$  and  $R_a$  are a measure of the width of the size distribution and/or distribution of correlation lengths of  $C_{12}E_5$  micelles. An idea about the width of such a distribution may also be obtained by calculating the distribution of decay times ( $A(\tau)$ ) from the field correlation function  $g^{(1)}(\tau)$  using CONTIN analysis. Such distributions are displayed in Figure SI7 and appear to be of similar width, but shifted in correlation time, for the three differently deuterated  $C_{12}E_5$  species. These results are confirmed by comparison of diffusion coefficients  $D$  and their standard deviation  $SD(D)$  displayed in Table SI3: With increasing degree of deuteration, an increase in  $D$  is observed, pointing towards smaller micelles and/or  $\xi$  in solutions of  $mC_{12}dE_5$  compared to  $hC_{12}hE_5$ . The ratio between  $SD(D)$  and  $D$  amounts to  $\approx 0.12$  or  $0.13$  in all cases, signalling a similar width of the distribution of  $D$  for all surfactants.

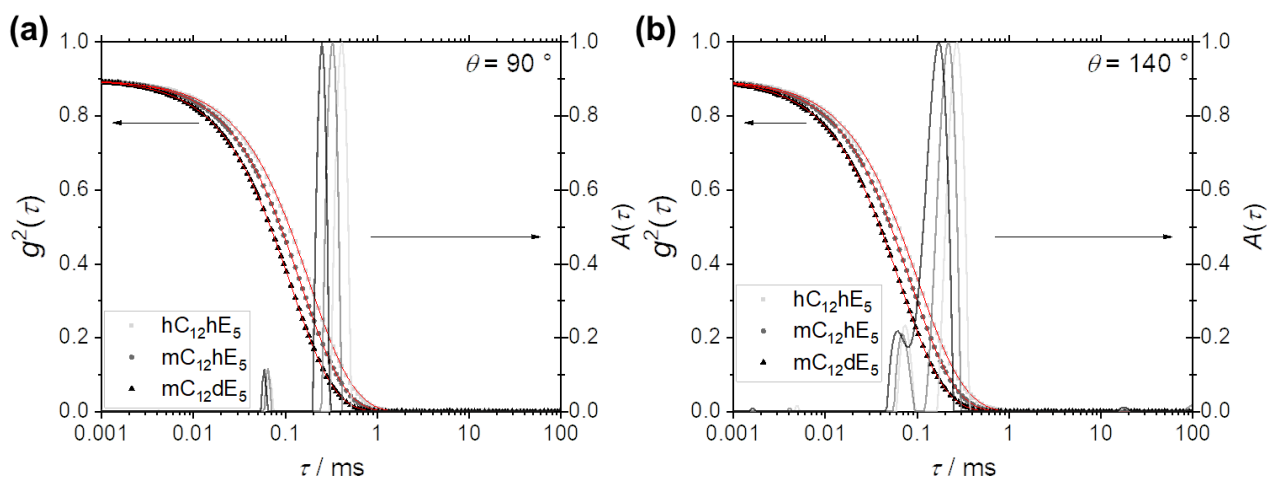


Figure SI7: Intensity autocorrelation functions  $g^{(2)}(\tau)$  of samples containing the respective  $C_{12}E_5$  species at a concentration of  $[C_{12}E_5] = 25$  mM in an isotonic NaCl solution prepared in  $D_2O$  at  $pD = 2$  and  $10^\circ C$ . The red lines show fits to  $g^{(2)}(\tau)$  according to the revised method of cumulants (eq (SI9)). Solid, grey lines display the distribution of decay times  $A(\tau)$  obtained from CONTIN analysis of respective field autocorrelation functions  $g^{(1)}(\tau)$ . The line colour corresponds to the symbol colour of the respective  $C_{12}E_5$  species. Data and distributions are shown for the scattering angles  $\theta = 90^\circ$  (a) and  $\theta = 140^\circ$  (b).

Figure SI8 displays Ornstein-Zernike plots of SLS data from solutions of the three differently deuterated  $C_{12}E_5$ -species. They were evaluated according to eq (SI7) to obtain correlation lengths of concentration fluctuations ( $\xi(\text{SLS})$ ) displayed in Table SI3. Apart from the linear dependency of  $R_\theta^{-1}$  on  $q^2$ , a small upturn of  $R_\theta^{-1}$  is observed at low values of  $q^2$ . In the  $R_\theta = f(q)$  scattering curve

this translates to a correlation peak, which appears due to spatial correlations with a correlation length of about  $2\pi q_{\text{peak}}^{-1} \approx 564 \text{ \AA}$  ( $q_{\text{peak}} \approx 0.011 \text{ \AA}^{-1}$ ). This value is larger than correlation lengths  $\xi(\text{SLS})$  found for concentration fluctuations. It is not clear, which domains in the sample cause the appearance of the correlation peak. Even though this additional feature slightly impairs an Ornstein-Zernike analysis of SLS data according to eq (SI7),  $\xi(\text{SLS})$  are still considered to be comparable among each other due to the low intensity of the correlation peak.

According to the analysis of SLS data, correlation lengths of concentration fluctuations become smaller with increasing degree of deuteration of the surfactant. This is consistent with the observed increase in the CT of solutions containing deuterated surfactant compared to  $\text{hC}_{12}\text{hE}_5$ . In qualitative agreement with SLS,  $R_a$  from DLS analysis yield a similar trend.

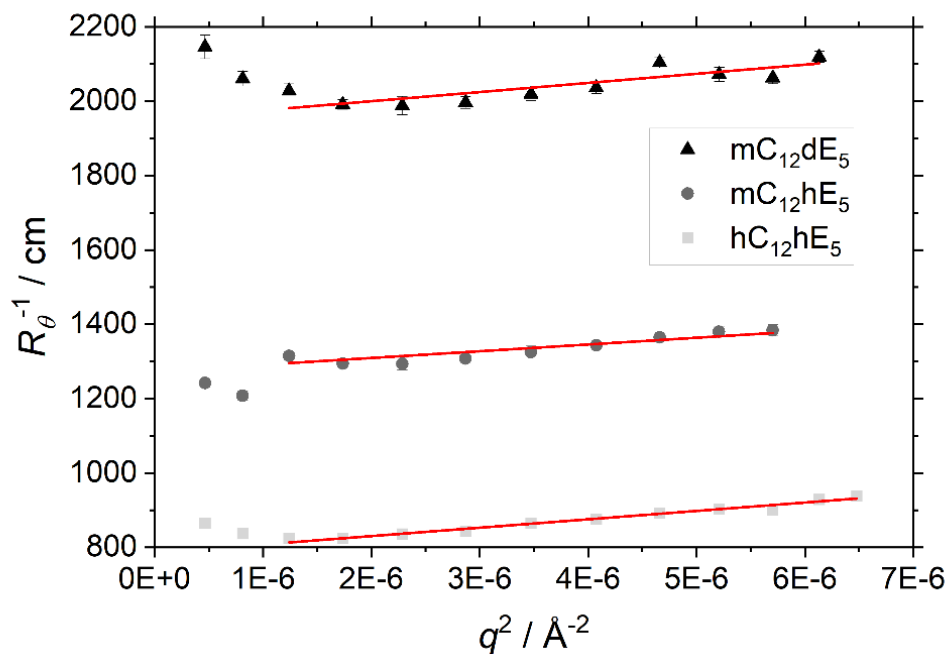
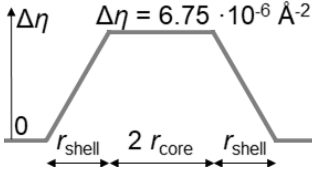
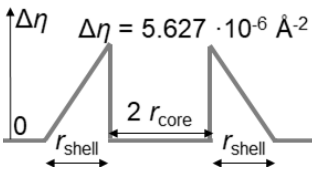
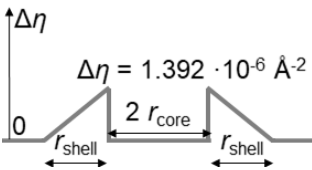


Figure S18: Ornstein-Zernike plots of SLS data from  $\text{C}_{12}\text{E}_5$  solutions according to eq (SI7) and corresponding fits. The reciprocal Rayleigh ratio is depicted as a function of the value of the scattering vector. Sample solutions contained the respective  $\text{C}_{12}\text{E}_5$  species at a concentration of  $[\text{C}_{12}\text{E}_5] = 25 \text{ mM}$  and were prepared in an isotonic  $\text{NaCl}$  solution in  $\text{D}_2\text{O}$  with  $\text{pD} = 2$ . Measurements were performed at a sample temperature of  $10 \text{ }^\circ\text{C}$ .

Table SI3: Comparison of the size and Ornstein-Zernike scattering parameters of C<sub>12</sub>E<sub>5</sub> micelles formed by C<sub>12</sub>E<sub>5</sub> molecules with different degrees of deuteration in their 25 mM solution in an isotonic NaCl solution in D<sub>2</sub>O at pD = 2 and 10 °C. Cross section dimensions were obtained from fitting the high-*q* region with the form factor of core-shell cylinders with a length of 90 Å and linearly decaying contrast towards the solvent in the shell region. The corresponding scattering length density difference ( $\Delta\eta$ ) profile is given. For hC<sub>12</sub>hE<sub>5</sub>, a logarithmic size distribution of the core radius was assumed. For this reason,  $r_{\text{core}}$  is the mean value of this distribution and  $SD(r_{\text{core}})$  its standard deviation calculated from  $r_{\text{core}}$  and the width of the log-normal distribution. Parameters for the Ornstein-Zernike scattering contribution were obtained from fitting the entire SANS curve with the form factor of an end-capped core-shell cylinder with a core length of  $L_{\text{core}} = 66$  Å.

	hC <sub>12</sub> hE <sub>5</sub>	mC <sub>12</sub> hE <sub>5</sub>	mC <sub>12</sub> dE <sub>5</sub>
<b>SANS</b>			
$\Delta\eta$ profile			
$r_{\text{core}} / \text{Å}$	$13.3 \pm 0.2$	$11.2 \pm 0.2$	$15.3 \pm 2$
$SD(r_{\text{core}}) / \text{Å}$	$3.45 \pm 0.06$ Log-normal distribution	0	0
$r_{\text{shell}} / \text{Å}$	$13.1 \pm 0.2$	$20.9 \pm 0.3$	$12 \pm 4$
$\kappa(\text{SANS})$	$8.88 \pm 0.02$	$5.58 \pm 0.07$	$35.3 \pm 11$
$\xi(\text{SANS}) / \text{Å}$	$140 \pm 0.2$	$119 \pm 2$	$418 \pm 76$
<b>SLS</b>			
$R_0(\text{SLS}) / 10^{-6} \text{ cm}^{-1}$	$1273 \pm 9$	$785 \pm 7$	$513 \pm 6$
$\xi(\text{SLS}) / \text{Å}$	$169 \pm 7$	$119 \pm 13$	$112 \pm 14$
<b>DLS</b>			
$D / 10^6 \text{ Å}^2 \text{ s}^{-1}$	788	986	1277
$SD(D) / 10^6 \text{ Å}^2 \text{ s}^{-1}$	105	123	151
$R_a / \text{Å}$	158	126	97
$SD(R_a) / \text{Å}$	21	16	12



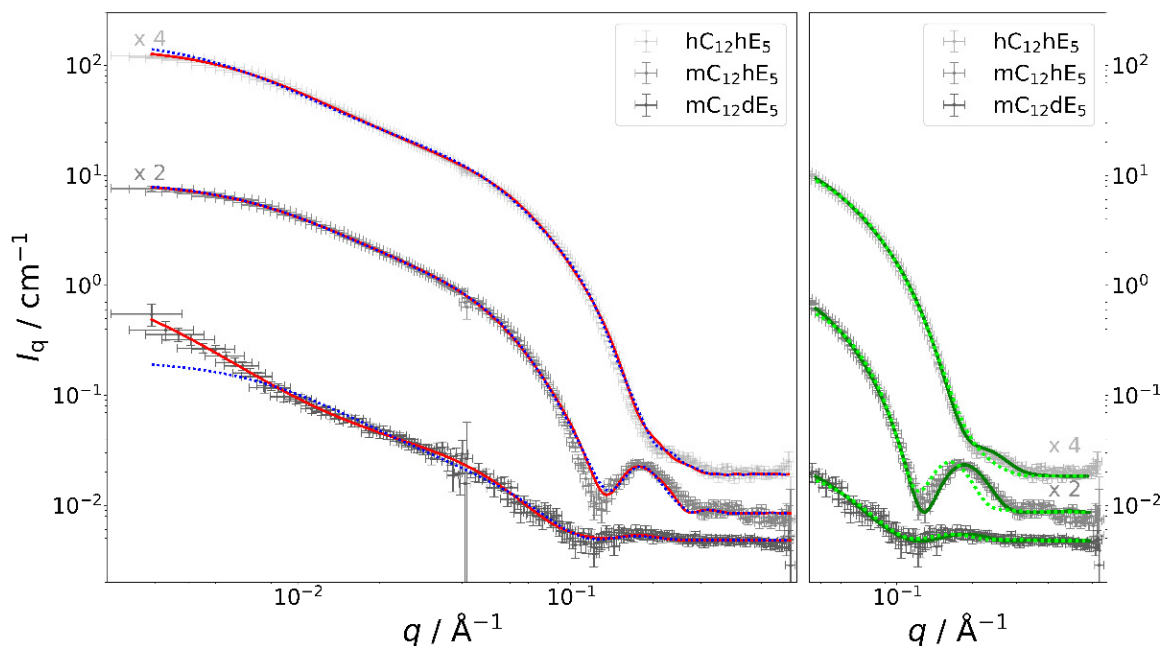


Figure S19: Full contrast SANS curves of solutions containing the respective  $C_{12}E_5$  species at a concentration of 25 mM and the indicated pD. An isotonic NaCl solution in  $D_2O$  was used as the solvent. SANS curves were recorded at a sample temperature of 10 °C. Red line (—): Fit with the form factor model of end-capped core-shell cylinders with a core length of 66 Å including Ornstein-Zernike scattering as a structure factor. Dotted, blue line (....): Fit with the same form factor model including Ornstein-Zernike scattering as the structure factor, but the correlation length  $\xi$  was kept constant to values obtained from the evaluation of static light scattering data in the Ornstein-Zernike plot (Figure S18). Dark green line (—): Form factor fit assuming core-shell cylinders with a total length of  $L = 90$  Å and a linearly decaying scattering length density difference ( $\Delta\eta$ ) profile within the shell region of the cylinder cross section. Lime green dotted line (....): Form factor fit assuming core-shell spheres and the same  $\Delta\eta$  profile.  $\Delta\eta$  profiles are displayed in Table SI3.

Figure S19 displays SANS curves from solutions containing the three differently deuterated  $C_{12}E_5$  surfactants. The right image displays the analysis of assembly cross sections analogous to investigations described in the main document, section 7.4 and in the SI, section 7.8.6. This was done by only fitting the high- $q$  region ( $q > 0.045 \text{ \AA}^{-1}$ ) with the form factor of a core-shell cylinder or with the form factor of a core-shell sphere. In both cases, the scattering contrast was assumed to linearly decay towards the solvent in the shell region. Assumed scattering length density difference profiles differ for each surfactant and are shown in the first line of Table SI3. The right plot in Figure S19 shows a fit with the form factor model of a core-shell cylinder with a total length of  $L = 90 \text{ \AA}$  and a fit with the form factor model of a core-shell sphere. The assumption of a cylindrical morphology resulted into the best fit in all cases and cross section dimensions from this analysis are therefore displayed in Table SI3. For fitting the SANS curve emerging from solutions of  $hC_{12}hE_5$ , a log-normal distribution of the core radius needed to be assumed to describe the data well. The standard deviation of  $r_{\text{core}}$  calculated from this distribution ( $SD(r_{\text{core}})$ ) is displayed in Table SI3 and  $r_{\text{core}}$  denotes the mean value of the distribution. For  $mC_{12}hE_5$  no

such distribution needed to be assumed, which indicates that the necessity to assume a distribution of  $r_{\text{core}}$  results from the small difference between the scattering length densities of the core and the shell for  $\text{hC}_{12}\text{hE}_5$ . For  $\text{mC}_{12}\text{dE}_5$ , no distribution of  $r_{\text{core}}$  was assumed either, which is mostly caused by the high signal-to-noise ratio of the experimental SANS curve. Core radii and shell thicknesses obtained from this analysis differ for all three differently deuterated  $\text{C}_{12}\text{E}_5$  species. This is attributed to the different contrast conditions. Total cross section radii ( $r_{\text{core}}+r_{\text{shell}}$ ) lay between 26.4 Å and 32.1 Å, but do not systematically vary with the degree of deuteration. As all surfactants possess the same chain lengths in their hydrophobic and their hydrophilic part, the apparent differences in cross section dimensions are likely caused by differences in contrast and actual cross section dimensions are expected to be similar.

Core radii shown in Table SI3 were successively used as fixed values in the fits to the total scattering curves. The left plot in Figure SI9 shows experimental SANS curves together with fits assuming the form factor of end-capped core-shell cylinders with a core length of  $L_{\text{core}} = 66$  Å and Ornstein-Zernike scattering. From Table SI3 it can be seen, that  $\kappa$  and  $\xi$  obtained from this fit differ for differently deuterated  $\text{C}_{12}\text{E}_5$  species. Correlation lengths obtained for  $\text{hC}_{12}\text{hE}_5$  and  $\text{mC}_{12}\text{hE}_5$  are fairly similar to values obtained from SLS. In contrast to that, values differ for  $\text{mC}_{12}\text{dE}_5$ . The dotted, blue line in Figure SI9 shows a fit, for which correlation lengths  $\xi$  were kept constant to values obtained from SLS measurements. SANS curves of  $\text{hC}_{12}\text{hE}_5$  and  $\text{mC}_{12}\text{hE}_5$  are well described with this approach. The SANS curve of  $\text{mC}_{12}\text{dE}_5$  is well described up until the low- $q$  upturn in scattering intensity. Considering the consistency of light scattering results with observed CT variations and the fact, that light scattering revealed a systematic decrease in  $\xi$  with increasing degree of deuteration, the high correlation length found with SANS for  $\text{mC}_{12}\text{dE}_5$  is questionable.

To conclude this section, isotope effects result in an increase of solution CT when  $\text{mC}_{12}\text{dE}_5$  instead of  $\text{hC}_{12}\text{hE}_5$  is used as a surfactant (Figure SI6). This goes along with a decrease in correlation lengths of concentration fluctuations with increasing degree of surfactant deuteration. Considering the given chemical structure of the surfactant, cross section dimensions of surfactant micelles are not expected to change significantly upon deuteration.

### 7.8.5. Light scattering from BlueH/C<sub>12</sub>E<sub>5</sub> solutions at pD = 2

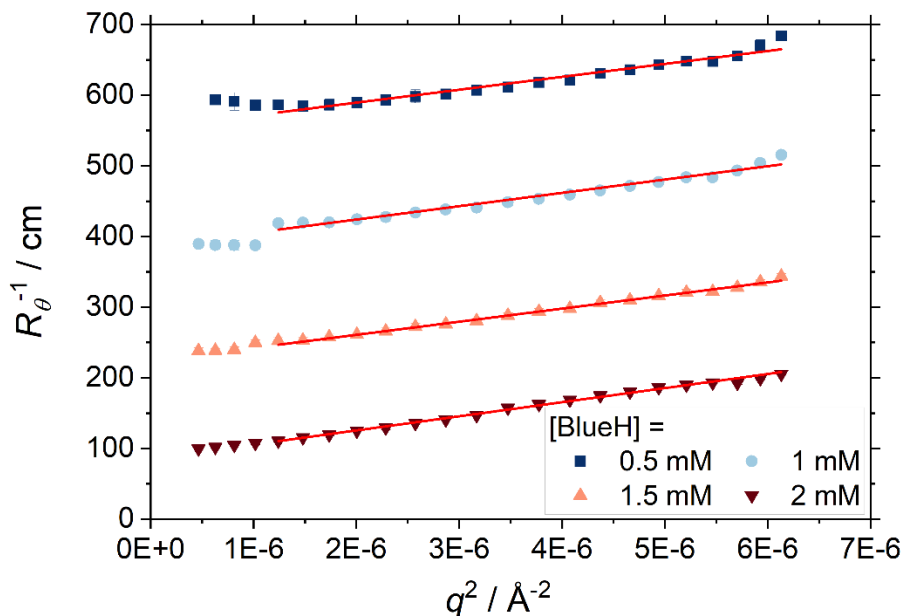


Figure SI10: Ornstein Zernike plots of SLS data obtained from solutions containing hC<sub>12</sub>hE<sub>5</sub> at a concentration of 25 mM and variable concentrations of BlueH. An isotonic NaCl solution prepared in D<sub>2</sub>O served as the solvent. The pD of each solution was pD = 2 and measurements were performed at a sample temperature of 10 °C.

Figure SI10 shows Ornstein-Zernike plots obtained from SLS-measurements of samples containing hC<sub>12</sub>hE<sub>5</sub> at a concentration of 25 mM and varying concentrations of Blue. Correlation lengths for concentration fluctuations were obtained from fits according to eq (SI7) and are shown in Table SI4 in comparison to  $\xi$  obtained from fitting of full contrast SANS curves for samples that were measured with SANS. For the sample containing [Blue] = 1 mM, SANS covered a sufficiently low  $q$ -range to obtain a correlation length  $\xi$ , which is comparable to  $\xi$  obtained from SLS. For the sample containing [Blue] = 2 mM, the Guinier plateau was not reached in the  $q$ -range covered by SANS, which entails that the analysis of SLS data provides a more reliable correlation length. Apart from the expected linear relationship between  $R_{\theta}^{-1}$  and  $q^2$ , Figure SI10 shows an upturn of  $R_{\theta}^{-1}$  at low values of  $q^2$ . The same observation was made in Figure SI8 and discussed in section 7.8.4 of the SI.

Intensity correlation functions obtained from DLS measurements were analysed using the revised method of cumulants (eq (SI9)). Figure SI11 displays  $g^{(2)}(\tau)$  for samples containing hC<sub>12</sub>hE<sub>5</sub> at a concentration of 25 mM and varying concentrations of Blue at a scattering angle of 90 °. The decay of  $g^{(2)}(\tau)$  becomes broader with increasing [Blue], but does not show two distinct shoulders. The broad decay points towards a high polydispersity of C<sub>12</sub>E<sub>5</sub> micelles, but does not permit to

identify two distinct species of micelles with different size. Apparent diffusion coefficients obtained by cumulant analysis at different angles are displayed in Figure S112 and were fitted according to eq (S111) to obtain diffusion coefficients  $D$ , which were used to calculate distances  $R_a$  that are displayed in Table S14.

Table S14: Comparison of Ornstein-Zernike parameters obtained from fitting full contrast SANS curves to correlation lengths obtained from the evaluation of SLS data and to apparent distances  $R_a$  obtained from the evaluation of DLS intensity correlation functions. The Ornstein-Zernike parameters  $\kappa$  and  $\xi$  were obtained from fitting full contrast SANS curves in the entire  $q$ -range with the form factor for end-capped core shell cylinders with a core length of 66 Å, including Ornstein-Zernike scattering. For [BlueH] = 0.5 mM and [BlueH] = 1.5 mM, no SANS curves exist.

[BlueH] :	0.5 mM	1 mM	1.5 mM	2 mM
<b>SANS</b>				
$\kappa(\text{SANS})$	-	$17.07 \pm 0.06$	-	$43.6 \pm 0.2$
$\xi(\text{SANS}) / \text{Å}$	-	$200.9 \pm 0.5$	-	$322 \pm 1$
<b>SLS</b>				
$R_0(\text{SLS}) / 10^{-6} \text{ cm}^{-1}$	$1809 \pm 12$	$2589 \pm 22$	$4469 \pm 28$	$11682 \pm 213$
$\xi(\text{SLS}) / \text{Å}$	$182 \pm 7$	$221 \pm 9$	$288 \pm 8$	$483 \pm 35$
<b>DLS</b>				
$R_a / \text{Å}$	$205 \pm 1$	$257 \pm 2$	$359 \pm 2$	$792 \pm 16$
$K\langle R_g^2 \rangle \cdot \xi(\text{SLS})^{-2}$	$0.33 \pm 0.3$	$0.51 \pm 0.03$	$0.58 \pm 0.02$	$0.76 \pm 0.06$

An increase of the slope in  $D_{\text{app}} = f(q^2)$ , which is proportional to  $K \cdot \langle R_g^2 \rangle$ , signals an increase in particle polydispersity and/or size, if the particle shape remains the same in all compared samples.<sup>57,62,63</sup> A systematic change of  $K$  with sample composition would potentially reveal a trend in particle polydispersity. If  $\langle R_g^2 \rangle$  was known,  $K$  could be calculated from the product  $K \cdot \langle R_g^2 \rangle$ , which is obtained by the analysis of  $D_{\text{app}} = f(q^2)$  according to eq S111. Unfortunately,  $\langle R_g^2 \rangle$  is unknown. However,  $\langle R_g^2 \rangle$  could be obtained from the slope of a Zimm plot and only differs from  $[\xi(\text{SLS})]^2$  by a constant. Therefore, the use of  $K\langle R_g^2 \rangle \cdot \xi(\text{SLS})^{-2}$  as a measure for sample polydispersity was considered reasonable and is displayed in Table S14. As all BlueH/C<sub>12</sub>E<sub>5</sub> co-assemblies are expected to possess a cylindrical shape and show fluctuation scattering, values of  $K\langle R_g^2 \rangle \cdot \xi(\text{SLS})^{-2}$  can be compared. From Table S14 it is visible, that the polydispersity of BlueH/C<sub>12</sub>E<sub>5</sub> co-assemblies increases with increasing concentration of BlueH. This is in accord with the increasing broadness of the  $g^{(2)}(\tau)$  decay with increasing [BlueH] (Figure S111).

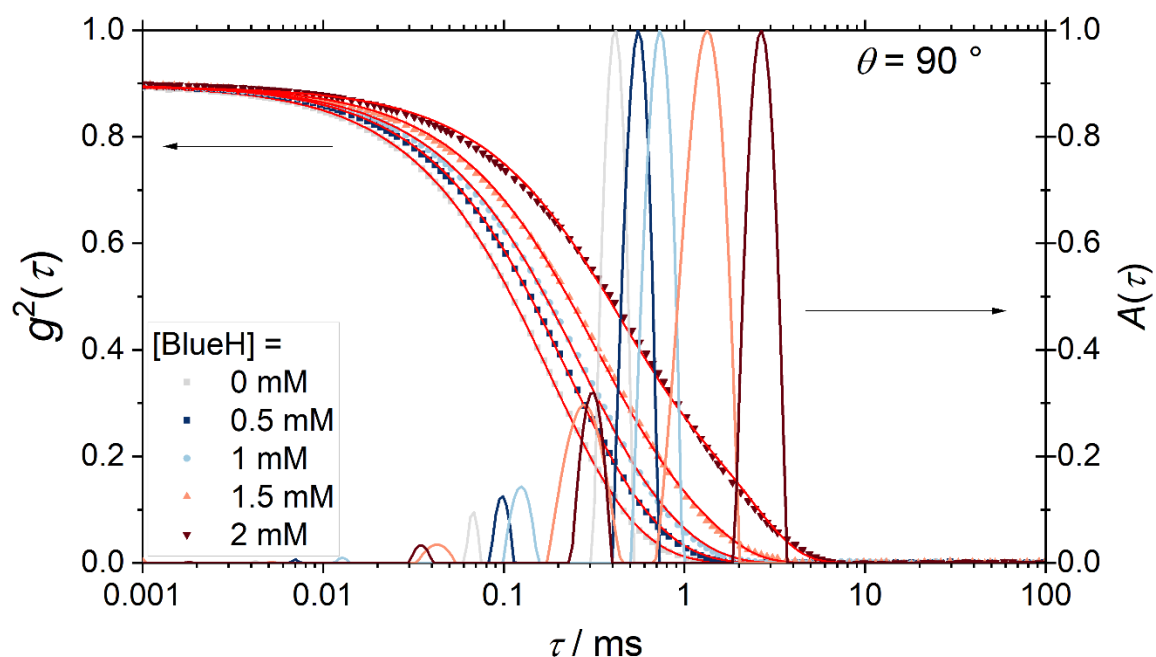


Figure S111: Intensity autocorrelation functions  $g^{(2)}(\tau)$  of samples containing  $hC_{12}hE_5$  at a concentration of 25 mM and variable concentrations of BlueH. An isotonic NaCl solution prepared in  $D_2O$  served as the solvent. The pD of each solution was pD = 2 and measurements were performed at a sample temperature of 10 °C. The red lines show fits to  $g^{(2)}(\tau)$  according to the revised method of cumulants (eq (S19)). The thicker, solid lines display the distribution of decay times  $A(\tau)$  obtained from CONTIN analysis of respective field autocorrelation functions  $g^{(1)}(\tau)$ . The line colour corresponds to the symbol colour of the respective concentration of BlueH. Data and distributions are shown for the scattering angle  $\theta = 90^\circ$ .

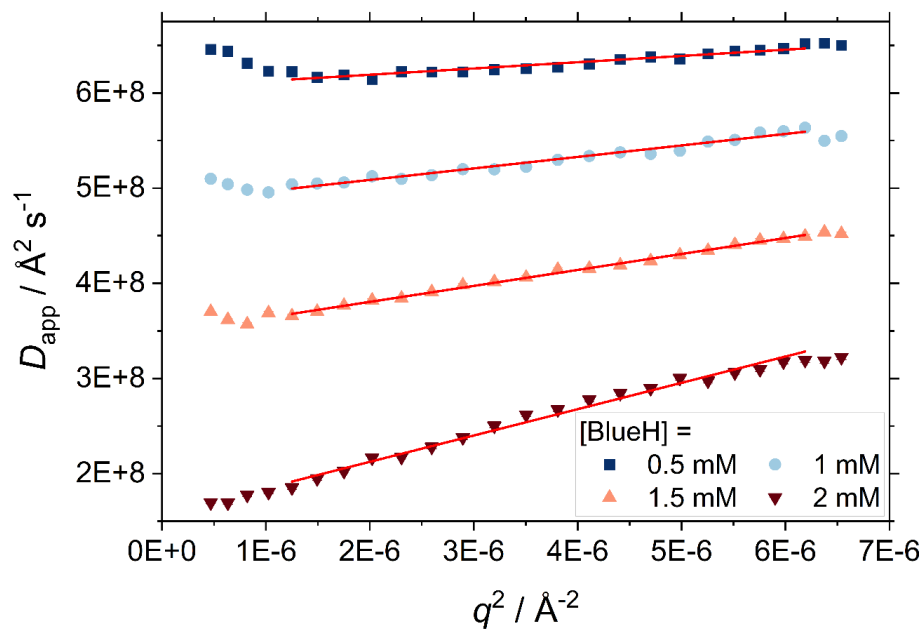


Figure S112: Apparent diffusion coefficients obtained by cumulant analysis of DLS intensity correlation functions from samples containing  $hC_{12}hE_5$  at a concentration of 25 mM and varying concentrations of BlueH. An isotonic NaCl solution in  $D_2O$  served as the solvent. Samples had a pD of 2 and were measured at a sample temperature of 10 °C.

To conclude this section, it was found that correlation lengths for concentration fluctuations of the number density of BlueH/C<sub>12</sub>E<sub>5</sub> co-assemblies ( $\xi$ ) can be obtained from Ornstein-Zernike plots of SLS data. They compare well to  $\xi$  obtained by SANS as long as the corresponding Guinier plateau is reached in the SANS curve. DLS data do not permit to observe the presence of two or more different types of micelles, but point towards a broad size distribution of BlueH/C<sub>12</sub>E<sub>5</sub> co-assemblies. The width of this distribution increases with increasing concentration of BlueH.

#### 7.8.6. Details on fits to full contrast SANS curves

For the analysis of full contrast SANS curves emerging from Blue/C<sub>12</sub>E<sub>5</sub> solutions, the following strategy was employed:

*In a first step*, only the high- $q$  range ( $q > 0.045 \text{ \AA}^{-1}$ ) was fitted with a core-shell model to obtain information on the ensemble average assembly cross section. No structure factor or Ornstein-Zernike contribution was assumed in this step.

*In a second step*, the entire  $q$ -range was fitted with various form factor models, including Ornstein-Zernike scattering or a structure factor. For this analysis, the core radius and its distribution were adapted from step one and kept constant during fitting. All other parameters, including shell thickness and scattering length densities, were fitted for a set of different form factors, including core-shell spheres and end-capped core-shell cylinders. The number density of assemblies ( $N$ ) was calculated as described in section 7.8.2 of the SI and fixed during fitting. The form factor model, which best described experimental SANS data, was identified by comparing the goodness-of-fit.

**Analysis of assembly cross section.** Information on the assembly cross section were obtained by form factor fits to the high- $q$  range ( $q > 0.045 \text{ \AA}^{-1}$ ). No structure factor was considered ( $S(q) = 1$ ). Two form factor models were applied to fit experimental data. Resulting fits were compared and cross section dimensions obtained from the fit with the form factor model, which best described experimental SANS curves with reasonable parameters.

*The first form factor model* assumes spherical micelles consisting of a core with homogeneous scattering length density ( $\eta$ ) and a shell with a linearly decaying scattering length density difference between particle and solvent ( $\Delta\eta$ ). This form factor is abbreviated as  $P_{\text{core-linshell-sphere}}(q)$ . The scattering length density profile for this analysis was displayed in the main document, Figure 4a. The contrast ( $\Delta\eta$ ) decay towards the solvent is caused by penetration of solvent molecules into the pentaethyleneglycol head group.<sup>64,65</sup> For polymeric surfactants containing longer polyethyleneglycol (PEG) head groups, specific form factor models were developed, which

take the radius of gyration of PEG head group chains into account.<sup>33</sup> However, in the case of C<sub>12</sub>E<sub>5</sub>, the head group is not long enough to justify the application of such a form factor.

The  $\Delta\eta$  profile shown in the main document (Figure 4a) is based on the theoretical scattering length density of the hC<sub>12</sub> alkyl chain ( $\eta = -0.392 \cdot 10^{-6} \text{ \AA}^{-2}$ ) and the scattering length density of the solvent ( $\eta = 6.358 \cdot 10^{-6} \text{ \AA}^{-2}$ ). As  $\eta$  of the hE<sub>5</sub> head group lays in between these values ( $\eta = 0.731 \cdot 10^{-6} \text{ \AA}^{-2}$ ), the largest  $\Delta\eta$  is achieved in the micellar core. Padia et al.<sup>6</sup> suggested intermixing of the core-shell interface in C<sub>n</sub>E<sub>m</sub> micelles, making it reasonable to assume that  $\Delta\eta$  does not suddenly drop when moving from the core into the shell region.

*The second form factor model* assumes the same scattering length density profile, but micelles with cylindrical rather than spherical morphology. The cylinder length was set to 90 Å for all fits using this model. This form factor is abbreviated as  $P_{\text{core-linshell-cylinder}}(q)$ .

Figure SI13 displays experimental SANS curves and best fits obtained upon application of the two above-described form factors ( $P_{\text{core-linshell-sphere}}(q)$  and  $P_{\text{core-linshell-cylinder}}(q)$ ).

For being able to fit the data sufficiently well, a log-normal distribution of the core radius  $r_{\text{core}}$  was required for both models. The standard deviation of  $\ln[r_{\text{core,median}}]$ ,  $\sigma$ , was fitted and lay in the range of  $0.18 < \sigma < 0.28$  in all cases, indicating standard deviations of  $r_{\text{core}}$  between 2.5 Å and 4 Å. The value of  $r_{\text{core}}$  denotes the mean of the number-weighted log-normal distribution of the core radius. The necessity to assume a size distribution of  $r_{\text{core}}$  may arise due to two phenomena: (1) The scattering length density profile shown in the main document (Figure 4a) was kept constant during the fit. Deviations from that profile due to interpenetration of alkyl- and EG-chains, incorporation of Blue or a non-linear decay of  $\Delta\eta$  are not considered by the model and may be compensated by a distribution of  $r_{\text{core}}$ . (2) It was previously shown, that wormlike and spherical micelles may coexist in a micellar solution.<sup>13,30,64,66</sup> For the C<sub>12</sub>E<sub>5</sub>-D<sub>2</sub>O system it was suggested, that the diameter of a cylindrical micelle is smaller by about 20 % compared to the diameter of a spherical micelle.<sup>13,15</sup> The necessity to introduce a distribution of  $r_{\text{core}}$  could therefore be indicative of the coexistence of spherical and cylindrical micelles. However,  $r_{\text{core}}$  and its standard deviation do not systematically change with sample composition (Figure SI14). This could either point to a negligible variation of the ratio between spherical and cylindrical micelles or to the existence of only one, polydisperse micellar geometry.

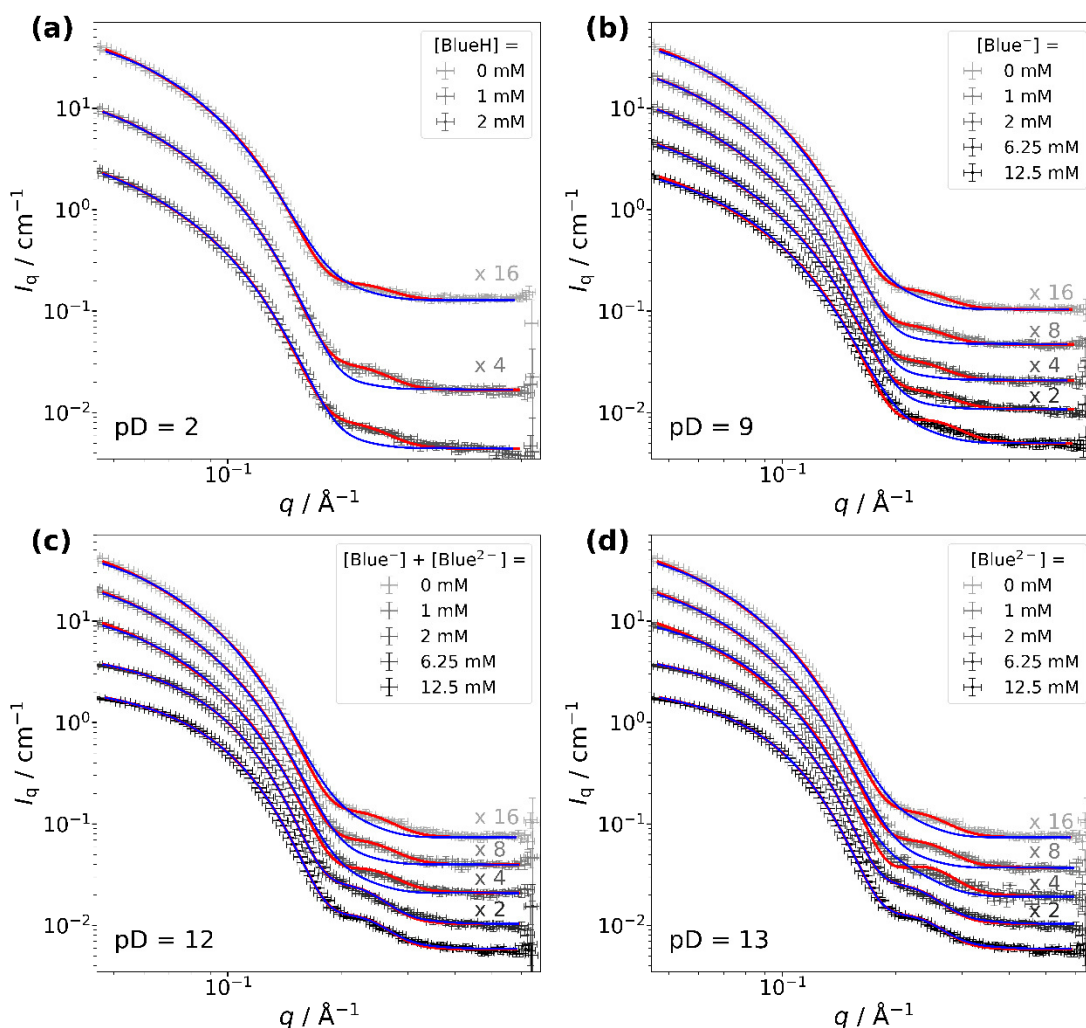


Figure S113: High- $q$  region of full contrast SANS curves recorded from samples containing  $[\text{hC}_{12}\text{hE}_5] = 25 \text{ mM}$ , and Blue at the indicated concentration at (a)  $\text{pD} = 2$ , (b)  $\text{pD} = 9$ , (c)  $\text{pD} = 12$  or (d)  $\text{pD} = 13$ . An isotonic NaCl solution ( $I = 0.154 \text{ M}$ ) in  $\text{D}_2\text{O}$  served as the solvent. SANS curves were recorded at a sample temperature of  $10 \text{ }^\circ\text{C}$ . Blue line (—): Form factor fit assuming core-shell spheres and a linearly decaying scattering length density difference ( $\Delta\eta$ ) profile within the shell region of the sphere ( $P_{\text{core-linshell-sphere}}(q)$ ). Red line (—): Form factor fit assuming core-shell cylinders with a total length of  $L = 90 \text{ \AA}$  and a linearly decaying scattering length density difference ( $\Delta\eta$ ) profile within the shell region of the cylinder cross section ( $P_{\text{core-linshell-cylinder}}(q)$ ).

The coexistence of spherical and cylindrical micelles may be detected with dynamic light scattering (DLS), if a correlation function is recorded, that permits the discrimination of two hydrodynamic radii. DLS was performed on the pure surfactant solution as well as on solutions containing BlueH and  $\text{C}_{12}\text{E}_5$ . Results were shown in Figure S17 and Figure S11. Correlation functions do not permit an unambiguous distinction of two shoulders and are rather broad. The interpretation of DLS data is complicated further by inter-micellar interactions. However, the absence of two distinct shoulders does suggest that spherical and cylindrical micelles, if present in equilibrium, do not strongly differ in their hydrodynamic radius. Blue<sup>-</sup> and Blue<sup>2-</sup> absorb light



throughout almost the entire visible range, therefore it was not possible to perform DLS on samples with pD = 9 or higher.

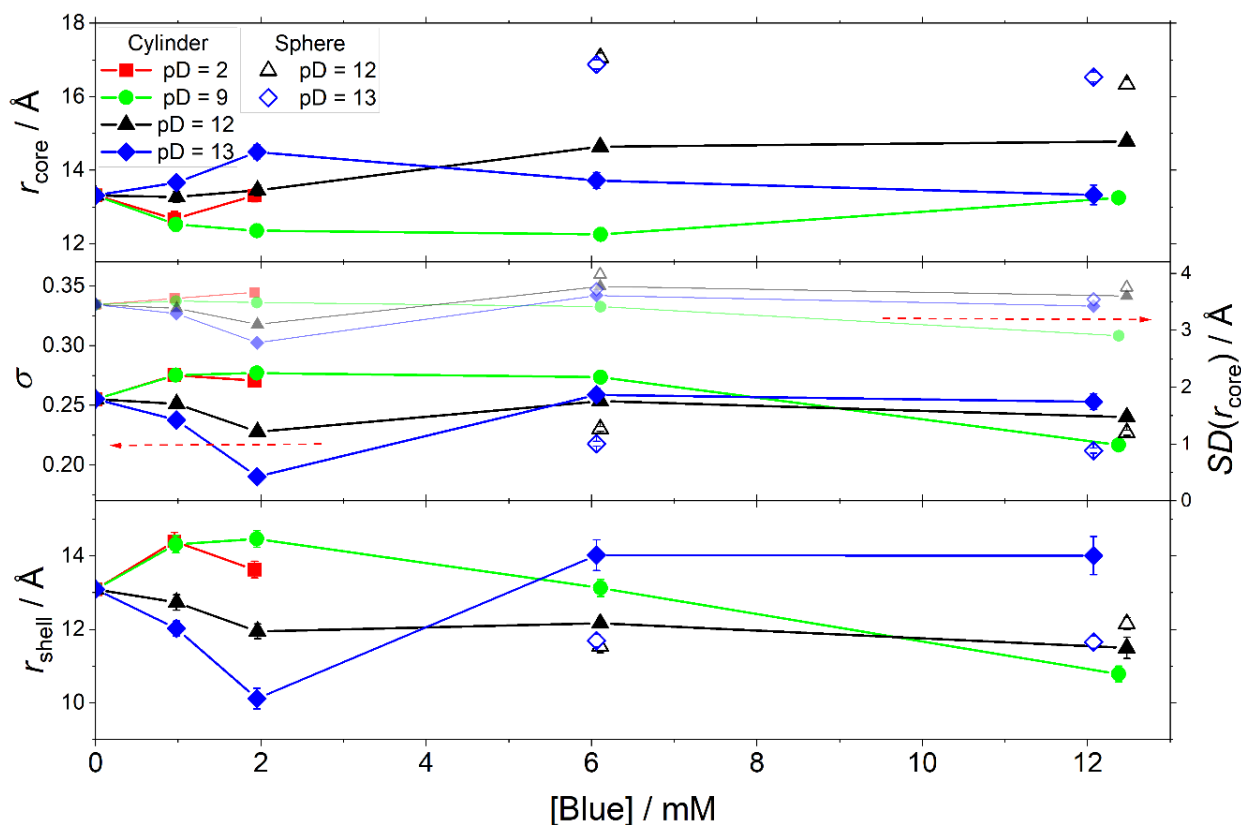


Figure S14: Size parameters for the cross section of Blue/C<sub>12</sub>E<sub>5</sub> micelles obtained from fitting the high- $q$  range ( $q > 0.045 \text{ \AA}^{-1}$ ) of full contrast SANS curves emerging from solutions containing hC<sub>12</sub>hE<sub>5</sub> at a concentration of 25 mM. An isotonic solution of NaCl in D<sub>2</sub>O was used as a solvent and measurements were performed at a sample temperature of 10 °C. The form factor model of a core-shell cylinder with a length of 90 Å and linearly decaying  $\Delta\eta$  in the shell region towards the solvent was used in most cases. In cases, where the form factor model of a core-shell sphere with the same  $\Delta\eta$  profile resulted in a better fit, resulting size parameters are displayed with open symbols in addition to parameters obtained upon assumption of a core-shell cylinder. The core radius is distributed according to a log-normal distribution. The parameter  $r_{core}$  is the mean value of this distribution. The parameter  $\sigma$  is the standard deviation of  $\ln[r_{core,median}]$  and  $SD(r_{core})$  is the standard deviation of  $r_{core}$ , which can be calculated from  $\sigma$  and  $r_{core}$ .

Table S15 compares  $\chi_{red}^2$  values obtained for fits to experimental SANS data in the high- $q$  range ( $q > 0.045 \text{ \AA}^{-1}$ ) with the two discussed form factor models. It furthermore displays  $\sigma$  as a measure for the polydispersity of the core radius.

By comparison of  $\chi_{red}^2$  (Table S15) it is easily seen, that most experimental SANS curves are better described assuming a cylindrical rather than a spherical morphology of the overall assembly. This goes along with high values of  $\sigma$  for spherical micelles in cases, where the cylindrical form factor describes experimental data better than the spherical one. This confirms, that high polydispersity of the core radius points towards anisometric micelles.

Following this observation, a cylindrical assembly morphology was considered to be the more reasonable description in cases, where  $\sigma > 0.3$  upon application of the form factor for spherical micelles ( $P_{\text{core-shell-sphere}}(q)$ ). Based on this cut-off and on lower  $\chi_{\text{red}}^2$ , cross section dimensions obtained from the fit with a cylindrical form factor were used for further analysis for all samples with  $pD \leq 9$  and for samples with  $[\text{Blue}] \leq 2$  mM for  $pD = 12$  and  $pD = 13$ .

Table S15:  $\chi_{\text{red}}^2$  values obtained from applying two different form factors to the high- $q$  region ( $q > 0.045 \text{ \AA}^{-1}$ ) of full contrast SANS curves from samples containing variable concentrations of Blue at variable  $pD$  and  $hC_{12}hE_5$  at a concentration of 25 mM. The standard deviation of  $\ln(r_{\text{core,median}})$  ( $\sigma$ ) resulting from the number-weighted log-normal distribution of the core radius is given as well. Solutions were prepared in an isotonic NaCl solution in  $D_2O$  and measured at a sample temperature of 10 °C.

[Blue] / mM	$P_{\text{core-linshell-sphere}}(q)$		$P_{\text{core-linshell-cylinder}}(q)$ Length $L = 90 \text{ \AA}$	
	$\chi_{\text{red}}^2$	$\sigma$	$\chi_{\text{red}}^2$	$\sigma$
0	7.74528	$0.44 \pm 0.02$	<b>2.0488</b>	$0.26 \pm 0.01$
pD = 2				
1	4.09144	$0.64 \pm 0.2$	<b>1.05111</b>	$0.28 \pm 0.01$
2	5.02672	$0.59 \pm 0.01$	<b>1.12636</b>	$0.27 \pm 0.01$
pD = 9				
1	4.14323	$0.64 \pm 0.01$	<b>0.919732</b>	$0.28 \pm 0.01$
2	3.9628	$0.66 \pm 0.02$	<b>0.741326</b>	$0.28 \pm 0.01$
6.25	3.64554	$0.62 \pm 0.01$	<b>1.14407</b>	$0.27 \pm 0.01$
12.5	3.82588	$0.43 \pm 0.01$	<b>3.05399</b>	$0.22 \pm 0.01$
pD = 12				
1	5.57002	$0.53 \pm 0.01$	<b>1.56856</b>	$0.25 \pm 0.01$
2	4.74567	$0.44 \pm 0.01$	<b>4.48411</b>	$0.23 \pm 0.01$
6.25	<b>2.17554</b>	$0.23 \pm 0.01$	2.30064	$0.25 \pm 0.01$
12.5	<b>2.88517</b>	$0.23 \pm 0.01$	3.31481	$0.24 \pm 0.01$
pD = 13				
1	6.17844	$0.49 \pm 0.01$	<b>2.08519</b>	$0.24 \pm 0.01$
2	<b>2.34835</b>	$0.34 \pm 0.01$	6.46766	$0.19 \pm 0.01$
6.25	<b>2.67611</b>	$0.22 \pm 0.01$	2.79508	$0.26 \pm 0.01$
12.5	<b>2.99752</b>	$0.21 \pm 0.01$	3.19957	$0.25 \pm 0.01$

The high- $q$  region of SANS curves emerging from samples containing  $[\text{Blue}] \geq 6.25$  mM at  $pD \geq 12$  was better described upon assumption of a spherical micelle geometry. Furthermore,  $\sigma$  is similar to that obtained for cylindrical micelles. For these reason, cross section dimensions obtained under the assumption of spherical micelles were used for further analysis for these four samples.

Fitted cross section dimension are summarized in Figure S114.

**Analysis of the entire  $q$ -range.** The second step of analysing experimental SANS curves consisted of fits to the entire  $q$ -range. For this purpose, form factors  $P(q)$  of end-capped core-shell cylinders with a core length  $L_{\text{core}}$  of either 20 Å, 40 Å, 66 Å, 100 Å or 200 Å and the form factor of a core-shell sphere were systematically applied to all SANS curves (main document, Figure 4b). Ornstein-Zernike scattering was included by substituting  $S(q)$  in eq (SI2) by the Ornstein-Zernike expression (eq. (SI3)). In contrast to form factors applied for the analysis of the high- $q$  regime, the form factors used in the analysis of the entire  $q$ -range exhibit a core with a homogeneous scattering length density ( $\eta_{\text{core}}$ ) and a shell with a homogeneous scattering length density ( $\eta_{\text{shell}}$ ). The choice of this model was based on the possibility to combine it with an Ornstein-Zernike scattering contribution using the SASfit software, which is not possible for the model of a core-shell cylinder with linearly decaying  $\Delta\eta$  in the shell (version 0.94.12).

The core radius  $r_{\text{core}}$  and its distribution were kept constant to values established in step 1 during fitting. The shell thickness  $r_{\text{shell}}$ , scattering length densities ( $\eta_{\text{core}}$  and  $\eta_{\text{shell}}$ ) and Ornstein-Zernike parameters were fitted for each of the described form factor models. The number density of assemblies ( $N$ ) was calculated from the micellar aggregation number and the known concentration of C<sub>12</sub>E<sub>5</sub> as described in section 7.8.2 of the SI. For the calculation of the micellar aggregation number, the core dimensions  $L_{\text{core}}$  and  $r_{\text{core}}$  were used.

Further information on the fitting procedure were given in the main document, section 7.4.

Figure SI15 to Figure SI18 display experimental SANS curves and best fits upon application of the form factor of a core-shell sphere (blue, dashed line), the form factor of an end-capped core-shell cylinder with a core length of 40 Å (red, dotted line) and the form factor of an end-capped core-shell cylinder with a core-length of 66 Å (red, solid line). Fits obtained from application of the other three models (end-capped core-shell cylinders with a core length of either 20 Å, 100 Å or 200 Å) are not shown. Except for fits to SANS curves from samples containing [Blue]  $\geq$  6.25 at pD  $\geq$  12, Ornstein-Zernike scattering was included as  $S(q)$ . SANS curves from samples containing [Blue]  $\geq$  6.25 at pD  $\geq$  12 were not well-described upon assumption of Ornstein-Zernike scattering. Therefore, the blue, dotted lines in Figure SI17 and Figure SI18 display best fits, when the form factor of core-shell spheres was applied while keeping  $S(q) = 1$ . The latter fit was improved by the inclusion of a structure factor based on hard sphere interactions (lime green, solid lines).

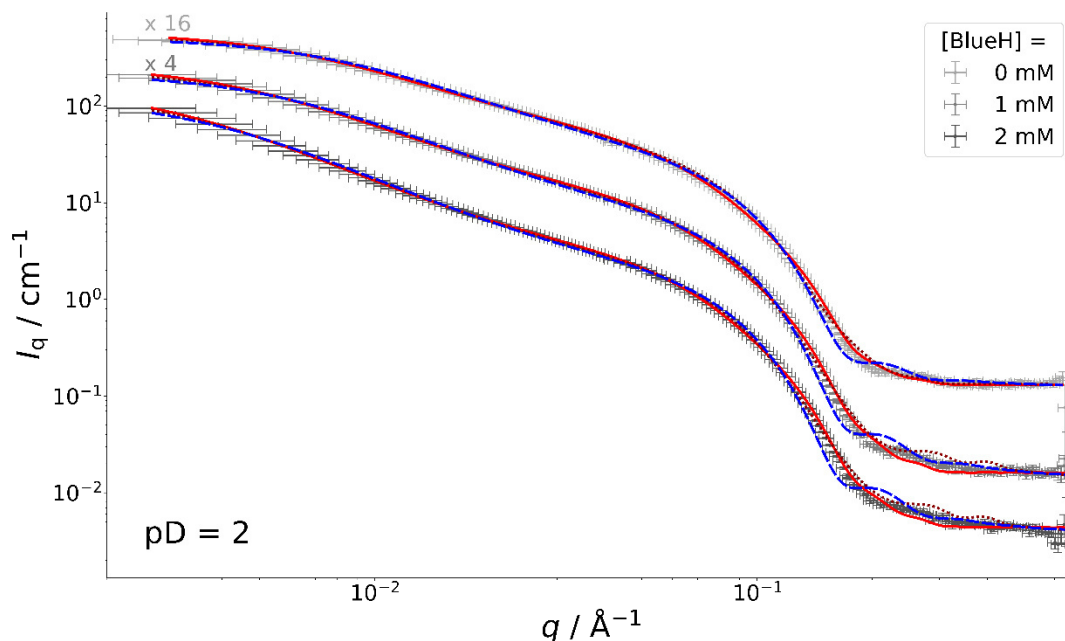


Figure SI15: Full contrast SANS curves of solutions containing  $[hC_{12}hE_5] = 25$  mM, and Blue at the indicated concentration at  $pD = 2$ . An isotonic NaCl solution ( $I = 0.154$  M) in  $D_2O$  served as the solvent. SANS curves were recorded at a sample temperature of  $10$  °C. Red line (—): Fit with the form-factor of end-capped core-shell cylinders with a core length of  $L_{core} = 66$  Å and Ornstein-Zernike scattering. Dark red dotted line (.....): Fit with the same model, but  $L_{core} = 40$  Å. Blue dashed line (---): Fit with the form factor of core-shell spheres and Ornstein-Zernike scattering.

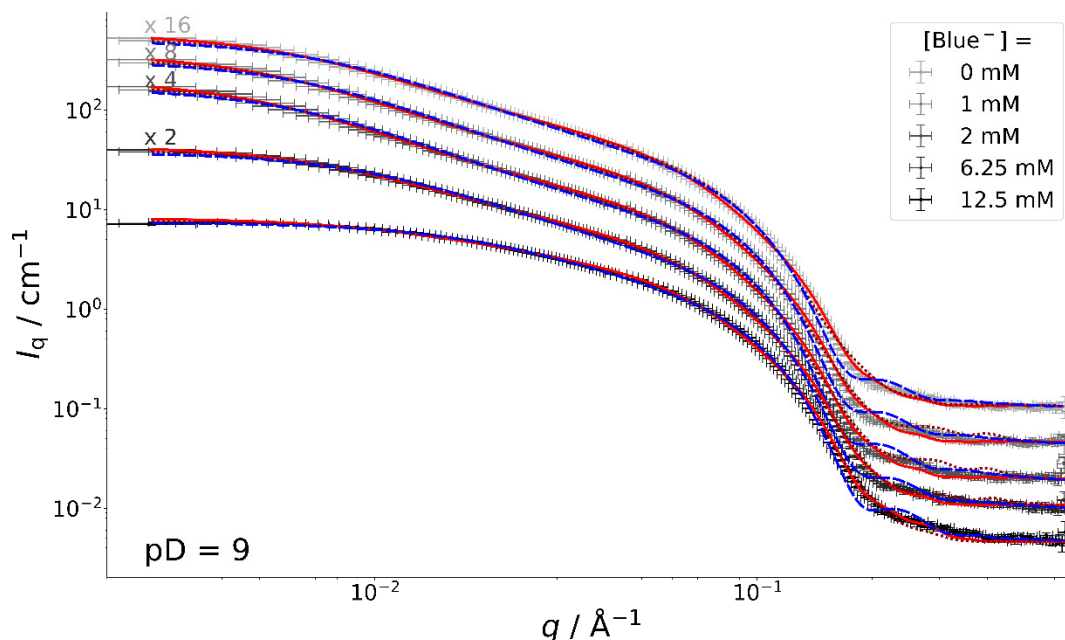


Figure SI16: Full contrast SANS curves of solutions containing  $[hC_{12}hE_5] = 25$  mM, and Blue at the indicated concentration at  $pD = 9$ . An isotonic NaCl solution ( $I = 0.154$  M) in  $D_2O$  served as the solvent. SANS curves were recorded at a sample temperature of  $10$  °C. Red line (—): Fit with the form-factor of end-capped core-shell cylinders with a core length of  $L_{core} = 66$  Å and Ornstein-Zernike scattering. Dark red dotted line (.....): Fit with the same model, but  $L_{core} = 40$  Å. Blue dashed line (---): Fit with the form factor of core-shell spheres and Ornstein-Zernike scattering.

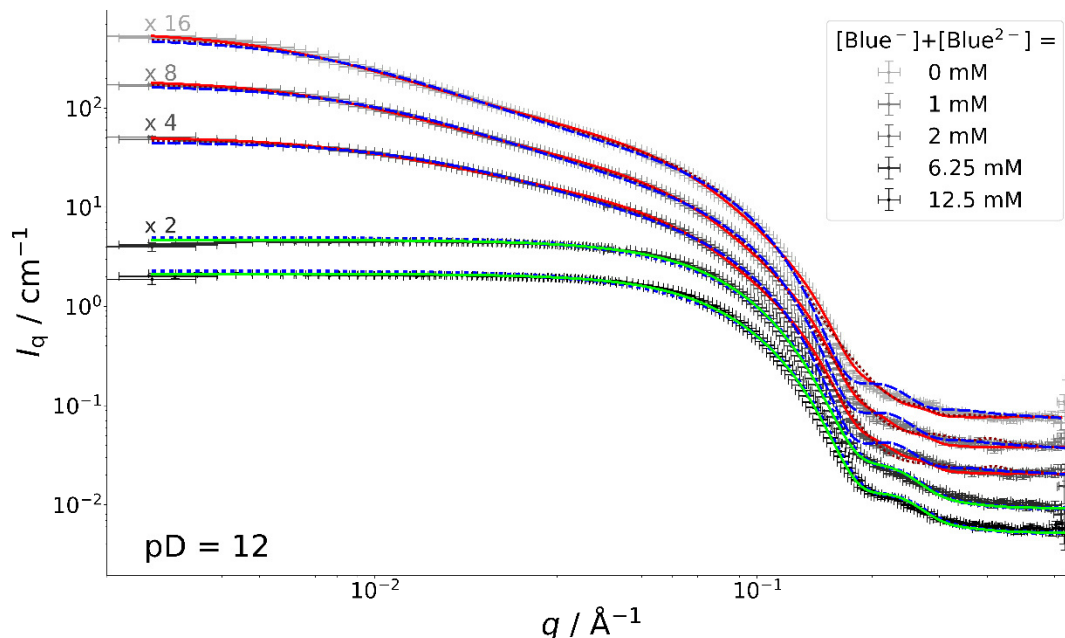


Figure SI17: Full contrast SANS curves of solutions containing  $[hC_{12}hE_5] = 25$  mM, and Blue at the indicated concentration at  $pD = 12$ . An isotonic NaCl solution ( $I = 0.154$  M) in  $D_2O$  served as the solvent. SANS curves were recorded at a sample temperature of  $10$  °C. Red line (—): Fit with the form-factor of end-capped core-shell cylinders with a core length of  $L_{core} = 66$  Å and Ornstein-Zernike scattering. Dark red dotted line (.....): Fit with the same model, but  $L_{core} = 40$  Å. Blue dashed line (---): Fit with the form factor of core-shell spheres and Ornstein-Zernike scattering. Blue dotted line (.....,  $[Blue] \geq 6.25$  mM): Fit with the form factor of core-shell spheres. Lime green line (—,  $[Blue] \geq 6.25$  mM): Fit with the form factor of core-shell spheres and a hard sphere structure factor.

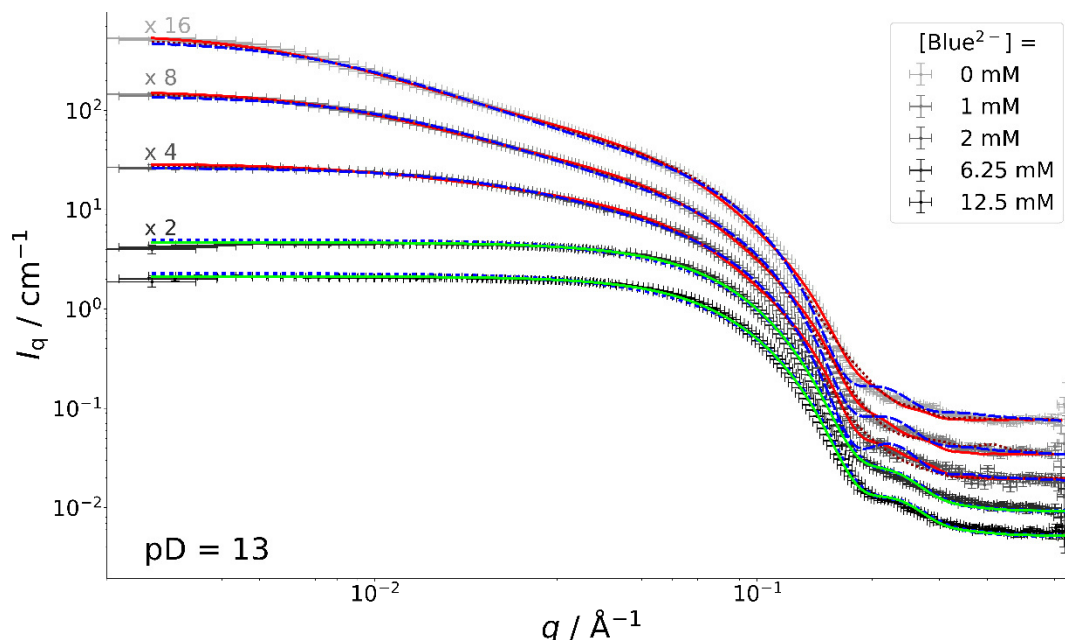


Figure SI18: Full contrast SANS curves of solutions containing  $[hC_{12}hE_5] = 25$  mM, and Blue at the indicated concentration at  $pD = 13$ . An isotonic NaCl solution ( $I = 0.154$  M) in  $D_2O$  served as the solvent. SANS curves were recorded at a sample temperature of  $10$  °C. Red line (—): Fit with the form-factor of end-capped core-shell cylinders with a core length of  $L_{core} = 66$  Å and Ornstein-Zernike scattering. Dark red dotted line (.....): Fit with the same model, but  $L_{core} = 40$  Å. Blue dashed line (---): Fit with the form factor of core-shell spheres and Ornstein-Zernike scattering. Blue dotted line (.....,  $[Blue] \geq 6.25$  mM): Fit with the form factor of core-shell spheres. Lime green line (—,  $[Blue] \geq 6.25$  mM): Fit with the form factor of core-shell spheres and a hard sphere structure factor.

The presented strategy serves to determine which form factor model best describes experimental SANS curves. This permits deductions on the morphology of the overall assembly. For this purpose, fit quality was compared in the mid- and low- $q$  regime ( $q < 0.134 \text{ \AA}^{-1}$ ) by means of  $\chi_{\text{red}}^2$ . By not including the high- $q$  regime into this analysis, distortions due to the use of a simplified scattering length density profile, which mostly affects the high- $q$  region, are avoided.

Table SI6 compares  $\chi_{\text{red}}^2$  values obtained from the application of different form factors to the mid- and low- $q$  regime ( $q < 0.134 \text{ \AA}^{-1}$ ) of experimental SANS curves. In cases, where fitting did not provide meaningful parameters upon inclusion of Ornstein-Zernike scattering no  $\chi_{\text{red}}^2$  values are given.

Table SI6:  $\chi_{\text{red}}^2$  values obtained from applying different models to the mid- and low  $q$  regime ( $q < 0.134 \text{ \AA}^{-1}$ ) of full contrast SANS curves. Solutions contained variable concentrations of Blue at variable pD and hC<sub>12</sub>hE<sub>5</sub> at a concentration of 25 mM. Solutions were prepared in an isotonic NaCl solution in D<sub>2</sub>O and measured at a sample temperature of 10 °C. The product of a core-shell particle form factor and an Ornstein-Zernike scattering contribution was applied in all cases. In cases, where the form factor of an end-capped core-shell cylinder was applied, the fixed core length is given by  $L_{\text{core}}$ . No values are given in cases, where fits including Ornstein-Zernike scattering did not improve  $\chi_{\text{red}}^2$  compared to fits without the Ornstein-Zernike contribution.

[Blue] / mM	$\chi_{\text{red}}^2$	$\chi_{\text{red}}^2$	$\chi_{\text{red}}^2$	$\chi_{\text{red}}^2$	$\chi_{\text{red}}^2$	$\chi_{\text{red}}^2$
	$P_{\text{core-shell-sphere}}(q)$	$P_{\text{cap-core-shell-cylinder}}(q)$	$P_{\text{cap-core-shell-cylinder}}(q)$	$P_{\text{cap-core-shell-cylinder}}(q)$	$P_{\text{cap-core-shell-cylinder}}(q)$	$P_{\text{cap-core-shell-cylinder}}(q)$
		$L_{\text{core}} = 20 \text{ \AA}$	$L_{\text{core}} = 40 \text{ \AA}$	$L_{\text{core}} = 66 \text{ \AA}$	$L_{\text{core}} = 100 \text{ \AA}$	$L_{\text{core}} = 200 \text{ \AA}$
0	56.1958	139.781	59.4544	<b>28.4856</b>	39.1214	59.3168
pD = 2						
1	109.797	74.1007	38.3013	<b>15.5627</b>	59.5742	111.887
2	143.608	90.7469	48.0338	<b>19.0937</b>	69.7645	147.802
pD = 9						
1	103.546	70.7841	36.5258	<b>15.4604</b>	59.778	107.03
2	125.742	87.2802	46.172	<b>14.5988</b>	51.6144	107.911
6.25	53.9567	32.2784	<b>15.1573</b>	15.8022	57.767	75.1715
12.5	18.9032	4.69194	<b>3.33927</b>	25.8871	65.9591	-
pD = 12						
1	47.0846	24.2802	<b>11.4717</b>	20.9485	67.2846	80.9147
2	29.3484	11.2277	<b>4.7245</b>	26.0071	87.3188	142.467
6.25	-	-	-	-	-	-
12.5	-	-	-	-	-	-
pD = 13						
1	37.3704	16.8482	<b>8.02013</b>	22.528	66.7001	77.0463
2	8.2244	1.83538	<b>1.78906</b>	15.0407	59.0167	140
6.25	-	-	-	-	-	-
12.5	-	-	-	-	-	-

Fitted parameters are displayed in Figure S119 for fits, where the form factor of an end-capped core-shell cylinder with a core length  $L_{\text{core}}$  of either 40 Å or 66 Å was applied. Correlation lengths of concentration fluctuations ( $\xi$ ) were fitted as well and were already displayed in the main document (section 7.4, Figure 8a).

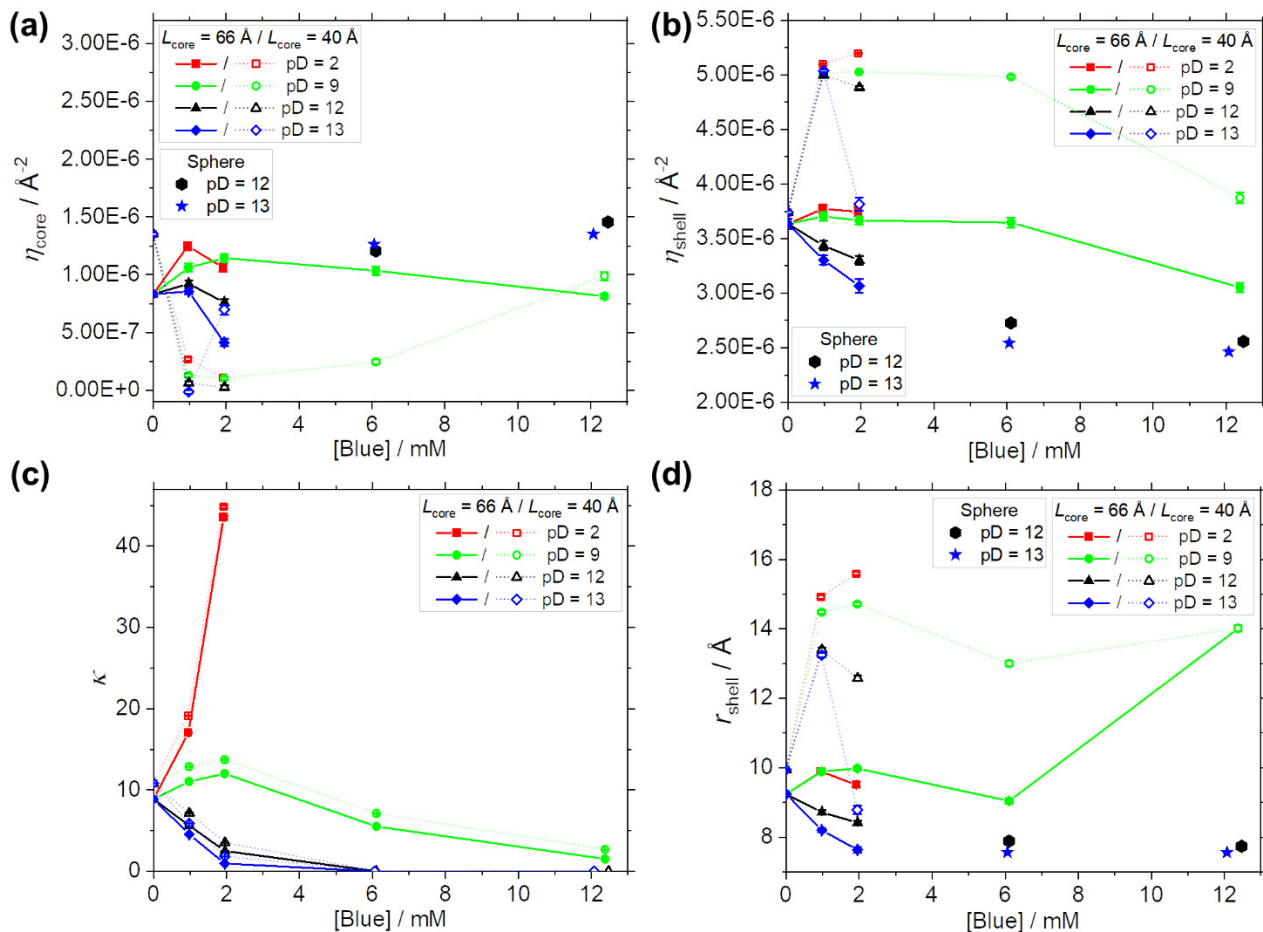
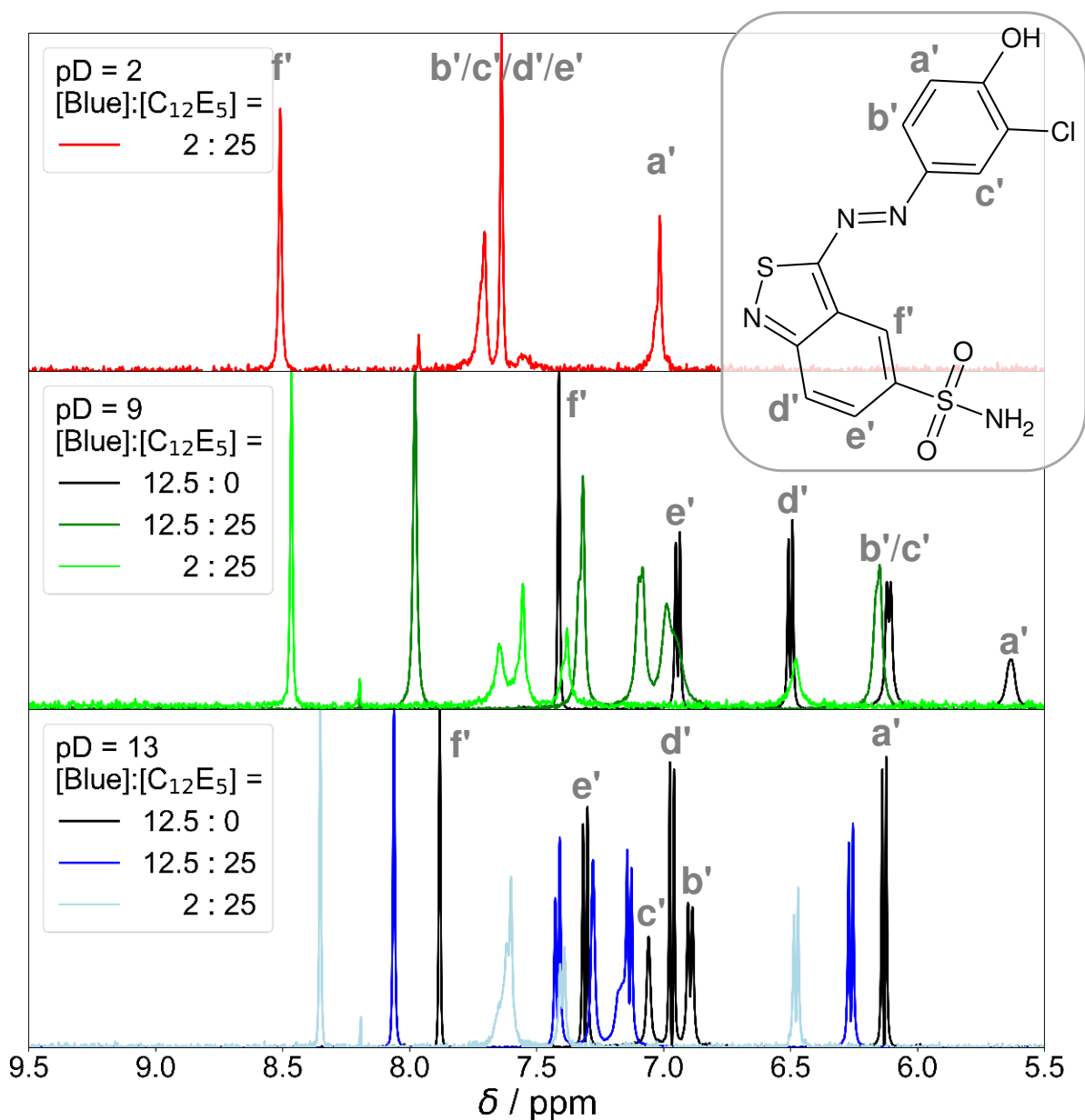


Figure S119: (a) Core scattering length density ( $\eta_{\text{core}}$ ), (b) shell scattering length density ( $\eta_{\text{shell}}$ ), (c) the scaling parameter for Ornstein-Zernike scattering ( $\kappa$ ) and (d) the shell thickness ( $r_{\text{shell}}$ ) obtained from fitting the entire  $q$ -range of full contrast SANS curves from solutions containing hC<sub>12</sub>H<sub>5</sub> at a concentration of 25 mM and variable concentration of Blue. An isotonic NaCl solution in D<sub>2</sub>O was used as the solvent. Measurements were performed at a sample temperature of 10 °C. Fits were performed with the form factor for end-capped core-shell cylinders with a core length ( $L_{\text{core}}$ ) of either 40 Å or 60 Å. Ornstein-Zernike scattering was included into the analysis. Correlation lengths were shown in Figure 8a of the main document (section 7.4). In cases, where the application of the core-shell sphere form factor with a hard sphere structure factor resulted in a better fit, dimensions resulting from such a fit are shown as well. The core radius  $r_{\text{core}}$  and its distribution were adopted from the corresponding high- $q$  fit (Figure S114) in all cases.

### 7.8.7. NMR-spectra





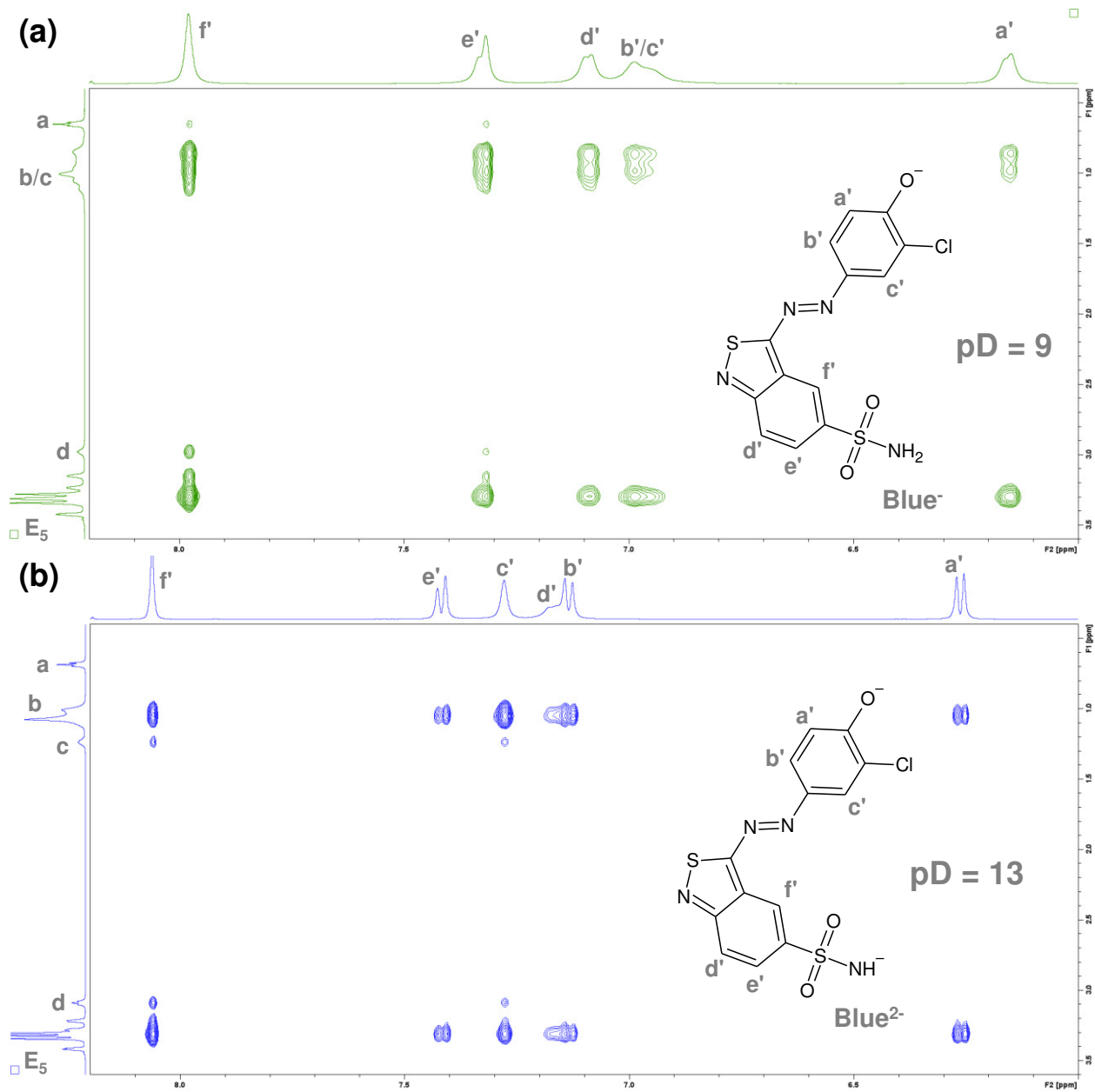


Figure S121: Section of NOESY spectra recorded from solutions containing Blue at a concentration of  $[Blue] = 12.5 \text{ mM}$  and  $hC_{12}hE_5$  at a concentration of  $[hC_{12}hE_5] = 25 \text{ mM}$ . An isotonic NaCl solution ( $I = 0.154 \text{ M}$ ) in  $D_2O$  served as the solvent. All measurements were performed at  $10 \text{ }^\circ\text{C}$ .

### 7.8.8. Self-aggregation of Blue and considerations on impurities

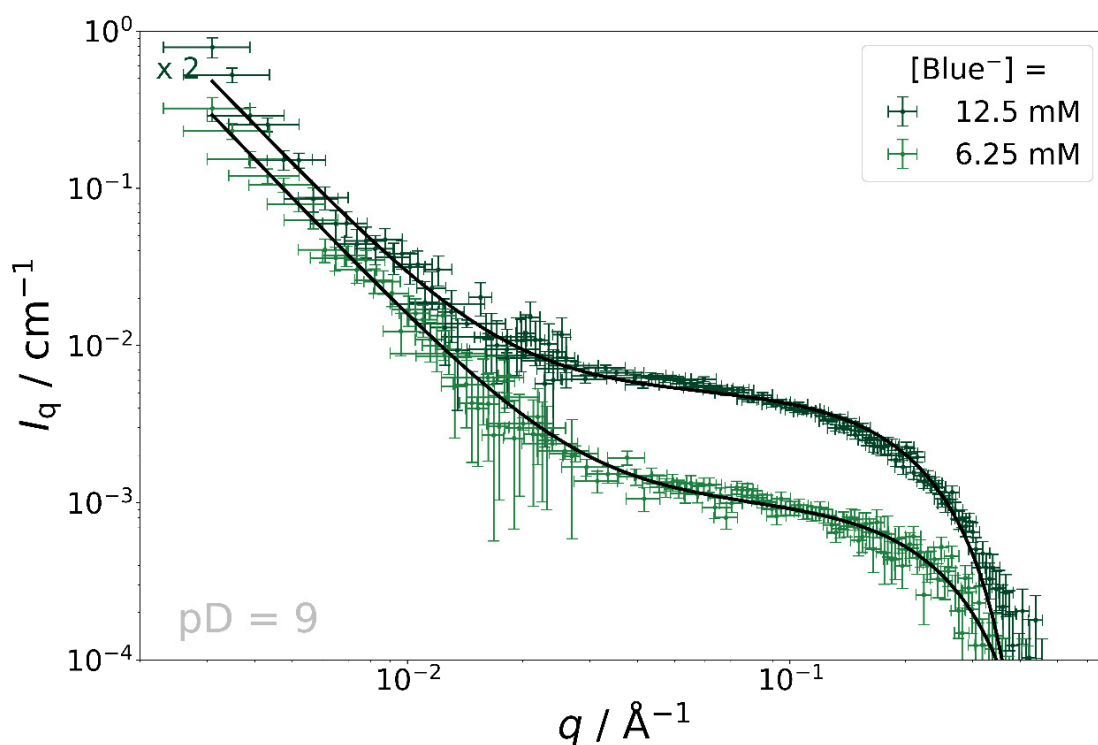


Figure SI22: SANS curves recorded from solutions containing Blue<sup>-</sup> at variable concentrations and at pD = 9. An isotonic NaCl solution ( $I = 0.154$  M) in D<sub>2</sub>O served as the solvent and measurements were performed at a sample temperature of 10 °C. Black lines show a fit with the form factor of spheres with a radius of either 9.0 Å ([Blue<sup>-</sup>] = 6.25 mM) or 10.5 Å ([Blue<sup>-</sup>] = 12.5 mM) that assemble into fractals with a characteristic dimension of either 42 Å ([Blue<sup>-</sup>] = 6.25 mM) or 68 Å ([Blue<sup>-</sup>] = 12.5 mM), a cut-off length for fractal correlations of 1500 Å, which was set due to the absence of a low- $q$  Guinier plateau and a fractal dimension of  $\approx 2.45$ .

Figure SI22 shows SANS curves from solutions containing only the azo dye Blue<sup>-</sup> at two different concentrations. The low- $q$  upturn of the scattered intensity signals the formation of large aggregates or fluctuations. The self-aggregation of Blue<sup>-</sup> in the absence of C<sub>12</sub>E<sub>5</sub> is furthermore confirmed by its NOESY spectrum (Figure SI23a), which displays cross peaks that implicate spatial proximity between protons of different molecules. Figure SI16 and Figure 10 in the main document show that the low- $q$  upturn in the scattering intensity, which is caused by Blue<sup>-</sup> self-assembly, vanishes in presence of C<sub>12</sub>E<sub>5</sub>. This means, that under the observed solution and concentration conditions, Blue<sup>-</sup> self-assemblies do not exist in the presence of C<sub>12</sub>E<sub>5</sub>.

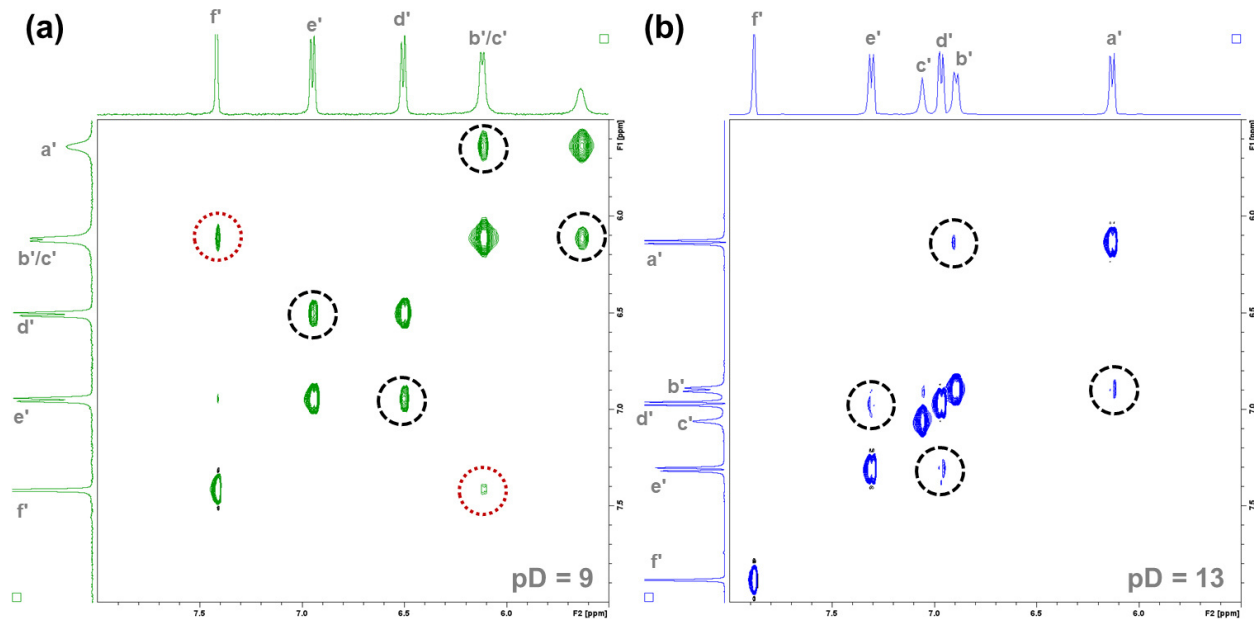


Figure SI23: NOESY spectra of solutions containing Blue at a concentration of  $[Blue] = 12.5 \text{ mM}$  in an isotonic solution of  $NaCl$  ( $I = 154 \text{ mM}$ ) in  $D_2O$  at (a)  $pD = 9$  or (b)  $pD = 13$ . Measurements were performed at a sample temperature of  $10 \text{ }^\circ\text{C}$ . The peak assignment is the same as in Figure SI20. Circles with black (dashed) outline highlight expected cross peaks due to the spatial proximity of protons within one molecule (intramolecular cross peaks). Circles with red (dotted) outline highlight cross peaks due to the spatial proximity of protons of different molecules (intermolecular cross peaks).

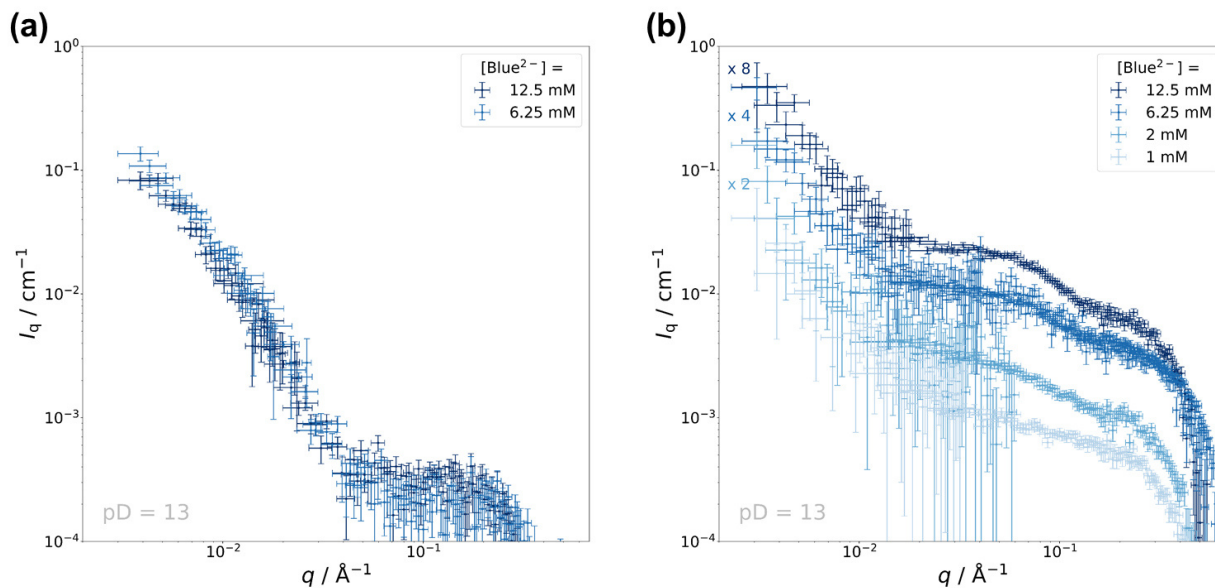


Figure SI24: (a) SANS curves of solutions containing Blue at different concentrations and at  $pD = 13$ . (b)  $C_{12}E_5$ -matched SANS curves containing Blue at different concentrations and  $mC_{12}mE_5$  at a concentration of  $[mC_{12}mE_5] = 25 \text{ mM}$  at  $pD = 13$ . An isotonic  $NaCl$  solution ( $I = 154 \text{ mM}$ ) in  $D_2O$  was used as a solvent in all cases and SANS curves were recorded at a sample temperature of  $10 \text{ }^\circ\text{C}$ . The low- $q$  upturn in  $I_q$  is attributed to impurities arising from  $Ca^{2+}$  contamination and the formation of finely dispersed, insoluble  $Ca(OD)_2$  salt.

Figure SI24 displays SANS curves of pure  $Blue^{2-}$  solutions and of  $C_{12}E_5$ -matched solutions containing  $Blue^{2-}$  at  $pD = 13$ . The low- $q$  ( $q < 0.02 \text{ } \text{\AA}^{-1}$ ) upturn of  $I_q$  does likely not result from Blue

self-aggregation, but could be a result of impurities in the sample, for instance finely dispersed  $\text{Ca}(\text{OD})_2$  salt due to contamination with  $\text{Ca}^{2+}$ . Several arguments supporting the absence of  $\text{Blue}^{2-}$  self-aggregation at  $\text{pD} = 13$  exist: (1) Electrostatic repulsion between two-fold negatively charged  $\text{Blue}^{2-}$  molecules may interfere with the formation of attractive  $\pi$ - $\pi$ - or hydrogen-bonding interactions between  $\text{Blue}^{2-}$  molecules. (2) The lowermost image in Figure SI20 shows the  $^1\text{H-NMR}$  spectrum of Blue at  $\text{pD} = 13$  in the absence of  $\text{C}_{12}\text{E}_5$  (black curve).  $^1\text{H-NMR}$  resonances are narrow, pointing either towards the absence of self-aggregation or towards the formation of highly symmetrical aggregates. (3) Figure SI23b displays the NOESY spectrum of a 12.5 mM solution of  $\text{Blue}^{2-}$  at  $\text{pD} = 13$ . Only cross peaks, which are expected from the chemical constitution of Blue are observed. Cross peaks that would point towards the spatial proximity of protons of different molecules are not present. For these reasons, the self-aggregation of  $\text{Blue}^{2-}$  is excluded. The low- $q$  upturn of  $I_q$  in SANS curves of pure Blue solutions with  $\text{pD} = 13$  and  $\text{C}_{12}\text{E}_5$ -matched solutions with  $\text{pD} = 13$  is therefore related to impurities. Such an impurity could be the contamination with  $\text{Ca}^{2+}$  ions. This contamination would solely change the ionic strength of the solvent for most samples, but result in the formation of insoluble  $\text{Ca}(\text{OD})_2$  at  $\text{pD} = 13$ , which is in accord with all observations. As stock solutions and the  $\text{DCl-}$  and  $\text{NaOD}$  solution used for  $\text{pD}$ -adjustment were filtered before  $\text{pD}$  adjustment, but SANS samples were not filtered after  $\text{pD}$ -adjustment, the formation of insoluble salts due to the high  $\text{pD}$  is therefore the most likely explanation of why scattering from impurities is solely observed at  $\text{pD} = 13$ . In full contrast SANS curves, the impurity-caused low- $q$  upturn of  $I_q$  is not apparent because of the high scattering intensity caused by  $\text{hC}_{12}\text{hE}_5$  scattering.

Given the above discussion, the evaluation of SANS curves emerging from samples with  $\text{pD} < 13$  considered, that molecularly dissolved small electrolyte salt does not influence the  $q$ -dependency of the scattering signal. For full contrast SANS curves from samples with  $\text{pD} = 13$ , the scattering contribution from small quantities of finely dispersed salt was considered to be insignificant compared to the strong scattering signal arising from  $\text{hC}_{12}\text{hE}_5$  and was therefore not considered. Only for  $\text{C}_{12}\text{E}_5$ -matched samples this contribution is significant due to low scattering intensities. Therefore, only the  $q$ -range within which the contribution of the impurity becomes negligible ( $q > 0.017 \text{ \AA}^{-2}$ ) was considered for these samples.

### 7.8.9. Comparison of parameters from fitting full contrast and C<sub>12</sub>E<sub>5</sub> contrast matched SANS curves

Table SI7 displays results from form factor fitting of SANS curves shown in the main document. The first column denotes the figure in the main document, where the corresponding fit is displayed. Applied form factor models and their combination with a structure factor are given in the table. Cross-section information from the best fit to full contrast data in the high- $q$  region ( $q > 0.045 \text{ \AA}^{-1}$ ) are displayed for comparison to results from fitting to C<sub>12</sub>E<sub>5</sub>-matched SANS curves. For fits to C<sub>12</sub>E<sub>5</sub>-matched SANS-curves,  $N$  corresponds to the number density of respective particles if the contrast, given by the scattering length density difference between particle and solvent ( $\Delta\eta$ ), equals  $\Delta\eta = 3.358 \cdot 10^{-6} \text{ \AA}^{-2}$ . If a core-shell structure was assumed for fits to C<sub>12</sub>E<sub>5</sub>-matched SANS curves, the contrast between solvent and shell was estimated to  $\Delta\eta = 3.358 \cdot 10^{-6} \text{ \AA}^{-2}$  and the contrast between the solvent and the core to  $\Delta\eta = 0$ . For fits to C<sub>12</sub>E<sub>5</sub>-matched data, no size distribution was assumed for any dimension. For fits to full contrast data at  $q > 0.045 \text{ \AA}^{-1}$ , a log-normal distribution of the core radius was assumed. Therefore,  $r_{\text{core}}$  is the mean core radius and SD its standard deviation calculated from the distribution. Ornstein-Zernike parameters obtained from fitting full contrast SANS curves with the model which resulted into the best fit according to Table 2 in the main document are given as well. If no error is displayed for a parameter, the value was fixed during fitting.

Table S17: Results from form factor fitting of SANS curves shown in the main document.

pD = 2											
C <sub>12</sub> E <sub>5</sub> -matched [mC <sub>12</sub> mE <sub>5</sub> ] = 25 mM			Full contrast [hC <sub>12</sub> hE <sub>5</sub> ] = 25 mM								
Model: $I(q)$ =	$N \cdot P_{\text{cylinder}}(q) \cdot C(q)$			$N \cdot P_{\text{core-linshell-cylinder}}(q)$ for $q > 0.045 \text{ \AA}^{-1}$			$N \cdot P_{\text{cap-core-shell-cylinder}}(q) \cdot C(q)$				
	Length $L$ / Å	Radius $R$ / Å	$N / 10^{16} \text{ cm}^{-3}$	$\kappa$	$\xi$ / Å	$\chi_{\text{red}}^2$	$r_{\text{core}}$ / Å	$SD(r_{\text{core}})$ / Å	$r_{\text{shell}}$ / Å	$\kappa$	$\xi$ / Å
[BlueH] = 1 mM											
Figure 9, dotted line	31.9 ± 0.8	3.0 ± 0.2	163 ± 22	17.1 (SANS)	201 (SANS)	3.5185					
Figure 9, dashed line	10.0 ± 34	5.7 ± 10	88 ± 6	41 ± 2	201 (SANS)	2.1851	12.7 ± 0.3	3.6 ± 0.2	14.4 ± 0.3	17.1 ± 0.1	201 ± 0.1
Figure 9, solid line	10.1 ± 300	5.8 ± 9	87 ± 5	48 ± 2	221 (SLS)	2.1513					
[BlueH] = 2 mM											
Figure 9, dotted line	93 ± 2	2.9 ± 0.2	40 ± 8	43.6 (SANS)	322 (SANS)	1.9923					
Figure 9, dashed line	54 ± 3	3.1 ± 0.2	59 ± 11	93 ± 6	322 (SANS)	1.6637	13.3 ± 0.3	3.7 ± 0.2	13.6 ± 0.3	43.6 ± 0.2	322 ± 1
Figure 9, solid line	60 ± 3	3.0 ± 0.2	55 ± 9	176 ± 11	483 (SLS)	1.5832					

pD = 9											
C <sub>12</sub> E <sub>5</sub> -matched [mC <sub>12</sub> mE <sub>5</sub> ] = 25 mM					Full contrast [hC <sub>12</sub> hE <sub>5</sub> ] = 25 mM						
Model: $I(q)$ =	$I_{q,Guinier}(q) + N \cdot P_{\text{core-shell-cylinder}}(q) \cdot C(q)$				$N \cdot P_{\text{core-linshell-cylinder}}(q)$ for $q > 0.045 \text{ \AA}^{-1}$				$N \cdot P_{\text{cap-core-shell-cylinder}}(q) \cdot C(q)$		
[Blue] = 1 mM	Length $L$ / $\text{\AA}$	$r_{\text{core}}$ / $\text{\AA}$	$r_{\text{shell}}$ / $\text{\AA}$	$\kappa$	$\xi$ / $\text{\AA}$	$X_{\text{red}}^2$	$r_{\text{core}}$ / $\text{\AA}$	$SD(r_{\text{core}})$ / $\text{\AA}$	$r_{\text{shell}}$ / $\text{\AA}$	$\kappa$	$\xi$ / $\text{\AA}$
Figure 10, solid line	66 (SANS)	7.4	21 ± 4	11.1 (SANS)	164 (SANS)	0.9000	12.5 ± 0.3	3.5 ± 0.2	11.2 ± 0.2	11.1 ± 0.1	164 ± 1
	$N / 10^{16} \text{ cm}^{-3}: 0.0014 \pm 0.0008$										
	$R_g$ from $I_{q,Guinier}(q)$ / $\text{\AA}: 6.0 \pm 0.2$										
[Blue] = 2 mM	Length $L$ / $\text{\AA}$	$r_{\text{core}}$ / $\text{\AA}$	$r_{\text{shell}}$ / $\text{\AA}$	$\kappa$	$\xi$ / $\text{\AA}$	$X_{\text{red}}^2$	$r_{\text{core}}$ / $\text{\AA}$	$SD(r_{\text{core}})$ / $\text{\AA}$	$r_{\text{shell}}$ / $\text{\AA}$	$\kappa$	$\xi$ / $\text{\AA}$
Figure 10, solid line	66 (SANS)	7.4	19 ± 2	12 (SANS)	174 (SANS)	1.4912	12.4 ± 0.3	3.5 ± 0.2	14.5 ± 0.3	12.0 ± 0.1	174 ± 1
	$N / 10^{16} \text{ cm}^{-3}: 0.006 \pm 0.002$										
	$R_g$ from $I_{q,Guinier}(q)$ / $\text{\AA}: 4.94 \pm 0.06$										
[Blue] = 6.25 mM	Length $L$ / $\text{\AA}$	$r_{\text{core}}$ / $\text{\AA}$	$r_{\text{shell}}$ / $\text{\AA}$	$\kappa$	$\xi$ / $\text{\AA}$	$X_{\text{red}}^2$	$r_{\text{core}}$ / $\text{\AA}$	$SD(r_{\text{core}})$ / $\text{\AA}$	$r_{\text{shell}}$ / $\text{\AA}$	$\kappa$	$\xi$ / $\text{\AA}$
Figure 10, solid line	40 (SANS)	7.9 ± 0.3	17.6 ± 0.2	7.1 (SANS)	97 (SANS)	3.2898	12.3 ± 0.3	3.4 ± 0.2	13.2 ± 0.3	7.1 ± 0.1	97 ± 1
	$N / 10^{16} \text{ cm}^{-3}: 0.0955 \pm 0.0004$										
	$R_g$ from $I_{q,Guinier}(q)$ / $\text{\AA}: 4.24 \pm 0.07$										
[Blue] = 12.5 mM	Length $L$ / $\text{\AA}$	$r_{\text{core}}$ / $\text{\AA}$	$r_{\text{shell}}$ / $\text{\AA}$	$\kappa$	$\xi$ / $\text{\AA}$	$X_{\text{red}}^2$	$r_{\text{core}}$ / $\text{\AA}$	$SD(r_{\text{core}})$ / $\text{\AA}$	$r_{\text{shell}}$ / $\text{\AA}$	$\kappa$	$\xi$ / $\text{\AA}$
Figure 10, solid line	40 (SANS)	6.9 ± 0.4	16.2 ± 0.3	2.7 (SANS)	52 (SANS)	2.9459	13.3 ± 0.2	2.91 ± 0.09	10.8 ± 0.3	2.7 ± 0.1	52 ± 1
	$N / 10^{16} \text{ cm}^{-3}: 0.191 \pm 0.0007$										
	$R_g$ from $I_{q,Guinier}(q)$ / $\text{\AA}: 6.5 \pm 0.2$										

pD = 13											
C <sub>12</sub> E <sub>5</sub> -matched [mC <sub>12</sub> mE <sub>5</sub> ] = 25 mM					Full contrast [hC <sub>12</sub> hE <sub>5</sub> ] = 25 mM						
Model: I(q) =	$I_{q,Guinier}(q) + N \cdot P_{\text{core-shell-cylinder}}(q) \cdot C(q)$				$N \cdot P_{\text{core-linshell-cylinder}}(q)$ for $q > 0.045 \text{ \AA}^{-1}$				$N \cdot P_{\text{cap-core-shell-cylinder}}(q) \cdot C(q)$		
[Blue <sup>2</sup> ] = 1 mM	Length L / Å	$r_{\text{core}} / \text{Å}$	$r_{\text{shell}} / \text{Å}$	$\kappa$	$\xi / \text{Å}$	$X_{\text{red}}^2$	$r_{\text{core}} / \text{Å}$	$SD(r_{\text{core}}) / \text{Å}$	$r_{\text{shell}} / \text{Å}$	$\kappa$	$\xi / \text{Å}$
Figure 11, solid line	40 (SANS)	13 ± 2	4.79 ± 1.7	5.9 (SANS)	87 (SANS)	1.3152	13.7 ± 0.2	3.3 ± 0.1	12.0 ± 0.3	5.9 ± 0.1	87 ± 1
	$R_g$	$N / 10^{16} \text{ cm}^{-3}: 0.08 \pm 0.02$ $R_g$ from $I_{q,Guinier}(q) / \text{Å}: 5.39$									
[Blue <sup>2</sup> ] = 2 mM	Length L / Å	$r_{\text{core}} / \text{Å}$	$r_{\text{shell}} / \text{Å}$	$\kappa$	$\xi / \text{Å}$	$X_{\text{red}}^2$	$r_{\text{core}} / \text{Å}$	$SD(r_{\text{core}}) / \text{Å}$	$r_{\text{shell}} / \text{Å}$	$\kappa$	$\xi / \text{Å}$
Figure 11, solid line	40 (SANS)	13.6 ± 0.7	4.79 ± 1.7	1.8 (SANS)	47 (SANS)	1.1606	14.5 ± 0.3	2.8 ± 0.2	10.1 ± 0.3	1.8 ± 0.1	47 ± 1
	$R_g$	$N / 10^{16} \text{ cm}^{-3}: 0.16 \pm 0.02$ $R_g$ from $I_{q,Guinier}(q) / \text{Å}: 5.39$									
Model: I(q) =	$I_{q,Guinier}(q) + N \cdot P_{\text{core-shell-sphere}}(q)$										
[Blue <sup>2</sup> ] = 6.25 mM	$R_g$	$r_{\text{core}} / \text{Å}$	$r_{\text{shell}} / \text{Å}$	$N / 10^{16} \text{ cm}^{-3}$	$X_{\text{red}}^2$	$r_{\text{core}} / \text{Å}$	$SD(r_{\text{core}}) / \text{Å}$	$r_{\text{shell}} / \text{Å}$	$\kappa$	$\xi / \text{Å}$	
Figure 11, solid line	5.39	21.1 ± 0.4	4.79 ± 1.7	0.13 ± 0.008	3.6223	16.9 ± 0.2	3.72 ± 0.07	11.7 ± 0.2	-	-	
[Blue <sup>2</sup> ] = 12.5 mM	$R_g$	$r_{\text{core}} / \text{Å}$	$r_{\text{shell}} / \text{Å}$	$N / 10^{16} \text{ cm}^{-3}$	$X_{\text{red}}^2$	$r_{\text{core}} / \text{Å}$	$SD(r_{\text{core}}) / \text{Å}$	$r_{\text{shell}} / \text{Å}$	$\kappa$	$\xi / \text{Å}$	
Figure 11, solid line	5.39	17.2 ± 0.3	4.79 ± 1.7	0.34 ± 0.02	1.8240	16.5 ± 0.2	3.55 ± 0.07	11.7 ± 0.2	-	-	



## 7.9 References

- (1) Klein, Ken. Shampoo Formulation: The Basics. *Cosmetics & Toiletries magazine* **2004**, 119 (5), 64–68.
- (2) Fiume, M. M.; Heldreth, B.; Bergfeld, W. F.; Belsito, D. V.; Hill, R. A.; Klaassen, C. D.; Liebler, D.; Marks, J. G.; Shank, R. C.; Slaga, T. J.; Snyder, P. W.; Andersen, F. A. Safety Assessment of Alkyl PEG Ethers as Used in Cosmetics. *Int J Toxicol* **2012**, 31 (5\_suppl), 169S-244S. <https://doi.org/10.1177/1091581812444141>.
- (3) Choi, F.; Zarate-Muñoz, S.; Acosta, E. J. Prediction of Cloud Point Curves of Alkyl Ethoxylates with the Hydrophilic–Lipophilic-Difference and Net-Average-Curvature (HLD-NAC) Framework. *Journal of Surfactants and Detergents* **2019**, 22 (5), 973–982. <https://doi.org/10.1002/jsde.12304>.
- (4) Liu, C.-L.; Nikas, Y. J.; Blankschtein, D. Novel Bioseparations Using Two-Phase Aqueous Micellar Systems. *Biotechnology and Bioengineering* **1996**, 52 (2), 185–192. [https://doi.org/10.1002/\(SICI\)1097-0290\(19961020\)52:2<185::AID-BIT1>3.0.CO;2-M](https://doi.org/10.1002/(SICI)1097-0290(19961020)52:2<185::AID-BIT1>3.0.CO;2-M).
- (5) Vicente, F. A.; Cardoso, I. S.; Sintra, T. E.; Lemus, J.; Marques, E. F.; Ventura, S. P. M.; Coutinho, J. A. P. Impact of Surface Active Ionic Liquids on the Cloud Points of Nonionic Surfactants and the Formation of Aqueous Micellar Two-Phase Systems. *J. Phys. Chem. B* **2017**, 121 (37), 8742–8755. <https://doi.org/10.1021/acs.jpcc.7b02972>.
- (6) Padia, F. N.; Yaseen, M.; Gore, B.; Rogers, S.; Bell, G.; Lu, J. R. Influence of Molecular Structure on the Size, Shape, and Nanostructure of Nonionic CnEm Surfactant Micelles. *J. Phys. Chem. B* **2014**, 118 (1), 179–188. <https://doi.org/10.1021/jp409808c>.
- (7) Zarate-Muñoz, S.; Troncoso, A. B.; Acosta, E. The Cloud Point of Alkyl Ethoxylates and Its Prediction with the Hydrophilic–Lipophilic Difference (HLD) Framework. *Langmuir* **2015**, 31 (44), 12000–12008. <https://doi.org/10.1021/acs.langmuir.5b03064>.
- (8) Berthod, A.; Tomer, S.; Dorsey, J. G. Polyoxyethylene Alkyl Ether Nonionic Surfactants: Physicochemical Properties and Use for Cholesterol Determination in Food. *Talanta* **2001**, 55 (1), 69–83. [https://doi.org/10.1016/S0039-9140\(01\)00395-2](https://doi.org/10.1016/S0039-9140(01)00395-2).
- (9) Lindman, B.; Carlsson, A.; Karlström, G.; Malmsten, M. Nonionic Polyethers and Surfactants - Some Anomalies in Temperature Dependence and in Interactions with Ionic Surfactants. *Advances in Colloid and Interface Science* **1990**, 32 (2), 183–203. [https://doi.org/10.1016/0001-8686\(90\)80018-U](https://doi.org/10.1016/0001-8686(90)80018-U).
- (10) Attwood, D. Light-Scattering Study of the Effect of Temperature on the Micellar Size and Shape of a Nonionic Detergent in Aqueous Solution. *J. Phys. Chem.* **1968**, 72 (1), 339–345. <https://doi.org/10.1021/j100847a066>.

- (11) Corti, M.; Degiorgio, V. Micellar Properties and Critical Fluctuations in Aqueous Solutions of Nonionic Amphiphiles. *J. Phys. Chem.* **1981**, *85* (10), 1442–1445. <https://doi.org/10.1021/j150610a033>.
- (12) Cebula, D. J.; Ottewill, R. H. Neutron Scattering Studies on Micelles of Dodecylhexaoxyethylene Glycol Monoether. *Colloid and Polymer Science* **1982**, *260* (12), 1118–1120. <https://doi.org/10.1007/BF01411231>.
- (13) Glatter, O.; Fritz, G.; Lindner, H.; Brunner-Popela, J.; Mittelbach, R.; Strey, R.; Egelhaaf, S. U. Nonionic Micelles near the Critical Point: Micellar Growth and Attractive Interaction. *Langmuir* **2000**, *16* (23), 8692–8701. <https://doi.org/10.1021/la000315s>.
- (14) Lindman, B.; Medronho, B.; Karlström, G. Clouding of Nonionic Surfactants. *Current Opinion in Colloid & Interface Science* **2016**, *22*, 23–29. <https://doi.org/10.1016/j.cocis.2016.01.005>.
- (15) Strey, R.; Glatter, O.; Schubert, K. -V.; Kaler, E. W. Small-angle Neutron Scattering of D<sub>2</sub>O–C<sub>12</sub>E<sub>5</sub> Mixtures and Microemulsions with N-octane: Direct Analysis by Fourier Transformation. *J. Chem. Phys.* **1996**, *105* (3), 1175–1188. <https://doi.org/10.1063/1.471960>.
- (16) Löf, D.; Tomšič, M.; Glatter, O.; Fritz-Popovski, G.; Schillén, K. Structural Characterization of Nonionic Mixed Micelles Formed by C<sub>12</sub>EO<sub>6</sub> Surfactant and P123 Triblock Copolymer. *J. Phys. Chem. B* **2009**, *113* (16), 5478–5486. <https://doi.org/10.1021/jp808442d>.
- (17) Al-Ghamdi, A. M.; Nasr-El-Din, H. A. Effect of Oilfield Chemicals on the Cloud Point of Nonionic Surfactants. *Colloids and Surfaces A: Physicochemical and Engineering Aspects* **1997**, *125* (1), 5–18. [https://doi.org/10.1016/S0927-7757\(96\)03860-5](https://doi.org/10.1016/S0927-7757(96)03860-5).
- (18) Sen, I. D.; Semwal, D.; Jayaram, R. V. Interaction of Imidazolium Based Ionic Liquids with Aqueous Triton X-100 Surfactant: Clouding, Fluorescence and NMR Studies. *Journal of Molecular Liquids* **2019**, *293*, 111481. <https://doi.org/10.1016/j.molliq.2019.111481>.
- (19) Tehrani-Bagha, A. R.; Holmberg, K. Solubilization of Hydrophobic Dyes in Surfactant Solutions. *Materials* **2013**, *6* (2), 580–608. <https://doi.org/10.3390/ma6020580>.
- (20) ASTM. ASTM D2024-09(2017): Standard Test Method for Cloud Point of Nonionic Surfactants. *Book of Standards* **2023**, *15.04*, 2. <https://doi.org/10.1520/D2024-09R17>.
- (21) Dewhurst, Charles. GRASP, 2023.
- (22) *Neutrons, X-Rays, and Light: Scattering Methods Applied to Soft Condensed Matter*, 1st ed.; Lindner, P., Zemb, T., Eds.; North-Holland delta series; Elsevier: Amsterdam ; Boston, 2002.
- (23) Breßler, I.; Kohlbrecher, J.; Thünemann, A. F. SASfit: A Tool for Small-Angle Scattering Data Analysis Using a Library of Analytical Expressions. *J Appl Cryst* **2015**, *48* (5), 1587–1598. <https://doi.org/10.1107/S1600576715016544>.

- (24) Gottlieb, H. E.; Kotlyar, V.; Nudelman, A. NMR Chemical Shifts of Common Laboratory Solvents as Trace Impurities. *J. Org. Chem.* **1997**, *62* (21), 7512–7515. <https://doi.org/10.1021/jo971176v>.
- (25) Yoshimura, S.; Shirai, S.; Einaga, Y. Light-Scattering Characterization of the Wormlike Micelles of Hexaoxyethylene Dodecyl C12E6 and Hexaoxyethylene Tetradecyl C14E6 Ethers in Dilute Aqueous Solution. *J. Phys. Chem. B* **2004**, *108* (40), 15477–15487. <https://doi.org/10.1021/jp0488214>.
- (26) Bulut, S.; Hamit, J.; Olsson, U.; Kato, T. On the Concentration-Induced Growth of Nonionic Wormlike Micelles. *Eur. Phys. J. E* **2008**, *27* (3), 261–273. <https://doi.org/10.1140/epje/i2008-10379-2>.
- (27) Einaga, Y. Wormlike Micelles of Polyoxyethylene Alkyl Ethers CiEj. *Polym J* **2009**, *41* (3), 157–173. <https://doi.org/10.1295/polymj.PJ2008244>.
- (28) Corti, M.; Minero, C.; Degiorgio, V. Cloud Point Transition in Nonionic Micellar Solutions. *J. Phys. Chem.* **1984**, *88* (2), 309–317. <https://doi.org/10.1021/j150646a029>.
- (29) Lindman, B.; Wennerstroem, H. Nonionic Micelles Grow with Increasing Temperature. *J. Phys. Chem.* **1991**, *95* (15), 6053–6054. <https://doi.org/10.1021/j100168a063>.
- (30) Bernheim-Groswasser, A.; Wachtel, E.; Talmon, Y. Micellar Growth, Network Formation, and Criticality in Aqueous Solutions of the Nonionic Surfactant C12E5. *Langmuir* **2000**, *16* (9), 4131–4140. <https://doi.org/10.1021/la991231q>.
- (31) Pedersen, J. S. Form Factors of Block Copolymer Micelles with Spherical, Ellipsoidal and Cylindrical Cores. *Journal of Applied Crystallography* **2000**, *33* (3–1), 637–640. <https://doi.org/10.1107/S0021889899012248>.
- (32) Kohlbrecher, Joachim. User Guide for the SASfit Software Package, 2023.
- (33) Castelletto, V.; Parras, P.; Hamley, I. W.; Bäverbäck, P.; Pedersen, J. S.; Panine, P. Wormlike Micelle Formation and Flow Alignment of a Pluronic Block Copolymer in Aqueous Solution. *Langmuir* **2007**, *23* (13), 6896–6902. <https://doi.org/10.1021/la700382y>.
- (34) Kotlarchyk, M.; Chen, S. Analysis of Small Angle Neutron Scattering Spectra from Polydisperse Interacting Colloids. *J. Chem. Phys.* **1983**, *79* (5), 2461–2469. <https://doi.org/10.1063/1.446055>.
- (35) Percus, J. K.; Yevick, G. J. Analysis of Classical Statistical Mechanics by Means of Collective Coordinates. *Phys. Rev.* **1958**, *110* (1), 1–13. <https://doi.org/10.1103/PhysRev.110.1>.
- (36) Baxter, R. J. Percus–Yevick Equation for Hard Spheres with Surface Adhesion. *The Journal of Chemical Physics* **2003**, *49* (6), 2770–2774. <https://doi.org/10.1063/1.1670482>.

- (37) Hayter, J. B.; Penfold, J. An Analytic Structure Factor for Macroion Solutions. *Molecular Physics* **1981**, *42* (1), 109–118. <https://doi.org/10.1080/00268978100100091>.
- (38) Berr, S. S. Solvent Isotope Effects on Alkyltrimethylammonium Bromide Micelles as a Function of Alkyl Chain Length. *J. Phys. Chem.* **1987**, *91* (18), 4760–4765. <https://doi.org/10.1021/j100302a024>.
- (39) Eriksson, J. C.; Gillberg, G. NMR-Studies of the Solubilisation of Aromatic Compounds in Cetyltrimethylammonium Bromide Solution II. *Acta Chem. Scand.* **1966**, *20* (8), 2019–2027. <https://doi.org/10.3891/acta.chem.scand.20-2019>.
- (40) Christenson, H.; Friberg, S. E. Spectroscopic Investigation of the Mutual Interactions between Nonionic Surfactant, Hydrocarbon, and Water. *Journal of Colloid and Interface Science* **1980**, *75* (1), 276–285. [https://doi.org/10.1016/0021-9797\(80\)90369-0](https://doi.org/10.1016/0021-9797(80)90369-0).
- (41) Shikata, T.; Hirata, H.; Kotaka, T. Micelle Formation of Detergent Molecules in Aqueous Media. 2. Role of Free Salicylate Ions on Viscoelastic Properties of Aqueous Cetyltrimethylammonium Bromide-Sodium Salicylate Solutions. *Langmuir* **1988**, *4* (2), 354–359. <https://doi.org/10.1021/la00080a019>.
- (42) Guo, L. N.; Arnaud, I.; Petit-Ramel, M.; Gauthier, R.; Monnet, C.; LePerchec, P.; Chevalier, Y. Solution Behavior of Dye-Surfactant Associations. *Journal of Colloid and Interface Science* **1994**, *163* (2), 334–346. <https://doi.org/10.1006/jcis.1994.1112>.
- (43) Onoda-Yamamuro, N.; Yamamuro, O.; Tanaka, N.; Nomura, H. NMR and Neutron Scattering Studies on Spherical and Rod-like Micelles of Dodecyltrimethylammonium Bromide in Aqueous Sodium Salicylate Solutions. *Journal of Molecular Liquids* **2005**, *117* (1), 139–145. <https://doi.org/10.1016/j.molliq.2004.08.009>.
- (44) Podo, Franca.; Ray, Ashoka.; Nemethy, George. Structure and Hydration of Nonionic Detergent Micelles. High Resolution Nuclear Magnetic Resonance Study. *J. Am. Chem. Soc.* **1973**, *95* (19), 6164–6171. <https://doi.org/10.1021/ja00800a003>.
- (45) Burrows, H. D.; Knaapila, M.; Monkman, A. P.; Tapia, M. J.; Fonseca, S. M.; Ramos, M. L.; Pyckhout-Hintzen, W.; Pradhan, S.; Scherf, U. Structural Studies on Cationic Poly[9,9-Bis[6-(N,N,N-Trimethylammonium)Alkyl]Fluorene-Co-1,4-Phenylene Iodides in Aqueous Solutions in the Presence of the Non-Ionic Surfactant Pentaethyleneglycol Monododecyl Ether (C12E5). *J. Phys.: Condens. Matter* **2008**, *20* (10), 104210. <https://doi.org/10.1088/0953-8984/20/10/104210>.
- (46) Furó, I. NMR Spectroscopy of Micelles and Related Systems. *Journal of Molecular Liquids* **2005**, *117* (1), 117–137. <https://doi.org/10.1016/j.molliq.2004.08.010>.

- (47) Patist, A.; Oh, S. G.; Leung, R.; Shah, D. O. Kinetics of Micellization: Its Significance to Technological Processes. *Colloids and Surfaces A: Physicochemical and Engineering Aspects* **2001**, *176* (1), 3–16. [https://doi.org/10.1016/S0927-7757\(00\)00610-5](https://doi.org/10.1016/S0927-7757(00)00610-5).
- (48) Claridge, T. D. W. Correlations through Space: The Nuclear Overhauser Effect. In *High-Resolution NMR Techniques in Organic Chemistry*; Tetrahedron Organic Chemistry Series; Elsevier, 2009; Vol. 27, pp 247–302. [https://doi.org/10.1016/S1460-1567\(08\)10008-3](https://doi.org/10.1016/S1460-1567(08)10008-3).
- (49) Lambert, J. B. *Spektroskopie: Strukturaufklärung in der Organischen Chemie*; Pearson, Higher Education, 2012.
- (50) Tanford, Charles. *The Hydrophobic Effect: Formation of Micelles and Biological Membranes*, 1st ed.; John Wiley & Sons, Inc: New York, London, Sydney, Toronto, 1973.
- (51) Parekh, P.; Yerramilli, Usha R.; Bahadur, P. Cloud Point and Thermodynamic Parameters of a Non-Ionic Surfactant Heptaoxyethylene Dodecyl Ether (C12E7) in Presence of Various Organic and Inorganic Additives. *Indian Journal of Chemistry* **2013**, *52A*, 1284–1290.
- (52) Intermolecular and Surface Forces. In *Intermolecular and Surface Forces (Third Edition)*; Israelachvili, J. N., Ed.; Academic Press: Boston, 2011; p iii. <https://doi.org/10.1016/B978-0-12-391927-4.10024-6>.
- (53) Israelachvili, J. N.; Mitchell, D. J.; Ninham, B. W. Theory of Self-Assembly of Hydrocarbon Amphiphiles into Micelles and Bilayers. *J. Chem. Soc., Faraday Trans. 2* **1976**, *72* (0), 1525–1568. <https://doi.org/10.1039/F29767201525>.
- (54) *Self-Assembly: From Surfactants to Nanoparticles*, First edition.; Nagarajan, R., Ed.; Wiley series on surface and interfacial chemistry; Wiley: Hoboken, NJ, 2019.
- (55) Weiss, A.-V.; Koch, M.; Schneider, M. Combining Cryo-TEM and Energy-Filtered TEM for Imaging Organic Core-Shell Nanoparticles and Defining the Polymer Distribution. *International Journal of Pharmaceutics* **2019**, *570*, 118650. <https://doi.org/10.1016/j.ijpharm.2019.118650>.
- (56) Atkins, P. W.; De Paula, J. *Atkins' Physical Chemistry*, 10th ed.; Oxford University Press: Oxford ; New York, 2014.
- (57) Schärftl, W. *Light Scattering from Polymer Solutions and Nanoparticle Dispersions*; Springer Laboratory; Springer Berlin Heidelberg: Berlin, Heidelberg, 2007. <https://doi.org/10.1007/978-3-540-71951-9>.
- (58) Kita, R.; Kubota, K.; Dobashi, T. Static and Dynamic Light Scattering of a Critical Polydisperse Polymer Solution. *Phys. Rev. E* **1998**, *58* (1), 793–800. <https://doi.org/10.1103/PhysRevE.58.793>.

- (59) Frisken, B. J. Revisiting the Method of Cumulants for the Analysis of Dynamic Light-Scattering Data. *Appl. Opt.* **2001**, *40* (24), 4087–4091. <https://doi.org/10.1364/AO.40.004087>.
- (60) Provencher, S. W. Inverse Problems in Polymer Characterization: Direct Analysis of Polydispersity with Photon Correlation Spectroscopy. *Die Makromolekulare Chemie* **1979**, *180* (1), 201–209. <https://doi.org/10.1002/macp.1979.021800119>.
- (61) Scotti, A.; Liu, W.; Hyatt, J. S.; Herman, E. S.; Choi, H. S.; Kim, J. W.; Lyon, L. A.; Gasser, U.; Fernandez-Nieves, A. The CONTIN Algorithm and Its Application to Determine the Size Distribution of Microgel Suspensions. *J. Chem. Phys.* **2015**, *142* (23), 234905. <https://doi.org/10.1063/1.4921686>.
- (62) Burchard, W.; Schmidt, M.; Stockmayer, W. H. Influence of Hydrodynamic Preaveraging on Quasi-Elastic Scattering from Flexible Linear and Star-Branched Macromolecules. *Macromolecules* **1980**, *13* (3), 580–587. <https://doi.org/10.1021/ma60075a020>.
- (63) Burchard, W.; Schmidt, M.; Stockmayer, W. H. Information on Polydispersity and Branching from Combined Quasi-Elastic and Intergrated Scattering. *Macromolecules* **1980**, *13* (5), 1265–1272. <https://doi.org/10.1021/ma60077a045>.
- (64) Glatter, O.; Strey, R.; Schubert, K.-V.; Kaler, E. W. III. Experimental Techniques: Small Angle Scattering Applied to Microemulsions. *Berichte der Bunsengesellschaft für physikalische Chemie* **1996**, *100* (3), 323–335. <https://doi.org/10.1002/bbpc.19961000319>.
- (65) Jerke, G.; Pedersen, J. S.; Egelhaaf, S. U.; Schurtenberger, P. Flexibility of Charged and Uncharged Polymer-like Micelles. *Langmuir* **1998**, *14* (21), 6013–6024. <https://doi.org/10.1021/la980390r>.
- (66) Creatto, E. J.; Okasaki, F. B.; Cardoso, M. B.; Sabadini, E. Wormlike Micelles of CTAB with Phenols and with the Corresponding Phenolate Derivatives - When Hydrophobicity and Charge Drive the Coacervation. *Journal of Colloid and Interface Science* **2022**, *627*, 355–366. <https://doi.org/10.1016/j.jcis.2022.07.044>.

## Chapter 8

### List of publications

#### This thesis is based on the following publications:

Müller, Wenke; Schweins, Ralf; Nöcker, Bernd; Egold, Hans; Huber, Klaus. Comparative Study of the Self-Assembly Behaviour of 3-Chloro-4-Hydroxy-Phenylazo Dyes. *Soft Matter* **2023**, *19* (24), 4579–4587. <https://doi.org/10.1039/D3SM00500C>.

Müller, Wenke; Schweins, Ralf; Nöcker, Bernd; Kohlbrecher, Joachim; Smales, Glen J.; Huber, Klaus. Comparative Study of the Co-Assembly Behaviour of 3-Chloro-4 Hydroxy-Phenylazo Dyes with DTAB. *Soft Matter* **2023**, *19* (24), 4588–4598. <https://doi.org/10.1039/D3SM00501A>.

Müller, Wenke; Schweins, Ralf; Nöcker, Bernd; Egold, Hans; Hannappel, Yvonne; Huber, Klaus. SANS contrast matching for the unambiguous localization of anionic dye in cationic surfactant micelles. Accepted with revisions by the journal *Nanoscale Advances* (Royal Society of Chemistry). Resubmitted version, 28.08.2023.

#### Other publications by the author:

Carl, Nico; Müller, Wenke; Schweins, Ralf; Huber, Klaus. Controlling Self-Assembly with Light and Temperature. *Langmuir* **2020**, *36* (1), 223–231. <https://doi.org/10.1021/acs.langmuir.9b03040>.

Bressel, Katharina; Müller, Wenke; Leser, Martin E.; Reich, Oliver; Hass, Roland; Wooster, Tim J. Depletion-Induced Flocculation of Concentrated Emulsions Probed by Photon Density Wave Spectroscopy. *Langmuir* **2020**, *36* (13), 3504-3513. <https://doi.org/10.1021/acs.langmuir.9b03642>.

## Chapter 9

### List of conference contributions

#### Oral presentations

- Müller, Wenke; Schweins, Ralf; Nöcker, Bernd; Huber, Klaus. Comprendre la coloration des cheveux grâce aux neutrons. *50 years of neutrons 2022* (Grenoble, France)
- Müller, Wenke; Schweins, Ralf; Nöcker, Bernd; Huber, Klaus. Localization of dye molecules in surfactant assemblies via SANS contrast variation. *SAS2022 Conference 2022* (Campinas, Brazil)
- Müller, Wenke; Schweins, Ralf; Nöcker, Bernd; Huber, Klaus. Localization of dye molecules in surfactant assemblies via SANS contrast variation. *3rd Joint ESS ILL User Meeting 2022* (Lund, Sweden)

#### Poster presentations

- Müller, Wenke; Schweins, Ralf; Nöcker, Bernd; Huber, Klaus. Investigation of dye-surfactant-mixtures in solution. *ESRF User Meeting 2021* (Grenoble, France – online)
- Müller, Wenke; Schweins, Ralf; Nöcker, Bernd; Huber, Klaus. Where is a direct dye located in a micellar solution? *ECIS Conference 2021* (Athens, Greece - online)
- Müller, Wenke; Schweins, Ralf; Nöcker, Bernd; Huber, Klaus. SANS contrast variation for the localization of anionic dyes in DTAB-micelles. *French-Swiss Meeting: SANS for Soft Matter 2022* (Strasbourg, France)
- Müller, Wenke; Schweins, Ralf; Nöcker, Bernd; Huber, Klaus. SANS contrast variation for the localization of anionic dyes in DTAB-micelles. *Symposium "50 years of D11" 2022* (Grenoble, France)
- Müller, Wenke; Schweins, Ralf; Nöcker, Bernd; Huber, Klaus. SANS contrast variation for the localization of anionic dyes in DTAB-micelles. *European conference on Neutron scattering 2023* (Munich, Germany)



